FATIGUE LIFE DETERMINATION OF A DAMAGE-TOLERANT COMPOSITE AIRFRAME

A Dissertation by

Waruna Prasanna Seneviratne

MS, Wichita State University, 2000

BS, Wichita State University, 1998

Submitted to the Department of Aerospace Engineering
and the faculty of the Graduate School of
Wichita State University
in partial fulfillment of
the requirements for the degree of
Doctor of Philosophy

December 2008

FATIGUE LIFE DETERMINATION OF A DAMAGE-TOLERANT COMPOSITE AIRFRAME

The following faculty have examined the final copy of this dissertation for form and content, and recommend that it be accepted impartial fulfillment of the requirement for the degree of Doctor of Philosophy with a major in Aerospace Engineering.

_____
John S. Tomblin, Committee Chair

_____
Larry Ilcewicz, Committee Member

_____
Charles Yang, Committee Member

_____
K. Suresh Raju, Committee Member

_____
Bob Minaie, Committee Member

Accepted for the College of Engineering

_____
Zulma Toro-Ramos, Dean

Accepted for the Graduate School

_____
J. David McDonald, Associate Provost for Research and Dean of the Graduate School

DEDICATION

To my beloved parents, wife, and kids–Natasha and Dimitri.

Predicting the future is complicated but examining the path ahead based on what was learned from the past is not.

ACKNOWLEDGMENTS

I would like to thank my mentor, Dr. John Tomblin, for his continued support that made this research possible, and for his valuable guidance and encouragement throughout the program. I also would like to thank my dissertation committee members for agreeing to be part of this research effort and for their valuable suggestions. This research program was sponsored by the William J. Hughes Technical Center of the Federal Aviation Administration (FAA) and the National Institute for Aviation Research (NIAR) at Wichita State University (WSU). The technical guidance and support of Dr. Larry Ilcewicz, Peter Shyprykevich (retired), and Curtis Davies of FAA were instrumental in keeping this research effort closer to the real world and thus more meaningful and practical.

This research would not have been as exciting and insightful without the support of Composites, Structures, and Full-Scale Structural Testing laboratories of NIAR. I would like thank Govind Ramakrishna Pillai and Jason Yeoh for coordinating experiments and Upul Palliyaguru for his programming support. I would also thank Kristie Bixby of Academic Affairs and Research at WSU for her editorial assistance. The enthusiasm and constructive criticism of the regulatory bodies (FAA, European Aviation Safety Agency, and Transport Canada), industry, and voluntary organizations such as the Composite Materials Handbook (CMH-17) committee were extremely encouraging and insightful.

I would also like to thank Hawker Beechcraft of Wichita, Kansas, for providing information that was very helpful during full-scale validations of the Beechcraft Starship forward wings, Cessna Aircraft of Wichita, Kansas, and Toray Composites (America), Inc., Tacoma, Washington, for providing material support during specimen fabrication, and Liberty Aerospace of Melbourne, Florida, for sharing some of their test data.

ABSTRACT

The methodology proposed in this research extends the current full-scale test approach based on the life factor and the load enhancement factor, and provides information necessary to define inspection intervals for composite structures by studying the effects of extremely improbable, high-energy impact damage. This methodology further extend the current practice during damage-tolerance certification to focus on the most critical damage locations of the structure and interpret the structural and loads details into the most representative repeated load testing in element level to gain information on the residual strength, fatigue sensitivity, inspection methods and inspection intervals during full-scale test substantiation. A reliability approach to determine the inspection intervals to mitigate risks of unexpected failure during the damage tolerance phase, especially with large impact damages, was discussed. This methodology was validated with several full-scale test examples of the Beechcraft Starship forward wings with large impact damages on the front and aft spars.

Procedures to generate reliable and economical scatter and load-enhancement factors necessary for a particular structural test by selecting the design details representing the critical areas of the structure is outlined with several examples and case studies. The effects of laminate stacking sequence, test environment, stress ratios, and several design features such as sandwich and bonded joints on the static-strength and fatigue-life shape parameters are discussed with detailed examples. Furthermore, several analytical techniques for obtaining these shape parameters are discussed with examples. Finally, the application of load enhancement factors and life factors for a full-scale test spectrum without adversely affecting the fatigue life and the damage mechanism of the composite structure is discussed.

A methodology synthesizing the life factor, load enhancement factor, and damage in composites is proposed to determine the fatigue life of a damage-tolerant composite airframe. This methodology narrows the variability of different aspects of the damaged structure to determine the remaining fatigue life of the structure. In order to prevent unintentional failure of a damaged article during DaDT testing, especially when investigating extremely improbable high-energy impact threats that reduce the residual strength of a composite structure to limit load, rigorous inspection intervals are required. The probability of failure of the damaged structure with the enhanced spectrum loads can be evaluated using the proposed cumulative fatigue unreliability model, which was validated through a full-scale test demonstration of a damaged article at the critical load path. Information from this model can be used also to allot economical and reliable inspection intervals during service based on a target reliability and a critical damage threshold.

Full-scale DaDT test conducted with a visual impact damage on the aft spar (secondary load path) using the improved LEFs based on the design details of Starship forward wing structure demonstrated the repeated life requirements according the proposed load-life-damage hybrid approach, and the post-DaDT residual strength requirements. The forward-wing DaDT test article with a large damage on the front spar (primary load path) demonstrated the capability of the cumulative fatigue unreliability model to predict the damage growth in terms of reliability and the capability of the model to determine the inspection levels. Although it is not a one-to-one correlation for the damage propagation or its size, the cumulative fatigue unreliability model highlighted load segments that resulted in gradual progression of local damage, such as possible matrix cracks, and the global impact of high loads that resulted in evident damage growth.

PREFACE

Over the past 25 years, the use of advanced composite materials in aircraft primary structures has increased significantly. In 1994, with the Advanced General Aviation Transport Experiments (AGATE) program, the National Aeronautics and Space Administration and the Federal Aviation Administration revitalized the use of composites in general and commercial aviation. Driven by the demand for fuel-efficient, light-weight, and high-stiffness structures that have fatigue durability and corrosion resistance, modern large commercial aircraft are designed with more than 50 percent composite materials. Although there are key differences between metal and composite damage mechanics and durability concerns, the certification philosophy for composites must meet structural integrity, safety, and durability requirements. Despite the many advantages, composite structural certification becomes challenging due to the lack of experience in large-scale structures, complex interactive failure mechanisms, sensitivity to temperature and moisture, and scatter in the data, especially in fatigue. The overall objective of this research was to provide guidance into structural substantiation of composite airframe structures through an efficient approach that weighs both the economic aspects of certification and the timeframe required for testing, while ensuring safety.

The main goal in this work was to develop a probabilistic approach synthesizing the life factor, load enhancement factor, and damage in composites to determine the fatigue life of a damage-tolerant aircraft. This robust approach, which can be tailored to a particular structural application, allows for the investigation of extremely improbably damage scenarios that define the critical damage threshold of composite structures during damage tolerance certification.

TABLE OF CONTENTS

TABLE OF CONTENTS (continued)

TABLE OF CONTENTS (continued)

TABLE OF CONTENTS (continued)

LIST OF TABLES

LIST OF TABLES (continued)

LIST OF TABLES (continued)

LIST OF FIGURES

LIST OF FIGURES (continued)

LIST OF FIGURES (continued)

LIST OF FIGURES (continued)

LIST OF FIGURES (continued)

LIST OF FIGURES (continued)

LIST OF FIGURES (continued)

LIST OF ABBREVIATIONS / NOMENCLATURE

5HS	5-harness satin weave fabric
8HS	8-harness satin weave fabric
A–Basis	95% lower confidence limit on first population percentile
ASTM	American Society for Testing and Materials
B–Basis	95% lower confidence limit on tenth population percentile
BVID	barely visible impact damage
CAI	Compression after impact
CF	Conversion factor
CTD	Cold temperature (-65°F) dry
CV	Coefficient of variation
DLL	Designed limit load
DLT	Designed lifetime
DNC	Double notched compression
DOT	Department of Transportation (United States)
DTH	Digital tap hammer
DUL	Designed ultimate load
ETW	Elevated-temperature (180°F) wet (moisture conditioned at 85% RH and 145 °F)
FAA	Federal Aviation Administration (United State)
FWS	Forward wing station
LEF	Load enhancement factor
LID	Large impact damage
LLRS	Linear-loss of residual strength

MLE	Maximum-likelihood estimation
MLSP	Modal fatigue-life shape parameter
MSSP	Modal static-strength shape parameter
NDI	Nondestructive inspections
OH	Open hole
OHC	Open-hole compression
OHT	Open-hole tension
PFS	Picture-frame shear
POF	Probability of failure
PW	Plain weave fabric
RRX	Rank regression in X
RTA	Room temperature ambient
RTW	Room temperature wet (moisture conditioned at 85% RH and 145 °F)
SLS	Single-lap shear
SMT	Shear-moment-torque loads
STDEV	Standard deviation
TAI	Tension after impact
UNI	Unidirectional tape
VID	Visible impact damage
VNRS	V-notched rail shear

LIST OF SYMBOLS

α	Weibull shape parameter
α_R	Modal static strength shape parameter
α_L	Modal fatigue life shape parameter
β	Weibull scale parameter
δ	Static-strength reduction factor
γ	degree of confidence
Γ	Gamma distribution
$\chi^2_\gamma(2n)$	Chi-square distribution with $2n$ degrees of freedom at γ level confidence
N	Full-scale test duration
N_F	Life factor
P_f	Probability of failure (POF)

CHAPTER 1

INTRODUCTION

In the early 1970s, composite materials were introduced to airframe structures to increase the performance and life of the airframe. In 1977, the National Aeronautics and Space Administration (NASA) Advanced Composite Structures Program introduced the use of composites in primary structures in commercial aircraft, i.e., the Boeing 737 horizontal stabilizer [1]. In 1994, the Advanced General Aviation Transport Experiments (AGATE) consortium, led by NASA and supported by the Federal Aviation Administration (FAA), industry, and academia, revitalized composite material product development in general aviation, thereby cost-effective composite airframe structures. Modern improved composite materials and matured processes have encouraged commercial aircraft companies to increase the use of composites in primary and secondary structures. Driven by the demand for fuel-efficient, light-weight, and high-stiffness structures that have fatigue durability and corrosion resistance, the Boeing 787 Dreamliner is designed with more than 50 percent of composite structures, marking a striking milestone in composite usage in commercial aviation. Meanwhile, the Airbus A350 commercial airplane is being designed with a similar percentage of composite materials in its structure. Figure 1 shows the use of composites in several commercial aircraft applications.

Although there are key differences between metal and composite damage mechanics and durability concerns, the certification philosophy for composites must meet structural integrity, safety, and durability requirements. Over the years, composite and hybrid structural certification programs have adopted methodologies utilized for metal structures that are based on several decades of experience in full-scale structural certification and service. Despite the advantages, such as high specific weight, tailorability, and fatigue resistance, composite structural

certification becomes challenging due to the lack of experience with large-scale structures, complex interactive failure mechanisms, sensitivity to temperature and moisture, and scatter in the data, especially relative to fatigue.

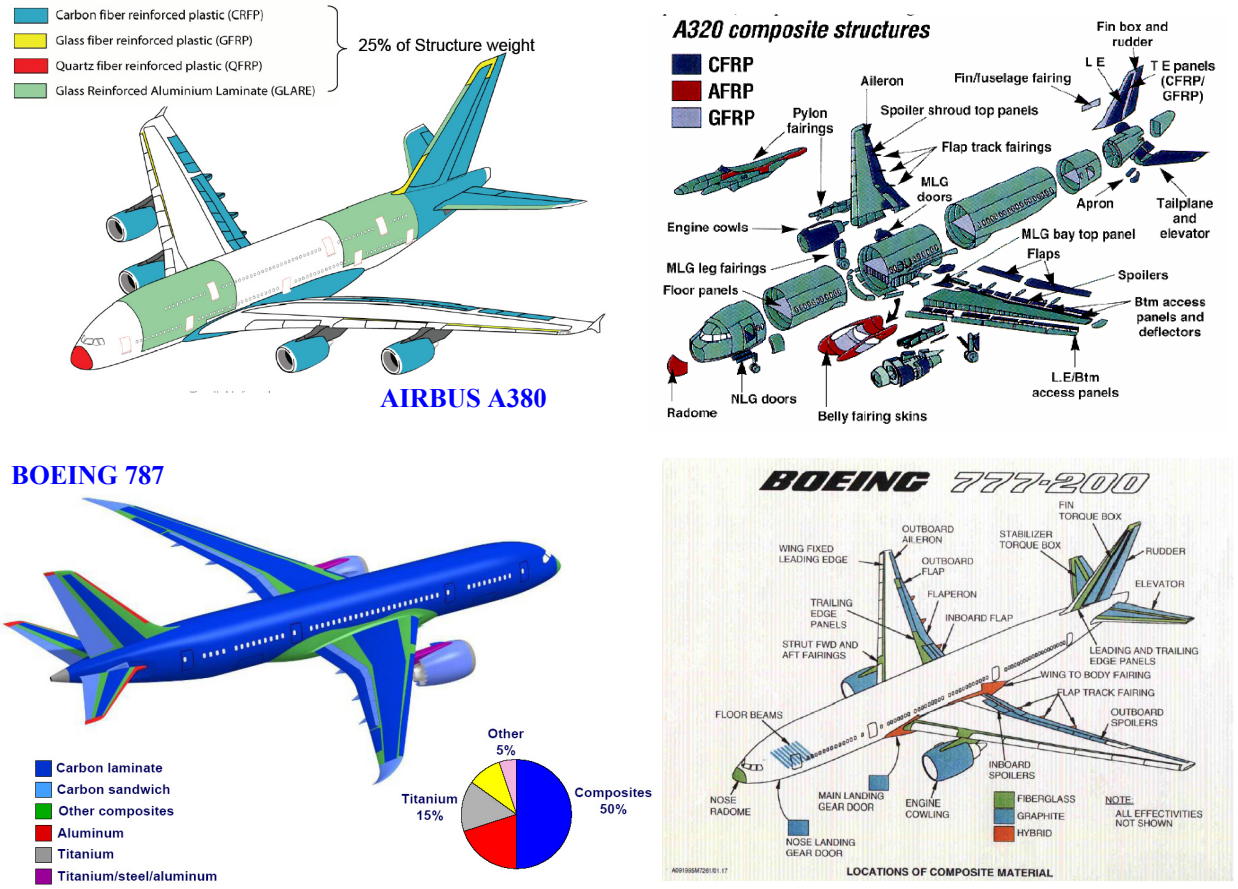

Figure 1. Composite materials applications in commercial aircraft.

Most current fatigue life-assessment methodologies for advanced composite structures rely on empirical S-N data in the lower levels of the building blocks of testing. Variation of material characteristics for different fiber-resin systems, layup configurations, environments, loading conditions, etc. often make the analysis and testing of composites challenging. Anisotropic heterogeneous characteristics and change in failure modes over the fatigue life as well as multiple failure mechanisms that interact with each other make it challenging to predict damage growth in composite structures. Consequently, most of the damage mechanisms and

wearout approaches discussed in the literature review section also depend on empirical data for refinement or calibration. Some approaches only discuss failure progression under certain loading configurations and often specific to a material system. Fatigue-life-assessment methodologies that are based on empirical data can be separated into two categories:

1. reliability or scatter analysis
2. curve-fit based on flaw growth

Both approaches require a considerable amount of empirical data. However, the first approach was extended to several programs through the concept of shared databases and in terms of general scatter of composite data in contrast to metal data. The major limitation in the second approach is that it is often specific to a certain material system, a loading configuration, and a failure mechanism. As part of the F/A-18 certification, a probabilistic methodology was developed to certify composite structures with the same level of confidence as metallic structures [2]. This methodology was formulated to account for the uncertainties of applied loads as well as the scatter in static strength and fatigue life related to composite structures. Over the years, several composite structural certification programs employed this certification methodology, which was developed for materials and test methods that were considered current at the time. Since then, materials and process techniques as well as test methods for evaluating composites have evolved. Consequently, test data often display significantly less scatter with high reliability. Thus, the probabilistic approach employed by Whitehead et al. [2] can be reevaluated for newer material forms and to represent structural details of current aircraft structures to obtain improved life and load-enhancement factors [3].

1.1. History of Damage-Tolerance Certification for Composite Structures

Damage-tolerance methodologies for metallic airframes, both military and commercial, have been implemented for certification since the 1970s in terms of crack growth. Although the fatigue life of composites is generally flat, the impact damage sensitivity, even at static loading, is a major concern. Thus, the ability of the structure to resist damage (damage resistance) and to perform with the presence of damage (damage tolerance) has been investigated in detail. Several certification approaches have been developed in terms of damage threat or probability of occurrence [4] as an extended methodology to the approach employed by Whitehead et al. [2]. In order to support Navy certification efforts in predicting the static strength capability of full-scale composite structures, a semi-empirical stiffness reduction model was developed by Horton and Whitehead [5] and assumed that the impact damage acted as a slit after initial failure and arrested at the nearest stiffeners causing a stress (strain) concentration at these stiffeners and adjacent bays. Using this approach, experimental results on several different material systems, impact locations, structural geometries, and energy levels show that the majority of the data points lies within ±10 percent of the predictive strain. It was recognized that several parameters influence the post-impact structural response. A detailed study conducted by Rapoff et al. [6] on several coupon, element, and full-scale composites with impact damages shows that simple test coupons can accurately represent mid-bay impact damage resistance and damage tolerance of a complex composite structure. This study also shows that the static scatter generally observed in composites is greatly reduced in coupon-level impact-damaged specimens subjected to in-plane loading, while fatigue-life scatter is similar to that for bolted composites. A fatigue study by Curtis et al. [7] shows that impact damage grows inconsistently under cyclic loading.

Current regulations require airframes to demonstrate adequate static strength, fatigue life, and damage-tolerance capability by testing and/or analysis with a high degree of confidence. These requirements are intended to account for uncertainties in usage and scatter exhibited by materials. The primary means of structural substantiation for most aircraft certification programs is by analysis. It is expected that the analysis will be supported by appropriate test evidence.

In order to develop a certification methodology for composite structures that has the same level of reliability as observed in metal certification approaches, accounting for the inherent difference between metal and composites, the FAA and U.S. Navy developed a certification approach for bolted composite structures [2,8] as part of the F/A-18 certification (Figure 2). This methodology is referred to as NAVY, or the load-life combined approach, throughout this report.

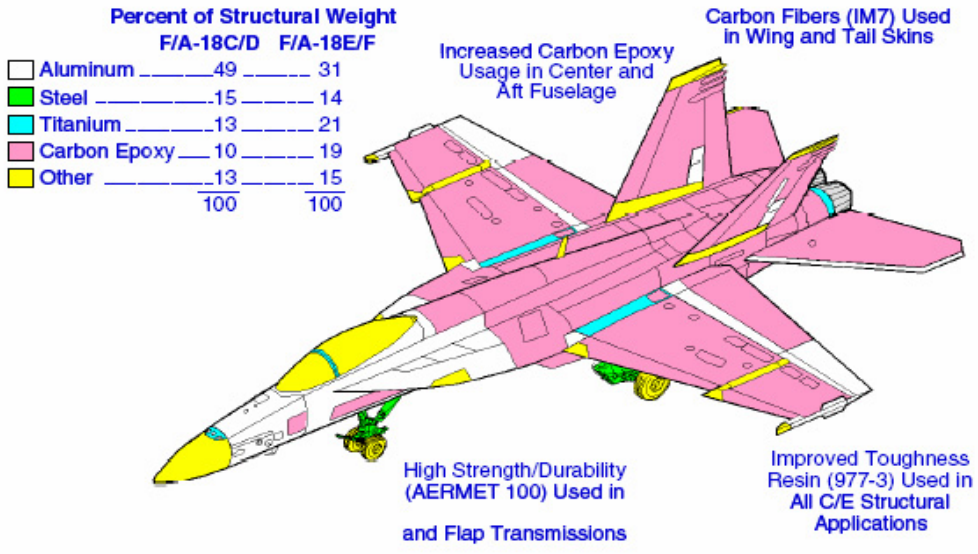

Figure 2. Material distribution for F-18 E/F aircraft [9].

This approach adopted two key requirements in metallic aircraft certification: (1) the full-scale static test article must demonstrate a strength that is equal to or exceeds 150 percent of the design limit load (DLL); and (2) the full-scale fatigue test article must demonstrate a life that is

equal to or exceeds twice the design service life. This approach analyzes the data scatter in the static strength and fatigue life of composites to establish a certification methodology that has the same level of reliability as for metal structures. Furthermore, this approach attempts to address the issues related to hybrid (composite and metallic) structures through a combined approach referred to as the load-life approach, which will be further discussed in this report. This approach was developed for what, at that time, was current composite usage and did not explicitly account for the damage in composite structures or adhesively bonded structural details. Kan and Whitehead [10] proposed a damage tolerance certification methodology to determine the reliability of impact damage on a composite structure and to calculate the allowable impact threat at a given applied load and specified reliability. Subsequent application of this methodology for an F/A-18 inner-wing structure demonstrated successful damage tolerance capabilities during certification.

The NAVY load-life methodology was adopted by Shah et al. [11] for certification of a stiffener runout detail. They found that the strength and life shape parameters are similar to that developed for the NAVY approach. This research successfully demonstrated the combined load-life approach for large component tests. Further, the applicability of the U.S. Navy damage tolerance approach by Kan and Whitehead [10] for certification of general and commercial aircraft was investigated by Kan and Dyer [12]. This study showed that the U.S. Navy damage-tolerant approach based on military requirements is too severe for the all-composite Lear Fan 2100 structure.

Early developments of the Boeing 737 graphite/epoxy horizontal stabilizer [13] and Airbus A310 [14] and A320 [15] all-composite vertical tail used the combined load-life approach for full-scale demonstrations and adopted the no-growth damage-tolerant design concept,

whereby a composite structure must demonstrate the ability to contain intrinsic manufacturing defects and the maximum allowable service damage(s) in adverse operational conditions and throughout the design life of the structure. Early composite certification programs recognized the need for damage-tolerant structural design concepts and certification approach for efficient composite structures. A damage-tolerant structure assumes to have a pre-existing defect or damage that requires a detailed inspection plan under repeated loading. This enables the incorporation of intrinsic and/or in-service damages into the damage-tolerance phase of the analysis and full-scale test substantiation. Damage-tolerance methodology should include information pertaining to the critical damage limit (CDL) as well as allowable damage limit (ADL) to support inspection intervals. Because of the highly heterogeneous nature of composite damage progression, the analytical predictions are application specific and require extensive empirical validation. Thus, probabilistic methods are commonly used for composite structures.

Followed by the early development approach for the NASA/Boeing 737 horizontal stabilizer, Boeing 777 empennage certification was primarily based on analysis supported by coupon and component test evidence [16]. The certification process includes general requirements for environmental effects in design allowables and impact damages, static strength, and fatigue and damage tolerance with a no-growth approach. By delivering predictions prior to testing, such demonstrations will contribute to a solid basis for acceptance of "certification by analysis" by the FAA and the aviation industry. This is consistent with current certification practices that allow the use of analysis for certification when supported by tests.

Several all-composite business aircraft, including the LearFan 2100 and Beech 2000 Starship, evolved in the early 1980s and completed FAA damage-tolerance certification requirements [17]. The LearFan 2100 was certified by the FAA after modifications following

wing and fuselage failure during initial structural testing. This first certified all-composite airplane flew in 1983. The all-composite Beechcraft Starship was certified in 1989 using the damage-tolerant approach, identifying environmental effects and concerns related to bonded joints. In order to meet FAA damage-tolerance requirements, major structural modifications had to be made to the wing. For full-scale durability and damage-tolerance tests, a combined load-life approach based on flaw-growth threshold stress was employed [18]. The environmental effects were addressed through an analytical approach validated by testing.

Under the Composite Affordability Initiative (CAI), Kan and Kane [19] explored the feasibility of extending probabilistic methodology for adhesive-bonded composite structures. The level of maturity in three areas was thoroughly reviewed: (1) probability theories and probabilistic methods, (2) probabilistic structural analysis tools, and (3) probabilistic structural criteria and requirements. This program identified that the same level of structural reliability with equivalent level of confidence can be achieved by the probabilistic method as compared to the deterministic method.

1.1.1. Fatigue Life Assessment of Fibrous Composite

Sumich and Kedward [20] investigated the use of the wearout model, on the basis of its applicability to matrix-dominant failure modes to examine the fatigue performance of the Rotor Systems Research Aircraft (RSRA) X-wing vehicle. Wearout models assume that structural degradation occurs with use and can be monitored by measuring parameters such as residual strength and stiffness. Halpin et al. [21] discussed this methodology in the early 1970s, and several certification programs, such as the A-7 outer wing and F-16 empennage have adopted this methodology for composite structures. This method, which was adopted by metal crack growth, determines fatigue failure when preexisting damage grows until the specimen can no

longer support the applied cyclic load. In addition, the residual strength of runout is related to crack length through fracture mechanics. This approach was improved by Sendeckyj [22] using a deterministic equation that converts static, fatigue, and residual strength data into a pool of equivalent static strength data. Sendeckyj's basic model assumes that the failure in a constant amplitude fatigue test occurs when the residual strength is equal to the maximum cyclic fatigue load. This pooling technique for fatigue data is useful for cases where there are not enough fatigue data in individual stress levels for Weibull analysis, which requires a minimum of six specimens in each stress level. This model is further improved for pooling fatigue tests with multiple stress ratios [23] but is not validated since it requires a significant amount of test data. Stress ratio or R ratio is the ratio of minimum and maximum cyclic stress in a fatigue test.

O'Brien and Reifsnider [24] studied fatigue life analytically using the fatigue modulus concept. This approach assumed that fatigue failure occurs when the fatigue secant modulus (residual stiffness) degrades to the secant modulus at the moment of failure in a static test. In this study, stiffness reductions resulting from fatigue damage were measured for unnotched $[\pm 45]_s$, $[0/90]_s$, and $[0/90/\pm 45]_s$ boron/epoxy laminates. Degradation in the various in-plane stiffness (axial, shear, and bending) was measured using a combination of uniaxial tension, rail shear, and flexure tests. Damage growth and stiffness loss were identified to be load-history dependent. Hence, the secant modulus criterion was not a valid criterion for general applications. A similar study was conducted on the fatigue behavior of $[0/\pm 45/90]_s$ glass/epoxy laminate by Hahn and Kim [25], in which the secant modulus was used as a measure of damage extent.

Following an extensive review of different damage models, Hwang and Han [26] identified various cumulative damage models using several physical variables such as fatigue

modulus and resultant strain. They introduced a new concept called "fatigue modulus," which is defined as the slope of applied stress and resultant strain at a specific cycle [27]. Fatigue modulus degradation assumes that the fatigue modulus degradation rate follows a power function of the fatigue cycle. The theoretical equation for predicting fatigue life is formulated using the fatigue modulus and its degradation rate. This relation is simplified by the strain failure criterion for practical applications. Mahfuz et al. [28] analytically studied the fatigue life of an S2-glass/vinyl-ester composite using the fatigue modulus concept. This study revealed that the fatigue modulus is not only a function of loading cycle but also a function of applied stress level and thickness of the test specimen. This life-prediction methodology requires two parameters that are obtained empirically either at two different stress levels or two different fatigue life times.

Halpin el al. [29] suggested that the fatigue behavior of composites should be based empirically under the design spectra. The main disadvantage of such an approach is that test results are specific to a loading spectrum. Also, a large number of test data is required for a complete analysis, like the extensive fatigue sensitivity study conducted by Jeans et al. [30] on bolted and bonded composite joints under various loading spectra. For metals, Miner's rule is often used to study the cumulative damage under a loading spectrum. However, Rosenfeld and Huang [31] conducted a fatigue study with different stress ratios to determine the failure mechanisms under compression of graphite/epoxy laminates and showed that Miner's rule fails to predict composite fatigue under spectrum loading. This is confirmed by several authors in the composite community. A study conducted by Agarwal and James [32] on the effects of stress levels on fatigue of composites confirmed that the stress ratio had a strong influence on the

fatigue life of composites. Further, they showed that microscopic matrix cracks are observed prior to gross failure of composites under both static and cyclic loading.

For practical consideration, Yang and Du [33] investigated the possibility of statistically predicting the fatigue behavior of composites under service-loading spectra, based on some baseline constant amplitude fatigue data. Although such a phenomenological statistical model does not account for the intrinsic failure mechanisms that are quite complex in composite materials, it can be very simple for practical applications and requires significantly less empirical effort.

Kassapoglou [34] presented a probabilistic approach for determining fatigue life for composite structures under constant amplitude loading. This approach assumes that the probability of failure during any cycle is constant and equal to the probability of failure obtained from static test results and associated statistically quantified scatter. This methodology does not require any fatigue data for calibration or for the expressions of the cycles to failure as a function of stress ratio. Comparison of fatigue life predictions for several stress ratios with a number of experimental data shows good correlation. However, the assumptions used in this model neglect the complex progressive damage mechanism that takes place during repeated loading.

1.1.2. Impact Damage on Composite Structures

A study conducted by Dost et al. [35] on the impact damage resistance of laminated composite transport aircraft fuselage structures empirically determined the relative importance and quantitative measure of the effect of numerous variables such as material, laminate, boundary condition, impactor type, and their interactions. An extensive study conducted on toughened-epoxy laminates by Dost et al. [36] shows that the damage state and the post-impact compressive strength behavior of composites is a strong function of the laminate stacking

sequence. A similar study conducted by Sharma [37] shows that strength degradation due to impact is dependent on the laminate configuration and fiber matrix combination. Also, laminates having more angle plies near the impact surface and unidirectional plies elsewhere seem to show extensive interply and intraply fiber delaminations at failure relative to laminates with a cross-ply on the impact surface.

Tomblin et al. [38] outlined the philosophy for the damage-tolerance certification approach for sandwich structures with several cases studies. This investigation identifies five major tasks for the damage resistance and tolerance characteristics of sandwich structures: (1) damage development due to low-velocity impact, (2) post-impact strength, (3) flaw-growth threshold and damage evolution under cyclic loading, (4) analytical model development, and (5) full-scale/sub-component testing and verification. These experimental observations should be used for developing and validating a semi-empirical model to predict the damage resistance and tolerance capabilities for a given sandwich panel configuration. Subsequent research by Tomblin et al. [39] investigated the effects of several impact parameters on damage resistance and tolerance, detectability of impact damage using field inspection techniques, and fatigue loading. Further studies by Tomblin et al. [40] on scaling studies of sandwich structures indicate that residual strength is affected by the ratio of specimen size to damage size and is dependent on the number of plies in the facesheets. Furthermore, the studies show that damage development is the dominant energy-dissipation mechanism and depends on the ratio of the impactor mass to the target mass. Based on an investigation conducted on honeycomb and form-core sandwich panels, Raju [41] showed a strong dependency of the indentation response and the failure mechanism on indenter size and core type. These studies show that information on both dent depth and planar damage size need to be included in certification of the composite structure. It is

clearly shown that visual inspection methods can be misleading and that residual indentation cannot be used as a reliable damage metric for static ultimate-strength and damage-tolerance criteria for sandwich structures.

1.2. Background for Current Approach

Based on current safety standards, composite materials are considered insensitive to fatigue failures. Most previous research efforts in damage tolerance have concentrated below the critical damage limit using fairly small coupons, and thus the results obtained are on the conservative side. With increased use of composite materials in primary structures, there is a growing need to investigate extremely improbable high-energy impact threats that reduce the residual strength of a composite structure to limit load. Currently, this issue is not explicitly addressed in full-scale substantiation, and no fatigue requirements exist, i.e., only "get home" loads. To verify that the structure has sufficient residual strength to sustain the expected in-service loads, once damages have been introduced, a typical certification program for composite structures is conducted in two phases: first, to demonstrate the durability of the structure, and second to include a damage-tolerance phase into the durability test. Alternately, the damage-tolerance phase can be introduced earlier in the testing with alternative requirements, i.e., rigorous inspection plans, repair after a certain test duration, etc.

Composite structural test loads are enhanced to reduce high test duration requirements, which are a direct result of the data scatter observed in composites relative to metals, using the load-life approach proposed for U.S. Navy F/A-18 certification [2] so that the same level of reliability as for metal structures can be achieved. Compared to the metal static and fatigue data, composite materials exhibit high data scatter due to their anisotropic heterogeneous characteristics such as layup, manufacturing defects and imperfections, test complications,

environment, etc. In order to interpret those information in a meaningful manner and to incorporate any effects of them into the certification of composite structures, life factor approach and load enhancement factor approach are two of the commonly used approaches that require composite scatter analysis, which is described in Chapter 3. The life factor approach, which has been successfully used for metallic structures to assure structural durability, accounts for the scatter in life (S-N) data in terms of the shape parameter of the population. The life shape parameter (often referred to as the modal life shape parameter) is obtained by analyzing the distribution of the shape parameters corresponds to S-N curves representing different design details of the structure as described in Chapter 5. The life factor corresponds to the central tendency (mean) of the population to the extreme statistics (allowable). The underlying objective of life factor approach is to ensure that the design service goal or life is representative of the weakest member of the population after a specified life in service. Thus, a successful repeated load test to mean fatigue life would demonstrate the B-basis reliability on the design lifetime. The NAVY approach showed that the life shape parameters of metal and composite are 4.00 and 1.25, respectively, and they correspond to life factors of 2.093 and 13.558, respectively, for B-basis reliability [2]. Therefore due to the large scatter in the composite test data, a composite structure is required to test additional fatigue life to achieve the desired level of reliability, i.e., test duration of more than 13 design lifetimes for composite in contrast to 2 design lifetimes for metal to achieve the B-basis reliability.

An alternative approach to the life factor, which requires an excessive test duration, is to increase the applied loads in the fatigue spectrum so that the same level of reliability can be achieved with a shorter test duration [2]. This approach is referred to as the load enhancement factor (LEF) approach and was derived from combining the life factor and the static factor (ratio

of mean to allowable fatigue strength) at one lifetime to form a relationship between the LEF and the test duration. The static factor is defined in terms of a static strength shape parameter that is obtained by analyzing the distribution of the shape parameters corresponds to static strength data sets representing different design details of the structure as described in Chapter 4. The formal relationship between the LEF and the test duration provides the flexibility of conducting durability test of a composite structure with different LEFs and the corresponding test durations to achieve the desired reliability. Although the materials, processes, layup, loading modes, failure modes, etc., are significantly different, most current certification programs use the load-life factors generated for the U.S. Navy F/A-18 certification program. Lameris [3] showed that both load and life factors can be significantly reduced by using strength and life-shape parameters generated for materials, processes, loading modes, failure modes, etc., applicable to a specific structure. However, guidance for developing these shape parameters is greatly needed.

Although fatigue life is adversely affected by damage (notch), the scatter in damaged composites, both in static and fatigue, tends to decrease due to localized stress concentration. This is favorable for generating static and life factors and will result in lower life and load-enhancement factors. Therefore, scatter analysis of coupons/elements in lower levels of testing building blocks can be used to develop a synergy among the life factor, load-enhancement factor, and damage in composites. This approach is beneficial for the damage-tolerance phase of full-scale substantiation and minimizes the risks associated with the introduction of large damage to durability test articles.

Development of scatter analysis applicable to current composite materials and processes using improved test methodologies will demonstrate lower requirements for the life factor and load-enhancement factors. Introduction of damage philosophy into the scatter analysis further

reduces these factors. The probabilistic approach employed in the NAVY load-life combined approach shows the potential use of improved shape parameters for estimating the effects of design changes, i.e., gross weight changes, on design life. This requires a probabilistic approach to redefine basis (A- or B-basis) fatigue life requirements set forth in the load-life combined approach to any deviation from the life (i.e., reduction in life factor due to damage introduction) or load factor (i.e., high spectrum fatigue loads due to gross weight change). For a full-scale test that was conducted using a higher load enhancement factor (LEF) or completed more than the required test duration, this technique can be used to redefine original design service goals (number of hours equivalent to one life) associated with the fatigue spectrum.

1.3. Objectives and Overview of Research

The key objective of this research was to develop a probabilistic approach to synthesizing the life factor, LEF, and damage in composite structures in order to determine the fatigue life of a damage-tolerant aircraft. This methodology was extended to the current certification approach to explore extremely improbable high-energy impact threats, i.e., damages that reduce the residual strength of aircraft to limit-load capability and allow incorporating certain design changes into full-scale substantiation without the burden of additional time-consuming and costly tests. Research was conducted in three phases (Figure 3):

1. Load-life combined approach.
2. Damage-tolerance and flaw-growth testing.
3. Load-life-damage (LLD) hybrid approach.

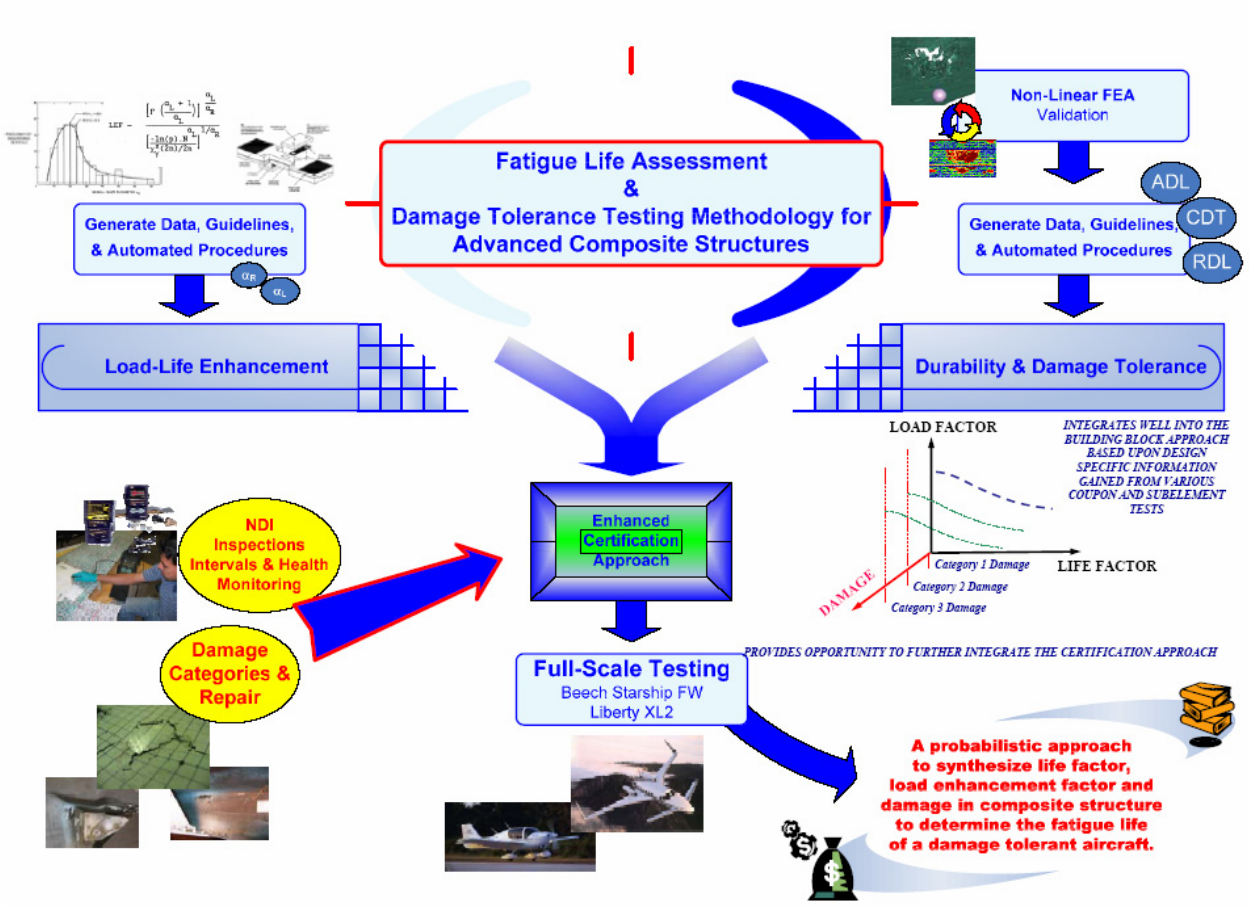

Figure 3. Overview of research.

The first subtask of phase 1 of the research was intended to generate a database of fatigue life data for several composite material systems that are commonly used in general aviation. The second subtask in this phase was to add static-strength shape parameters to the database and generate improved load-enhancement factors for several example materials. These data were then used to generate necessary load-life combined data, for example, full-scale demonstrations included in the final stage of the research. The improvements in materials and processes, and test methods produced life and load factors lower than the values commonly used in most certification programs based on the NAVY approach. Data gathered in this phase were used to provide guidance for generating safe and reliable load and life factors pertaining to a specific

structure. In addition, a user-friendly computer code that can be used for scatter analysis of composites was developed. This code alleviates misinterpretation of any statistical or mathematical processes during the analysis and provides guidance for selecting different techniques appropriate for a particular application.

Although the composite data scatter for unnotched specimens is considerably high due to heterogeneous nature of laminated composites and competing failure modes, the notched or damaged composite data show significant reduction in the data scatter due to the localized stress concentration. The primary goal of the damage-tolerance phase of the research was to capture the effects of damage on the composites data scatter in element level, and interpret this information in a meaningful manner for damage-tolerance testing of composite structures. During the damage-tolerance phase of the research, fatigue characteristics of different categories of damages were studied. These data were combined with data obtained in phase 1 and were used in methodology development and full-scale validation in the final phase. When simulating high-energy damage, especially if it is incorporated in the early phases of testing, care must be taken to control its intensity so as not to exceed the required damage threat level. Further, a methodology was introduced to investigate the impact of a large defect on the probability of failure of the structure during the DaDT phase. This approach can also be use to allot inspection intervals economically to prevent unintentional failure of the damaged structure.

The final phase combined data from the first two phases and developed the improved damage-tolerance test methodology, a synergy of life factor, load-enhancement factor, and damage. This methodology highlights the reductions in data scatter due to the improvements in material and process techniques and test methods of composites, and provides flexibility of using appropriate life factor and LEF requirements during different phases of the durability and

damage tolerance testing of composite structure. This methodology further extend the current practice during damage-tolerance certification to focus on the most critical damage locations of the structure and interpret the structural and loads details into the most representative repeated load testing in element level to gain information on the residual strength, fatigue sensitivity, inspection methods and inspection intervals during full-scale test substantiation. A reliability approach to determine the inspection intervals to mitigate risks of unexpected failure during the damage tolerance phase, especially with large impact damages, was discussed. This methodology was validated with several full-scale test examples of the Beechcraft Starship forward wings with large impact damages on the front and aft spars (Figure 4).

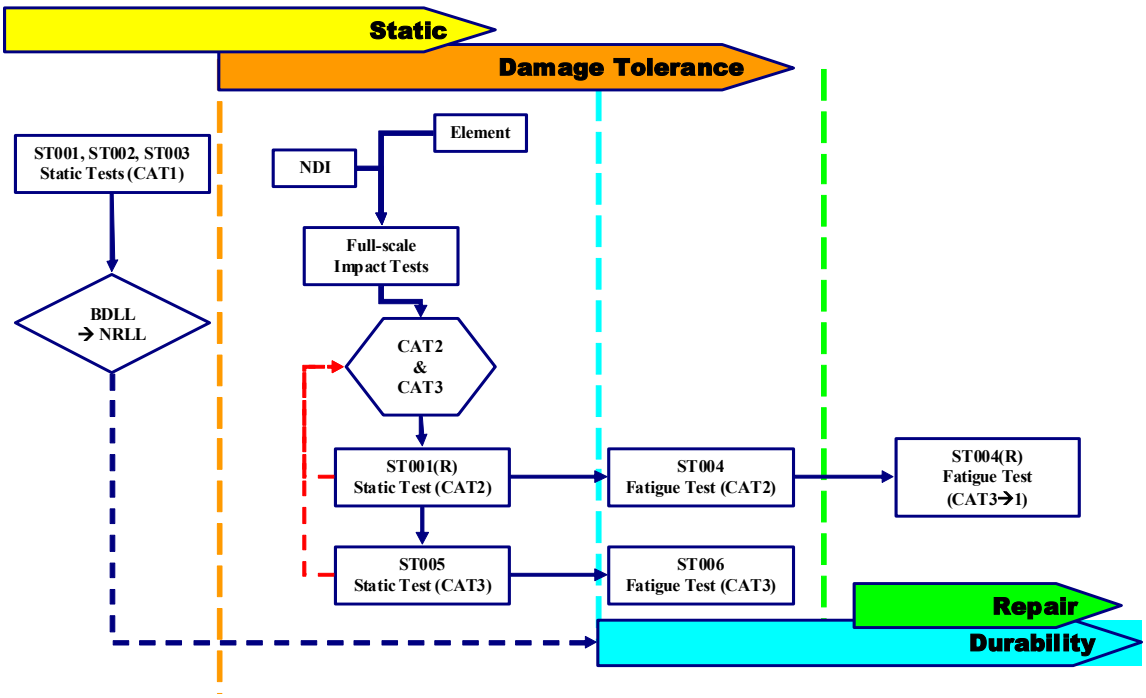

Figure 4. Outline of full-scale testing.

The front spar of the forward-wing structure is the primary load path and a large impact damage that result in a decrease of the residual strength to its limit-load was considered as a

category 3 (CAT3) damage. A large impact damage that was on the aft spar was considered as a category 2 (CAT2) damage and its contribution to the final failure of the structure was secondary. Several element-level tests were conducted to determine the impact parameters for inflicting these damage on full-scale structures. Strategic placement of strain gages around the damage and near critical areas provided real-time feedback during damage tolerance tests. The strain data provide information similar to a built-in health monitoring system and provide details in real time to assess the state of the damage, i.e., propagation or not, and any global effects on the structure due to possible damage growth.

CHAPTER 2

EXPERIMENTAL PROCEDURE

As shown in Figure 3, this research was conducted in three major phases: (1) load-life factor generation, (2) damage-tolerance and flaw-growth testing, and (3) load-life-damage hybrid approach. The coupon and element testing required for the first two phases were carried out together. The primary goal in phase 1 was to develop and document a methodology for the development of Weibull parameters to be used in the load-life combined approach. Two key parameters were needed: static-strength and the fatigue-life Weibull shape parameters. The first subtask in this phase was to investigate the life factor for several composite material systems using the fatigue-life shape parameter. Then, using fatigue-life and static-strength shape parameters, the load-enhancement factor for several material systems was calculated. Finally, a comparison of the load-life approach for several material systems and design scenarios was shown with two benchmark case studies: Beech Starship forward wing and Liberty XL2 fuselage. The second phase incorporated different damage categories into a full-scale test article and investigated the effects of damages on life and load factors. The final phase was intended to develop a hybrid approach using the life factor, load-enhancement factor, and damage in the composite. Once the load-life factors were generated for the Starship material, full-scale fatigue testing of the last phase was started to verify the load-life-damage approach.

2.1. Development of Weibull Shape Parameters

The primary goal was to evaluate factors affecting scatter analysis, such as material, process, layup, loading mode, failure modes, etc., and to propose a simplified reduced test matrix that could be used to generate a reliable life factor and load enhancement factor for a particular composite certification program. This task was also intended to establish guidance to the scatter

analysis with several examples for commonly used general aviation composite material systems. The purpose of this exercise was to incorporate this type of data, not only into the individual certification plans but also into shared databases as well. Non-autoclave materials (graphite and glass) were the primary focus of the data generated. In addition, the approach was extended for elements and structural details, i.e., characterization of sandwich materials (foam and honeycomb), which are commonly used in the primary structures of general aviation airframes.

Three different scatter analyses (section 3.1) were used to calculate the fatigue-life shape parameters:

1. Individual Weibull analysis.
2. Joint Weibull analysis.
3. Sendeckyj equivalent wearout model.

A user-friendly computer program was developed so that the fatigue test data could be analyzed using these three techniques. This program was designed to guide the analyst to select the most suitable approach for a given set of test data.

2.1.1. Material Systems

The three main material systems studied in this investigation for the purpose of generating static and fatigue shape parameters were Cytec AS4/E7K8 plain-weave fabric (AS4-PW), Toray T700SC-12K-50C/#2510 plain-weave fabric (T700-PW), and 7781/#2510 8-Harness glass-fiber fabric (7781-8HS) [43]. The test data for these three materials are referred to as FAA-LEF data throughout this report. In addition to FAA-LEF data, a detailed static scatter analysis was conducted on Toray T700G-12K-31E /#2510 unidirectional tape and T700SC-12K-50C/#2510 plain-weave fabric, Advanced Composites Group (ACG) MTM45/AS4C 12K unidirectional tape and MTM45/AS4C 6K 5-harness graphite fabric, and NelCote (formally

FiberCote) T700-24K/E765 unidirectional tape and T300-3K/E765 plain-weave fabric that are available through an extensive laminate database [44], which was generated to analyze the lamina variability method (LVM) [45] on generating laminate allowables. This data set is referred to as FAA-LVM data throughout this report.

In addition to the above two data sets, fatigue scatter analysis for Loctite, Hysol EA9696, and PTM&W ES6292 adhesive systems are included from the data obtained from FAA research to investigate the durability of adhesive joints [46]. These test specimens were fabricated according to American Standards for Testing Materials (ASTM) standard test method for thick-adhered metal lap-shear joints in order to determine the shear stress-strain behavior of adhesives in shear by tension (ASTM D5656). This data set is referred to as FAA-D5656 data throughout this report. Finally, element test data of adhesively bonded composite joints that were loaded in picture-frame shear and single-lap shear [47] test configurations were included in the analysis. Data from this database are referred to as FAA-EOD data throughout this report. Once the scatter analysis was completed, load enhancement factors were generated, combining scatter analysis of the above data sets for available fatigue cases.

Note that the additional material databases included in the scatter analysis (FAA-LVM, FAA-D5656, and FAA-EOD) are authors previous work that were funded by the FAA.

The Beechcraft Starship was primarily fabricated using an AS4/E7K8 epoxy material system (original manufacturer U.S. Polymeric). Hercules AS4 fibers are continuous carbon filaments made from a PAN precursor, and their surface is treated to improve handling characteristics and structural properties. Typical fiber tensile modulus and strength are 34 Msi and 550 ksi [48]. The E7K8 medium-flow epoxy resin system with good tack characteristics for handling has a 20-day out-time at ambient temperature. The AS4/E7K8 3K plain weave material

system (AS4-PW) has an aerial weight of 195 g/m^2, a typical cured-ply thickness of 0.0087 inch, and a low-exotherm profile for processing thick parts. This material is currently being used by Hawker Beechcraft and Cessna Aircraft in Wichita, Kansas, for several aircraft applications.

2.1.2. Test Matrices

Testing included various "element type" tests and concentrated on tests that are "generic" in nature and would be representative of various loading modes and construction techniques. In general, this program primarily focused on stress ratios within the wing and fuselage envelopes for the development of the Weibull fatigue shape parameter. Using the data gathered in the lamina, laminate, and element tests, the methodology used to develop the Weibull static strength parameters was compared for various scenarios.

Commonly used laminate stacking sequences ("hard" (50/40/10 for unidirectional tape and 40/20/40 for fabric), quasi-isotropic[1] (25/50/25), and "soft" (10/80/10) laminate constructions) were used for the FAA-LEF database (Table 1).

TABLE 1

LAMINATE CONFIGURATIONS FOR FAA-LEF DATABASE

Laminate	Layup % 0°/45°/90°	Ply Stacking Sequence	Total Plies
Hard	40/20/40 (weave)	$[0/90/0/90/45/-45/90/0/90/0]_S$	20
Quasi-isotropic	25/50/25	$[\ (45/0/-45/90)_2\ ]_S$	16
		$[\ (45/0/-45/90)_4\ ]_S$	32
Soft	10/80/10	$[45/-45/90/45/-45/45/-45/0/45/-45]_S$	20
		$[45/-45/90/45/-45/45/-45/0/45/-45]_{2S}$	40
All ±45	0/100/0	$[(45/-45)_5\ ]_S$	20

[1] Material properties are similar in all in-plane directions.

In addition, sandwich specimens were fabricated with three-ply facesheets with plies in the 0° direction with a 0.25-inch HRH-10 Nomex core. Test methods and fixture requirements for FAA-LEF testing is shown in Table 2.

TABLE 2

FAA-LEF TEST METHODS AND FIXTURE REQUIREMENTS

Test Description	Abbreviation	Test Method	Test Fixture
Tension, Open Hole	OHT	ASTM D5766	No
Compression, Open Hole	OHC	ASTM D6484	Yes
Double-Notched Compression	DNC	Modified ASTM D3846	Yes
Single-Lap Shear, Tension	SLS-T	Modified ASTM D3165	No
Single-Lap Shear, Compression	SLS-C	Modified ASTM D3165	Yes
Sandwich 4-Point Bend	4PB	ASTM C393	Yes
Compression After Impact	CAI	ASTM D7137	Yes
Tension After Impact	TAI	Modified ASTM D3518	No

Although these test methods are recommended for static testing, a similar test setup was used for fatigue testing as well. DNC specimens were modified to have similar geometry as OHC (12 x 1.5 inches), and the OHC fixture was used for both static and fatigue testing. Similarly, the ASTM D3165 specimen was modified to have the same overall specimen dimensions with a 1.5-inch overlap so that the OHC fixture could be used for compression loading.

The basic FAA-LEF test matrix is shown in Table 3. All 10/80/10 laminates in this table were fabricated with a 20-ply stacking sequence, as shown in Table 1. In order to support the

full-scale demonstration and the damage-tolerance effort discussed in section 8.1, a supplemental test matrix was added for AS4-PW (Table 4). These test matrices represents different layups, test environments, loading modes, bonded joints, and sandwich structures. Sandwich specimens were fabricated with HexWeb® HRH-10 manufactured from Nomex® aramid fiber sheets. This core was selected because of its applications in the Beechcraft Starship.

TABLE 3

BASIC FAA-LEF TEST MATRIX

Laminate	Test Method	Loading Condition	Standard	Static Test Environment		RTA - Cyclic Test R-Ratio (Three Stress Levels)			
				RTA	ETW	-0.2	0	-1	5
10/80/10 Laminate	OH	Tension	ASTM D5766	6	6	18	18		18
		Comp.	ASTM D6484	6	6			18	
	SLS (t=0.01")	Adhesive In-Plane Shear	Modified ASTM D3165	6	6	18		18	
	SLS (t=0.06")			6	6	18		18	
	DNC	Interlaminar Shear	Modified ASTM D3846	6	6	18		18	
Sandwich	4PB	Flexure	Modified ASTM C393	6	6		18		

The 10/80/10 CAI specimens in Table 4 were fabricated with the 40-ply stacking sequence, while the 25/50/25 CAI specimens were fabricated using the 32-ply stacking sequence, as shown in Table 1. Extensive testing of coupons [49] and components [50] of adhesive joints have shown a significant decrease in static strength for thick bondlines. Thus, the adhesive joints with different bondline thicknesses were included in the test matrix. ASTM D3518 was modified to have a four-inch width for the TAI specimen, with impact at the center.

TABLE 4

SUPPLEMENTAL FAA-LEF TEST MATRIX

Laminate	Test Method	Loading Condition	Standard	Static Test Environment		Cyclic Test R-Ratio (Three Stress Levels)			
				RTA	ETW	-0.2	0	-1	5
10/80/10 Laminate	CAI	Comp. BVID	ASTM D7137	6					18
		Comp. VID		6					18
25/50/25 Laminate	OH	Comp. RTA	ASTM D6484	6				18	
		Comp. ETW			6			6	
	CAI	Unimpacted RTA	ASTM D7137	6					
		Comp. BVID/RTA		6					18
		Comp. VID/RTA		6					18
		Comp. LID/RTA		6					18
40/20/40 Laminate	CAI	Comp. VID	ASTM D7137	6					18
0/100/0 Laminate	OH	Comp. RTA	ASTM D6484	6				18	
	TAI	Shear BVID/RTA	Modified ASTM D3518	6					18
		Shear VID/RTA		6					18

The 25/50/25 CAI specimens were included primarily to support the damage-tolerance element test. Thus, these specimens were machined to 6 by 9 inches to minimize the edge effects for larger damages and to leave room for damage propagation during cyclic loading. Further details are discussed in Chapter 6.

2.2. Experimental Setup for LEF and Element Testing

This section contains information regarding the experimental setup and equipment used for impacting, non-destructive inspections (NDI), and residual strength testing of the FAA-LEF test specimens.

2.2.1. Impact Testing

CAI and TAI test specimens were impacted using an Instron Dynatup 8250 drop-weight impact tester (Figure 5). The impact force was measured using a piezoelectric load cell attached to the impact mass assembly. This impact tester was equipped with a pneumatic rebound catch mechanism, which prevents secondary impacts on the test specimens, and a photo-detector/flag system, which provides impact velocity information. Data-acquisition software, which runs on a computer connected to each drop-weight impact tester, collected and reduced the impact test data. A sensor (flag), which was placed closer to the impact location, triggered the data acquisition system a few milliseconds prior to the impact event. This sensor and another flag placed a known distance adjacent to that were used for calculating impact velocity (velocity = distance/time).

Prior to impacting, specimens were placed in the support fixtures, as shown in Figure 6, and held rigidly. These fixtures use dowel pins for aligning the specimens. The total impact event time duration for the specimens and energy levels used in this investigation was about 10 milliseconds or less. Therefore, a very high-frequency triggering mechanism was used to collect data during the impact event in order to minimize unnecessary data before and after. An Instron Dynatup 8250 drop tower was equipped with an Instron Dynatup Impulse data acquisition system.

Figure 5. Instron Dynatup drop-weight tester.

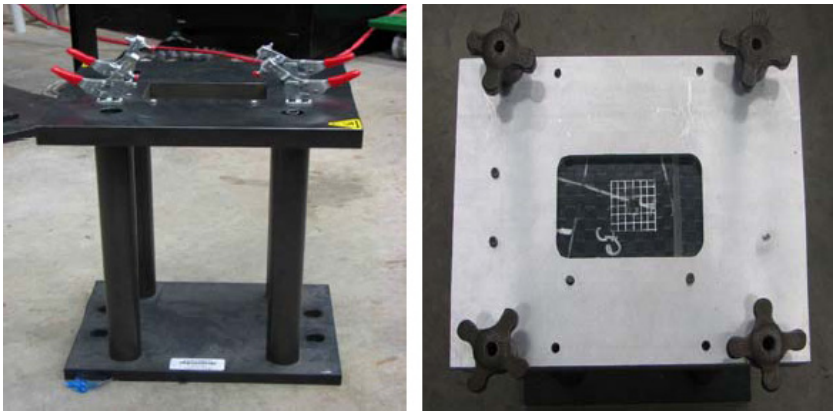

Figure 6. Support fixture for CAI and TAI impact specimens.

2.2.2. Non-Destructive Inspections

Impacted specimens were subjected to through-transmission ultrasonic (TTU) NDI that generated C-scans to quantify the planner-damaged areas using image-analysis software (Figure 7). Additional inspections techniques, e.g., microscopy, thermal imaging, were also used for the damage-tolerance investigation and are briefly discussed later in this report. For those cases

involving glass fiber composite, damage can be seen clearly with the naked eye due to the translucent nature of these fibers.

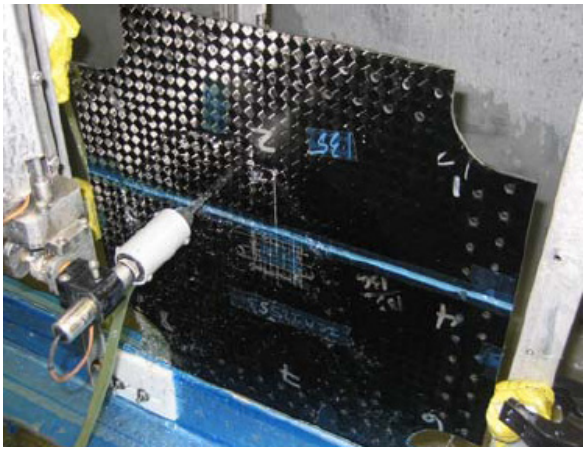

Figure 7. TTU scanning of PFS test specimen.

In addition to TTU C-scans, test specimens were inspected with the Sonic 1200 ultrasonic flaw detector and BondMaster^{TM} 1000 hand-held NDI inspection units, when the specimens were in the test setup. The BondMaster^{TM} 1000 is capable of resonance, mechanical impedance analysis (MIA), and pitch/catch mode, and the user has the ability to select the method best suited for inspecting a particular composite structure. The MIA technique, which was used for inspecting test specimens in this program, measures the stiffness and mass of the material under test and requires no coupling agents. The output was measured in both amplitude and phase. Both of these hand-held units are equipped with color displays and provide real-time data.

2.2.3. Full-Field Strain Evolution

The ARAMIS photogrammetry full-field strain measurement system was utilized to measure localized buckling in the region of disbonds/defects. ARAMIS [51] is a non-contact, optical, three-dimensional deformation measuring system. It uses two high-definition cameras to track translation and rotation of the surface details (object characteristics) with sub-pixel

accuracy. Surface details are obtained by applying a stochastic color pattern that follows surface displacement during loading. ARAMIS uses this pattern to recognize the surface structure and uses digitized images through both cameras for triangulation of surface details (micro-pattern) to determine the precise location of each point. Therefore, this system has the capability of digitizing the precise shape (surface) of the structure during loading. The first set of coordinates for object characteristics are obtained in the undeformed stage. After load application, a new set of coordinates (digital images) is recorded. Then, ARAMIS compares the digital images and calculates the displacement and deformation of the object characteristics.

Figure 8. Portable version of ARAMIS photogrammetry system [51].

ARAMIS is capable of three-dimensional deformation measurements under static and dynamic load conditions in order to analyze deformations and the strain of real components. In addition, this system is able to eliminate the rigid body motion component from the displacement results. Therefore, it can be used for specimens that exhibit large displacements. Strain sensitivity of the system is approximately 100-200 microstrains, and the scan area can be as large as 47 by 47 inches. Full-field displacement/strain data are then used to examine any propagation of the defects according to the procedures outlined by Tomblin et al. [52], which assesses the localized skin buckling (out-of-plane displacement) around the disbonded or delaminated region.

The full-field strain evaluation on CAI specimens during static loading (Figure 9) and during fatigue loading was measured using ARAMIS photogrammetry system.

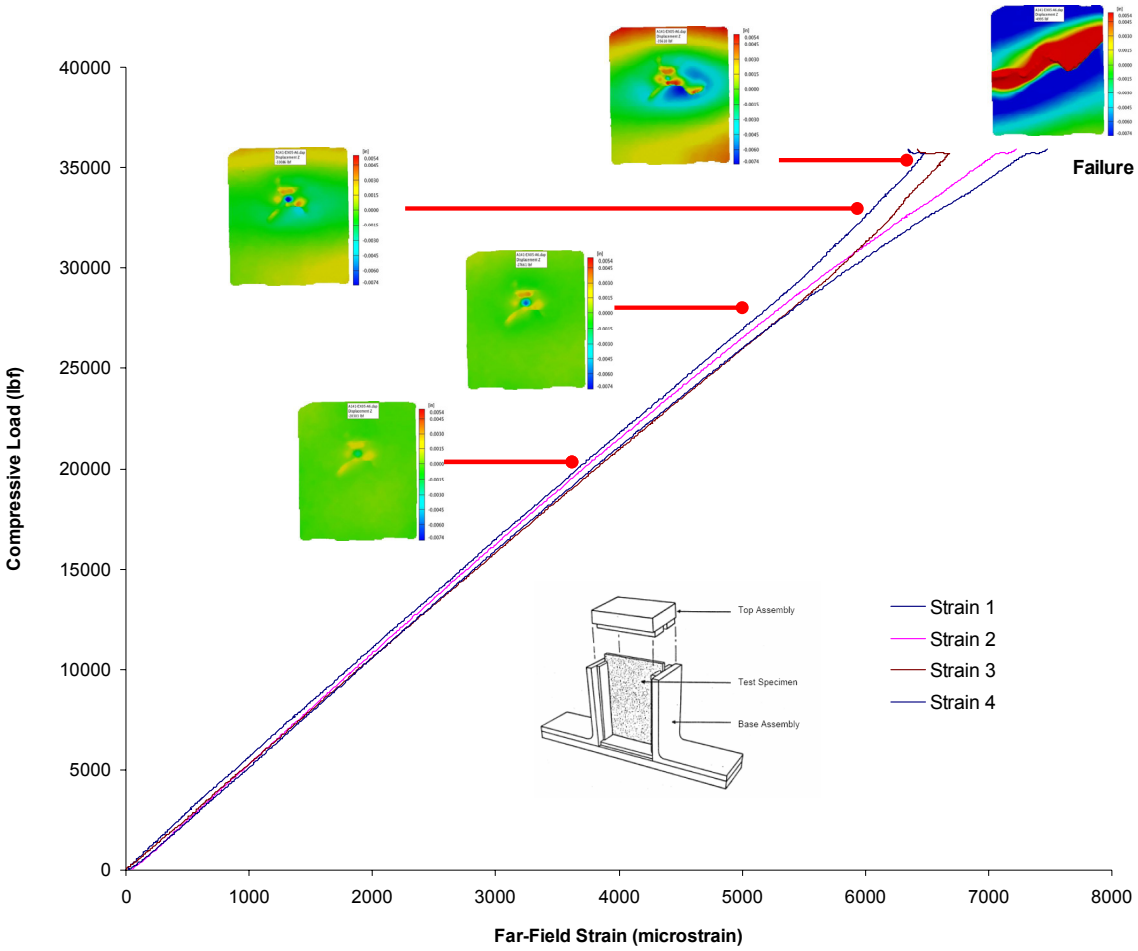

Figure 9. Damage evolution of a CAI specimen under static loading.

2.2.4. Static and Residual Strength Testing

All static testing and residual strength testing were conducted using Material Test Systems (MTS) servo-hydraulic test frames. Test specimens that did not require fixtures were mounted to the test frame using a hydraulic grip assembly, as shown in Figure 10. While gripping the specimens, the actuator was programmed in load-control mode to prevent unnecessary preloading due to grip pressure. Static tests were conducted in displacement-control mode with a rate of 0.05 in/min, while acquiring data at a rate of 10 Hz.

Figure 10. MTS servo-hydraulic test frame.

2.2.5. Fatigue Life Evaluation

Fatigue tests were conducted in load-control mode with a frequency of 5 Hz. Fatigue specimens included several R-ratios that represented loading levels in different parts of the aircraft (section 2.1.2). Fatigue testing was conducted at three different stress levels with a minimum of six specimens per stress level to support the minimum requirements of individual Weibull analysis. Specimen compliance degradation was monitored throughout fatigue duration to examine damage evolution.

In order to investigate the damage progression, full-field strain data were interpreted according to the NDI method outlined by Tomblin et al. [52]. Both ARAMIS and C-scan data were used to establish guidelines for determining the fatigue failure of specimens that was not obvious, i.e., the four-point bend sandwich specimen did not indicate any sign of complete delamination across the width and continued to hold applied cyclic loading (Figure 11).

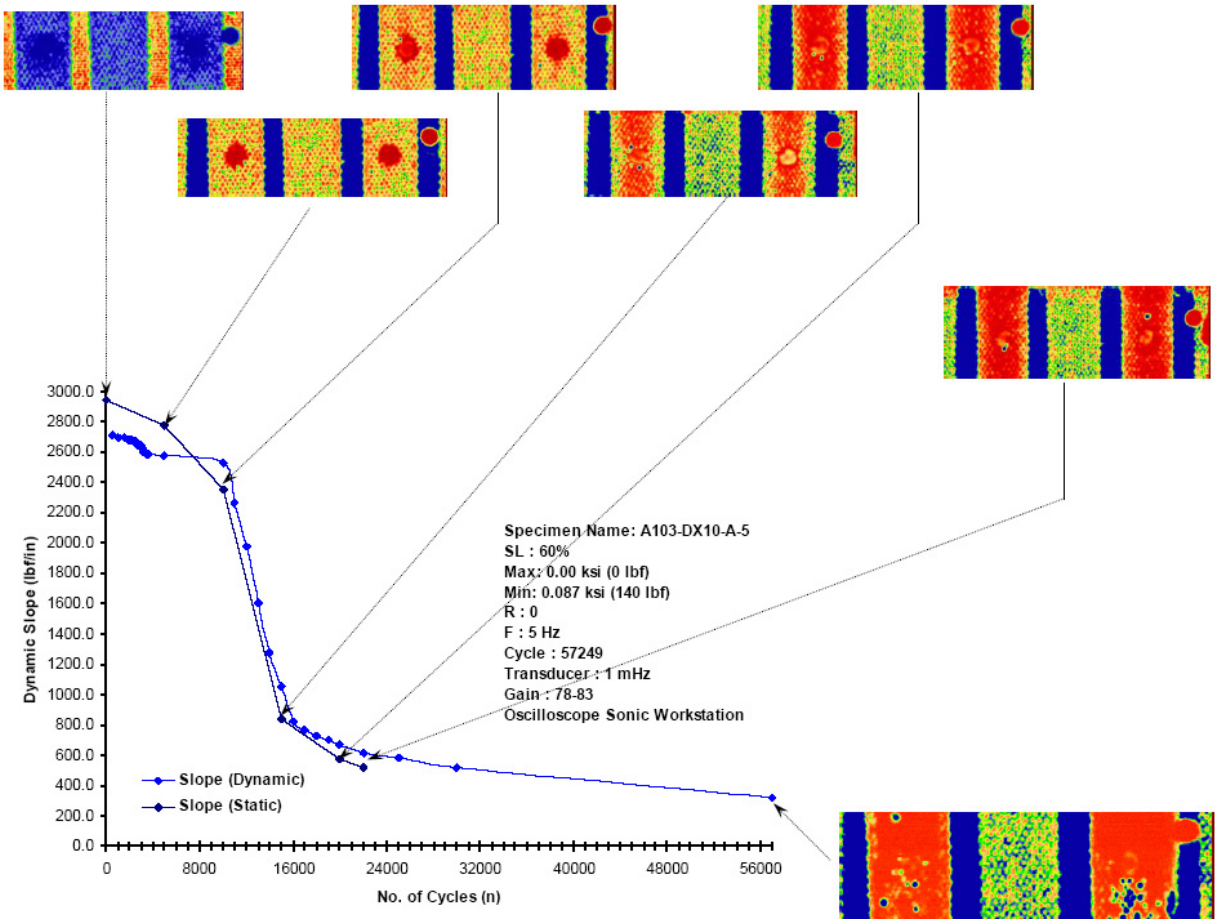

Figure 11. Compliance change and damage area during fatigue testing of 4PB sandwich specimen.

Anti-buckling fixtures were used for compression fatigue specimens such as OH, DNC, and CAI to prevent premature failure. The OHC fixture, which is designed for static tests, indicated wear, as the specimen compliance changed during fatigue testing and required modifications to prevent further damage to the fixture and load misalignment during fatigue testing. The change in temperature was monitored for several specimens with defects and found insignificant, i.e., less than 10°F.

Several trial specimens were used at the beginning of each loading mode and layup to determine appropriate stress levels so that at least two provided fatigue failures. Fatigue loads

for each specimen were calculated with respect to static strength using the actual specimen dimensions.

2.3. Full-Scale Test Substantiation

The Beechcraft Starship forward wing was designed with a significant amount of conservatism. Thus, the Beechcraft design limit and ultimate loads were adjusted following several static tests using a conversion factor (CF). These redefined limit and ultimate loads are referred to as NIAR research limit and ultimate loads (NRLL and NRUL, respectively). Full-scale tests were conducted to address four different aspects of certification of composite structures as shown in Figure 4: static, damage tolerance, durability, and repair.

For durability test articles with impact damages, the original whiffletree locations needed to be modified around damages so that the load was redistributed without significantly influencing the overall shear-moment-torque (SMT) loads. Since damages induced on the structure were significantly larger compared to the ones typically introduced during certification, aggressive NDI and health-monitoring strategies (sections 8.3 and 8.4) in addition to scheduled inspections were utilized. Once the load-enhancement factors were generated and CF was determined, the fatigue spectrum loads were generated so that the gross min/max loads were enhanced by preserving stress ratios.

CHAPTER 3

SCATTER ANALYSIS OF COMPOSITES

Compared to metal static and fatigue data, composite materials exhibit high data scatter due to their anisotropic heterogeneous characteristics such as layup, manufacturing defects and imperfections, test complications, environment, etc (Figure 12). In order to interpret this information in a meaningful manner and to incorporate any effects of this into the certification of composite structures, several approaches are used. Life factor, load enhancement factor, and the load-life combined approach are three of the commonly used approaches that require composite scatter analysis.

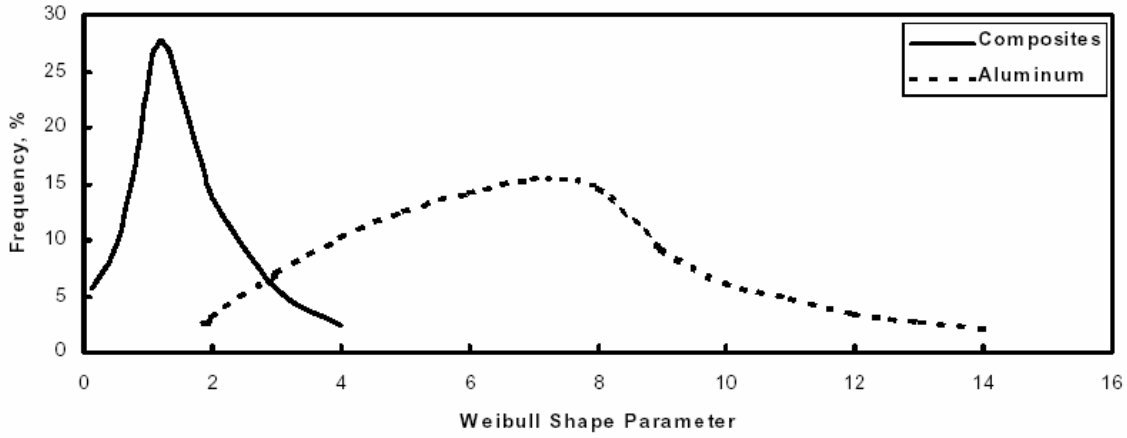

Figure 12. Life scatter in composites and metal [2].

3.1. Scatter Analysis

The primary goal in scatter analysis of composites is to interpret the variability in data in lower levels of the building blocks of testing and translate the statistical significance of such phenomenon into full-scale test substantiation. In order to determine the shape parameters for static strength and fatigue life for the purpose of full-scale test substantiation, test matrices must

be designed so that at least the design details and loading modes of critical locations of the structure are represented by coupon and/or element tests. The influence of material, layup sequence, loading mode, sandwich construction, joints, environmental effects, etc. is considered typically during static strength scatter analysis. Fatigue analysis includes the influence of the stress ratio in addition to the above-mentioned design details.

Scatter in composites can be analyzed as Weibull distribution or normal distribution. Due to simplistic functionality and the ability to handle smaller sample sizes, the two-parameter Weibull distribution is commonly used in composite static and fatigue analyses. Fatigue scatter in composite test data can be analyzed using several different techniques. These techniques are mainly subdivided into two categories: individual analysis and pooling. Joint Weibull and Sendeckyj are two pooling techniques discussed in this report.

First, the shape parameters corresponding different data sets representing different design detail are obtained using Weibull analysis, and then the shape parameter corresponding to their Weibull distribution, which is referred to as the static-strength or fatigue-life shape parameter, is obtained. In order to be conservative, the modal value of the distribution of shape parameters is selected as the strength or life shape parameter, rather than the mean value (Figure 13), and this is referred to as the modal static-strength shape parameter (MSSP) or modal fatigue-life shape parameter (MLSP), respectively.

Determination of fatigue life scatter requires a large number of test replications at different stress levels. In order to reduce cost and test duration, while maintaining the reliability of data analysis, it is recommended that the fatigue scatter analysis be conducted using pooling methods such as the joint Weibull or Sendeckyj wearout analysis.

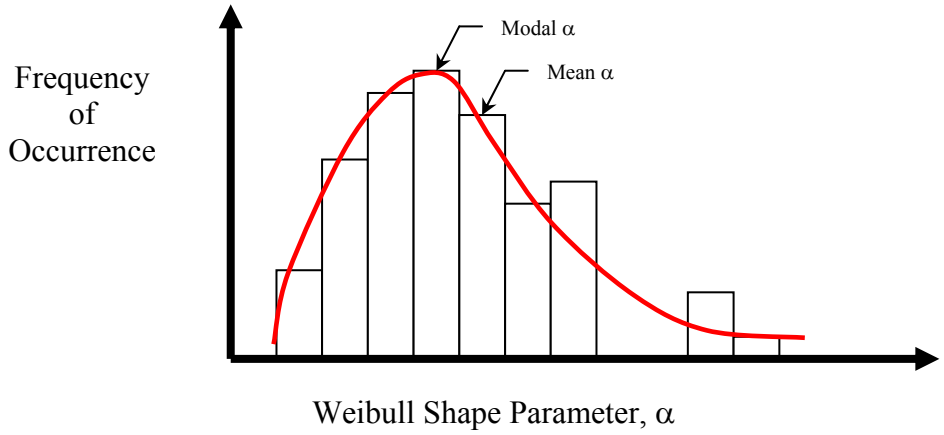

Figure 13. Scatter analysis using Weibull distribution of shape parameters.

3.1.1. Individual Weibull Method

Weibull distribution is used in statistical analysis of composites, especially for small samples, due to its simple functionality and ease of interpretation. The commonly used two-parameter Weibull distribution expressed by the cumulative survival probability function is shown as

$$P(X \le x) = e^{-(x/\beta)^{\alpha}} \tag{1}$$

where, x is the random variable, α is the shape parameter, and β is the scale parameter.

The population mean, μ, and standard deviation, σ, are calculated with the Gamma (Γ) distribution function, as in equation (2) and (3), respectively.

$$\mu = \beta \cdot \Gamma\left(\frac{\alpha+1}{\alpha}\right) \tag{2}$$

$$\sigma = \beta\sqrt{\Gamma\left(\frac{\alpha+2}{\alpha}\right) - \Gamma^2\left(\frac{\alpha+1}{\alpha}\right)} \tag{3}$$

The shape parameter and scale parameter are estimated from an iterative process using either the maximum likelihood estimation (MLE) or rank regression [53]. Rank regression in X

(RRX) tends to produce reliable results for small samples, while MLE works well for samples containing more than 20 or 30 data points.

During the individual Weibull analysis of fatigue data, each stress level is analyzed, and then the shape parameters are arithmetically averaged to define life scatter. Since Weibull analysis considers only the data at a certain stress level at a time, five or more data points must be included in each stress level. For S-N data that has less than five data points per stress level, either joint Weibull analysis or Sendeckyj analysis must be used.

3.1.2. Joint Weibull Method

In the joint Weibull analysis, M groups of data having a common shape parameter, but different scale parameters, are pooled [54]. The common shape and scale parameters are obtained using the joint maximum likelihood estimate method, as shown in equations (4) and (5).

$$\sum_{i=1}^{M}\left[\frac{\sum_{j=1}^{n_i} x_{ij}^{\alpha}\cdot\ln(x_{ij})}{\sum_{j=1}^{n_i} x_{ij}^{\alpha}}\right]-\frac{M}{\alpha}-\sum_{i=1}^{M}\left[\frac{\sum_{j=1}^{n_{fi}}\ln(x_{ij})}{n_{fi}}\right]=0 \tag{4}$$

$$\beta_i=\left(\frac{1}{n_{fi}}\cdot\sum_{j=1}^{n_i} x_{ij}^{\alpha}\right)^{1/\alpha} \tag{5}$$

where n_i = number of data points in the i^{th} group of data (i=1,2,….,M)

n_{fi} = number of failures in the i^{th} group of data (i=1,2,….,M)

3.1.3. Sendeckyj Equivalent Static Strength Model

The Sendeckyj equivalent static strength (wearout) model [22] uniquely relates the static strength and residual strength to fatigue life. Thus, the analysis pools static strength, fatigue life, and residual static strength data and converts it into equivalent static strength data. The basic Sendeckyj model is shown as

$$\sigma_e = \sigma_a \left[\left(\frac{\sigma_r}{\sigma_a} \right)^{1/S} + (N_f - 1) \cdot C \right]^S \tag{6}$$

where σ_e is the equivalent static strength, σ_a is the maximum applied cyclic stress, σ_r is the residual strength, N_f is the number of fatigue cycles, and S and C are Sendeckyj fitting parameters. Setting the maximum amplitude cyclic stress equal to residual strength for fatigue failures, the power law is obtained as

$$\sigma_a \cdot (1 - C + C \cdot N_f)^S = \sigma_u \tag{7}$$

where σ_u is the static strength.

Using Sendeckyj analysis, fatigue life and residual strength data for each S-N curve are converted into a pool of equivalent static strength data points. Then, this data set is fitted into a Weibull distribution to obtain the life shape parameter as described by Sendeckyj [22].

3.2. Life-Factor Approach

The life factor approach has been successfully used for metal to assure structural durability. In this approach, the structure is tested for additional fatigue life to achieve the desired level of reliability. The underlying objective of the life factor is to ensure that the design life is representative of the condition of the weakest member of the population after a specified life in service. This is graphically illustrated in Figure 14 in terms of B-basis statistics, i.e., successful repeated load test to mean fatigue life would demonstrate B-basis reliability on design lifetime.

The ratio of the mean repeated load life to A- or B-basis repeated life is defined as life factor, N_F, and given by equation (8). The derivation of the general form of this equation is included in section 7.3.

$$N_F = \frac{\Gamma\left(\frac{\alpha_L + 1}{\alpha_L}\right)}{\left\{\frac{-\ln(R)}{\left[\chi^2_\gamma(2n)/2n\right]}\right\}^{1/\alpha_L}} \tag{8}$$

where α_L is the modal life shape parameter (MLSP), n is the number of articles, and R is the reliability. For γ=0.95, A- and B-basis reliabilities are 0.99 and 0.90, respectively. $\chi^2_\gamma(2n)$ is the Chi-square distribution with $2n$ degrees of freedom at γ level confidence.

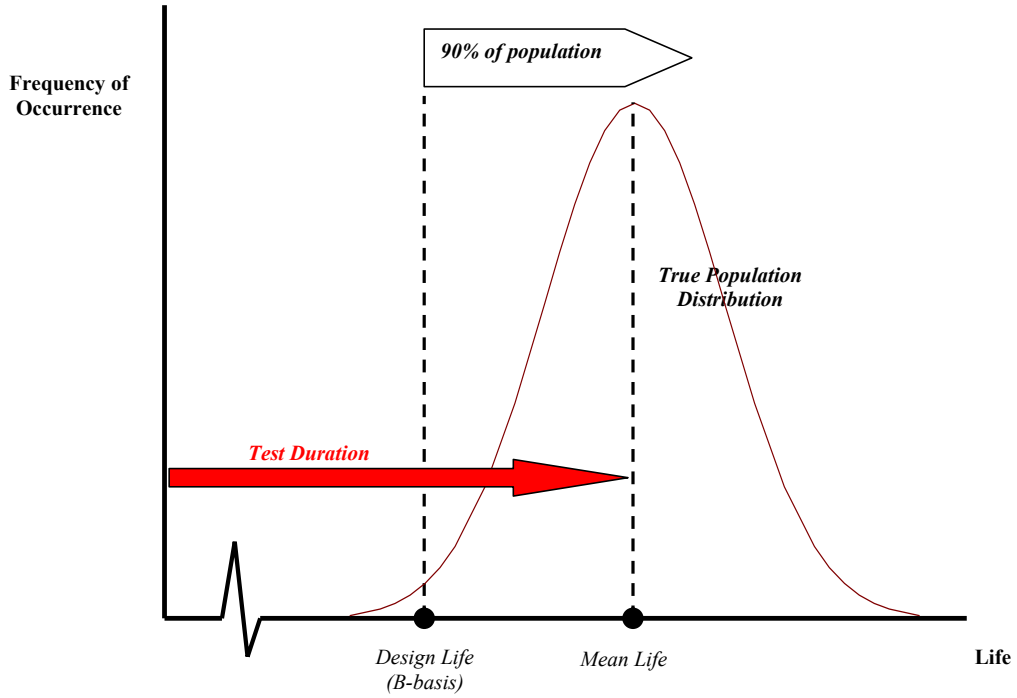

Figure 14. Life-factor approach for substantiating.

Figure 15 shows the influence of the shape parameter on the life factor, which is the ratio between mean repeated life to B-basis life [2]. This figure shows that the life factor rapidly increases for fatigue life shape parameters that are less than 2. Due to large scatter in the composite test data, the life shape parameter of composite was found to be 1.25 for the data

analyzed for the NAVY approach, while it was found to be 4.00 for metal. Therefore, a composite structure is required to test additional fatigue life to achieve the desired level of reliability, i.e., test duration of more than 13 design lifetimes (DLTs) for composite in contrast to 2 DLT for metal. As can be seen in equation (8), life factor is a function of MLSP. Thus, improvements in MLSP for newer forms of materials that exhibit less scatter can significantly reduce the life factor.

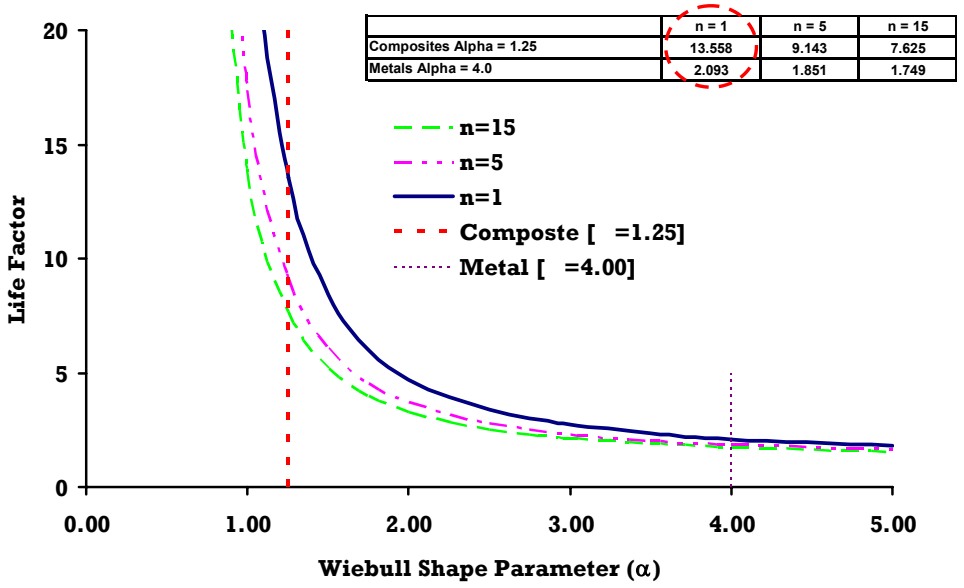

Figure 15. Influence of fatigue life shape parameter on life factor.

Furthermore, the analysis in section 6.2.3 shows that the data scatter of notched or damaged composite elements can be significantly less than that of the unnotched composite specimens. Such improvements in fatigue-life shape parameter can significantly reduce the life factor. However, the life factor becomes insensitive to small changes in the life-shape parameter beyond a value of 4, which is considered to be the life-shape parameter for metal. The composite modal life-shape parameter of 1.25, which was used for the NAVY approach, lies within the highly sensitive region of life factor vs. shape parameter curve (Figure 15), thus even

a small improvement resulted in a dramatic reduction of life factor, which reflects the required number of test durations to achieve a certain level of reliability in the design life. The modal life-shape parameter is obtained from a distribution of shape parameters representing numerous S-N curves of different critical structural details. Thus, it is common to have large scatter in S-N data of design details that have competing failure modes and less scatter in notched test data due to stress concentration. For example, a V-notched rail shear test specimen that has a soft (10/80/10) laminate stacking sequence has majority of its fibers aligned with the tensile and compressive load resultant axes during in-plane shear loading. Although the applied (external) load is an in-plane shear load, the tensile and compressive (internal) loads along fiber directions often cause a fiber break and fiber buckling, respectively, and significantly contribute to the final failure. In some cases, the competing (tensile and compressive) loading configurations will result in unacceptable failure modes of these in-plane shear specimens. Often, the complex state of stress and these competing failure modes coupled with other variabilities associated with composites such as batch variability, porosity, and fiber misalignments tend to cause large scatter in both static strength and fatigue life. On the other hand, the stress concentrations in notched composite cause the final failure of the specimen negating or minimizing the collective effects of the above-mentioned secondary variables.

3.3. Load-Factor Approach

An alternative approach to the life factor, which requires an excessive test duration, is to increase the applied loads in the fatigue spectrum so that the same level of reliability can be achieved with a shorter test duration [2]. This approach is referred to as the load enhancement factor (LEF) approach. A formal relationship between LEF and the test duration, N, as shown in equation (9), is formed for composite structural certification [2].

$$LEF(N) = \frac{\Gamma\left(\frac{\alpha_L + 1}{\alpha_L}\right)^{\alpha_L/\alpha_R}}{\left\{\frac{-\ln(R)\cdot N^{\alpha_L}}{\left[\chi^2_\gamma(2n)/2n\right]}\right\}^{1/\alpha_R}} \tag{9}$$

LEF for test duration of 1 DLT, referred to as load factor (*LF*), is calculated as

$$LF = \lambda \cdot \frac{\Gamma\left(\frac{\alpha_R + 1}{\alpha_R}\right)}{\left\{\frac{-\ln(R)}{\left[\chi^2_\gamma(2n)/2n\right]}\right\}^{1/\alpha_R}} \tag{10}$$

where, α_R is the modal static strength shape parameter (MSSP), and λ is a function of both MSSP and MLSP, as defined in equation (11). Equation (10) has the same form as equation (8), except α_L is replaced by α_R, and the new parameter λ is included so that both life factor and load factor have the same level of reliability.

$$\lambda = \frac{\Gamma\left(\frac{\alpha_L + 1}{\alpha_L}\right)^{\alpha_L/\alpha_R}}{\Gamma\left(\frac{\alpha_R + 1}{\alpha_R}\right)} \tag{11}$$

3.4. Combined Load-Life Approach

The life-factor approach requires an excessive test duration and, by itself, may not be practical for full-scale test demonstration. In contrast, the load factor approach requires increasing the fatigue loads so that the same level of reliability can be achieved with one test duration. However, for hybrid structures, overloads may cause crack growth retardation, buckling, and premature failure of some of the metal components. Another approach, which has

been applied in the past, is a combined approach using load and life factors, which is the general form of LEF given in equation (9). The procedure in this approach would be to apply a combined life factor with the load factor to achieve a compromise in the full-scale test requirements as well as the load spectrum. This approach allows using a lower load-enhancement factor as a trade-off for more life cycles, which would reduce the severity of the overload on the metallic parts.

By combining equations (8) and (9), the LEF is defined in terms of test duration, as shown in equation (12). This is a condensed form of equation (9).

$$LEF = \left(\frac{N_F}{N} \right)^{\frac{\alpha_L}{\alpha_R}} \tag{12}$$

As shown in Figure 16, LEF is significantly influenced by MSSP and MLSP. Thus, improvements in these shape parameters for newer forms of materials that exhibit less scatter can significantly reduce LEF.

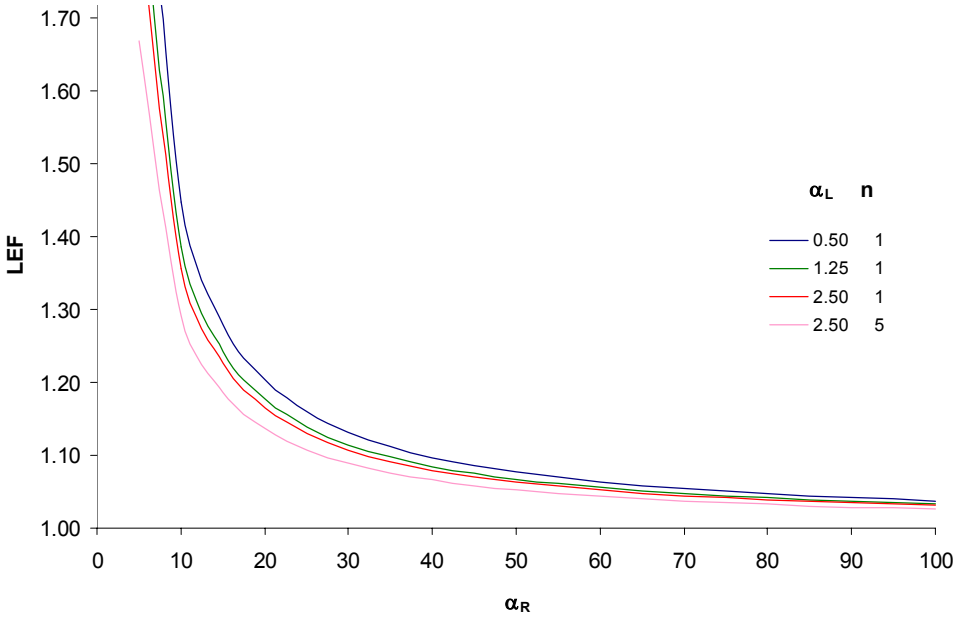

Figure 16. Influence of strength and life parameter on LEF.

As shown in Figure 17, a significant reduction in LEF is achieved simply by increasing the test duration to 1.5 DLT. Furthermore, the influence of strength and life shape parameter on

LEF changes as the test duration is increased. For example, as the test duration is increased, the influence of the fatigue-life shape parameter on LEF increases. This is understood, as N_F is only influenced by MLSP. Also, note for small test durations, the influence of MSSP on LEF is significant due to the increased influence of load factor.

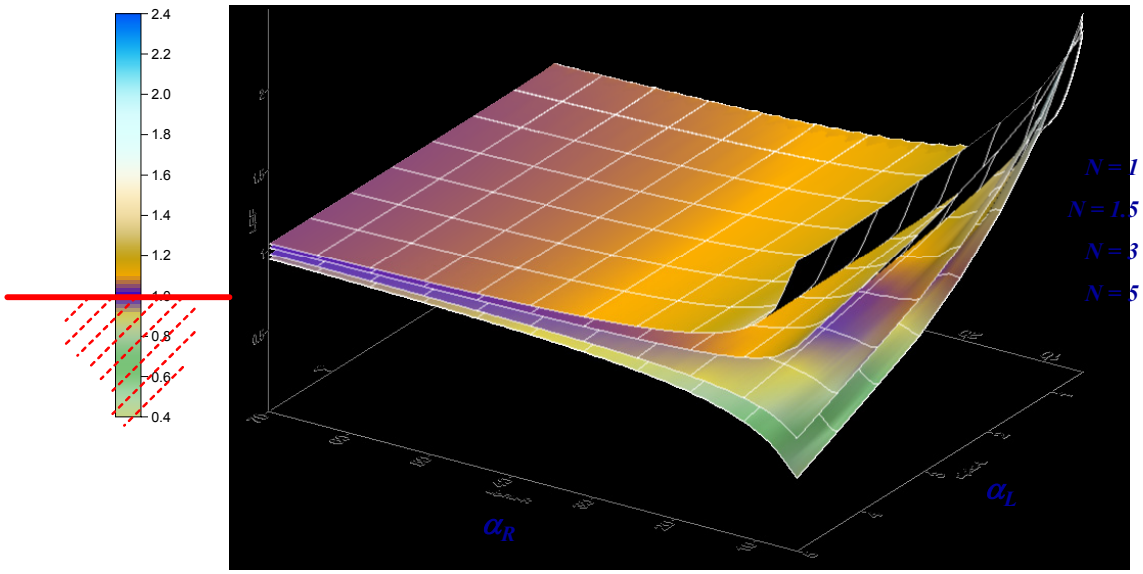

Figure 17. Influence of MSSP and MLSP on LEF (combined load-life approach).

Application of the combined load-life approach is illustrated in Figure 18. The LEF is calculated as the ratio of the maximum applied load to the design maximum fatigue stress. This curve is generated by calculating LEF for several different test durations. Note that the LEF required for the test duration that is equal to the life factor, N_F, is one, and N_F is obtained from Figure 15 for the corresponding fatigue-life shape parameter. If the design maximum load in the repeated load test (P_F) is increased to the mean residual strength at one lifetime (P_T), then the A- or B-basis residual strength of the structure would be equivalent to the design maximum fatigue stress. Thus, a successful repeated load test to one lifetime at applied stress, P_T, or a repeated test to N_F at applied stress P_F (no LEF) would both demonstrate the corresponding reliability.

Furthermore, a successful repeated load test to a test duration (less than N_F) with the corresponding LEF would demonstrate the same level or reliability on the design lifetime.

The combined load-life approach can be used in two different ways: (1) apply the same LEF, which is calculated for a certain test duration, to the entire spectrum or (2) apply a different LEF for different load blocks in the spectra based on the severity of enhanced load, i.e., cycles that have high loads are repeated for a longer test duration (with lower LEF) than the rest of the spectrum. This approach is particularly useful for hybrid structures that exhibit metallic component failure due to high LEF (overloads) and to avoid premature failure due to buckling. Both of these applications are illustrated in Figure 19.

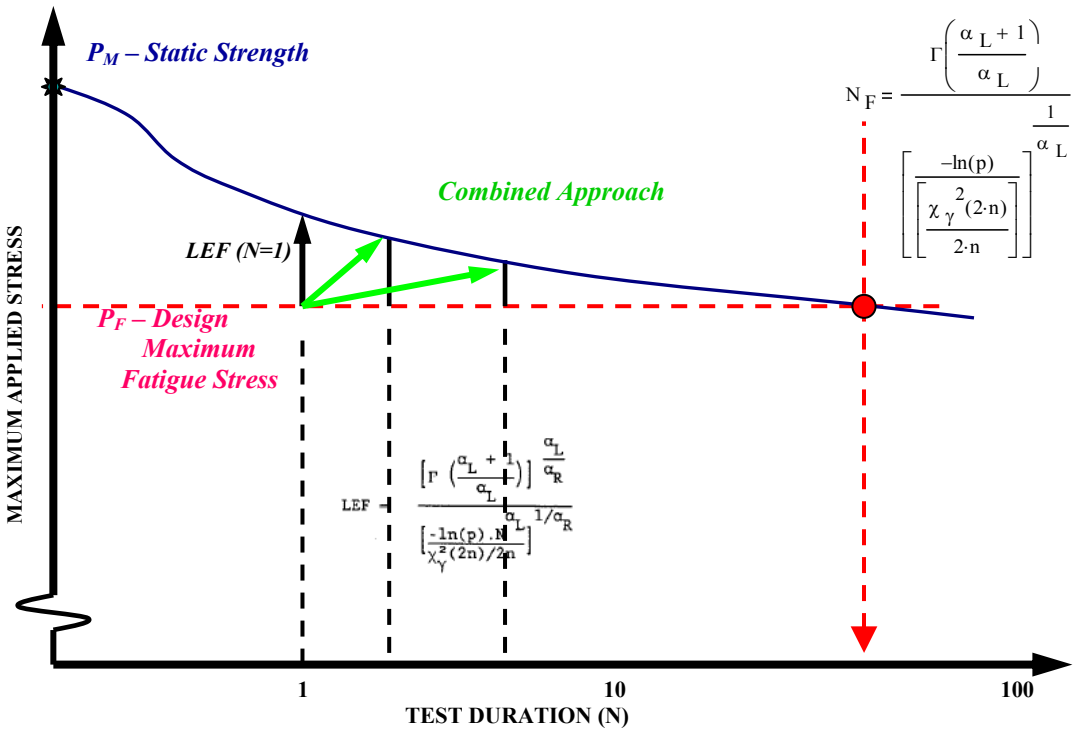

Figure 18. Combined load-life approach for composite structures.

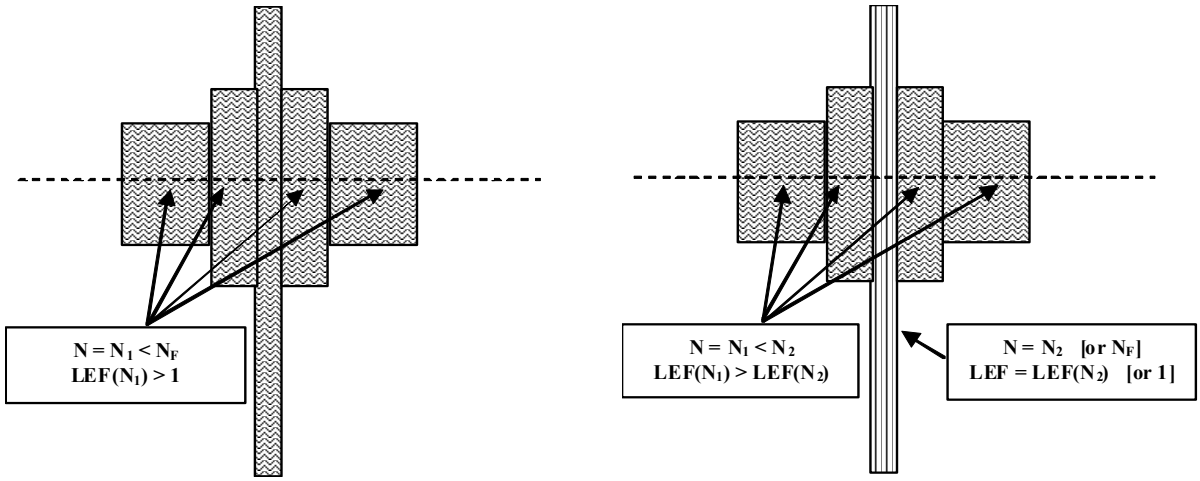

(a) Combined load-life test (b) Combined load-life spectrum

Figure 19. Application of combined load-life approach.

One common practice for composite full-scale test substantiation is a two-lifetime test, which is adopted from metallic structural certification (Figure 15) using the design spectrum with the corresponding LEF under room temperature ambient test conditions. Often times, the test duration of 1.5 DLT is used with corresponding LEF. The LEF approach accounts for the variability in design details and loading modes. In order to account for the service environmental effects on composite, additional factors are calculated from the design allowable tests. These additional factors for composite structures account for the difference between composite and metallic structure during design and analysis, and are beyond what is normally done for metallic certifications. Such factors, accounting for both moisture and temperature effects on composites, significantly depend on the material system and the layup configuration, and can be as high as 1.4.

In order to reduce the test duration, the fatigue test spectrum is truncated by eliminating the segments with stress levels below an endurance limit (stress level corresponds to an infinite

life). The endurance limit of a particular composite material varies based on the parameters such as the layup configuration, test environment, stress ratio. The S-N curves that are generated to obtain the life shape parameters can be used to determine the endurance limit for different design details of a composite structure. The life factor and/or load-enhancement factor are to be applied after truncation of the load spectrum as shown in Figure 20.

Composite material properties are susceptible to heat and moisture. Therefore when a full-sale test is conducted at RTA conditions, environmental compensation factors are applied to the load spectrum. The environmental factors are recommended to be applied to the truncated load spectrum. Although this approach provides an efficient way to assure the structural life reliability, the cumulative effects of the above-mentioned enhancement factors may result in an undesirably high cumulative load enhancement factor. For these cases, an approach similar to Figure 19(b) is recommended to reduce the required LEFs for high spectrum loads, i.e., test for additional life. However, these additional high-stress cycles must be spread throughout the spectrum so that the damage growth mechanism is not adversely altered, and the practical limits of spectrum load sequence must be preserved. Although there are not significant load-sequencing effects on fatigue life, composites are extremely sensitive to variation in the number of high loads in the fatigue spectrum [2]. It is imperative that the effects of these parameters do not change the fatigue failure mode (and the failure mechanism) or reach static strength of the structure. Furthermore, the application of load enhancements must preserve the stress ratio of each load cycle throughout the spectrum as discussed in section 8.1.5.

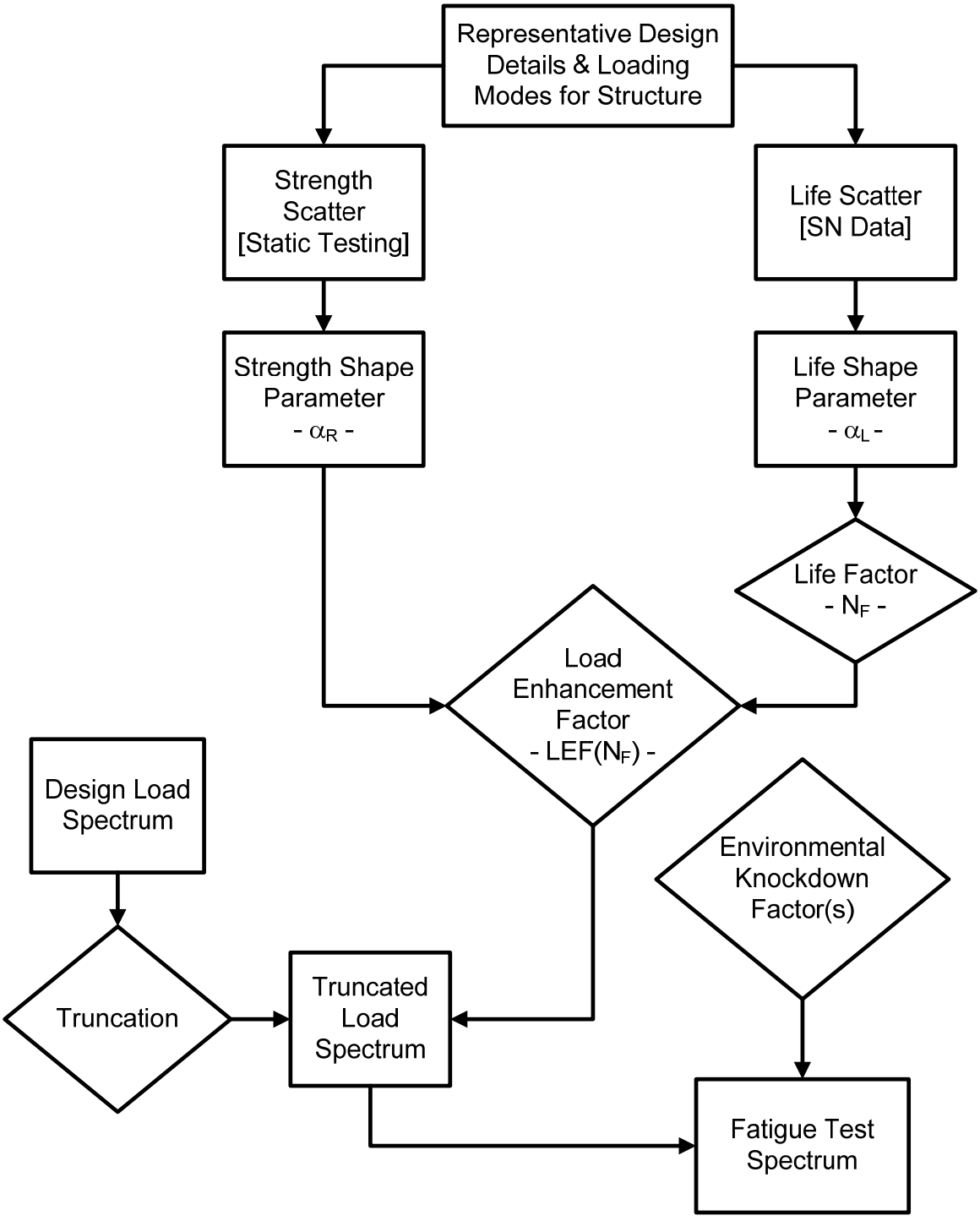

Figure 20. Fatigue test spectrum development for composite structural test.

3.5. Scatter Analysis Computer Code (SACC)

The scatter analysis conducted for this report was carried out by using a combination of Microsoft Excel, Visual Basic, and ReliaSoft Weibull software. Sendeckyj analysis was coded in a Microsoft .NET Framework software. In order to alleviate the dependency on multiple software packages, the complete analysis with multiple analysis options was coded using Microsoft Visual Basic that could be run in Excel.

A user-friendly computer code, Scatter Analysis Computer Code (SACC), was developed (Figure 21) so that the fatigue test data could be analyzed using the individual Weibull distribution, joint Weibull distribution, and Sendeckyj equivalent static strength model. This program is designed to guide the analyst to select the most suitable approach for a given set of test data.

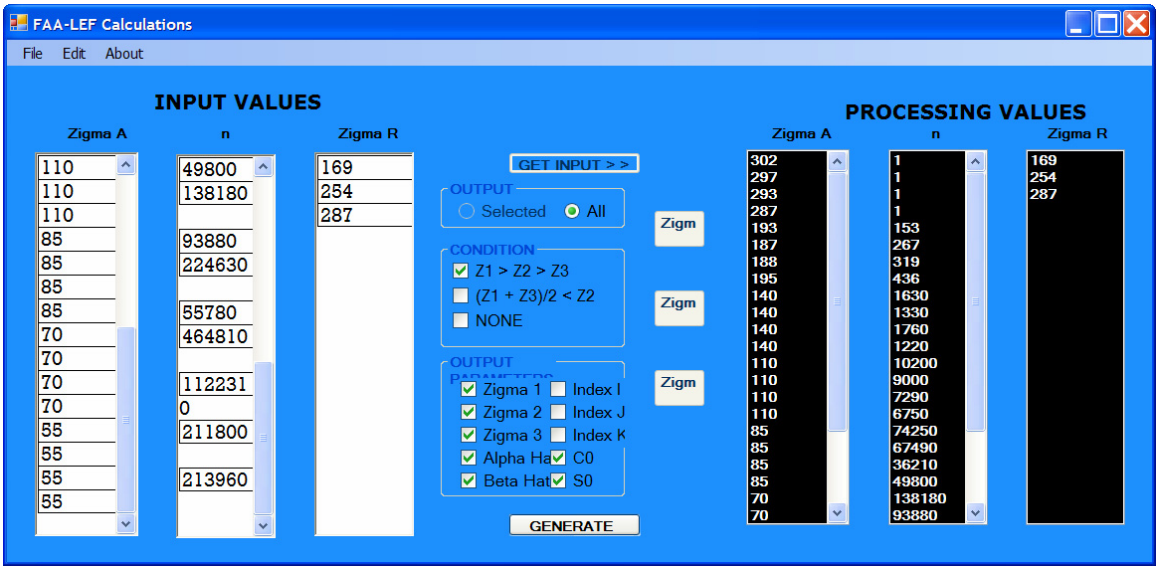

Figure 21. Sendeckyj analysis using SACC.

CHAPTER 4

STATIC STRENGTH DATA SCATTER ANALYSIS

An extensive static scatter analysis was conducted to support U.S. Navy F/A-18 certification [2] on several material databases. These data represented several structural details and variables such as laminate layup, loading mode, load transfer, specimen geometry, and environment. For increasing the accuracy of Weibull analysis, only the datasets containing six or more specimens were included. Also, the Navy program only included autoclaved 350°-cure graphite-epoxy materials. This analysis was conducted primarily on fiber-dominated failures. In addition, these data were summarized primarily for laminated construction and did not include sandwich construction or bonded joints. The goal of the current research was to produce data for materials commonly used in aircraft applications and to promote the development of this type of data, not only for individual certification plans but also for shared databases as well.

4.1. Structural Details for Static Scatter Analysis

The current research obtained the static data points from several material databases, which are described in section 2.1.1. These data included additional details such as bonded joints, sandwich details, impact damage, disbonds, lightening strikes, process variability, in-plane shear and interlaminar shear specimens, in addition to the variables studied in the Navy F/A-18 certification program. These structural details were included in the analysis to represent design variables/details in present aircraft applications. Data generated from coupons and elements were used to investigate the dependence of the static-strength shape parameter, which is a representation of static data scatter, on various coupon geometries, loading modes, environments, and layups. The degree to which these parameters affect the overall LEF factors from a parametric basis is discussed in section 5.4. Several examples are shown for obtaining MSSP or

α_R by pooling different data sets. When pooling data to estimate MSSP, the user is advised to select appropriate design details that are applicable to a certain application.

The material databases described in this section were selected primarily to support the full-scale structure tests included in section 8. These materials are used in several ongoing certification programs and certified general aviation aircraft. The databases include coupon-level static-strength data for the following primary variables:

1. Different layups – hard, quasi-isotropic, and soft (typically 50/40/10, 25/50/25, and 10/80/10, respectively, for unidirectional material and 40/20/40, 25/50/25, and 10/80/10, respectively, for fabric material) and all ±45° plies (0/100/0)
2. Environments – CTD, RTA, RTW, ETD, ETW
3. Tension – no hole, open hole, filled hole
4. Compression – no hole, open hole, filled hole
5. Bearing – single shear, double shear, bearing-bypass
6. In-plane shear – V-notched rail shear
7. Interlaminar shear – double-notched compression, short-beam shear

In addition to the coupon-level data, element-level static-strength data were included in the analysis that represents the following design details/requirements:

1. Sandwich – core materials, face sheet
2. Bonded joints – single-lap shear, picture frame
3. Damage tolerance – CAI, TAI, sandwich
4. Four-point bending – laminate, sandwich

The following sections include the generation of the shape parameter for several different material systems along with knowledge of the effects of different geometries, environments, layups, and loading modes.

4.1.1. AS4/E7K8 3K Plain-Weave Fabric

Static strength results of AS4/E7K8 plain-weave fabric (AS4-PW) for both RTA and ETW environmental conditions are shown in Table 5.

TABLE 5

STATIC STRENGTH TEST RESULTS FOR AS4-PW

Specimen Configuration		RTA Strength (ksi)			ETW Strength (ksi)		
Layup	**Test Description**	**Average**	**STDEV**	**CV**	**Average**	**STDEV**	**CV**
10/80/10	OHT	43.455	0.773	1.778	35.175	0.296	0.842
	OHC	40.472	1.571	3.882	28.579	1.156	4.045
	SLS–C (t=0.01”)	5.532	0.381	6.880			
	SLS–T (t=0.01”)	4.528	0.163	3.601			
	SLS–T (t=0.01”) No anti-buckling	2.301	0.058	2.532			
	SLS–T (t=0.06”)	5.057	0.591	11.685	2.038	0.330	16.196
	DNC	3.988	0.160	4.022	3.004	0.154	5.130
	CAI – BVID (20 plies)	34.605	1.541	4.454			
	CAI – VID (40 plies)	30.263	0.814	2.690			
Sandwich	4PB – HRH 10	0.145	0.003	2.071	0.128	0.003	2.388
0/100/0	TAI – BVID	21.875	0.350	1.600	11.912	1.295	10.876
	TAI – VID	15.118	0.626	4.143			
	OHC	17.799	0.387	2.172			
25/50/25	OHC	45.375	1.624	3.579	32.019	1.347	4.208
	Unimpacted	55.736	0.839	1.505			
	CAI – BVID	36.025	0.851	2.361			
	CAI – VID	29.671	0.891	3.003			
	CAI – LID	25.445	0.692	2.721			
40/20/40	CAI – VID	31.845	1.026	3.223			

Using ReliaSoft® Weibull software, the shape parameter (α) and the scale parameter (β) of each data set was obtained and shown in Table 6.

TABLE 6

WEIBULL PARAMETERS FOR STATIC STRENGTH DISTRIBUTIONS OF AS4-PW

Specimen Configuration		Test Environment	Weibull Statistics		
Layup	**Test Description**		**α**	**β (ksi)**	**n**
10/80/10	OHT	RTA	58.036	43.826	6
		ETW	61.970	35.653	6
	OHC	RTA	26.930	41.205	6
		ETW	33.290	29.081	8
	SLS–C (t=0.01")	RTA	22.665	5.683	6
	SLS–T (t=0.01")	RTA	31.165	4.602	5
	SLS–T (t=0.01") No anti-buckling	RTA	40.072	2.239	6
	SLS–T (t=0.06")	RTA	12.358	5.286	6
		ETW	6.919	2.174	8
	DNC	RTA	28.130	4.061	6
		ETW	23.845	3.072	6
	CAI – BVID (20 plies)	RTA	35.461	35.185	3*
	CAI – VID (40 plies)	RTA	49.383	30.608	6
Sandwich	4PB – HRH 10	RTA	47.621	0.146	6
		ETW	43.177	0.129	6
0/100/0	TAI – BVID	RTA	44.694	17.992	5
	TAI – VID	RTA	34.344	15.379	6
	OHC	RTA	63.247	22.046	6
		ETW	11.766	12.431	5
25/50/25	OHC	RTA	33.424	46.101	6
		ETW	28.157	32.613	6
	CAI – BVID[#]	RTA	45.771	36.413	6
	CAI – VID[#]	RTA	32.222	30.103	6
	CAI – LID[#]	RTA	36.676	25.776	6
40/20/40	CAI – VID	RTA	32.984	32.324	6

* Not included in the combined analysis to obtain MSSP.
[#] Tests included in damage-tolerance section and not included in MSSP. Further details may be found in Chapter 6.

Weibull statistics obtained from maximum-likelihood estimate (MLE) and both X and Y rank regression (RRX and RRY, respectively) are shown in Table 7.

TABLE 7

WEIBULL STATISTICS FOR COMBINED DISTRIBUTION OF SCATTER IN STATIC STRENGTH DISTRIBUTIONS OF AS4-PW

Analysis Method	Weibull Parameter	Analysis Cases		
		All	RTA	ETW
MLE	α	2.514	3.1323	1.782
	β	39.387	41.777	33.629
	α_{Modal}	32.193	36.950	21.183
RRX	α	2.188	2.900	1.441
	β	39.882	41.980	34.452
	α_{Modal}	30.167	36.284	15.148
RRY	α	2.103	2.790	1.417
	β	40.285	42.288	34.665
	α_{Modal}	29.644	36.068	14.621

The probability density function of Weibull shape parameters and the reliability plot for both RTA and ETW static data (combined case denoted as All) is shown in Figure 22. The shape and scale parameters for this distribution from MLE are 2.514 and 39.387, respectively. The corresponding modal value is 32.193. The difference between Weibull statistics obtained from different analysis methods is least significant for the RTA dataset, while it is most significant for the ETW dataset. The scatter in ETW datasets is reflected in the combined case for all three analysis methods. Statistics from MLE portray the least scatter for all three cases, while RRY portrays the most scatter. However, the 90% confidence bounds on reliability from all three analysis methods for the combined dataset do not vary significantly (Figure 22 shows confidence bounds for MLE).

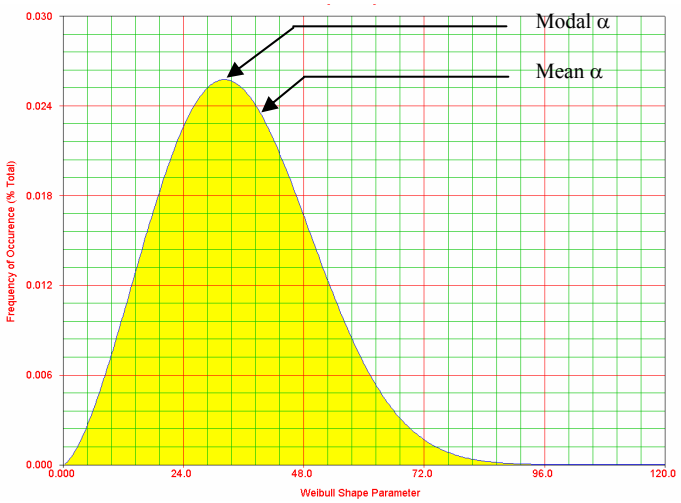

(a)

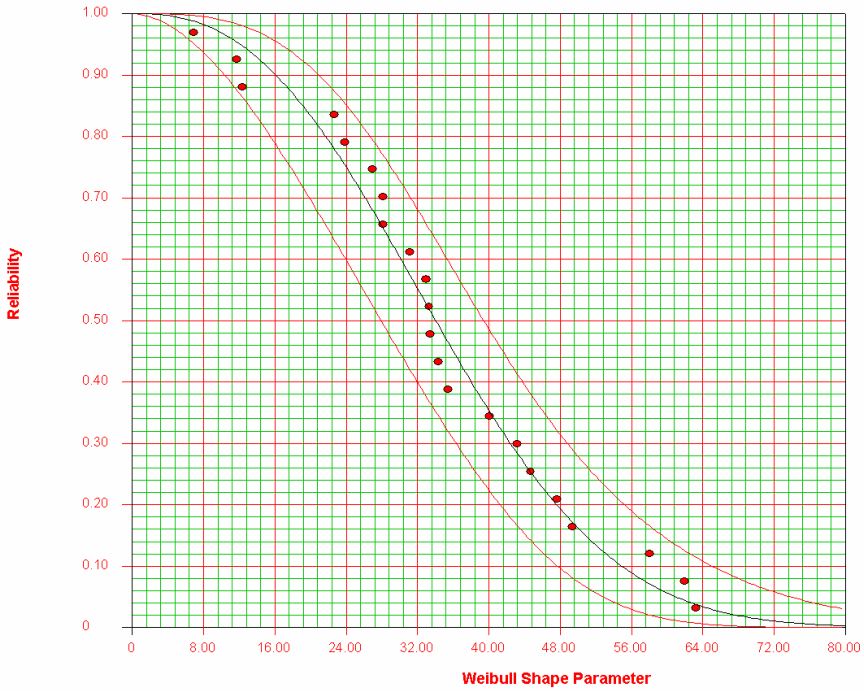

(b)

Figure 22. (a) Probability density function and (b) reliability plot of shape parameters for AS4-PW static strength distributions

For large datasets, i.e., more than 20-30 samples, MLE produces reliable Weibull statistics, while for small datasets, RRX tends to produce relatively accurate data. This will be further investigated during this research in terms of the reliability of analysis results. Consequently, a procedure to obtain reliable Weibull statistics and recommendations will be documented in the final report along with examples and case studies for typical aircraft applications. For example, if the structure does not contain adhesive joints, the shape parameters for adhesive static strength distributions do not have to be pooled to determine MSSP.

4.1.2. T700/#2510 Plain-Weave Fabric

Toray T700/#2510 plain-weave fabric (T700-PW) data from several material databases (section 2.1.1) are analyzed in this section. Static strength results obtained from FAA-LEF data are shown in Table 8.

TABLE 8

STATIC-STRENGTH TEST RESULTS FOR T700-PW

Specimen Configuration		RTA Strength (ksi)			ETW Strength (ksi)		
Layup	**Test Description**	**Average**	**STDEV**	**CV**	**Average**	**STDEV**	**CV**
10/80/10	OHT	41.686	0.889	2.133	38.961	0.886	2.273
	OHC	34.986	0.923	2.639	28.626	0.788	2.752
	SLS-T (t=0.06")	5.064	0.197	3.900			
	DNC	3.007	0.197	6.568	3.242	0.179	5.530
40/20/40	CAI – BVID	43.408	0.610	1.405			
Sandwich	4PB – HRH 10	0.137	0.003	2.333	0.125	0.005	3.626

The corresponding Weibull statistics are shown in Table 9 along with the number of specimens used for analysis. Although the Weibull analysis was conducted for 40/20/40 CAI specimens, the shape parameter was not included in the analysis for calculating MSSP of AS4-PW because this data set has less than the minimum recommended number of specimens for a reliable analysis.

TABLE 9

WEIBULL PARAMETERS FOR STATIC-STRENGTH DISTRIBUTIONS OF T700-PW

Specimen Configuration		Test Environment	Weibull Statistics		
Layup	**Test Description**		α	β **(ksi)**	**n**
10/80/10	OHT	RTA	48.872	42.108	6
		ETW	45.242	39.387	6
	OHC	RTA	41.540	35.408	6
		ETW	40.170	28.989	7
	SLS-T (t=0.06)	RTA	36.927	5.144	6
	DNC	RTA	17.989	3.094	6
		ETW	25.000	3.317	6
40/20/40	CAI	RTA	67.713	43.700	3*
Sandwich	4PB – HRH 10	RTA	42.068	0.139	6
		ETW	42.190	0.127	6

* Not included in combined analysis

FAA-LVM data [44] that contain additional 48 datasets containing 863 specimens for T700-PW [44] were added to the static-strength scatter analysis. These datasets represent hard or 40/20/40 (Table 10), quasi-isotropic or 25/50/25 (Table 11), and soft or 10/80/10 (Table 12) layup sequences, as well as a wide range of loading modes and environmental conditions (CTD, RTA, and ETW). Furthermore, each dataset contains specimens from three distinct material batches.

Distribution of shape parameters calculated for T700-PW using the static data in FAA-LEF and FAA-LVM are shown in Figure 23. The scatter in shape parameters of 10/80/10 laminate is significantly higher than that for the other two laminate stacking sequences.

TABLE 10

WEIBULL PARAMETERS FOR STATIC-STRENGTH DISTRIBUTIONS OF 40/20/40 T700-PW (FAA-LVM)

Test Description	Test Environment	Shape Parameter, α	Number of Specimens
Single-Shear Bearing Tension	RTA	45.409	18
Double-Shear Bearing Tension	RTA	49.696	30
Bearing-Bypass 50% Compression	RTA	42.102	15
Bearing-Bypass 50% Tension [t/D=0.475]	RTA	40.040	18
Bearing-Bypass 50% Tension [t/D=0.570]	RTA	42.594	18
Bearing-Bypass 50% Tension [t/D=0.712]	RTA	43.426	15
Bearing-Bypass 50% Tension [t/D=0.949]	RTA	38.198	18
No-Hole Tension	RTA	29.820	18
No-Hole Compression	RTA	20.584	18
Open-Hole Compression	RTA	30.453	19
Filled-Hole Tension	CTD	29.908	19
Filled-Hole Tension	RTA	20.296	19
Filled-Hole Tension	ETW	25.192	18
V-Notched Rail Shear	RTA	59.208	18
Open-Hole Tension [w/D=3]	RTA	20.594	18
Open-Hole Tension [w/D=4]	RTA	27.054	18
Open-Hole Tension [w/D=6]	RTA	27.202	20
Open-Hole Tension [w/D=8]	RTA	25.441	18

TABLE 11

WEIBULL PARAMETERS FOR STATIC-STRENGTH DISTRIBUTIONS OF 25/50/25 T700-PW (FAA-LVM)

Test Description	Test Environment	Shape Parameter, α	Number of Specimens
Double-Shear Bearing Tension	CTD	25.721	18
Double-Shear Bearing Tension	RTA	43.827	18
Double-Shear Bearing Tension	ETW	34.775	18
Single-Shear Bearing Tension	CTD	28.956	18
Single-Shear Bearing Tension	RTA	18.132	18
Single-Shear Bearing Tension	ETW	33.850	18
Bearing-Bypass 50% Tension	RTA	44.264	15
Bearing-Bypass 50% Compression	RTA	48.028	15
Open-Hole Tension [w/D=6]	CTD	35.816	18
Open-Hole Tension [w/D=6]	RTA	34.049	18
Open-Hole Tension [w/D=6]	ETW	25.223	21
No-Hole Tension	CTD	51.153	18
No-Hole Tension	RTA	40.186	18
No-Hole Tension	ETW	38.383	18
No-Hole Compression	CTD	31.498	18
No-Hole Compression	RTA	27.074	18
No-Hole Compression	ETW	23.676	19
Open-Hole Compression	CTD	34.475	19
Open-Hole Compression	RTA	46.999	18
Open-Hole Compression	ETW	33.319	21
V-Notched Rail Shear	RTA	16.458	18

Shape parameters obtained from static strength distributions were combined for several different analysis scenarios to investigate the degree to which these parameters affect the MSSP of T700-PW (Table 13). Adhesively bonded T700-PW element data from FAA-EOD material database are included in section 4.1.9.

TABLE 12

WEIBULL PARAMETERS FOR STATIC-STRENGTH DISTRIBUTIONS OF 10/80/10 T700-PW (FAA-LVM)

Test Description	Test Environment	Shape Parameter, α	Number of Specimens
Bearing-Bypass 50% Tension	RTA	65.445	15
Bearing-Bypass 50% Compression	RTA	74.360	15
Open-Hole Tension [w/D=6]	RTA	51.713	8
No-Hole Tension	RTA	58.084	19
No-Hole Compression	RTA	36.056	18
Open-Hole Compression	RTA	50.909	18
V-Notched Rail Shear	CTD	9.963	18
V-Notched Rail Shear	RTA	17.278	19
V-Notched Rail Shear	ETW	13.103	18

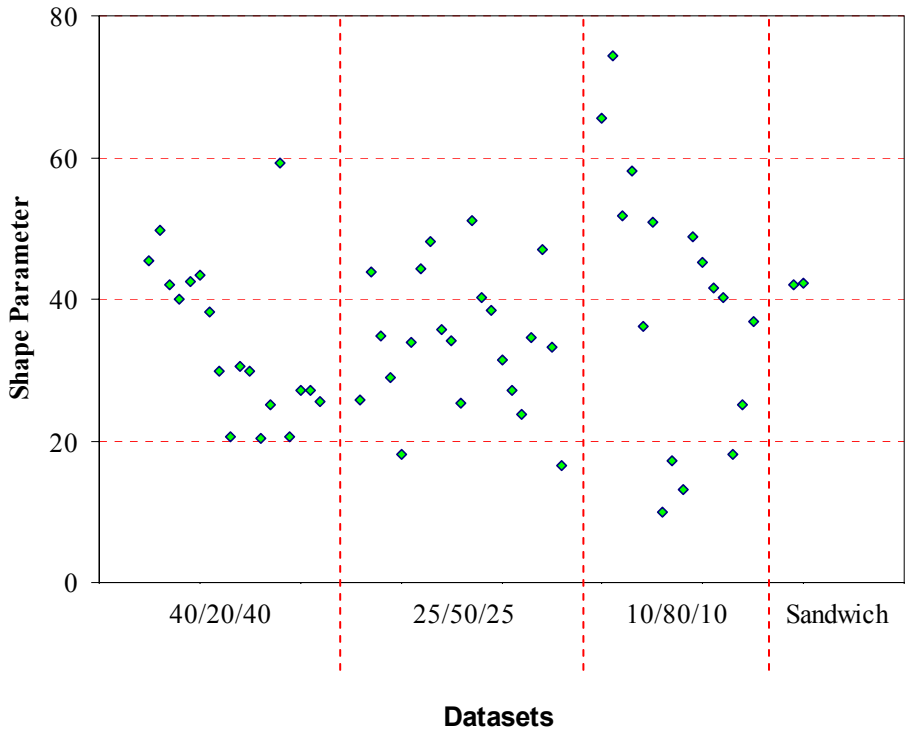

Figure 23. Shape parameters for T700-PW static-strength distributions.

TABLE 13

SUMMARY OF WEIBULL SHAPE PARAMETER ANALYSIS OF T700-PW

Analysis Case	Analysis Variable	Weibull Statistics			Number of Datasets
		α	β (ksi)	α_{Modal}	
Database	FAA-LVM	2.801	40.038	34.196	48
	FAA-LEF	5.405	41.184	39.654	9
	Combined	2.961	40.307	35.071	57
Test Environment	CTD	3.164	34.467	30.569	8
	RTA	2.912	43.359	37.524	32
	ETW	4.545	31.252	29.589	8
Layup	40/20/40	3.391	38.218	34.477	18
	25/50/25	4.139	37.585	35.155	21
	10/80/10	1.925	47.172	32.239	9
Loading Mode	All bearing	3.412	46.947	42.409	17
	OH/FH	3.550	35.976	32.773	16
	VNRS	1.449	25.941	11.559	5
	NH	3.379	39.728	35.809	10

4.1.3. 7781/#2510 8-Harness Satin-Weave Fabric

Toray 7781/#2510 8-harness satin-weave fabric (7781-8HS) data from the FAA-LEF material database are analyzed in this section. Static strength results for 7781-8HS are shown in Table 14, and the corresponding Weibull statistics are shown in Table 15.

TABLE 14

STATIC-STRENGTH TEST RESULTS FOR 7781-8HS

Specimen Configuration		RTA Strength (ksi)			ETW Strength (ksi)		
Layup	Test Description	Average	STDEV	CV	Average	STDEV	CV
10/80/10	OHT	26.808	0.366	1.364	21.120	0.186	0.882
	OHC	33.227	0.324	0.974	21.824	0.335	1.533
	DNC	3.494	0.170	4.861	2.364	0.264	11.167
Sandwich	4PB – HRH 10	0.139	0.002	1.795	0.128	0.002	1.206

TABLE 15

WEIBULL PARAMETERS FOR STATIC-STRENGTH DISTRIBUTIONS OF 7781-8HS

Specimen Configuration		Test Environment	Weibull Statistics		
Layup	**Test Description**		**α**	**β (ksi)**	**n**
10/80/10	OHT	RTA	76.115	26.983	6
		ETW	116.288	21.211	6
	OHC	RTA	104.824	33.385	6
		ETW	62.351	21.998	6
	DNC	RTA	32.221	3.561	6
		ETW	10.116	2.476	6
Sandwich	4PB – HRH 10	RTA	80.260	0.142	6
		ETW	86.690	0.128	6

Table 16 shows the analysis results for the Weibull distribution of shape parameters in Table 15. Compared to RRX and RRY analyses, MLE data indicate significant skewness, possibly due to an insufficient number of datasets. It is important to explore the other two regression techniques for such cases. For this case, RRX method was selected to determine the static-strength shape parameter.

TABLE 16

WEIBULL STATISTICS FOR COMBINED DISTRIBUTION OF SCATTER IN STATIC-STRENGTH DISTRIBUTIONS OF 7781-8HS

Analysis Method	Weibull Parameter	Analysis Cases	
		All	**RTA**
MLE	α	2.185	3.295
	β	79.512	82.038
	α_{Modal}	60.092	73.510
RRX	α	1.438	2.079
	β	83.239	84.814
	α_{Modal}	36.416	61.868
RRY	α	1.278	1.868
	β	87.043	87.042
	α_{Modal}	26.385	57.748

4.1.4. T700/#2510 Unidirectional Tape

Toray T700/#2510 unidirectional tape (T700-UT) data from the FAA-LVM material database [44] are analyzed in this section. This database contains 853 T700-UD specimens from 47 datasets (Appendix A). These datasets represent hard (50/40/10), quasi-isotropic (25/50/25), and soft (10/80/10) layup sequences, as well as a wide range of loading modes and environmental conditions (CTD, RTA, and ETW). Furthermore, each dataset contains specimens from three distinct material batches. Shape parameters obtained from static-strength distributions (section A.5) were combined for several different analysis scenarios to investigate the degree to which these parameters affect the MSSP of T700-UT (Table 17). The distribution of shape parameters calculated for T700-UT using the static data in FAA-LVM are shown in Figure 24. As seen for T700-PW, scatter in the distribution of 10/80/10 static-strength shape parameters is significantly higher than that for the other two laminate stacking sequences.

TABLE 17

SUMMARY OF WEIBULL SHAPE PARAMETER ANALYSIS OF T700-UT

Analysis Case	Analysis Variable	Weibull Statistics			Number of Datasets
		α	β (ksi)	α_{Modal}	
All	T700-UT	2.255	37.176	28.671	47
Test Environment	CTD	3.465	35.279	31.977	8
	RTA	2.174	39.519	29.763	31
	ETW	3.139	29.188	25.830	8
Layup	50/40/10	3.006	37.479	32.760	17
	25/50/25	2.246	36.083	27.760	21
	10/80/10	1.648	38.205	21.678	9
Loading Mode	All bearing	2.772	47.451	40.375	17
	OH/FH	4.197	30.659	28.734	16
	VNRS	2.471	15.719	12.743	5
	NH	3.949	32.859	30.517	10

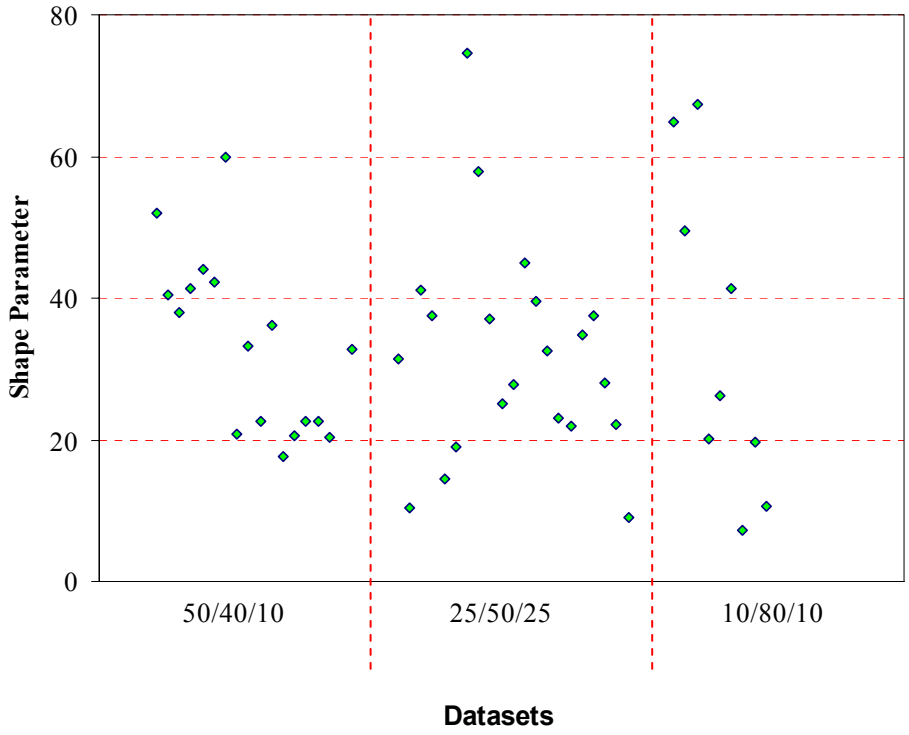

Figure 24. Shape parameters for T700-UT static-strength distributions.

4.1.5. AS4C/MTM45 Unidirectional Tape

ACG AS4C/MTM45 12K unidirectional tape (AS4C-UT) data from the FAA-LVM material database [44] are analyzed in this section. This database contains 1151 AS4C-UT specimens from 86 datasets (Appendix A). These datasets represent hard (50/40/10), quasi-isotropic (25/50/25), and soft (10/80/10) layup sequences, as well as a wide range of loading modes and environmental conditions (CTD, RTA, ETD, and ETW). Most of these datasets contain specimens from multiple distinct material batches. Shape parameters obtained from static-strength distributions (section A.6) were combined for several different analysis scenarios to investigate the degree to which these parameters affect the MSSP of AS4C-UT (Table 18). The distribution of shape parameters calculated for AS4C-UT using the static data in FAA-LVM are shown in Figure 25.

TABLE 18

SUMMARY OF WEIBULL SHAPE PARAMETER ANALYSIS OF AS4C-UT

Analysis Case	Analysis Variable	Weibull Statistics			Number of Datasets
		α	β (ksi)	α_{Modal}	
All	AS4C-UT	2.151	34.779	26.004	86
Test Environment	CTD	2.213	31.603	24.084	16
	RTA	3.094	35.541	31.329	30
	ETW	1.905	35.777	24.208	38
Layup	50/40/10	2.040	36.953	26.560	14
	25/50/25	2.731	36.635	31.002	19
	10/80/10	2.378	46.883	37.267	19
	Lamina	3.0435	25.5518	22.4171	34
Loading Mode	All bearing	2.729	33.131	28.028	6
	OH/FH	2.632	36.646	30.561	30
	NH	2.252	51.868	39.964	12

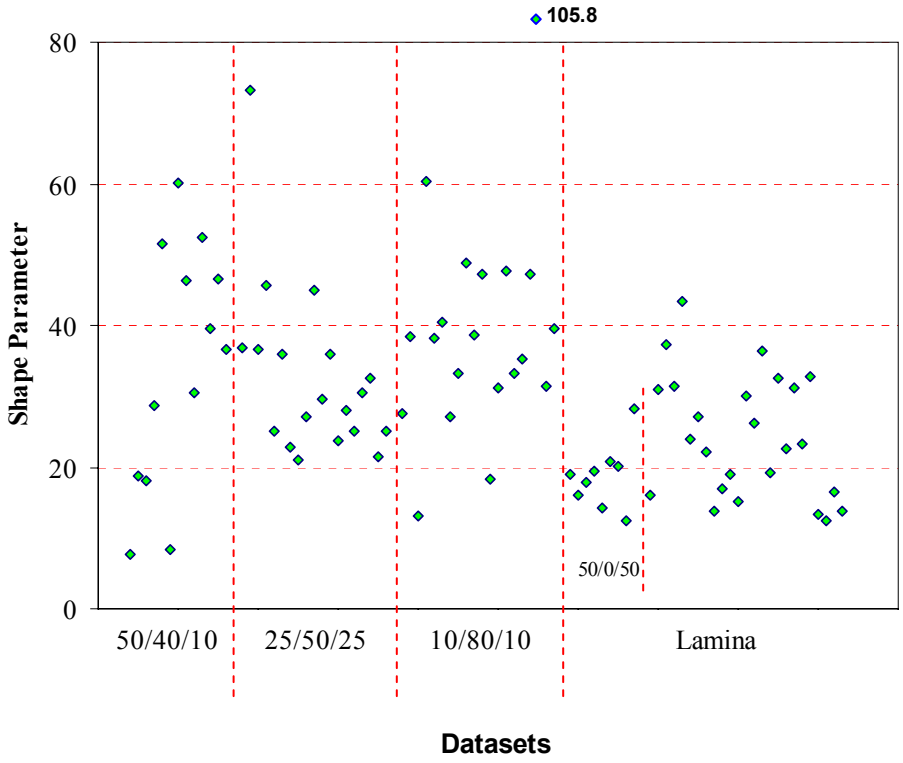

Figure 25. Shape parameters for AS4C-UT static-strength distributions.

4.1.6. AS4C/MTM45 5-Harness Satin-Weave Fabric

ACG AS4C/MTM45 5-harness satin-weave fabric (AS4C-5HS) data from the FAA-LVM material database [44] are analyzed in this section. This database contains 1083 AS4C-5HS specimens from 78 datasets (Appendix A). These datasets represent hard (40/20/40), quasi-isotropic (25/50/25), and soft (10/80/10) layup sequences, as well as a wide range of loading modes and environmental conditions (CTD, RTA, ETD, and ETW). Most of these datasets contain specimens from multiple distinct material batches. Shape parameters obtained from static-strength distributions (section A.7) were combined for several different analysis scenarios to investigate the degree to which these parameters affect the MSSP of AS4C-5HS (Table 19). Distribution of shape parameters calculated for AS4C-5HS using the static data in FAA-LVM are shown in Figure 26.

TABLE 19

SUMMARY OF WEIBULL SHAPE PARAMETER ANALYSIS OF AS4C-5HS

Analysis Case	Analysis Variable	Weibull Statistics			Number of Datasets
		α	β (ksi)	α_{Modal}	
All	AS4C-5HS	2.104	35.694	26.267	78
Test Environment	CTD	2.263	37.711	29.144	14
	RTA	2.284	36.714	28.534	26
	ETW	1.976	34.586	24.207	34
Layup	40/20/40	2.926	29.475	25.549	13
	25/50/25	1.985	36.759	25.828	18
	10/80/10	2.834	46.860	40.190	16
	Lamina	2.062	26.579	19.266	20
Loading Mode	All bearing	2.643	21.535	17.990	5
	OH/FH	2.454	41.192	33.279	29
	NH	2.293	42.576	33.163	16

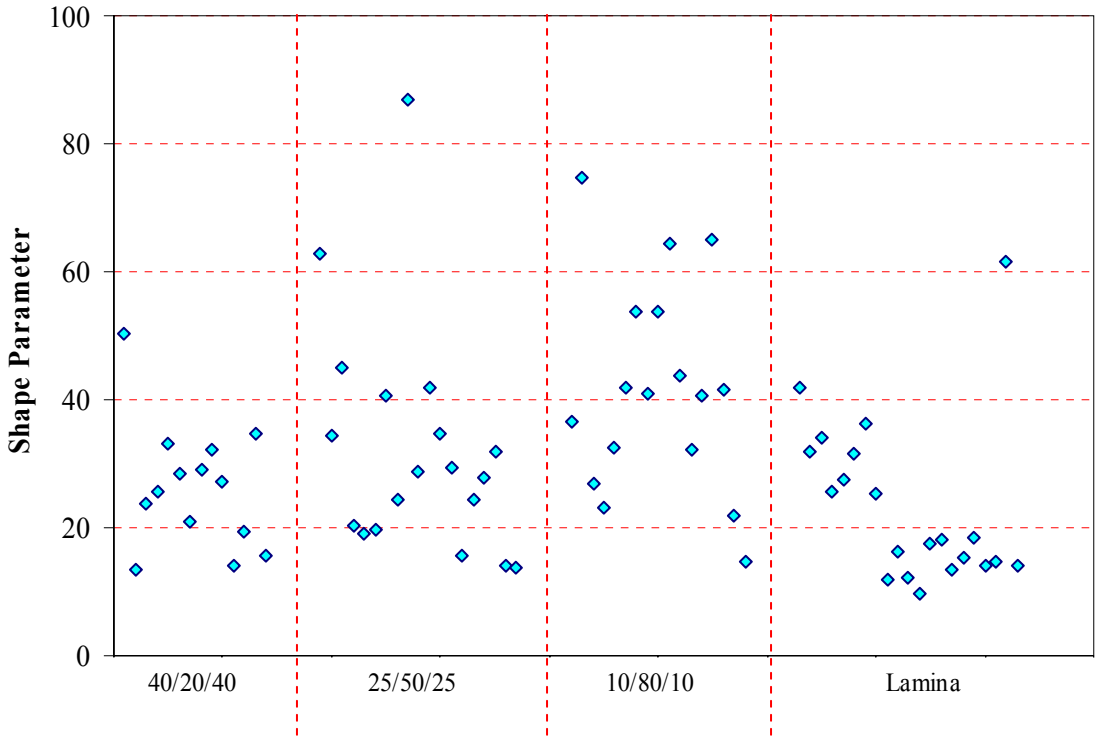

Figure 26. Shape parameters for AS4C-5HS static-strength distributions.

4.1.7. T700/E765 Graphite Unidirectional Tape

Nelcote (formally FiberCote) T700/E765 24K graphite unidirectional tape (E765-UT) material from the FAA-LVM material database [44] are analyzed in this section. This database contains 834 E765-UT specimens from 47 datasets (Appendix A). These datasets represent hard (50/40/10), quasi-isotropic (25/50/25), and soft (10/80/10) layup sequences, as well as a wide range of loading modes and environmental conditions (CTD, RTA, and ETW). Most of these datasets contain specimens from multiple distinct material batches. Shape parameters obtained from static-strength distributions (section A.8) were combined for several different analysis scenarios to investigate the degree to which these parameters affect the MSSP of E765-UT (Table 20). Distribution of shape parameters calculated for E765-UT using the static data in FAA-LVM are shown in Figure 27.

TABLE 20

SUMMARY OF WEIBULL SHAPE PARAMETER ANALYSIS OF E765-UT

Analysis Case	Analysis Variable	Weibull Statistics			Number of Datasets
		α	β (ksi)	α_{Modal}	
All	E765-UT	2.0867	30.719	22.471	47
Test Environment	CTD	2.241	22.254	17.095	7
	RTA	2.117	31.091	22.98	29
	ETW	1.779	23.739	14.920	7
Layup	40/20/40	1.976	32.334	22.627	16
	25/50/25	2.158	29.647	22.215	20
	10/80/10	2.445	30.220	24.372	8
Loading Mode	All bearing	3.280	31.484	28.180	16
	OH/FH	2.343	39.705	31.312	14
	VNRS	3.229	14.368	12.810	4
	NH	2.222	23.345	17.838	9

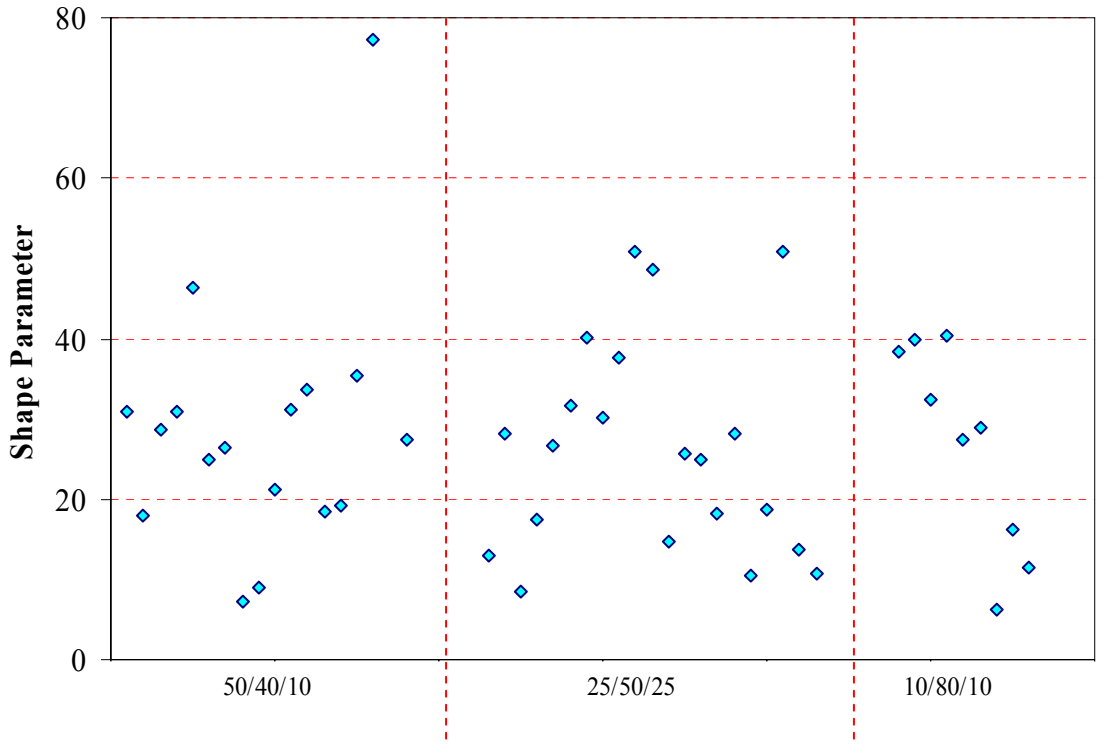

Figure 27. Shape parameters for E765-UT static-strength distributions.

4.1.8. T300/E765 3K Plain-Weave Fabric

Nelcote (formally FiberCote) T700/E765 plain-weave fabric (E765-PW) material from the FAA-LVM material database [44] are analyzed in this section. This database contains 722 E765-PW specimens from 48 datasets (Appendix A). These datasets represent hard (40/20/40), quasi-isotropic (25/50/25), and soft (10/80/10) layup sequences, as well as a wide range of loading modes and environmental conditions (CTD, RTA, and ETW). Most of these datasets contain specimens from multiple distinct material batches. Shape parameters obtained from static-strength distributions (section A.9) were combined for several different analysis scenarios to investigate the degree to which these parameters affect the MSSP of E765-PW (Table 21). Distribution of shape parameters calculated for E765-PW using the static data in FAA-LVM are shown in Figure 28.

TABLE 21

SUMMARY OF WEIBULL SHAPE PARAMETER ANALYSIS OF E765-PW

Analysis Case	Analysis Variable	Weibull Statistics			Number of Datasets
		α	β (ksi)	α_{Modal}	
All	E765-PW	2.389	32.735	26.089	48
Test Environment	CTD	2.434	24.535	19.740	7
	RTA	2.535	35.837	29.400	31
	ETW	2.751	27.714	23.516	7
Layup	40/20/40	2.484	37.800	30.723	17
	25/50/25	2.947	30.194	26.233	20
	10/80/10	1.907	27.820	18.843	8
Loading Mode	All bearing	2.200	30.491	23.148	16
	OH/FH	3.098	32.641	28.782	15
	VNRS	1.288	26.488	8.269	4
	NH	4.619	38.055	36.097	9

4.1.9. Adhesive Effects of Defects Data

The FAA effects of defects (FAA-EOD) database [47] contains more than 70 bonded-joint picture-frame shear (PFS) element tests that have disbonds, lightening strikes, and low-

velocity impact damages. These specimens were fabricated using T700-PW and 7781-8HS, and bonded with the EA9394 two-part paste adhesive system. Only datasets that contain more than five specimens were included in the Weibull analysis (Table 22).

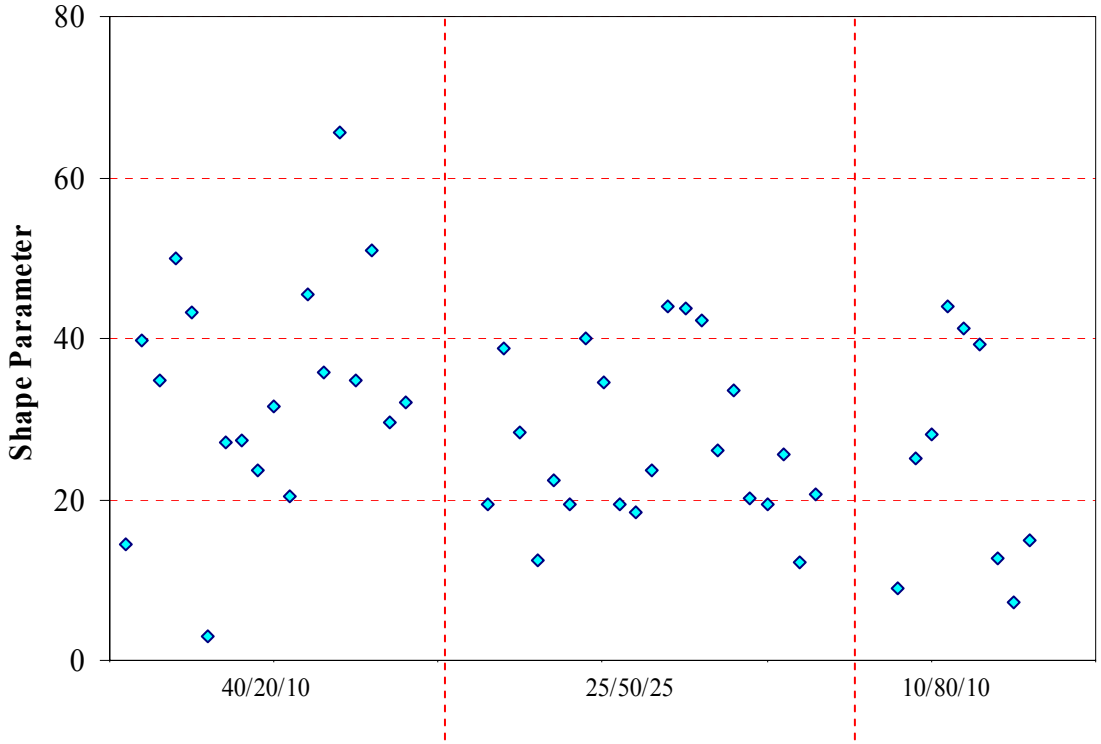

Figure 28. Shape parameters for E765-PW static-strength distributions.

TABLE 22

WEIBULL PARAMETERS FOR BONDED-JOINT PICTURE-FRAME ELEMENT TESTS

Adherend Material	Defect Description	Shape Parameter, α	Number of Specimens
T700-PW	No disbonds	11.358	9
	Small disbonds (circle, diamond)	18.319	6
	Large rectangular disbonds	14.181	9
	Lightning strikes	22.390	6
	Low-velocity impact damages	20.255	20
7781-8HS	No disbonds	19.701	5

In addition to the above data, 60 bonded joints (elements) impacted with different energy levels [47] and tested in single-lap shear (SLS) were analyzed. Specimens with a 4 by 4 inch gage section were fabricated using the following material systems, which are commonly used in aircraft applications, and bonded using EA9394 two-part paste adhesive system.

1. Newport NB321/7781 E-glass satin weave (FGSW)

2. Toray T700G-12K/3900-2 carbon fabric plain weave (CFPW)

3. Toray T800S/3900-2B carbon tape unidirectional (CFU)

Although three different impactor diameters (0.50-, 0.75-, and 1.00-inch) and three different energy levels (88.5-, 221-, and 354-in-lbf) were used to inflict damages, the impact damages were contained mostly within the elastic trough and away from the side edges. Thus, although the damage states, i.e., residual indentation, damage area, were different, the residual strength was not significantly influenced by the impact parameters. Thus, the data for each material were pooled and analyzed for scatter (Table 23).

TABLE 23

WEIBULL PARAMETERS FOR BONDED SLS ELEMENT TESTS

Adherend	**Adhesive**	**Weibull Statistics**			**Number of Specimens**
		α	β (ksi)	α_{Modal}	
FGSW	EA9394	14.134	847.347	842.96	20
CFPW		25.657	867.356	866.013	20
CFU		19.890	986.267	983.713	20

4.2. Summary

Figure 29 shows that ETW data have the highest scatter, while RTA has the least scatter, for most cases analyzed in this section. The scatter in ETW data can be attributed to variations in total moisture absorption among test specimens and the time to reach the elevated test temperature prior to test. Furthermore, the shape parameter obtained by pooling test data from all environmental conditions is close to the shape parameter obtained by analyzing RTA test data of each material system. Also, the pooled values are higher than the MSSP of 20, which was the value used for F/A-18 certification, for all the material systems analyzed in this paper. This can be attributed to the improvements in materials, process techniques, and test methodologies of modern composite materials.

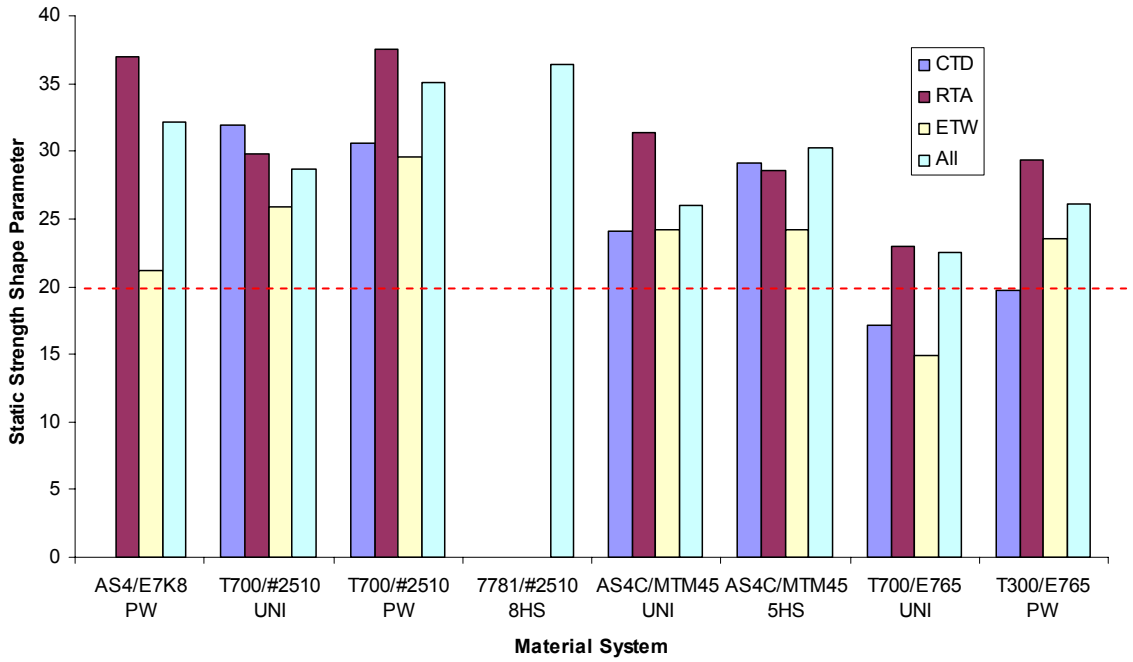

Figure 29. Comparison of composite static-strength shape parameters for different environments.

Figure 30 indicates that the shape parameters of T700-PW and E765-UNI are independent of layup sequence, while other material systems indicate large variations among layup sequences. Also, the shape parameter obtained by pooling test data from all laminate

stacking sequences is close to the shape parameter obtained by analyzing the quasi-isotropic laminate (25/50/25) test data of most of the material systems. For both ACG material systems (AS4C-UT and AS4C-5HS), the soft laminate (10/80/10) test data indicate the least scatter, while for T700-UNI and for E765-PW, they indicate the most scatter. The hard laminate (50/40/10) test data indicate the reverse trend for these four material systems.

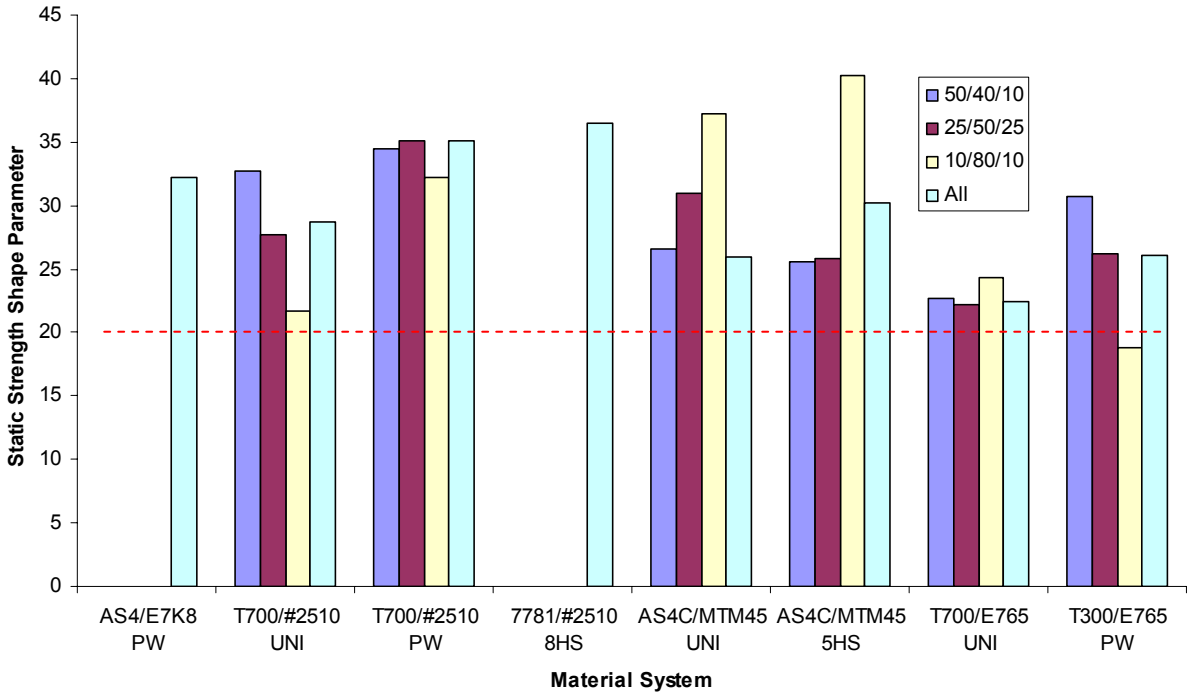

Figure 30. Comparison of composite static-strength shape parameters for different layups.

Figure 31 shows that the loading mode significantly influences the static scatter for all five material systems. For both NelCote material systems (E765-UNI and E765-PW) unnotched (NH) test data indicate the most scatter resulting shape parameters significantly lower than 20, while OH and FH data indicate the least scatter. For both ACG material systems, bearing test data indicate the most scatter. For both Toray material systems (T700-UNI and T700-PW), OH and FH data indicate the most scatter that is closer to the scatter in unnotched test data, while bearing test data indicate the least scatter.

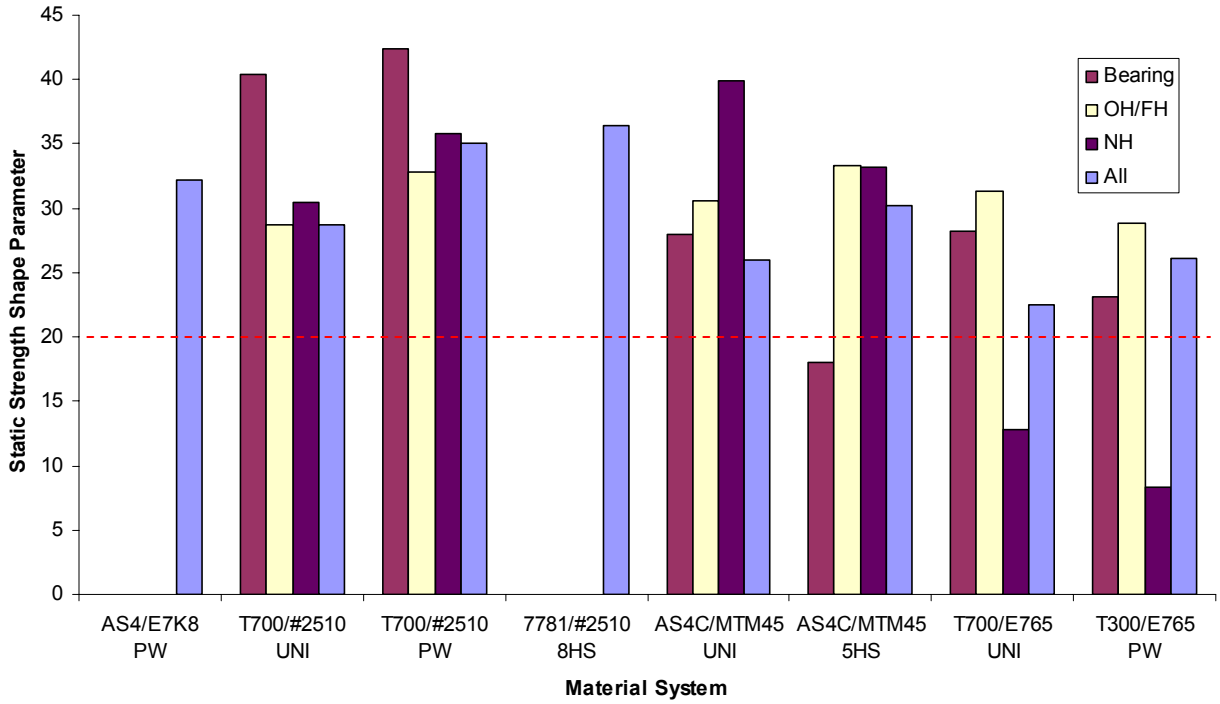

Figure 31. Comparison of composite static-strength shape parameters for different loading modes.

The scatter analysis results in this section provide guidance to design a cost-effective test matrix for generating reliable MSSP. The data are documented so that they can be readily available for a particular case, and the user does not have to generate new data or analyze the scatter.

CHAPTER 5

FATIGUE LIFE DATA SCATTER ANALYSIS

An extensive fatigue scatter analysis was conducted by Whitehead et al. [2] on various material databases. These databases represented several structural details and variables such as R-ratio, laminate layup, loading mode, load transfer, specimen geometry, and test environment. The material database of Badaliance and Dill [54] included 204 graphite/epoxy datasets, while Whitehead and Schwarz [55] included 2,925 data points from 120 datasets of graphite/epoxy, 450 data points from 26 datasets of E-glass/epoxy, and 419 step-lap bonded joints from 23 datasets. To increase the accuracy of Weibull analysis, only the datasets containing five or more specimens were included in the individual Weibull analysis.

Typically, an S-N curve contains fatigue failures for multiple stress levels in addition to static-strength data points and runouts, if any. In this paper, the fatigue life scatter was analyzed using individual Weibull, joint Weibull, and Sendeckyj analyses. Only datasets containing more than five specimens within a stress level were included in the individual Weibull analysis. Residual strength data for all runouts were included in the Sendeckyj analysis.

5.1. Structural Details for Fatigue Life Scatter Analysis

This section includes over one thousand data points from the following three different composite material systems that are commonly used in aircraft applications:

1. AS4/E7K8 plain-weave fabric (AS4-PW)
2. T700/#2510 plain-weave fabric (T700-PW)
3. 7781/#2510 8-harness satin-weave fabric (7781-8HS)

In addition, adhesive fatigue data from the FAA-D5656 material database [46] in the following three different test environments for three adhesive systems are included:

1. Hysol EA9696 film adhesive
2. PTM&W ES6292 paste adhesive
3. Cessna Aircraft proprietary paste adhesive (Loctite)

Data generated from coupons and elements were used to investigate the dependence of the fatigue-life shape parameter, which is a representation of fatigue-life scatter, on various coupon geometries, loading modes, environments, and layups. The degree to which these parameters affect the overall LEF factors from a parametric basis is discussed in section 5.4. Since fatigue-life data inherently exhibit significantly more scatter than static-strength data, the modal fatigue-life shape parameter (MLSP or α_L) is noticeably smaller than the modal static-strength shape parameter (MSSP or α_R). Several examples are shown for obtaining MLSP by pooling different data sets. When pooling data to estimate MLSP, the user is advised to select appropriate design details that are applicable to a certain structure.

The material databases described in this section were primarily selected to support the full-scale structure tests proposed in section 8. These materials are used in several ongoing certification programs and certified general aviation aircraft. The databases include coupon-level static-strength data for the following primary variables:

1. Layups – hard, quasi-isotropic, and soft (typically 50/40/10, 25/50/25, and 10/80/10, respectively, for unidirectional material, and 40/20/40, 25/50/25, and 10/80/10, respectively, for fabric material – all ±45° plies) and all ±45° plies (0/100/0)
2. Environments – CTD, RTA, RTW, ETW
3. Tension – open hole
4. Compression – open hole
5. Interlaminar shear – double-notched compression

In addition to coupon-level data, element-level static-strength data were included in the analysis that represents the following design details/requirements:

1. Sandwich – core materials, face sheet
2. Bonded joints – single-lap shear
3. Damage tolerance – CAI, sandwich

The following sections include the generation of the shape parameter for several different material systems along with knowledge of the effects of different geometries, environments, layups, and loading modes.

5.2. Fatigue Scatter Analysis

ReliaSoft Weibull software and SACC were used for the Sendeckyj analysis of fatigue data in two steps: with and without static-strength data. Residual strength data of all runout specimens were included in the Sendeckyj analysis. Individual and joint Weibull analyses were conducted only using the fatigue data. Kassapoglou [34] life predictions based only on static-strength scatter were compared with Sendeckyj analysis of experimental data in Appendix A. As shown in Appendix A, currently Kassapoglou methodology either under predicts or over predicts the fatigue life significantly for some S-N curves.

5.2.1. AS4/E7K8 Plain Weave Fabric

Fatigue analysis of 385 AS4-PW specimens from 14 datasets is included in this section. Each dataset contains a minimum of three fatigue stress levels and at least six static-strength data points (Figure 32). S-N curves for AS4-PW are included in Appendix A. Fatigue-life scatter analysis data are shown in Table 24.

Figure 33 shows a comparison of AS4-PW OHC fatigue data, where R= -1 for quasi-isotropic (25/50/25) and two resin-dominant layup configurations (10/80/10 and 0/100/0). The

same data are normalized with respect to the ultimate static strength (average) and are shown in Figure 34. Both of these figures show that the 0/100/0 layup with all ±45° plies has the critical fatigue life but not the dataset that has the highest scatter.

Figure 35 shows a comparison of AS4-PW OH measured data for different R-ratios, and Figure 36 shows a comparison of normalized data. Both figures indicate that R= -1 is the critical fatigue life and has the least scatter when pooled with static data points.

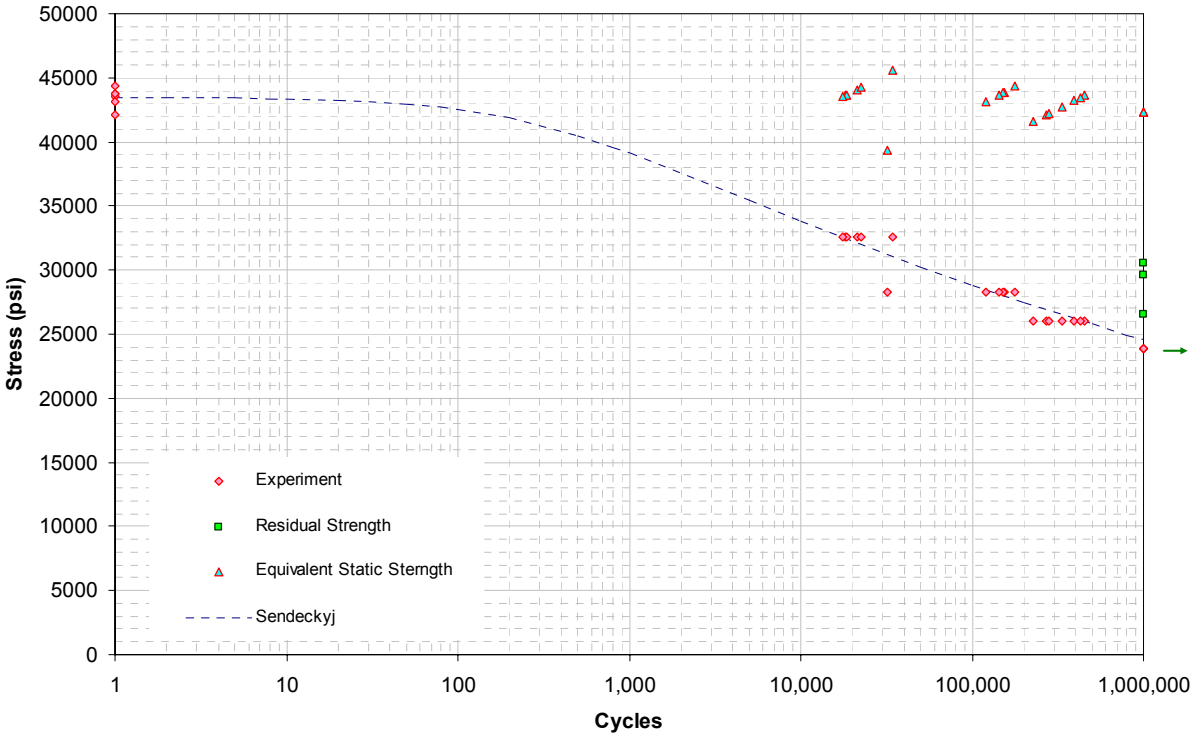

Figure 32. Sendeckyj wearout analysis prediction of fatigue life of OHT (R=0) – AS4-PW.

TABLE 24

FATIGUE-LIFE SCATTER ANALYSIS FOR AS4-PW

Specimen Configuration			Sendeckyj		Weibull*	
Layup	**Test Description**	**R-Ratio**	**$\alpha_{Sendeckyj}$ (w/static)**	**$\alpha_{Sendeckyj}$ (w/o static)**	**$\alpha_{Ind.\ Weibull}$**	**$\alpha_{Joint\ Weibull}$**
10/80/10	OH	-1	2.068	2.604	3.304	2.630
	OHC	5	1.792	2.328	3.223	2.502
	OHT	0	3.434	3.686	5.555	3.825
	OH	-0.2	3.319	4.090	4.003	4.314
	CAI – BVID (20-ply)	5	2.870	3.321	3.968	3.387
	CAI – VID (40-ply)	5	2.103	2.221	2.778	2.288
	DNC	-1	3.837	3.905	6.636	3.842
	DNC	-0.2	2.025	1.962	2.278	2.235
0/100/0	OH	-1	2.495	3.480	5.528	3.559
	TAI – BVID	0	1.640	1.515	2.477	1.514
	TAI – VID	0	1.111	1.065	1.974	1.870
Sandwich	4PB – HRH 10	0	1.924	2.020	5.131	2.287
25/50/25	OH	-1	3.224	3.661	5.713	3.673
	CAI – BVID[#]	5	1.774	2.234	2.446	2.355
	CAI – VID[#]	5	2.182	2.658	2.991	2.779
	CAI – LID[#]	5	2.466	2.799	3.272	3.250
40/20/40	CAI – VID	5	2.337	3.522	4.392	3.938

[*] Life scatter analysis using Weibull only includes fatigue data.
[#] Test data not included in the combined analysis for MLSP generation. Further details may be found in Chapter 6.

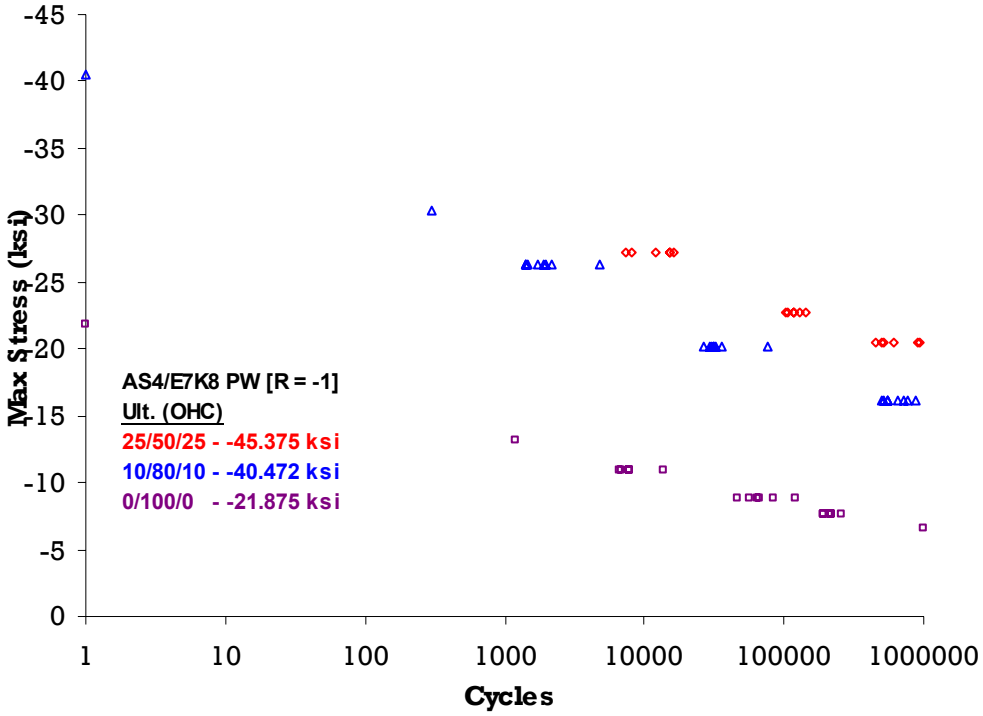

Figure 33. Effects of layup sequence, AS4/E7K8, OH fatigue data – measured.

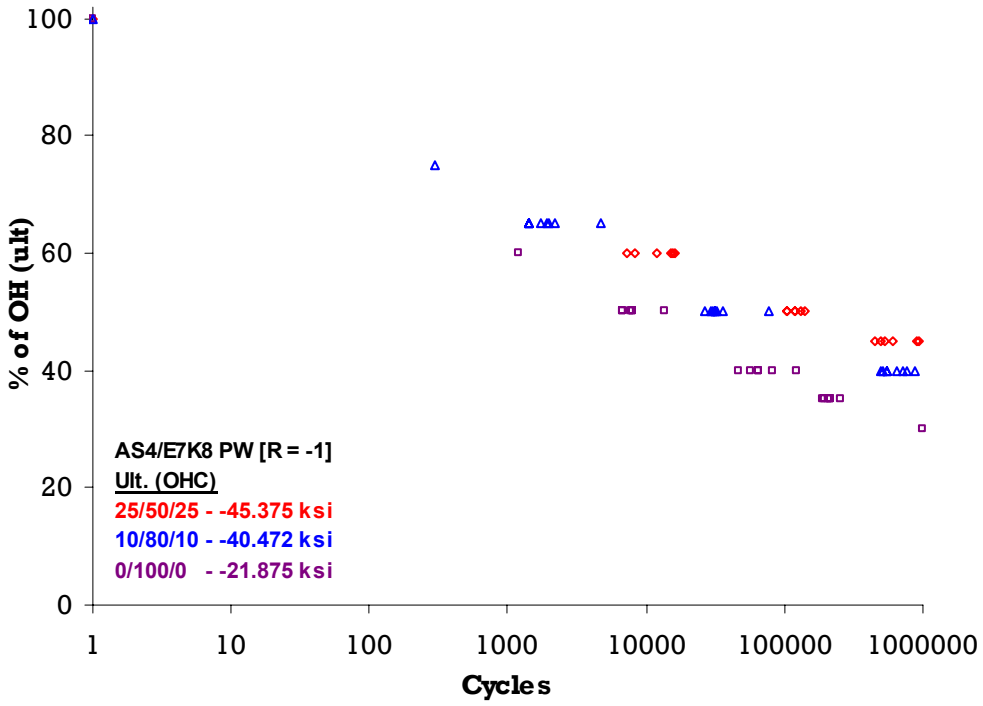

Figure 34. Effects of layup sequence, AS4/E7K8, OH fatigue data – normalized.

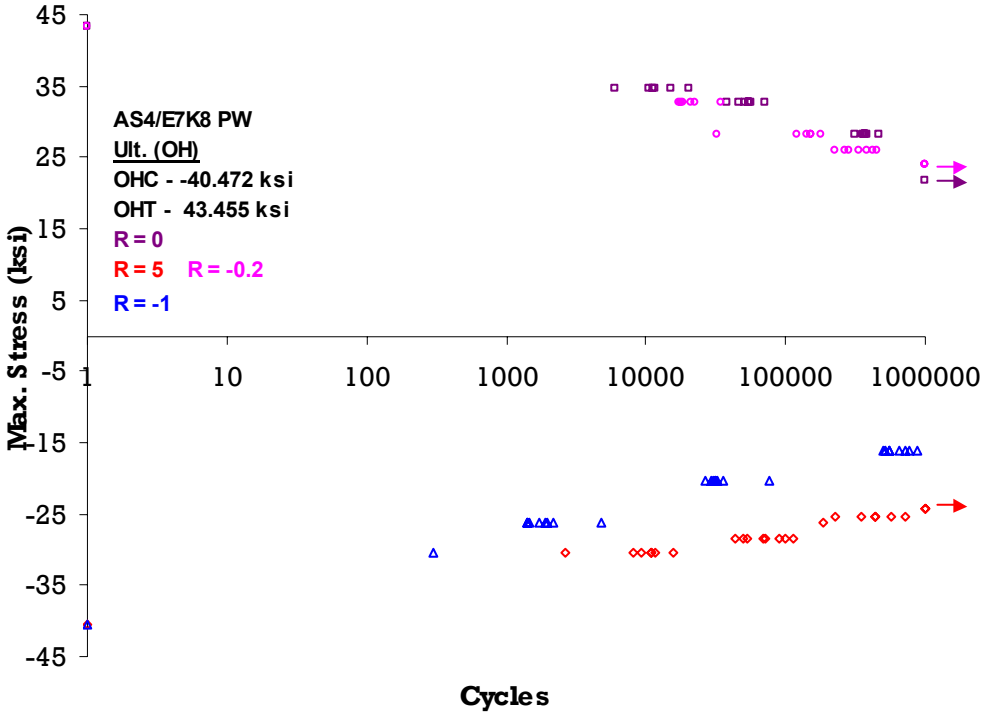

Figure 35. Effects of stress ratio for AS4-PW OH fatigue data – measured.

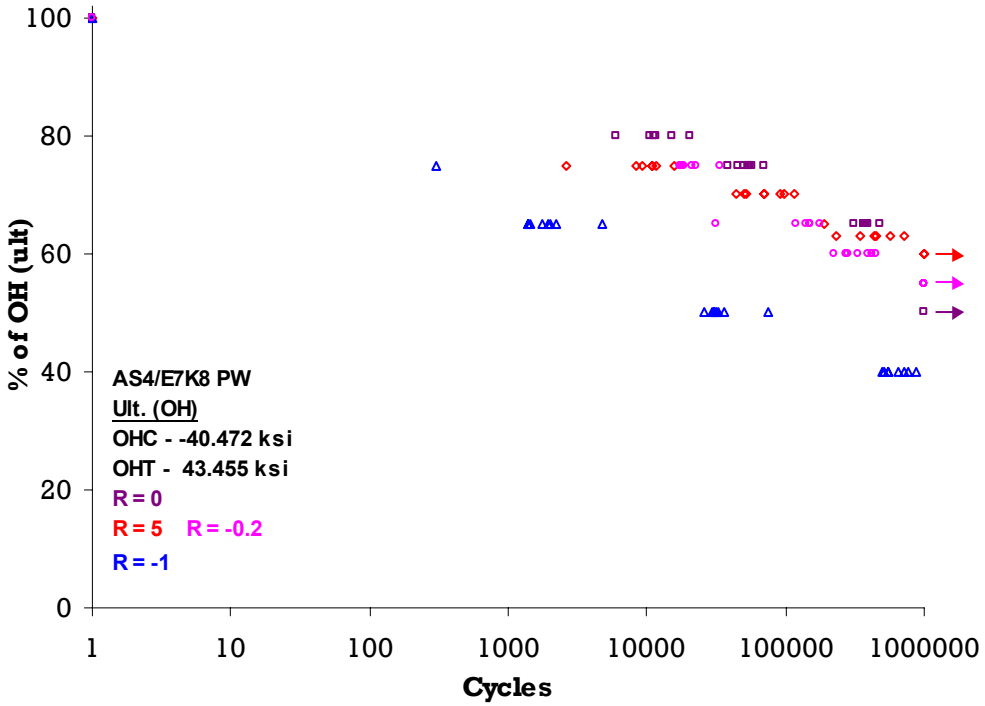

Figure 36. Effects of stress ratio for AS4-PW OH fatigue data – normalized.

Figure 37 shows a comparison of AS4-PW CAI data for different layups and energy levels. Normalized data indicate that the fatigue life is independent of layup and up to 1500 in-lbf/in impact energy. Figure 38 shows a comparison between CAI and TAI for different energy levels. Normalized data indicate that the fatigue life for TAI is independent impact energy levels up to 1500 in-lbf/in but significantly lower than that for CAI. The lower fatigue life for TAI can also be attributed to the fact that these specimens are all ±45°, while the CAI specimens are 10/80/10 layup. TAI data also indicate significant scatter compared to CAI data.

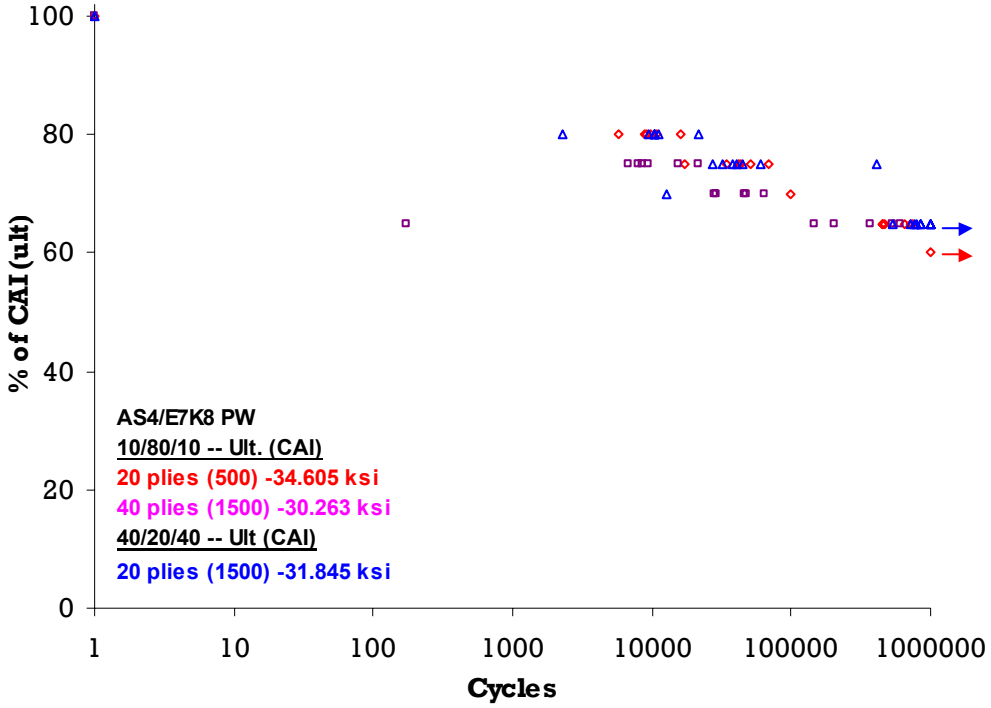

Figure 37. Effects of layup sequence for AS4-PW CAI fatigue data – normalized.

Figure 39 shows a comparison of fatigue-life scatter data obtained from different analysis techniques. It includes runout and corresponding residual strength data points as well as the equivalent static strength based on the Sendeckyj model. The Sendeckyj analysis produces a higher scatter as it is unbiased compared to the arithmetically averaged individual Weibull shape parameters (Figure 39).

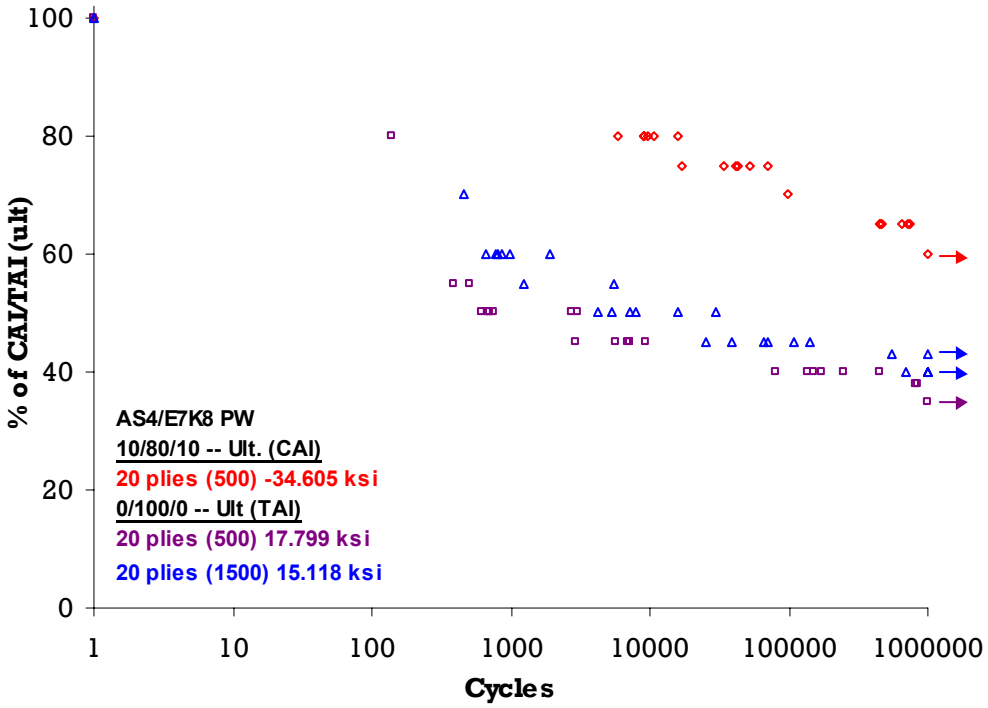

Figure 38. Comparison of CAI and TAI for AS4-PW.

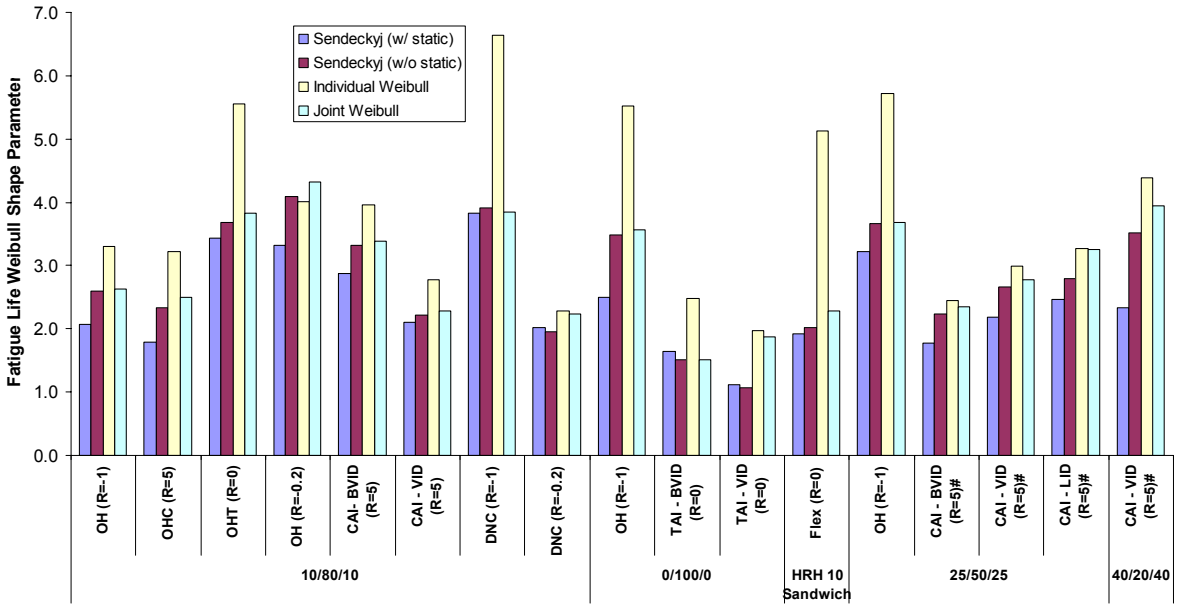

Figure 39. Fatigue-life shape parameters of AS4-PW from different analysis methods.

The Sendeckyj analysis is the most conservative of the above-mentioned methods because it includes static, fatigue failures, runouts, and residual strength data. This analysis produces the equivalent static strength for each fatigue data point. These strength values are pooled and compared against the tested static-strength data in Table 25 and graphically shown in Figure 40.

TABLE 25

COMPARISON OF STATIC STRENGTH OF AS4-PW FROM TEST AND SENDECKYJ ANALYSIS

Specimen Configuration			Static Test		Pooled (Sendeckyj)	
Layup	**Test Description**	**R-Ratio**	**Strength (ksi)**	**CV**	**Strength (ksi)**	**CV**
10/80/10	OH	-1	40.472	3.882	42.608	3.848
	OHC	5			41.360	2.783
	OHT	0	43.455	1.778	42.823	4.217
	OH	-0.2			42.942	5.055
	CAI–BVID (20-ply)	5	34.605	4.454	35.581	3.238
	CAI–VID (40-ply)	5	30.263	2.690	30.329	2.060
	DNC	-1	3.988	4.022	3.975	4.456
	DNC	-0.2	3.988	4.022	4.008	5.843
0/100/0	OH	-1	21.875	1.600	22.058	3.420
	TAI – BVID	0	17.799	2.172	16.709	9.695
	TAI – VID	0	15.118	4.143	14.807	5.112
Sandwich	4PB – HRH 10	0	0.145	2.071	0.141	8.411
25/50/25	OH	-1	45.375	3.579	45.882	2.499
	CAI – BVID	5	36.025	2.361	36.289	2.002
	CAI – VID	5	29.671	3.003	29.990	2.438
	CAI – LID	5	25.445	2.721	25.614	2.259
40/20/40	CAI – VID	5	31.845	3.223	31.586	3.945

The fatigue-life shape parameters for AS4-PW shown in Table 25 are then fitted into another Weibull distribution, and the shape parameter corresponding to the new distribution and the model shape parameter are obtained from three different techniques: MLE, RRX, and RRY. As can be seen in Table 26, there are no significant differences between different techniques.

The Sendeckyj-model shape parameter (with static) for life scatter is 2.427, while it is 3.974 for individual Weibull.

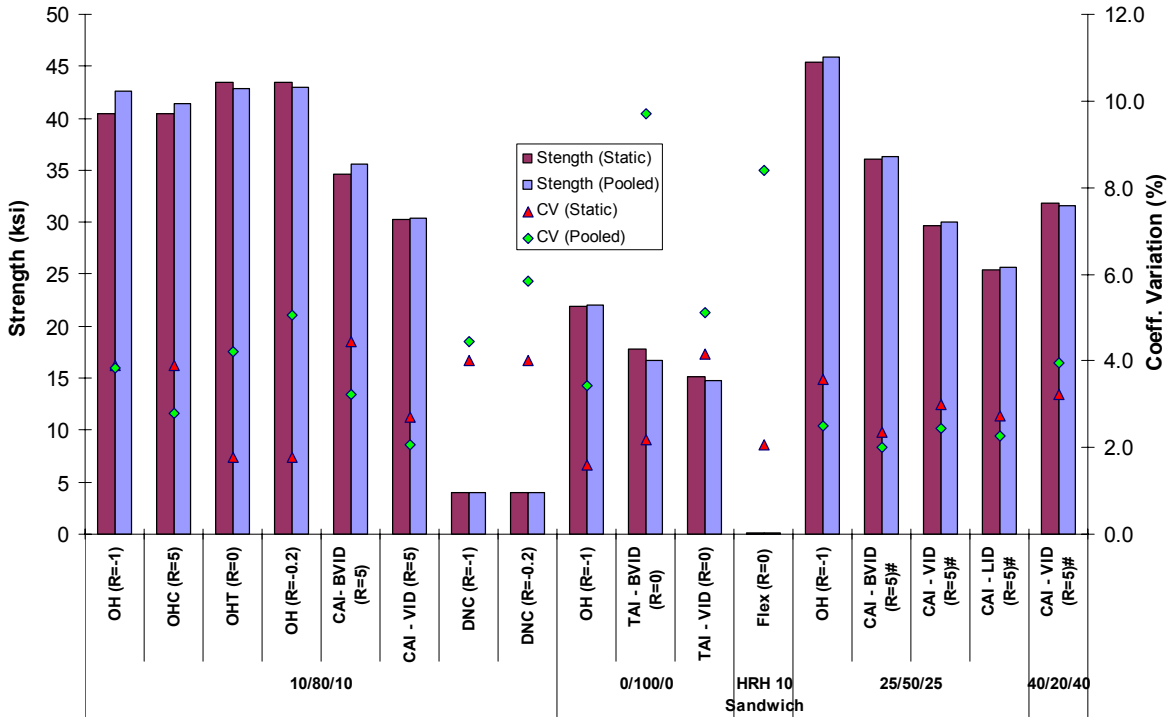

Figure 40. Comparison of static strength and CV of AS4-PW from test and Sendeckyj analysis.

TABLE 26

WEIBULL STATISTICS FOR COMBINED DISTRIBUTION OF SCATTER IN FATIGUE-LIFE DISTRIBUTIONS OF AS4-PW

Analysis Method	Weibull Parameter	Fatigue Scatter Analysis Method			
		$\alpha_{Sendeckyj}$ (w/static)	$\alpha_{Sendeckyj}$ (w/o static)	$\alpha_{Ind.\ Weibull}$	$\alpha_{Joint\ Weibull}$
MLE	α	3.553	3.511	3.207	4.030
	β	2.716	3.138	4.558	3.311
	α_{Modal}	2.475	2.852	4.056	3.085
RRX	α	3.443	2.901	3.065	3.652
	β	2.710	3.163	4.541	3.308
	α_{Modal}	2.453	2.734	3.992	3.030
RRY	α	3.323	2.798	2.953	3.474
	β	2.725	3.184	4.572	3.333
	α_{Modal}	2.447	2.719	3.974	3.022

5.2.2. T700/#2510 Plain-Weave Fabric

Fatigue analysis of 240 T700-PW specimens from 7 S-N curves is included in this section. Each dataset contains a minimum of three fatigue stress levels and at least six static-strength data points. Similar to AS4-PW, T700-PW OH data show that R= -1 is the most critical stress ratio for both measured (Figure 41) and normalized (Figure 42) data comparisons. Fatigue-life scatter analysis data are shown in Table 27. Figure 43 shows a comparison of fatigue-life scatter data obtained from different analysis techniques. Similar to AS4-PW, Sendeckyj analysis produces a higher scatter for T700-PW, as it is unbiased compared to the arithmetically averaged individual Weibull shape parameters. However, Sendeckyj data exhibit significantly less scatter compared to AS4-PW. As a result, the difference between Sendeckyj and individual Weibull fatigue-life shape parameters is not prominent for T700-PW (Table 28).

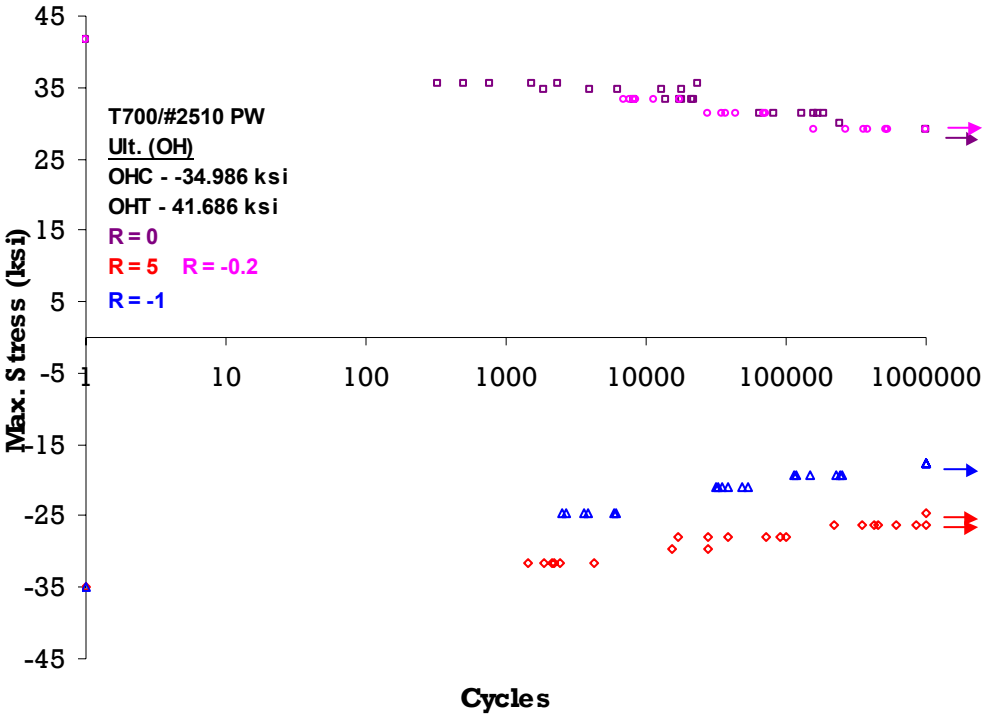

Figure 41. Effects of stress ratio for T700-PW OH fatigue data – measured.

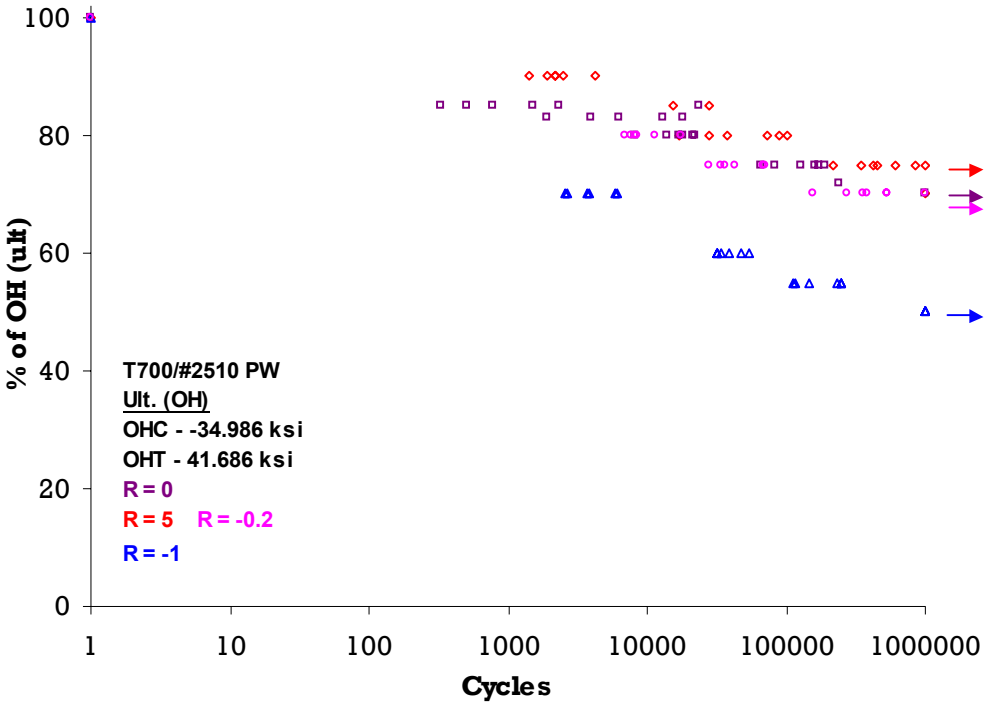

Figure 42. Effects of stress ratio for T700-PW OH fatigue data – normalized.

TABLE 27

FATIGUE-LIFE SCATTER ANALYSIS FOR T700-PW

Specimen Configuration			Sendeckyj		Weibull	
Layup	Test Description	R-Ratio	$\alpha_{Sendeckyj}$ (w/static)	$\alpha_{Sendeckyj}$ (w/o static)	$\alpha_{Ind.\ Weibull}$	$\alpha_{Joint\ Weibull}$
10/80/10	OH	-1	2.796	3.389	3.932	3.747
	OHC	5	1.481	1.992	2.344	2.224
	OHT	0	1.367	2.086	2.721	1.515
	OH	-0.2	1.904	2.079	2.615	2.261
	DNC	-1	1.496	1.464	1.714	1.606
	DNC	-0.2	1.547	1.635	2.489	1.763
Sandwich	4PB – HRH 10	0	1.764	2.315	2.881	2.409

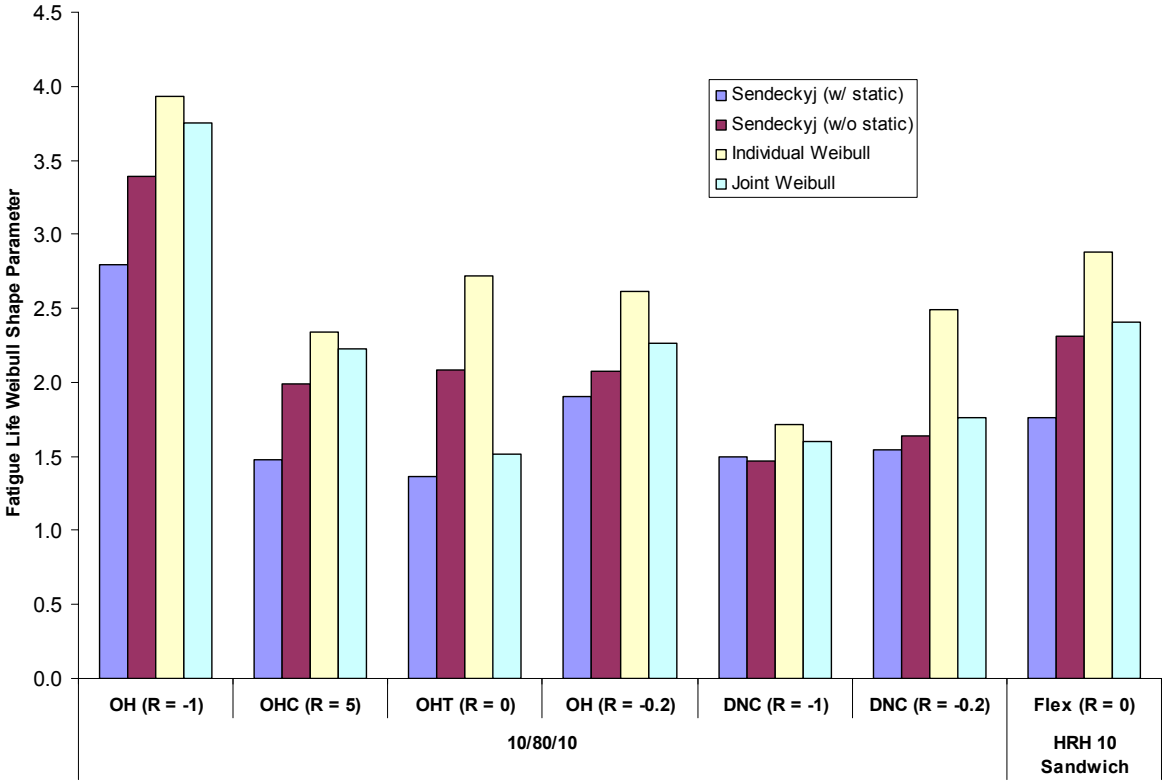

Figure 43. Fatigue-life shape parameters of T700-PW from different analysis methods.

TABLE 28

WEIBULL STATISTICS FOR COMBINED DISTRIBUTION OF SCATTER IN FATIGUE-LIFE DISTRIBUTIONS OF T700-PW

Analysis Method	Weibull Parameter	Fatigue Scatter Analysis Method			
		$\alpha_{Sendeckyj}$ (w/static)	$\alpha_{Sendeckyj}$ (w/o static)	$\alpha_{Ind.\ Weibull}$	$\alpha_{Joint\ Weibull}$
MLE	α	3.795	3.728	4.433	3.228
	β	1.944	2.359	2.919	2.470
	α_{Modal}	1.793	2.170	2.756	2.202
RRX	α	5.255	4.344	4.570	3.838
	β	1.892	2.326	2.908	2.425
	α_{Modal}	1.817	2.190	2.755	2.241
RRY	α	3.780	3.729	4.145	3.197
	β	1.965	2.371	2.941	2.490
	α_{Modal}	1.811	2.181	2.752	2.214

5.2.3. 7781/#2510 8-Harness Satin-Weave Fabric

Fatigue analysis of 204 7781-8HS specimens from 7 S-N curves is included in this section. Each dataset contains a minimum of three fatigue stress levels and at least six static-strength data points. As shown for the previous two material systems, OH with R= -1 data indicate the lowest fatigue life (Figure 44). Normalized OH data for R=5 indicate the lowest level of fatigue degradation for this material (Figure 45). Fatigue life scatter analysis data are shown in Table 29. Figure 46 shows a comparison of fatigue-life scatter data obtained from different analysis techniques. Similar to AS4-PW and T700-PW, Sendeckyj analysis produces a higher scatter for 7781-8HS than individual Weibull shape parameters. Except for R=5, OH data without static data show significantly high shape parameters, indicating an unrealistic skewness in OH fatigue data. Table 30 includes a summary of the fatigue-life parameter for 7781-8HS.

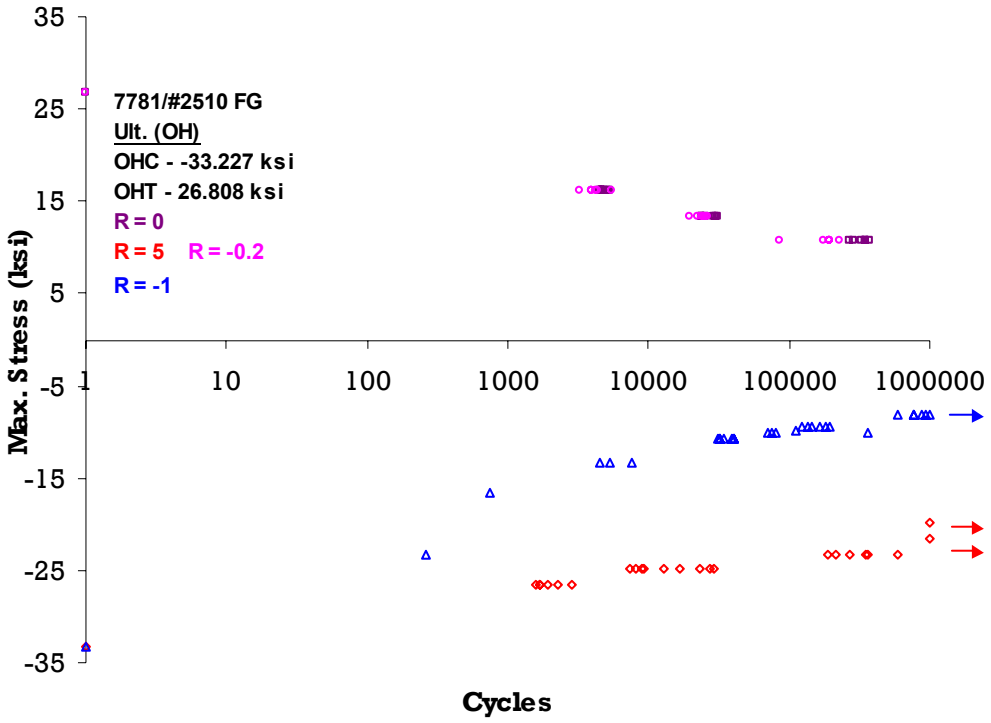

Figure 44. Effects of stress ratio for 7781-8HS OH fatigue data – measured.

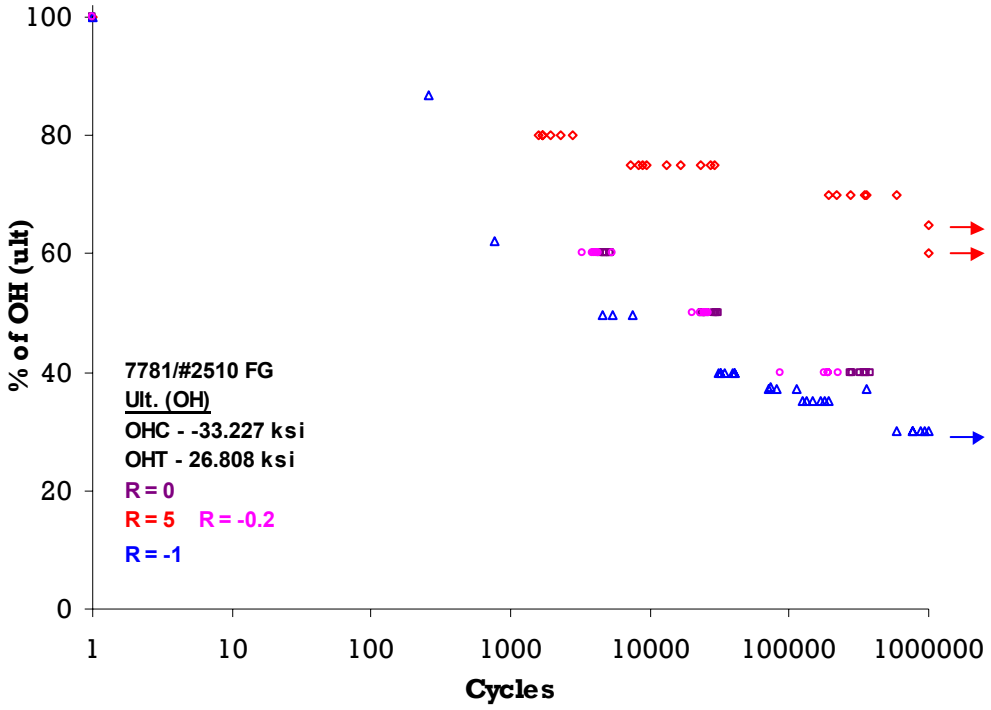

Figure 45. Effects of stress ratio for 7781-8HS OH fatigue data – normalized.

TABLE 29

FATIGUE-LIFE SCATTER ANALYSIS FOR 7781-8HS

Specimen Configuration			Sendeckyj		Weibull	
Layup	Test Description	R-Ratio	$\alpha_{Sendeckyj}$ (w/static)	$\alpha_{Sendeckyj}$ (w/o static)	$\alpha_{Ind. Weibull}$	$\alpha_{Joint Weibull}$
10/80/10	OH	-1	1.876	1.730	6.258	1.930
	OHC	5	2.727	2.580	3.169	2.532
	OHT	0	1.769	9.794	13.866	9.831
	OH	-0.2	1.575	7.335	8.998	7.361
	DNC	-1	1.163	1.056	2.035	1.150
	DNC	-0.2	2.724	2.643	3.346	2.628
Sandwich	4PB – HRH 10	0	2.358	3.429	4.034	3.569

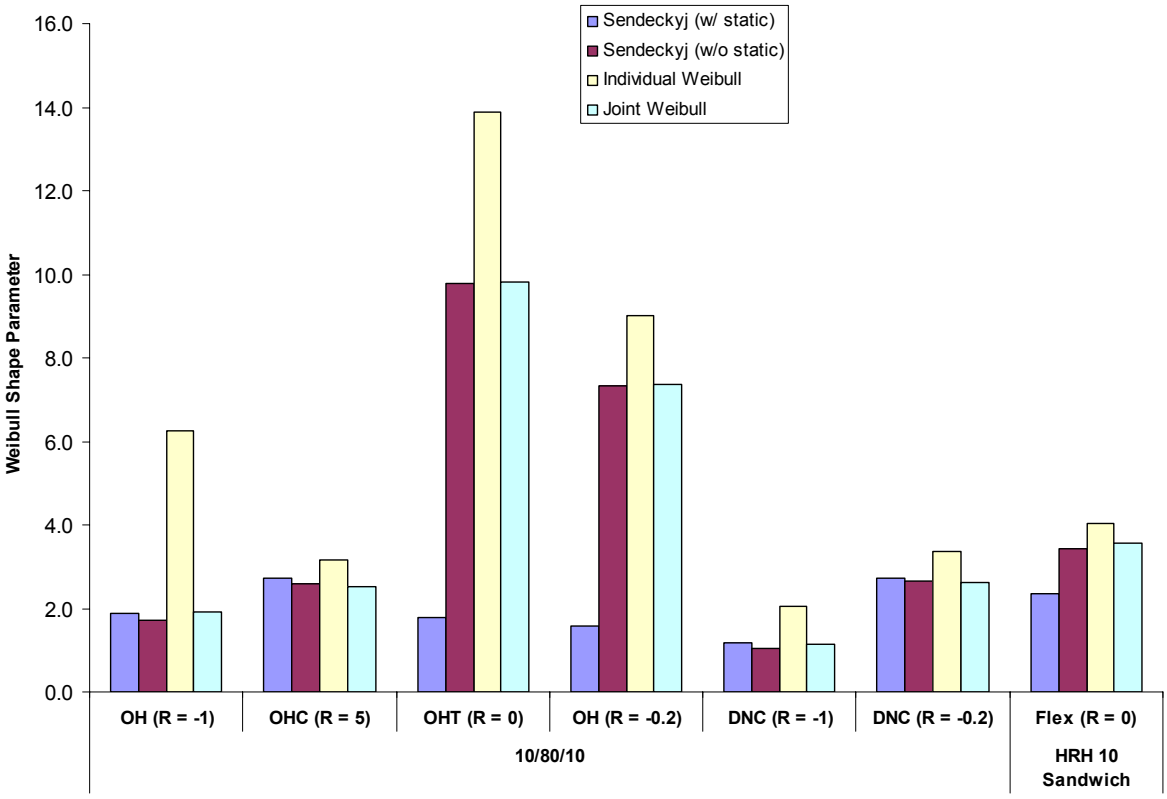

Figure 46. Fatigue-life shape parameters of 7781-8HS from different analysis methods.

TABLE 30

WEIBULL STATISTICS FOR COMBINED DISTRIBUTION OF SCATTER IN FATIGUE-LIFE DISTRIBUTIONS OF 7781-8HS

Analysis Method	Weibull Parameter	Fatigue Scatter Analysis Method			
		$\alpha_{Sendeckyj}$ (w/static)	$\alpha_{Sendeckyj}$ (w/o static)	$\alpha_{Ind.\ Weibull}$	$\alpha_{Joint\ Weibull}$
MLE	α	4.232	1.459	1.662	1.500
	β	2.237	4.542	6.726	4.630
	α_{Modal}	2.099	2.056	3.864	2.224
RRX	α	3.519	1.441	1.698	1.508
	β	2.251	4.482	6.614	4.552
	α_{Modal}	2.047	1.971	3.918	2.211
RRY	α	3.410	1.338	1.554	1.384
	β	2.262	4.605	6.801	4.692
	α_{Modal}	2.043	1.647	3.501	1.857

5.2.4. Adhesive Fatigue Data

Fatigue scatter analysis of FAA-D5656 material database [46] that contains ASTM D5656 single-lap shear adhesive joints from four different adhesive systems is included in this section. This database contains 390 adhesive specimens from 12 S-N curves, which represent three different test environments: CTD, RTA, and RTW. Each dataset contains a minimum of three fatigue stress levels and at least nine data points in each stress level in addition to static-strength data. Fatigue-life scatter analysis data are shown in Table 31. Figure 47 shows a comparison of fatigue-life scatter data obtained from different analysis techniques.

TABLE 31

FATIGUE-LIFE SCATTER ANALYSIS FOR FAA-D5656

Specimen Configuration		**Sendeckyj**		**Weibull**	
Adhesive	**Test Environment**	$\alpha_{\text{Sendeckyj}}$ **(w/static)**	$\alpha_{\text{Sendeckyj}}$ **(w/o static)**	$\alpha_{\text{Ind. Weibull}}$	$\alpha_{\text{Joint Weibull}}$
Loctite	CTD	0.805	0.821	1.069	0.946
	RTA	0.662	1.624	1.226	1.044
	RTW	0.682	0.644	1.109	0.738
EA9696	CTD	0.847	4.119	2.372	2.475
	RTA	0.403	1.389	2.077	1.752
	RTW	0.379	2.189	1.110	1.034
PTM&W (0.06")	CTD	0.870	1.376	1.541	1.093
	RTA	1.051	1.483	1.179	1.153
	RTW	0.681	1.169	1.417	1.014
PTM&W (0.16")	CTD	0.363	0.669	1.165	0.889
	RTA	0.856	4.296	2.170	1.193
	RTW	0.671	1.618	1.061	0.888

Individual Weibull shape and scale parameters of PTM&W for six shape parameters shown in Table 31 are 3.870 and 1.568, which result in a fatigue-life shape parameter of 1.451. Overall, the Sendeckyj analysis exhibits high scatter, especially for the case with static strength,

compared to individual Weibull analysis. This is due to the scatter observed in adhesive fatigue data at each stress level.

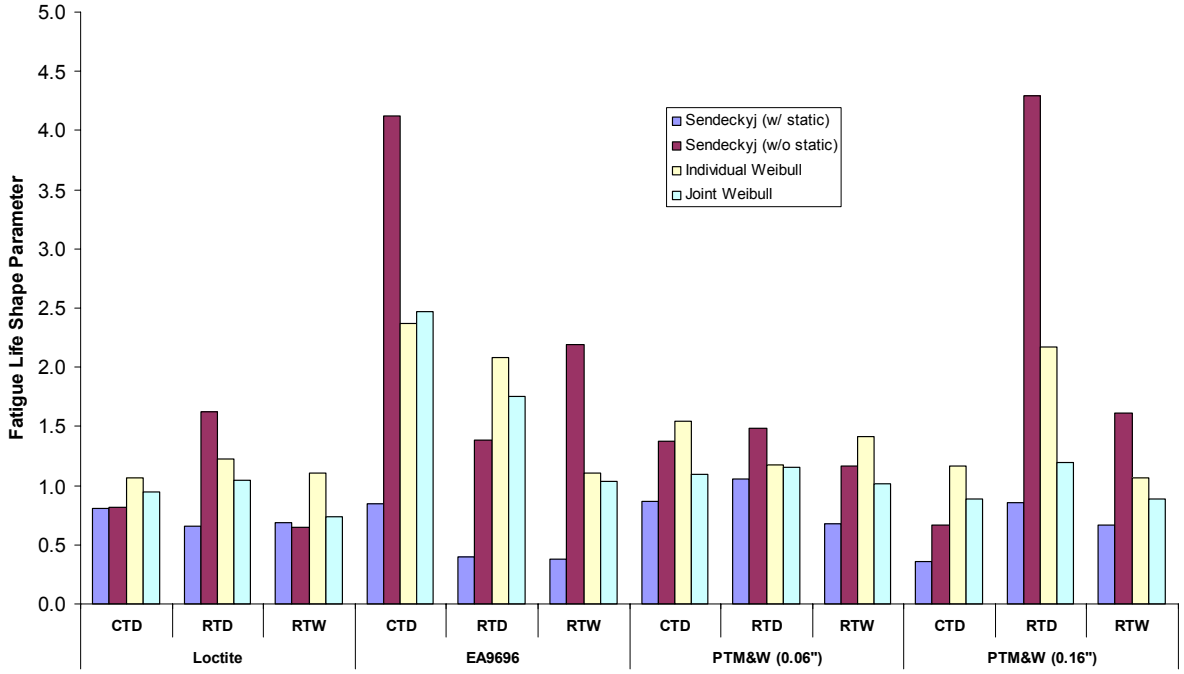

Figure 47. Fatigue-life shape parameters of FAA-D5656 data from different analysis methods.

Typically, the scatter in adhesive test data is significantly higher than that of composite test data. This is primarily due to the processing parameters and the multiple secondary loading modes occur during testing of adhesive joints, i.e., peel stress at the ends of the overlap during single-lap shear test. Post-fatigue microscopic analysis of Loctite paste adhesive test specimens indicated that fractures initiated from the clusters of glass beads, which were mixed into the adhesive to control bondline thickness. Further, the moisture-conditioned specimens indicated localized swelling around glass beads. The random distribution of glass beads and the effects of the above-mentioned two phenomena resulted in large data scatter. Furthermore, the change in bondline thickness and the amount of adhesive that squeeze out at the ends of the overlap will cause significant changes to the stress distribution of the adhesive layer, and consequently a large

data scatter. For the adhesive fatigue data in the current analysis, fatigue-life scatter significantly increases with test duration. Therefore, individual Weibull analysis is recommended for adhesive test data. Also, the modal shape parameters obtained for individual Weibull analysis data are consistent throughout RRX, RRY, and MLE (Table 32).

As shown in Figure 47, the Sendeckyj model with static data indicate significant scatter in the adhesive data, while without static data in some cases, scatter is higher than that for individual Weibull analysis. When including static data for the Sendeckyj analysis, it is recommended that a minimum of six static data points be included. At this point, it is recommended that adhesive S-N curves are analyzed using individual Weibull analysis. Thus, these S-N curves must have a minimum of six data points in each stress level, and each S-N curve must have minimum of three stress levels in addition to static data.

TABLE 32

WEIBULL STATISTICS FOR COMBINED DISTRIBUTION OF SCATTER IN FATIGUE-LIFE DISTRIBUTIONS OF FAA-D5656 DATA

Analysis Method	**Weibull Parameter**	**Fatigue Scatter Analysis Method**			
		$\alpha_{Sendeckyj}$ (w/static)	**$\alpha_{Sendeckyj}$ (w/o static)**	**$\alpha_{Ind.\ Weibull}$**	**$\alpha_{Joint\ Weibull}$**
MLE	α	3.854	1.679	3.339	2.889
	β	0.764	2.016	1.626	1.214
	α_{Modal}	0.707	1.176	1.461	1.091
RRX	α	3.374	1.993	4.487	4.777
	β	0.765	1.944	1.572	1.214
	α_{Modal}	0.689	1.371	1.486	1.156
RRY	α	3.064	1.741	3.247	3.440
	β	0.777	2.020	1.644	1.268
	α_{Modal}	0.683	1.237	1.468	1.147

5.3. Summary of Fatigue Scatter Analysis

Overall, the individual Weibull analysis provides the highest fatigue-life shape parameter, while the Sedeckyj analysis provides the lowest (conservative) fatigue-life shape parameter. For most cases, when the static data are included in the Sendeckyj analysis, the analysis resulted in significantly lower fatigue-life shape parameters than that without the static test data. For example, 7781-8HS OHT (R=0) S-N data resulted in a fatigue-life shape parameter of 9.794 for Sendeckyj analysis without static data. When the static test data are included in the analysis, this value was reduced to 1.769. For most composite analysis cases, the Sendeckyj analysis without static test data and the joint Weibull analysis resulted in similar shape parameters.

Figure 48 shows a comparison of fatigue-life shape parameters calculated using the Sendeckyj model for three composite material systems and three adhesive systems discussed in this chapter. Sendeckyj analysis for each composite and adhesive S-N curve is conducted with and without static data. Then, shape parameters for adhesive S-N curves are combined with shape parameters for each composite system. Fatigue-life scatter with static and adhesive data indicate the highest scatter for all three composite materials. Removing the adhesive data have the greatest effect on 7781-8HS life scatter, while removing the adhesive data and static data have the greatest effect on AS4-PW life scatter. For all three composites, removal of static and adhesive data result in significantly less scattered life shape parameters. For both AS4-PW and T700-PW, the shape parameter distribution obtained without static and adhesive data indicate the least scatter.

For composite material systems included in this chapter, R= -1 stress ratio resulted in the most critical open-hole fatigue life. For T700-PW, this stress ratio resulted in the least scatter. Typically, the load reversal (R<0) causes low fatigue life and less scatter in test data.

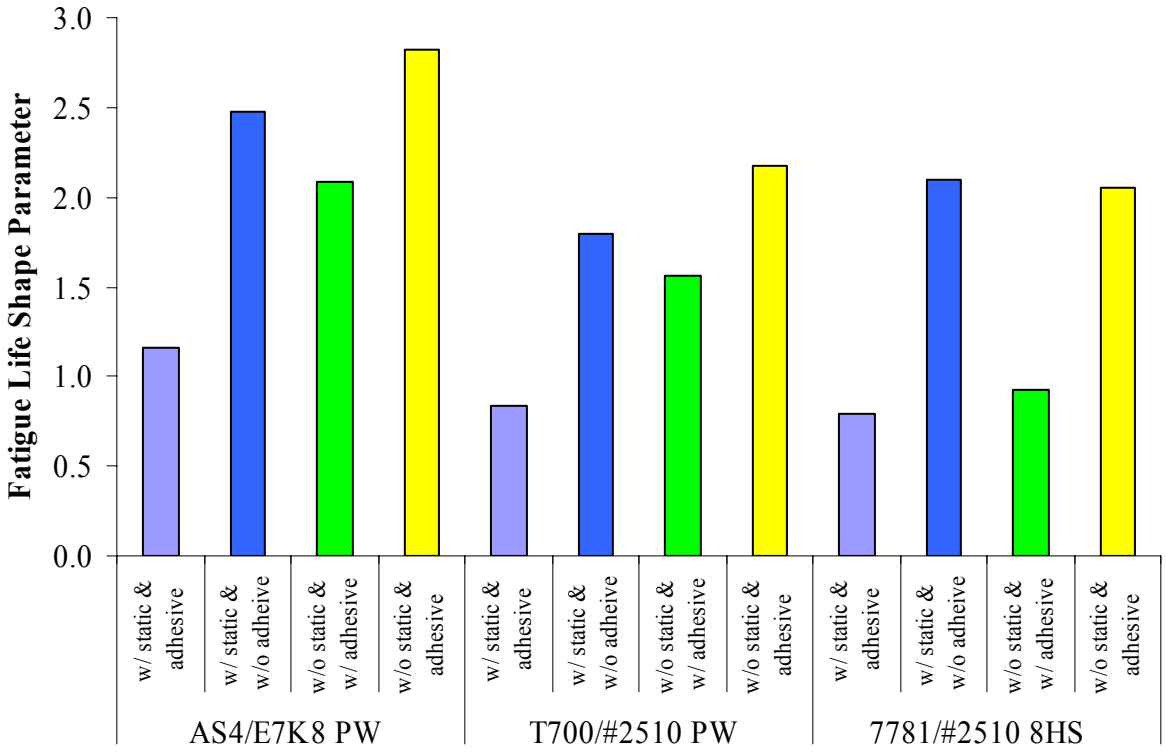

Figure 48. Comparison of fatigue-life shape parameter for FAA-LEF database.

5.4. Load Enhancement Factor

This section includes the effects of static-strength and fatigue-life scatter on the load-enhancement factor and the combined load-life approach. Data for three different composite material systems in the FAA-LEF data set were combined with adhesive fatigue data in the FAA-D5656 material database to obtain life and load enhancement factors. As discussed in section 3.2, the life factor, N_F, is a function of modal life shape parameter (MLSP or α_L) and is not influenced by the modal-strength shape parameter (MSSP or α_R). However, LEF is a function of both parameters.

Different combinations of MSSP and MLSP from sections 4.2 and 5.3, respectively, are combined to calculate the corresponding LEF curves. Table 33 shows the life factor for MLSP obtained by combining adhesive fatigue-life shape parameters obtained from individual Weibull

analysis for adhesives and Sendeckyj analysis for composites. MSSP for T700-PW also includes element test data from the FAA-EOD database. The influence of test duration on the B-basis load-enhancement factor for these three materials is shown in Figure 49 for one test article. Table 34 and Figure 50 show a comparison of MLSP obtained for AS4-PW by using different analytical techniques, i.e., individual Weibull or Sendeckyj model, for composites and adhesives.

TABLE 33

WEIBULL STATISTICS FOR COMBINED COMPOSITES AND ADHESIVES

Composite Material	α_R	α_L	N_F
AS4/E7K8 PW	32.193	1.880	5.267
T700/#2510 PW	32.845	1.576	7.516
7781/#2510 8HS	60.092	1.660	6.715

TABLE 34

WEIBULL STATISTICS FOR AS4-PW COMPOSITES AND ADHESIVES FROM DIFFERENT ANALYTICAL TECHNIQUES

Analysis Method	α_R	α_L	N_F
Individual Weibull (C)	32.193	4.056	2.070
Individual Weibull (C+A)	32.193	2.082	4.418
Sendeckyj (C)	32.193	2.475	3.431
Sendeckyj (C+A)	32.193	1.021	26.296
Sendeckyj (C) +Individual Weibull (A)	32.193	1.880	5.267

C and A represent AS4-PW composites and adhesives, respectively.

As can be seen from these examples, the LEF calculated as a function of test duration for these materials is significantly lower than that for NAVY. In addition, application of the life factor, rather than LEF, for high loads in spectrum requires fewer repetitions for improved MLSP than that for NAVY. However, guidance for generating reliable shape parameters must be established to prevent unrealistic LEF that will compromise the structural integrity of composite aircraft. It is recommended that specimens or elements representative of features representing

materials, design details, failure modes, loading conditions, environments, etc., are included in the analysis rather than pooling various material databases. Also, it is noted that the primary goal in scatter analysis is not selecting shape parameters from the critical layup, R-ratio, environment, etc., (which may result in skewed data that will produce unconservative LEF), but rather selecting the design details representing the critical areas of the structure.

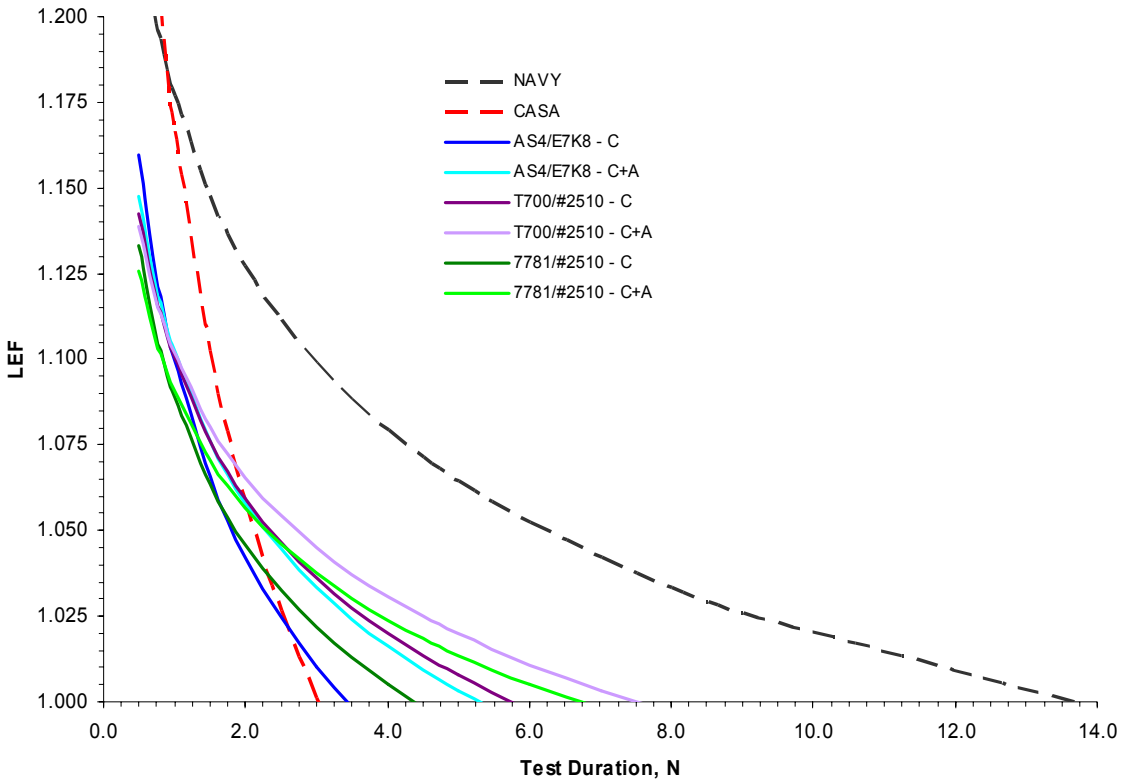

Figure 49. Influence of test duration on B-basis load-enhancement factors for different materials.

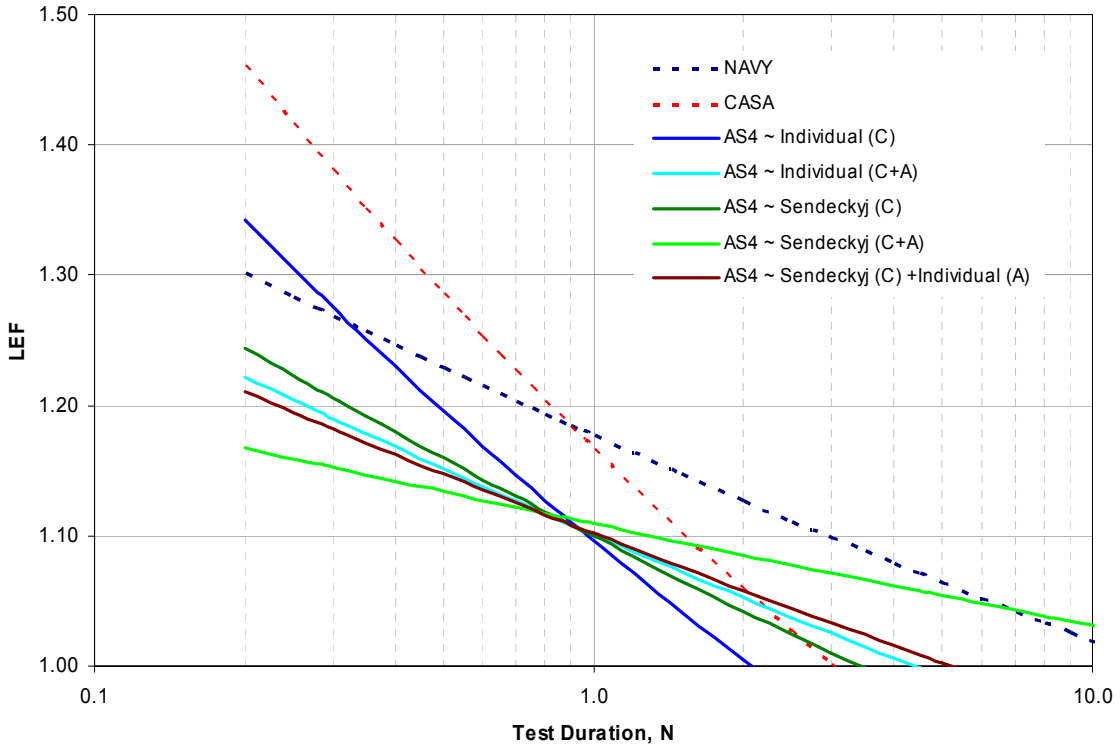

Figure 50. Influence of test duration on B-basis load-enhancement factors of AS4-PW from different analytical techniques.

The primary objective of the analysis in Chapters 4 and 5 was to evaluate the parameters affecting MSSP (α_R) and MLSP (α_L) so that minimum requirements to generate safe and reliable, yet economical, load-enhancement factors and life factors (N_F) can be outlined along with a recommendation for benchmark test matrices. The secondary objective was to create a readily available shared database of static-strength and fatigue-life shape parameters for commonly used composite materials and structural details to support on-going and future certification programs to reduce testing time and cost. Finally, well-documented procedures and a user-friendly computer code for generating statistically reliable life factor and load enhancement factors were developed. Using equation (9), Tables A.28 and A.29 in Appendix A include A- and B-basis LEFs, respectively, for different combinations of MSSPs and MLSPs for different test durations and number of test articles.

5.5. Case Studies

5.5.1. Beechcraft Starship Forward Wings

The Beechcraft Starship forward wing structure was fabricated primarily using AS4/E7K8 material system. This structure contains sandwich (HRH-10) and bonded joints (AF163) as shown in Figure 51. The LEFs calculated in section 5.4 for AS4-PW includes these details. The MSSP and MLSP for pooled composite (Sendeckyj) and adhesive (individual Weibull) data are 32.193 and 1.880, respectively, resulting in a life factor of 5.267. As shown previously in Figure 50, the LEFs corresponding to a 1.5 test duration is reduced to 1.076 from 1.148 (NAVY). Full-scale fatigue testing conducted in this research (chapter 8) used the modified B-basis LEFs and life factor, whenever necessary, instead of the historically used NAVY values.

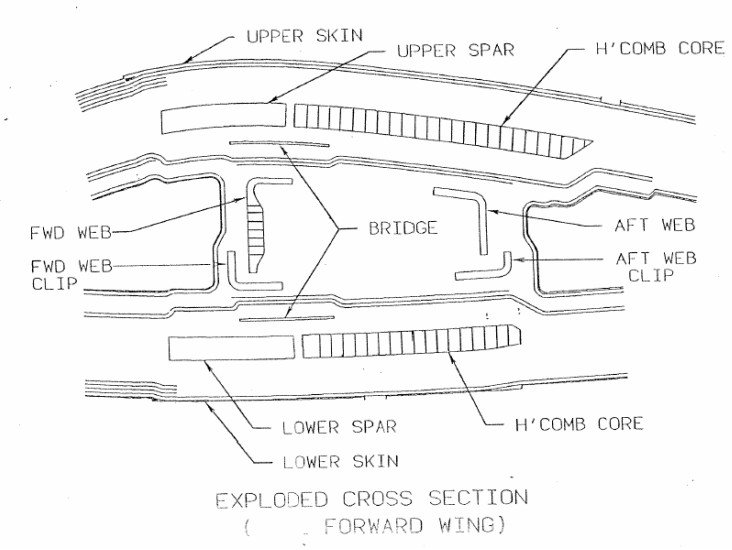

Figure 51. Beechcraft Starship front wing (detailed construction).

The details of the durability and damage tolerance testing of Starship forward wing structures are included in Chapter 8. Prior to load application, large impact damages were

inflicted on the fatigue test articles. Also, these full-scale tests were conducted by applying the improved LEFs based on the scatter analysis conducted in Chapters 4 and 5 on AS4/E7K8 material system. The load spectrum was also multiplied by an additional conversion factor based on three static-full scale tests conducted to determine the load capacity of the structure (section 8.1.3). This would account for additional factors applied to the structural design such as environmental factors. As can been seen from the detailed test data analysis in Chapter 8, the test article with a large impact damage on the aft spar demonstrated residual strength capacity after 2-DLT of spectrum loading with an LEF.

5.5.2. Liberty Aerospace XL2 Fuselage

This section demonstrates an application of LEF for a composite fuselage of the Liberty Aerospace XL2 aircraft (Figure 52) that was primarily fabricated using T700/#2510 PW (T700-PW) and Airex R82-80 foam core. In order to generate LEF for the fuselage material systems, several sandwich coupon configurations were tested.

Figure 52. Liberty Aerospace XL2 aircraft.

A reduced test matrix was developed, including compression and shear-loaded sandwich coupons using an R82-80 core. Both notched and unnotched compression sandwich specimens

were tested using open-hole anti-buckling fixtures. One, two, and three plies for face sheet layups and 3 and 5 mm thick cores with and without core splices were included in the test matrix. Several ETD static-compression specimens were also included. The total Liberty database included 198 static data points and 82 fatigue data points. Each static dataset had a minimum of six specimens (Table 35).

TABLE 35

WEIBULL ANALYSIS RESULTS OF LIBERTY SANDWICH STATIC TEST DATA

Specimen Configuration	Loading Configuration	Core Size (mm)	Plies per Facesheet	Core Splice	Number of Specimens	Weibull Parameters	
						Shape	Scale
RTA Unnotched	Compression	3	1		6	17.234	2.606
	Compression	3	2		6	51.431	5.307
	Compression	3	3		6	35.754	7.011
RTA Notched	Compression	3	1		6	22.962	2.133
	Compression	3	2		6	19.597	4.224
	Compression	3	3		6	105.229	5.438
RTA Shear	Shear	3	1		6	23.376	0.226
	Shear	3	2		6	30.213	0.245
	Shear	3	3		6	30.058	0.251
	Shear	5	1		6	14.520	0.196
	Shear	5	2		6	16.305	0.209
	Shear	5	3		6	53.031	0.190
ETD Static	Compression	3	1		6	7.450	2.525
	Compression	3	2		6	12.065	5.046
	Compression	3	3		6	28.349	6.296
	Compression	3	1	YES	6	14.895	2.543
	Compression	3	2	YES	6	38.642	4.690
	Compression	3	3	YES	6	17.858	6.327
	Compression	3	1		6	8.145	1.975
	Compression	3	2		6	29.879	3.736
	Compression	3	3		6	33.781	4.689
	Compression	3	1	YES	6	9.153	2.802
	Compression	3	2	YES	6	17.646	3.730
	Compression	3	3	YES	6	31.001	5.414

However, fatigue datasets did not have the minimum recommended five specimens per stress level to generate accurate individual Weibull shape parameters. Therefore, MLSP was

generated using the Sendeckyj method for fatigue datasets that had a minimum of three stress levels, in which fatigue failures were in at least two (Table 36). MSSP was generated using several scenarios: (1) only Liberty database [56], (2) Liberty (without adhesive data) and FAA-LVM databases, (3) Liberty (with adhesive data) and FAA-LVM databases, and (4) Liberty, FAA-LVM, and FAA-EOD databases.

TABLE 36

SENDECKYJ ANALYSIS RESULTS OF LIBERTY SANDWICH FATIGUE TEST DATA

Specimen Configuration	**Loading Configuration**	**Core Size (mm)**	**Plies per Facesheet**	**Core Splice**	**Number of Specimens**	**Shape Parameter**
Unnotched	Compression	3	3		10	1.346
	Compression	5	3	YES	9	17.410
Notched	Compression	3	3		7	4.559
	Compression	5	3		7	3.972
Shear	Shear	3	1		9	7.254
	Shear	3	2		8	4.965
	Shear	3	3		9	1.229
	Shear	5	1		7	4.016
	Shear	5	2		7	7.024
	Shear	5	3		9	0.804

Since the Liberty XL2 fuselage is primarily T700-PW with ±45° layup and T700-UT around some of the highly loaded areas, only 10/80/10 T700-PW and 50/40/10 T700-UT data from the FAA-LVM database were included in the fatigue analysis of the Liberty XL2 fuselage materials [56]. This is an example of using a shared database for generating reliable LEFs with minimum testing efforts, i.e., only testing the R82-80 core. B-basis load-enhancement factors are shown for all four analysis scenarios with respect to different test durations in Table 37. These data are also illustrated in Figure 53.

TABLE 37

COMPARISON OF WEIBULL STATISTICS FOR LIBERTY XL2 DATABASE

Test Duration (*N*)	**NAVY**	**CASA**	**Analysis Scenario for Liberty XL2**			
			1	**2**	**3**	**4**
1.00	1.177	1.167	1.166	1.141	1.148	1.157
1.10	1.170	1.151	1.158	1.131	1.138	1.146
1.25	1.161	1.131	1.147	1.118	1.124	1.132
1.50	1.148	1.103	1.133	1.100	1.106	1.112
1.75	1.137	1.079	1.121	1.085	1.090	1.095
2.00	1.127	1.059	1.110	1.073	1.076	1.081
3.00	1.099	1.001	1.079	1.035	1.037	1.039
4.00	1.079		1.057	1.009	1.009	1.010
MSSP (α_R)	20.000	19.630	20.886	23.526	22.419	21.199
MLSP (α_L)	1.250	2.740	1.469	2.082	2.082	2.082
Life Factor (N_F)	13.558	3.019	8.837	4.422	4.422	4.422

Since MLSP from the Liberty data (Scenario 1) are lower than that for the NAVY database, the life factor is reduced to 8.837 from 13.558. This is further reduced to 4.422 after adding FAA-LVM data. For a given MLSP, the life factor is fixed since it does not depend on MSSP. Therefore, further improvements to MSSP result in a decrease in the slope of the curve, which pivots about N_F (LEF=1), as shown in Figure 53. Consequently, this lowers the LEF, especially for smaller test durations. In Scenario 3, MSSP is reduced when the Liberty adhesive data are included, indicating a small increase in scatter for the Weibull distribution of static scatter parameters. MSSP is further decreased in scenario 4, when element level adhesive joint data from FAA-EOD are included. FAA-EOD element test specimens are bonded using EA9394. However, the Liberty XL2 is bonded using EPIBOND 1590. Therefore, Scenario 3 is more applicable to this structure.

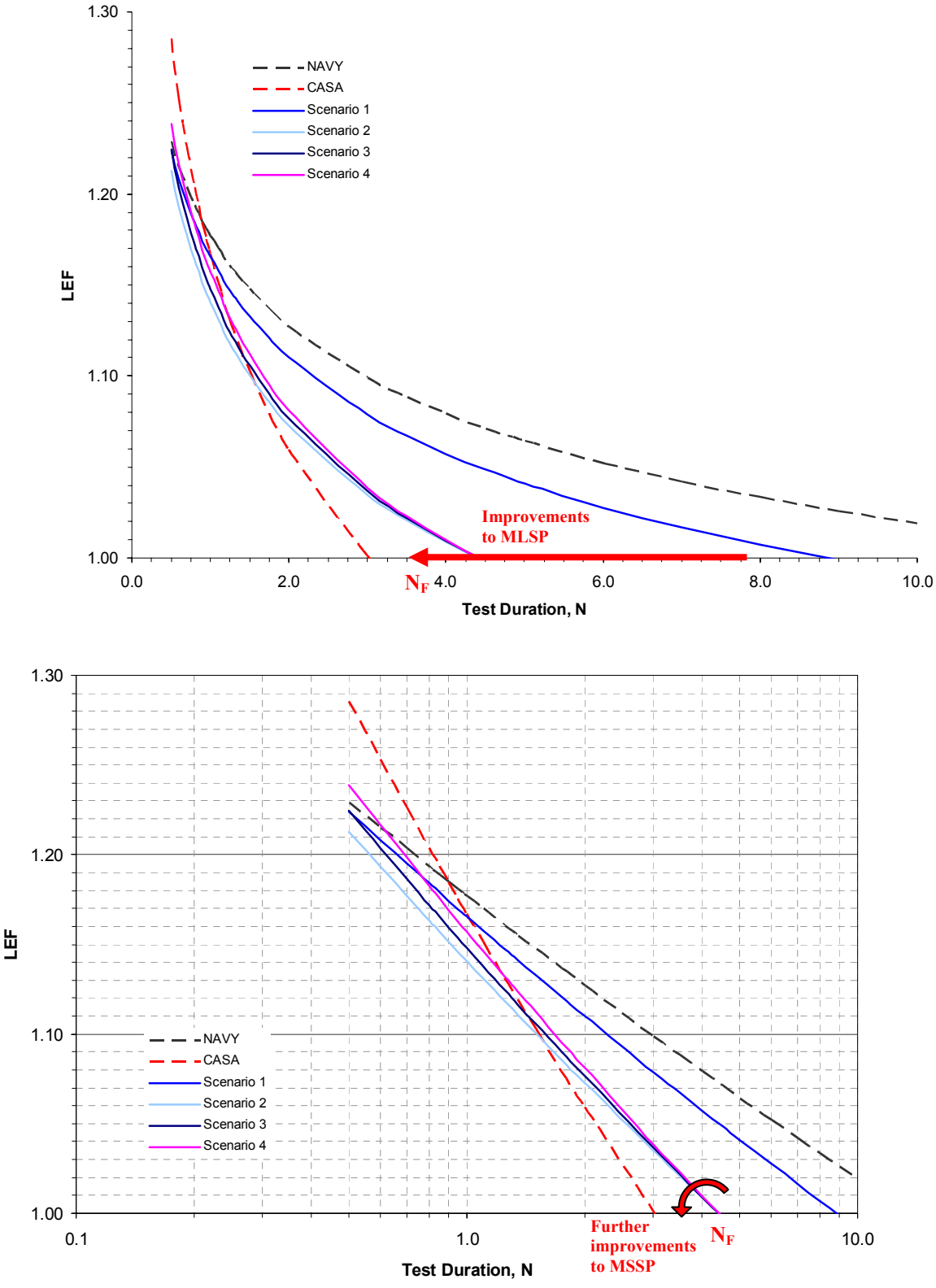

Figure 53. Influence of test duration on B-basis LEFs for Liberty XL2.

Although Scenario 3 does not show significant improvements for LEF, the life factor is about 50 percent lower than that for Scenario 1. Also, B-basis LEFs for this scenario are considerably lower than that for NAVY. The original fatigue testing of the Liberty XL2 fuselage was conducted using the NAVY life factor and a LEF of 1.15, which corresponds to a test duration of 1.5 DLT. The Liberty fuselage fatigue test was conducted for three test lives with NAVY LEF and included a damage tolerance phase as well. According to Scenario 3, an LEF of 1.15 corresponds to a test duration of 1 DLT. Thus, the full-scale test with an LEF of 1.15 corresponds to a B-basis life factor of 1. The actual test was conducted with two DLTs more than what is required to achieve the same level of reliability demonstrated by the metal structure. This increases the confidence on DLT, i.e., number of hours corresponding to test duration of 1 DLT.

During full-scale testing, certain spectrum load cycles above a percentage of the design limit loads (high-load cycles) were multiplied by the NAVY life factor rather than applying LEF, as described in section 3.4. Due to the improvement in data scatter, the life factor was reduced to 4.422 from the value of 13.558 proposed for composites by Whitehead et al. [2]. Therefore, the high-load cycles were repeated approximately three times more than the required number of repetitions to achieve the B-basis life factor. This further increased the level of confidence on DLT.

In order to compare the B-basis LEF requirements based on different databases, the Liberty XL2 fuselage durability and damage tolerance (DaDT) test was compared against two scatter analysis material databases: (1) NAVY and (2) Liberty data (scenario 4 in **Error! Reference source not found.**). This approach evaluated the modified DLT in the event that a certification test duration or LEF was different from the minimum required to achieve B-basis

reliability. Figure 54 shows the B-basis LEF requirements with respect to different test durations based on data from the above-mentioned two databases. Liberty LEF requirements reflect the material and process as well as test method improvements related to composites, which consequently reduced the data scatter as compared to the test data used for the NAVY approach. Points C and Z correspond to the life factor for Liberty and NAVY databases, respectively. Points X and Y show the LEF required for 1.5- and 3-DLT test durations, respectively, according to the NAVY approach. For the same test durations, points A and B show the LEF requirements for the improved composite test data for Liberty XL2 fuselage materials.

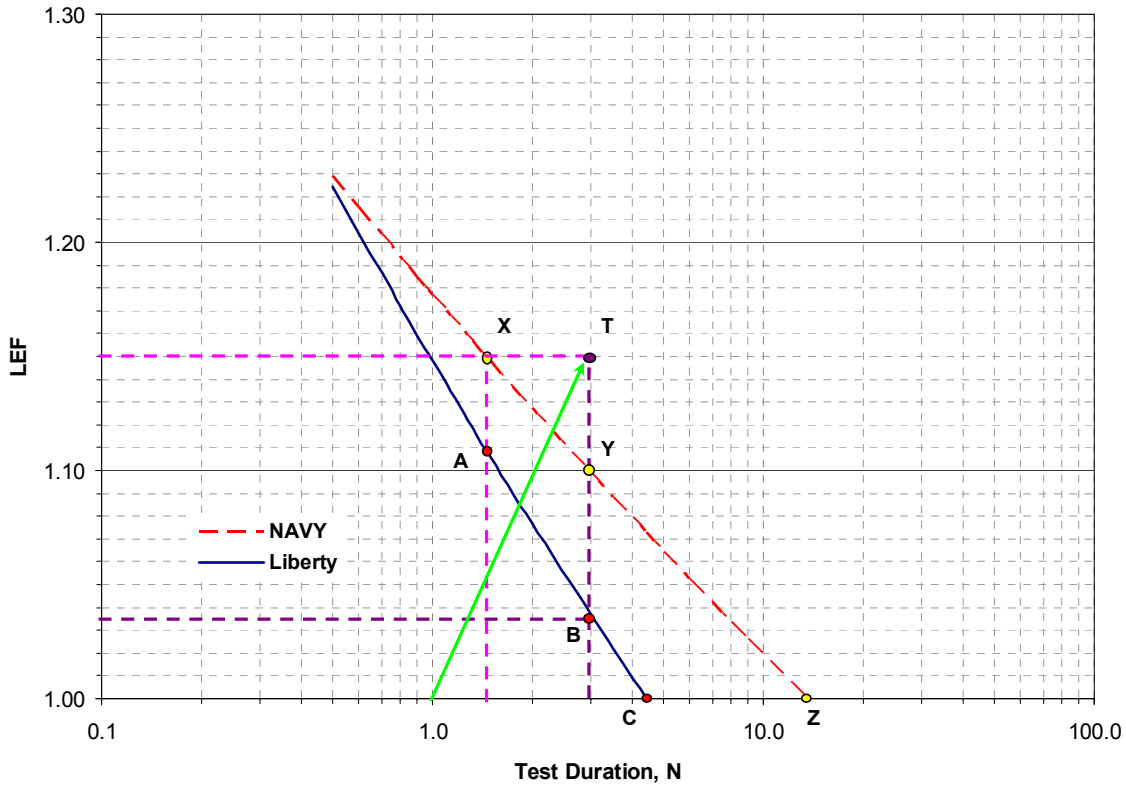

Figure 54. Comparison of tested and required LEFs for Liberty XL2.

A full-scale DaDT test of the 1653-pound Liberty XL2 fuselage was performed at NIAR for three lifetimes. Point T in Figure 54 shows the LEF used during the DaDT full-scale test substantiation. The load spectra used for cyclic loading was developed using the exceedance curves from DOT/FAA/CT-91/20 [58] (maneuver and gusts) and AFS-120-73-2 [59] (taxi and landing). The test spectra has been truncated below 30 percent design limit load (DLL) in order to shorten the test without significant effects on the fatigue characteristics of the structure. No load in excess of DLL was applied during cyclic testing.

Since testing of the Liberty LEF was in progress at the time of full-scale test substantiation, an LEF of 1.15 corresponding to 1.5-lifetime per NAVY approach [2] was applied to loads below an 80 percent limit load, and an N_F of 28.5 was applied for loads above an 80 percent limit load, similar to the approach outlined in Figure 19(b). This approach allowed for using a lower load-enhancement factor in a trade-off for more life cycles, which would reduce the severity of the overload for high stress levels.

Based on the NAVY approach, B-basis reliability was obtained either by increasing the loads by an LEF of 1.15 with test duration of 1.5 DLTs or by applying N_F of 13.6. This is equivalent to N_F of 2 DLTs, which is typically used to demonstrate B-basis reliability of metal structures. However, as can be seen in Figure 54, the Liberty XL2 fatigue test article was tested twice the required test duration (3-DLTs) with no indication of damage growth and demonstrating residual strength after repeated loading. Therefore, it is evident that the test article demonstrated B-basis reliability for twice the design lifetime of 5,000 hours. Typically, this argument alone would not justify the new design lifetime as the load segments above 80 percent DLL are multiplied by N_F instead. However, in this case, N_F should have been 13.6 or 4.422, based on the NAVY or Liberty approach, respectively. The applied N_F is more than twice

compared to the NAVY approach and six times compared to the Liberty approach. Thus, the above-mentioned argument for a design lifetime of 10,000 hrs is justified. An N_F of 28.5 corresponds to a MLSP or α_L of 1.00 (Figure 15), which corresponds to materials that exhibit higher scatter in fatigue life data than the dataset in the NAVY approach.

Alternately, considering only the NAVY approach and based on the difference between applied and required LEFs for B-basis reliability, it can be shown that this structure is capable of carrying 5 percent more load than the tested load spectrum for substantiation of a 5,000-hour DLT. Based on the test data applicable to Liberty XL2 fuselage materials and design details, an LEF of 1.035 for three lifetimes (Table 37) or an N_F of 4.422 was sufficient to demonstrate B-basis reliability on a 5,000-hour DLT. Therefore, considering the improved LEF curve and based on the difference between applied and required LEFs for B-basis reliability, it can be shown that a 1,653-pound fuselage structure is capable of carrying 11.5 percent more loads than the designed load spectrum for DLT of 5,000 hours. This additional information can be used to support design changes that result in higher load requirements, given that the load spectra, failure modes, and critical locations of the structure are not changed.

This case study addresses concerns related to the application of LEF and N_F during full-scale test substantiation. Once the LEF curve is generated, as shown in Figure 54, any combination of LEF and test duration, N, is going to provide the same level of reliability that is required to be demonstrated by metal structures, N=2-DLT. Thus, the test duration and life factor are not further required to be multiplied by two to achieve B-basis reliability of the designed lifetime.

CHAPTER 6

DAMAGE-TOLERANCE ELEMENT TESTING

A detailed damage-tolerance element (DTE) study was conducted to determine the flaw growth and data scatter in damaged composite structures. This study focused mainly on impact damages and their effects on the extent of the damaged area, residual strength, fatigue life, flaw growth, and data scatter. The data gathered in this section also provide guidance to scaling of damage extents for full-scale testing.

6.1. Experimental Procedure

In addition to data included for scatter analysis conducted on AS4/E7K8 plain-weave fabric material, a total of 72 compression-after-impact (CAI) specimens and 6 unimpacted (baseline) specimens were tested (Table 38). Stress levels were selected to obtain fatigue failures rather than runouts.

TABLE 38

DAMAGE-TOLERANCE ELEMENT TEST MATRIX

Category of Damage	Damage Definition	Impact Energy Level (in-lbf/in)	Stress Level	% of Static Strength	Number of Specimens
Unimpacted	UI	N/A	Static	100	6
CAT1	BVID	750	Static	100	6
			SL1	80	6
			SL2	75	6
			SL3	70	6
CAT2a	VID	1500	Static	100	6
			SL1	75	6
			SL2	70	6
			SL3	65	6
CAT2b	LID	3000	Static	100	6
			SL1	75	6
			SL2	65	6
			SL3	60	6

The main objective was to evaluate the data scatter with respect to the damage energy level or damage threat. Test panels were fabricated with a 32-ply quasi-isotropic layup, $[45/0/-45/90]_{4S}$. Test specimens were machined to 6 by 9 inches, instead of the ASTM standard test method for compressive residual strength properties of damaged polymer matrix composite plates (D7137) recommended to be 4 by 6 inches, to minimize the edge effects of large damages and to leave sufficient material for damage propagation during cyclic loading. Based on several trial impact and residual strength tests, 750, 1500, and 3,000 in-lbf/in impact energy levels were selected to represent CAT1, CAT2a, and CAT2b damage, respectively. The damage definitions corresponding to these energy levels are as follows:

CAT1 – Barely visible impact damage (BVID)

CAT2a – Visible impact damage (VID)

CAT2b – Large impact damage (LID)

Although these definitions may not have a one-to-one correlation to damages on a full-scale structure, the information pertaining to the scatter analysis is relevant to a damage structure at its critical load path, i.e., minimal global load redistribution due to damage. Following infliction of the impact damage, residual dent depth and damage extent (using TTU C-scan) were measured. During fatigue loading, the damage extent was inspected using a BondMaster^{TM} 1000 hand-held NDI inspection unit using mechanical impedance analysis at several predetermined number of cycles. Furthermore, ARAMIS full-field strain and displacement data were acquired at the maximum fatigue load at these intervals to delineate the extent of damage. This also allowed for measuring the residual stiffness or the compliance change of these specimens at these fatigue intervals.

All tests were conducted in an RTA environment. Fatigue tests were conducted at a frequency of 5 Hz with an R-ratio of 5 using the load control mode. For flaw growth studies, the strain control mode provides more progressive damage data since the maximum and minimum fatigue loads are gradually decreased as the compliance decrease; however, fatigue tests in this study were conducted using the load control mode to simulate fatigue damage on a critical load path that has minimal load redistribution due to loss of stiffness or compliance, i.e., front spar of Starship forward wing. This control mode maintains the initial minimum and maximum fatigue loads by increasing the strain ($+\Delta_\varepsilon$) throughout the fatigue test, in contrast to the strain control mode that reduces the loads ($-\Delta_P$) to maintain the initial strain limits (Figure 55). Furthermore, because of the high sensitivity in strain feedback during fatigue testing, this control may result in frequent test interruptions due to interlocks set to prevent over-straining of the test specimen.

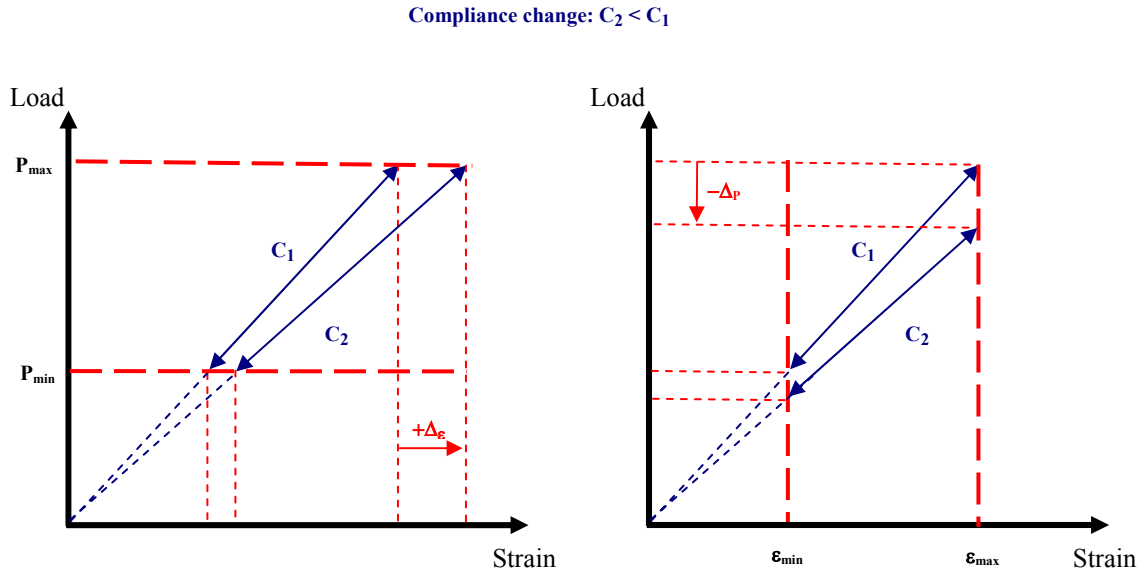

(a) Load control mode (b) Strain control mode

Figure 55. Load-strain response for different test control modes.

6.2. Damage-Tolerance Element Test Results

This section contains the NDI, residual strength, and fatigue life of DTE tests. Incipient curves during impact and post-impact inspection results are also included. Further, the scatter analysis of S-N data and flaw-growth data are included for these specimens. Figure 56 shows the energy history for different impact energy levels. The plateau regions depict the total energy transferred to the specimen.

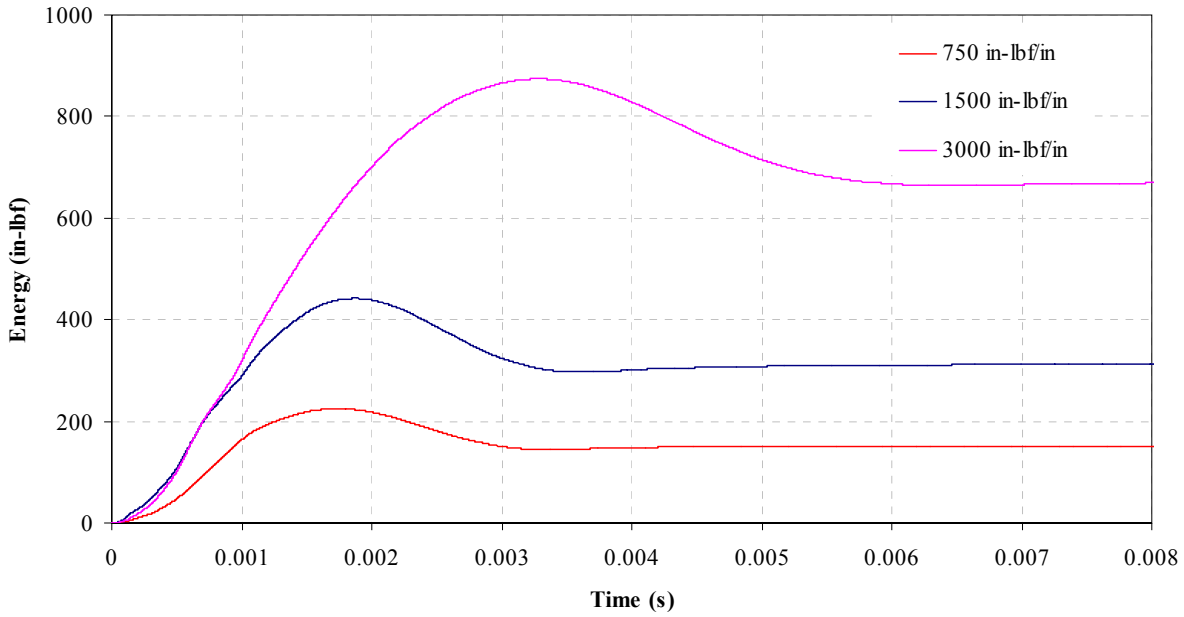

Figure 56. Comparison of energy history for different impact energy levels

6.2.1. Post-Impact Inspections

This section contains the NDI, residual strength, fatigue life, and scatter analysis of damage-tolerance element tests. As can be seen in Figure 57, VID was manifested as a large cross-shaped back-side damage. Although some of the BondMaster™ 1000 NDI data followed the cross-shaped damage, post-impact TTU C-scans indicated mostly circular damage patterns.

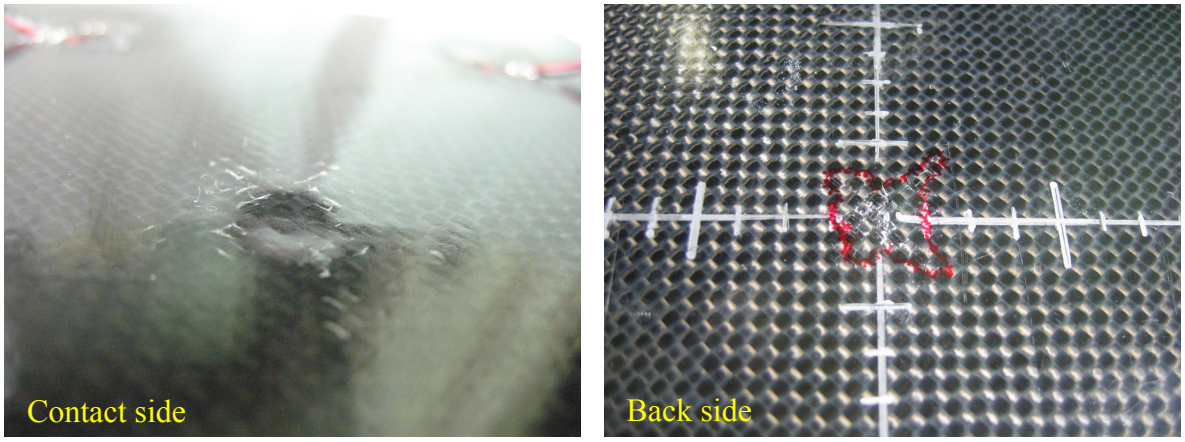

(a) 1500 in-lbf/in

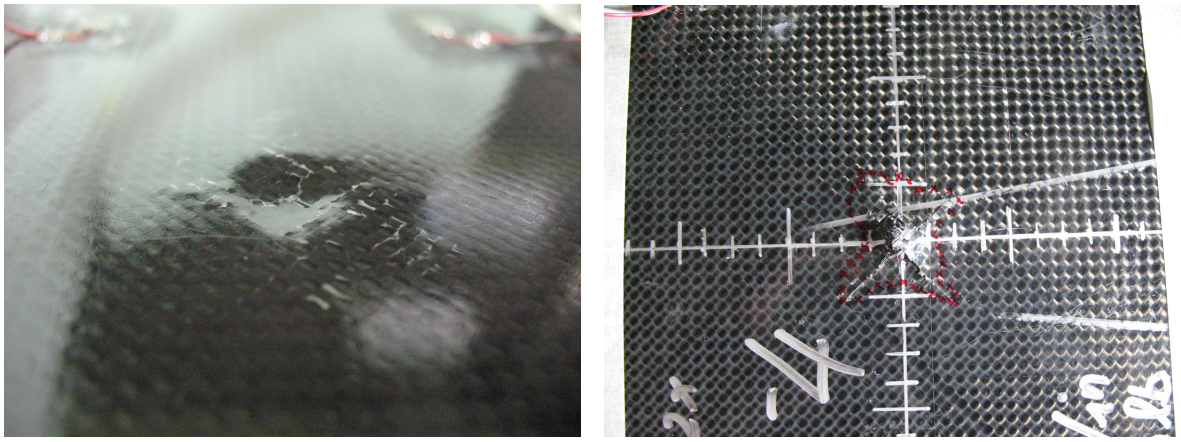

(b) 3000 in-lbf/in

Figure 57. Post-impact damage inspection of DTE test specimens.

During the impact event, matrix cracks and fiber breakage resulted in a complex damage morphology that was difficult to predict, especially for impacts that do not result in complete penetration. There was a significant compressive stress due to contact stress and the resulting bending moment, which was concentrated at the impact location resulting in fracture along the fiber directions of the composite fabric layers. This was evidenced by the cross-shaped fracture on the back side of the specimens where the outermost fibers were in ±45° orientation (Figure 58). The stiffness mismatch in fiber and matrix caused the cracks to form along the fiber directions during deflection.

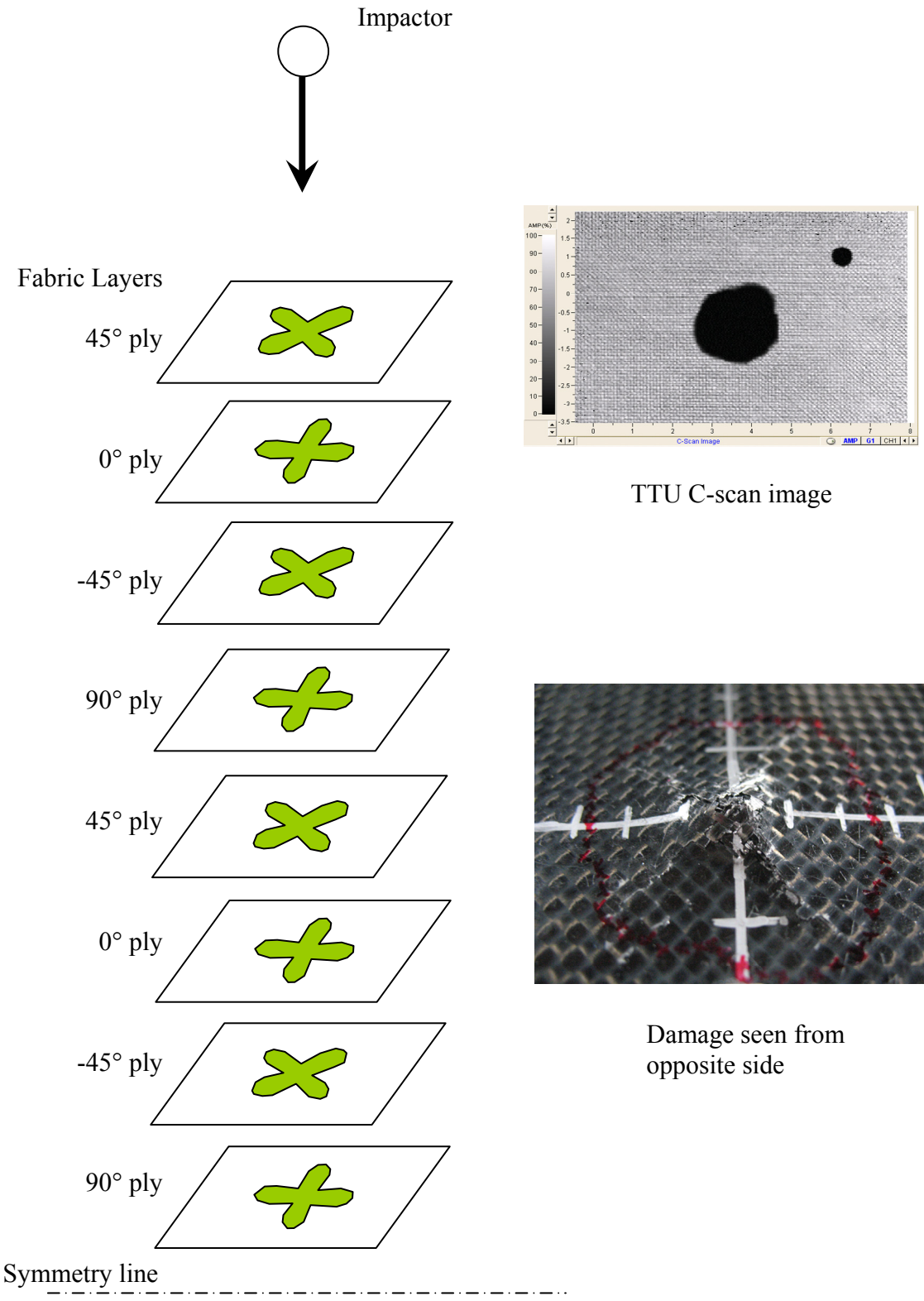

Figure 58. Orientation of matrix crack concentrations due to impact.

For a unidirectional composite, the damage took an oblong or "peanut" shape with the major axis oriented in the fiber direction [57]. As shown by Tomblin et al. [47] for low-velocity impact damages on bonded composite joints, since the layup of AS4-PW is quasi-isotropic, i.e. $[45°/0°/-45°/90°]_{2S}$, these cross-shaped damage zones possibly concentrated in a 45° radial spacing, along fiber directions, at each layer through the thickness and smaller cracks in between, resulting a circular damage shape as seen in TTU C-scans. In addition to cracks, localized contact stress resulted in fiber breaks and transverse cracks on first few plies that resulted in cracks through the thickness of these plies. At these crack tips, where they meet the lower ply, a high peel stress was created at the ply interface, which resulted in interfacial cracks or delamination. Because of the intralaminar matrix cracks along the fiber directions, the delamination propagated along the fiber directions of adjacent plies. Since the adjacent fabric plies were oriented 45° apart, the delamination spread in a circular pattern, as shown in Figure 58, i.e., matrix cracks in adjacent layers coalesce within the small layer of matrix material between plies. Additional microscopic analysis and three-dimensional NDI data are required to verify this conjecture.

As can be seen in Figure 59, the damage area increased as the impact energy increased. For 3000 in-lbf/in (VID) test specimens, a significant amount of energy was translated into large fractures and significantly large deformation (Figure 60); thus, the rate of increase in the damage area was reduced. As can be seen in Figure 61, the contact force reached a maximum of 4,000 lbf as the energy level increased, which resulted in a significant perforation, thereafter reducing the delaminated area in the planner direction.

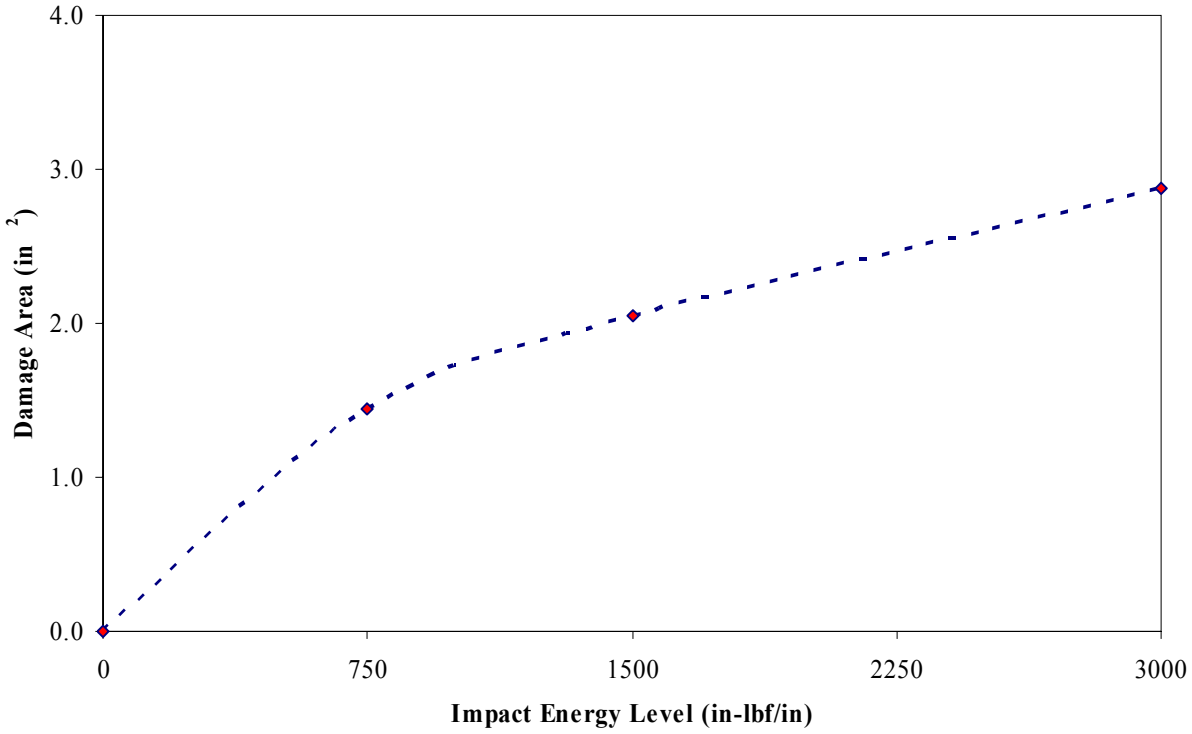

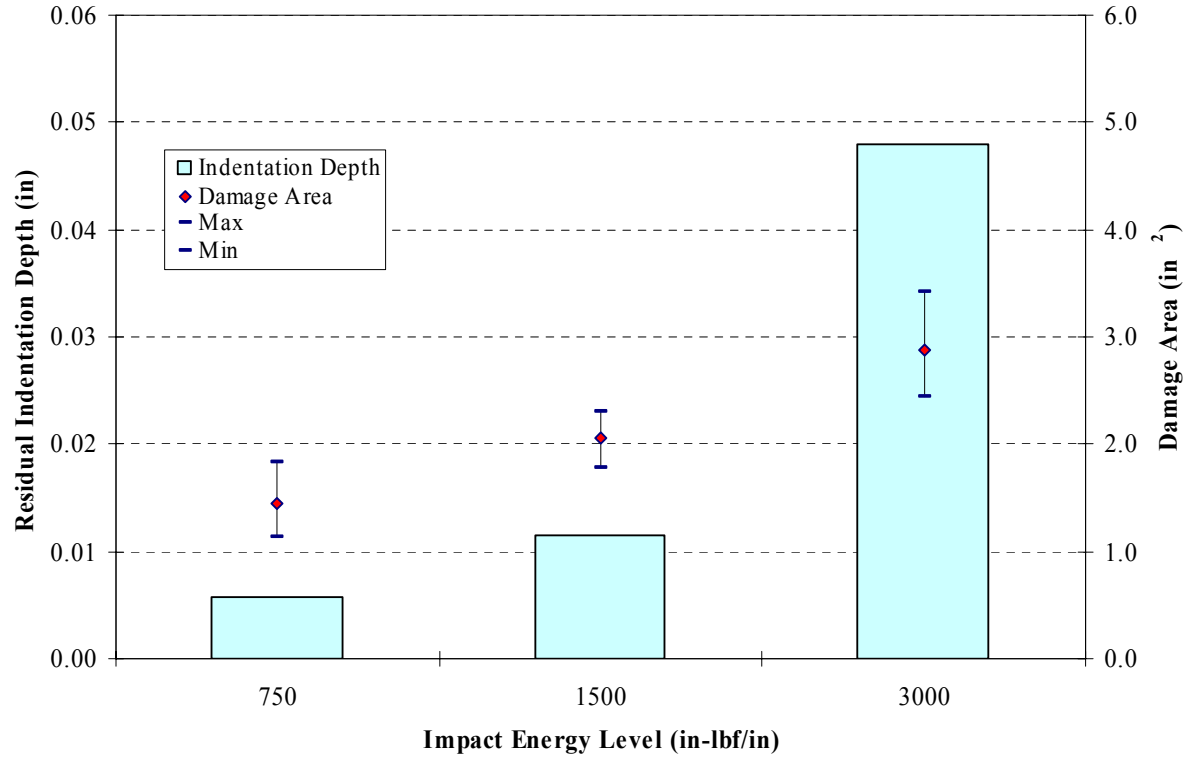

Figure 59. Post-impact inspection results for DTE tests.

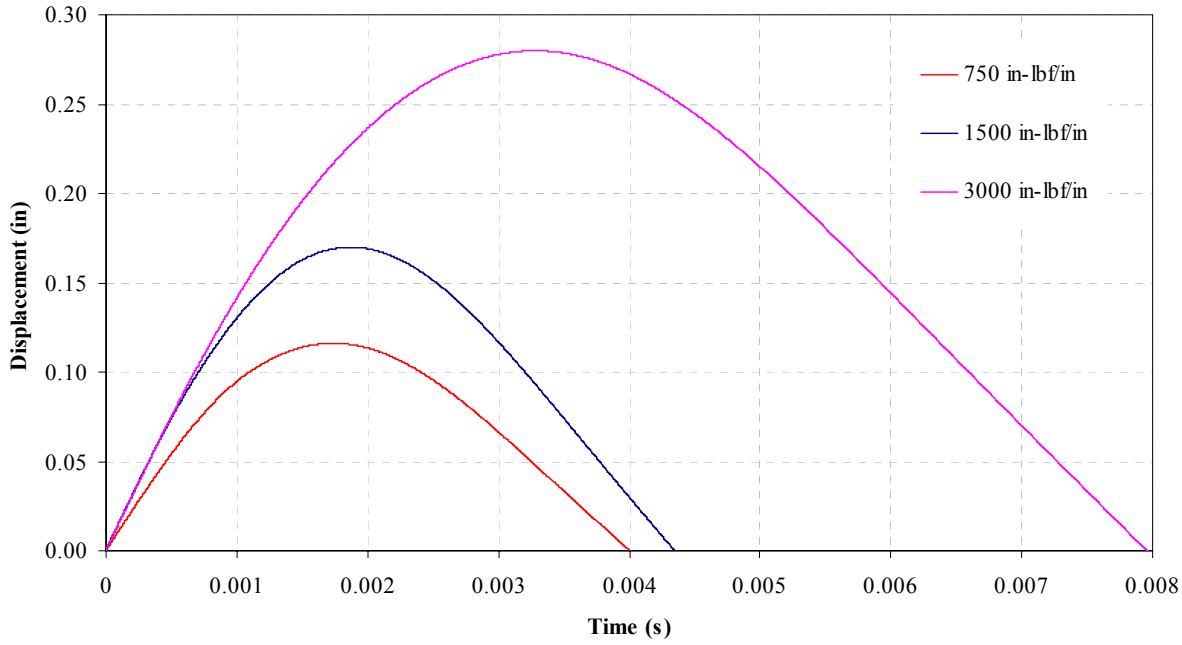

Figure 60. Comparison of displacement history for different energy levels.

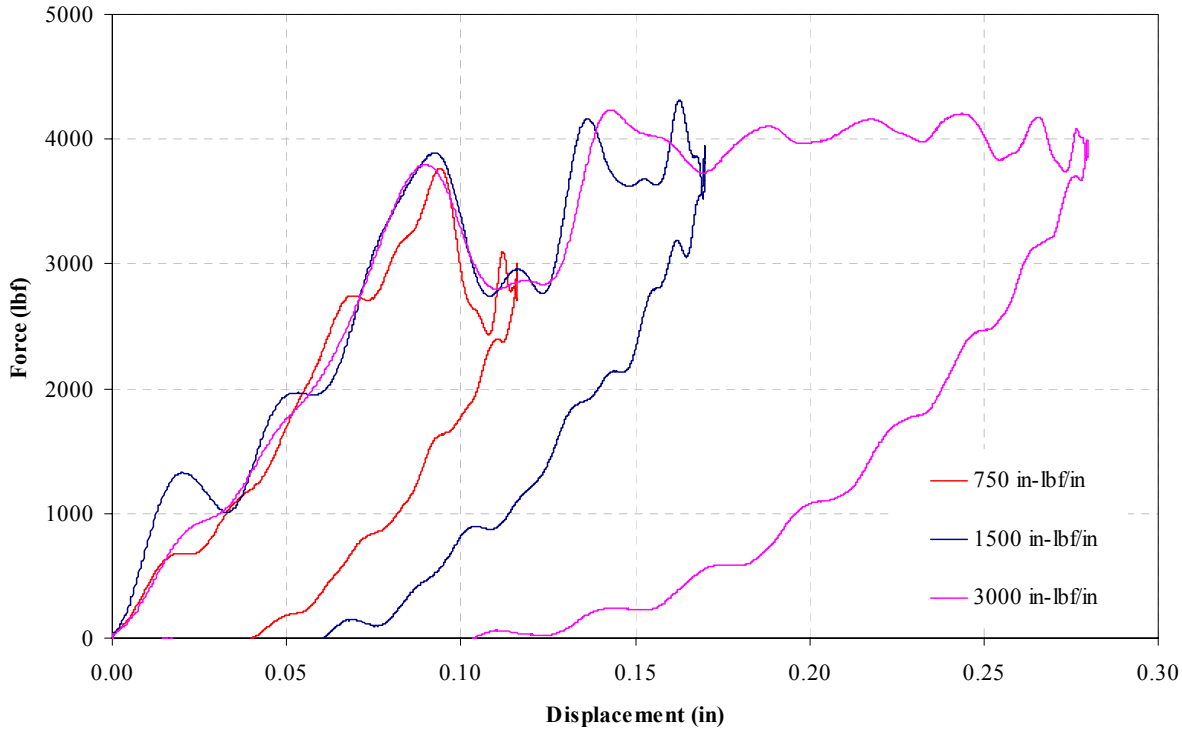

Figure 61. Comparison of force displacement for different energy levels.

As shown in Figure 62, there was about 29 percent reduction in residual strength for LID compared to BVID, while it was approximately 17 percent for VID. Damage areas were 99 and 42 percent for LID and VID, respectively, compared to BVID. The stress concentration factor (SCF)–the stress amplifications in the vicinity of the defect (geometric discontinuity)–is calculated as 1.55, 1.87, and 2.19, for BVID, VID, and LID, respectively. These SCFs correspond to a damaged structure assuming that the post-impact load path has not significantly changed. The loss of residual strength and post-impact damage inspections showed that LID specimens were sufficient to mimic CAT2b damage at the element level. Thus, the scatter in the CAT2b damage structure was assumed to be represented by the scatter analysis of the LID specimen, as shown in section 6.2.3.

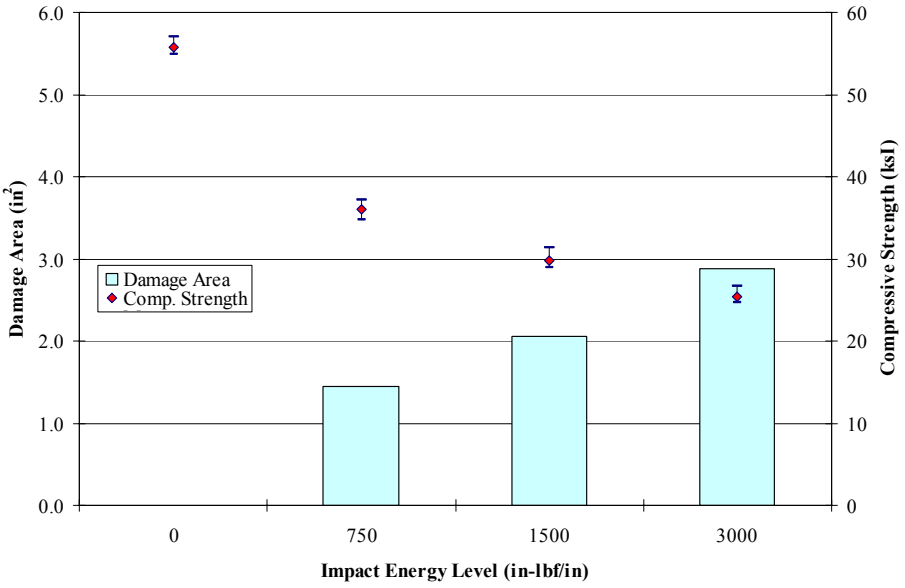

Figure 62. Damage area and residual strength results comparison for DTE tests.

Figure 63 shows a summary of DTE test data for all three damage categories. The S-N data are also compared with the Sendeckyj wearout model data. For LID specimens that had larger perforations than either BVID or VID, the initial stiffness degradation was not prominent as majority of the damage had already propagated through the thickness (initial plateau region in

Figure 63). Note that the residual strength and the fatigue life of CAI specimens tested in this section are likely affected by the finite specimen width, especially for LID.

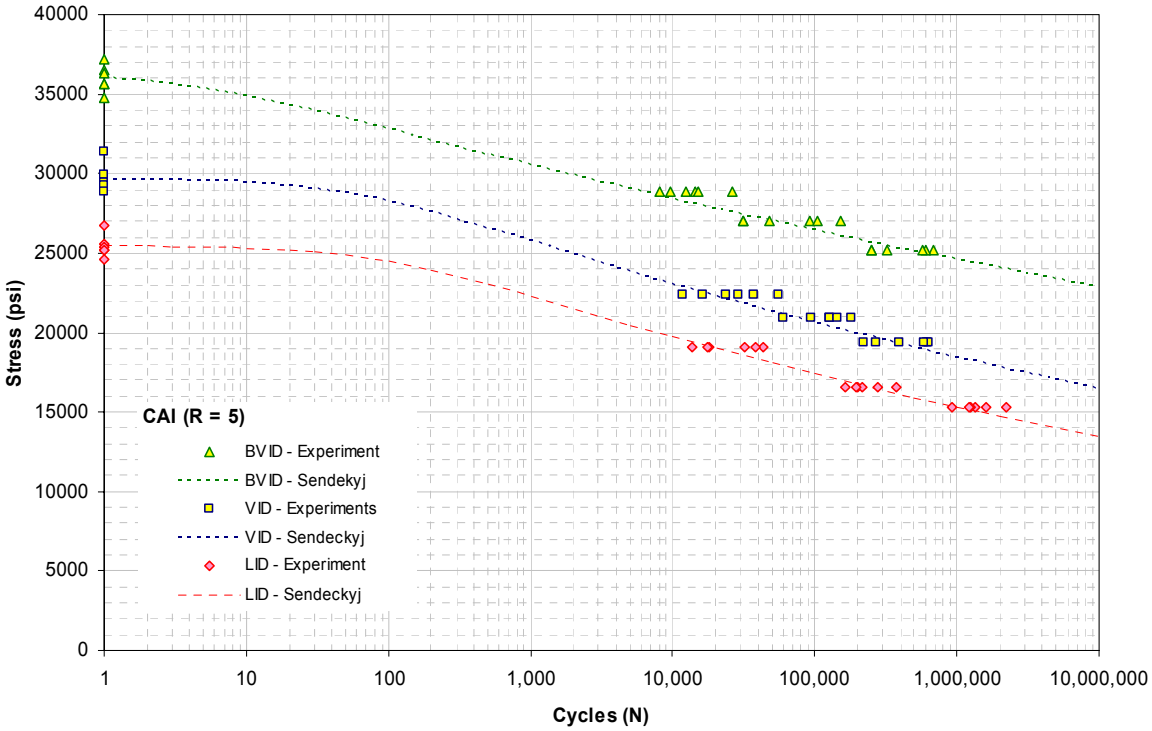

Figure 63. S-N curves for DTE test specimens.

6.2.2. Flaw-Growth and Compliance Change

Typically during fatigue loading, specimen compliance gradually decreases (section A.2), primarily due to stiffness degradation in the matrix material and when a sudden drop in load-carrying capabilities is observed, i.e., when the fiber failure occurs, the specimen fails. For the case of DTE specimens, the impact damage propagated as shown in Figure 64 for the LID fatigue specimen at SL2 (65%). As can be seen in this figure, the initial cross-shaped damage area, which was delineated by BondMaster™ 1000 as opposed to the circular C-scan damage, rapidly grew into a circular shape. As explained in Figure 58, this is due to the coalition of small cracks that were present (C-scan images) but not detectible to BondMaster™ 1000 prior to

fatiguing. Although the damage stopped growing in the load direction (height) after about 75,000 cycles, it grew continuously in the direction perpendicular to the load until final failure (260,091 cycles).

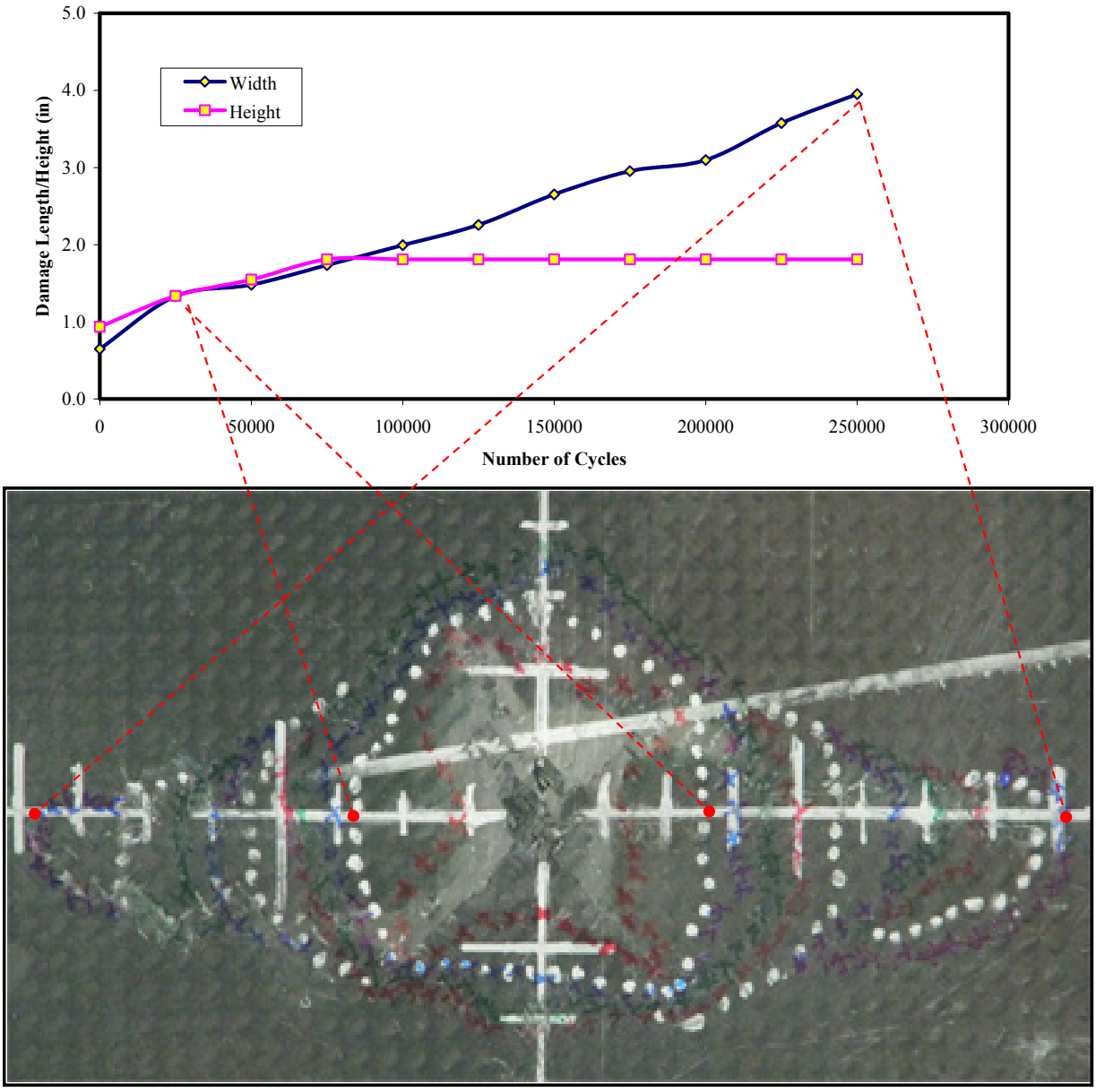

Figure 64. Progressive damage propagation for SL2 of LID.

As can be seen in Figure 65 for SL3 (60%) of LID, the height of the damage remained steady throughout the test. However, the width of the damage remained contained up to 200,000

cycles and then increased steadily until final failure at 492,163 cycles. ARAMIS full-field displacement measurements also confirmed the increase in damage width and significant out-of-plane displacement after 200,000 cycles. Thus, the flow growth threshold for this damage scenario and stress level is 200,000 cycles. More ARAMIS data are included in Appendix B.

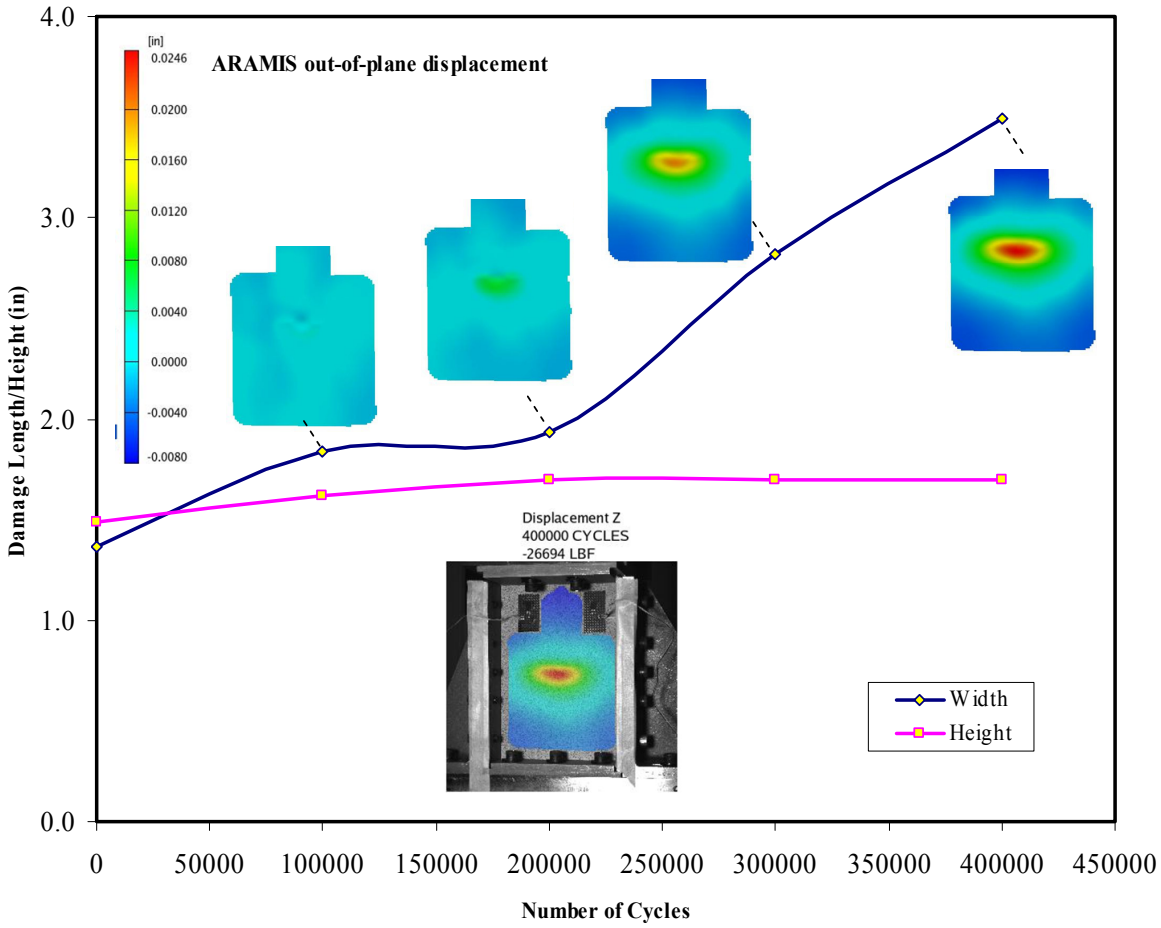

Figure 65. Progressive damage propagation and out-of-plane displacement for SL3 of LID.

Typically, the NDI or full-field displacement/strain measurements are not acquired during a fatigue test, as they are time consuming and not economical. However, specimen compliance can be calculated by simply outputting data during fatigue testing, without interrupting the fatigue test, and calculating the slope of the load-displacement curve. As can be seen in Figure 66, the compliance of the SL3 specimen dramatically dropped after 200,000

cycles, thus confirming the NDI observations. Compliance of the SL2 specimen gradually decreased after 50,000 cycles. Thus, it is recommended that specimen compliance, especially for notched specimens, be monitored throughout the fatigue test to better understand the failure mechanism and the damage propagation.

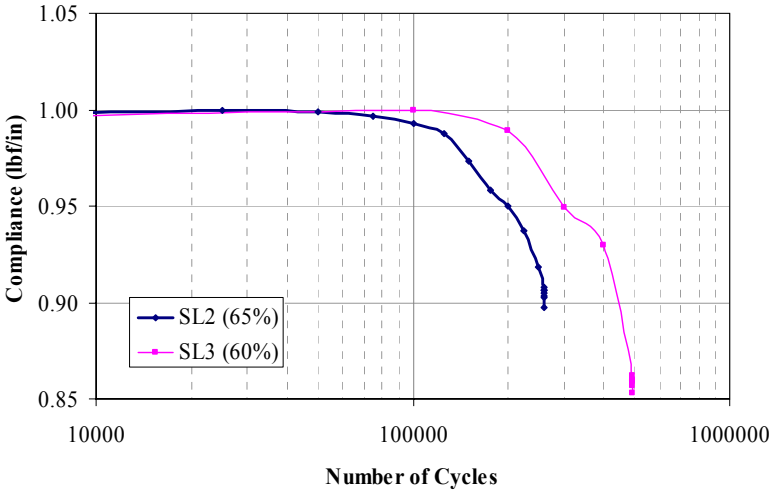

Figure 66. Compliance change in LID fatigue specimens.

6.2.3. Scatter Analysis of DTE Test Data

The scatter analysis of S-N data shown in Table 39 was conducted using individual Weibull, joint Weibull, and Sendeckyj analyses (Figure 67). The later two are pooled analytical techniques for calculating the shape parameter of fatigue-life distribution.

TABLE 39

SCATTER ANALYSIS RESULTS OF DTE TESTS

Damage Category	Static Strength		Durability and Damage Tolerance			
	Weibull Analysis		Sendeckyj Analysis		Weibull Analysis	
	α	β	With Static	Without Static	Individual	Joint
BVID	45.771	36413	1.774	2.234	2.446	2.355
VID	32.222	30103	2.182	2.658	2.991	2.779
LID	36.676	25776	2.466	2.799	3.272	3.250

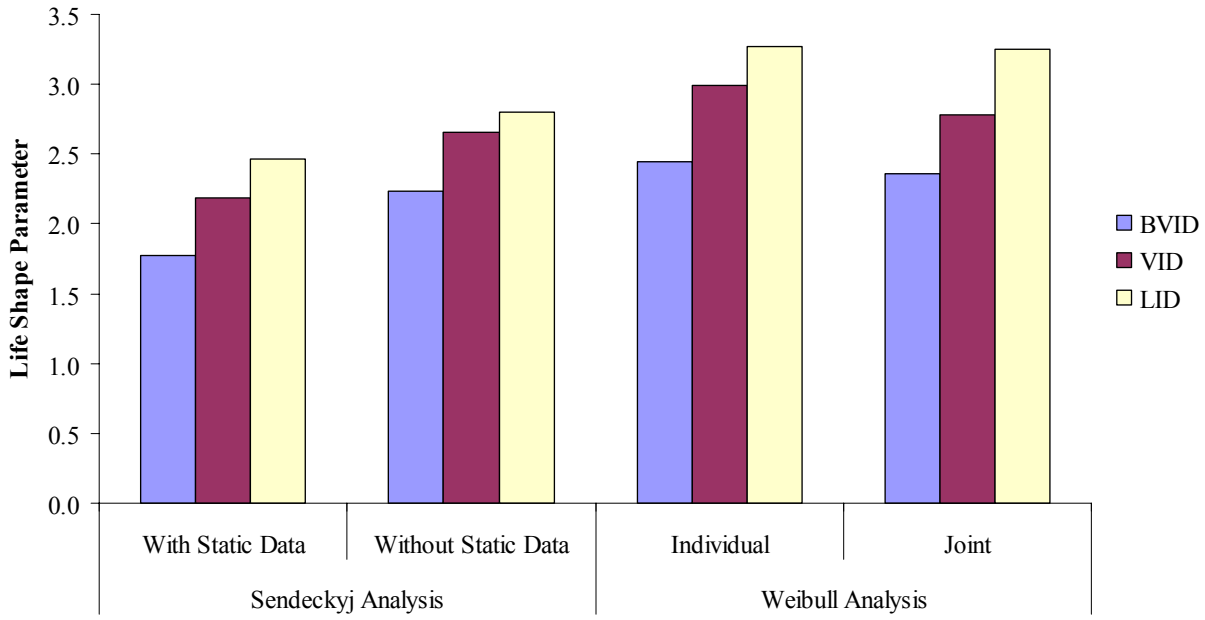

Figure 67. Comparison of DTE life shape parameters.

Sendeckyj analysis was conducted with and without static data. As shown for LEF data in Chapter 5, life scatter increased when the static data points were included in the analysis. All four analysis methodologies showed that the scatter in fatigue data was reduced as the damage threat level increased, mainly due to the stress concentration caused by the increased severity of impact damage. The post-impact visual inspections revealed that the probability of detection of a damage increases proportionally with the increased energy level or severity. In a service environment, the latter will mitigate the risk of a severe damage, such as a CAT2b, being left undetected. Thus, the damage will be found within a few flights. The reduction in scatter, on the other hand, supports the analysis of static strength or fatigue life of a damaged structure using scatter-based methods and results in less rigorous requirements to achieve a certain level of reliability. These items will be further discussed in Section 7.3.3, in terms of application to a full-scale DaDT test article.

CHAPTER 7

DAMAGE TOLERANCE OF COMPOSITE STRUCTURES

The primary goal in a damage-tolerance certification program is to avoid catastrophic failure due to fatigue, corrosion, or accidental damage throughout the operational life of the aircraft. The damage-tolerance philosophy is well established for metallic airframes, where proven methods (structural analysis and inspection procedures) and supporting databases exist to detect damage and predict crack growth and residual strength. However, damage characteristics, inspection procedures, analysis methods, and experimental databases are not well understood to apply the damage-tolerance philosophy to composite structures, including sandwich construction. Determination of damage-tolerance characteristics of sandwich panels has been limited in previous investigations to relatively few sandwich configurations and damage states [42]. Thus, there is a growing interest in damage-tolerance methodology to determine the fatigue life of composite structures under repeated loading.

7.1. Certification Approach

The state of damage within a composite structure is complex and dependent on a number of variables that define the intrinsic properties of the sandwich constructions and the extrinsic damage-causing event. Further, the barely visible impact damage (BVID), allowable damage limit (ADL), and critical damage threshold (CDT) are not clearly defined in terms of a rational damage metric. Traditionally, visual inspection procedures have been used for detecting damage in composite structures (in-service); hence, BVID came into existence. The current definitions of BVID are based on the residual indentation depth, which has been clearly shown to be configuration-dependent and often misleading. Another issue coupled with this is the choice of NDI techniques, which dictates the damage metric defining the BVID criterion.

7.1.1. Damage-Tolerance Design Philosophy

The general philosophy applied during damage-tolerance certification, shown schematically in Figure 68, relates representative damage size to design load requirements. As in the case of metal aircraft, ultimate strength and damage-tolerance philosophies are used to maintain a reliable and safe operation of composite structures. As shown in Figure 68, this philosophy may be described typically using three distinct regions: (1) barely visible impact damage, (2) allowable damage limit, and (3) critical damage threshold.

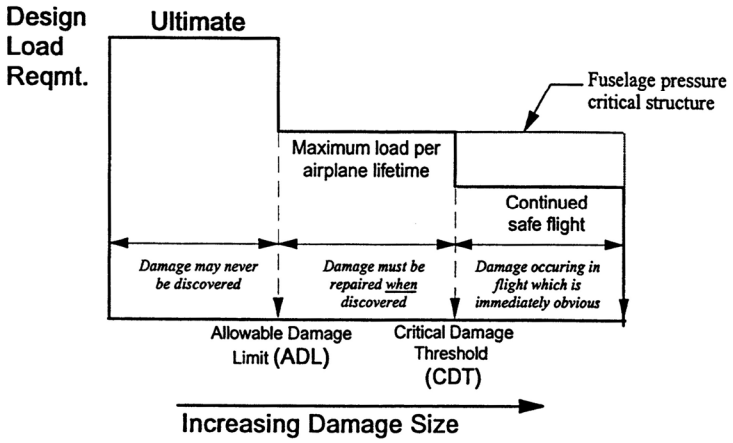

Figure 68. FAA damage-tolerant design philosophy.

Non-visible or BVID or defects that are not detectable during manufacturing inspections and service inspections must withstand ultimate flight loads in the most adverse temperature and humidity environments and not impair operation of an aircraft throughout its lifetime (DLT). In this region, it is assumed that the damage may never be discovered during the DLT and must support ultimate design load. Once damage that is larger than ADL is observed, it must be repaired when discovered. This damage is visible during service inspections and must withstand a once-per-lifetime load (design limit load or DLL) for the specified inspection interval. It is necessary in a damage-tolerant design that service damage falling in this region be found and characterized using practical inspection techniques. The last region represents a damage state

that should be immediately obvious and found with an extremely high probability using the selected inspection scheme. Usually, this damage occurs in flight and is apparent to the operator. Under this condition, the CDT is executed, and the aircraft must withstand loads specified under limited maneuvers with and without pressure necessary for continued safe flight.

Figure 69 illustrates the extent of the impact damage that needs to be considered in the damage-tolerance and fatigue evaluation. Both the energy level associated with static-strength demonstration and the maximum energy level associated with the damage-tolerance evaluation are dependent on the part of the structure under evaluation and a threat assessment. Obvious impact damage is used here to define the threshold from which damage is readily detectable and appropriate actions taken before the next flight.

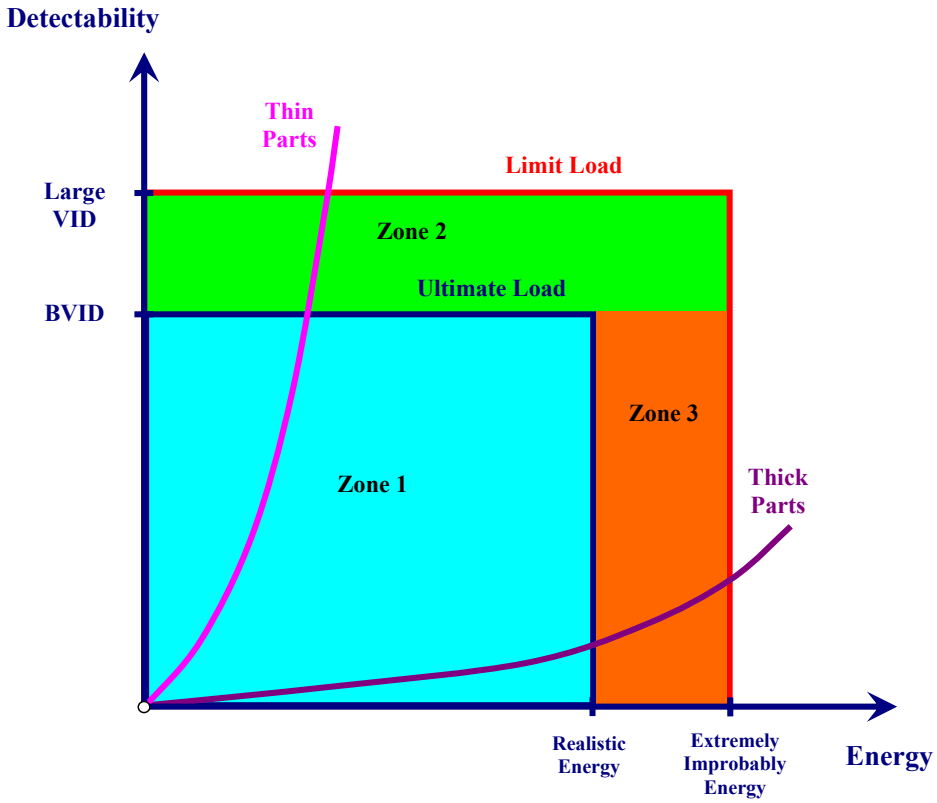

Figure 69. Characterization of impact damage.

7.1.2. Characterization of Impact Damage

Barely visible impact damage defines the state of damage at the threshold of detectability for the approved inspection procedure. BVID is that threshold associated with a detailed visual inspection procedure. Detectable damage defines the state of damage that can be reliably detected at scheduled inspection intervals. Visible impact damage (VID) is that state associated with a detailed visual inspection.

Three damage zones are defined in Figure 69:

Zone 1: Because the damage is not detectable, design ultimate load (DUL) capability is required.

Zone 2: Because the damage can be detected at scheduled inspection, design limit-load capability is the minimum requirement for this damage.

Zone 3: Because the damage is not detectable with the proposed in-service inspection procedures, ultimate load capability is required, unless an alternate procedure can show an equivalent level of safety. For example, residual strength lower than ultimate may be used in association with improved inspection procedures or with a probabilistic approach showing that the occurrence of energy levels is low enough so that an acceptable level of safety can be achieved.

7.1.3. Categories of Damages

Table 40 categorizes damage and defect considerations, with some guidelines for identification and safety considerations pertaining to such defects in primary composite airframe structures [60]. Most certification approaches consider both category 1 (CAT1) and category 2 (CAT2) defects. It is not standard practice to demonstrate category 3 (CAT3) damages in full-scale test substantiation. Damage-tolerance testing in elements, components, and full-scale

articles that are included in this program will address the "fail safety" of composite structures for very low-probability impact damages that may lower the residual strength of the structure to limit-load capacity.

TABLE 40

CATEGORIES OF DAMAGE AND SAFETY CONSIDERATIONS FOR PRIMARY COMPOSITE AIRFRAME STRUCTURES [60]

Category	Examples	Safety Considerations (Substantiation, Management)
Category 1: Damage that may go undetected by field inspection methods (or allowable defects)	BVID, minor environmental degradation, scratches, gouges, allowable mfg. defects	Demonstrate reliable service life Retain Ultimate Load capability Design-driven safety
Category 2: Damage detected by field inspection methods @ specified intervals (repair scenario)	VID (ranging small to large), mfg. defects/mistakes, major environmental degradation	Demonstrate reliable inspection Retain Limit Load capability Design, maintenance, mfg.
Category 3: Obvious damage detected within a few flights by operations focal (repair scenario)	Damage obvious to operations in a "walk-around" inspection or due to loss of form/fit/function	Demonstrate quick detection Retain Limit Load capability Design, maintenance, operations
Category 4: Discrete source damage known by pilot to limit flight maneuvers (repair scenario)	Damage in flight from events that are obvious to pilot (rotor burst, bird-strike, lightning)	Defined discrete-source events Retain "Get Home" capability Design, operations, maintenance
Category 5: Severe damage created by anomalous ground or flight events (repair scenario)	Damage occurring due to rare service events or to an extent beyond that considered in design	Requires new substantiation Requires operations awareness for safety (immediate reporting)

7.2. Load-Life-Damage Hybrid Approach

During full-scale fatigue testing, it is common to use a combination of the life factor and load-enhancement factors, as described in section 3.4. This research proposes the generation of these factors for a specific certification program using design details, such as materials, layup, loading conditions, etc., that are related to the composites structure, rather than using the factors generated for U.S. Navy F/A-18 certification [2] by pooling material test data from several databases that were then current. As shown in section 5.4, scatter in the composite data is reduced considerably due to the improvements in materials, process technologies, and composite

test methods. Furthermore, it is shown that the scatter in composite data tends to be less for notched or damaged specimens (section 6.2). In Chapter 6, the composite data scatter was evaluated based on the extent of the damage and related to the definitions in section 7.1.3. When a DaDT article is impacted with a certain damage, such as CAT3, the following assumptions can be made with a high degree of confidence:

a. The impact-damaged region becomes the critical location of the structure.
b. Imminent damage initiation at this location will cause structural collapse or load distribution that can be predicted by analysis for subsequent test validation,

Then elements or sub-components that represent the details of the impacted location can be tested to obtain a new life shape parameter for that particular structural detail and critical load conditions associated with the failure mode. The first condition is essential, as the modal life shape parameter that was obtained as the procedure outlined in section 5.1 is replaced by the shape parameter of the fatigue analysis of element or sub-component tests, i.e., the analysis conducted in section 6.2.3 on impact-damaged elements. The second condition is required, as the failure mode of the structure is assumed to occur as a direct result of damage instigation of impact damage. If load is redistributed instead of complete structural failure, then the use of a newly defined life shape parameter must be superseded by corresponding life shape parameters of the subsequent damage state of the structure for the remainder of the test, i.e., if CAT2 damage is transferred to a CAT3 damage as a result of the damage propagation, then the remainder of the DaDT test requires the use of a CAT3 life shape parameter instead of a CAT2 life shape parameter. DaDT element or sub-component tests must be designed to address the expected outcome. This approach is graphically illustrated in Figure 70 for a full-scale structural

test that was initiated with standard LEFs for the durability phase and then continued using LLD hybrid approach for the DaDT phase.

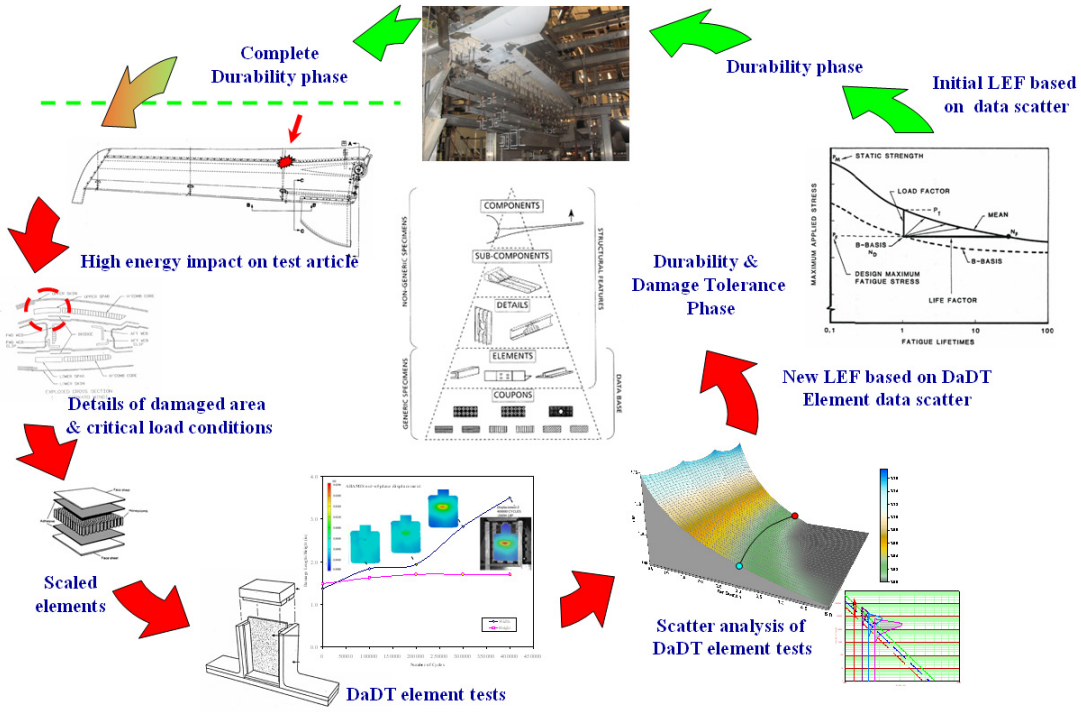

Figure 70. DaDT test demonstration with Load-Life-Damage hybrid approach.

Based on the design analysis and strain surveys, the most critical locations of the structure are selected for damage infliction. Then, the impact parameters are determined to inflict a certain damage, i.e., CAT2 or CAT3. This step requires an analysis of the local details such as materials, laminate stacking sequence, critical loading modes, etc. For example, a nonlinear finite element analysis of the local details with a continuum damage model, i.e., stiffness degradation due to fiber/matrix cracking and plastic deformation under shear loading, and a contact algorithm to model surface erosion (element removal) on multiple contact bodies during impact, i.e., impactor and the contact surface as well as the interior ply interfaces, can be used to determine the extent of the damage for a particular impact scenario. A model with such

details requires significant computing time and often extremely sensitive to the mesh density, element type, input required for the damage model, etc. Therefore, scaled element tests are recommended, where possible, not only to cross-examine the impact parameters prior to impacting the full-scale test article but also to validate the nonlinear finite element models. The element test also can be used for the scatter analysis of a particular damage scenario. Consequently, the LEFs and life factor corresponding to the selected damage scenario can be calculated for the damage-tolerance phase of the full-scale test.

As shown in Figure 70, the LLD hybrid approach focus on the most critical details of the structure and interpret the structural and loads details into the most representative repeated load testing in element level to gain information on residual strength, fatigue sensitivity, inspection methods, and inspection intervals during full-scale test substantiation. Typically, a critical damage such as a category 3 is readily detectible during a short walk-around inspection. In the safety stand point, the goal is to focus on the most critical yet least detectible damage that may occur during service. This may be a category 2 or 3 depending on the detectability and the inspection methods that can be practically applied, i.e., short walk-around inspection or a scheduled inspection at heavy maintenance.

In order to demonstrate the application of LLD hybrid approach, the element test data in section 6.2 were used, considering only the effects of impact damage on the fatigue life scatter, and three sets of LEFs were generated with respect to the extent of the damage and combined with the original AS4-PW LEFs to generate a surface plot of LEFs, as shown in Figure 71. First, the LEF corresponding to three DLTs using AS4-PW data was selected but the test was only conducted up to two DLTs. Then, the structure was impacted with a LID and the corresponding LEF curve was used to select the LEF for the remainder of the test. The LLD approach

introduces the use of multiple LEFs for a particular composite structure, based on the damage category, i.e., use of different LEF curves representing different damage severities.

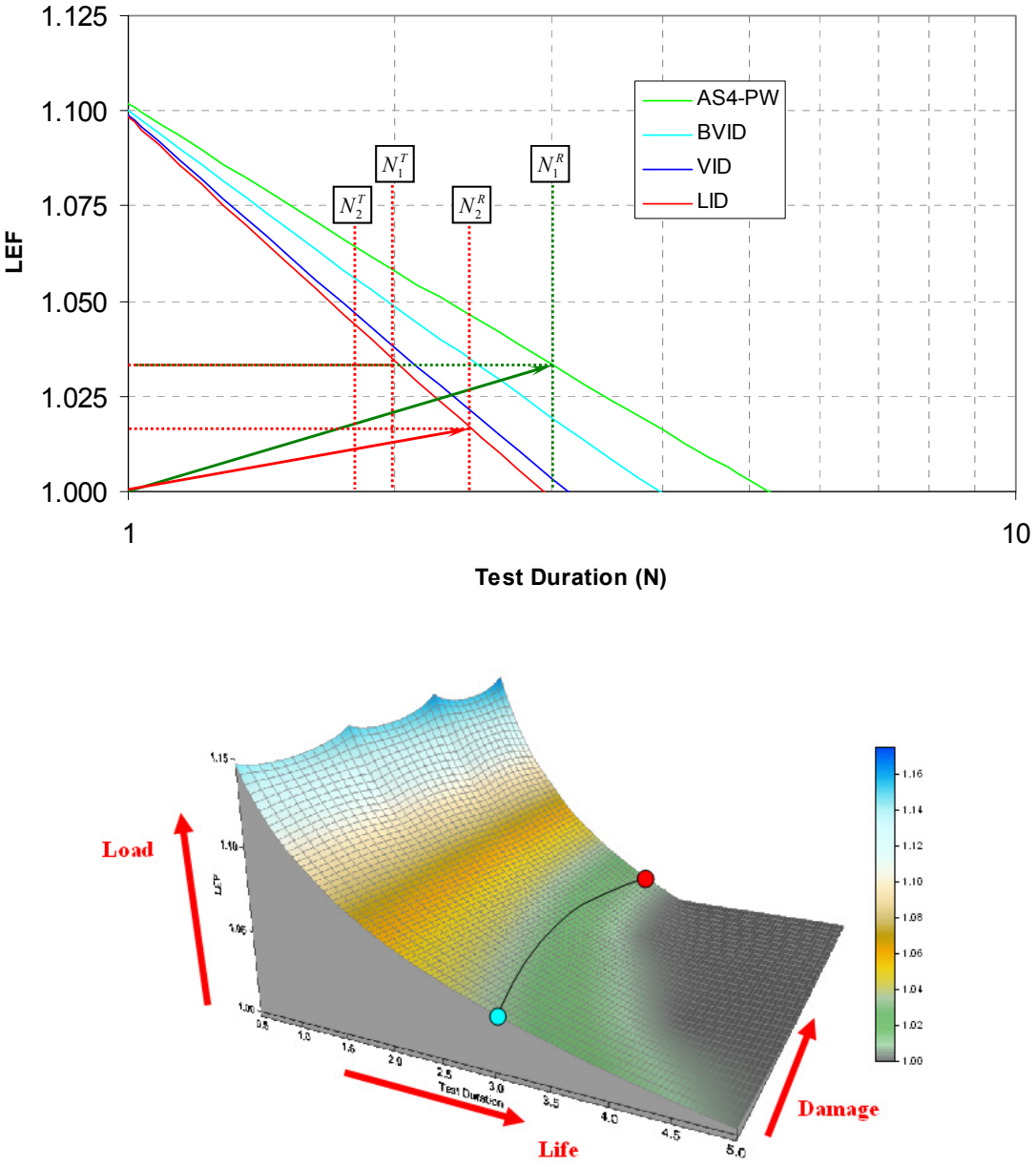

Figure 71. Load-life-damage (LLD) hybrid approach.

When multiple LEF (load-life) curves are used for different damage scenarios, a concept called the load-life shift was introduced to calculate the remaining test duration upon introduction of the new damage to test article. The load-life shift given in equation (13) calculates the remaining test duration based on the percentage of unsubstantiated design life in the previous test phase.

$$N_2^T = \left(1 - \frac{N_1^T}{N_1^R}\right) \cdot N_2^R \tag{13}$$

In equation (13), the subscripts *1* and *2* correspond to the test phase, and the superscripts *R* and *T* denote the corresponding repeated life for a particular LEF and the actual test duration, respectively, to demonstrate the reliability of design lifetime. For example, the test duration of 3 DLTs (N_1^R) from AS4-PW curve corresponds to an LEF of 1.033 (Figure 71). The test is conducted for 2 DLTs (N_1^T), and the structure is inflicted with a LID. The test duration of 2.5 DLTs (N_2^R) from LID curve corresponds to an LEF of 1.014 (Figure 71). Since 2 out of 3 DLTs required in the first phase of the test is completed, using equation (13), the remaining test duration (for phase 2) is calculated as 0.83 DLT (N_2^T). Therefore, the total test duration is 2.83 DLTs. The application of LID coupled with LLD hybrid approach not only reduces the LEF requirements but also reduces the total test duration. If the impact damage is repaired, the reminder of the test must use the LEFs from the original AS4-PW curve. The load-life shift calculation must now consider the percentage of unsubstantiated design life prior to the repair for calculating the remainder of the test duration.

The impact of the reduction in the life shape parameter on the life factor is clearly demonstrated in Figure 71. Thus, the test duration and/or LEF required to demonstrate a certain level of reliability on the DLT or the remaining test life is significantly reduced. However, the

risk of structural failure due to large impact can be significantly increased with the extent of the damage. This is addressed in the next section in terms of probability of failure and inspection intervals. Once the new LEF corresponding to the large damage is applied, the spectrum loads of the required test duration can be analyzed in terms of the probability of failure to ensure that the structure can tolerate them, i.e., no or stable damage growth. Inspection intervals can be allotted to monitor the damage state during test to avoid unintentional failure during the test, as large damage has a high probability of growth. In the event that a repair of the impacted damage is deemed necessary to prevent premature failure, then the LEF requirements must be adjusted to reflect the fact that the structure is restored back to its undamaged state.

One possible application to the LLD hybrid approach is illustrated in Figure 72 [61]. This example requires defining ADL and CDT, as well as the necessary inspection interval for damage-tolerant composite structures. Although current certification requirements do not include substantiation of large damages like CAT3 and beyond, this approach will help determine load-life enhancement factors related to such a test article with large damage(s). The extra information obtained from such an exercise is beneficial for determining the inspection levels to mitigate risks to the structural integrity as a result of a rare damage threat from a high-energy impact. This approach can be extended also for hybrid structures, as the LEF requirement will be considerably less than the current practice for a composite test article with damage, i.e., LEF of 1.15 for a test duration of 1.5 DLT.

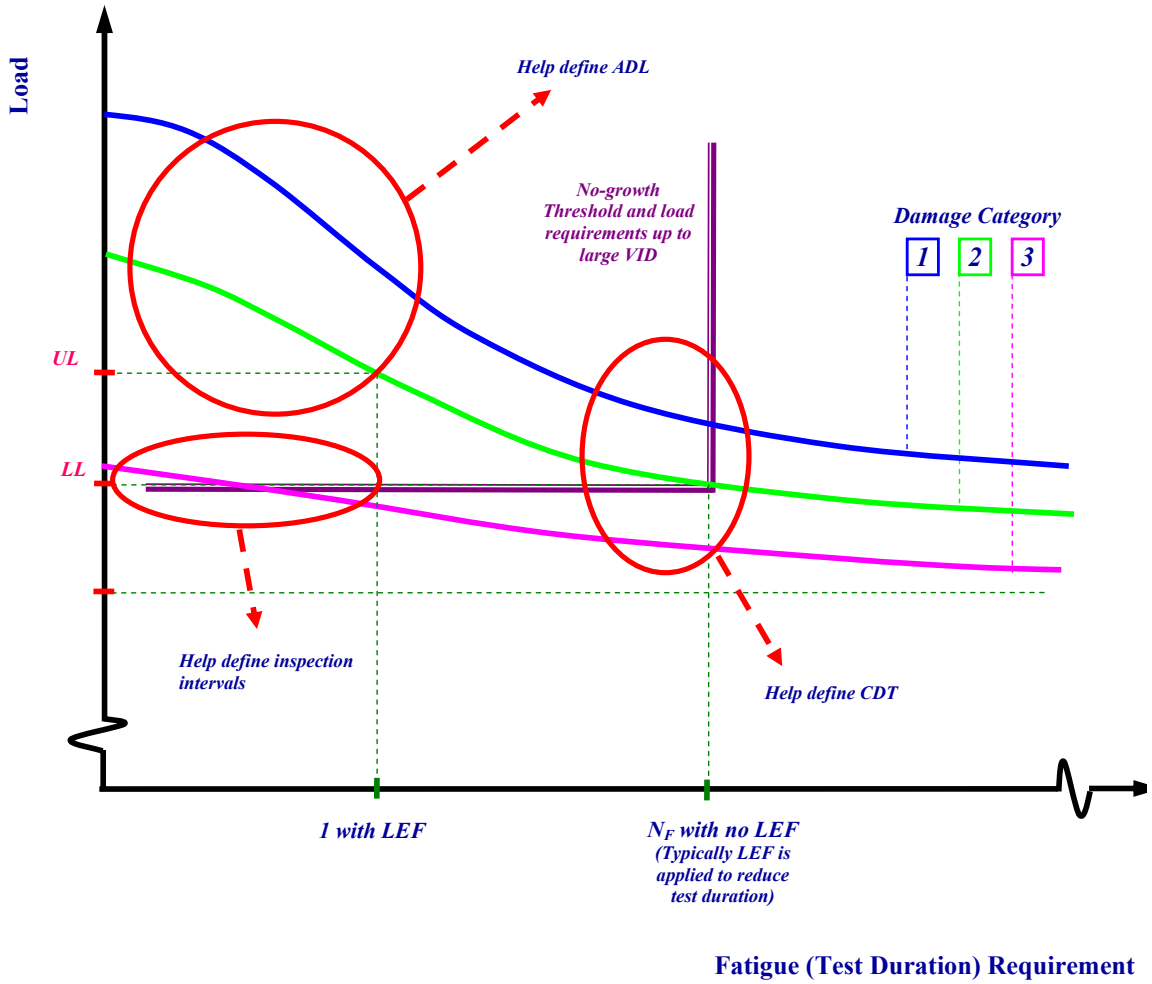

Figure 72. Application of LLD hybrid approach for full-scale demonstration.

7.3. Damage Threat Assessment Based on Reliability

In order to ensure no unintentional failure of the structure when using the LLD approach, a reliability-based approach is proposed in this section to evaluate the enhanced spectrum for the remaining test duration after impact resulting in large damage. This approach, based on the fundamental reliability concepts used for both the life-factor and load-enhancement-factor approaches, can be used to evaluate the reliability of damaged test articles and determine the necessary inspection intervals so that the damage is detected prior to it threatening the structural integrity.

Assuming that the residual strength or fatigue life of a composite structure, denoted by the random variable x, follows a two-parameter Weibull distribution, the cumulative distribution function of residual strength or fatigue life can be expressed as

$$P(x;\alpha,\hat{A}) = 1 - \exp\left[-\left(\frac{x}{\hat{A}}\right)^{\alpha}\right] \tag{14}$$

where $\hat{A}$ is the characteristic residual strength/fatigue life, and α is the shape parameter that determines the scatter of the distribution of random variable x. The shape parameter that corresponds to residual strength or fatigue life is calculated as shown in Chapters 4 and 5, respectively. These shape parameters estimate the distribution of strength or life of the full-scale structures. Therefore, the test matrices for determining these parameters must include critical design details and loading parameters that are representative of the full-scale structure. $\hat{A}$, which is also known as the scale parameter or the location parameter, is calculated as

$$\hat{A} = \left[\frac{1}{n_f}\cdot\sum_{i=1}^{n_f}\left(A_i^{\alpha}\right)\right]^{1/\alpha} \tag{15}$$

where n_f is the number of data points in the data group. Assuming that the distribution of $\hat{A}$ follows a Chi-squared distribution with $2n$ degrees of freedom, and α is known, the lower-bound estimate of $\hat{A}$ with a γ-level of confidence is given by [62]

$$\breve{A}_{\gamma} = \hat{A}\cdot\left[\frac{2\cdot n}{\chi^2_{\gamma}(2\cdot n)}\right]^{1/\alpha} \tag{16}$$

where the probability of the lower bound estimate is shown as

$$P(\breve{A}_{\gamma} \le \hat{A}) = \gamma \tag{17}$$

The probability of failure (POF) with a γ-level of confidence for an applied stress or fatigue life ($\breve{A}_R$) is shown in equation (18).

$$P(\breve{A}_R) = 1 - \exp\left[-\left(\frac{\breve{A}_R}{\breve{A}_\gamma} \right)^{\alpha} \right] \tag{18}$$

Given that $\breve{A}_R$ is the designed stress or fatigue life of a structure, the reliability of the design (=1-[POF]) with a γ-level of confidence is given in equation (19).

$$R = \exp\left[-\left(\frac{\breve{A}_R}{\breve{A}_\gamma} \right)^{\alpha} \right] \tag{19}$$

For γ=0.95, A- and B-basis reliabilities are 0.99 and 0.90, respectively. Substituting equation (16) for the lower-bound characteristic value in equation (19) and solving for the designed stress or life or the allowable statistics, $\breve{A}_R$, for the desired reliability, R, can be expressed as

$$\breve{A}_R = \hat{A} \cdot \left[-\ln(R) \frac{2 \cdot n}{\chi^2_\gamma (2 \cdot n)} \right]^{1/\alpha} \tag{20}$$

For a Weibull distribution with an α-shape parameter, the mean value of the population, $\bar{A}$, is given in equation (21) with respect to the characteristic value.

$$\overline{A} = \hat{A} \cdot \Gamma\left(\frac{\alpha + 1}{\alpha} \right) \tag{21}$$

The scatter factor, the ratio of mean to design (allowable) value, for desired reliability, R, with γ-level of confidence can be expressed as

$$X = \frac{\overline{A}}{\breve{A}_R} = \frac{\Gamma\left(\frac{\alpha+1}{\alpha} \right)}{\left[-\ln(R) \frac{2 \cdot n}{\chi^2_\gamma (2 \cdot n)} \right]^{1/\alpha}} \tag{22}$$

The scatter factor signifies the relation between the central tendency of a data set (mean) and the extreme statistics (allowables) as the life factor given in equation (8) and illustrated in

Figure 14. The scatter factor for fatigue life and static strength data are referred to as life factor and static factor (S_F), respectively. Solving for the reliability, equation (22) yields

$$R = \exp\left\{-\frac{\chi^2_\gamma(2\cdot n)}{2\cdot n}\cdot\left[\frac{\Gamma\left(\frac{\alpha+1}{\alpha}\right)}{X}\right]^\alpha\right\} \tag{23}$$

and the probability of failure is defined as

$$P_f = 1 - R \tag{24}$$

Equation (22) shows that the reliability of a particular scatter factor depends upon the shape parameter, α, of the data set and the degrees of freedom, $2n$, where n is the sample size or, in this case, the number of scaled test articles. Figure 73 shows that the B-basis reliability for DLT is achieved with scatter (life) factors of 13.6 and 4.7 for MSFPs of 1.25 and 2.00, respectively. Similarly, the B-basis reliability on DLL is achieved with scatter (static) factors of 1.15 and 1.10 for MSSP of 20 and 30, respectively, indicating that the typical scatter factor of 1.5 on DUL (1.5·DLL) is more than sufficient to demonstrate B-basis reliability for both of these scatter factors. However, equation (23) does not account for the unintentional deviations from service load, service environmental effects, and structural response variability. The effects of these parameters must be evaluated to completely understand the level of safety provided by the static factor of 1.5.

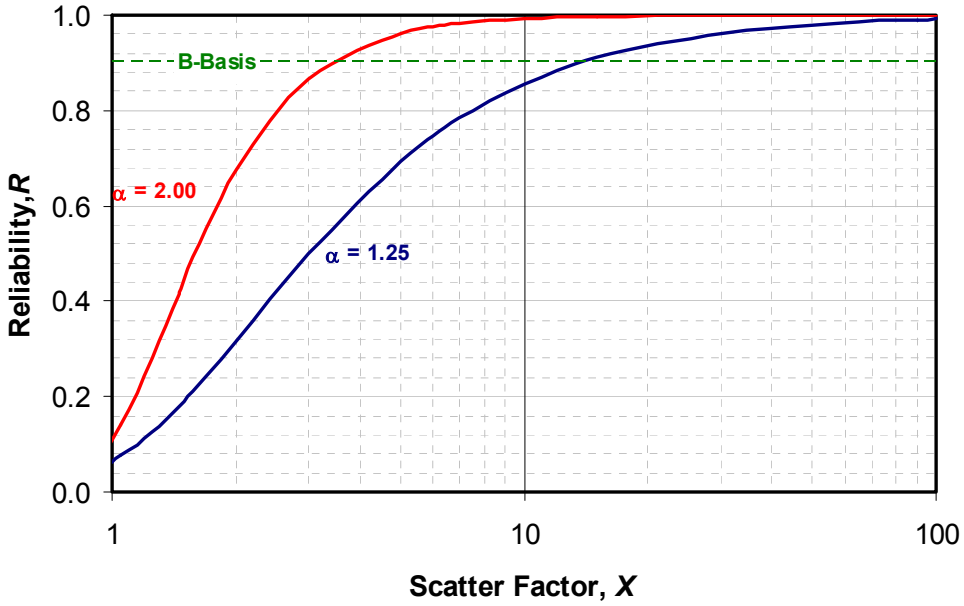

(a) Typical MFSPs

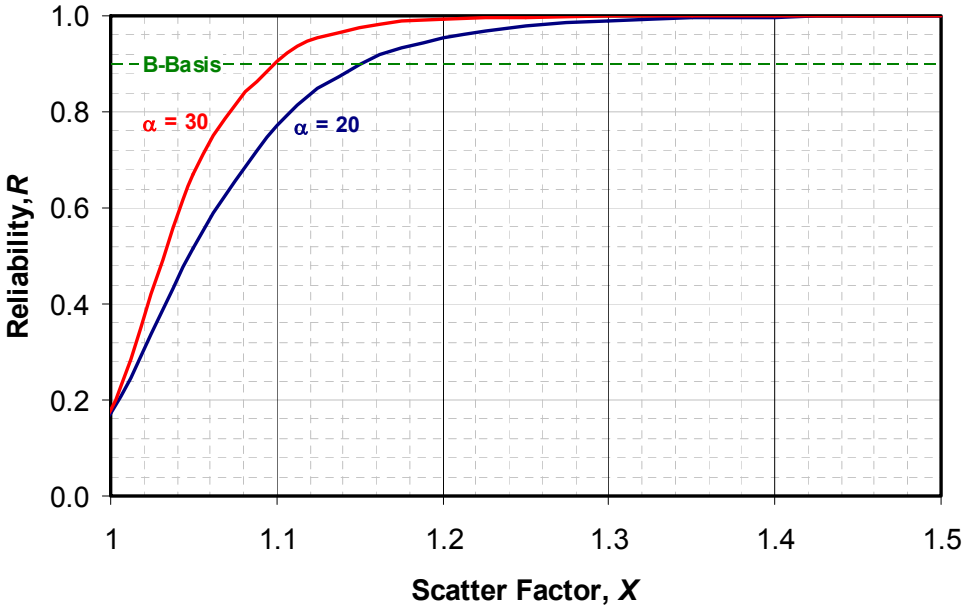

(b) Typical MSSPs

Figure 73. Effects of scatter factor on reliability.

7.3.1. Cumulative Fatigue Unreliability (CFU) Model

In the even of impact damage to a structure that is designed with a static factor of 1.5, the residual strength is reduced based on the category of the damage, as shown in Table 40. The reduction to residual strength is denoted by the static-strength reduction factor, δ, and the scatter factor is written as

$$S_F = \frac{\delta \cdot DUL}{DLL} = \delta \cdot \hat{X} \tag{25}$$

where $\hat{X}$ (=1.5) is the static factor prior to the damage. The probability of failure at a fatigue load segment can be determined by combining equations (23), (24), and (25) as

$$P_{f_i} = 1 - \exp\left\{ -\frac{\chi_\gamma^2(2 \cdot n)}{2 \cdot n} \cdot \left[\frac{\Gamma\left(\frac{\alpha+1}{\alpha}\right)}{\hat{X}_i} \right]^\alpha \right\} \tag{26}$$

where $\hat{X}_i$ is the static factor for i^{th} segment, i.e., ratio of the residual strength and maximum load at i^{th} segment. Also, the initial static factor for a structure is given in equation (27) with the static-strength reduction factor, δ.

$$\hat{X}_0 = \delta \cdot \hat{X} \tag{27}$$

The probability of failure of the structure during a particular fatigue load segment in the spectrum (load sequence) can now be calculated by summing the probability of failure at each segment up to the current segment (n_s), including the current load segment, as shown in equation (28).

$$P_f = \sum_{i=1}^{n_S} P_{f_i} \tag{28}$$

Since reliability is calculated based on the residual strength degradation or wearout, the sequencing effects are reflected in the cumulative fatigue reliability (CFU) model. When the cumulative probability of failure, P_f, during a load segment in the fatigue spectrum reaches unity, it constitutes the structural failure during that load segment as

$$P_f \geq 1 - TR \rightarrow Failure \tag{29}$$

where TR is the target reliability. The CFU model is a measure of the state of a structure with certain damage and certain number of fatigue cycles, but it is not directly related to the damage propagation. Information pertaining to the damage propagation and the residual strength degradation are incorporated into the model through the coupon and element tests, as illustrated in section 7.3.3.

7.3.2. Considerations for Application of CFU Model

When applying the CFU model to a structural application, several factors need to be considered to accurately predict safe and economical inspection intervals and fatigue life. Because of the robustness of the CFU model, depending on the criticality, i.e., primary load path or redundant structure, and probability of certain damage threat scenarios related to a structure, it can be customized to reduce the amount of test data and computations required to achieve a safe, reliable, and economical DaDT test validation program and inspection intervals.

7.3.2.1. Static-Strength Shape Parameter and Static Factor

For a category 3 damage, the residual strength of the structure will be reduced to its limit load (Table 40), thus δ=2/3, and S_F=1.0. Substituting a static factor for category 3 damage in equation (23), the reliability of the damaged structure can be determined. Consequently, the probability of failure at DLL is calculated using equation (24) and plotted in Figure 74 with respect to MSSP. As can be seen in this figure, the probability of failure is significantly

increased for MSSP less than 15. The value of MSSP obtained using the NAVY approach is 20, while it is 32.193 for AS4-PW material based on the scatter analysis in section 4.1.1. These values results in 17.4 and 17.8 percent reliability or 82.6 and 82.2 percent probability of failure for DLL, respectively.

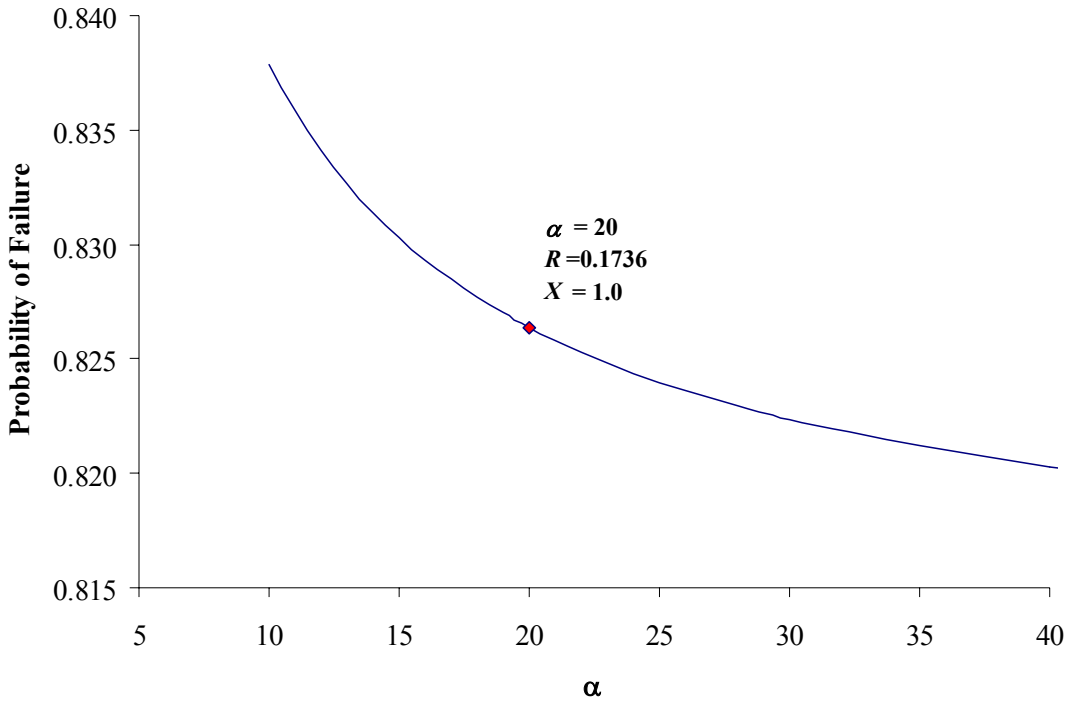

Figure 74. Probability of failure for S_F=1.0.

It was shown in Chapter 6 that the static-strength scatter is reduced significantly for damaged-element testing due to stress concentration. Thus, the reliability of a structure with category 3 damage, a population representing less scatter (assume α=30), is compared with the traditionally used MSSP (NAVY approach), α_R=20, and with no impact damage in Figure 75. Although the B-basis (90 percent with 95 percent confidence) reliability is diminished at DLL, the post-impact reliability of the structure for some operational loads (simulated by spectrum during DaDT test) still remains above the B-basis reliability level, as shown in Figure 75, i.e., the

B-basis reliability of a category 3 damaged article (based on α=30) is still maintained for operational loads below 91 percent of DLL, assuming no residual strength degradation.

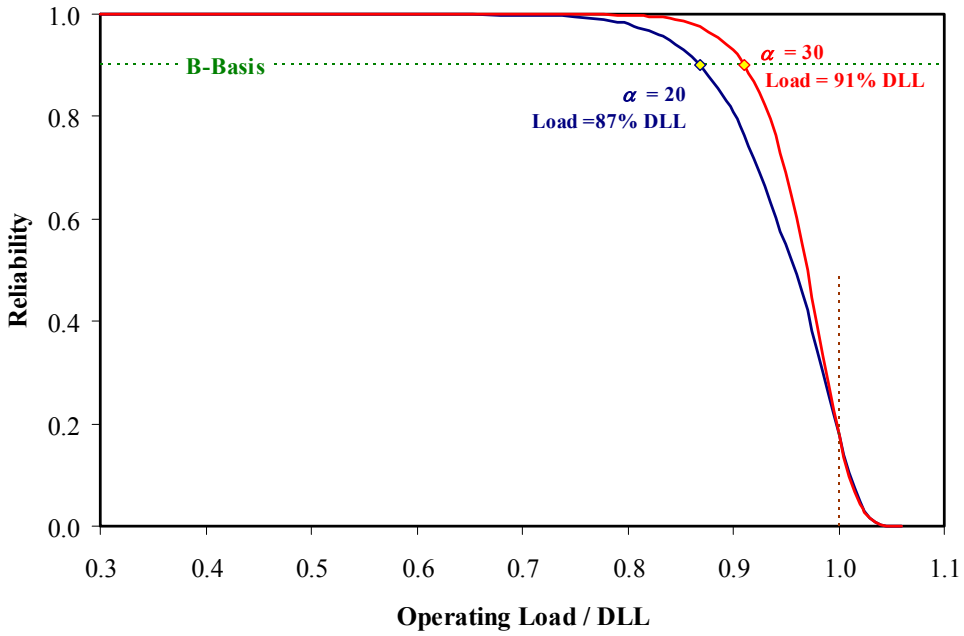

Figure 75. Static-strength reliability at operating loads for a structure with a category 3 damage.

Figure 76 compares the post-impact reliability of a category 3 damaged article that belongs to a relatively skewed population (α=30) to the reliability of the undamaged structure that belongs to a population with MSSP of 20 for different operational loads. The B-basis reliability that was maintained for a one-time load application of 130 percent DLL is reduced to 91 percent as a result of the category 3 damage. Since a category 3 damage is expected to be detected within a few flights, it can be repaired and the residual strength of the structure can be restored to DUL.

Note that these reliability calculations do not account for the stiffness degradation or wearout of structural capacity due to repeated loading and do not compare with the one-time application of the operational or applied loads to DLL. It is imperative that residual strength

degradation throughout the spectrum is investigated to assess fatigue reliability and consequently the probability of failure.

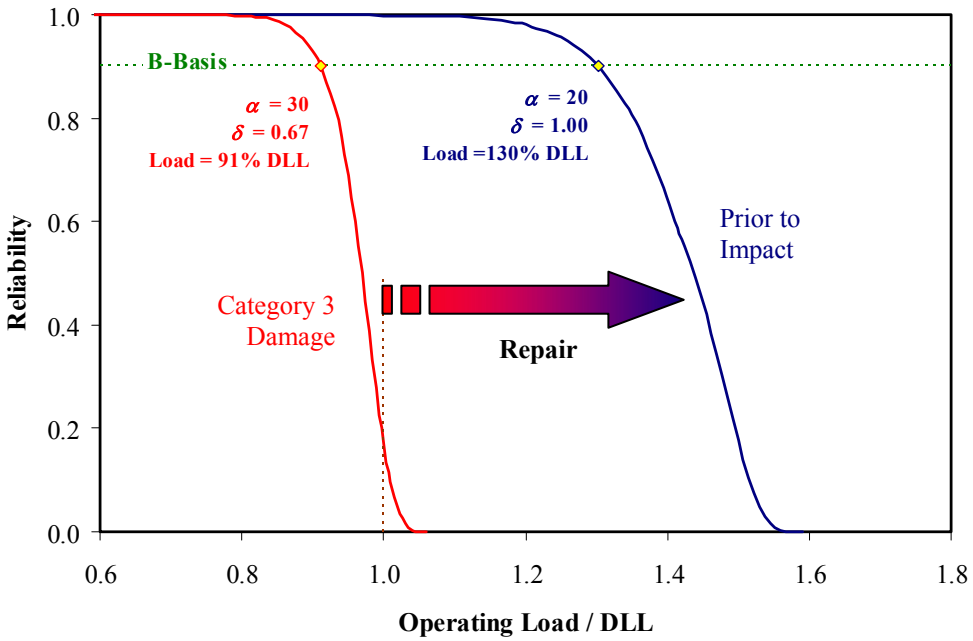

Figure 76. Static-strength reliability comparison before and after impact.

7.3.2.2. Residual Strength Degradation–Wearout Models

In order to obtain the correct reliability, the residual strength of the structure must be reevaluated after each cycle using a residual strength degradation or wearout technique, and the static factor for the i^{th} segment, $\hat{X}_i$, must be recalculated based on the new residual strength. For a typical aircraft spectrum, this may result in a significant number of calculations, depending on the selection of the wearout model. A closer examination of the reliability results for static strength shape parameters of 20 and 30, shown in Figure 75, reveals that for maximum operational loads below 70 and 80 percent of limit load, respectively, the probability of failure is negligible.

For load cases that are above the truncation levels, a wearout model is required for evaluating the residual strength of the structure after each fatigue load cycle. Rearranging

equation (6), the Sendeckyj residual strength degradation for constant amplitude fatigue testing can be expressed as a monotonically decreasing function of the number of fatigue cycles, n_f, as shown in equation (30).

$$\sigma_r = \sigma_a \left[\left(\frac{\sigma_e}{\sigma_a} \right)^{1/S} - C(n_f - 1) \right]^S \tag{30}$$

Figure 77 shows a comparison of the residual strength degradation of LID fatigue specimens in section 6.2 (only SL1 and SL3 are shown) based on the Sendeckyj wearout model and linear loss of residual strength (LLRS) for n_f constant amplitude fatigue cycles as

$$\sigma_r = \sigma_e + \left(\frac{\sigma_a - \sigma_e}{N_f(\sigma_a)} \right) \cdot n_f \tag{31}$$

where $N_f(\sigma_a)$ is the number of cycles to failure for constant amplitude fatigue loading at the maximum applied cyclic stress, σ_a.

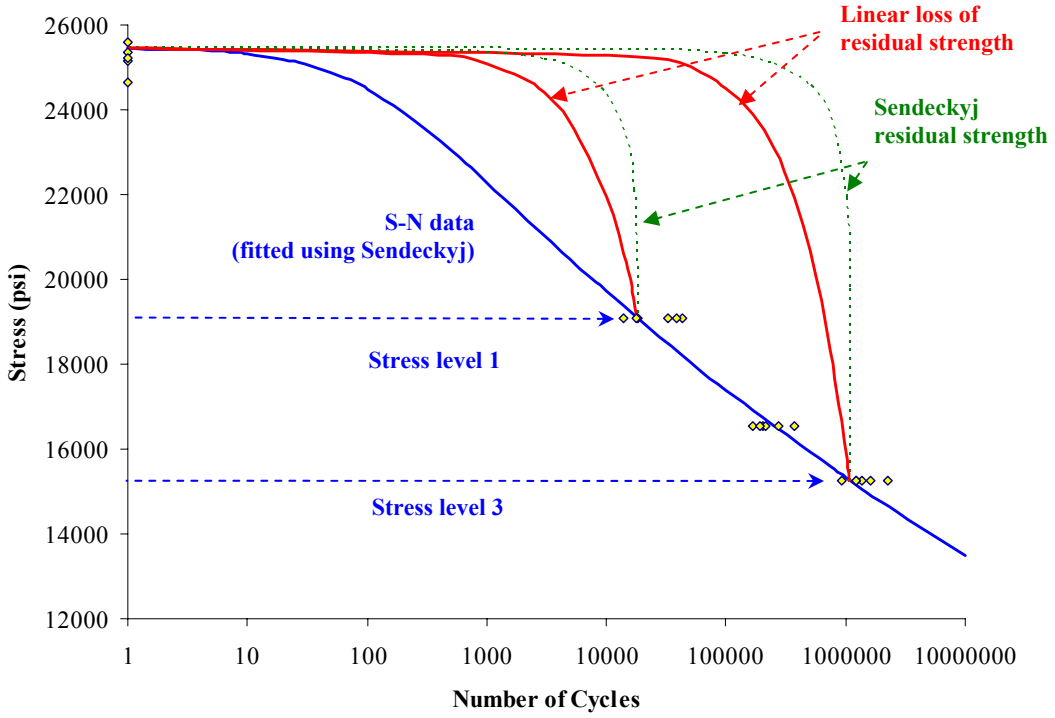

Figure 77. Residual strength degradation for constant amplitude fatigue loading.

When fatigue failure occurs at the n_f^{th} cycle, residual strength is reduced to the maximum applied cyclic stress, and n_f becomes $N_f(\sigma_a)$. Thus, $N_f(\sigma_a)$ can be solved by rearranging the terms in equation (30) as

$$N_f(\sigma_a) = \frac{1}{C}\left[\left(\frac{\sigma_e}{\sigma_a}\right)^{1/S} + C - 1\right] \tag{32}$$

As can be seen in Figure 77, when there are not sufficient S-N data to obtain Sendeckyj fitting parameters, the LLRS can be used to conservatively approximate the residual strength, and $N_f(\sigma_a)$ can be obtained using a graphical method from the S-N curve. Note that for both wearout equations (30) and (31), fatigue failure occurs when the residual strength reaches the maximum amplitude fatigue stress level. Further, the CFU model is not restricted to the above two wearout models, but welcomes any appropriate model for calculation of the residual strength after each load cycle. Since these models require a significant number of calculations and most of the loads in a typical fatigue spectrum are below 80 percent of the limit load, a simplified approach is proposed in section 7.3.3. Once the residual strength is determined, the static factor for the i^{th} cycle can be written as

$$\hat{X}_i = \sigma_{r_i} / \sigma_{a_i} \tag{33}$$

For example, by substituting equation (30) or (31), the scatter factor can be determined. Then it can be substituted into equation (23) to calculate the reliability. Finally, the probability of failure after the corresponding number of fatigue cycles can be calculated for the applied stress. This exercise was carried out for LID S-N data in section 6.2, and the scatter analysis of LID S-N data is summarized in Table 39. The Sendeckyj model was used to fit the S-N data. Residual strength as a function of the number of fatigue cycles was calculated using both the

Sendeckyj model and the LLRS. Using the Sendeckyj residual strength, the probability of failure was calculated and is shown in Figure 78. Two stress levels were selected for this simulation: 77.5 and 61 percent of a static failure load that corresponds to 10,000 and 800,000 cycles, respectively. According to the CFU model, the number of cycles corresponding to these two stress levels at 90 percent reliability or 10 percent probability of failure was 9,625 and 799,625, respectively.

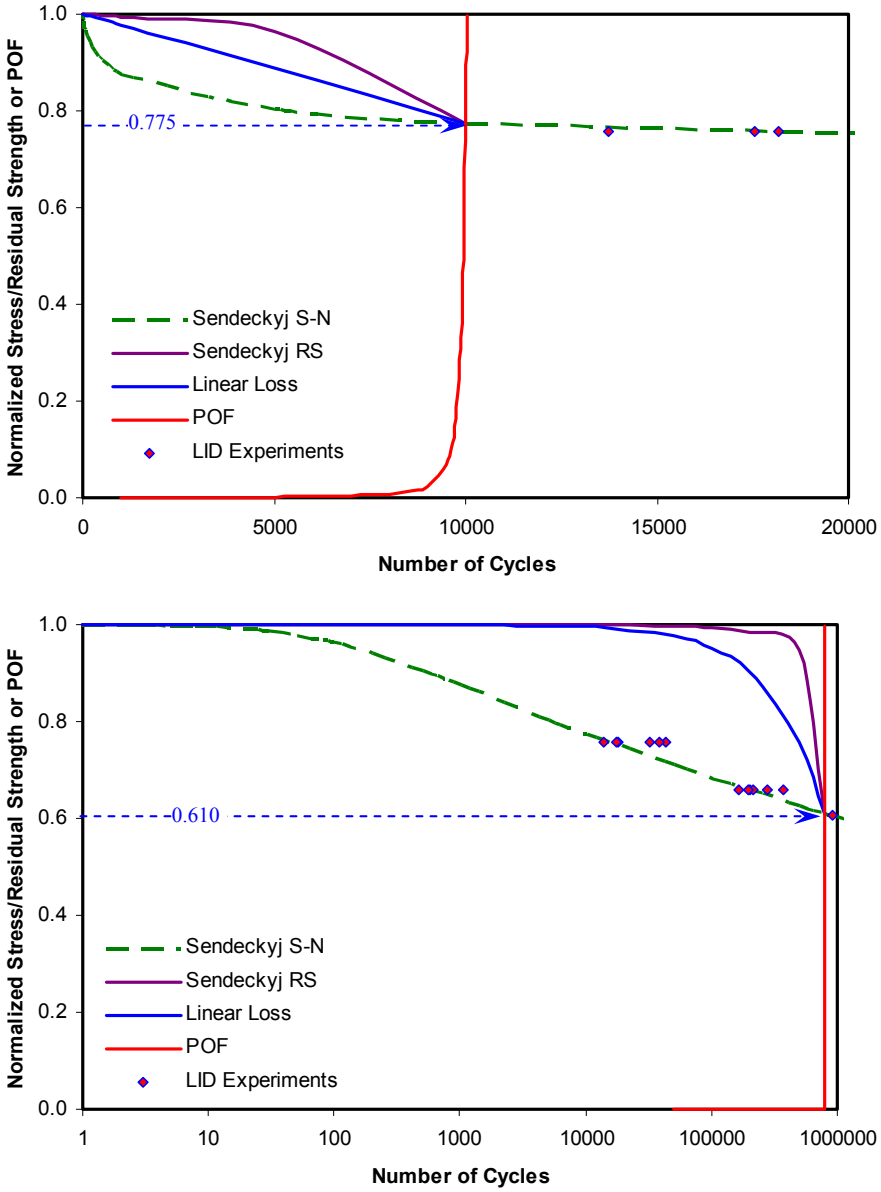

Figure 78. Example of CFU model for constant amplitude fatigue tests.

7.3.3. Benchmark Application of CFU Model

Due to the robustness of the CFU model, it can be customized to a particular application to obtain reliable inspection intervals and to evaluate the reliability of the structure for operational loads. In order to demonstrate an application of the CFU model, the Starship forward wing with a category 3 impact damage on its primary load path, forward spar cap, is considered.

Fatigue test spectrum loads are typically developed using exceedance curves (Appendix C) and arranged so that several different blocks representing different flight conditions, i.e., maneuver, gust, etc., are repeated based on their probabilities of occurrence for a certain mission profile for which the aircraft is designed. Within a block, there are several subsets of load blocks (SLBs) that are arranged low to high and high to low as shown in Figure 79 (each bar in this figure represent an SLB). These subsets can be considered as constant amplitude SLBs that construct the load spectrum. Therefore, CFU calculations can be significantly reduced by considering these SLBs rather than each cycle separately. In order to be conservative, the residual strength at the last cycle in each SLB is considered as the residual strength throughout that particular SLB.

The next observation is that, except for blocks C and D, all loads are below 80 percent of the DLL. These loads represent 99.98 percent of all cycles within the spectrum. Loads in the block A-M, which constitute 89.73 percent of load cycles, are below the truncation load levels. The S-N data in section 6.2 confirm that the stress levels corresponding to these loads are below the endurance limit of LID specimens. Thus, the residual strength degradation for these loads can be neglected. The majority of loads in blocks B-M and B-G are below 60 percent DLL, while

the SLBs that are above that load level have only a limited number of occurrences within a SLB. Thus, the residual strength degradation is extremely small.

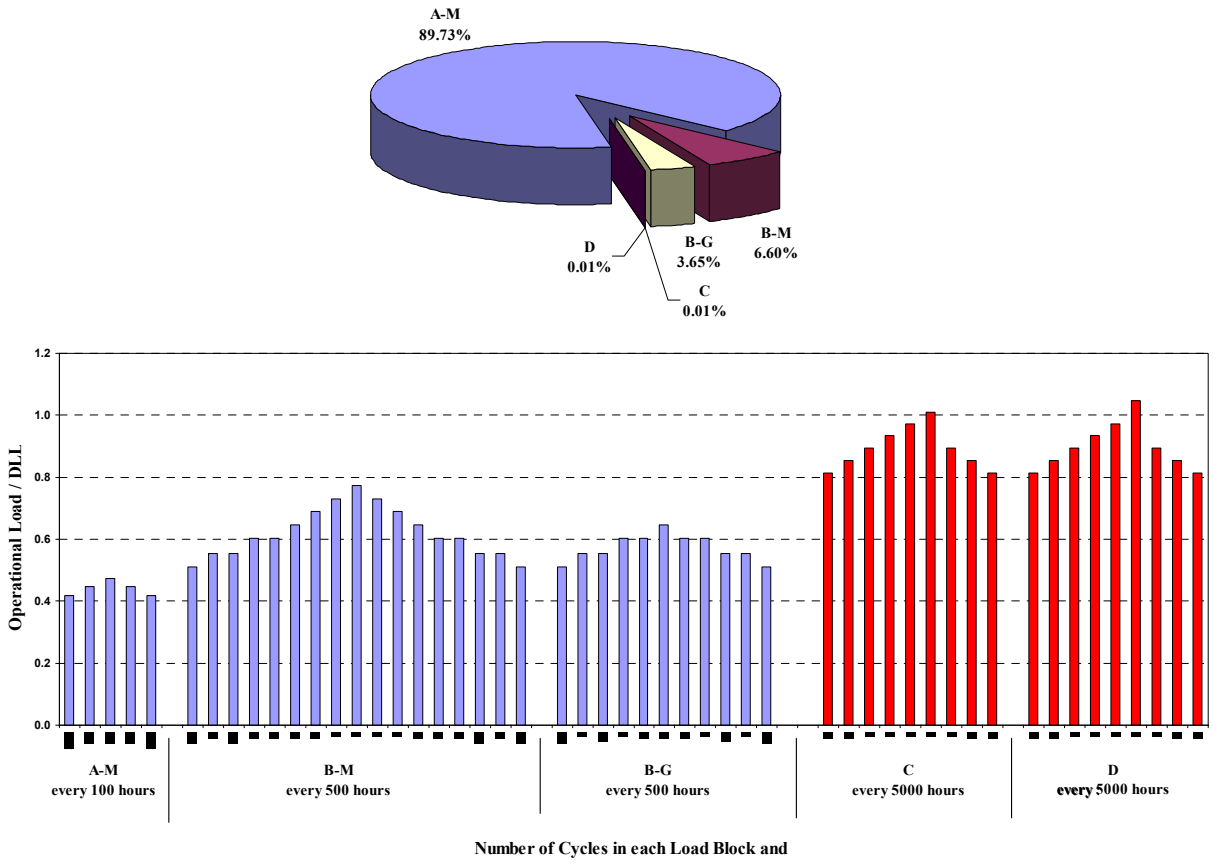

Figure 79. Forward-wing cycle count per DLT.

The linear loss of residual strength, which is an overly conservative wearout model, as shown in Figure 77, only showed 0.3 percent residual strength loss at one DLT, and about 0.03 and 0.04 percent of that are due to the loads in blocks C and D, respectively. Thus, for the purpose of establishing inspection intervals and assessing the structural reliability for category 3 damage, the lower-bound estimate of residual strength with γ-level of confidence can be calculated using equation (16) so that this value can be used throughout the spectrum as the residual strength. For one test article and shape parameters of 20 and 32.193, the lower-bound estimate indicates a reduction of 5.3 and 3.4 percent, respectively. This reduction factor results

in a residual strength that is considerably less than that using the linear loss of residual strength and has a significantly higher impact on the probability of failure than that from varying MSSP from 20 to 32.193 (Figure 80). These two scenarios predict structure failure during 40,007 and 80,025 cycles, respectively.

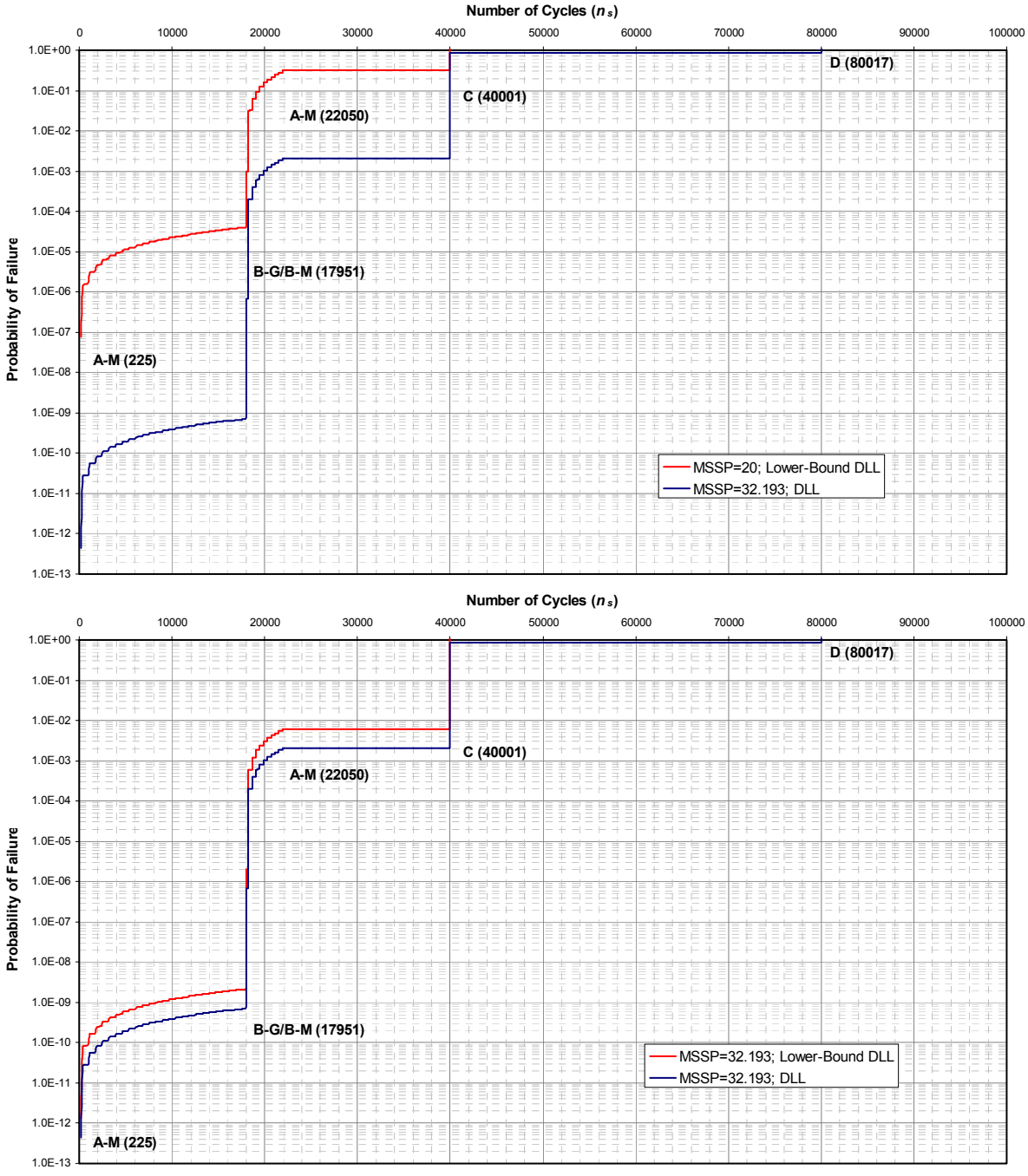

Figure 80. Cumulative probability of failure for Starship forward wing.

7.3.3.1. Determination of Inspection Intervals

The primary objective of establishing inspection intervals is to discover dormant failures as a result of an accident or degradation, which will eventually threaten the structural integrity and mitigate the risk of structural failure. Regardless of the damage threat level, the approach discussed in the previous benchmark example graphically exemplifies the effects of different load conditions. A sudden increase in the probability of failure (note that the probability in Figure 80 is a logarithmic scale) can be attributed to the likelihood of damage propagation; thus, the inspection levels during testing can be allotted to detect such phenomenon. When considering the inspection intervals during operation, it is important to consider a target reliability level and a probable damage threat so that the inspection intervals can be allotted to maintain the unreliability or the probability of failure under this threshold. Since the definition of category 3 damage in Table 40 delineates limit-load capability as a requirement, considering such an extremely improbable yet easily detectable damage that defines the critical damage threshold is practical to establish inspection intervals. It is also expected that this critical damage will not grow before it is detected by scheduled inspection.

Figure 81 shows an example of establishing inspection intervals with a target reliability of 90 percent using the CFU model for the load spectrum used for the Starship DaDT testing. As shown, 11 possible incidents cross the target reliability threshold. During blocks C and D, the probability of failure rapidly increases over 20 and 30 percent, respectively; thus, an additional count is added for every 10 percent increment. Using this graphical method will alleviate any confusion about whether this sudden increase in POF is due to one cycle or multiple cycles that are not clearly visible due to the x-scale of the graph. Furthermore, this will reduce the size of

the inspection interval for load spectrums that have multiple high-load segments that increase the POF significantly.

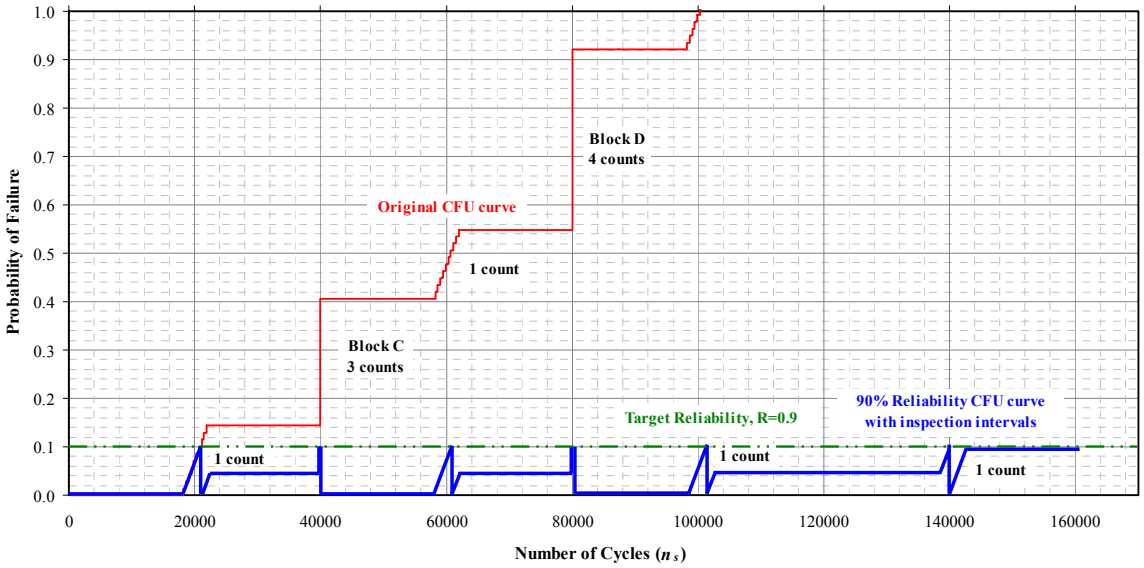

Figure 81. Establishing inspections intervals using CFU curve for target reliability.

Inspection intervals in this example (Figure 81) are allotted so that the probability of failure does not increase more than 10 percent (reliability=1-POF). Also, it is assumed that the damage is detected during inspections and that the structure is restored to its condition prior to the damage; thus, the POF is set to zero prior to calculating the remainder using the CFU model. As can be seen in Figure 81, the smallest interval between two points at which the POF reaches the reliability threshold is approximately 19,000 cycles. This value is divided by the life factor (e.g., 9.6) to obtain the inspection interval of 1,979 cycles. On the other hand, if the total number of cycles in DLT (160,033 cycles) is divided by the number of times that POF reaches the reliability threshold per DLT (11, for this example), then 1,458 cycles result. Since this is smaller than the previously calculated inspection interval of 1,979 cycles, the latter should be set as the minimum inspection interval.

If the minimum inspection interval is beyond the cost restrictions and is not practical, the probability of occurrence of high loads and a more practical damage threat level can be considered to reduce the number of inspections required. Regardless of the scheduled inspections intervals, if an event that is similar to block C or D is experienced or if damage was detected during a walk-around, the structure must be immediately inspected and repaired, if necessary, to ensure continued airworthiness. This example also shows that the imminent structural failure due to CAT3 damage, which was around 100,000 cycles, was eliminated with scheduled inspections and the DLT was reestablished.

7.3.3.2. Fail Safety of Composite Structures

Of the three zones in Figure 69, only zone 3 can have a residual strength requirement that can vary with alternate procedures and/or the probability of damage occurrence. In either case, any compromise for residual strength requirements less than the ultimate load requirement should only be considered when pursuing one of the options under the damage-tolerant fail-safe means of compliance.

One example of the use of alternate procedures is for the rare damage threat from a high-energy blunt impact (e.g., service vehicle collision). Depending on the selected maintenance inspection scheme, such damage may fall under the category of zone 3. When considering such damage in the design of a composite structure, it may be shown to be damage-tolerant fail safe, even though the damage is not detectable, based on a very low probability of occurrence. As a result, the design would have sufficiently high residual strength (e.g., below DUL, but well above the DLL to ensure safety without detection for long periods of time). If it is further determined that such impact events usually occur with the knowledge of maintenance or aircraft service personnel, then alternate procedures may be added to the instructions for continued

airworthiness. For example, advanced inspection methods, which can detect damage from high-energy blunt impacts, may be used as alternate procedures to minimize the risk of catastrophic failure for such zone 3 damage.

7.4. Durability and Damage-Tolerance Testing

Previous research efforts [42] have concentrated on the first two areas shown in Figure 68 up to the critical damage limit using fairly small coupons, and thus the results obtained are on the conservative side. This research addressed the philosophies, within the scope of this program, and investigated larger damages using larger elements and full-scale subcomponents and components.

To verify that the structure has sufficient residual strength to sustain the expected in-service loads once damages have been introduced, a typical certification program for a composite structure was conducted in two phases. During certification of the Starship forward wing, durability of a minimum quality structure was demonstrated for 1 DLT with a LEF of 1.15, and then damage was included in the durability test and continued for an additional 1 DLT (Figure 82). At the end of 2 DLT, residual strength was demonstrated.

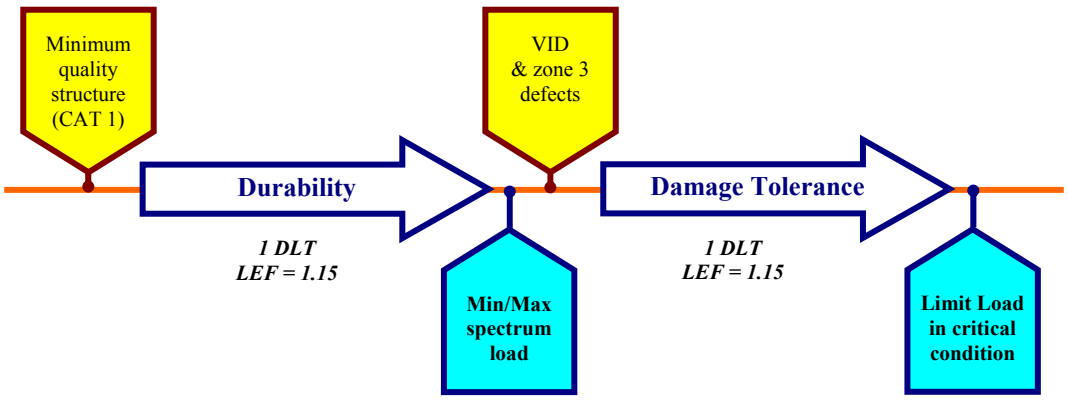

Figure 82. Typical durability and damage-tolerance certification test.

In order to validate the proposed methodology in sections 5.4 and 7.3.1, large category 2 and 3 damages were explored through several full-scale tests. Damage-tolerance element tests were conducted in Chapter 6 to investigate the methodology to simulate the damage severities described in Table 40 into full-scale test articles. Once LEF results and damage-tolerance element tests were completed, the LEF required for the LLD hybrid approach that incorporates scatter in the damage categories into the load-life approach was developed. Full-scale test articles were impacted at the beginning of the test phase, as shown in Figure 83. As shown in Figure 72, these tests provided information related to establishing inspection intervals and damage-tolerant capability of category 3 damage.

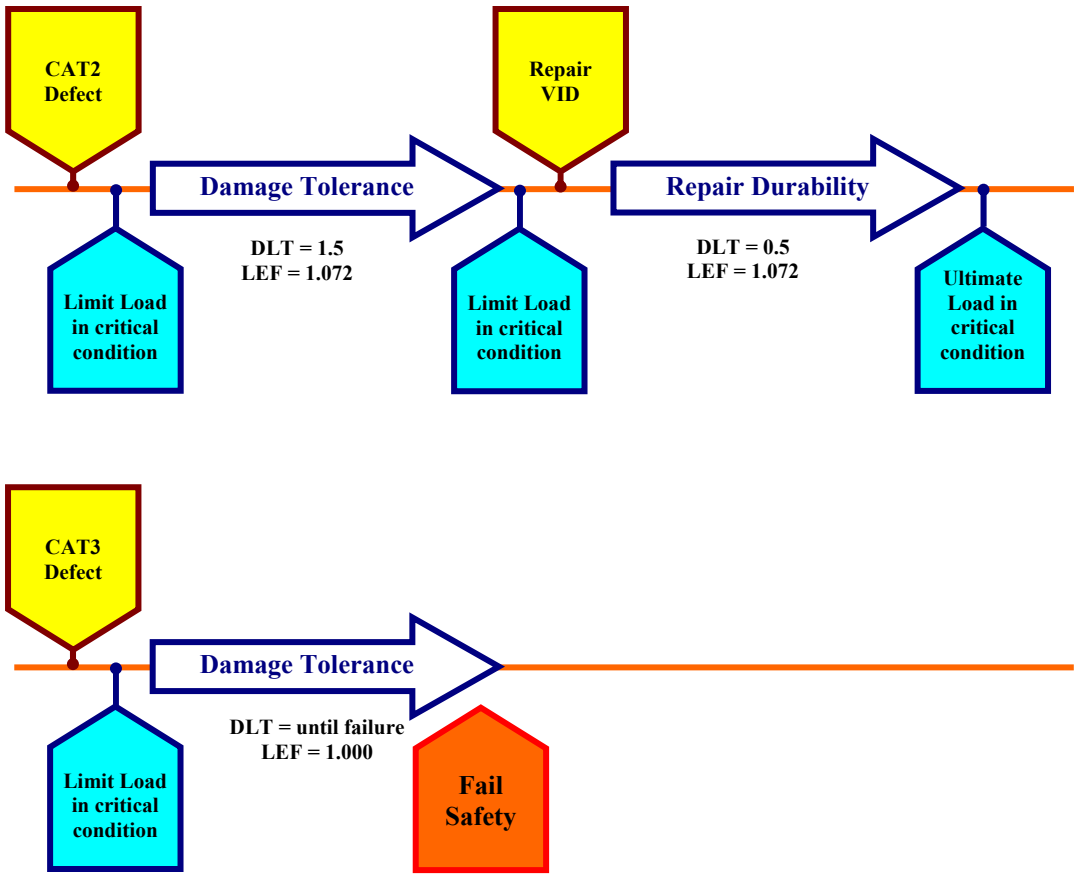

Figure 83. Durability and damage-tolerance testing with CAT2 and CAT3 damages.

7.4.1. Damage Infliction

Depending on the certification program, the introduction of defects, especially high-threat and low-probability cases, into the full-scale test article varies, i.e., after 1.5 or 2 DLT. Some damages such as disbonds, delaminations, and simulation of porous details may require inclusion during fabrication of the test article.

Several methods are commonly used to produce defects in the full-scale test article. Surface impacts produce internal delamination, core crush for sandwich structures, or puncture damage at high energies. Edge impact with a sharp object, such as a chisel, produces edge delamination, which simulates disbonds in joints. Cross-head puncture, which produces a cross-shaped defect with severe delaminations, simulates severe impact or lightning-strike damages. Use of a welding torch to burn surface plies simulates lightening strikes and engine-burn fire damage. Drilling holes and saw-cuts (in metal parts) are also commonly used to disrupt the load path in attachment members and joints.

Extreme care must be exercised especially when inflicting large defects, so that the mechanical means of inflicting damage does not demolish the test article. Procedures must be carried out following finite element analysis and careful investigation of strain gage data from the initial fatigue test phase. These data along with manufacturing experience of typical causes for rejection of parts help identify the areas where such defects are least desirable, thus threatening the structural integrity. Information related to the scaling effects of damage is crucial, identifying necessary energy levels for impact damages, especially in the simulation of severe damage scenarios such as category 3 and above.

For the case of Starship forward wing, the threshold of detectability (BVID) for an impact damage and the limit load envelop are close, as shown in Figure 84. Unlike a layered

composite, due to its construction that is similar to a bundle of fibers, the spar cap on the contact side bends and crushes the web, which is a honeycomb construction, and bounces back as shown in Figure 84. Therefore, thick, mostly unitape-wound spar caps required a significant amount of energy and very sharp impactor geometry for perforation, as discussed in section 8.2.2.

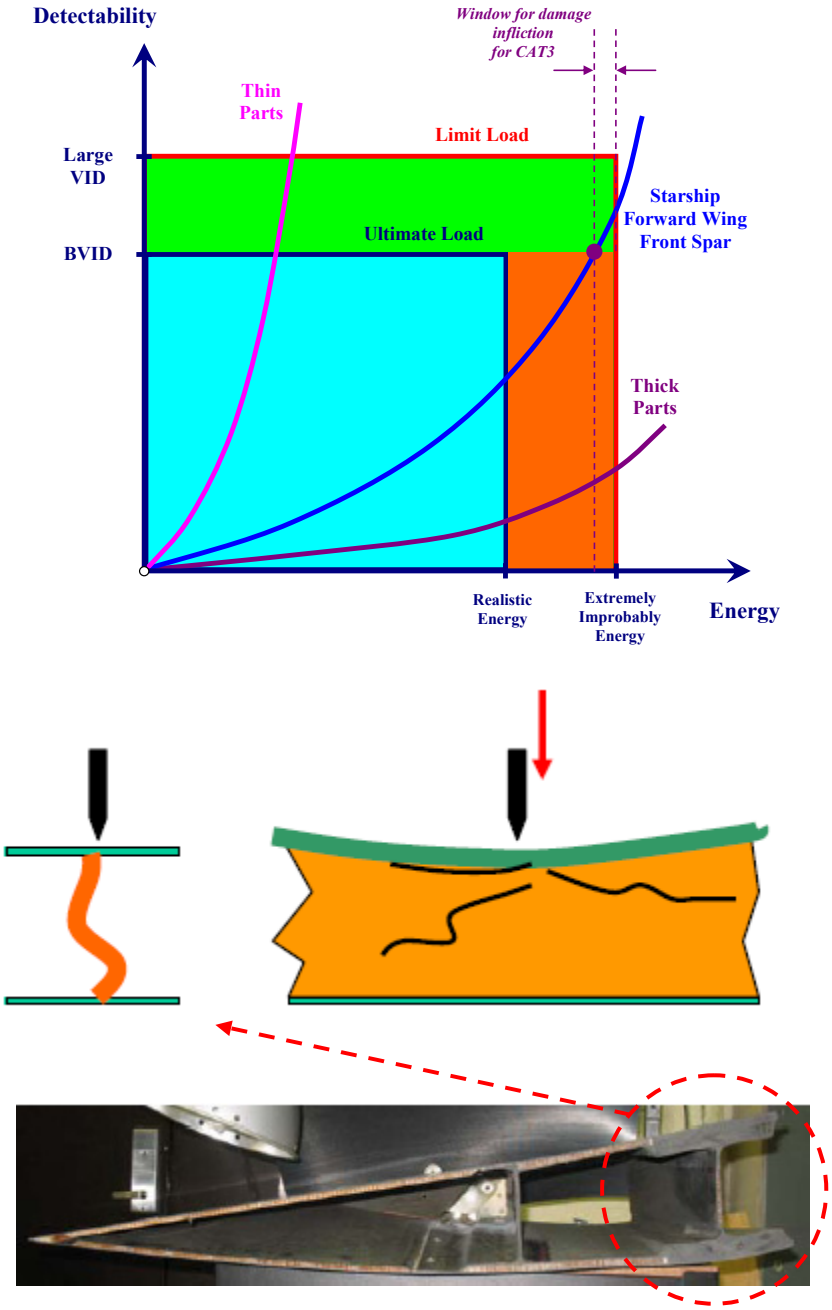

Figure 84. Damage infliction on Starship forward wing.

7.4.2. Nondestructive Inspections for Progressive Damage

Unlike for a standard certification program, damages inflicted on a full-scale article are more severe, i.e., large category 2 and 3 damages. Therefore, NDI requirements for damage-tolerance testing require detailed NDI inspections. Standard tap testing was utilized for scanning the test articles, while detailed inspections were conducted using ultrasound, RD3 electronic digital tap hammer (DTH), the BondMaster™ 1000, and thermogrpahy (Figure 85).

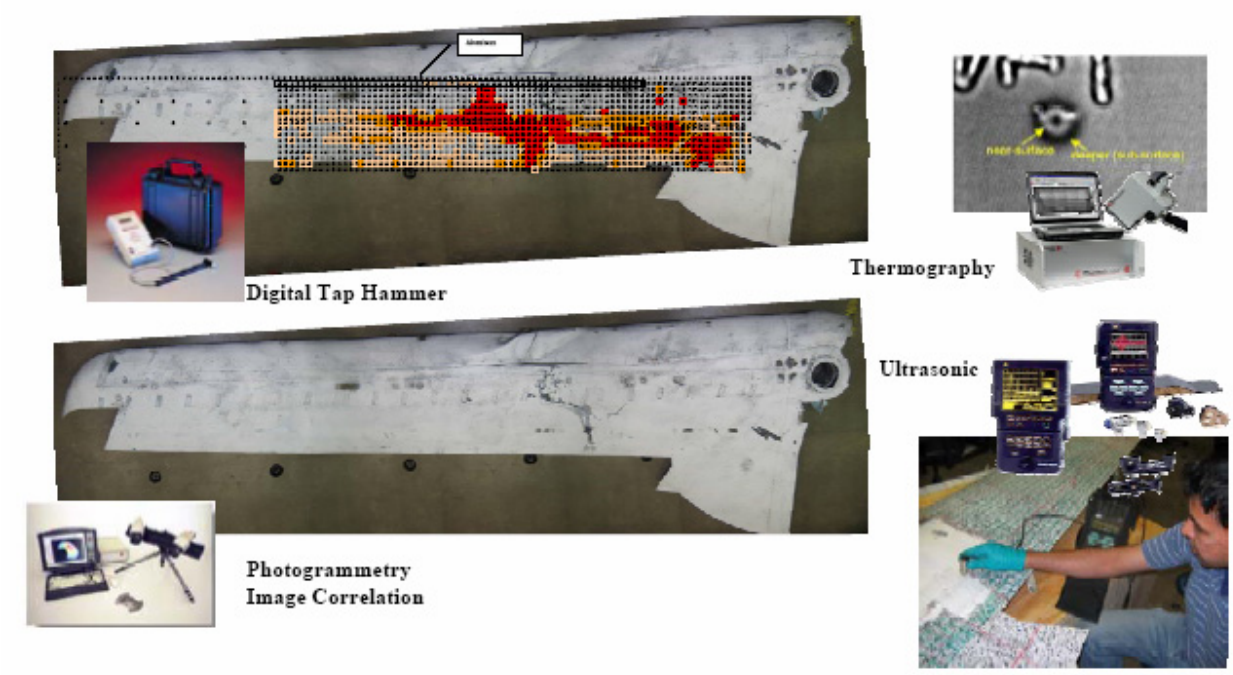

Figure 85. Pulsed thermography inspections of ST004-R impact damage.

Signs of internal damage included, but was not limited to, strain and displacement anomalies, fracture or delamination, relative motion of attachment members or joints, audible noises, and localized shift or relaxation in the whiffletree assembly. When these signs were detected, the structure was inspected and observations were documented in detail with corrective actions, if any. If a localized disassembly was required for an unscheduled detail inspection, care was taken not to damage or alter the structure prior to restarting the test.

CHAPTER 8

FULL-SCALE TEST SUBSTANTIATION

Previously, Figure 4 shows an overview of the full-scale test plan. First, several static test articles were used to determine the ultimate loads and the corresponding limit load for the durability and damage-tolerance tests outlined in this section. The appropriate conversion factor along with the load enhancement factors developed in section 5.4 for the Beechcraft Starship material and design details were used to generate the load spectrum. Unlike the original certification program, the defects were introduced to the structure at the beginning of fatigue testing. The damages introduced to the structure also represent considerably larger and higher impact damages than that used for the original certification program. The durability test articles were inspected periodically using conventional and detailed inspection procedures in addition to monitoring strain anomalies for possible damage progression.

8.1. Full-Scale Test Program

As shown in Figure 4, the results from five static and two fatigue tests of the Starship forward wings were included in this program. These wings were used to demonstrate various means of compliance, validate the approach for full-scale demonstration based on LEF and N_F as outline in section 5.4, and validate the methodology in section 7.3.1. Full-scale tests were planned to address static, damage tolerance, durability, and repair. In order to reduce the number of tests required, these tests were planned with some overlap of the above-mentioned four core categories as outlined in Figure 4. The outline test plans for these tests consist of two stages: (1) static with strain survey and damage tolerance phases, and (2) durability with damage tolerance and repair phases. Phase 1 of stage 1 included three forward-wing static tests to generate static-strength data for baseline comparison and to accomplish strain surveys of these articles. These

surveys were used to establish the spectrum-loading magnitudes relative to durability tests. In phase 2 of stage 1, two static articles were tested with category 2 and 3 damages to ensure baseline residual-strength requirements for damage-tolerance fatigue test articles.

In phase 1 of stage 2, two fatigue articles were tested under spectrum loading with category 2 and 3 damages that were similar to the ones in phase 2 of stage 1. CAT2 damage in the first fatigue article was intended to investigate damage behavior at the ADL and the residual strength of the structure to sustain expected in-service loads. Such information is crucial for determining inspection intervals. Test duration was selected based on the calculated LEF and N_F related to design details of the Starship forward wing to verify the methodology presented in section 5.4. The second fatigue test article with CAT3 damage was intended to obtain information pertaining to the onset of damage growth on a primary load path. This damage was selected as it would provide vital data for the definition of the critical damage threshold and help help defining the inspection intervals. Further, the construction of this test article demonstrated that the global failure mechanism is insensitive to damages inflicted on the secondard load path. Post-impact residual strength of the article was closer to limit-load capabilities. Thus, no LEF was applied to the fatigue spectrum. It was understood that damage would grow in this article, and therefore the damage growth was closely monitored.

Real-time data monitoring was crucial to identifying damage propagation during the full-scale DaDT test, especially since large damage scenarios were expected to grow. The monitoring provided instant feedback of the structural response for applied loads and mitigated risks of unexpected test failures or anomalies that would have been otherwise left undetected. The strategic allocation of and placement of strain gages for these articles was crucial to achieve this goal. The strain data provided information similar to a built-in health monitoring system and

provided details in real time to assess the state of the damage, i.e., propagation or not, and any global effects on the structure due to possible damage growth.

8.1.1. Forward-Wing Stations

The Starship forward-wing station (FWS) references the center of the attach pin as FWS 19.76. For data in this report, the FWS is measured along the front web.

8.1.2. Non-Destructive Inspections

Strain gages were mounted at critical locations and around damages to detect possible flaw growth and were periodically monitored throughout the test. The test articles were inspected in detail prior to and after each ¼ DLT of cyclic loading (either by removing the whiffletree or by removing the specimen completely from the test setup) using ultrasound, in addition to periodic inspections based on strain anomalies around the defect. For initial static testing, full-field strain measurements were used to monitor the damage containment and propagation.

8.1.3. Conversion of Beechcraft Design Loads to NIAR Research Loads

Initially, four full-scale static tests were conducted in an up-bending configuration to evaluate the load-carrying capability of forward wings beyond the Beechcraft-designed ultimate load (BDUL) so that the baseline loads for fatigue tests could be established. Therefore, limit and ultimate loads for this research (NRLL and NRUL, respectively) were redefined based on the preliminary static full-scale test data. ST001, ST002, and ST003 test articles were tested as is, assuming CAT1 damages. ST001 was loaded up to 200% of the BDLL and unloaded. Since the strain/displacement responses were linear, this article was later inflicted with CAT2 damage on the aft spar-top skin at FWS 45, renamed as ST001(R), and static tested to evaluate structural capacity. Initial static test results along with strain measurements are found in Appendix D, and

a summary of loads data is shown in Table 41. For the first three cases, the first sign of fracture that affected the global strain responses of the test article was noted based on axial gage A4, which was located on the upper skin at FWS 34.0 on the aft spar (Figure 86). Strain gage diagrams were different based on the areas of interest in each test article. Details of strain and displacement gage locations are found in Appendix D.

TABLE 41

LOAD SUMMARY FOR FULL-SCALE STATIC STRENGTH TESTS

Test Article	Wing	Damage Category	Load (lbf)		
			Onset of Damage Propagation - Local	First Sign of Fracture - Global	Fracture
ST001	Right	CAT1	-	11091.56	unloaded
ST002	Left	CAT1	-	11304.44	14640.43
ST003	Right	CAT1	-	10231.09	16123.50
ST001(R)	Right	CAT2	9149.90	11627.80	14694.60

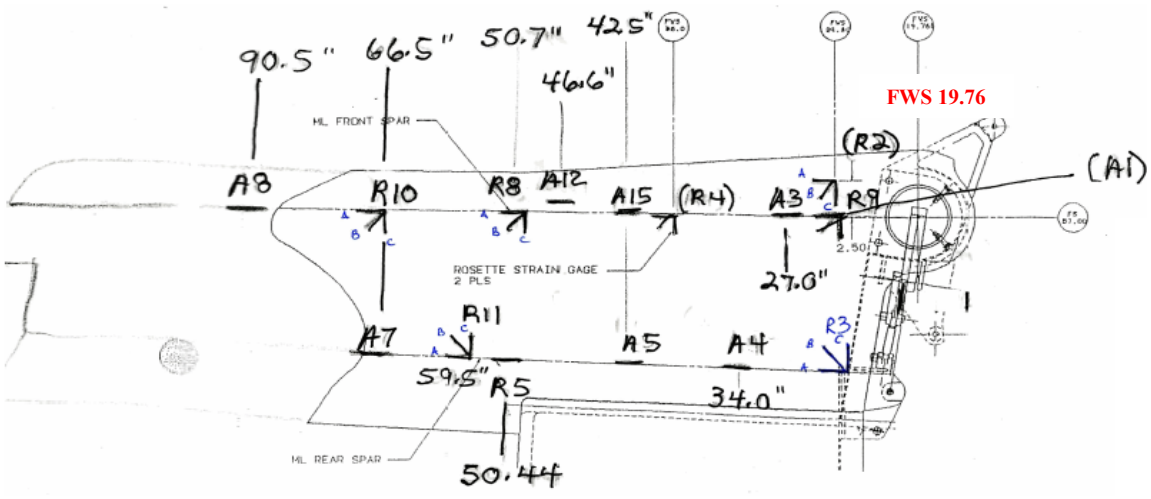

( ) indicates gages on lower surface

Figure 86. Strain gage locations for ST003.

Strain data and post-test failure analysis indicated an initial bondline fracture between the aft spar and top skin toward the root rib, which resulted in skin buckling around this area. For ST001(R), the axial gage A1, located on the lower skin FWS 24.8 on the front spar, indicated the first sign of global fracture. Prior to that, strain gages around the impact damage indicated the onset of local damage propagation around 9150 lbf. Although data points were not sufficient to generate a reliable basis value, Weibull analysis was conducted using rank regression in fracture loads (RRX) for fracture data in Table 41 (Figure 87). Shape and scale parameters for the Weibull distribution of fracture loads are 20.977 and 15,472, respectively. Then, the B-basis of fracture load was calculated using equation (20). The B-basis fracture load is approximately 87 percent of the average fracture load for an up-bending load configuration and is presumed conservative. Furthermore, this load is considered the ultimate load for tests conducted in this research (NRUL). Consequently, the NIAR research limit load (NRLL) was calculated as two-thirds of the NRUL, which resulted in a conversion factor (CF) of 1.4 to convert BDLL to NRLL (Table 42).

TABLE 42

NIAR RESEARCH LIMIT-LOAD SUMMARY

	Positive Limit	**Negative Limit**
Moment (in-lb)	511,168	-124,431
Shear (lb)	8,533	-2,212
Torque (in-lb)	-27,090	6,962

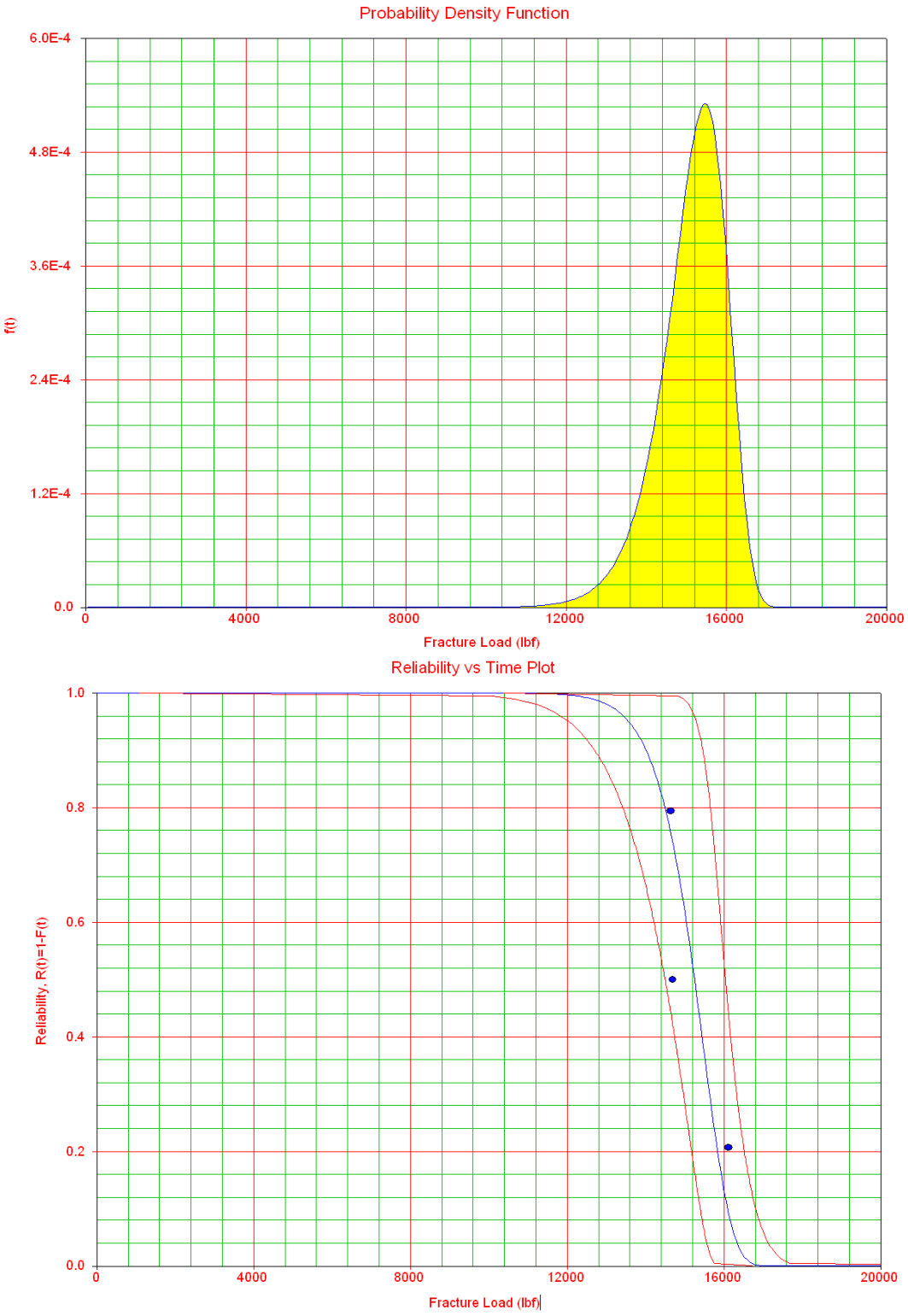

Figure 87. Probability density function and reliability plot for fracture loads.

8.1.4. LEFs for Starship Forward-Wing Testing

Table 43 shows a comparison of load enhancement factors (LEFs) calculated for AS4/E7K8 PW material and NAVY data [2]. The LEF for AS4/E7K8 plain-weave fabric material was first calculated using the individual Weibull method, which was used for NAVY analysis. Next, pooled S-N data were analyzed using the Sendeckyj wearout model to generate the second set of LEFs.

TABLE 43

COMPARISON OF LEFS FOR AS4/E7K8 (STARSHIP MATERIAL) AND NAVY

Number of Test Lives (*N*)	**NAVY**	**Individual (AS4/E7K8)**	**Sendeckyj (AS4/E7K8)**	**Sendeckyj (AS4/E7K8) +Individual (Adhesive)**
1.00	1.177	1.096	1.099	1.102
1.25	1.161	1.066	1.081	1.088
1.50	1.148	1.041	1.066	1.076
2.00	1.127	1.004	1.042	1.058
2.50	1.111		1.025	1.044
3.00	1.099		1.010	1.033
4.00	1.079			1.016
5.00	1.064			1.003
6.00	1.052			
9.00	1.026			
14.00	0.998			
MSSP	20.000	32.193	32.193	32.193
MLSP	1.250	4.056	2.475	1.880
N_F	13.558	2.070	3.431	5.267

Individual Weibull analysis resulted in unconservative LEFs and N_F, i.e., same as traditional metal life factors, as both fatigue data included in the analysis had significantly less scatter. However, fatigue specimens were obtained from the same batch of materials, and only six specimens were tested per stress level. Such data may not be sufficient for individual

Weibull analysis. In contrast, Sendeckyj analysis pooled the test data from all stress levels, including residual strength data, and created a large sample size. Since forward-wing construction of the Starship included several adhesive joints, both adhesive strength and life shape parameters (obtained using individual Weibull due to large scatter observed in adhesive data) were pooled with composite analysis data to generate LEFs and are included in Table 43. For full-scale DaDT testing in this research, the latter LEFs were used, although the adhesive data included in the analysis are for different adhesive than what was used in the structure.

The ST004 DaDT article was tested for 2 DLT (N=2), thus an LEF of 1.058 was required. However, the test article was run with an LEF of 1.072, which was calculated based on the data available at the time the ST004 DaDT test was executed. Based on FAA-LEF data, except for the DTE test data, the LEF of 1.072 corresponds to a test duration of 1.6 DLT. This, along with the conversion factor (CF=1.4), resulted in a cumulative factor of 1.5.

8.1.5. Application of LEF

The LEF can be applied to the fatigue spectrum in several ways: (1) to 1-g mean fatigue load, (2) to amplitude (Δg), and (3) to minimum and maximum load. In addition to the LEF, the CF is an additional factor that was applicable to this research, and these factors were combined to obtain the cumulative load enhancement (equations [33] through [36]) in several ways.

$$P_{1-g} = \left[\left(Load_{1-g} \right) \cdot CF \cdot LEF + \left(\frac{\Delta Load}{\Delta g} \right) \cdot \Delta g \right] \tag{34}$$

$$P_{\Delta g} = \left[\left(Load_{1-g} \right) \cdot CF + \left(\frac{\Delta Load}{\Delta g} \right) \cdot \Delta g \cdot LEF \right] \tag{35}$$

$$P_{Moment} = \left[\left(Load_{1-g} \right) \cdot CF + \left(\frac{\Delta Load}{\Delta g} \right) \cdot \Delta g \right] \cdot LEF \tag{36}$$

$$P_{Cumulative} = \left[\left(Load_{1-g} \right) + \left(\frac{\Delta Load}{\Delta g} \right) \cdot \Delta g \right] \cdot CF \cdot LEF \tag{37}$$

When applying the LEFs to mean fatigue loads, as shown in equations (34), (35), and (36), the mean load is offset in either the positive (for positive mean loads) or negative (for negative mean loads) direction. For cycles with load reversal (stress ratio, $R < 0$), this will cause a reduction in load magnitudes in the opposite loading direction, i.e., shifts the mean load, as shown in Figure 88. Consequently, this will alter the damage growth caused by reversible loads to the composite structure. Furthermore, for higher LEF values, this may convert a tension-compression cycle to a tension-tension cycle or compression-compression cycle for positive and negative enhanced mean loads, respectively. Specimen-level data for composite materials show that reversible load cases ($R < 0$) are critical and have a significantly lower fatigue life than that of tension-tension or compression-compression ($R > 0$) cases (Figure 36). Therefore, equations (34) through (36) are not recommended for applying the LEF to a spectrum loading with negative stress ratios (tension-compression loading) to avoid changes to stress ratios and unintentional reduction in fatigue damages to the test article.

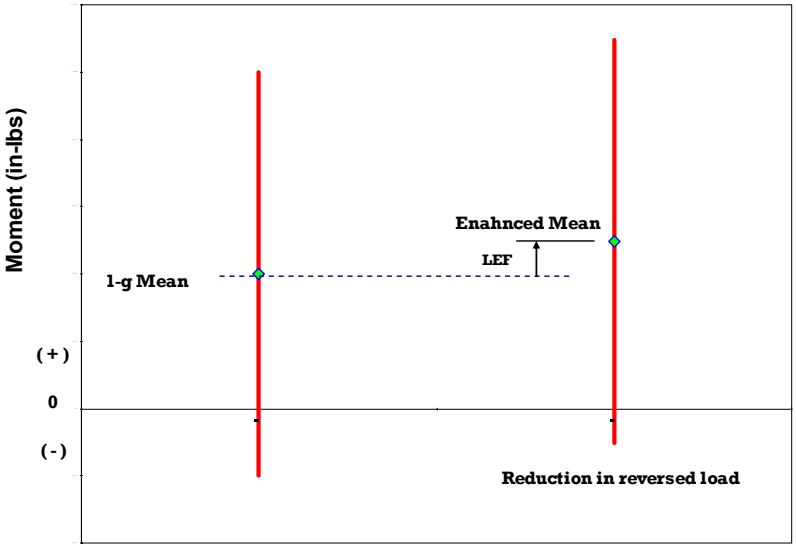

Figure 88. Application of LEF only to mean load.

Application of the CF and LEF to both 1-g mean and amplitude as in equation (37) results in considerably high loads but maintains the same stress ratios throughout the spectrum. Therefore, full-scale fatigue test spectrum loads are generated by applying the CF and LEF (a cumulative load-enhancement factor) to the minimum and maximum shear-moment-torque (SMT) loads so that the reversible loads are not shifted but rather enhanced, depending on the sign of the maximum or minimum SMT load, and the stress ratio is maintained after load enhancement. A comparison of these four methods of applying CF (=1.4) and LEF (=1.072) to SLBs in the Starship forward-wing spectrum is shown in Figure 89 for each load block. During a typical full-scale substantiation program where the CF=1.0, equations (36) and (37) become identical and apply the LEF to minimum or maximum SMT load. As shown in Figure 89, except for the cumulative method in equation (37), most of the reversible loads were converted into positive shear loads.

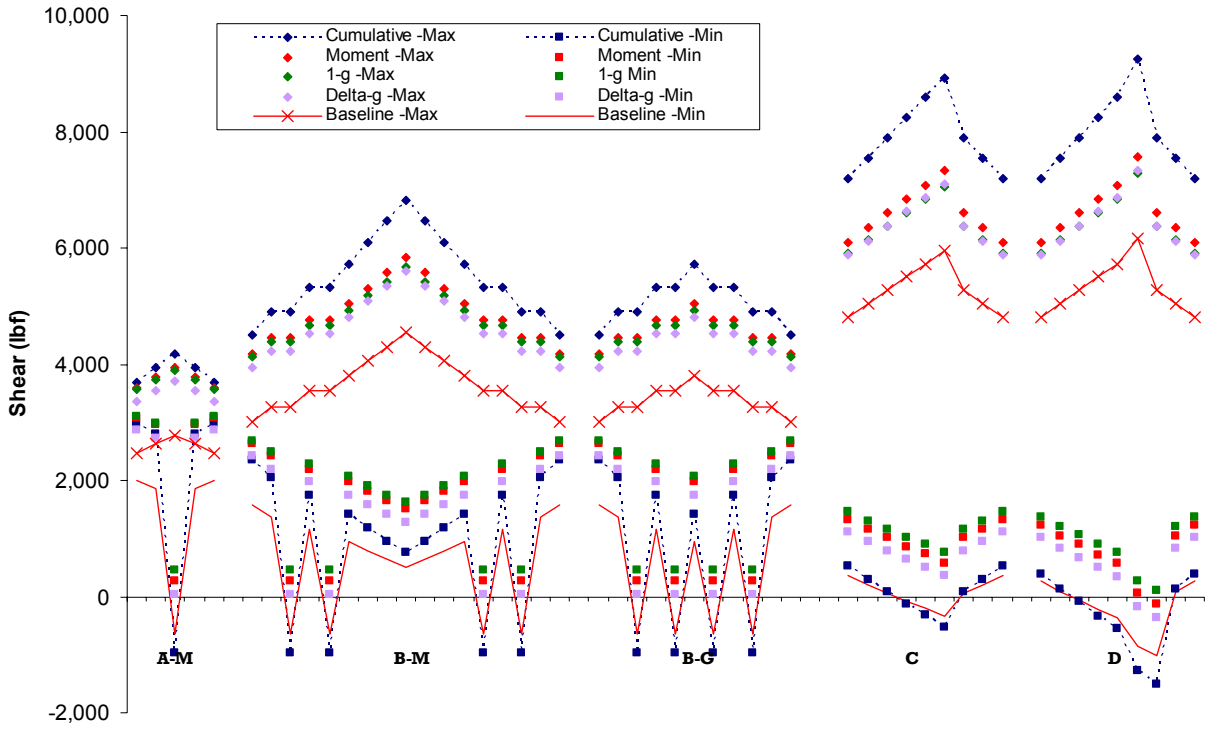

Figure 89. Comparison of methods for applying LEF to a load spectrum.

8.1.6. Fatigue Spectrum Generation

One Beechcraft designed lifetime (1 DLT) of the test article is equivalent to 20,000 flight hours (Figure 90) and corresponds to a spectrum of 160,034 full cycles, which includes 1-g and 3-g maneuvers as well as positive and negative gust conditions. Sequencing of the load blocks in the fatigue spectrum is shown in Table 44 for 1 DLT. In order to adopt the nomenclature of the LEF according to the NAVY approach [2], a fatigue spectrum that is equivalent to 1 DLT of the test article was considered as one test duration (N=1). Prior to fatigue loading, the test articles were used to demonstrate both positive and negative limit loads. At predetermined intervals, durability test articles were loaded to static positive and negative limit loads to compare possible compliance changes, i.e., due to stiffness loss or damage propagation.

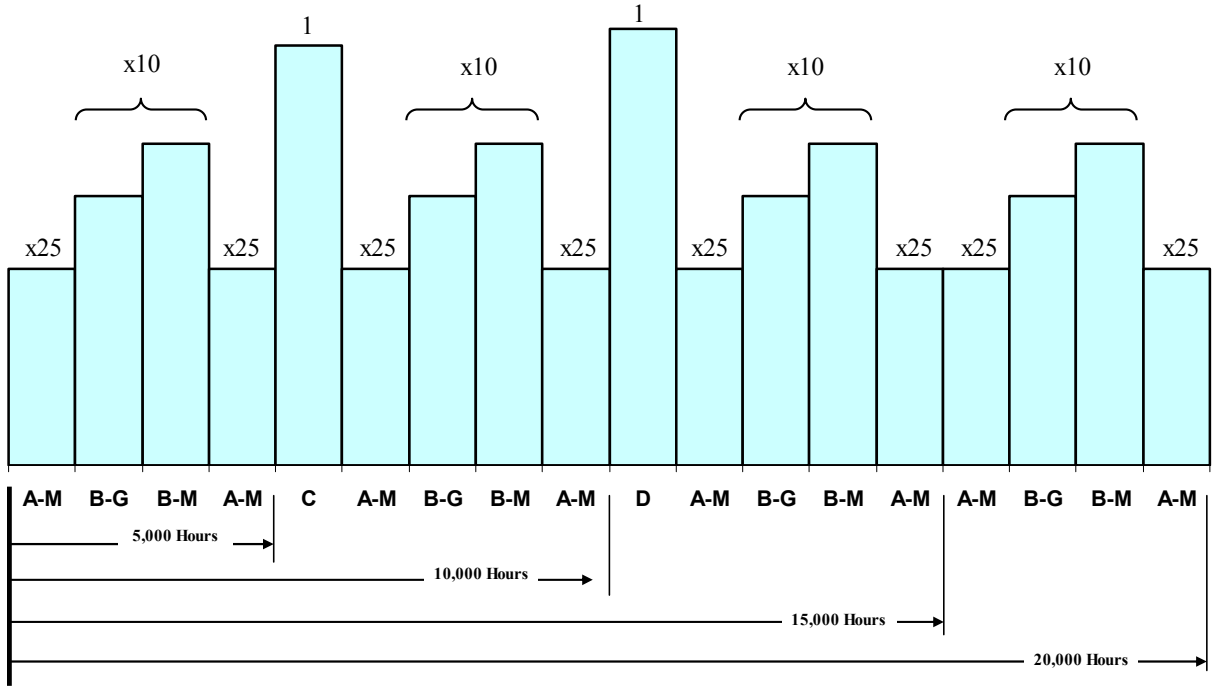

Figure 90. Loading sequence (spectrum) for 1 DLT.

TABLE 44

LOAD SEQUENCE FOR 1-DLT TEST

Sequence	Loading Block	Repetitions	n per Block	Σn	Cumulative Flight Hours	Life Times
a	Start					0
b	Ramp to NRLL+	1				
c	Ramp to: Zero	1				
d	Ramp to: NRLL-	1				
e	Ramp to: Zero	1				
f	Ramp for fatigue	1				
1	Block A-M	25	718			
2	Block B-G	1	146			
3	Block B-M	1	264			
4	Repeat 2 and 3	9	410			
5	Block A-M	25	718	40000	4999	0.250
6	Ramp to: Zero	1				
7	Repeat a through f (50% Load)	1				
8	Block C	1	16			
9	Block A-M	25	718			
10	Repeat 2 and 3	10	410			
11	Block A-M	25	718	80016	10000	0.500
12	Ramp to: Zero	1				
13	Repeat a through f (50% Load)	1				
14	Block D	1	17			
15	Block A-M	25	718			
16	Repeat 2 and 3	10	410			
17	Block A-M	25	718	120033	15001	0.750
18	Ramp to: Zero	1				
19	Repeat a through f (50% Load)	1				
20	Block A-M	25	718			
21	Repeat 2 and 3	10	410			
22	Block A-M	25	718	160033	20000	1.000
23	Ramp to: Zero	1				

The Starship forward-wing original certification test spectrum [63] was modified for the current research. This modification included converting maneuver and gust SMT loads at 1-g by the CF to define new limit and ultimate conditions as discussed in section 8.1.3, and application of the LEF to the spectrum as discussed in section 8.1.5. The spectrum contained gust and maneuver load blocks that were repeated several times as recommended [59], with shear-load sequences arranged from low to high and high to low within each block (Figure 91). Blocks A-M and B-M represent maneuver conditions, while block B-G represents gust conditions. Blocks C and D are torque conditions, where positive and negative Δg loads were calculated based on maneuver and gust torque conditions, respectively.

The gust and maneuver exceedance curves and ±Δg loads used for fatigue SMT loads are found in Appendix C. The resultant bending moments and torque for the applied shear loads in Figure 91 are shown in Figures 92 and 93, respectively.

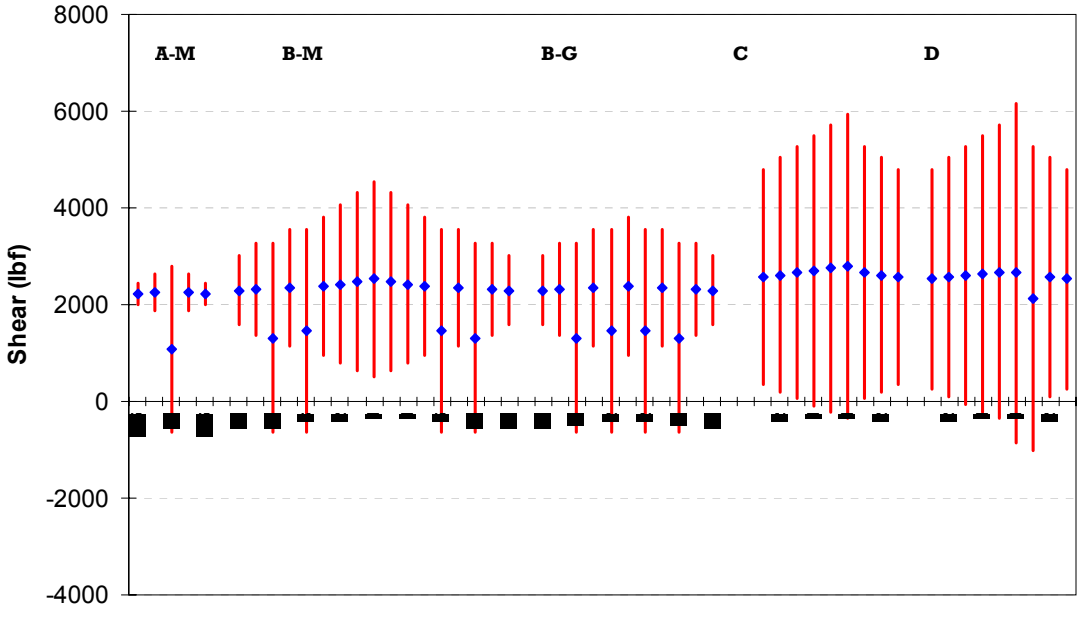

Figure 91. Maneuver and gust shear-load spectrums, CF= 1.0 and LEF=1.0.

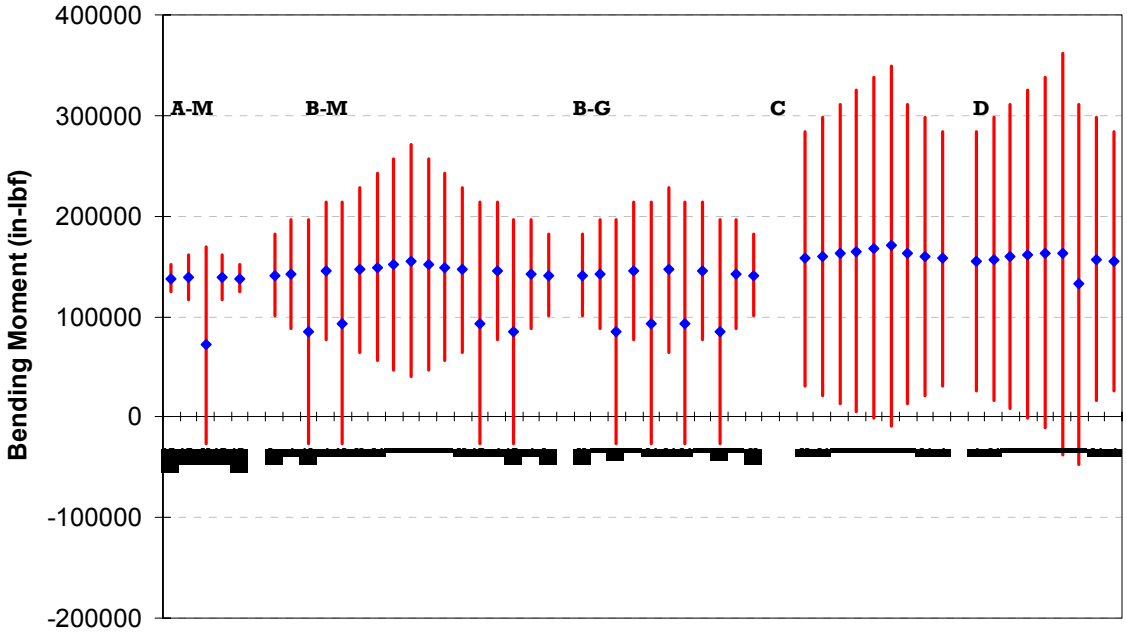

Figure 92. Maneuver and gust bending moments, CF= 1.0 and LEF=1.0.

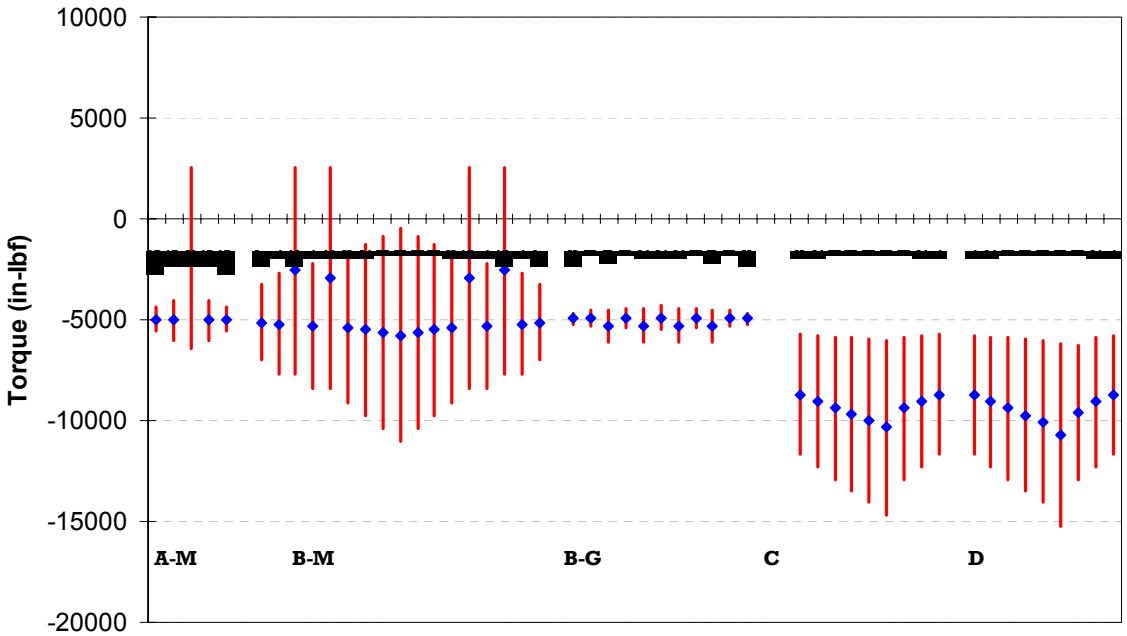

Figure 93. Maneuver and gust torque, CF= 1.0 and LEF=1.0.

8.1.7. Modified Load Patches

Application of significantly large damages, i.e., CAT2 and CAT3 damages, which are beyond original certification requirements, resulted in removal of several load patches around the damages of ST004 and ST006 DaDT test articles to accommodate damage growth, make room for strain gage installation, and minimize localized out-of-plane loads. Such modifications were carried out with caution so that SMT loads would not be severely altered, especially around the damage area, as shown in Figure 94.

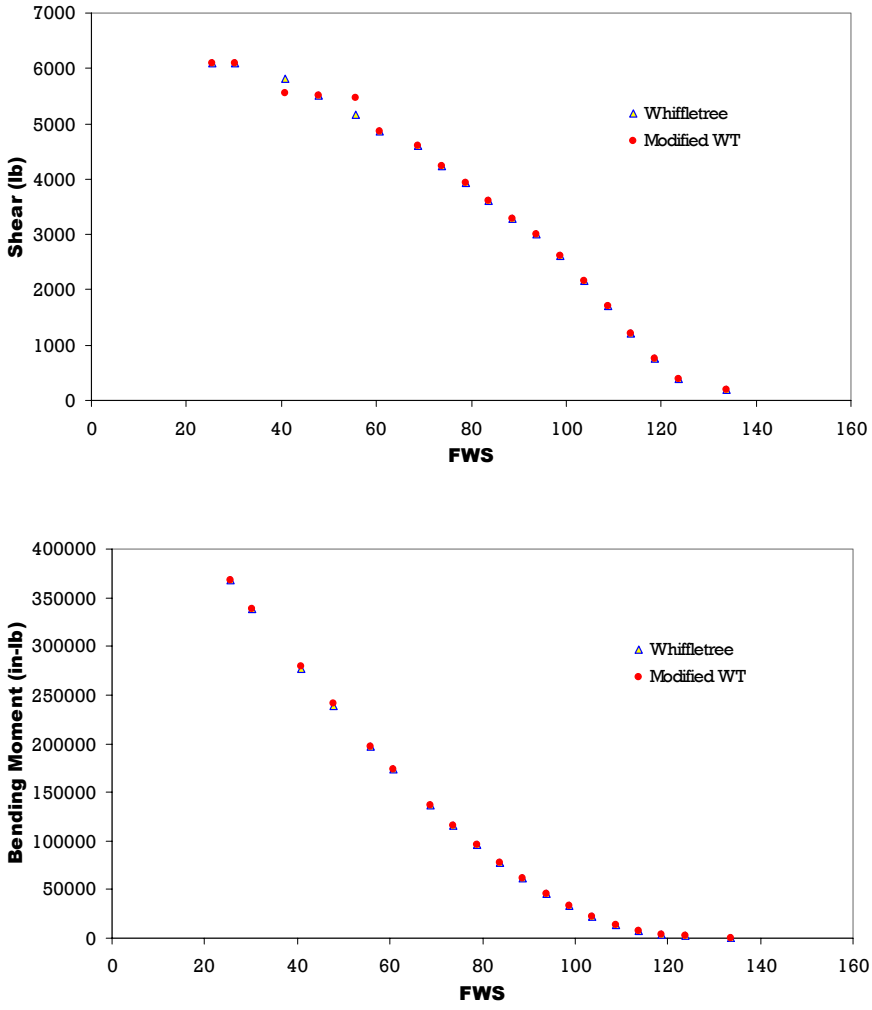

Figure 94. Effects of modified patch locations of ST004 on shear and moment.

8.1.8. Durability and Damage-Tolerance Test Results

Both ST001(R) and ST004 test articles were impacted with 225g ft-lb energy impact with a three-inch diameter metal sphere to obtain CAT2 damage at FWS 45 on the top skin of the rear spar. ST001(R) was static tested to evaluate the structural capacity, while ST004 article was fatigue tested with an LEF for two DLTs. Following 2 DLTs, ST004 was tested to evaluate residual strength in the up-bending loading configuration. The ST005 article was impacted with 1000g ft-lb energy using a sharp wedge impactor at FWS 65 at the front spar (top skin) and static tested in the up-bending configuration to evaluate structural capacity. This energy level was selected to represent CAT3 damage to the structure, while the location was selected to investigate the effects of such a defect on the primary load path of the structure. Similar damage was inflicted on the ST006 fatigue test article. Following impacting, test articles were inspected non-destructively to quantify the damage using ultrasonic and digital tap-hammer inspection techniques.

8.2. Damage Infliction

In order to obtain CAT2 and CAT3 damages that satisfied load and visibility requirements as shown in Table 40, several trial impact tests were conducted using static-tested forward wings. Due to the design details shown in Figure 84 and the failure mechanism during impact, damaging the forward wing to satisfy these requirements was challenging. Energy level requirements for both impact categories were significantly higher than what is typically used during certification programs. However, these energy levels were selected after numerous trial tests to satisfy both load and visibility requirements for each damage category. In order to penetrate the front spar cap and satisfy visibility requirements for CAT3 damage, even with extremely high energy levels, a sharp impactor (wedge) was used.

8.2.1. CAT2 Damage on ST001(R) and ST004

Table 45 summarizes the impact trials conducted to determine CAT2 impact parameters. Based on the information gathered from these impact trials, damage was inflicted on the aft spar of ST001(R) with an energy level of 225g ft-lb using a three-inch steel sphere at FWS 45 (Figure 95). For comparative purposes, the durability article ST004 was impacted with a similar energy level at the same location.

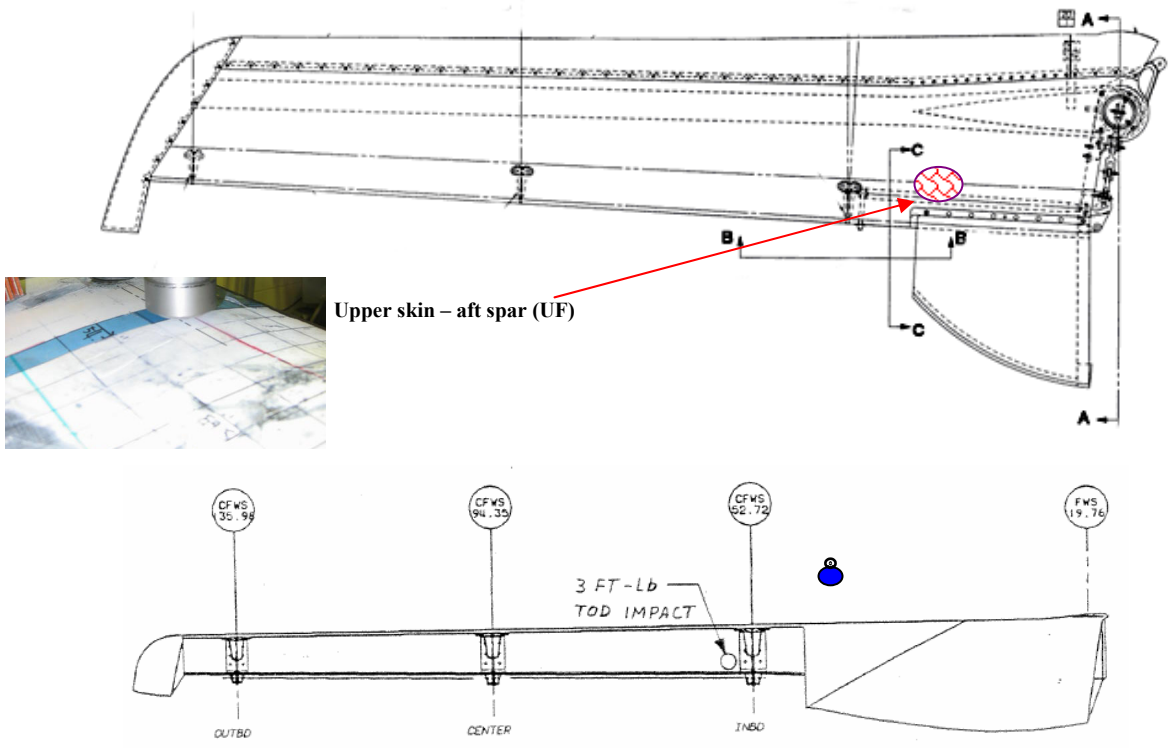

Figure 95. Damage location on ST001(R) and ST004.

Figure 96 shows the visual inspections following CAT2 impact on the ST004 test article. Damage to the top skin at the contact location and to the aft web was clearly visible. Detailed post-impact nondestructive inspection results are included in section 8.3 of this report.

TABLE 45

SUMMARY OF IMPACT TRIALS TO DETERMINE CAT2 IMPACT PARAMETERS

Spar	Location (FWS)	Mass (lb)	Impactor	Support Span (in)	Height (in)	Energy Level		Notes
						in-lb	ft-lb	
Front	126.0	14.5	Bowling Ball	12	40	580	48	no visible damage on the surface or on the web
Front	126.0	14.5	Bowling Ball	Steel base	80	1160	97	no visible damage on the surface; some fracture along web-flange intersection
Front	126.0	14.5	Bowling Ball	Steel base	110	1595	133	no visible damage on the surface; some fracture along web-flange intersection
Front	112.0	31	3-inch Sphere	16	36	1116	93	no visible damage on the surface; some fracture along web-flange intersection
Front	106.0	31	3-inch Sphere	16	80	2480	207	no visible damage on the surface; some fracture along web-flange intersection
Front	51.0	31	3-inch Sphere	16	110	3410	284	no visible damage on the surface; some fracture along web-flange intersection
Aft	78.7	31	3-inch Sphere	16	72	2232	186	skin fracture + indent (web is not visible)
Aft	54.7	31	3-inch Sphere	16	72	2232	186	skin fracture + indent; no damage to web (close to control surface mount)
Aft	124.5	14.5	Bowling Ball	16	72	1044	87	indent + possible 2.75” fracture in the aft web
Aft	114.5	20.5	Bowling Ball	16	110	2255	188	indent + possible 5.5” fracture in the aft web
Aft	102.5	45.5	Bowling Ball	16	72	3276	273	indent + possible 8” fracture in the aft web
Aft	89.5	37.5	3-inch Sphere	16	72	2700	225	skin fracture + indent (web is not visible)
Front	89.5	37.5	3-inch Sphere	16	72	2700	225	no visible damage on the surface; web fracture
Aft	45.0	37.5	3-inch Sphere	16	72	2700	225	Visible Damage on surface + fracture in the web away from the control surface mount

Events are listed in chronological order.

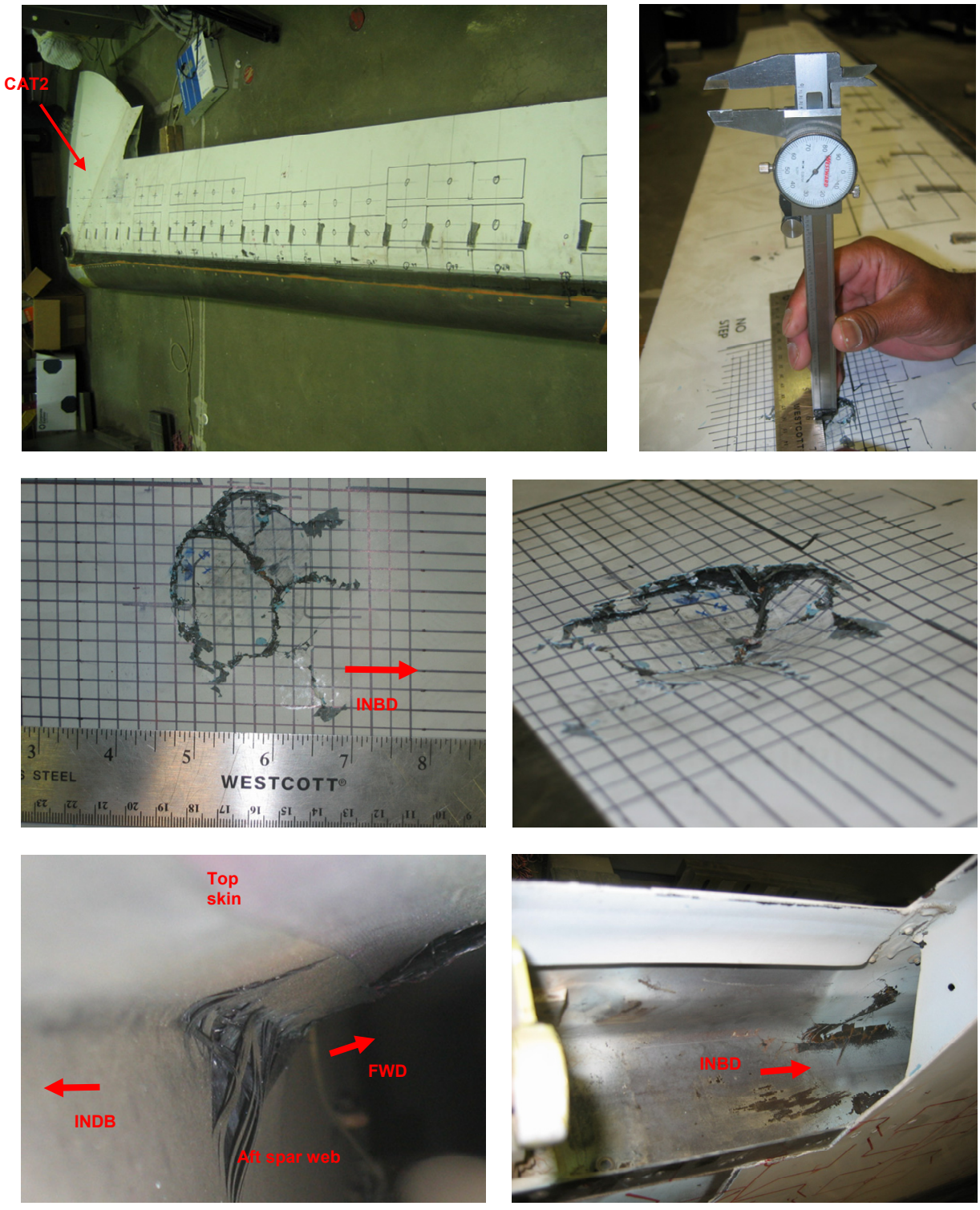

Figure 96. Visual inspections of CAT2 damage on ST004.

8.2.2. CAT3 Damage on ST005 and ST006

ST005 was inflicted with CAT3 impact damage and static tested for residual strength. The required energy level and impact geometry were selected based on several impact trials, as listed in Table 46. For these trials, one- and three-inch-wide wedges (Figure 97) were selected as impactors. Even with the maximum energy level of 997g ft-lb, damage to the spar cap was limited to localized surface damage at the contact line, as shown in Figure 98(a), and did not satisfy visibility requirements of CAT3 damage. However, there was a substantial amount of fracture and delamination to the front web, which is not visible unless the leading edge is removed (Figure 98[b]).

TABLE 46

SUMMARY OF IMPACT TRIALS TO DETERMINE CAT3 IMPACT PARAMETERS

Test Article	FWS (Front Spar)	Wedge	Mass (lb)	Height (ft)	Energy Level (ft-lb)
ST002	120.5	1-inch	15	6	90
		1-inch	15	10	150
		1-inch	50.5	10	505
	108.5	3-inch	50.5	15	758
		3-inch	50.5	10	505
ST001	66.5	3-inch	73.3	13.6	997

In order to increase the contact force and drive penetration, the top front spar cap of the ST005 static article was impacted with a 1000g ft-lb energy level using a machined one-inch sharp-wedge impactor at FWS 65. This forward-wing station was selected because of the aluminum secondary web that is located forward of the front spar to stabilize the thick front-spar caps from rotating on the thin web. This secondary web runs from FWS 26.76 to FWS 64.5 and

is mechanically attached to the top and bottom skin overhang (flange) forward of the front spar and leading-edge closeout rib.

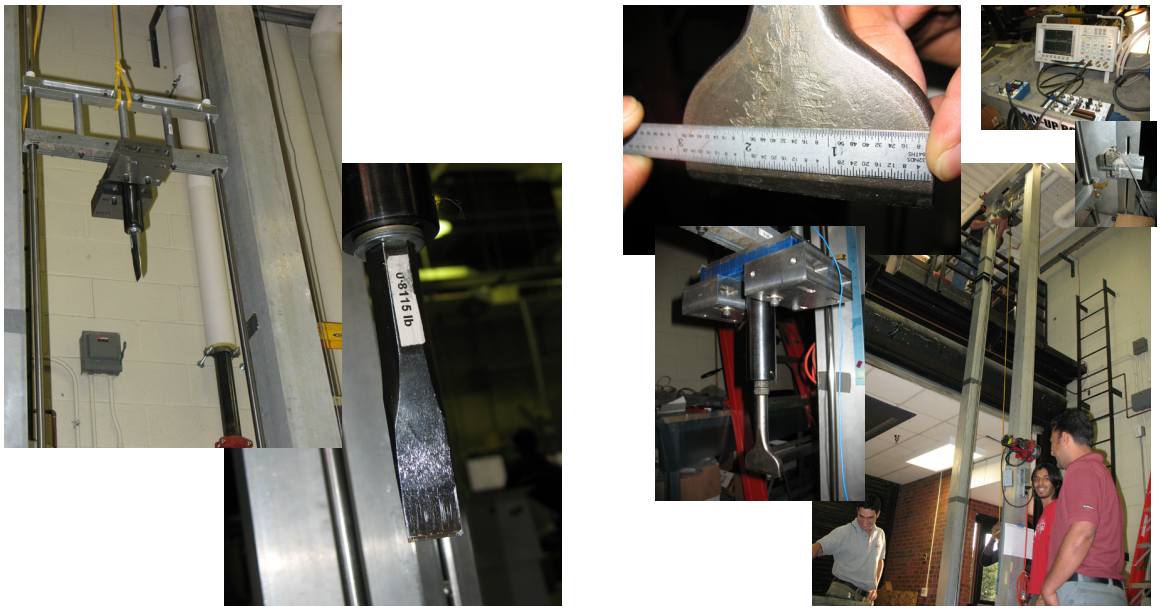

(a) 1-inch wedge (b) 3-inch wedge

Figure 97. Gravity-assisted drop-tower setup for CAT3 impact trial tests.

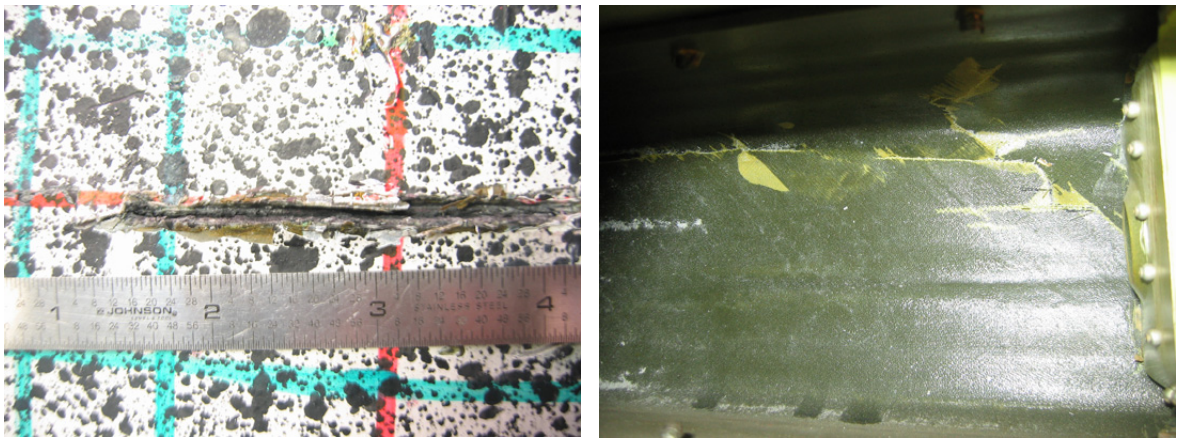

(a) front-spar (top skin) impact location (b) damage to web below impact location

Figure 98. CAT3 impact damage results for trials

An aluminum closeout rib at FWS 64.5 was mechanically fastened to the secondary web, and bonded to the upper and lower spar caps and front spar web (Figure 99). This provided additional strength in the direction of impact at the contact location (FWS 65), thus minimizing front-spar web crush, as illustrated in Figure 84. This resulted in penetration rather than springback of the spar caps (and web crush) that was seen in trial tests conducted on ST002 (Table 46).

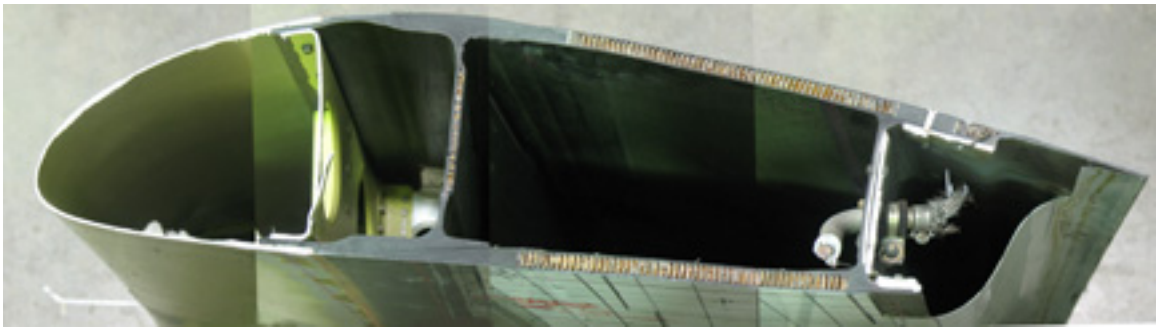

Figure 99. Cross-sectional view near FWS 65.

In order to rigidly hold the test article during impact, a cradle fixture was built with a matching wing profile at supports (Figure 100). Unlike the case of trial impacts, this fixture arrangement resulted in complete penetration, which was clearly visible during a walk-around inspection. In order to inspect the damage to the front side of the front-spar web, a 1.75-inch hole was drilled on the leading edge using a hole saw. Based on the law of conservation of energy (and assuming no frictional effects on the drop-weight guide), the velocity of the impactor assembly was calculated as approximately 30 ft/sec prior to contact. Figure 101 shows the one-inch circular damage on the top front spar cap of ST005, which was later tested to determine the residual strength under up-bending load configuration. As seen in this figure, significant delamination and fracture were observed on the web, especially closer to the upper-

spar cap. Ultrasonic NDI inspections as well as DTH tests were performed to delineate the damage extent, and results are included in section 8.3.

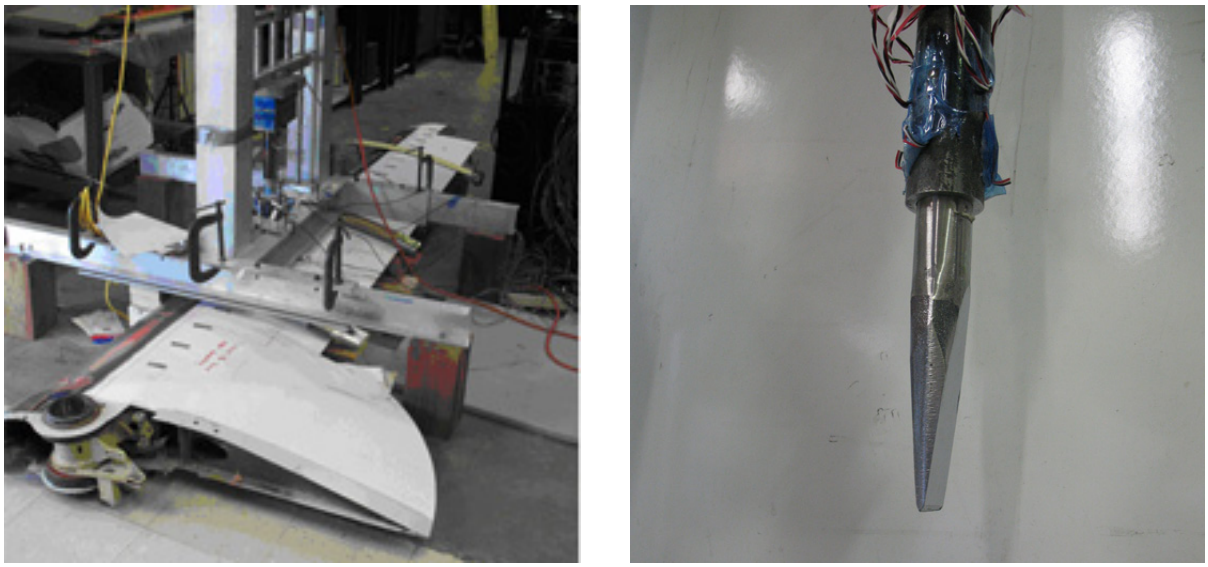

(a) Gravity-assisted drop tower (b) Sharpe wedge impactor

Figure 100. CAT3 impact test setup for ST005 and ST006.

The DaDT test article ST006 was impacted with the same energy level using the same impactor at the same location, front spar top skin at FWS 65, for comparison purposes. Figure 102 shows the 1.25-inch circular damage on the top front-spar cap of ST006, which was tested for durability and damage tolerance (DaDT). As seen on ST005, this impact damage was clearly visible during a walk-around inspection, and there were significant delamination and fractures observed on the web. Furthermore, post-impact visual inspection revealed that the lower bottom aft flange of the front spar was disbonded, and the bottom skin (opposite the contact location) was delaminated, as shown in Figure 102. Ultrasonic NDI inspections as well as DTH tests were performed to determine the extent of damage, and results are included in section 8.3.

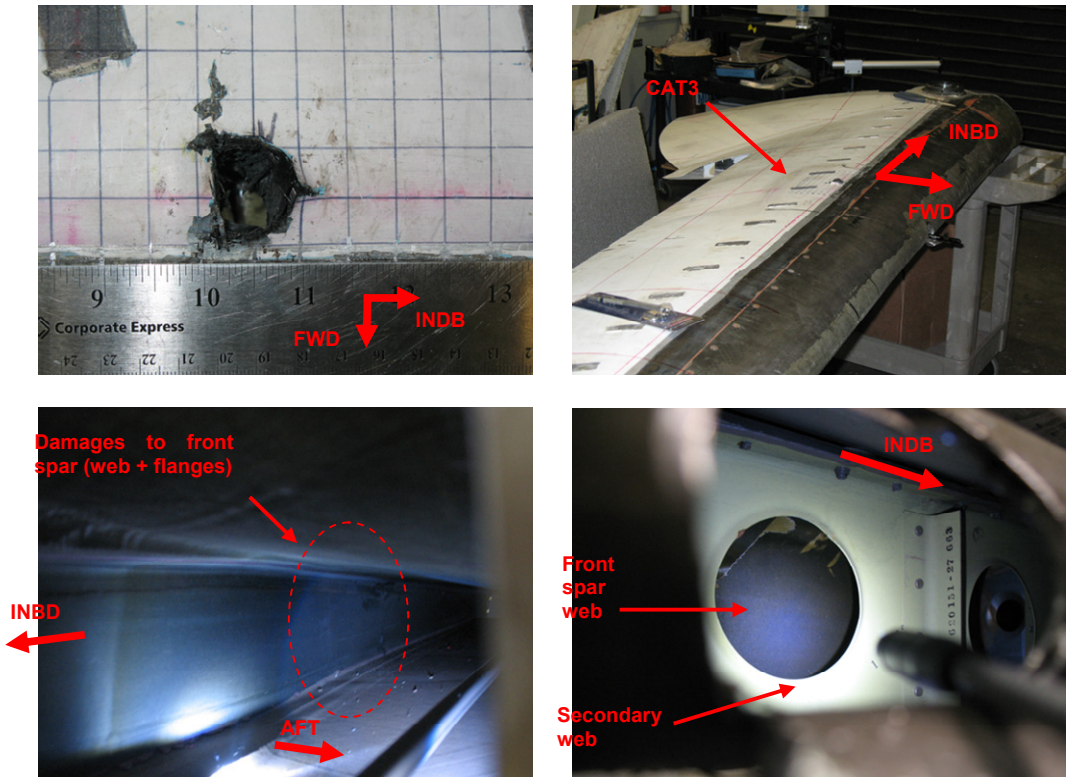

Figure 101. CAT3 impact damage on ST005 at FWS 65.

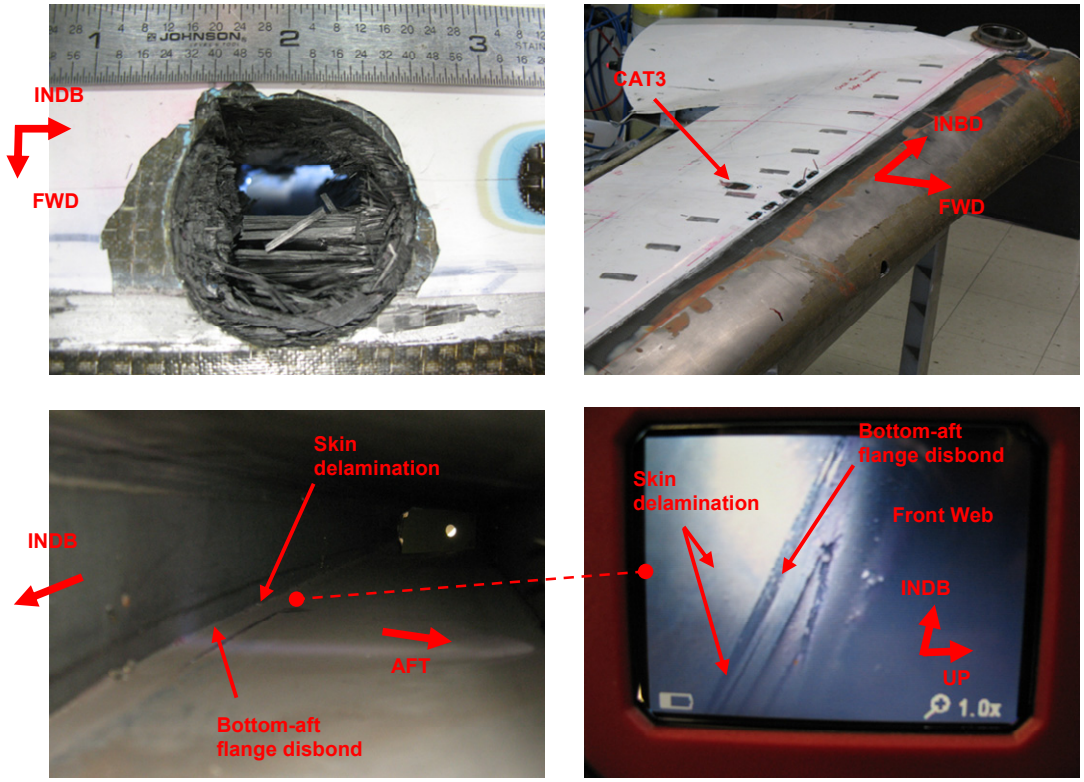

Figure 102. CAT3 impact damage on ST006 at FWS 65.

8.3. Non-Destructive Inspections Results

Several NDI techniques were used to inspect the test articles following damage infliction to delineate the extent of damage to the structures. Figure 103 shows the NDI results of CAT2 damage inflicted on ST004 prior to cyclic loading. This unit consists of a lightweight hammer containing an accelerometer, which is connected by a flexible cable to components and a liquid crystal display. It supplements the subjective tonal discrimination of the operator with a quantitative, objective numeric readout that can be correlated to fractures, delaminations, or debonds in the structure. Baseline data were recorded prior to impact using a grid, as shown in Figure 103(b). Since the thickness of the structure changes significantly around the inspection area, these baseline data were essential for subsequent NDI inspections, i.e., post-impact and during fatigue testing, so that the localized relative stiffness change could be measured by isolating the inherent tonal variations due to thickness or stiffness changes. Initial DTH readings confirmed ultrasonic A-scan (pulse-echo) inspections. In addition, a Thermoscope II, a hand-help high-speed infrared camera, was used to track changes in the surface temperature following a brief pulse of a xenon flash lamp. As the local structure cooled down, the surface temperature was affected by internal flaws, such as disbonds, voids, or inclusions, which obstruct the flow of heat into the structure. This unit was used only on ST004 due to the availability of the system.

Figure 104 shows the NDI results obtained from Sonic 1200 ultrasonic, BondMaster^{TM} 1000, and DTH following the CAT3 impact damage on ST005 test article. The first two methods show the localized damaged region, while the latter delineated an approximately 5.5-inch-long (along the spar cap) and 3.75-inch-wide damaged area. Ultrasonic reading in this area was weak but confirmed DTH findings. Conversely, NDI results obtained from these techniques on ST006 correlated well, defining a 6.5-inch-long and 3-inch-wide damaged area (Figure 105).

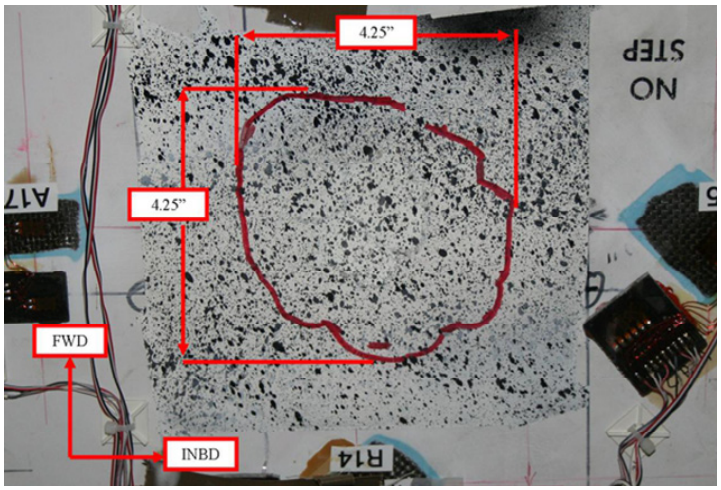

(a) Ultrasonic (pulse-echo)

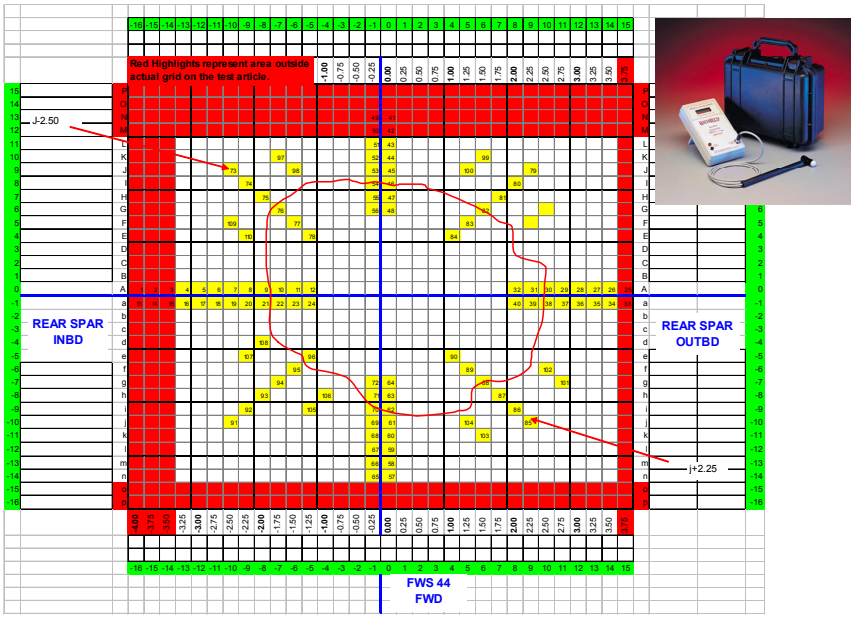

(b) Digital tap hammer

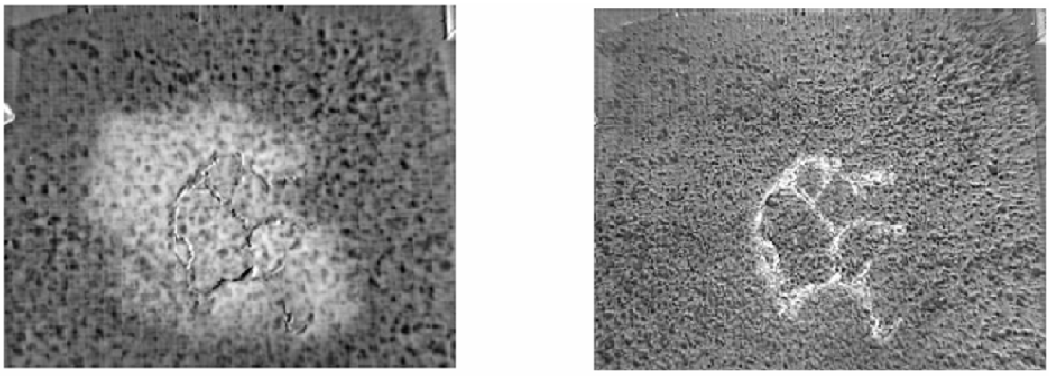

(c) Pulsed thermography

Figure 103. NDI results of CAT2 damage on ST004 prior to cyclic load.

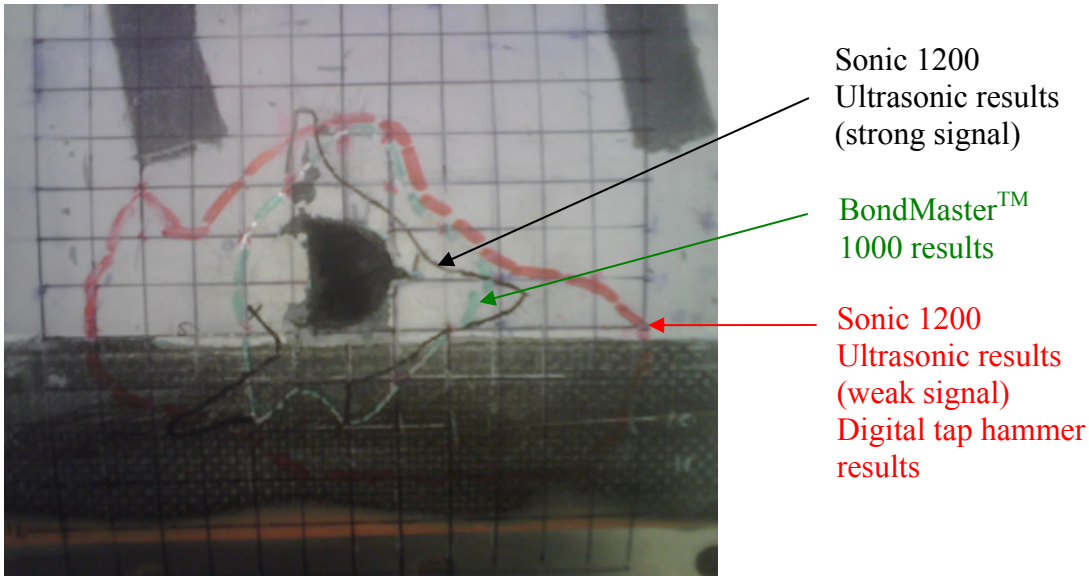

Figure 104. NDI results for CAT3 damage on ST005.

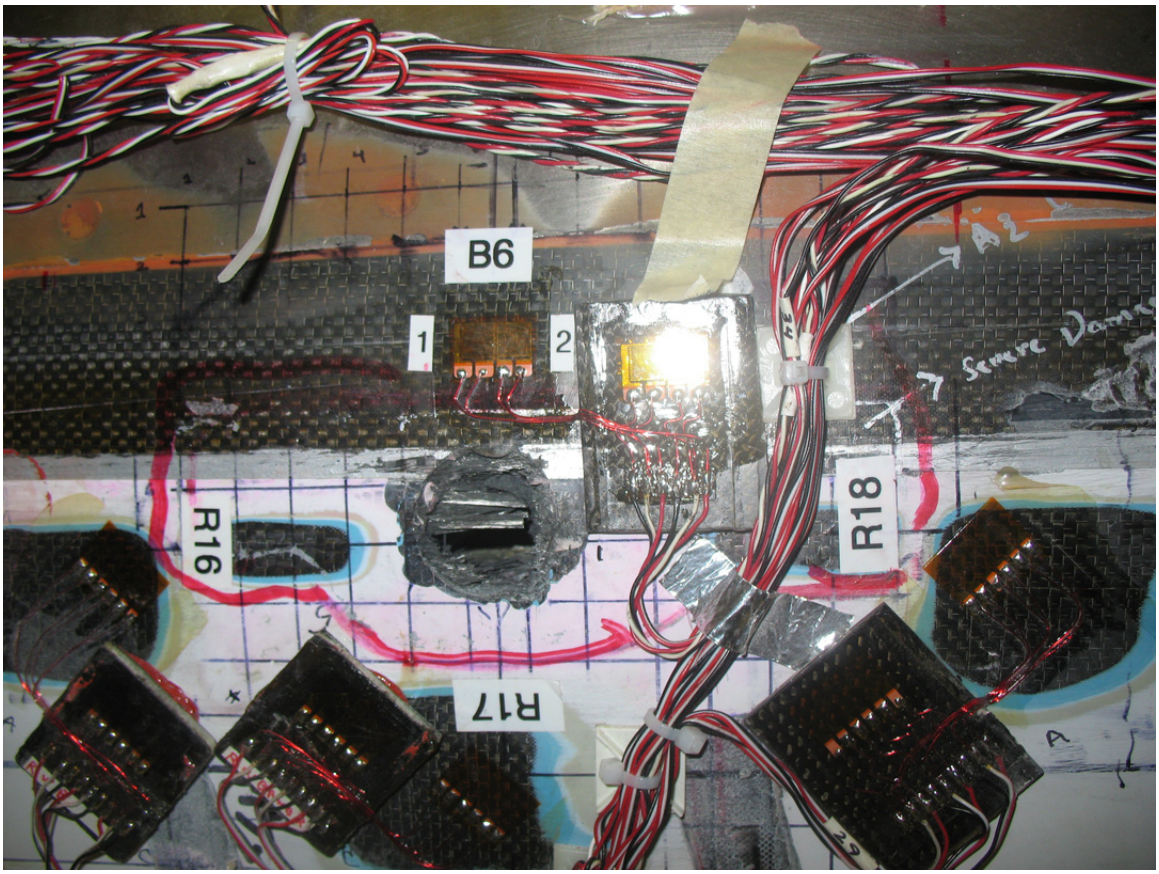

Figure 105. NDI results for CAT3 damage on ST006.

8.4. Damage Containment and Propagation

Additional strain gages were mounted adjacent to impact damage to detect possible damage initiation and flaw growth. During static loading, strains should gradually increase, thus maintaining the original distribution (in linear elastic region), unless there is damage propagation, as seen in Figure 107, which disrupts the original strain distribution.

8.4.1. Quasi-Static Loading

This section contains the static test results for ST001(R) and ST005 articles with CAT2 and CAT3 damages, respectively. Additional strain and displacement data for both test articles are found in Appendix D.

8.4.1.1. ST001(R) – CAT2 Damage on Aft Spar

The strain gage diagram for ST001(R) is shown in Figure 106. Several additional gages were mounted closer to the damage to monitor damage propagation during quasi-static loading. According to the damage definition, a structure must withstand the limit load with CAT2 damage. As shown in Figure 107, CAT2 damage propagation was initiated around 107 percent of NRLL. As shown in Figure 108, the strain data adjacent to the impact damage indicate that the damage propagation initiated around NRLL. This strain gage was located one inch inboard of the damage boundary and was extremely sensitive to any anomalies around the damage. These strain data indicate that ST001(R) was able to contain the CAT2 defect until NRLL. Note that the ultimate fracture load for this article was significantly higher than NRLL.

Figure 109 shows that prior to failure, axial strains along both top and bottom skins of the front spar were not affected by CAT2 damage on the aft spar of ST001(R). This comparison was based on strain values observed on the ST002 test (with CAT1 damage) article at the same load level. Axial strain along both front and aft spars indicated that the anomalies in Figure 107 were

localized and did not affect the final fracture. This was largely due to the fact that for the up-bending loading configuration, the front spar, which is significantly stiffer than the aft spar, was the primary load path. Therefore, for the CAT3 damage configuration, the front spar was selected.

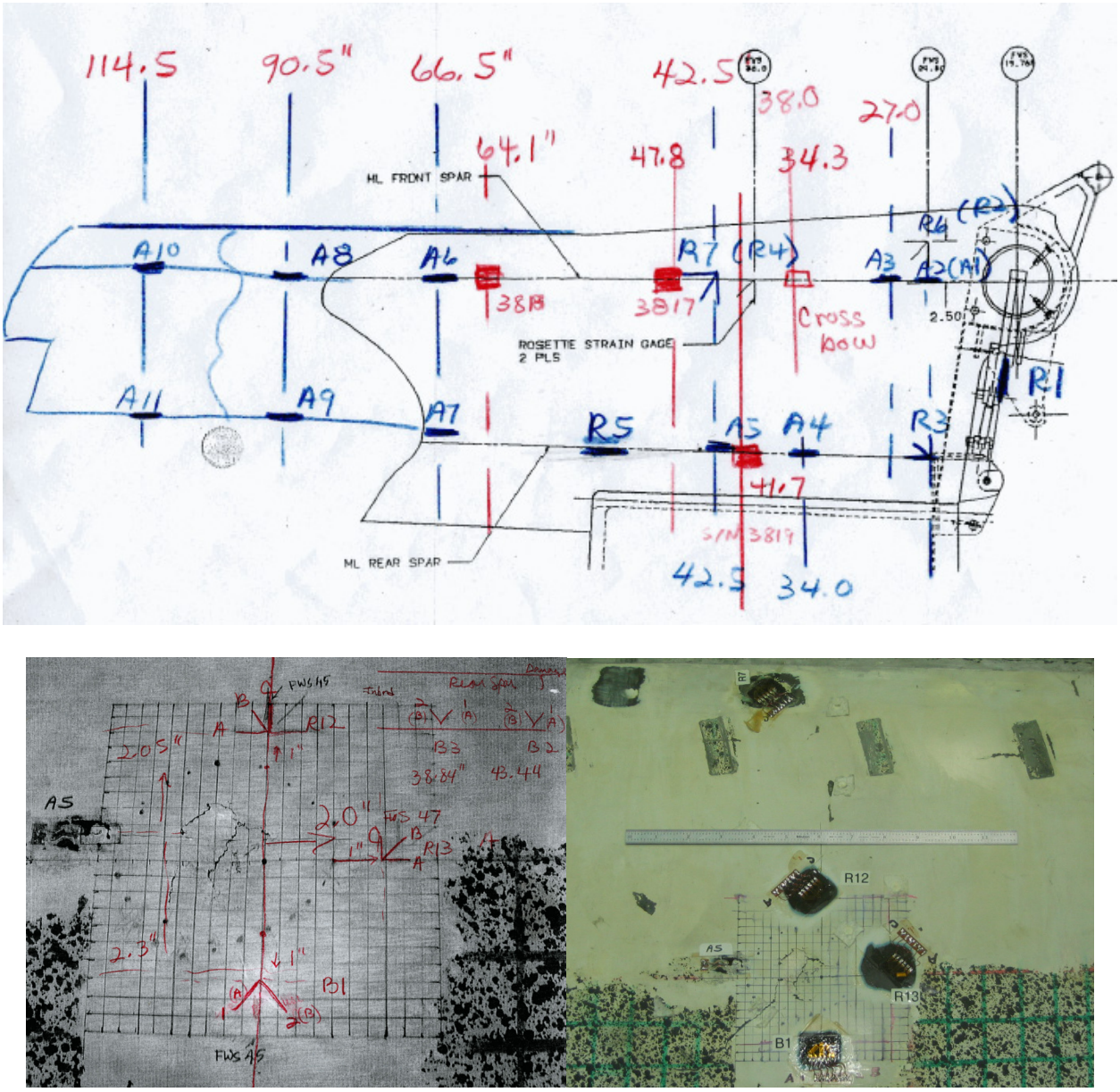

Figure 106. Strain gage location for ST001(R) static test article.

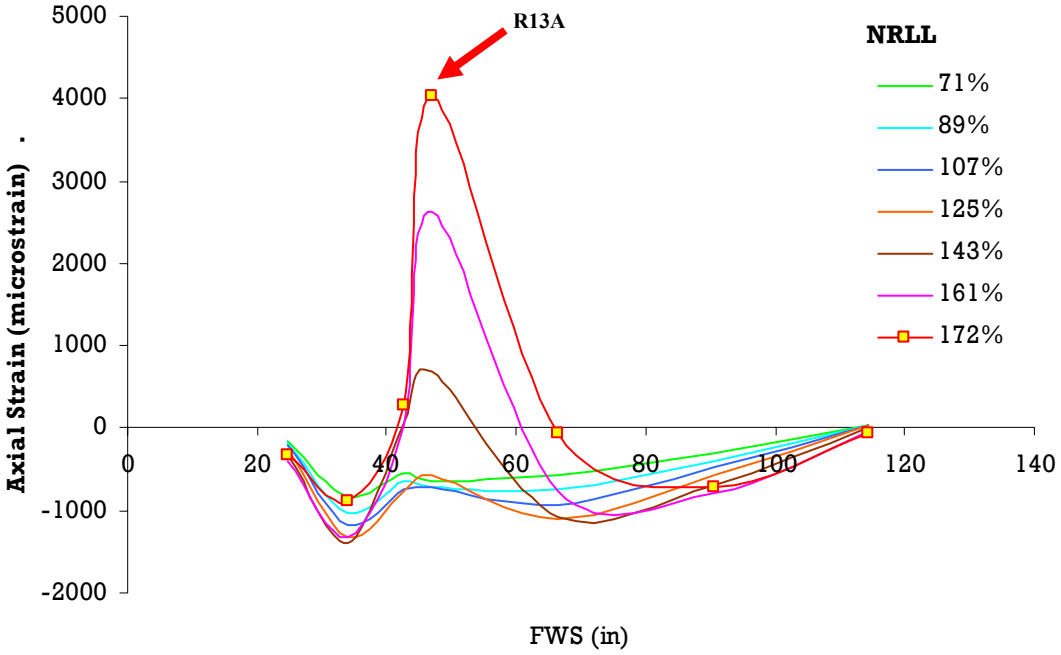

Figure 107. Strain evolution on upper skin of aft spar of ST001(R).

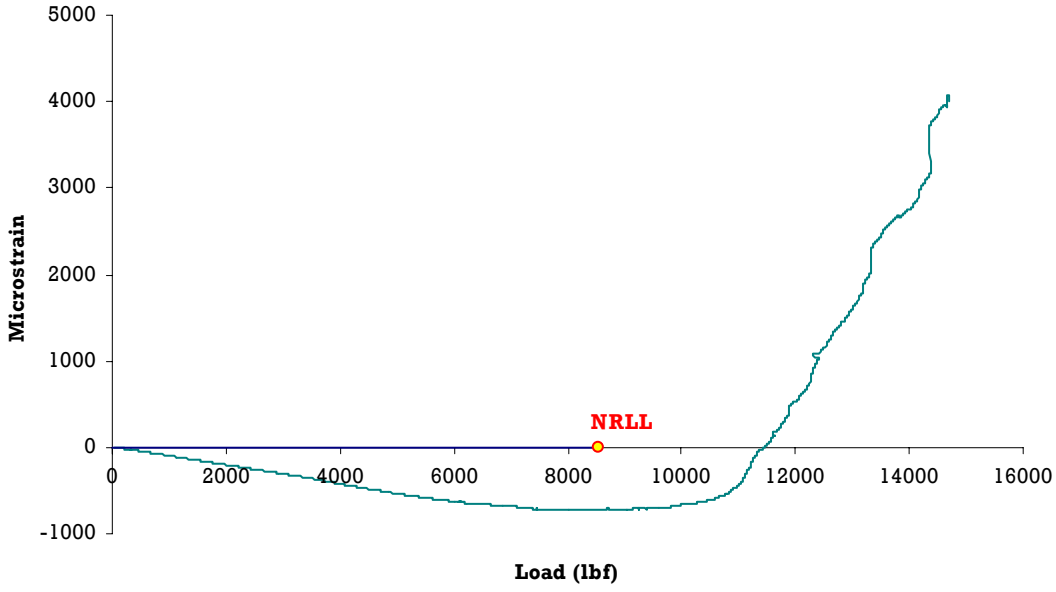

Figure 108. Strain evolution of R13A of ST001(R).

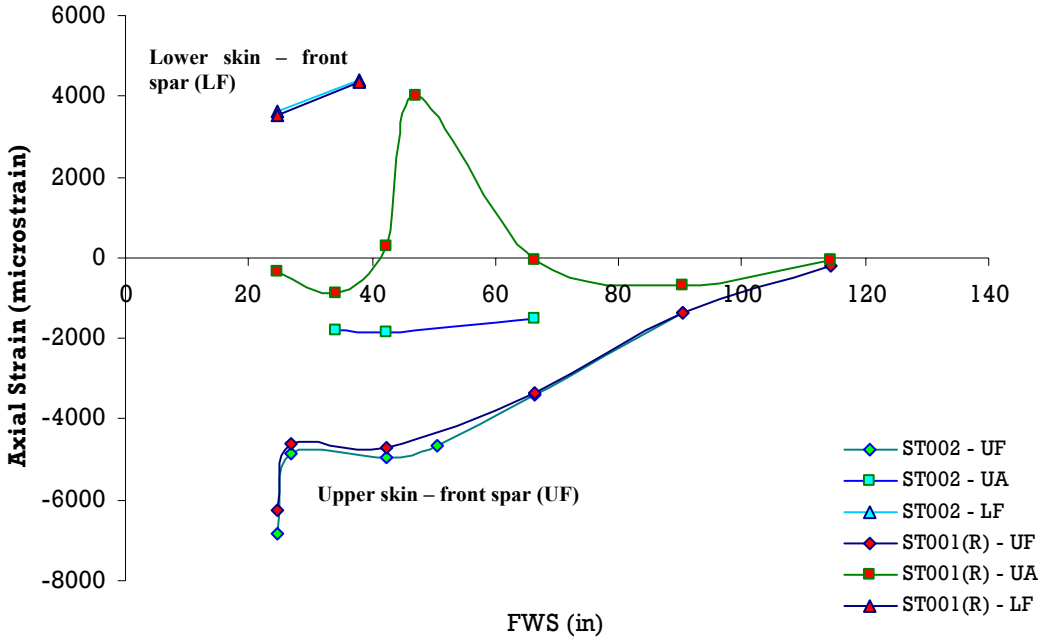

Figure 109. Axial strain comparison of ST001(R) and ST002 (172% NRLL).

8.4.1.2. ST005 – CAT3 Damage on Front Spar

Figure 110 shows the locations of strain gages for the ST005 static test article. Several additional gages were mounted adjacent to the damage to monitor damage propagation during quasi-static loading. During loading of the ST005 test article, strains in the aft spar increased gradually, as shown in Figure 111. Figure 111 also shows that inboard of FWS 40, the strain along the aft spar was reduced significantly, indicating that the loads were diverted to the steel lug at the end of front spar. At around 60 percent of NRLL, there was a gradual strain drop at FWS 66.5 on the rear spar, which is directly aft of the CAT3 damage, and then an increase in strain toward the failure. This was primarily due to skin buckling at this location, which may have later resulted in skin disbond. The rest of the rear spar indicated a linear response until failure.

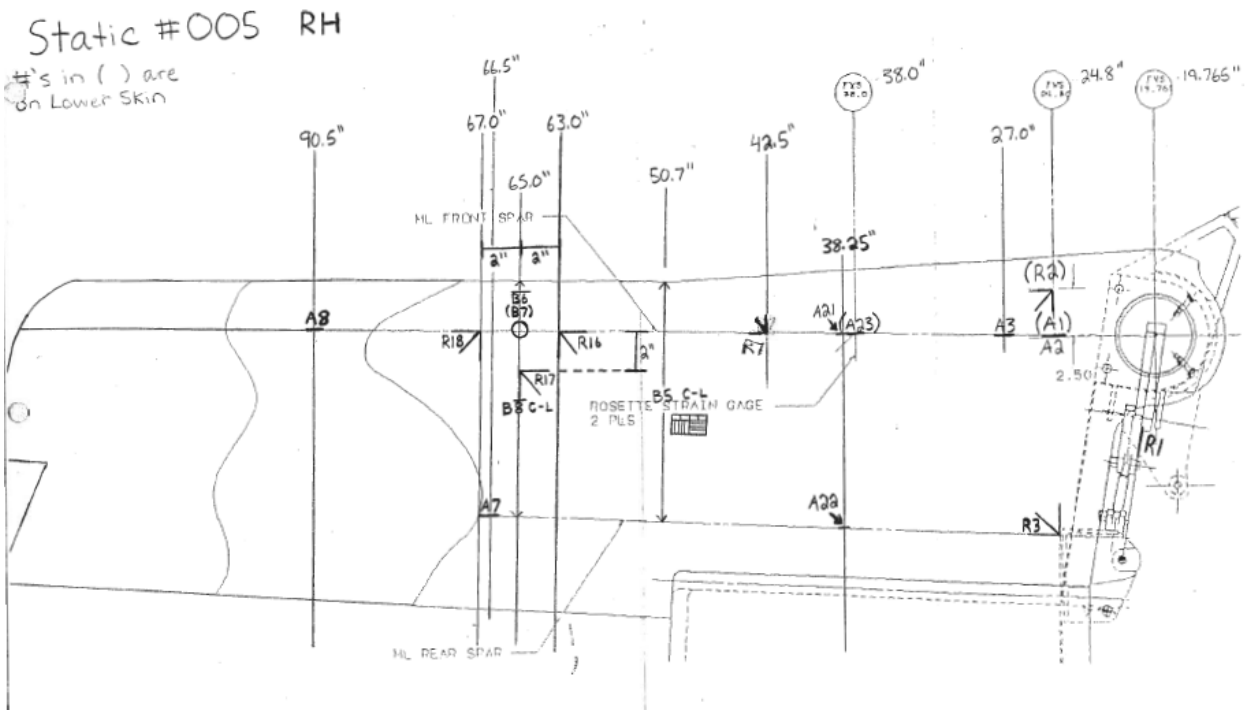

Figure 110. Strain gage locations for ST005 static test article.

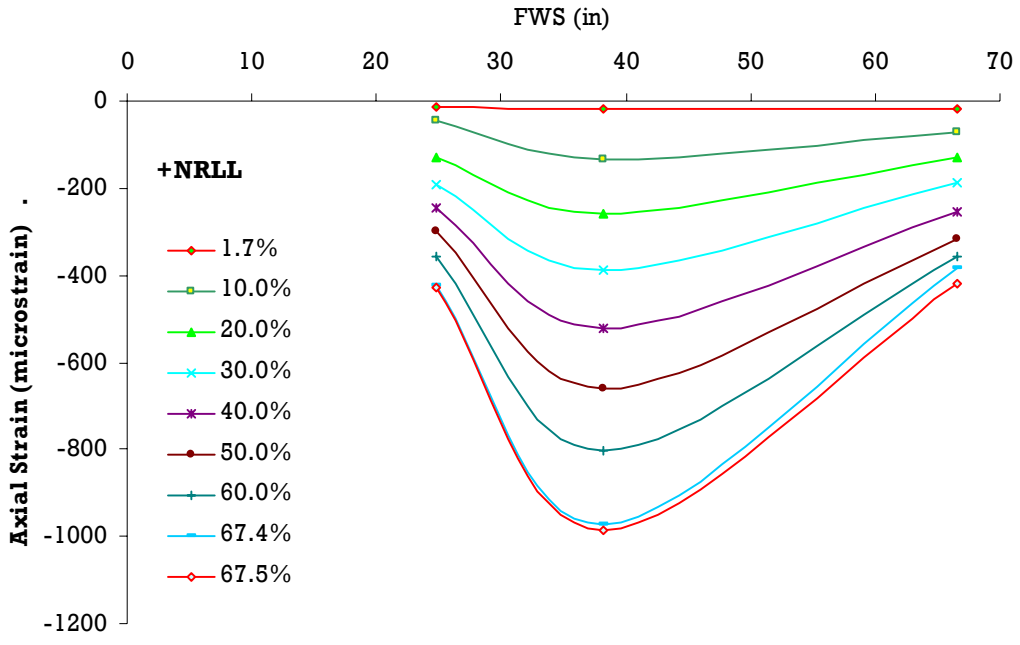

Figure 111. Strain evolution on upper skin of aft spar of ST005.

As expected, damage propagation was noted adjacent to CAT3 damage on the front spar just prior to failure, following a series of audible cracking noises (Figure 112). Unlike the case of ST001(R), this directly resulted in catastrophic failure of the structure. The rosette located two inches aft of the damage also indicated significant nonlinear strain anomalies after 60 percent NRLL, indicating skin buckling, as noted on the aft spar, and a possible load redistribution due to damage growth. A similar anomaly was noted from a gage located forward of the damage but around 65 percent of NRLL, indicating possible damage growth, as this area is relatively thick, and thus buckling was not the case. Both of these gages were located in an axis perpendicular to the direction of the compressive stress on the upper spar cap caused by the bending moment, the direction in which damage growth was expected to occur. All of these strain anomalies on the front spar were limited to the vicinity of the impact damage, as the rest of the gages had a linear response until failure.

Unlike for the case of CAT2 damage on the rear spar, CAT3 damage on the front spar had a significant impact on limit-load carrying capability and failure mode. Failure load (5,768 lbf) corresponded to 68 percent of NRLL, which was 94 percent of BDLL.

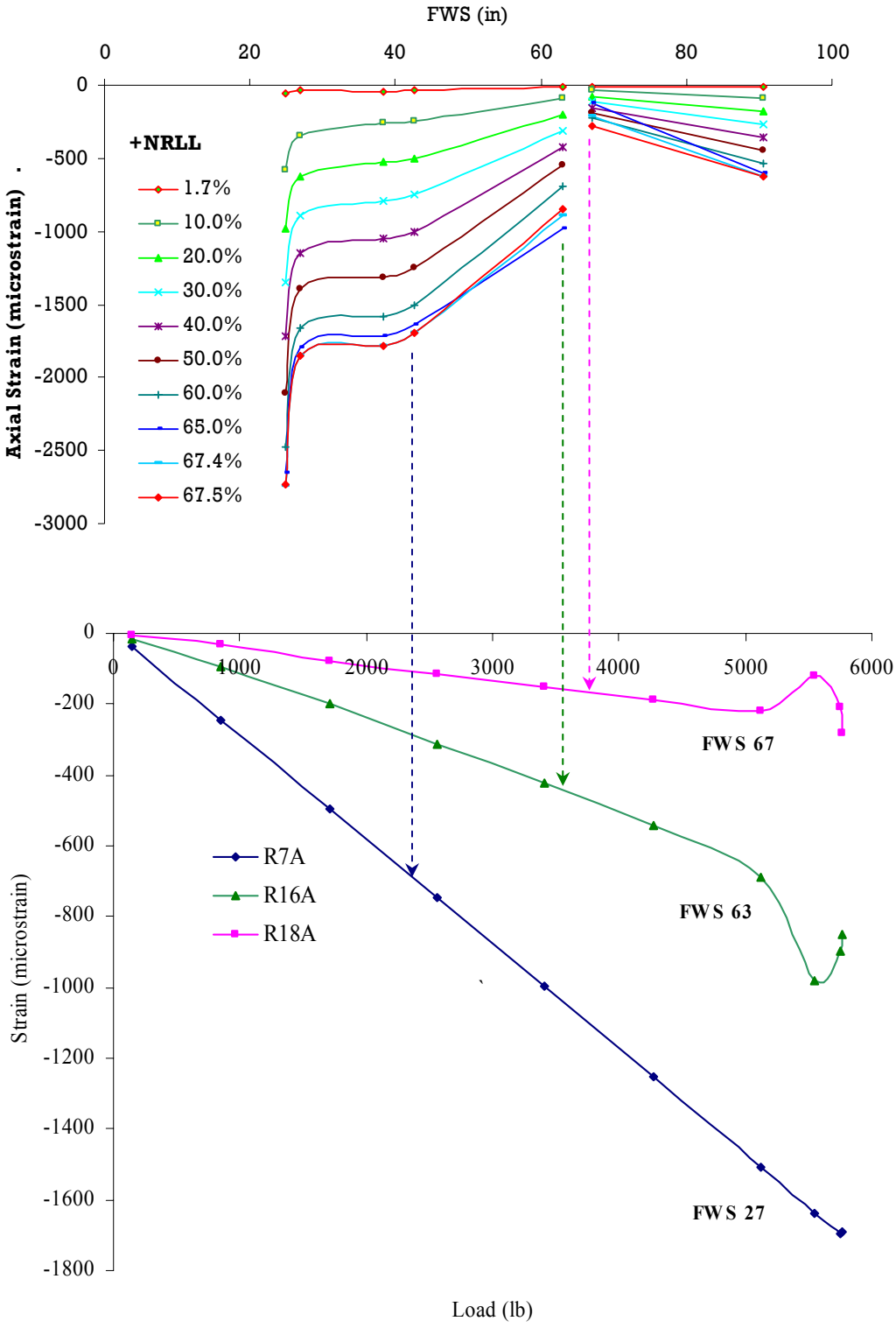

Figure 112. Axial strain along front spar top skin of ST005.

8.4.2. Spectrum Fatigue Loading

This section contains the DaDT test results for ST004 and ST006 articles with CAT2 and CAT3 damages, respectively. Additional strain and displacement data for both test articles are found in Appendix D. In addition to NDI techniques outlined in section 8.3, strain gage data, especially around the damage, were used as a health monitoring of the test article during cyclic loading. Strain data were accumulated from all channels at middle SLBs of A-M, B-M, and B-G. Since blocks C and D had the highest loads and only a limited number of cycles, strain data were acquired during each of their load cycles. Strain data were able to detect the onset of damage propagation as well as the load redistribution, thus indicating that they were more efficient than ultrasonic NDI and able to provide information in real time with minimal interruptions to the test progress. In order to isolate possible environmental effects, temperature-compensation gages were mounted throughout the durability test articles.

8.4.2.1. ST004 – CAT2 Damage on Aft Spar

Prior to cyclic testing, the ST004 DaDT test article was loaded to positive and negative limit loads, as shown in Table 44. A strain gage diagram showing the location of the main gages is shown in Figure 113. Axial strains from ST001(R) static and ST004 DaDT test articles along the top and bottom front spar caps as well as the upper skin along the aft spar are compared in Figure 114. Strain data on ST004 were somewhat higher than that of ST001(R). This can partially be attributed to the fact that ST001(R) is a right wing and ST004 is a left wing, thus requiring minor changes to the fixture assembly. Furthermore, load-former and load-patch whiffletree loading assemblies in static and durability testing, respectively, may have caused some of these discrepancies (Figure 115).

The ST004 fatigue test article was periodically monitored throughout fatigue testing. It was inspected in detail prior to cyclic loading and after each ¼ DLT of cyclic loading. Periodic inspections and strain anomalies around the defect were monitored to investigate damage containment and propagation. As can be seen in Figure 116, at the beginning of cyclic loading, there was a strain drop inboard of impact damage, possibly due to settling of the structure around the impact damage during initial cyclic loading. This also resulted in an increase in strain at FWS 24.8, possibly due to load redistribution. Furthermore, impact damage propagated outboard between 1.5 and 2.0 DLT (Figure 116) and then arrested, as shown in Figure 117.

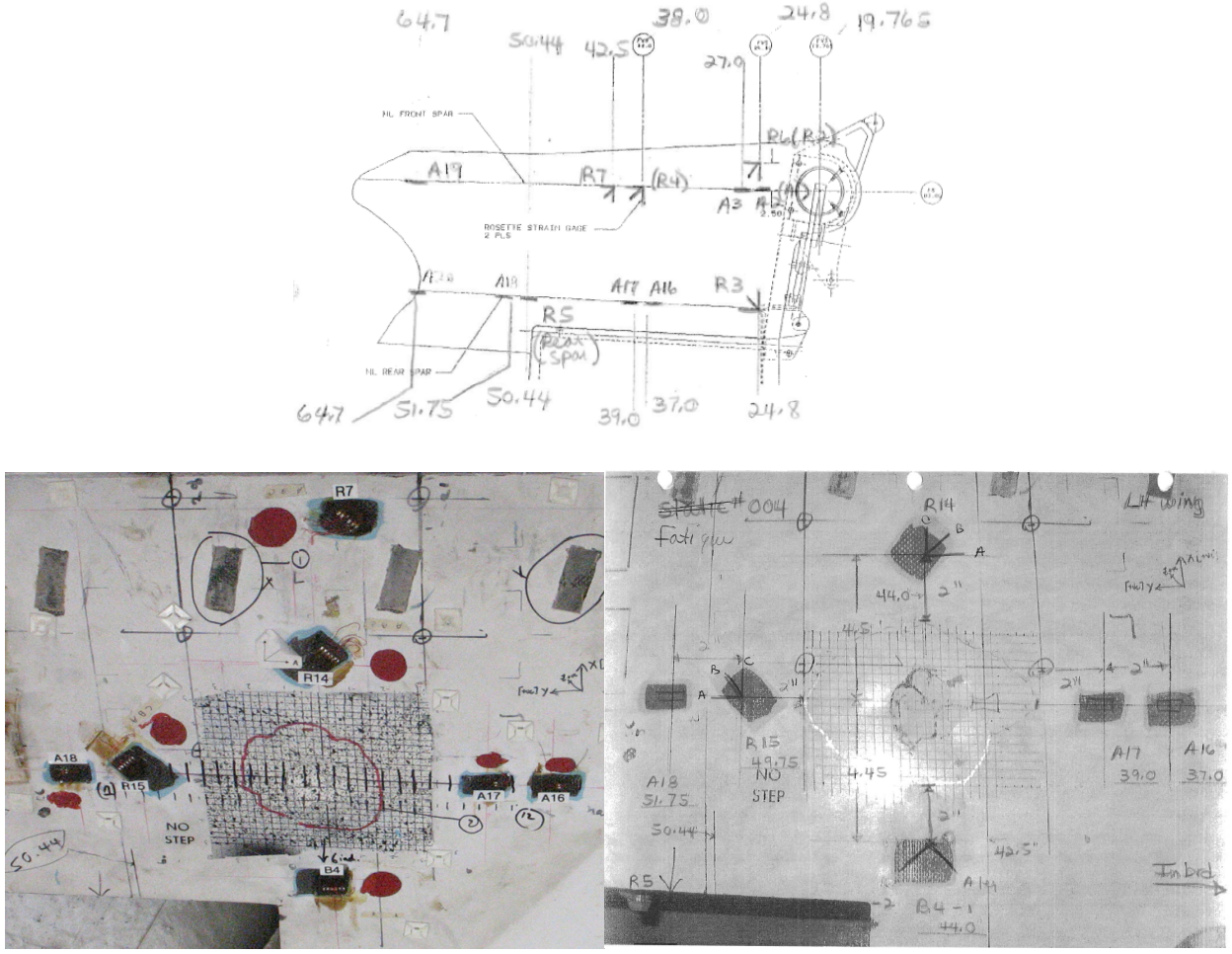

Figure 113. Strain gage location for ST004 DaDT test article.

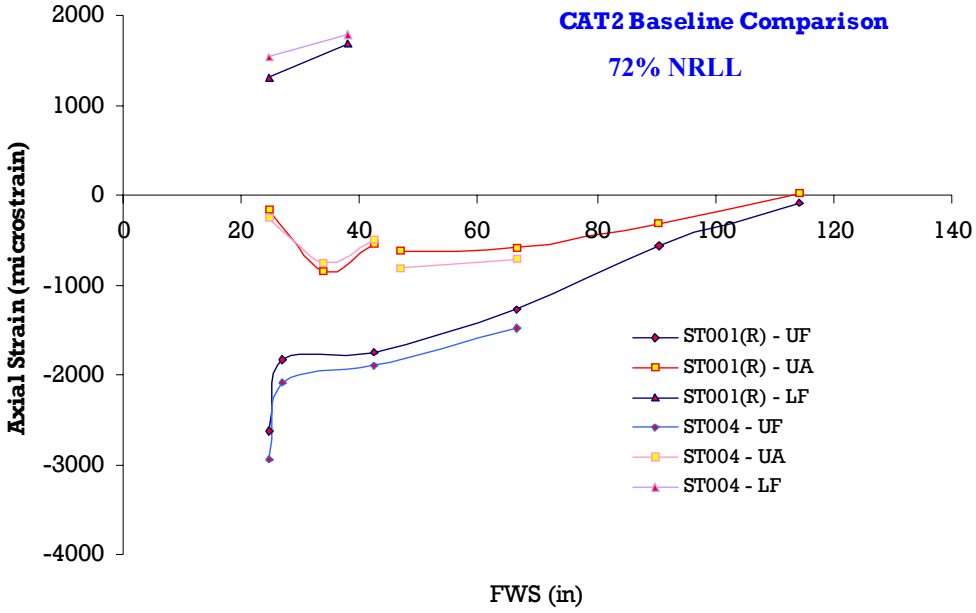

Figure 114. Axial strain comparison of ST001(R) and ST004 prior to cyclic loading.

(a) Load formers - static (b) Load patches - fatigue

Figure 115. Full-scale test setup for quasi-static and fatigue loading.

During the residual strength test of ST004 after 2-DLT, a loud cracking noise was heard around 155 percent of NRLL, and strain anomalies around the damage were noted. Figure 117 shows that the impact damage rapidly propagated outboard along the aft spar between 155 and 165 percent of NRLL and gradually propagated thereafter. Far-field strain gages along the aft

spar did not increase beyond 160 percent of NRLL, indicating that the load did not redistribute around the damaged area. Thus the aft spar reached its maximum structural capacity. All strain and global displacement data show several spikes and significant strain anomalies after 155 percent of NRLL, indicating structural failure.

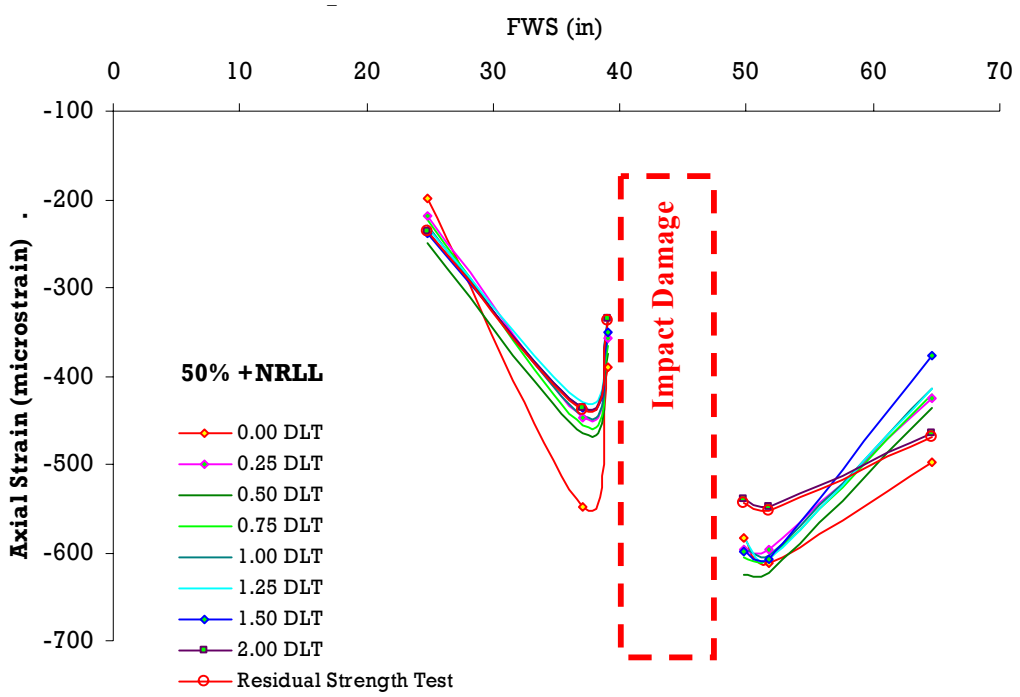

Figure 116. Damage progression along aft spar top skin of ST004 during DaDT test.

Furthermore, strain data during the residual strength test of ST004 after 2-DLT are compared with ST001(R) static test data at 50, 100, and 150 percent of NRLL in Figure 118. Data show that the structural stiffness of ST004 decayed after 50 percent of NRLL, as compared to the data obtained from the ST001(R) test, i.e., strains on ST004 were lower than that of ST001(R) after 50 percent of NRLL. This was confirmed by the strain and global displacement data that indicated a nonlinear response around 50 percent of NRLL. Moreover, an audible noise, i.e., a loud pop, was noted around 40 percent of NRLL, and that may have caused an internal failure, resulting in a nonlinear strain/displacement response.

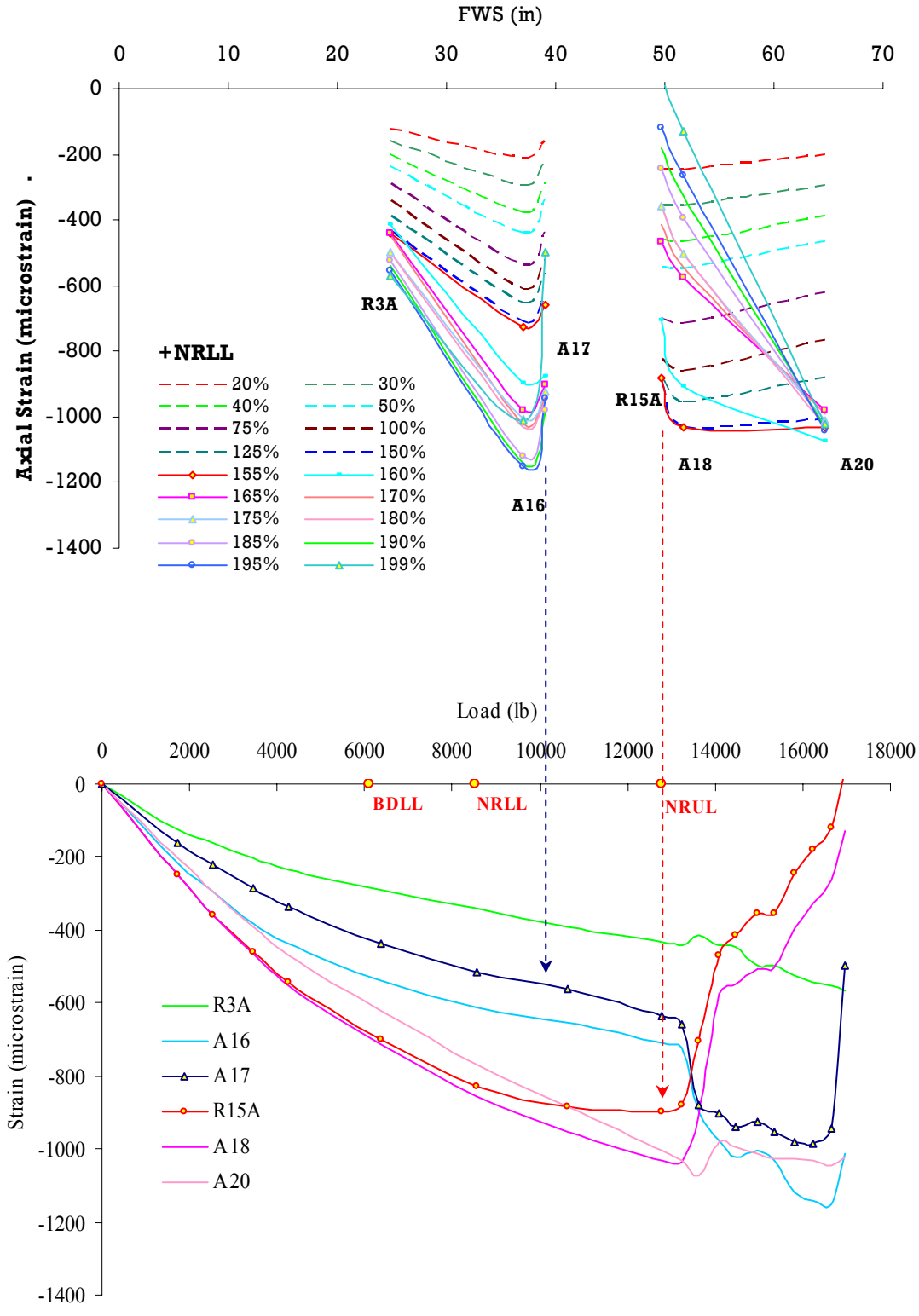

Figure 117. Damage progression along aft spar (top skin) of ST004 during residual strength test after 2-DLT cyclic test

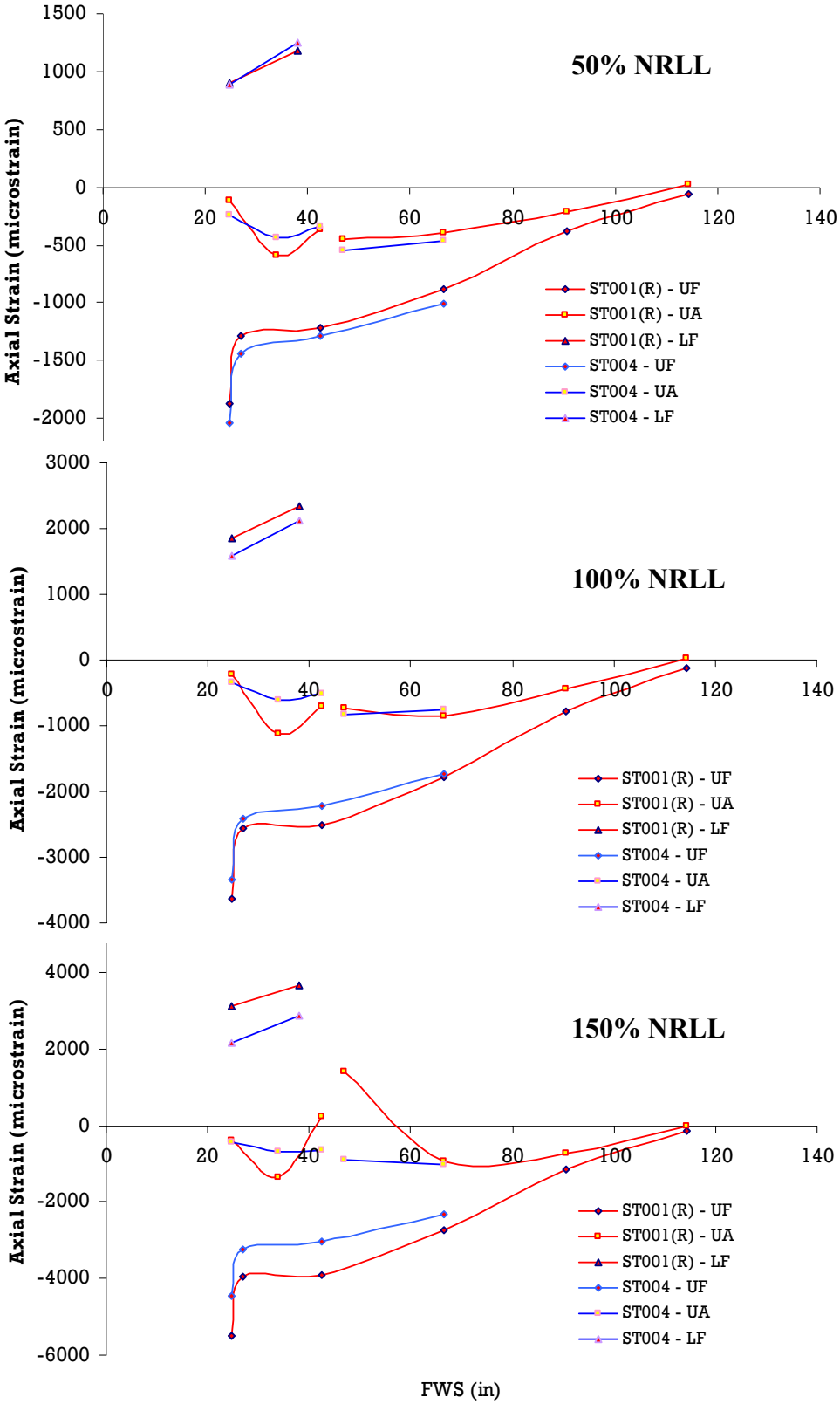

Figure 118. Comparison of axial strain evolution along forward and aft spar of ST001(R) and ST004 during residual strength test after 2-DLT cyclic test.

8.4.2.2. ST006 – CAT3 Damage on Front Spar

For ST006 fatigue testing, a conversion factor of CF=1.4 would result in some spectrum loads that were higher than the load corresponding to the static residual strength of NRLL (5768 lbf) with a similar damage, especially in blocks C and D. Blocks C and D were inserted in the spectrum after 0.25 and 0.50 DLT, respectively. Since the first inspection was scheduled prior to 0.25 DLT, the damage would be located and repaired in-service, assuming that the structure survived. The majority of loads, except three center load segments (Figure 79), in blocks B-M were below 5768 lbf. All spectrum loads in blocks A-M and B-G were below 68 percent NRLL. In order to ensure that the fatigue loads were below the static failure load of ST005, neither the CF nor the LEF was applied to the load spectrum. This simulated a composite primary structure that had a CAT3 damage in the primary load path undergoing typical service loads. The load sequence was the same as shown in Table 44, except the periodic limit load checks were limited to 50 percent of BDLL, and the residual strength test was conducted after block D, just after half of DLT. The inspection intervals were allotted as shown in Table 47 to closely monitor any damage propagation and to validate the benchmark predictions in section 7.3.3.

Figure 119 shows the strain gage location for the ST006 DaDT test article. Periodic health monitoring results using strain gages on the front spar are shown in Figure 120. This figure only shows data from the main inspection intervals for clarity, excluding the data acquired periodically during fatigue loading. During the first set of B-G/B-M blocks, the axial gage immediately outboard of the damage decreased, while the rest of the strains in the front spar increased. This indicated that there was a damage propagation outboard of the defects with a global influence, unlike in the case of CAT2 damage on the aft spar, since the front spar is the primary load path.

TABLE 47

LOAD SEQUENCE FOR ST006 DADT TEST AND INSPECTION INTERVALS

Sequence	Loading Block	Repetitions	n-Block	Σn	Flight Hours	Life Times	Scheduled Inspections
a	Start						**X**
b	Ramp to **k*BDLL+**	1					
c	Ramp to: **Zero**	1					
d	Ramp to: **k*BDLL-**	1					
e	Ramp to: **Zero**	1					
f	Ramp for fatigue **(k=50%)**	1					
1	Block A-M	10	718	7180			X
2	Block A-M	15	718	17950			X
3	Block B-G	1	146	18096			
4	Block B-M	1	264	18360			
5	Repeat 3 and 4	4	410	20000			X
6	Repeat 3 and 4	5	410	22050			X
7	Block A-M	10	718	29230			X
8	Block A-M	15	718	40000	**4999**	**0.250**	**X**
9	Ramp to: **Zero**	1					
10	Repeat a through f	1					
11	Block C	1	16	40016			**X**
12	Block A-M	10	718	47196			X
13	Block A-M	15	718	57966			X
14	Repeat 2 and 3	5	410	60016			X
15	Repeat 3 and 4	5	410	62066			X
16	Block A-M	10	718	69246			
17	Block A-M	15	718	80016	**10000**	**0.500**	**X**
18	Ramp to: **Zero**	1					
19	Repeat a through f	1					
20	Block D	1	17	80033	10002	0.500	**X**
21	Ramp to: **Zero**	1					
22	Residual strength test	1					

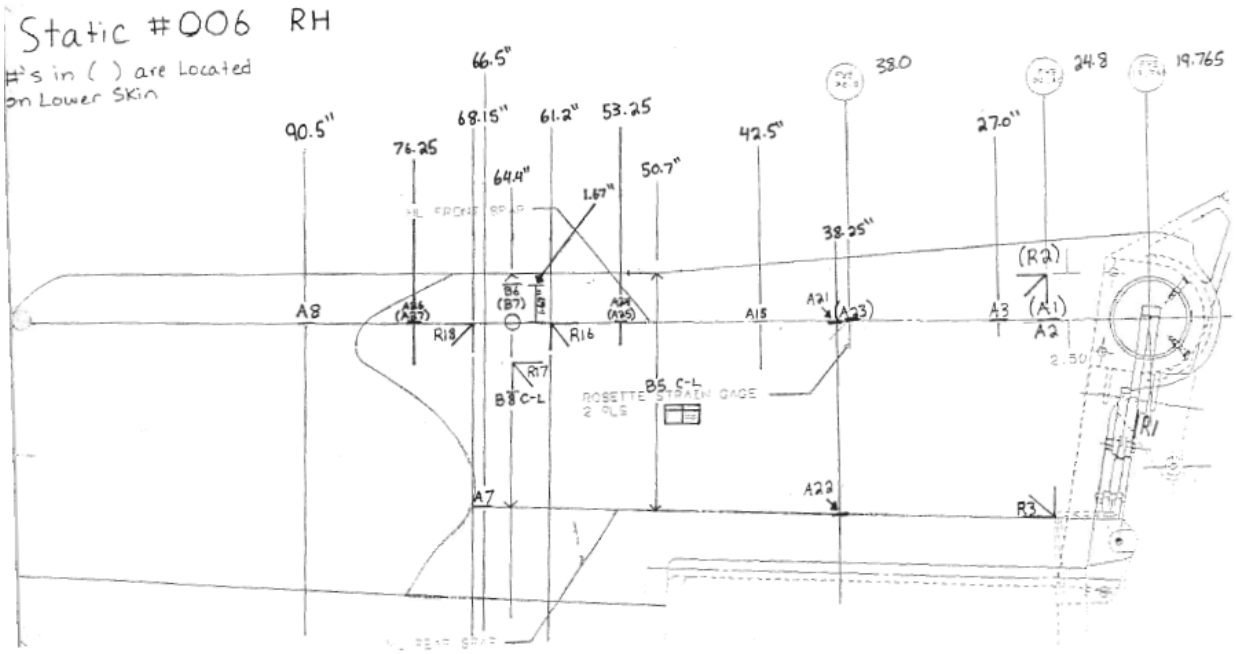

Figure 119. Strain gage locations for ST006 DaDT test article.

In addition to the gages on the front spar, both gages that were front and aft of the damage, B6-1 and R17A, respectively, indicated that the stress field around the damage increased during the first set of B-G/B-M blocks, possibly due to minor damage propagation. This set of load blocks was not as severe as the ones in blocks C and D, but they had significantly higher repetitions (4,100 cycles) than that for the case of latter load blocks. Thus, the damage progressed gradually, as shown in Figure 120, during the first and second set of B-G/B-M blocks, resulting in minor matrix fracture that consequently caused localized material degradation (compliance change), which was not severe enough to be detected by ultrasonic inspection equipments. To the contrary, blocks C and D had only 16 and 17 cycles, respectively, but significantly higher loads than was the case for B-G/B-M loads, which caused about the same amount of strain increment. Furthermore, ultrasonic equipment was able to detect damage growth, and visual inspections confirmed damage to other parts of the structure as well (section 8.5.2).

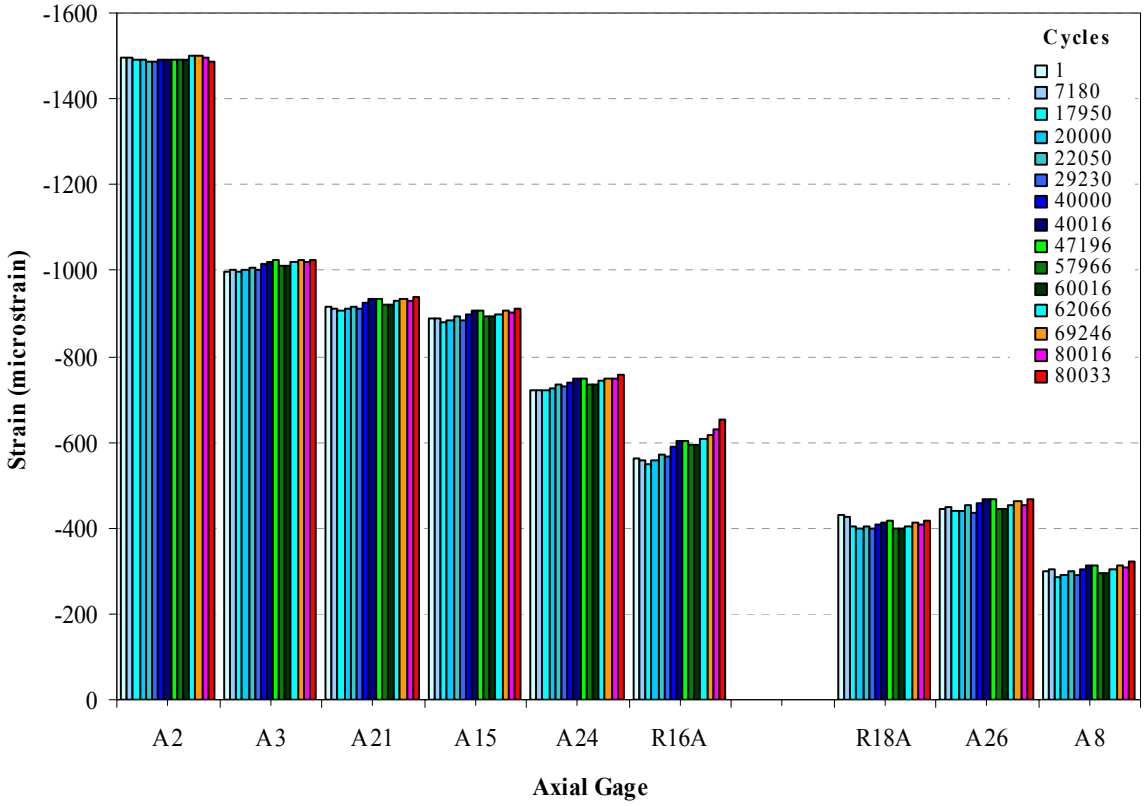

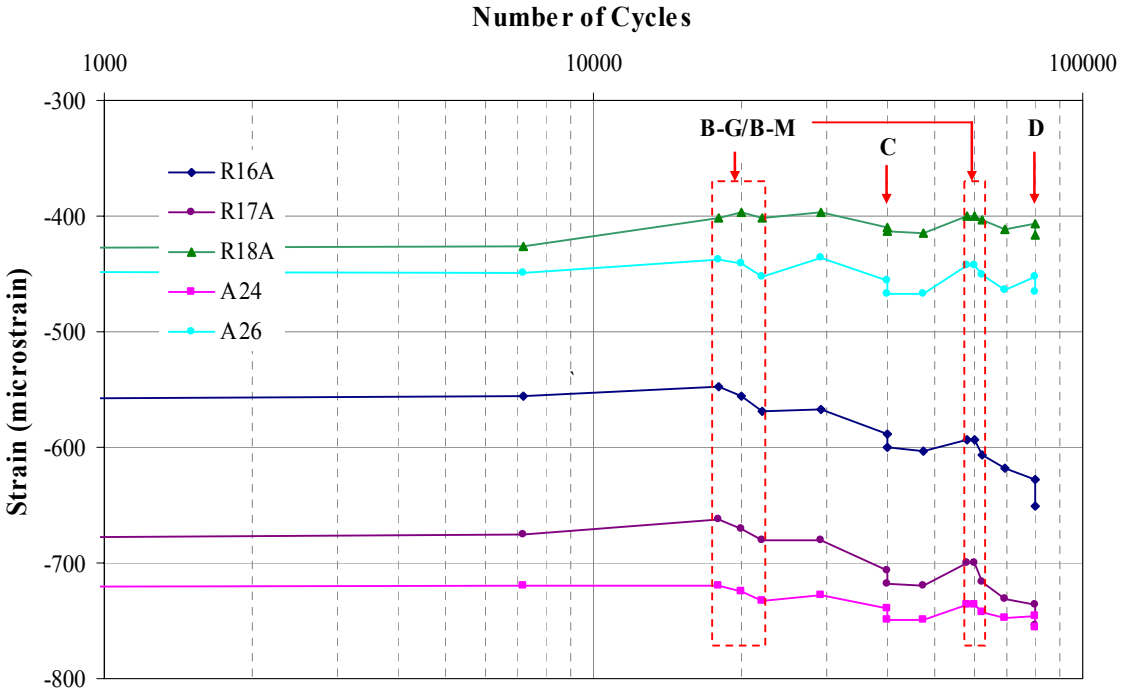

Figure 120. Strain evolution on front spar of ST006 DaDT test article.

Damage growth during B-G/B-M, C, and D is depicted in terms of probability of structural failure due to damage progression in Figure 80. Although this is not a one-to-one correlation for the damage propagation or its size, in a linear scale (Figure 121), the CFU model shows the gradual progression of local damage, such as possible matrix cracks observed during B-G/B-M blocks of fatigue testing of ST006 as well as the global impact of high loads such as blocks C and D on the structure.

After cycling through block D, ST006 was tested quasi-statically to evaluate the residual strength. Figure 122 shows a comparison of axial strain along front and aft spars of ST005 and ST006 (before and after fatigue loading). Except for the strain adjacent to the damage, the front spar indicated a similar strain distribution for all three cases, while ST005 static test strains on the aft spar were somewhat higher than that of ST006. The discrepancy of strain data around the damage can largely be attributed to the difficulties associated with achieving CAT3 damage on a thick part such as the spar cap, as illustrated in Figure 84, and minor changes to damage parameters can significantly change the state of damage in such an article. The residual strength test failed at 95.5 percent NRLL, soon after a fracture through the CAT3 damage, as was observed during static testing of the ST005 article. Examination of strain evolution on the front and aft spars (Figure 123) shows that the CAT3 damage further propagated outboard, between 80 and 85 percent of NRLL, which was significant enough to affect the aft spar at the same FWS. Strain gage A7, which was located on aft spar at FWS 66.5, indicated a sudden drop at 7,039 lbf, and a loud cracking noise was heard from the back side closer to this gage, possibly due to the top skin disbonding from the aft spar or skin delamination. At this point, several gages around the CAT3 damage also indicated sudden changes, possibly due to stress relief and damage

propagation. Although strains inboard of CAT3 damage did not indicate sudden changes, the R16 gage indicated possible local skin buckling in a 45° direction with respect to the front spar.

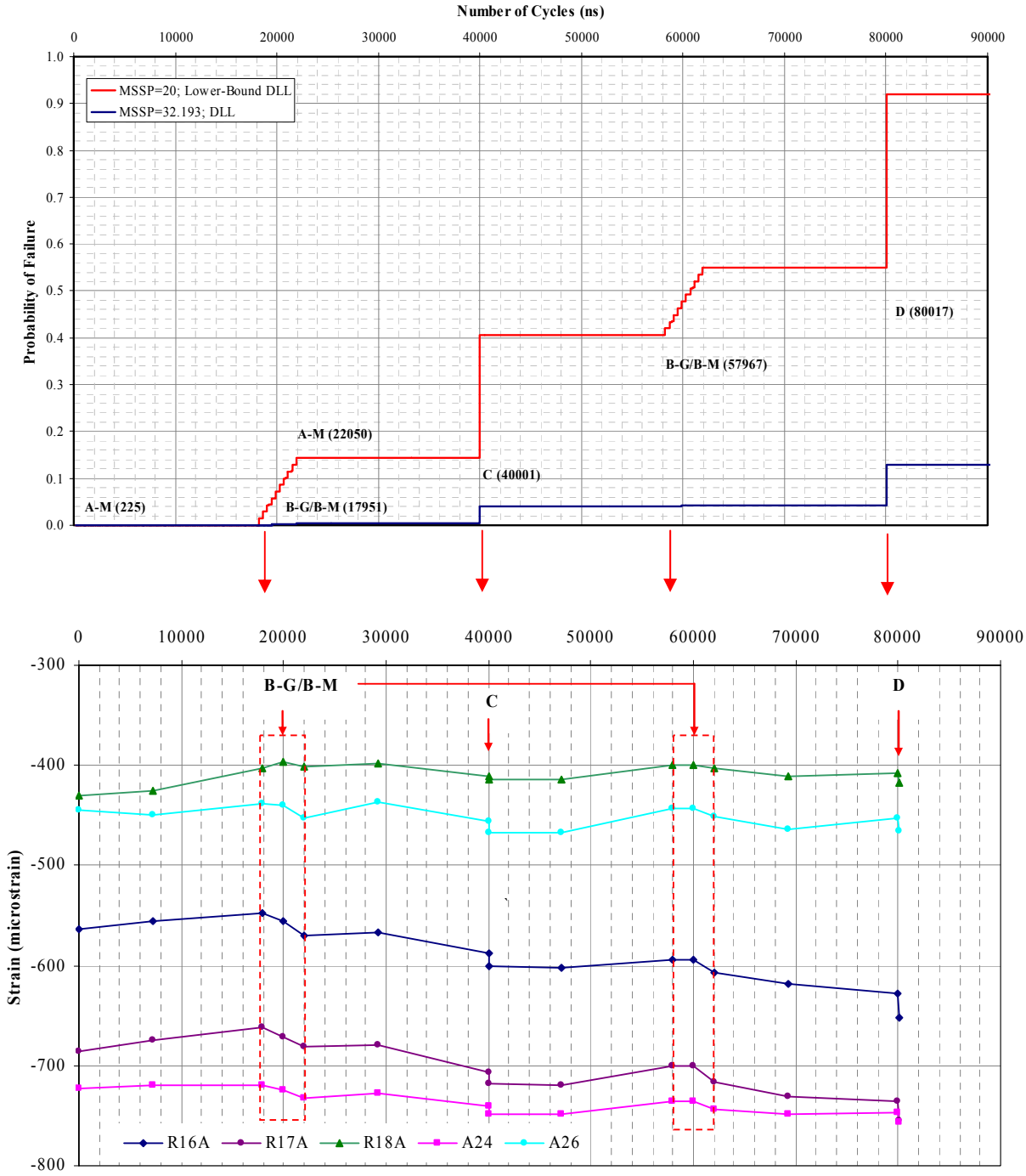

Figure 121. Cumulative probability of failure for Starship forward wing and strain data for ST006 DaDT test article.

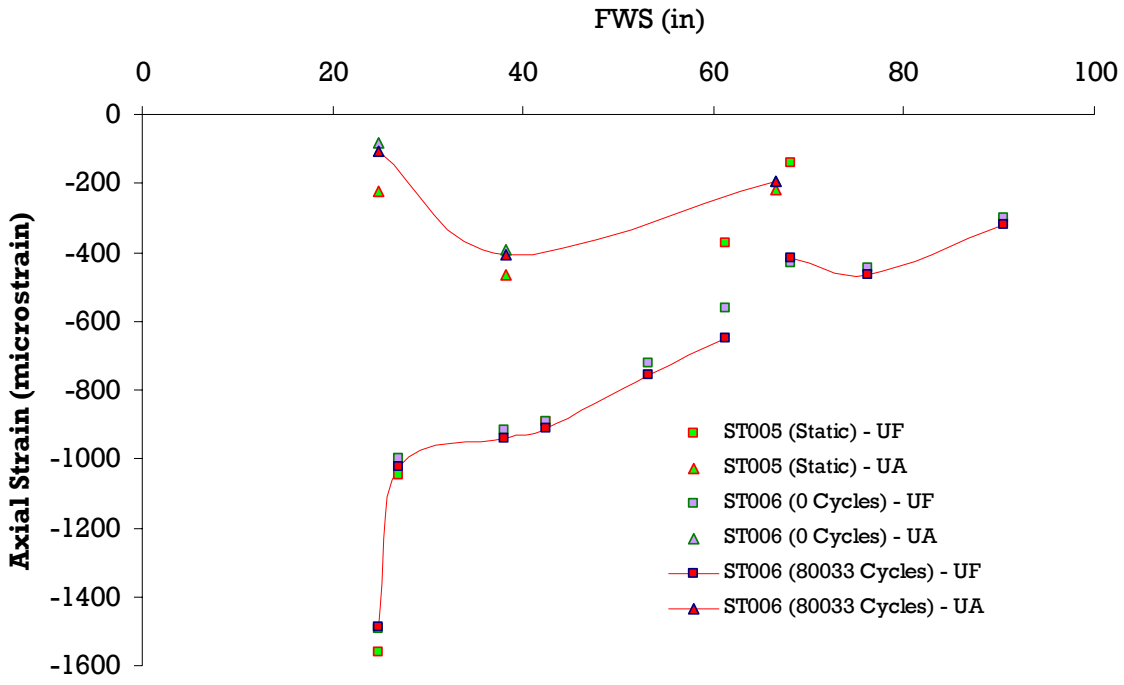

Figure 122. Comparison of axial strains along front and aft spars (36% NRLL).

Once the residual strength test was completed, the CFU model was reanalyzed by modifying the post-impact residual strength (prior to fatigue cycling) so that the linear loss of residual strength at the end of fatigue was equal to the failure load (post-DaDT residual strength). The probability of failure during post-DaDT quasi-static loading for different load levels is shown in Figure 124. As can be seen in this figure, the probability of failure between 80 and 85 percent NRLL, the load level in which the loud cracking noise and strain anomalies were observed during the ST006 post-DaDT residual strength test, increases dramatically. Based on an MSSP of 20 and a post-impact residual strength equal to the lower bound limit load, the probability of failure at 82.5 percent of NRLL (corresponding to 7039 lbf) was approximately 24 percent. It was decreased to 4.2 percent for an MSSP of 32.193.

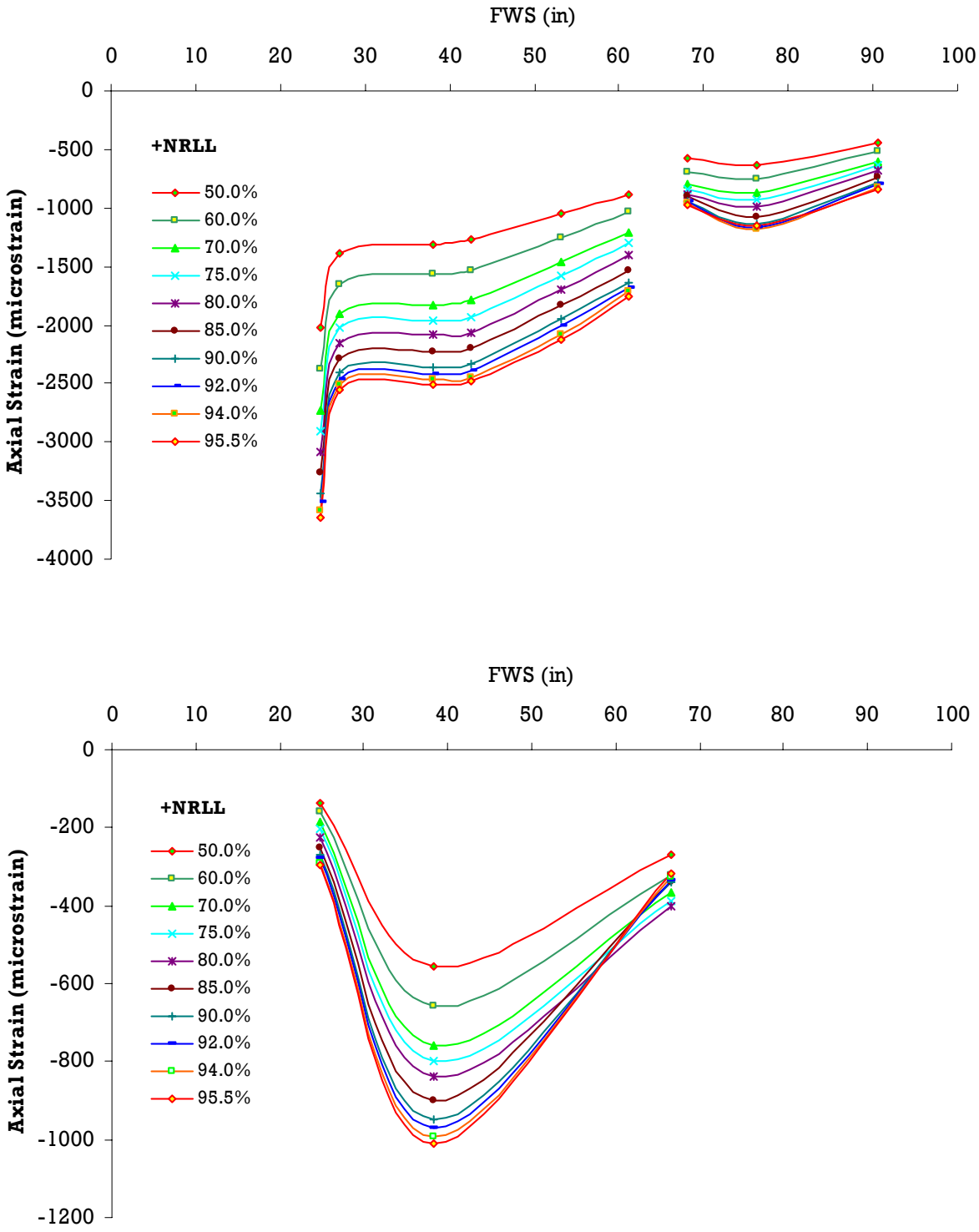

Figure 123. Stain evolution on front and aft spars during residual strength test after 80033 cycles.

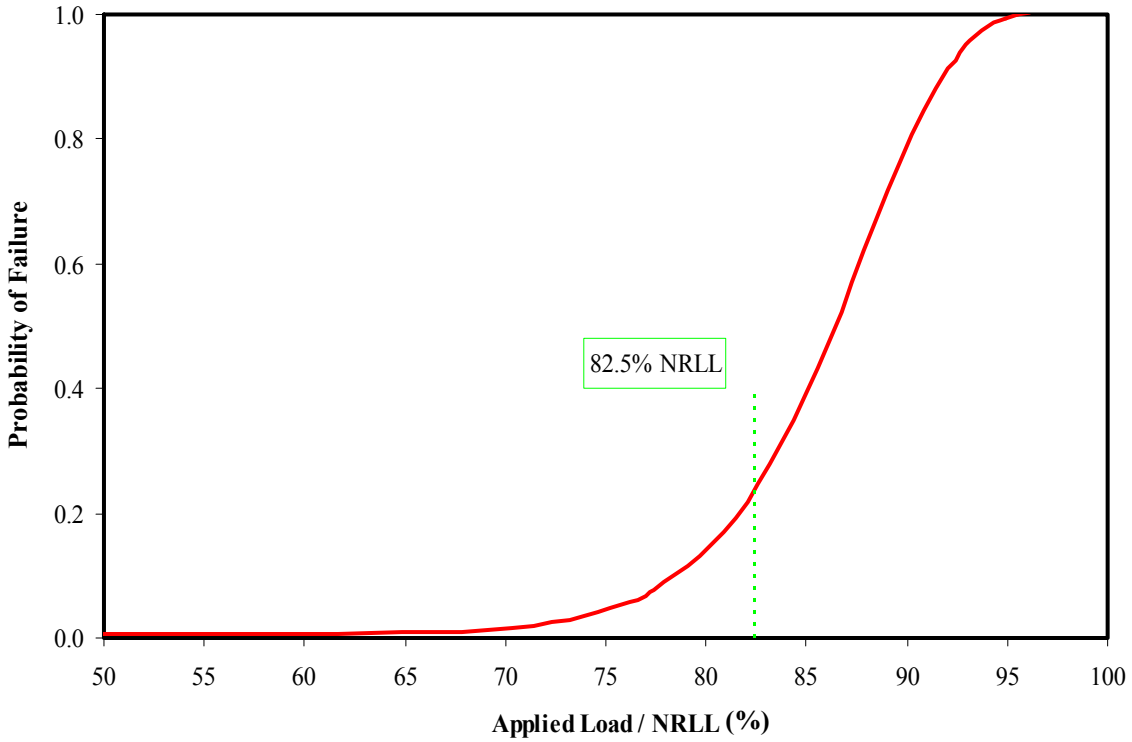

Figure 124. Probability of failure for corrected residual strength after block D (80033 cycles).

Although use of the lower-bound limit load for residual strength of a CAT3 damaged article resulted in an overly conservative fatigue life, it accentuated the loads that may cause damage instigation in terms of small matrix cracks that can coalesce to form larger cracks or trigger the onset of propagation of an existing damage. Thus, this criterion can be used to determine the inspection intervals necessary to detect damage prior to imminent failure. This approach can be used as a starting point, and then, based on the probability of occurrence of such a high-energy impact scenario and the probability of detectability following such an impact scenario, it can be tailored to a particular structure to address economic concerns.

8.5. Scheduled Inspections of DaDT Test Articles

In addition to the strain surveys discussed in section 8.4.2, periodic NDI and visual inspections were carried out for DaDT test articles. In addition to the damage surroundings, visual inspection on critical areas and heavily loaded areas such as root lug, test fixture attachments, and some of the leading edge load patches were periodically inspected to prevent unexpected failure of these test articles so that corrective action, if necessary, could be taken immediately.

8.5.1. ST004 – CAT2 Damage

Around 0.25 DLT, one of the fasteners at FWS 43 that attaches the leading edge to the top spar cap (flange) indicated pull-though failure and resulted in local skin buckling, as shown in Figure 125(a). Since the focus of this test was on the composite structure, the test was resumed. By 1.5 DLT, this fastener had completely failed through the leading edge. Shortly after completing 1.5 DLT, fatigue testing of article ST004 was halted, and the article was removed from the test fixture to investigate significant displacements observed around the fixed end of the test article. Although there was no significant propagation of the impact damage inflicted on the aft spar at FWS 45, several fasteners along the leading edge indicated pull-through failure (Figure 125). Initially, this was observed only around FWS 43 during up-bending, and later, several fasteners outboard and inboard of FWS 43 indicated fastener pull-through failures and severe leading-edge buckling around these locations.

In addition to leading-edge fastener failures, a fracture was observed on the bottom skin overhang adjacent to the sleeve of the steel lug at the fixed-end (Figure 126). Significant relative (rotational) displacements between the composite structure and the steel lug were observed during fatigue loading, thus indicating internal damage to the structure. The test article was

removed from the fixture and inspected for possible fracture on the steel tube or on the composite structure. Once the lug was removed from the ST004 fatigue article, several fractures and hole damages were noted, as shown in Figure 126. Top and bottom flanges of the root rib were disbonded from the skin closer to the lug area. Further inspection revealed that the backside of the root rib was still attached to the skin. Thus, no repairs were performed. Also, the fastener holes located at the web to attach the main lug, skin, and surface fractures were noted, but they were not repaired. Furthermore, the leading-edge fastener-pullout failed sections were left unrepaired. A fastener hole adjacent to the sleeve was damaged during lug removal and repaired using EA9394 paste adhesive and chopped fibers (Figure 127).

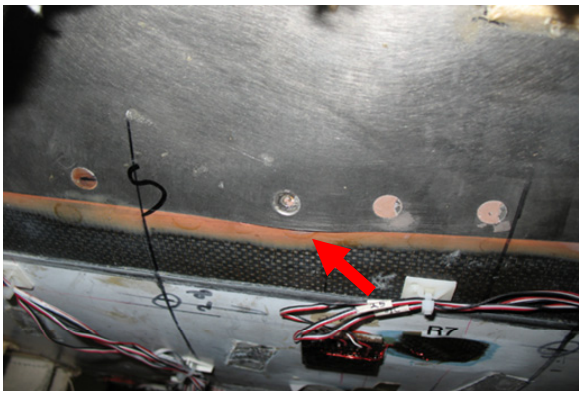

(a) 0.50 Life

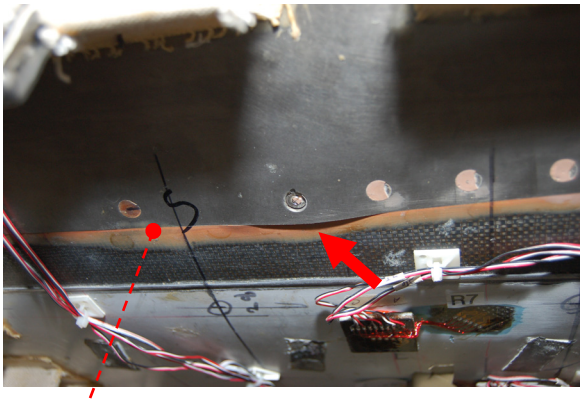

(b) 1.50 Life

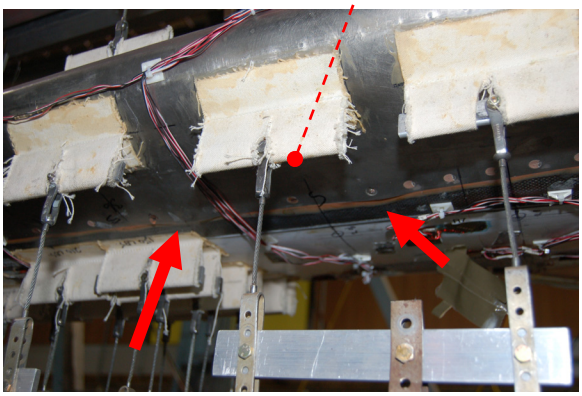

(c) 1.50 Life

Figure 125. Leading edge fastener-pullout failure (top surface).

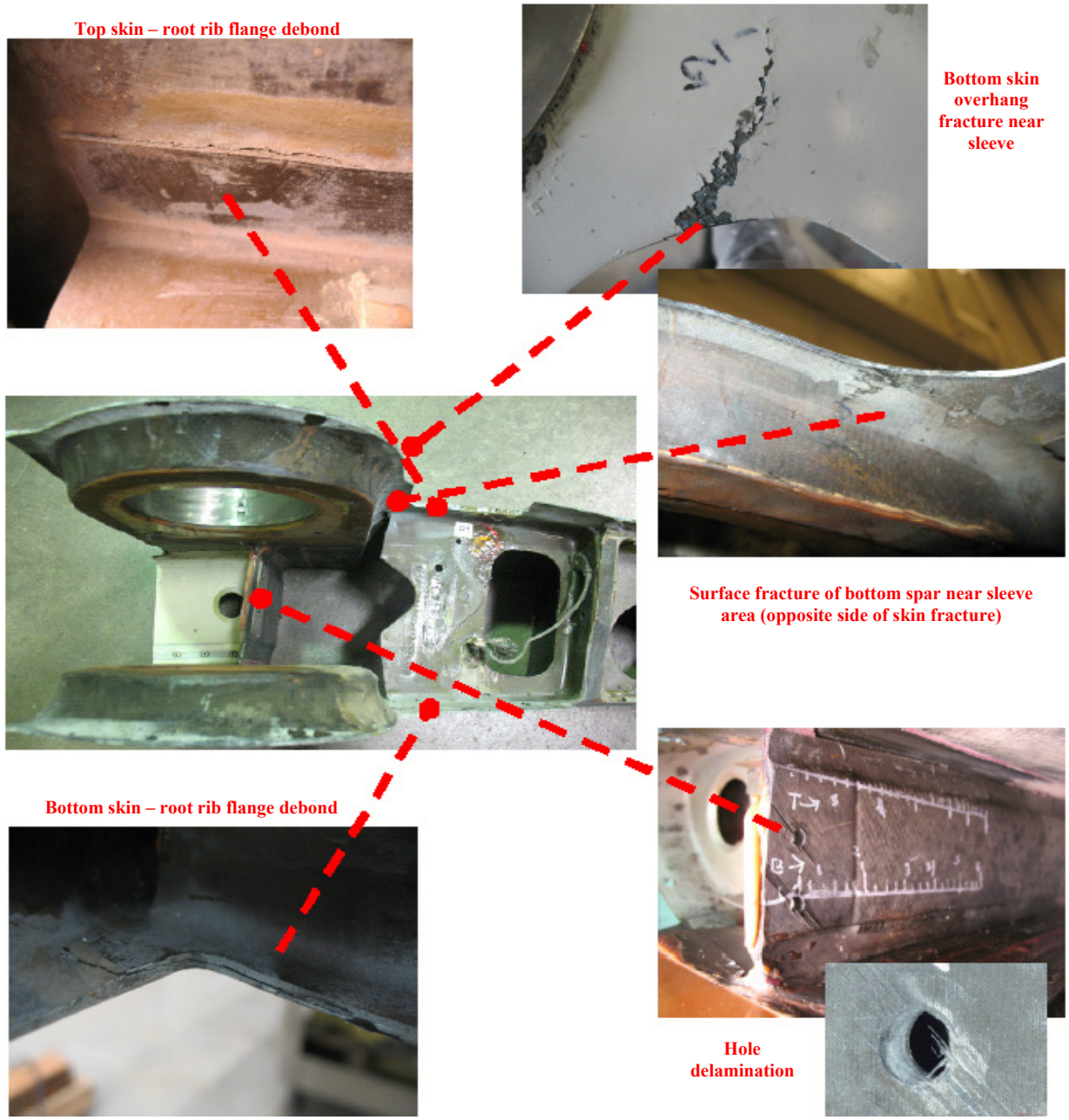

Figure 126. Damages noted on ST004 fatigue article after 1.5 DLT.

The lug area and the web closer to the lug were further inspected using ultrasound and DTH, which found no evidence of failure or delaminations other than the damages shown in Figure 126. Therefore, the test article was mounted back in the test fixture, and cyclic loading

was continued until 2 DLTs. Positive and negative limit-load tests revealed no evidence of compliance change or significant strain anomalies.

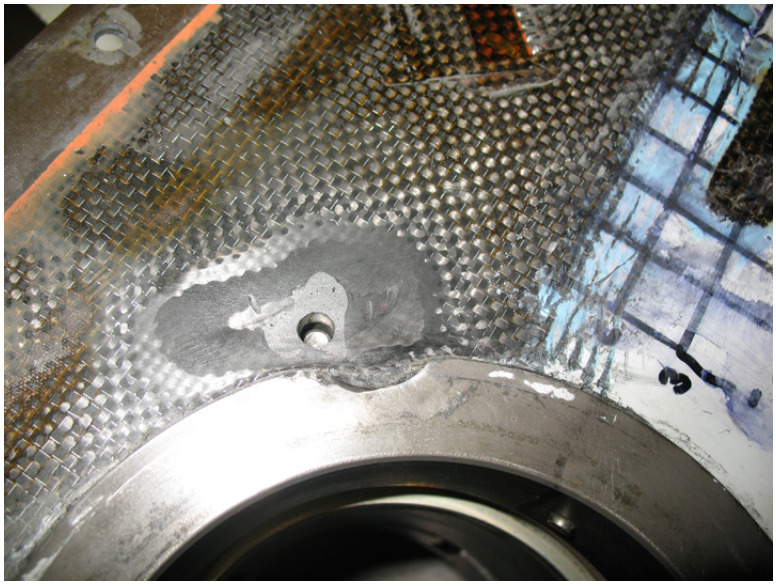

Figure 127. Hole repair after 1.5 DLT inspections.

An inspection of ST004 following 2 DLTs of cyclic loading noted a leading-edge fastener-pullout failure on the bottom skin that spread from FWS 64 to 85 (Figure 128). In this area, no damage to the composite structure was found. Furthermore, the bottom skin fracture near the sleeve grew approximately five more inches between 1.5 and 2 DLTs of cyclic loading.

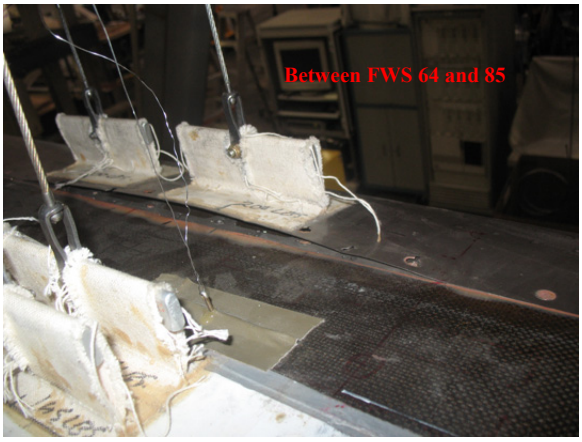

Figure 128. Leading-edge fastener pullout failure (bottom surface) after 2.0 DLT.

In order to minimize risks of damaging strain gages around the damage, DTH readings were taken only on the colored areas in Figure 129. DTH inspections revealed that the initial damage grew along the red areas. Blue sections indicate minor stiffness degradation, possibly due to fracture or microcracks. Green sections indicate no growth. Figure 129 also indicates that the damage area continued to grow until 2 DLTs. A standard tap test or ultrasonic inspections was unable to detect these anomalies.

8.5.2. ST006 – CAT3 Damage

Since the CAT3 damage on the primary load path of ST006 was expected to grow before 0.25 DLT, as depicted in Figure 80, and the fatigue loads were closer to the failure load of ST005 that was impacted with a similar damage, the inspection intervals were shortened and fatigue testing was conducted by closely monitoring the strain gages and conducting frequent visual and NDI inspections. Although the strain anomalies were detected during B-G/B-M load blocks (section 8.4.2.2) and creaking/popping sounds increased, neither visual nor ultrasonic inspections detected any changes to the damage boundary delineated prior to the test.

Inspections following block C indicated that the leading edge at the root separated from the bottom skin (Figure 130). Also, the squeezed-out adhesive at the attachment doubler located at the root end of the aft spar disbonded from the close-out rib. Strain anomalies around this region (gage R3) also confirmed a sudden strain drop after block C, thus confirming a local failure and/or load redistribution. Furthermore, ultrasonic NDI results indicated possible damage progression along FWS across the CAT3 damage (Figure 131). Red and black markings indicate the damage boundary prior to fatiguing and after load block C, respectively. This confirms the explanation given in section 8.4.2.2 for strain anomalies around CAT3 damage.

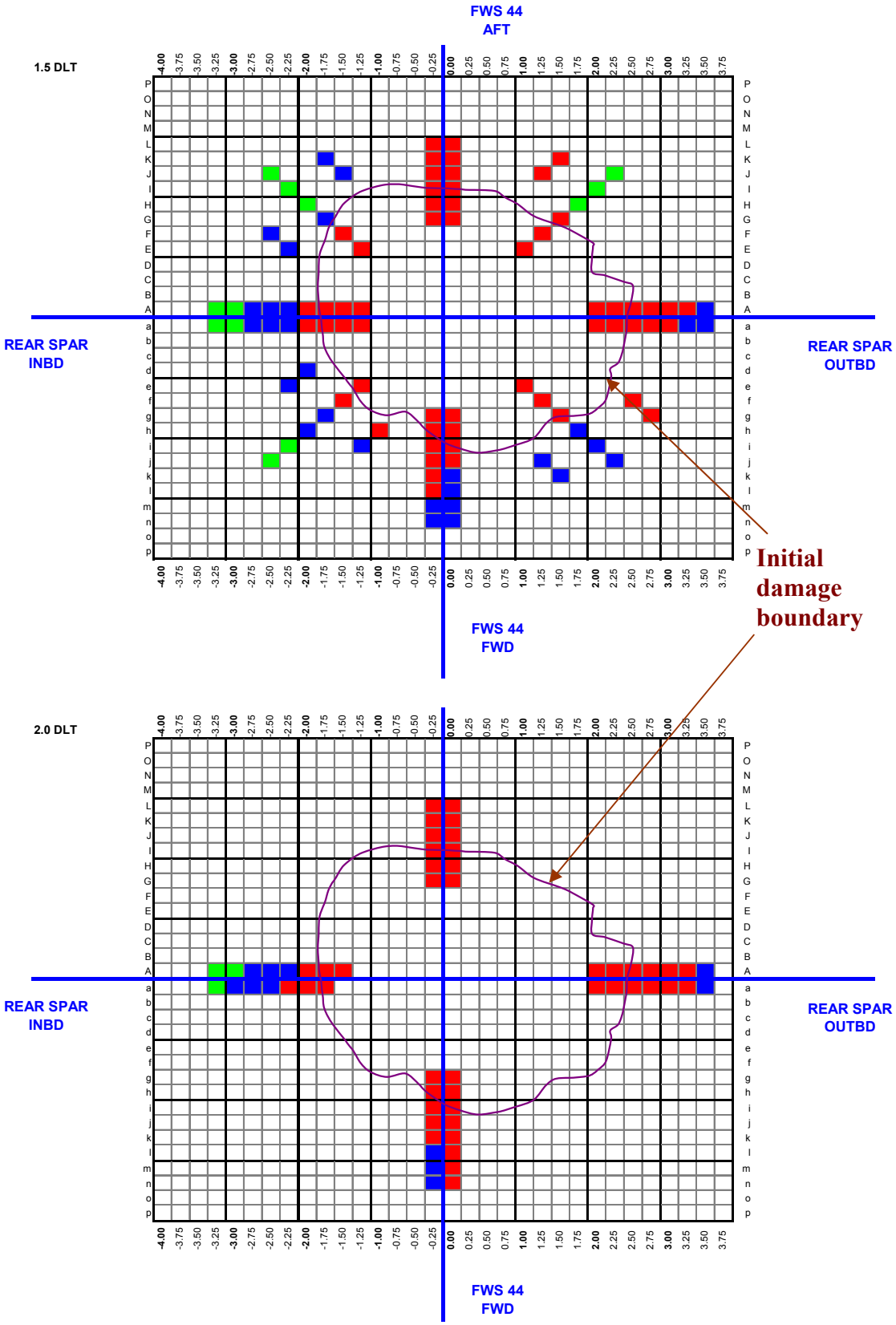

Figure 129. Damage propagation of ST004 DaDT article – digital tap hammer.

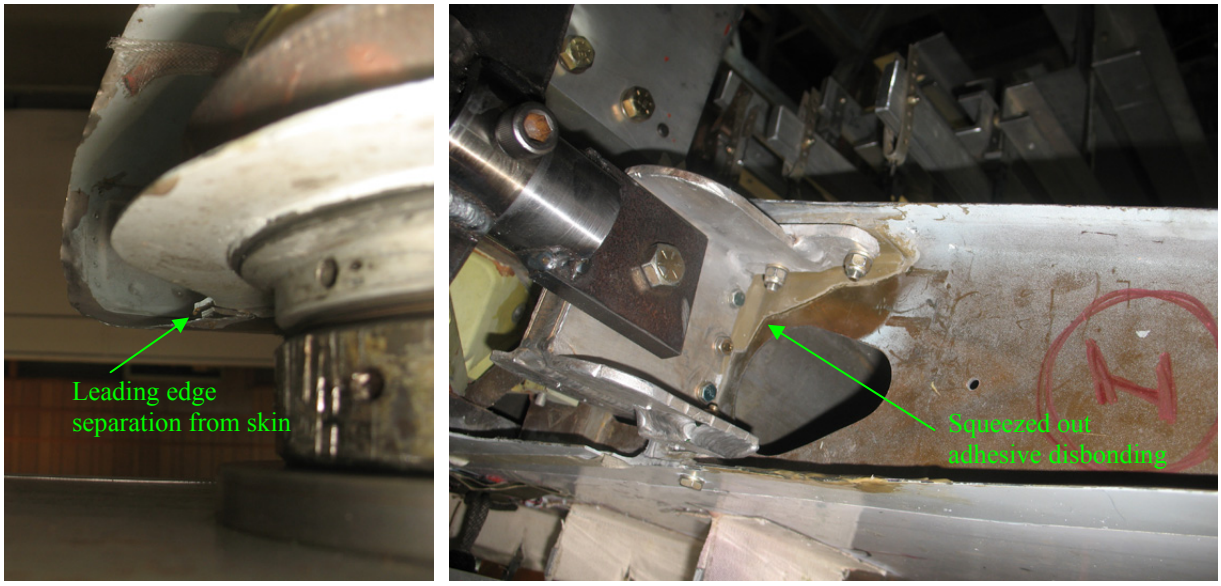

Figure 130. Visual inspection findings after load block C (40016 cycles).

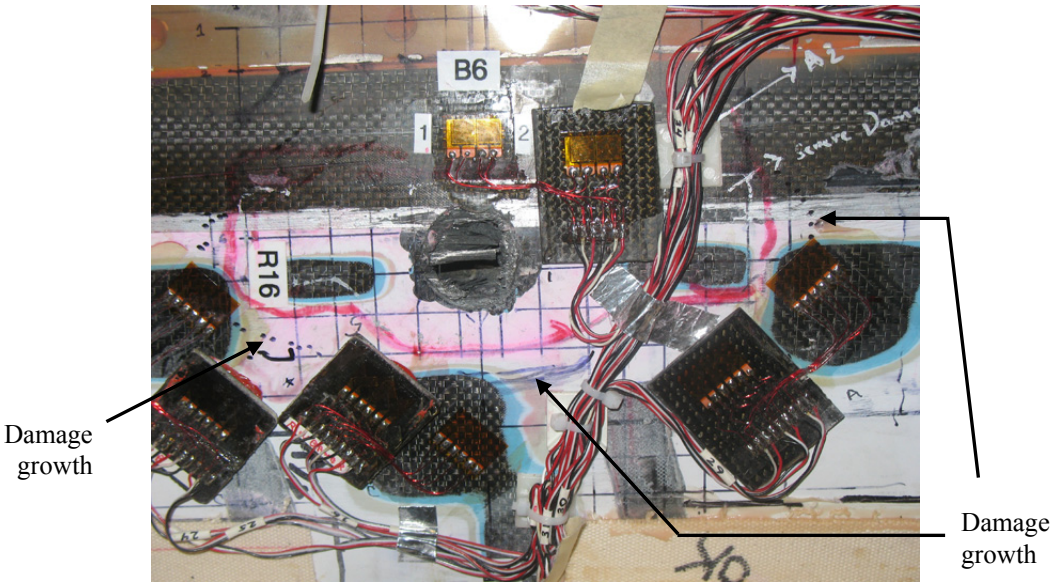

Figure 131. Ultrasonic NDI results after load block C (40016 cycles).

No significant damage was detected until after load block D. Following block D, the damages noted in Figure 130 increased, as shown in Figure 132. Furthermore, the leading edge indicated that local buckling between rivets on both top and bottom sides ruptured the orange filler material that was applied closer to the root end between the periphery of the leading edge and skin.

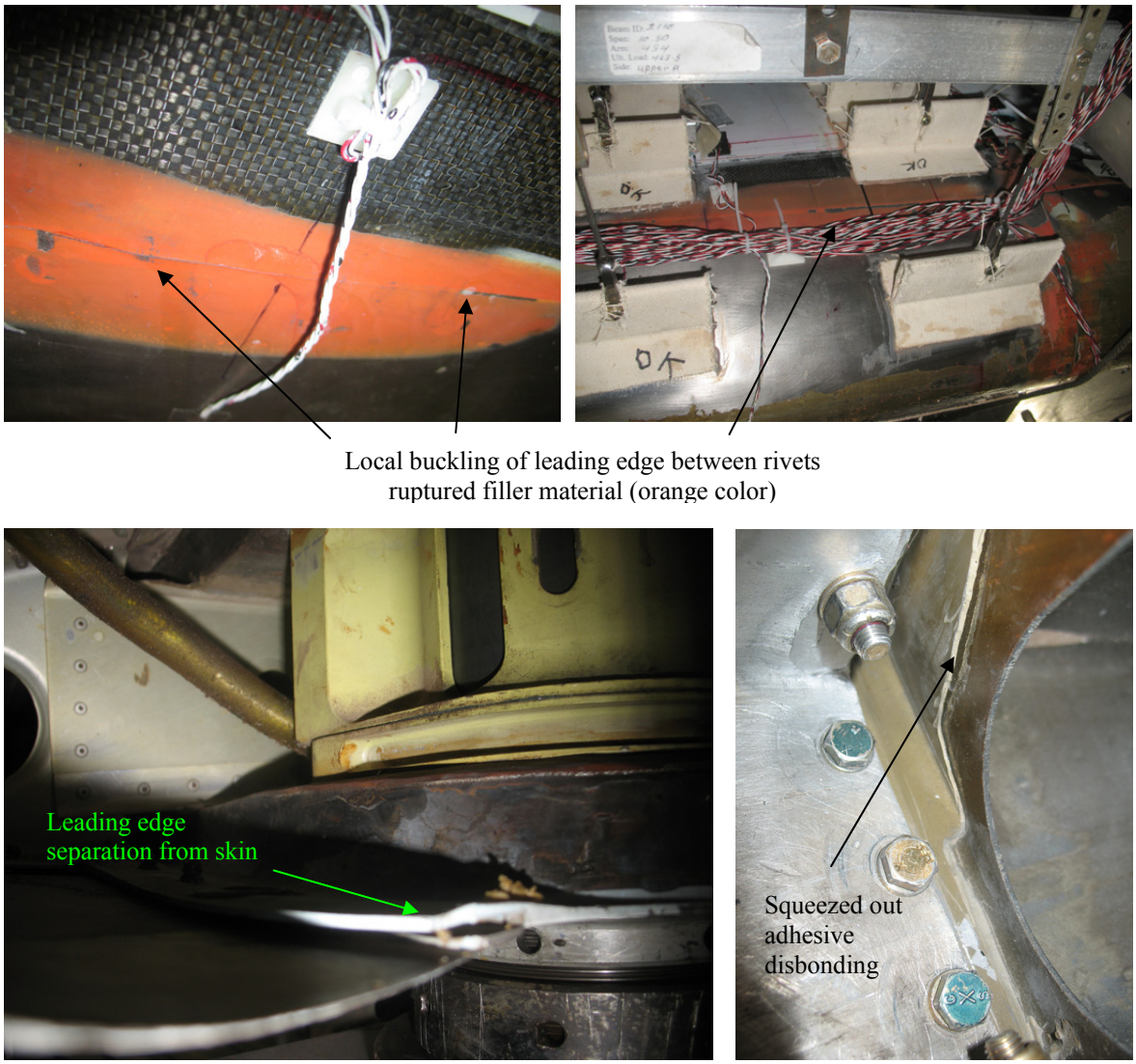

Figure 132. Visual Inspection findings after load block D (80033 cycles).

8.6. Post-Test Failure Analysis

Once the static and residual strength tests were completed, detailed post-inspections along with video and strain gage data were used to evaluate the failure mechanism of each Starship forward wing. In addition, DTH was used to determine the fractured areas with respect to the untested forward wing.

8.6.1. Static Test Articles

Both static test articles, ST002 and ST003, indicated a similar failure mechanism and fracture surface (Figure 133). Visual inspections and tap tests showed the following:

- Widespread upper-skin fracture, leading-edge permanent buckling (yielding), and skin debond/delaminations between FWS 51 and FWS 76.
- Upper skin debond around rear spar toward root end.
- Lower skin fracture along aft spar.
- Multiple skin delamination and fracture toward root end.

Once the leading edge was removed, severe damages to the web and front-spar flanges were noted, especially around the outboard closeout rib of the aluminum secondary spar (Figure 134). This closeout rib and aluminum spar were also severely deformed due to high brazier loads due to wing-box bending [64]. Flexural stress on the front web due to bending resulted in 45° fractures, as shown in Figure 134. After sectioning the test article around these stations, it was determined that the top and bottom spar caps were intact with no fractures.

Figure 135 shows primary damage locations delineated by DTH inspections of ST002 and ST003. A major fracture on the top skin indicated that the skin fracture initiated as a result of shear buckling (45° alignment). Results also indicated that top-skin delamination of the aft spar toward the root end possibly was due to mode I or pullout loading that resulted from torsional buckling of the top skin. Based on DTH data, damages to the bottom skin was limited to the area directly under the major fracture on the top skin and closer to the root end of the aft spar.

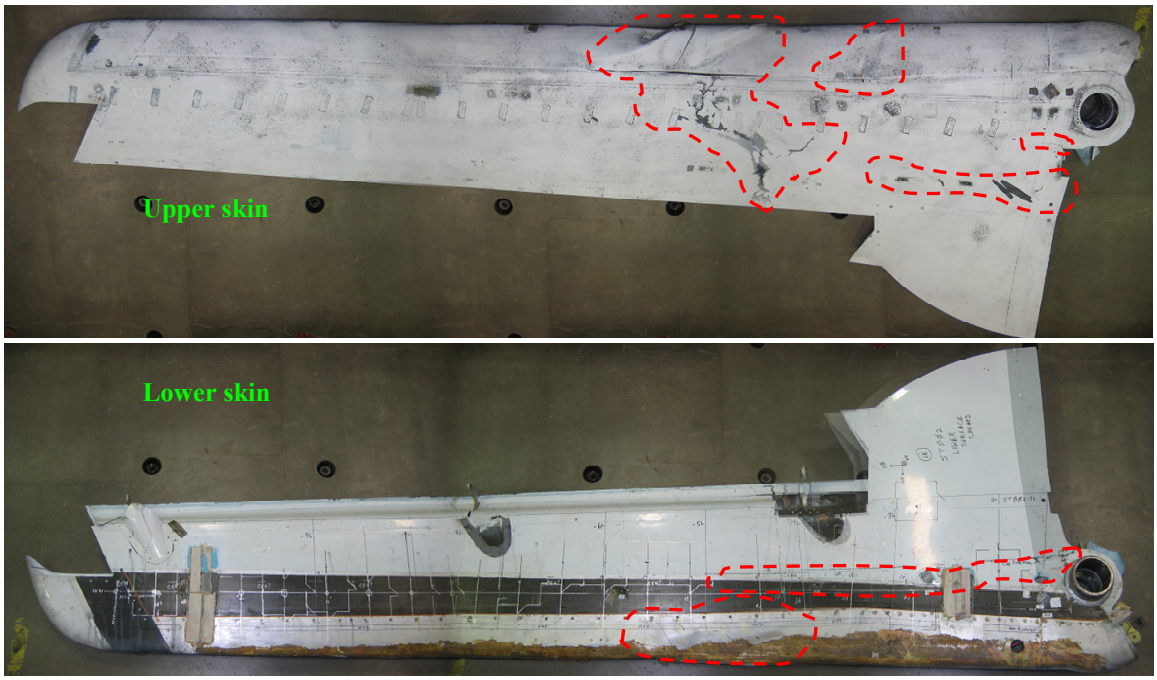

(a) ST002 static test article

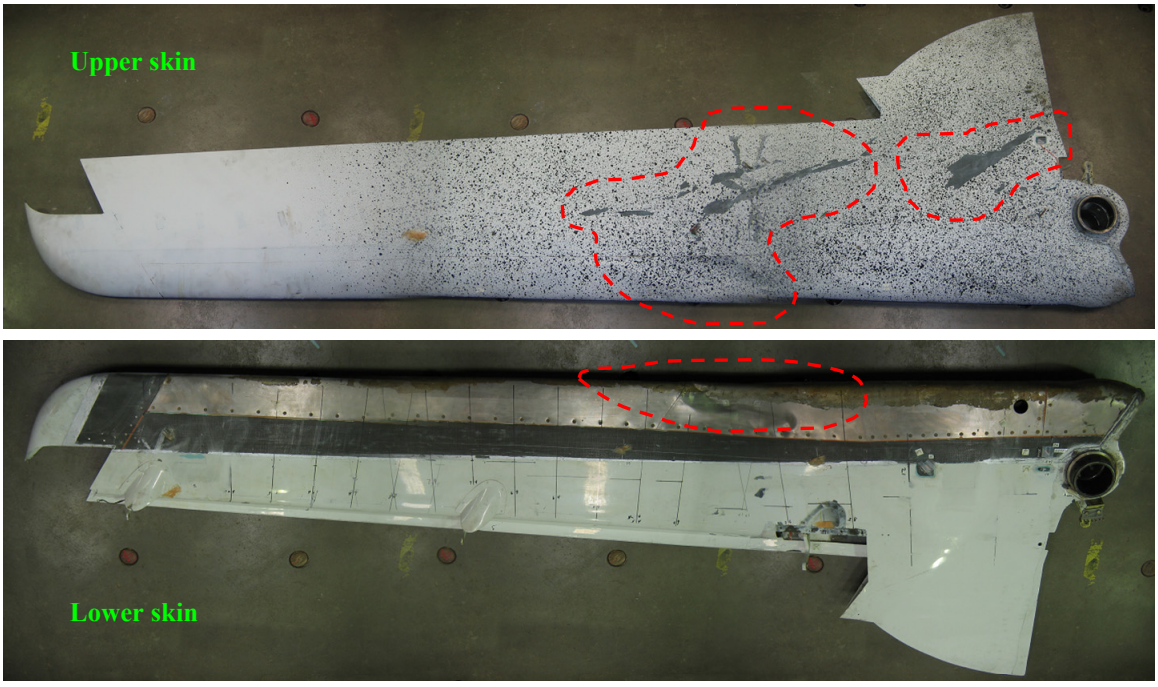

(b) ST003 static test article

Figure 133. Post-test visual inspections.

Figure 134. Post-test inspections of ST003 upon removal of leading edge.

Strain gages of ST002 on the rear spar toward the root end (A4) indicated sudden decrease in strain followed by an audible noise, indicating initial debond/delamination around 11,275 lbf (Figure 136). A video captured during testing also indicated significant skin buckling and twisting of the structure around 14,000 lbf and notable aft skin disbonding around 14,600 lbf. The strain anomalies indicated that the disbond started from the root and propagated outboard toward the failure. The first major failure, which was not related to the skin delamination, occurred just outside the elevator attachment hinge bracket at FWS 52.7 due to compressive loads on the top flange of the aft spar. Following that, the aft web continued to be crushed as the load increased. Consequently, the article started twisting as the aft lost its load-carrying capability. Immediately following, the major fracture occurred as the load redistribution caused the front web to fail under increased brazier and torsional loads.

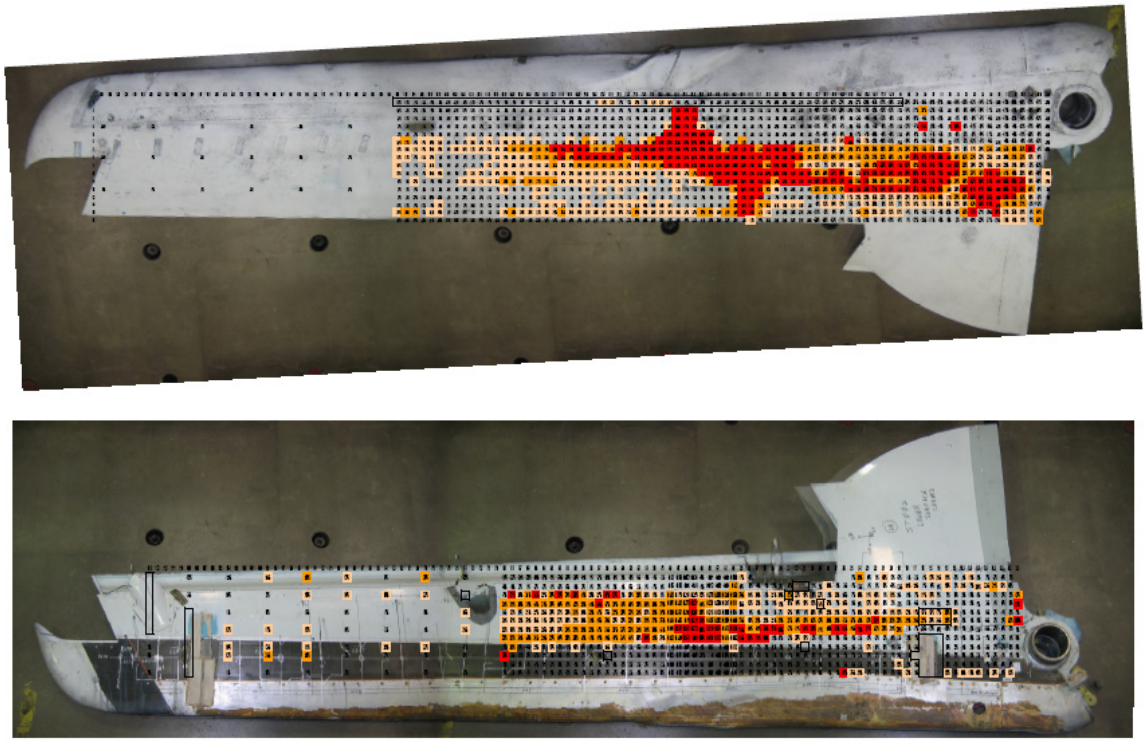

(a) ST002 static test article

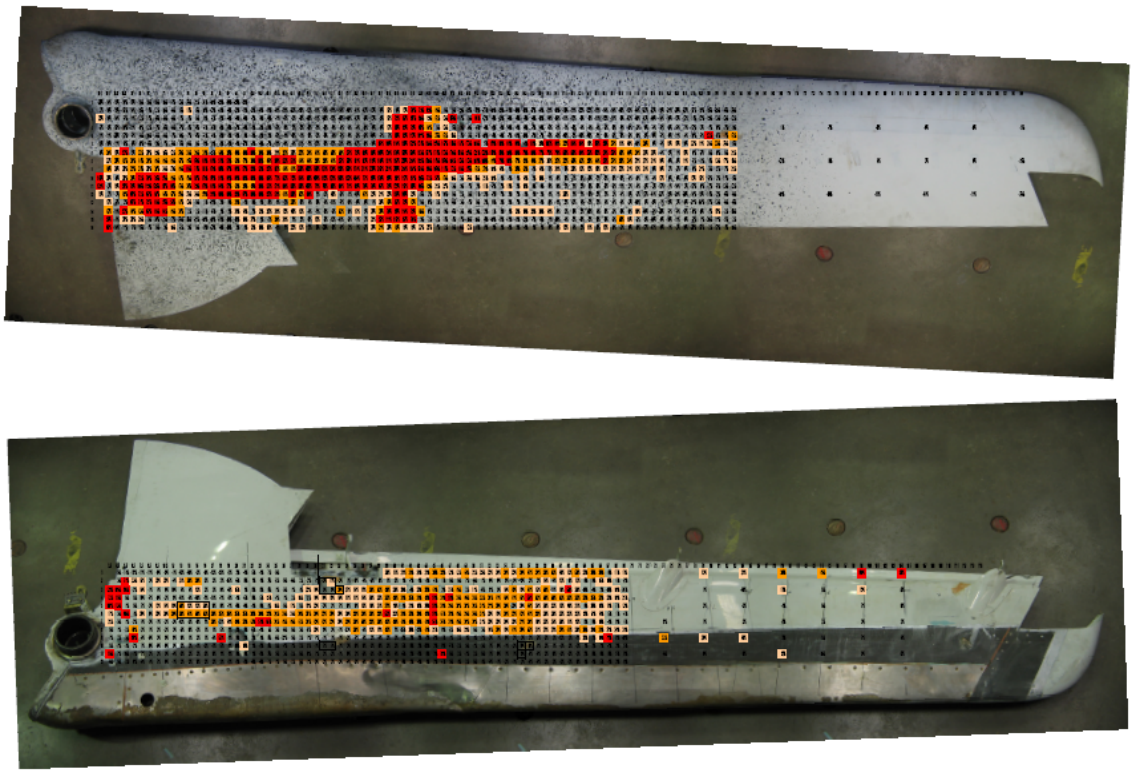

(b) ST003 static test article

Figure 135. Post-test digital tap hammer results overlay.

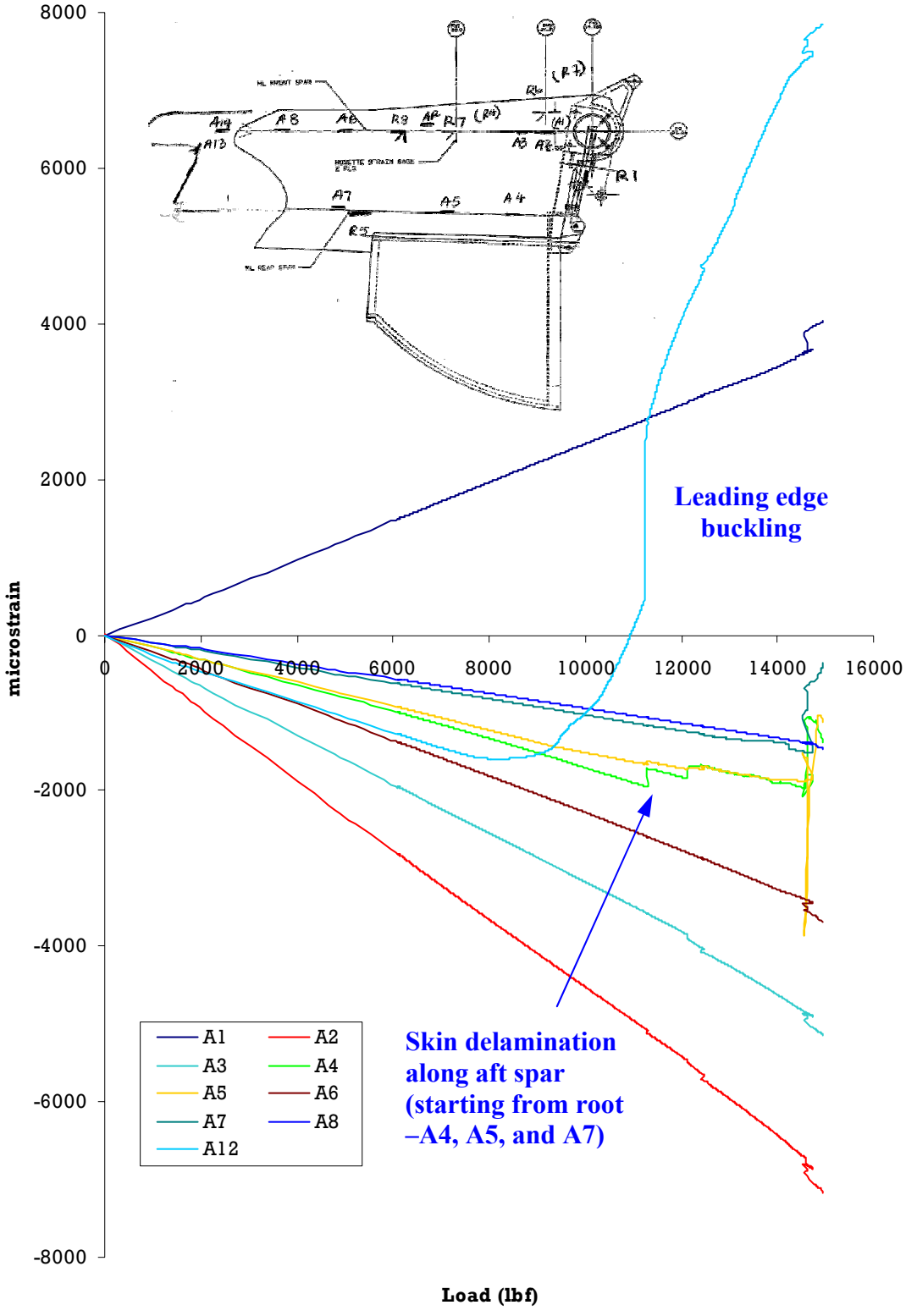

Figure 136. Failure mechanism determination using strain anomalies – ST002.

8.6.2. CAT2 Damage on Aft Spar – ST001(R) and ST004

The primary failure mode of ST001(R) and ST004 was the same as it was for ST002 and ST003, i.e., aft web crush due to brazier loads causing rotation, which caused high brazier loads and torsional loads on the front web followed by shear buckling. However, no major fracture that propagated across front and aft spars was seen in both ST002 and ST003. Instead, a large diagonal delamination propagated instantaneously across CAT2 damage following a loud cracking noise (Figure 137). Based on the videos and strain data around the damage, this occurred at 13,330 lbf (167 percent NRLL) for ST001(R), and at 13,370 lbf (157 percent NRLL) for ST004 during residual strength after 2-DLT.

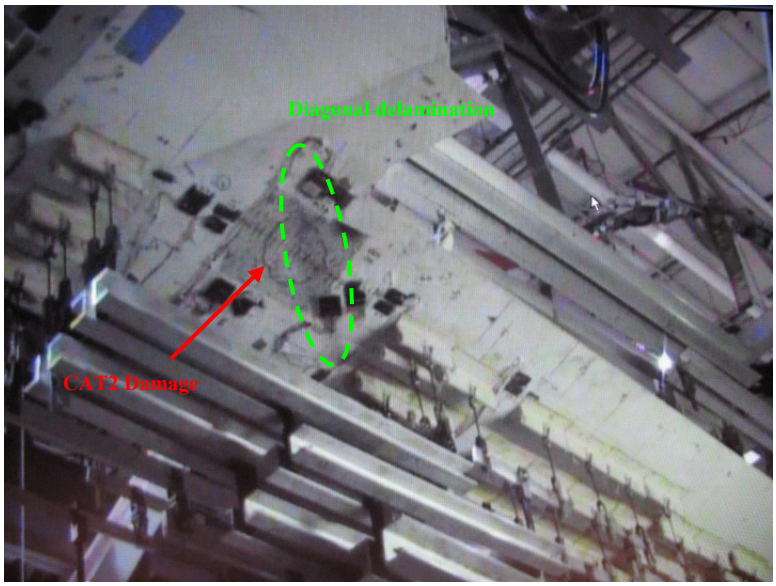

Figure 137. Diagonal delamination across CAT2 damage on aft spar after 160% NRLL.

Visual inspections after residual strength tests revealed no indication of apparent fractures in addition to post-impact and post-DaDT damages for ST001(R) and ST004, respectively.

8.6.3. CAT3 Damage on Front Spar – ST005 and ST006

Both ST005 and ST006 test articles with CAT3 damages on the front spar failed across the damage following skin delamination at the trailing edge just outboard of the elevator attachment hinge (Figures 138 and 139, respectively). The video showed that prior to failure, the skin undergoes compression buckling rather than shear buckling mode, which is observed during previous tests (sections 8.6.1 and 8.6.2). It also indicated that the primary failure was initiated at CAT3 damage. This is understandable, as the CAT3 damage creates a significant stress concentration around the damage. Furthermore, damage to the front web below the CAT3 damage resulted in a significant reduction in flexural strength of the front spar. Once the top spar cap fractured across the damage instantaneously, the aft spar failed and a major crack formed across FWS 66.5. As shown in Figure 138, damage was primarily across the region delineated by ultrasonic inspections, trailing-edge delamination, and leading-edge buckling around FWS 66.5. Also, both front and aft webs and top flanges across this region indicated severe fracture and delamination due to compressive loads.

8.7. Summary of Full-Scale Test Validation

Based on initial full-scale static testing, a conversion factor of 1.4 was established to convert Beechcraft design loads to NIAR research loads. The ST001(R) static test article with CAT2 damage on the top skin of the aft spar at FWS 45 indicated no growth until NRLL. Detailed investigation of strain data, videos, and post-test inspections revealed that the compressive loads were responsible for failure of the aft web, which was damaged during impact testing. Following that and after NRUL, a long delamination formed diagonally across the CAT2 damage due to shear buckling and increased mode I stress. Subsequently, the rotation of the article increased the torsional loads, and redistributed loads increased the brazier loads on the

front web, just outboard of the secondary aluminum spar (in front of front spar), causing that to fail as well.

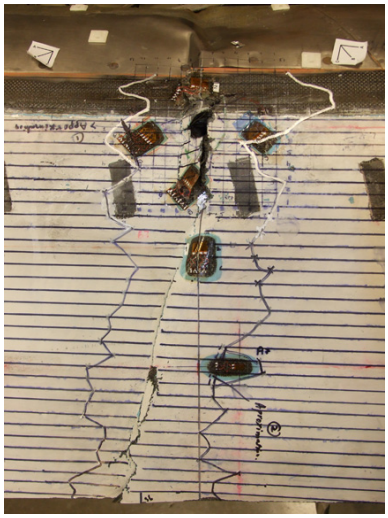

(a) Ultrasonic results

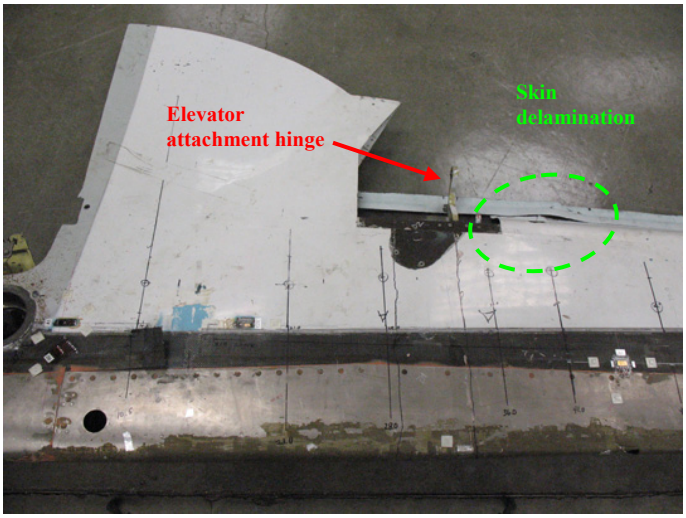

(b) Trailing edge skin delamination

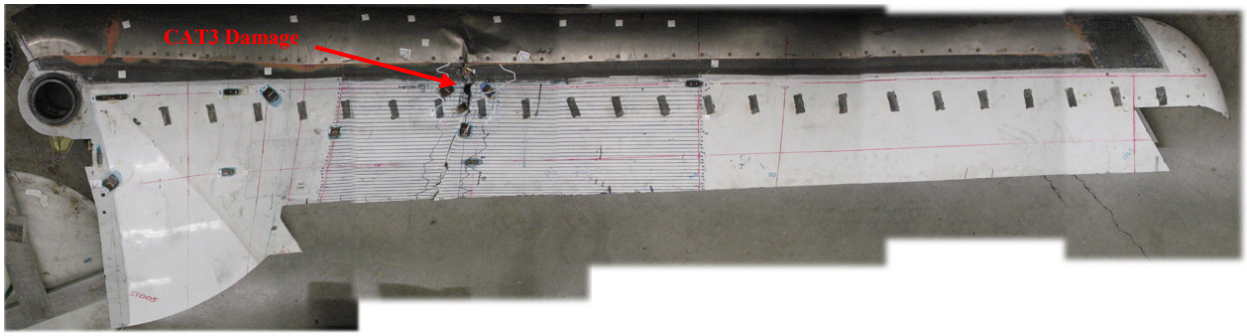

(c) Top view

(d) Bottom view

Figure 138. Ultrasonic and visual post-test inspections of ST005 static test article.

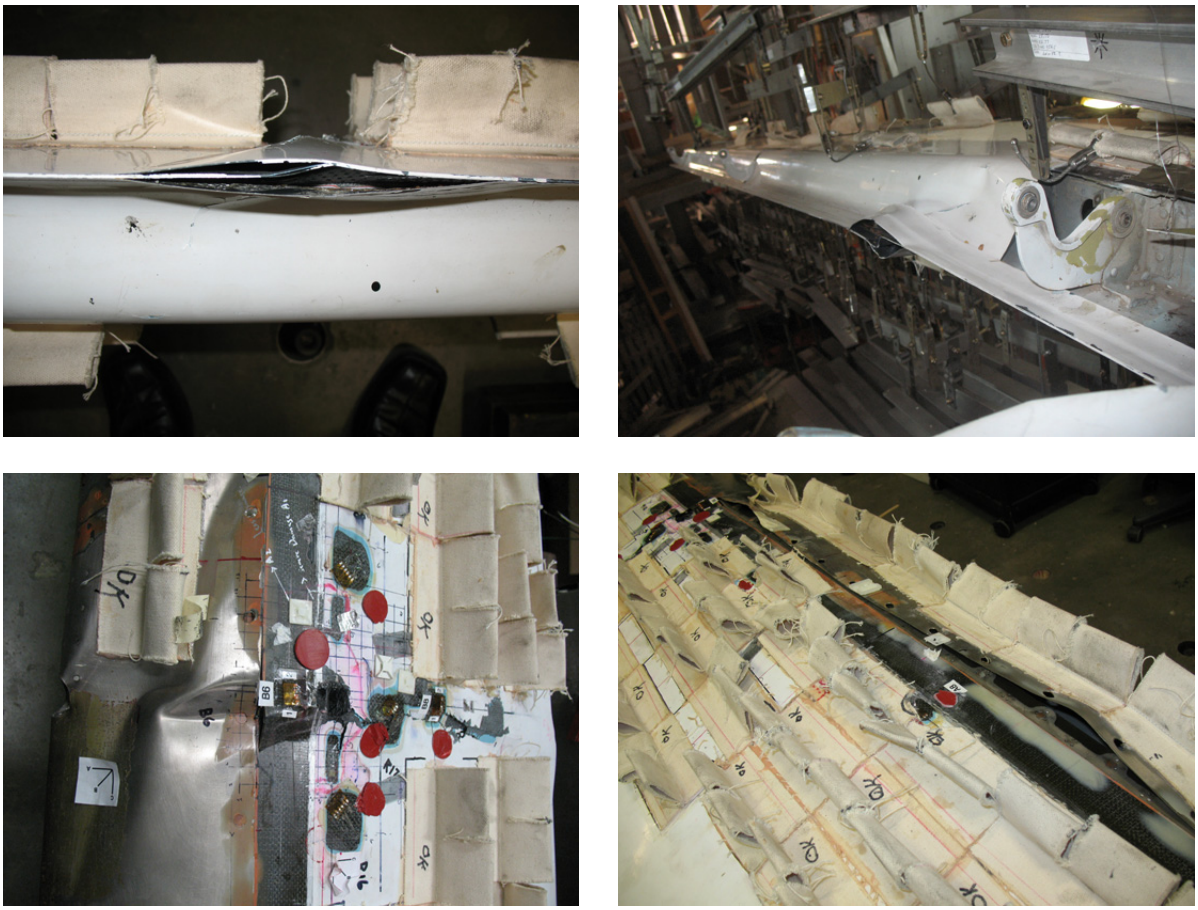

Figure 139. Post-test visual inspections of ST006 DaDT test article after residual strength test.

Cyclic testing of the DaDT test article with CAT2 damage for 2 DLTs with LEF=1.072 indicated no significant damages to the composite structure but several fastener pull-through failures in the leading edge. The LEF was based on the materials used for the construction of the forward wing and considerably lower than that based on the NAVY approach. Furthermore, in addition to the LEF, spectrum loads were multiplied by CF=1.4, resulting in a cumulative enhancement factor of 1.5. Standard tap testing revealed no growth, but DTH data and strain anomalies indicated minor damage growth after 1-DLT. The post-DaDT residual strength test of this article indicated nonlinear strain/displacement anomalies and audible cracking noise around 40 percent of NRLL and final failure around 157 percent of NRLL. Therefore, the ST004 DaDT test article demonstrated ultimate load capability after a required test duration with an LEF based

on the approach outline in section 8.1.4. Based on the scatter analysis of VID element test results and the LLD hybrid approach (Figure 71), it was found that the required test duration for LEF of 1.072 corresponds to 1.35 DLTs.

In order to disrupt the primary load path by creating CAT3 damage, the front spar of ST005 was impacted. Catastrophic failure was observed at 68 percent of NRLL, indicating that this damage was more severe than typical CAT3 damage. For comparative purposes, the ST006 DaDT test article was impacted with similar impact parameters at the same location and cyclic tested. Based on the residual strength after impact, the CF=1.4 resulted in spectrum loads that would be higher than the residual strength of this article. Although the scheduled inspections would occur prior to these high loads, for the fatigue spectrum of ST006 DaDT article, the CF was not applied to ensure that the maximum fatigue load was below the post-impact residual strength. The inspection intervals were designed with a target (minimum) reliability of 90 percent, i.e., the inspection intervals were allotted prior to the probability of failure of a structure with CAT3 damage reaching 10 percent. Strain anomalies and periodic inspections confirmed the CFU predictions for damage growth, in terms of probability of failure. Quasi-static testing conducted after half DLT of ST006 indicated that the post-DaDT residual strength of the article was approximately 95.5 percent NRLL.

CHAPTER 9

CONCLUSIONS AND RECOMMENDATIONS

The primary objective of this research was to develop an approach to synthesizing the life factor, load-enhancement factor, and damage in composite structures to determine the fatigue life of a damage-tolerant aircraft. The methodology proposed in this research extends the current damage-tolerance test approach and provides information necessary to define inspection intervals for composite structures by studying the effects of extremely improbable, high-energy impact damage.

Research was completed in three major phases. First, the effects of generating load enhancement factors based on the most critical design details of a composite structure in coupon level was interrogated. The approach for obtaining the modal static strength shape parameter and modal fatigue life shape parameter to calculate the load-enhancement factors for different test durations was investigated in details using static and fatigue test data for several different composite material systems, respectively. Secondly, the process of scaling different impact threats in a full-scale structure down to a representative element-level was discussed. It was shown that the scatter in notched (damaged) composite test data is significantly lower than unnotched composite. Such improvements in fatigue-life shape parameter can significantly reduce the life factor. However, the life factor becomes insensitive to small changes in the life-shape parameter beyond a value of 4, which is considered to be the life-shape parameter for metal. The composite modal life-shape parameter of 1.25, which was used for the NAVY approach, lies within the highly sensitive region of life factor vs. shape parameter curve, thus even a small improvement resulted in a dramatic reduction of life factor, which reflects the required number of test durations to achieve a certain level of reliability in the design life. The

main goal in this phase was to carry out the scatter analysis to support the durability testing of a damage-tolerance full-scale test article with large damages. The analysis in this step forms the supporting data for the load-life-damage hybrid approach that can be applied to a full-scale durability test article during the damage-tolerance phase. Finally, several full-scale tests were conducted by combining the load enhancement factors developed in the first phase and the scatter analysis conducted on damage-tolerance element-tests in the second phase to validate the load-life-damage hybrid approach for determining the fatigue life.

9.1. Scatter Analysis for Generating Load Enhancement Factors

As shown in this paper, there are several approaches for the scatter analysis of fatigue data, including the individual Weibull, joint Weibull, and Sendeckyj wearout models. When analyzing small fatigue data sets, the latter two methods can be used to pool data across fatigue stress levels. Further, Sendeckyj analysis allows the user to include the static and residual strength of runout specimens. In addition to a probabilistic description of the data scatter, the Sendeckyj wearout model provides a deterministic equation to define the shape of the S-N curve and an expression for the monotonically decreasing residual strength as a function of the number of cycles.

Compared to metals, composite materials are known for higher scatter in both static and fatigue test data due to their heterogeneous nature, higher sensitivity to batch variability, environment, and complex failure modes. Over the years, improvements in test methods, materials, and process techniques have resulted in significant reduction in data scatter. A detailed scatter analysis conducted on several material test databases (authors current and past FAA-funded research programs) representing multiple batches, loading modes, environments, and laminate stacking sequences for several commonly used composite material systems has

shown that both static-strength and fatigue-life scatter have been reduced significantly. These improvements have a direct impact on the probabilistic or reliability-based analysis technique for predicting the life of a composite structure such as life factor and load-enhancement factor analysis.

It is recommended that specimens or elements representative of features of a particular structure, i.e., materials, design details, failure modes, loading conditions, environments, etc., be included in the analysis rather than pooling various material databases. Also, it is noted that the primary goal in scatter analysis is not to select shape parameters from the critical layup, R-ratio, environment, etc. (which may result in skewed data that will produce unconservative LEF), but rather select the design details representing the critical areas of the structure. It is important that the test matrix include sufficient information to translate the statistical significance of such phenomenon in a meaningful manner into a full-scale test substantiation. Such test matrices can be significantly reduced by focusing on critical aspects of the structure to address the minimum requirements. As demonstrated in the case study of the Liberty XL2 fuselage, the use of shared databases can significantly reduce the amount of additional tests and time required for a certain application, but care must be taken to make certain that the shared data are equivalent to what is used for that application. Adhesive joints, if applicable, may require the use of individual Weibull analysis rather than polling techniques such as Sendeckyj, as adhesive joints tend to produce large scatter, mainly due to imperfections during bonding and high sensitivity to load eccentricity especially in asymmetric joints. Although the shape parameters can be varied within a large spectrum of values, care must be taken to address unrealistic values and address them individually to produce safe and reliable scatter analysis. For example, the Sendeckyj model provides a way to graphically inspect the data fit, as illustrated in Appendix A, to evaluate the

quality of the fitting parameters, which are used to generate the S-N curve fit and for the scatter analysis. For Weibull analysis, the maximum-likelihood estimation can be used to generate shape parameters when there are more than 18 data points, while regression in the number of cycles is recommended for small datasets. For the modal fatigue-life shape parameter calculations of composite data in this report, both of these techniques produced similar values, while for adhesives, regression in the number of cycles produced higher shape parameters than that from the maximum-likelihood estimation.

9.2. Load-Life-Damage Hybrid Approach for Full-Scale Substantiation

Typically, the load spectrum of a full-scale test article is truncated by eliminating the segments with stress levels below the endurance limit. In order to further reduce the required test duration to achieve the desired level of reliability on the design lifetime, life factor and LEFs are combined and applied to the truncated load spectrum. In addition, for the room-temperature ambient test, environmental factors should be applied to the truncated spectrum to account for the environmental effects on composite materials. When applying these factors, the stress ratio of the original spectrum and the expected failure mode must be preserved, and the final loads must be below the static strength to avoid unintentional failures. When damage is introduced to the structure, care must be taken to prevent unintentional failures. If the damage region becomes the critical location of the structure and imminent damage instigation at this location results in catastrophic failure of the structure or a load redistribution that can be predicted by analysis, the scatter analysis can be conducted on elements that represent the critical location with an equivalent damage (LLD approach). Specimen design and the loading mode for such an exercise has a direct impact on the fatigue test results and the data scatter, and may require rigorous NDI techniques to monitor flaw growth, i.e., finite-width CAI specimens that are fatigue tested in load

control test mode will represent damage on a critical load path with no load redistribution due to damage growth. The new life shape parameter can be used to calculate the life factor corresponding to the structure, given the above-mentioned conditions are met. Due to the notch sensitivity of composites, it is shown that their life scatter is reduced as the impact energy level is increased. Thus the LLD approach, in most cases, will result in a lower life factor and LEF requirements than the values obtained from the original MSSP and MLSP of the structure. In the event that a repair of the impacted damage is deemed necessary to prevent premature failure or that damage propagation resulted in a load redistribution predicted by analysis, then the LEF requirements must be adjusted to reflect the fact that the structure is restored back to its undamaged state.

9.2.1. Load-Life Shift

The LLD approach introduces the use of multiple LEFs for a particular composite structure, based on the damage category, i.e., use of different LEF curves representing damage severity. The load-life shift calculates the remaining percentage of the design life to be substantiated after completing a certain number of repeated lives with respect to the required repeated lives for the corresponding LEF. Once the test article is inflicted with damage, the remaining test duration is calculated by multiplying the required repeated lives corresponding to the new LEF and the above-mentioned percentage of design life. The example discussed in this paper showed that this approach not only reduced the LEF requirements for a test article with a large damage but also reduced the remaining test duration as a result of the reduction in data scatter of notched (damaged) composite element test data.

9.2.2. Determination of Inspection Intervals using Cumulative Fatigue Unreliability Model

In order to prevent unintentional failure of a damaged article during DaDT testing, especially when investigating extremely improbable high-energy impact threats that reduce the residual strength of a composite structure to its limit load, rigorous inspection intervals are required. The probability of failure of the damaged structure for the enhanced spectrum loads can be evaluated using the cumulative fatigue unreliability (CFU) model proposed in this research. The information obtained from this model can also be used to allot economical and reliable inspection intervals to detect the extent of damage prior to imminent failure or unstable propagation that will threaten the structural integrity. This approach can also be extended to determine the inspection interval during service based on a target reliability and a critical damage threshold.

9.3. Full-Scale Test Substantiation

The first three full-scale static tests were conducted to determine the structural capacity (ultimate load) of Beechcraft Starship forward wing structure. It was determined to be 1.4 times the design ultimate load, thus the load spectrum of ST004 durability tests was multiplied by a factor of 1.4 prior to applying the LEF. The static residual strength test of the test article, ST001(R), with a category 2 damage on the aft spar indicated that the damage grew just after the newly defined ultimate load. Following that, there were significant whiffletree shifting, thus the test was aborted.

9.3.1. Validation of Load-Life-Damage Hybrid Approach

The LEFs developed based on the critical design details of Starship forward wing were significantly lower than the LEFs developed for F/A-18 certification (NAVY approach). The scatter analysis of damage-tolerance element test showed that the initial LEF requirements can

be further reduced by introducing large impact damages to the tests article. Full-scale test validation of the LLD approach that was carried out using a Starship forward-wing DaDT test article with category 2 damage on the aft spar demonstrated no significant fatigue damage to the composite structure or no significant damage propagation that could be detected by standard NDI techniques. The strain anomalies indicated minor damage propagation, which was later arrested, between 1.5 and 2 DLT. Based on the scatter analysis of VID element test results and the LLD hybrid approach, it was found that the applied LEF of 1.072 corresponds to a required test duration of 1.35 DLT. However, the DaDT test was conducted for 2 DLTs, and then the post-DaDT residual strength was evaluated. The test article demonstrated ultimate strength capacity during a post-DaDT residual strength test. These data showed that the damage growth occurred after satisfying the repeated load requirements according to LLD hybrid approach, and the minor damage growth on the secondary load path (aft spar) did not alter the residual strength capacity of the structure. Furthermore, the failure mode of the post-DaDT test was similar to the post-impact static residual strength test, thus the minor damage growth observed through strain anomolies did not alter the overall failure mechanism.

9.3.2. Validation of Cumulative Failure Unreliability Model

The forward-wing DaDT test article with category 3 damage on the front spar, which is the primary load path, demonstrated the capability of the CFU model to predict the damage growth in terms of reliability and the capability of the model to determine the inspection levels. Although it is not a one-to-one correlation for the damage propagation or its size, the CFU model highlighted load segments that resulted in gradual progression of local damage, such as possible matrix cracks, and the global impact of high loads that resulted in evident damage growth. Although the standard NDI techniques were unable to detect the minor damage growth during

certain spectrum loads, the CFU model highlighted the probability of damage growth for those loads and the strain gage data confirmed the growth.

Real-time data monitoring is crucial to identifying damage propagation during the full-scale DaDT test, especially since large damage scenarios are expected to grow. The monitoring provided instant feedback of the structural response for applied loads and mitigated risks of unexpected test failures or anomalies that would have been otherwise left undetected. The strategic allocation of and placement of strain gages for these articles is crucial to achieve this goal. The strain data provide information similar to a built-in health monitoring system and provide details in real time to assess the state of the damage, i.e., propagation or not, and any global effects on the structure due to possible damage growth.

A realistic target reliability must be used for determination of inspection intervals accounting the safety and the cost considerations. Although a category 3 damage is recommended for determining the inspection intervals, more realistic damage threat levels can be used considering the probability of occurrence so that more practical or economical inspection levels can be determined. In order to further extend the CFU model for determination of inspection intervals for a fleet, the fleet size and the probability of detectability may have to be considered in addition to the above-mentioned parameters.

REFERENCES

REFERENCES

[1] Aniversario, R. B., Harvey, S. T., Mccarty, J. E., Parson, J. T., Peterson, D. C., Pritchett, L. D., Wilson, D. R., and Wogulis, E. R., "Full-Scale Testing, Production and Cost Analysis Data for the Advanced Composite Stabilizer for Boeing 737 Aircraft," Vol. 2, NASA CR-166012, December, 1982.

[2] Whitehead, R. S., Kan, H. P., Cordero, R., and Saether, E. S., "Certification Testing Methodology for Composite Structures," Report No. NADC-87042-60, Volumes I and II, October, 1986.

[3] Lameris, J., "The Use of Load Enhancement Factors in the Certification of Composite Aircraft Structures," NLR Report: NLR TP 90068 U, February, 1990.

[4] Kan, H. P., Cordero, R., and Whitehead, R. S., "Advanced Certification Methodology for Composite Structures," DOT/FAA/AR-96/111, April, 1997.

[5] Horton, R. E., and Whitehead, R. S., "Damage Tolerance of Composites," Report No. AFWAL-TR-87-3030, Volumes I, II and III, July, 1988.

[6] Rapoff, A. J., Dill, H. D., Sanger, K. B., and Kautz, E. F., "Certification of Damage Tolerant Composite Structure," Eighth DoD/NASA/FAA Conference on Fibrous Composites in Structural Design, NASA CP-3087, Part 2, November, 1989, pp. 499-514.

[7] Curtis, P. T., Lawrie, D., and Young, J. B., "The Effects of Impact on Pre-Fatigued Fiber Composites," in J. Morton, ed., *Structural Impact and Crashworthiness*, Elsevier, London, 1984, pp. 494-509.

[8] Sanger, K. B., "Certification Testing Methodology for Composite Structures," Report No. NADC-86132-60, January, 1986.

[9] Deo, R., Starnes, Jr., J. H., and Holzwarth, R., "Low-Cost Composite Materials and Structures for Aircraft Applications," NATO Applied Vehicle Technology Panel (AVT) Specialists' Meeting, RTO-MP-069(II), Leon, Norway, May, 2001.

[10] Kan, H. P., and Whitehead, R. S., "Damage Tolerance Certification Methodology for Composite Structures," *Proceedings of Eighth DoD/NASA/FAA Conference on Fibrous Composites in Structural Design,* NASA CP-3087, Part 2, November, 1989, pp. 479-498.

[11] Shah, C. H., Kan, H. P., and Mahler, M., "Certification Methodology for Stiffener Termination," DOT/FAA/AR-95/10, April, 1996.

[12] Kah, H. P., and Dyer, T. A., "Structural Integrity Evaluation of the Lear Fan 2100 Aircraft," DOT/FAA/AR-95/13, May, 1996.

[13] McCarty, J. E., Johnson, R. W., and Wilson, D. R., "737 Graphite-Epoxy Horizontal Stabalizer Certification," *Proceedings of the 23rd AIAA/ASME/ASCE/AHS Structures,* Structural Dynamics and Materials Conference, May, 1982, pp. 307-322.

[14] Gogkol, O., "A310-300 CRFP Fin – Damage Tolerance Demonstration," *Proceedings of the 7th International Conference of SAMPE,* European Chapter, Munich, June, 1986.

[15] Brandecker, B., and Hilgert, R., "A320 Full Scale Structural Testing for Fatigue and Damage Tolerance Certification of Metallic and Composite Structure," *Proceedings of the 16th Congress of the International Council of the Aeronautical Sciences,* ICAS-88-5.8.1, Jerusalem, Israel, 1988.

[16] Fawcett, A., Trostle, J., and Ward, S., "777 Empennage Certification Approach," *Proceedings of the 11th International Conference on Composite Materials,* Australia, July, 1997.

[17] Vosteen, L. F., and Hadcock, R. N., "Composite Chronicles: A Study of the Lessons Learned in the Development, Production, and Service of Composite Structures," NASA CR-4620, November, 1994.

[18] Wong, R., and Abbott, R., "Durability and Damage Tolerance of Graphite/Epoxy Honeycomb Structures," *Proceedings of the 34th International Symposium,* Anaheim, CA, 1990.

[19] Kan, H. P., and Kane, D. M., "Probabilistic Certification of Integrally Bonded Composite Structures – an Assessment," *Proceedings of the 43rd AIAA/ASME/ASCE/AHS/ASC Structures,* Structural Dynamics and Materials, Denver, CO, April, 2002.

[20] Sumich, M., and Kedward, K. T., "Development of a Fatigue-Life Methodology for Composite Structures Subjected to Out-of-Plane Load Components," NASA TM-102885, February, 1991.

[21] Halpin, J. C., Jerina, K. L., and Johnson, T. A., "Characterization of Composites for the Purpose of Reliability Evaluation," *Analysis of Test Methods for High Modulus Fibers and Composites, ASTM STP 521,* American Society for Testing Materials, 1973, pp. 5-64.

[22] Sendeckyj, G. P., "Fitting Models to Composite Materials Fitting Data," *Test methods and Design Allowables for Fibrous Composites, ASTM STP 734,* in C. C. Chamis, ed., American Society for Testing and materials, 1981, pp. 245-260.

[23] Sendeckyj, G. P., "Life Prediction for Resin Matrix Composite Materials," in K. L. Reifsnider, ed., *Fatigue of Composite Materials,* Elsevier, Amsterdam, 1990.

[24] O'Brien, T. K., and Reifsnider, K. L., "Fatigue Damage Evaluation through Stiffness Measurements in Boron-Epoxy Laminates," *Journal of Composite Materials,* No. 15, 1981, pp. 55-70.

[25] Hahn, H. T., and Kim, R. Y., "Fatigue Behavior of Composite Laminates," *Journal of Composite Materials,* Vol. 10, No. 2, 1976, pp. 156-180.

[26] Hwang, W., and Han, K. S., "Cumulative Damage Model and Multi-Stress Fatigue Life Prediction," *Journal of Composite Materials,* Vol. 20, No. 2, 1986, pp. 125-153.

[27] Hwang, W., and Han, K. S., "Fatigue of Composites—Fatigue Modulus Concept and Life Prediction," *Journal of Composite Materials,* Vol. 20, No. 2, 1986, pp. 154-165.

[28] Mahfuz, H., Zaman, K., Haque, A., Foy, C., Mohamed, H., and Jeelani, S., "Fatigue Life Prediction of Thick-Section S2-Glass/Vinyl-Ester Composites Under Flexural Loading," *Journal of Engineering Materials and Technology,* Vol. 122, No. 4, October, 2000, pp. 402-408

[29] Halpin, J.C., Jerina, K. L., Johnson, T. A., "Characterization of Composites for the Purpose of Reliability Evaluation," AFML-TR-77-289, WPAFB, Ohio, 1972.

[30] Jeans, L. L., Grimes, G. C., and Kan, H. P., "Fatigue Spectrum Sensitivity Study for Advanced Composite Materials," U.S. Air Force Flight Dynamic Laboratory, Technical Report AFWAL-TR-80-3130, Volumes I, II and III, 1980.

[31] Rosenfeld, M.S., and Huang, S. L., "Fatigue Characteristics of Graphite/Epoxy Laminates under Compression Loading," *Journal of Aircraft,* Vol. 15, No. 5, 1978, pp. 264-268.

[32] Agarwal, B. D., and James, W. D., "Prediction of Low-cycle Fatigue Behavior of GFRP: An Experimental Approach," *Journal of Materials Science,* Vol. 10, No. 2, 1975, pp. 193–199.

[33] Yang, J. N., and Du, S., "An Exploratory Study into the Fatigue of Composites under Spectrum Loading," *Journal of Composite Materials,* Vol. 17, No. 6, 1983, pp. 511-526.

[34] Kassapoglou, C., "Fatigue Life Prediction of Composite Structures under Constant Amplitude Loading," *Journal of Composite Materials,* Vol. 41, No. 22, 2007.

[35] Dost, E. F., Avery, W. B., Ilcewicz, L. B., Grande, D. H., and Coxon, B. R., "Impact Damage Resistance of Composite Fuselage Structure, Part 1," *Proceedings of the Ninth DoD/NASA/FAA Conference on Fibrous Composites in Structural Design,* vol. 2, Lake Tahoe, NV, November, 1991. pp. 1037-1069.

[36] Dost, E. F., Ilcewicz, L. B., Avery, W. B., and Coxon, B. R., "Effects of Stacking Sequence on Impact Damage Resistance and Residual Strength for Quasi-Isotropic Laminates," *Composite Materials: Fatigue & Fracture (Third Volume), ASTM STP 1110,* In T. K. O'Brien, Ed., American Society for Testing Materials, Philadelphia, 1991, pp. 476-500.

[37] Sharma, A. V., "Low-Velocity Impact Tests on Fibrous Composite Sandwich Structures," *Proceedings of the Symposium on Test Methods and Design Allowables for*

Fibrous Composites, American Society for Testing and Materials, Dearborn, MI, October, 1979, Philadelphia, PA, 1981, pp. 54-70.

[38] Tomblin, J., Lacy, T., Smith, B., Hooper, S., Vizzini, A., and Lee, S., "Review of Damage Tolerance for Composite Sandwich Airframe Structures," DOT/FAA/AR-99-49, August, 1999.

[39] Tomblin, J., Raju, K. S., Liew, J., and Smith, B., "Impact Damage Characterization and Damage Tolerance of Composite Sandwich Airframe Structures," DOT/FAA/AR-00/44, January, 2001.

[40] Tomblin, J., Raju, K. S., and Arosteguy, G., "Damage Resistance and Tolerance of Composite Sandwich Panels – Scaling Effects," DOT/FAA/AR-03/75, February, 2004.

[41] Raju, K.S., "The Static Indentation Behavior of Composite Sandwich Panels With Thin Quasi-Isotropic Skins," Ph.D. Dissertation, Department of Aerospace Engineering, Wichita State University, December, 2001.

[42] Shyprykevich, P., Tomblin, J., Ilcewicz, L., Vizzini, A., Lacy, T., and Hwang, Y., "Guidelines for Analysis, Testing, and Nondestructive Inspection of Impact Damaged Composite Sandwich Structures," DOT/FAA/AR-02-121, March, 2003.

[43] Tomblin, J. S., and Seneviratne, W. P., "FAA Research on Large-Scale Test Substantiation," FAA Damage Tolerance and Maintenance Workshop, Rosemont, IL, July, 2006.

[44] Tomblin, J. S., and Seneviratne, W. P., "Laminate Statistical Allowable Generation for Fiber Reinforced Composite Materials – Lamina Variability Method (LVM)," DOT/FAA/AR-06/53, Federal Aviation Administration, National Technical Information Service, Springfield, VA, 2006.

[45] Shyprykevich, P., Seneviratne, W. P., and Tomblin, J. S., "Lamina Variability Method for Determining Laminate Basis Values," 22nd Annual Technical Conference of the American Society for Composites (ASC), Seattle, WA, September, 2007.

[46] Tomblin, J. S., Seneviratne, W. P., Escobar, P., and Yap, Y., "Fatigue and Stress Relaxation of Adhesives in Bonded Joints," DOT/FAA/AR-03/56, April, 2003.

[47] Tomblin, J. S., Seneviratne, W. P., and Pillai, G. R., "Effects of Disbonds, Lightning Strikes, and Low-Velocity Impact Damages on Adhesively Bonded Composite Joints," Federal Aviation Administration, National Technical Information Service, Springfield, VA (under review).

[48] Composite Material Handbook, Volume 2: Polymer Matrix Composites Material Properties, Chapter 4 – Carbon Fiber Composites.

[49] Tomblin, J., Harter, P., Seneviratne, W., and Yang, C., "Characterization of Bondline Thickness Effects in Adhesive Joints", *ASTM Journal of Testing and Evaluation, JCTRER,* Vol. 24, No. 2, 2002, pp. 332-344.

[50] Tomblin, J. S., Seneviratne, W. P., Kim, H., and Lee, J., "Box Beam Lap Shear Torsion Testing for Evaluating Structural Performance of Adhesive Bonded Joints," *Joining and Repair of Composites Structures, ASTM STP 1455,* In K. T. Kedward and H. Kim, Eds., ASTM International, 2004, pp. 42-54.

[51] ARAMIS, v. 5.3.0 User Manual, GOM mbH.

[52] Tomblin, J. S., Seneviratne, W. P., and Borgman, M. D., "Electronic Speckle Pattern Interferometry for Investigating Defect Propagation of Honeycomb Sandwich Specimens," SAMPE Technical Conference, Baltimore, MD, November, 2001.

[53] Life Data Analysis Reference, ReliaSoft Corporation, Tucson, AZ.

[54] Badaliance, R., and Dill, H. D., "Compression Fatigue Life Prediction Methodology for Composite Structures," NADC-83060-60, Volumes I and II, September, 1982.

[55] Whitehead, R. S., and Schwarz, M. G., "The Role of fatigue Scatter in the Certification of Composite Structures," ASTM Symposium on the Long Term Behavior of Composites, Williamsburg, VA, March, 1982.

[56] Seneviratne, W. P., "Fatigue Analysis of Liberty XL2 Fuselage Materials," National Institute for Aviation Research, STR-RP-2008-005, September, 2008.

[57] Abrate S., *Impact on Composite Structures,* Cambridge University Press, United Kingdom, 1998.

[58] Gabriel, E.A., DeFiore, T., Locke, J.E., and Smith, H.W., "General Aviation Aircraft—Normal Acceleration Data Analysis and Collection Project," DOT/FAA/CT-91/20, Department of Transportation, Federal Aviation Administration, Washington, D.C., 1993.

[59] "Fatigue Evaluation of Wing and Associated Structure of Small Airplanes," AFS-120-73-2, May, 1973.

[60] Ilcewicz, L., "Composite Damage Tolerance and Maintenance Safety Issues," FAA Damage Tolerance and Maintenance Workshop, Rosemont, IL, July, 2006.

[61] Tomblin, J. S., and Seneviratne, W. P., "Research on Structural Test and Analysis Protocol: Progress & Plan," Commercial Aircraft Composite Repair Committee (CACRC) Meeting & Workshop for Composite Damage Tolerance & Maintenance, Amsterdam, Netherlands, May, 2007.

[62] Whittaker, I. C., and Besuner, P. M., "A Reliability Analysis Approach to fatigue Life Variability of Aircraft Structures," AFML-TR-69-65, April, 1969.

[63] Stover, P., and Wong, R., "Forward Wing Damage Tolerance Test (FT-556) Model 2000," Report No. 122E349S, Beech Aircraft Corporation, Wichita, KS, January, 1986.

[64] Krog, L., Tucker, A., Kemp, A., and Boyd, R., "Topology Optimization of Aircraft Wing Box Rib," *Proceeding of the 10th AIAA/ISSMO Multidisciplinary Analysis and Optimization Conference,* AIAA-2004-4481, Albany, New York, August, 2004.

APPENDICES

APPENDIX A

SCATTER ANALYSIS RESULTS

This section contains the Wohler (S-N) curves that were used for the fatigue life scatter analysis of FAA-LEF database. Sendeckyj analysis was conducted for the S-N data, and the fitting curves are displayed here for a graphical confirmation that the analysis represents a reasonable trend. S-N curves based on the Sendeckyj analysis are compared with the life predictions based on Kassapoglou method, which only uses static-strength data to predict fatigue life. In addition, for several selected fatigue specimens, the compliance change and the damage growth are compared.

A.1. S-N Data for AS4/E7K8 Plain-Weave Fabric

This section contains the S-N data for AS4-PW test data included in the FAA-LEF database. Tables A.1 through A.6 include the individual data points, while Figures A.1 through A.14 show the S-N curves that were used for generating LEFs for AS4-PW. Figure A.15 shows the Goodman diagram for AS4-PW OH test data. In these tables, n is the number of cycles survived and n=1 indicate static failure. Also, σ_A and σ_R correspond to the fatigue stress level (or static failure stress level) and the residual strength after surviving the corresponding number of cycles, respectively.

TABLE A.1

S-N DATA FOR AS4-PW 10/80/10 OPEN-HOLE TESTS (FAA-LEF)

OHC/T (R = -1)			OHC (R = 5)			OHT (R = 0)			OHT (R = -0.2)		
σ_A	n	σ_R	σ_A	n	σ_R	σ_A	n	σ_R	σ_A	n	σ_R
41228	1		41228	1		43792	1		43792	1	
39404	1		39404	1		44405	1		44405	1	
40497	1		40497	1		43580	1		43580	1	
39811	1		39811	1		43112	1		43112	1	
43154	1		43154	1		42126	1		42126	1	
38740	1		38740	1		43717	1		43717	1	
30354	301		30354	2645		34764	20505		32591	18137	
26307	2195		30354	15660		34764	15422		32591	18575	
26307	1407		30354	11740		34764	10607		32591	21301	
26307	1412		30354	9151		34764	11684		32591	22457	
26307	1751		30354	10990		34764	6077		32591	34293	
26307	1996		30354	8239		34764	11195		32591	17588	
26307	1442		30354	11057		32591	38373		28246	153000	
26307	1927		28330	69069		32591	55456		28246	119454	
26307	4746		28330	44082		32591	46146		28246	31998	
20236	36171		28330	98781		32591	71250		28246	151318	
20236	29470		28330	90522		32591	57471		28246	142394	
20236	31608		28330	114108		32591	54131		28246	178984	
20236	32681		28330	52521		28246	474638		26073	226885	
20236	30972		28330	50311		28246	377554		26073	390390	
20236	26187		28330	70955		28246	368844		26073	451383	
20236	30657		26307	188105		28246	314495		26073	270902	
20236	75965		25497	229685		28246	365748		26073	425390	
16189	549419		25497	445665		28246	389959		26073	281893	
16189	652440		25497	348791		21728	1000000	41546	26073	332591	
16189	545138		25497	443210					23900	1000000	30517
16189	715247		25497	726570					23900	1000000	29613
16189	519140		25497	574103					23900	1000000	26546
16189	503585		24283	1000000	36385						
16189	881812		24283	1000000	34324						
16189	771513										

TABLE A.2

S-N DATA FOR AS4-PW 10/80/10 CAI AND DNC TESTS (FAA-LEF)

CAI (R = 5) [20-ply] - BVID			CAI (R = 5) [40-ply] - VID			DNC (R = -1)			DNC (R = -0.2)		
σ_A	n	σ_R	σ_A	n	σ_R	σ_A	n	σ_R	σ_A	n	σ_R
34974	1		28945	1		4236	1		4236	1	
35928	1		31307	1		3804	1		3804	1	
32913	1		30476	1		3836	1		3836	1	
27684	9071		30525	1		3948	1		3948	1	
27684	5856		29743	1		4037	1		4037	1	
27684	8980		30585	1		4068	1		4068	1	
27684	16161		22698	9471		1595	7231		1994	25321	
27684	10644		22698	15663		1595	7524		1994	28298	
27684	9777		22698	7994		1595	6586		1795	27417	
25954	34539		22698	21448		1595	8621		1795	17379	
25954	66766		22698	6833		1595	8212		1795	10624	
25954	42237		22698	8538		1595	7256		1795	28230	
25954	17223		21184	29471		1595	7150		1795	54216	
25954	43665		21184	47593		1196	25573		1795	27694	
25954	46917		21184	28418		1196	35487		1795	16090	
24224	99627		21184	63444		1196	34290		1595	72855	
22493	454828		21184	46077		1196	47904		1595	99058	
22493	740070		19671	601081		1196	48215		1595	50752	
22493	650366		19671	203021		1196	59366		1595	39812	
22493	468695		19671	145252		997	262210		1595	40000	
22493	450007		19671	538785		997	361803		1595	34484	
22493	709191		19671	374069		997	271419		1595	170739	
20763	1000000	35656				997	307399		1396	393302	
						997	194263		1396	238336	
						997	104738		1396	265252	
						678	1000000	3591	1396	170266	
									1396	221148	
									1396	121619	
									1196	711710	
									1196	1000000	3381
									1196	1000000	3540

TABLE A.3

S-N DATA FOR AS4-PW 0/100/0 CAI AND DNC TESTS (FAA-LEF)

OHT (R = -1)			TAI (R = 0) - BVID			TAI (R = 0) - VID		
σ_A	n	σ_R	σ_A	n	σ_R	σ_A	n	σ_R
21231	1		17631	1		15690	1	
21970	1		17409	1		15744	1	
22082	1		17550	1		14612	1	
21821	1		18326	1		14150	1	
22254	1		18078	1		15333	1	
21890	1					15180	1	
13125	1211		14239	137		10583	464	
10937	6730		9789	500		9071	860	
10937	13547		9789	392		9071	808	
10937	7729		8899	3001		9071	976	
10937	7957		8899	2709		9071	1933	
10937	7893		8899	695		9071	667	
10937	6812		8899	675		9071	768	
8750	57561		8899	717		8315	1226	
8750	83056		8899	621		8315	5471	
8750	47243		8899	745		7559	4243	
8750	65033		8009	7164		7559	15903	
8750	121089		8009	9277		7559	5396	
8750	66003		8009	2982		7559	7275	
7656	210460		8009	7037		7559	7844	
7656	191852		8009	7196		7559	29967	
7656	194105		8009	5607		6803	66940	
7656	216642		7120	249488		6803	38624	
7656	216727		7120	448722		6803	70854	
7656	254909		7120	79665		6803	142973	
6562	990178		7120	138485		6803	107914	
			7120	173554		6803	25250	
			7120	153293		6501	556214	
			6764	807275		6501	1000020	
			6764	840693		6047	698405	
			6230	1000027	12663	6047	1000011	13543
						6047	1000022	14565

TABLE A.4

S-N DATA FOR AS4-PW 25/50/25 OHT AND CAI TESTS (FAA-LEF)

OHT (R = -1)		CAI (R = 5) - BVID		CAI (R = 5) - VID		CAI (R = 5) - LID	
σ_A	n	σ_A	n	σ_A	n	σ_A	n
44593	1	37188	1	29149	1	25147	1
46643	1	34745	1	31335	1	25601	1
43391	1	35658	1	29443	1	24627	1
44080	1	36526	1	29282	1	25370	1
45918	1	36364	1	29950	1	25228	1
47623	1	35669	1	28866	1	26695	1
27225	14982	28820	12243	22374	37690	19083	42897
27225	11988	28820	14342	22374	24001	19083	38476
27225	15400	28820	9651	22374	55768	19083	18155
27225	7335	28820	8152	22374	28958	19083	13719
27225	8149	28820	15155	22374	11897	19083	32463
27225	16101	28820	26005	22374	16335	19083	17564
22687	129345	27019	92926	20882	127451	16539	201380
22687	105310	27019	31634	20882	94625	16539	214807
22687	142170	27019	104891	20882	128689	16539	374375
22687	103758	27019	152023	20882	59749	16539	278234
22687	117594	27019	47635	20882	143030	16539	165086
22687	117183	27019	31642	20882	180742	16539	193821
20419	446962	25217	678421	19391	626039	15267	2233805
20419	524270	25217	596825	19391	397153	15267	1352887
20419	604378	25217	323026	19391	270784	15267	1618147
20419	498321	25217	252255	19391	638545	15267	1236307
20419	949760	25217	575983	19391	222775	15267	928401
20419	916940	25217	252433	19391	595875	15267	1228113

TABLE A.5

S-N DATA FOR AS4-PW 40/20/40 CAI TESTS (FAA-LEF)

CAI (R = 5) - VID		
σ_A	n	σ_R
30623	1	
31444	1	
33538	1	
31473	1	
32526	1	
31465	1	
25476	11230	
25476	21414	
25476	10473	
25476	9354	
25476	10449	
23884	37414	
23884	27422	
23884	31761	
23884	40216	
23884	59635	
23884	45263	
20699	538811	
20699	800295	
20699	849092	
20699	774653	
20699	860179	
20699	726956	
20699	1000030	31056
20699	1000032	31272
20699	1000051	30183

TABLE A.6

S-N DATA FOR AS4-PW SANDWICH TESTS (FAA-LEF)

Flexure (R = 0)		
σ_A	n	σ_R
143.828	1	
145.592	1	
146.042	1	
146.530	1	
147.151	1	
139.028	1	
87.000	26661	
87.000	26077	
87.000	23272	
87.000	20000	
87.000	22000	
87.000	18898	
87.000	19928	
72.500	48648	
72.500	170000	
72.500	60000	
72.500	80000	
72.500	145000	
72.500	190000	
72.500	235000	
65.250	150000	
58.000	470000	
58.000	580000	
58.000	340000	
58.000	500000	
58.000	250000	
58.000	420000	
58.000	1000000	145.545

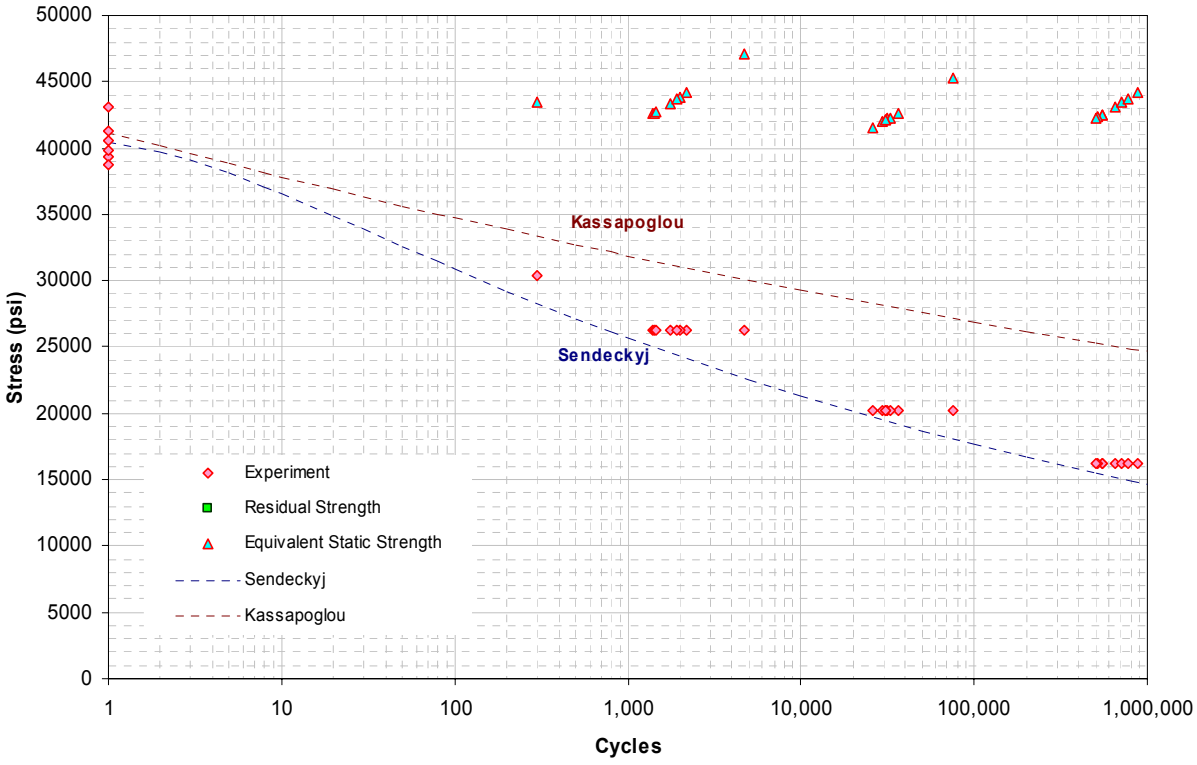

Figure A.1. AS4/E7K8 PW - 10/80/10, Open-hole, R =-1.

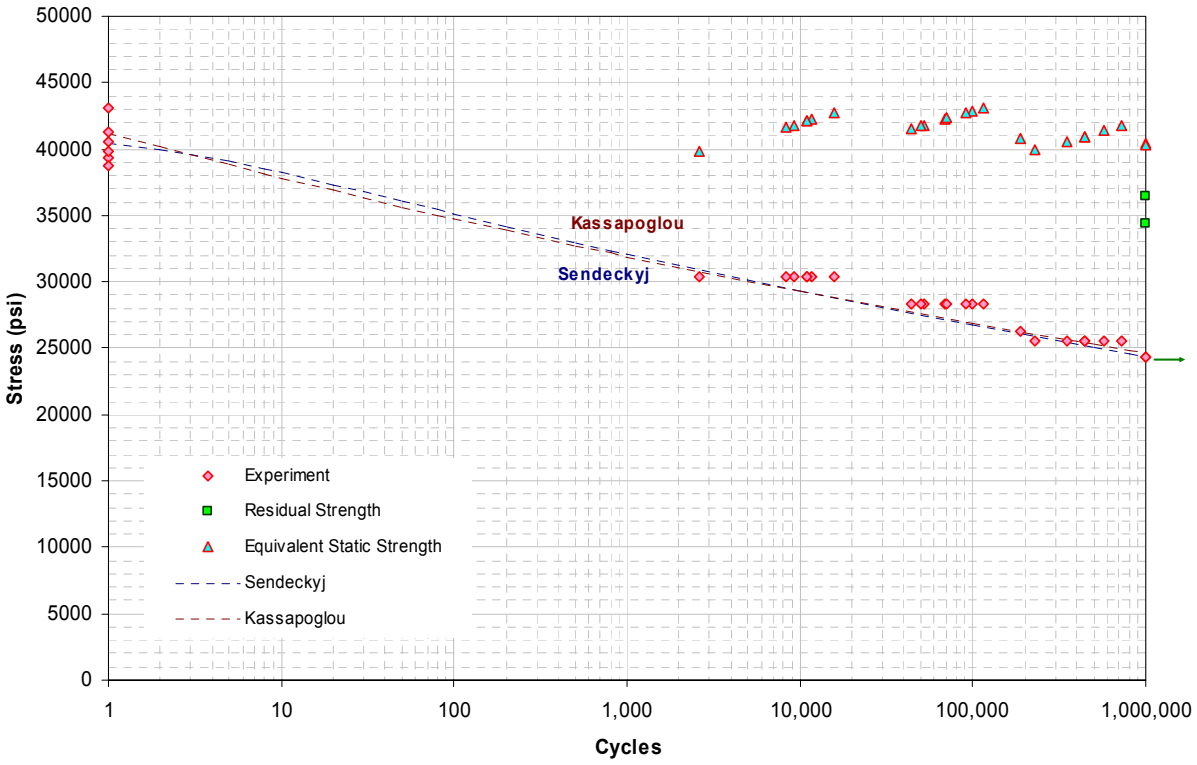

Figure A.2. AS4/E7K8 PW - 10/80/10, Open-hole, R=5.

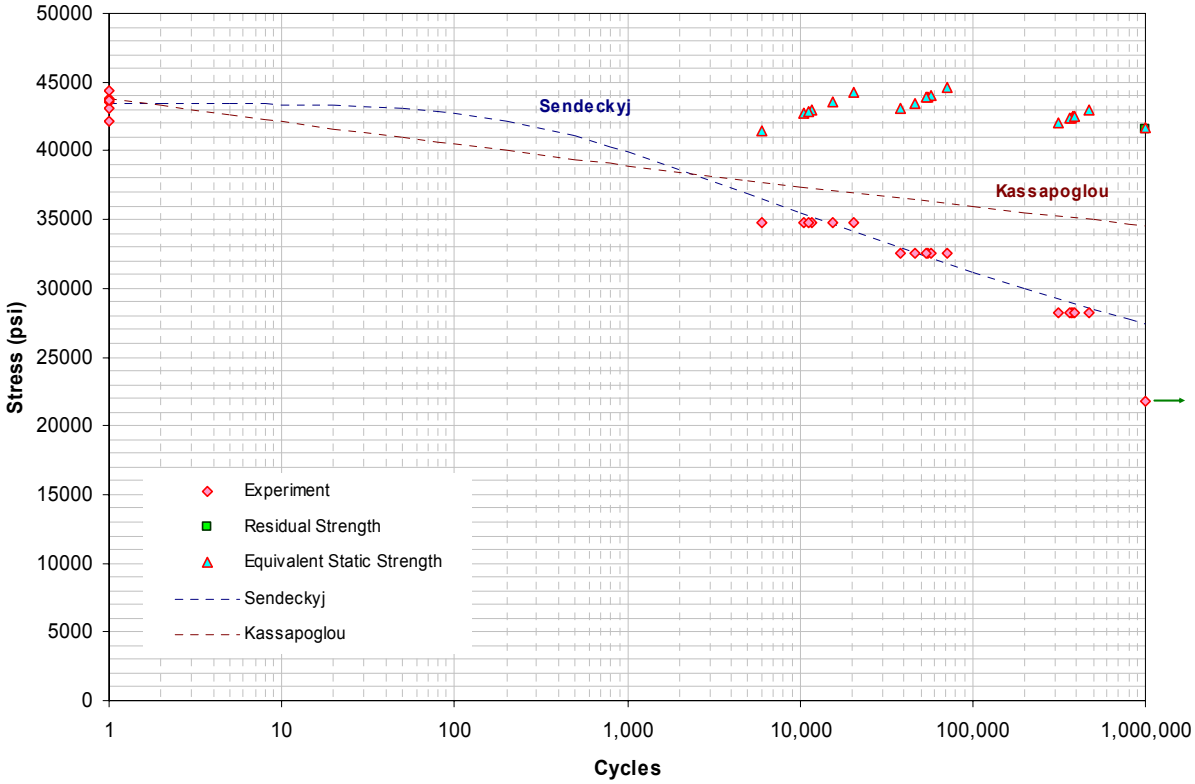

Figure A.3. AS4/E7K8 PW - 10/80/10, Open-hole, R=0.

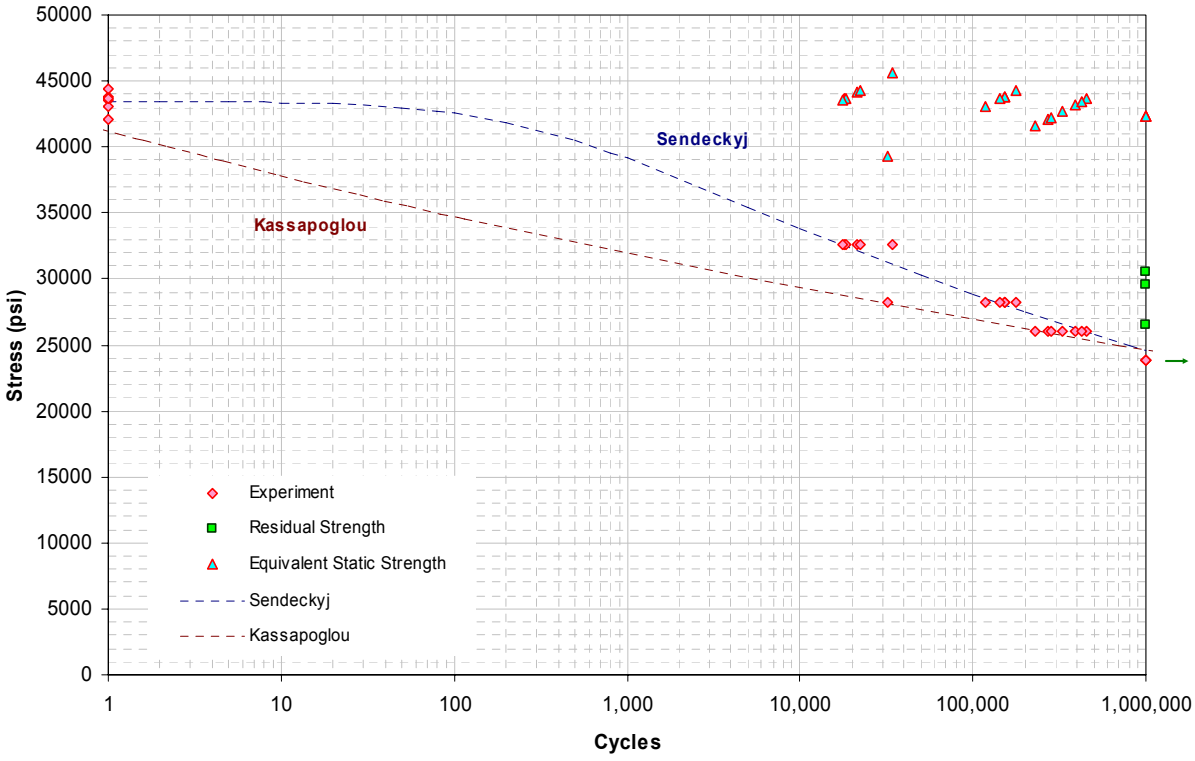

Figure A.4. AS4/E7K8 PW - 10/80/10, Open-hole, R=-0.2.

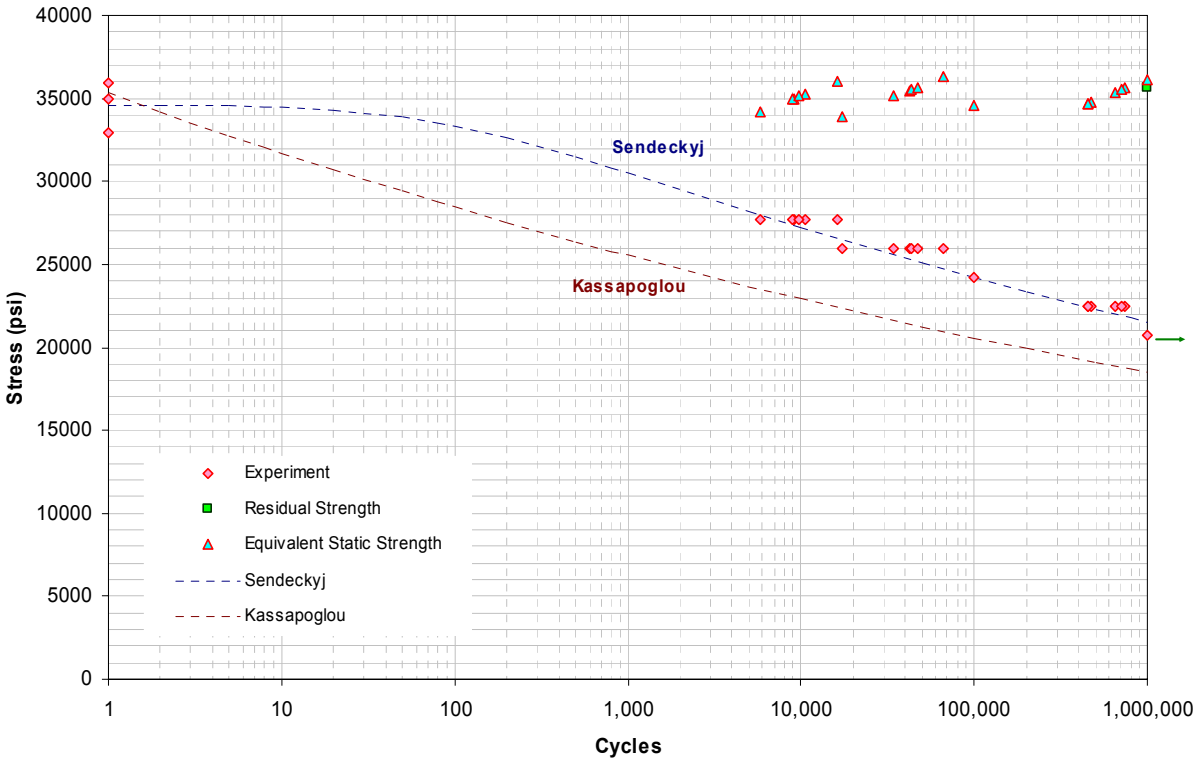

Figure A.5. AS4/E7K8 PW - 10/80/10, CAI (20-ply) – BVID, R=5.

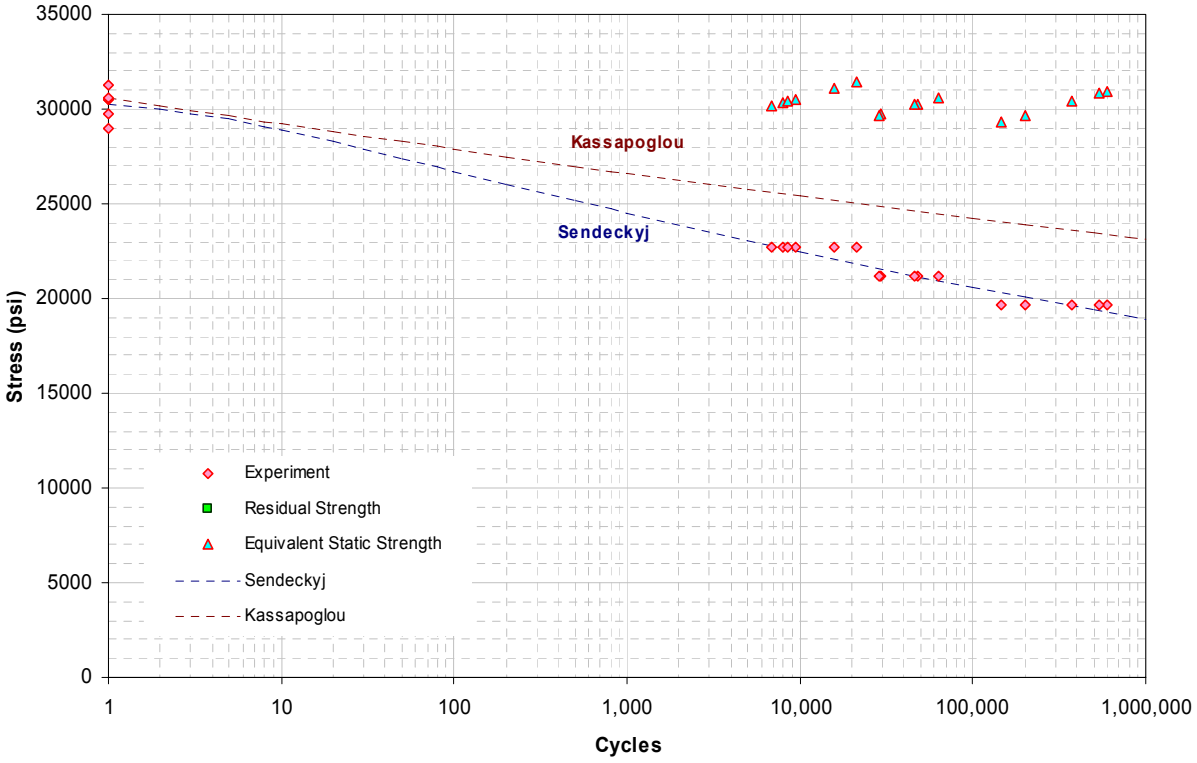

Figure A.6. AS4/E7K8 PW - 10/80/10, CAI (40-ply) – BVID, R=5.

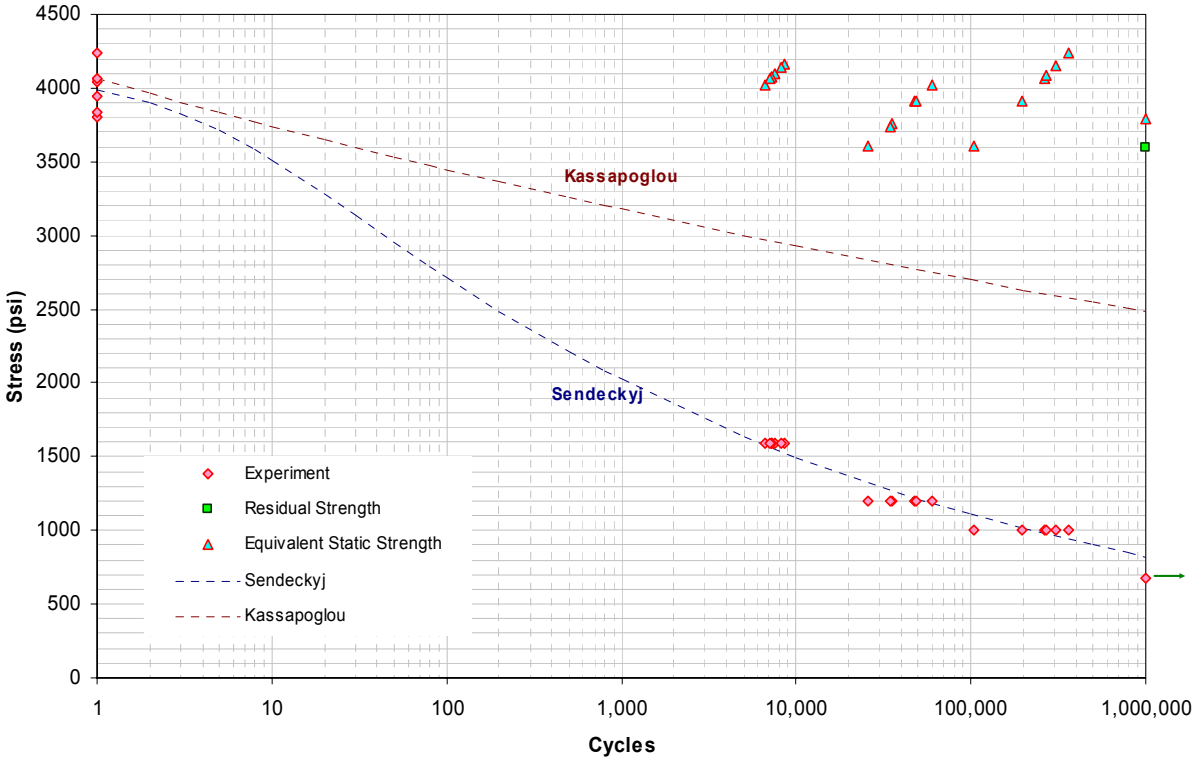

Figure A.7. AS4/E7K8 PW - 10/80/10, DNC, R=-1.

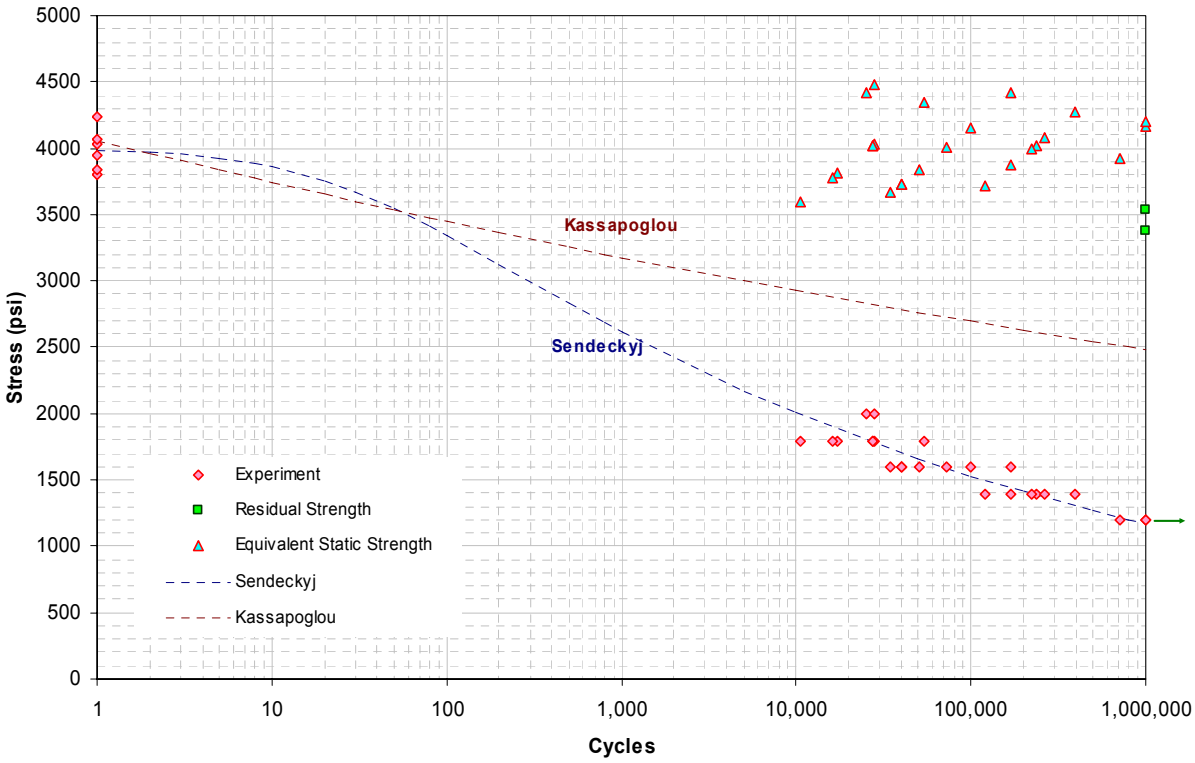

Figure A.8. AS4/E7K8 PW - 10/80/10, DNC, R=-0.2.

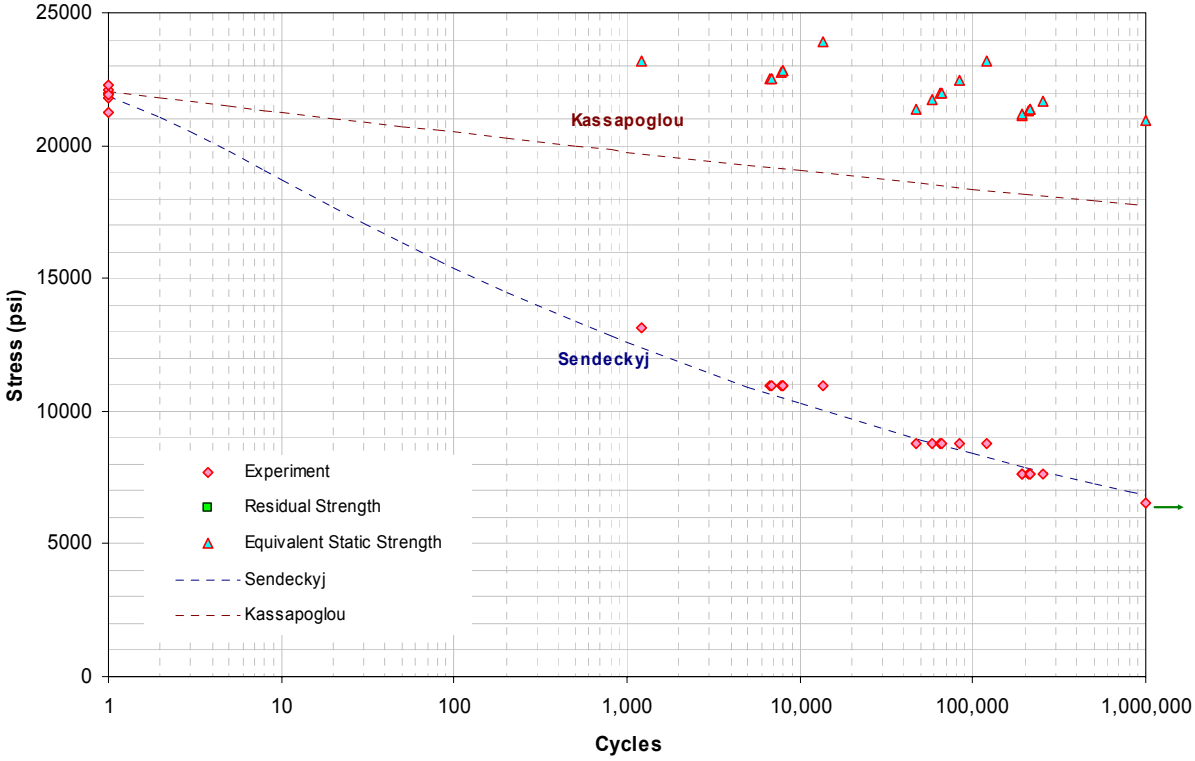

Figure A.9. AS4/E7K8 PW – 0/100/0, OH, R=-1.

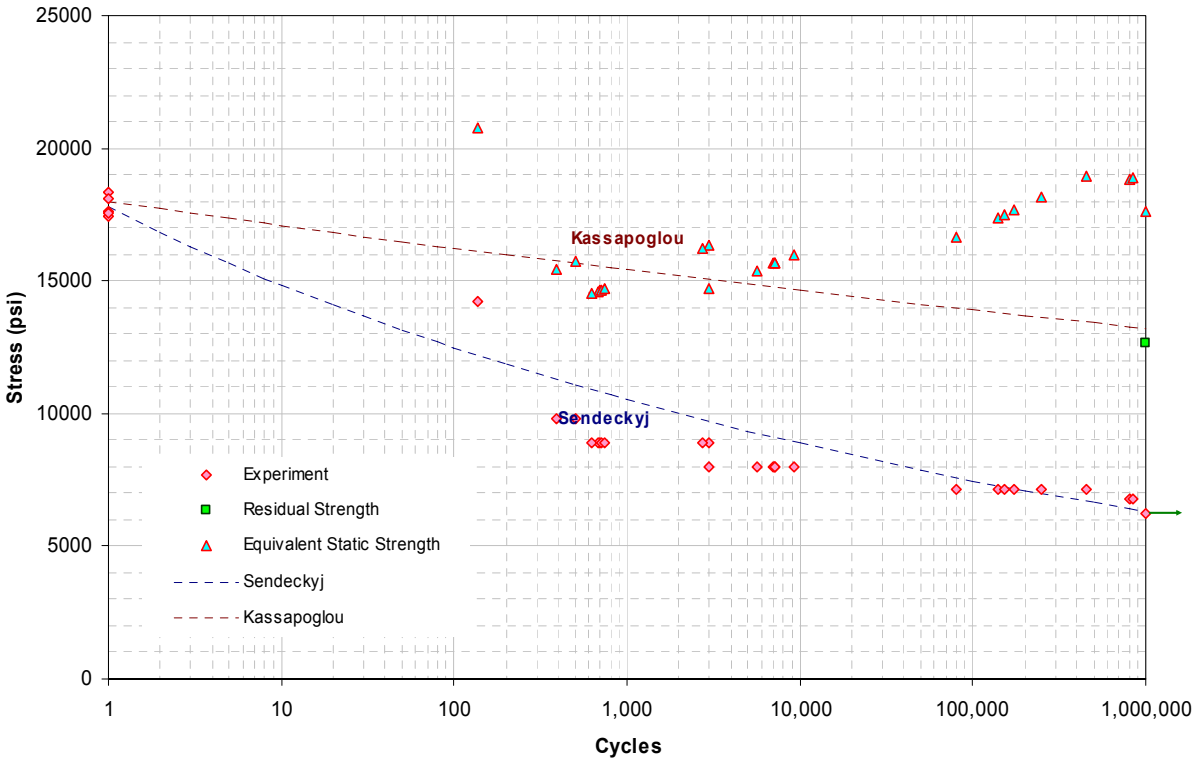

Figure A.10. AS4/E7K8 PW – 0/100/0, TAI - BVID, R=0.

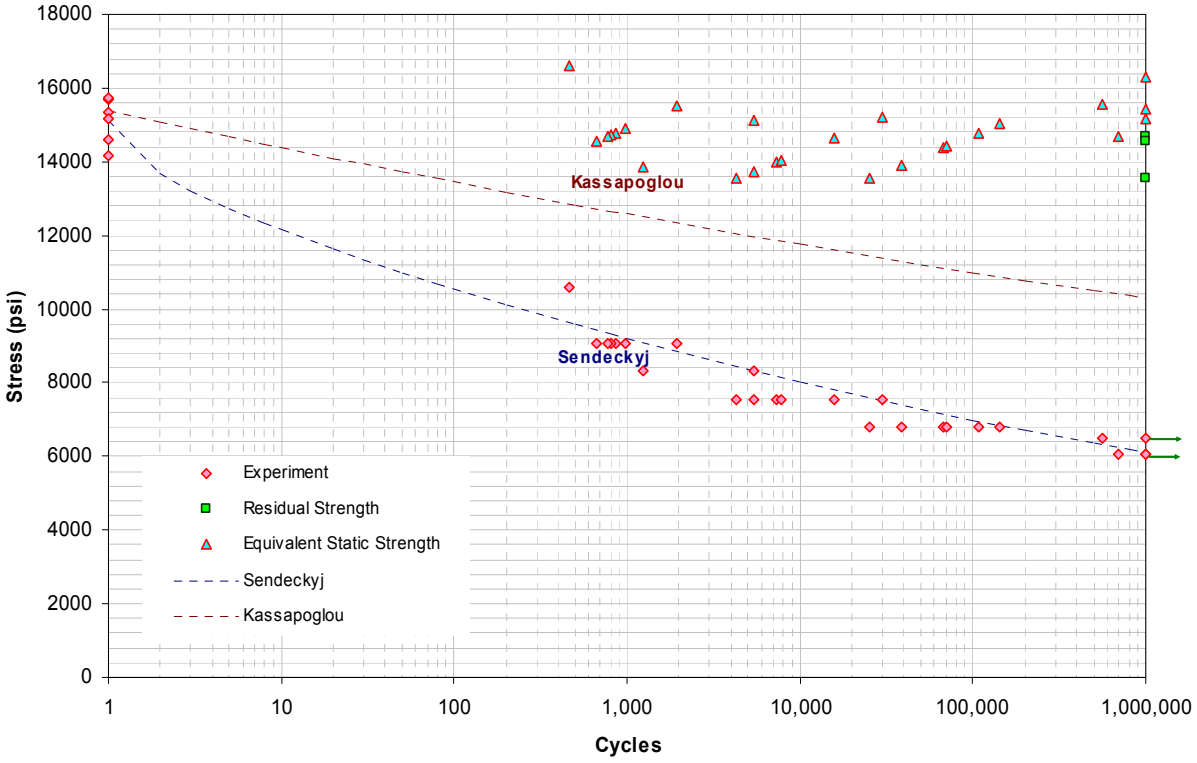

Figure A.11. AS4/E7K8 PW – 0/100/0, TAI - VID, R=0.

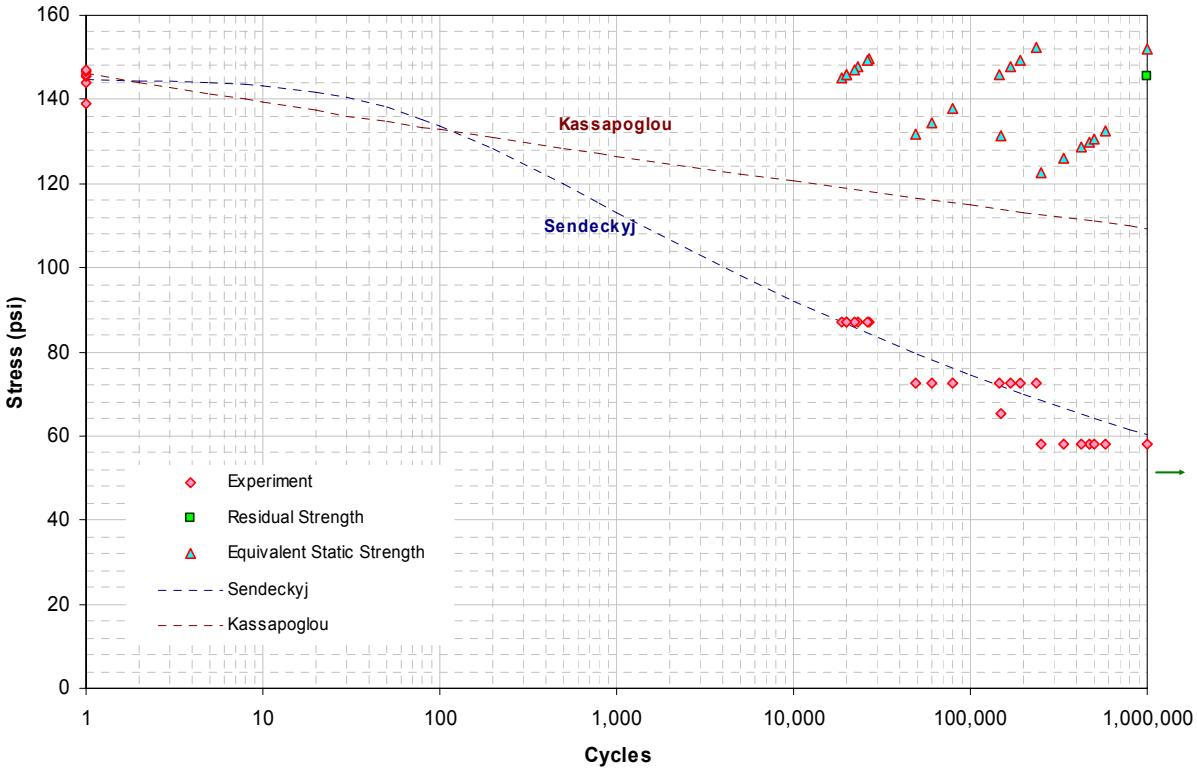

Figure A.12. AS4/E7K8 PW – HRH 10, Flexture, R=0.

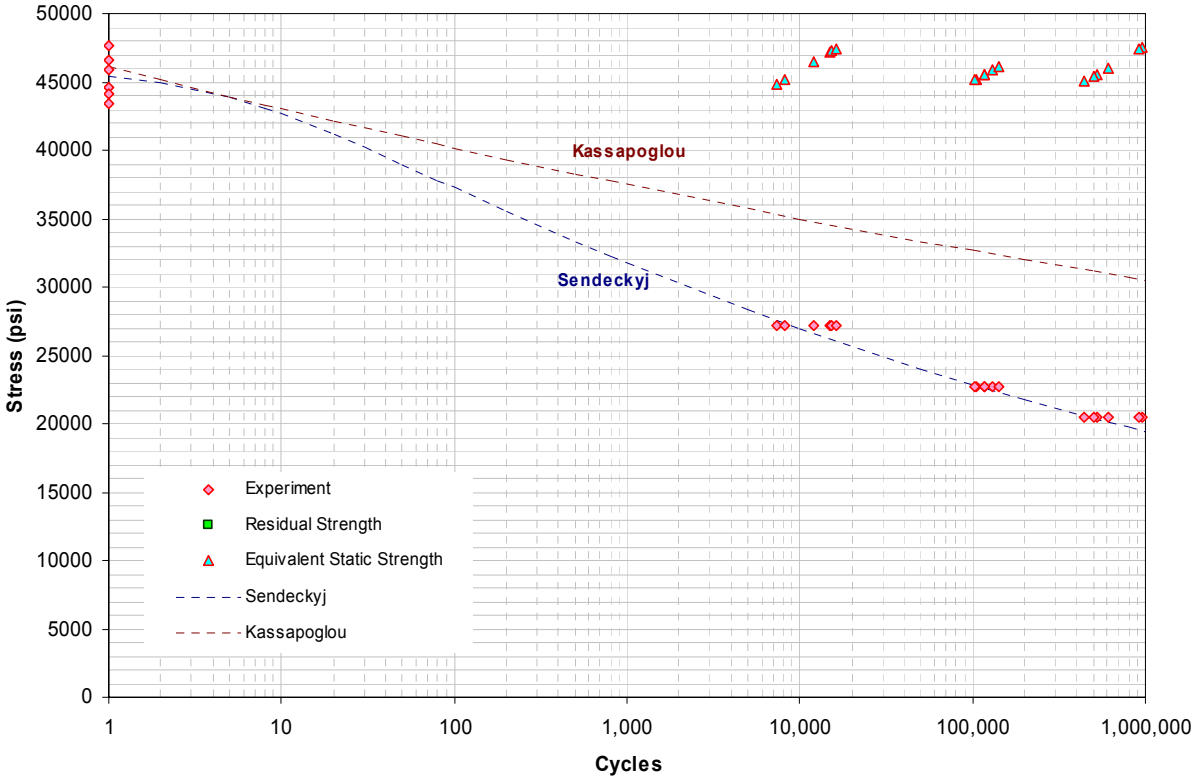

Figure A.13. AS4/E7K8 PW – 25/50/25, OH, R=-1.

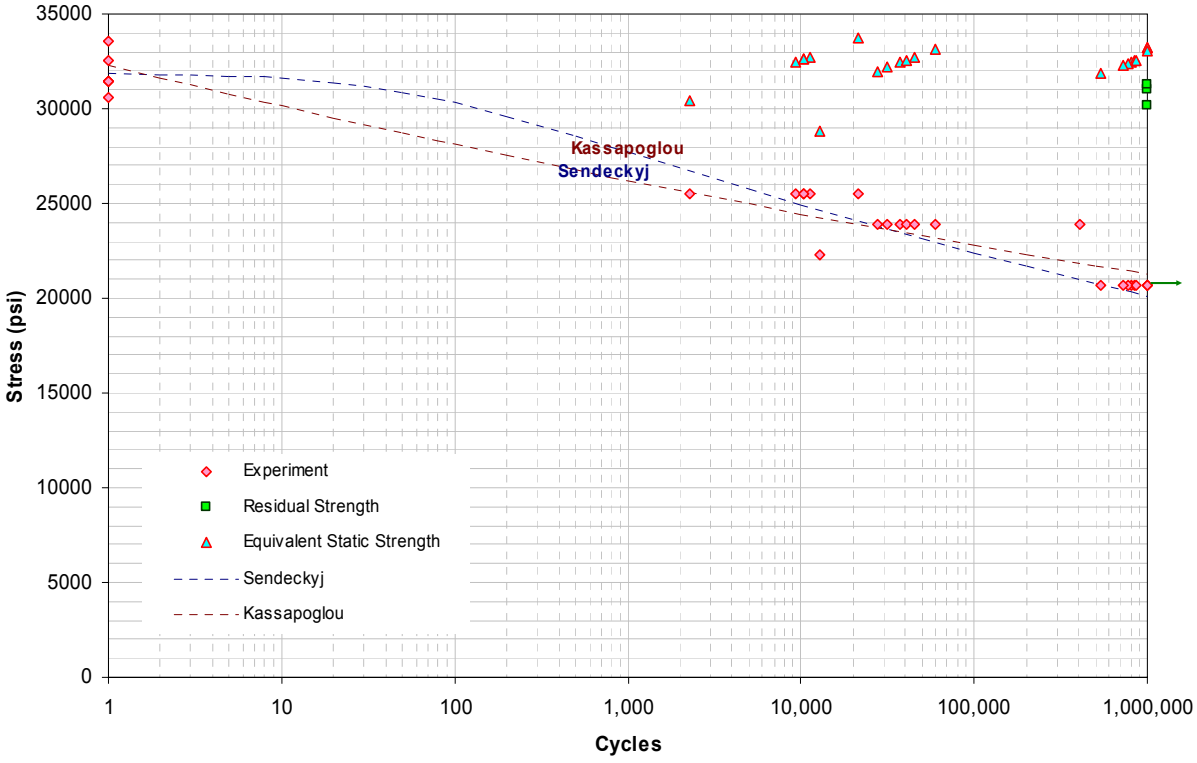

Figure A.14. AS4/E7K8 PW – 40/20/40, CAI - VID, R=5.

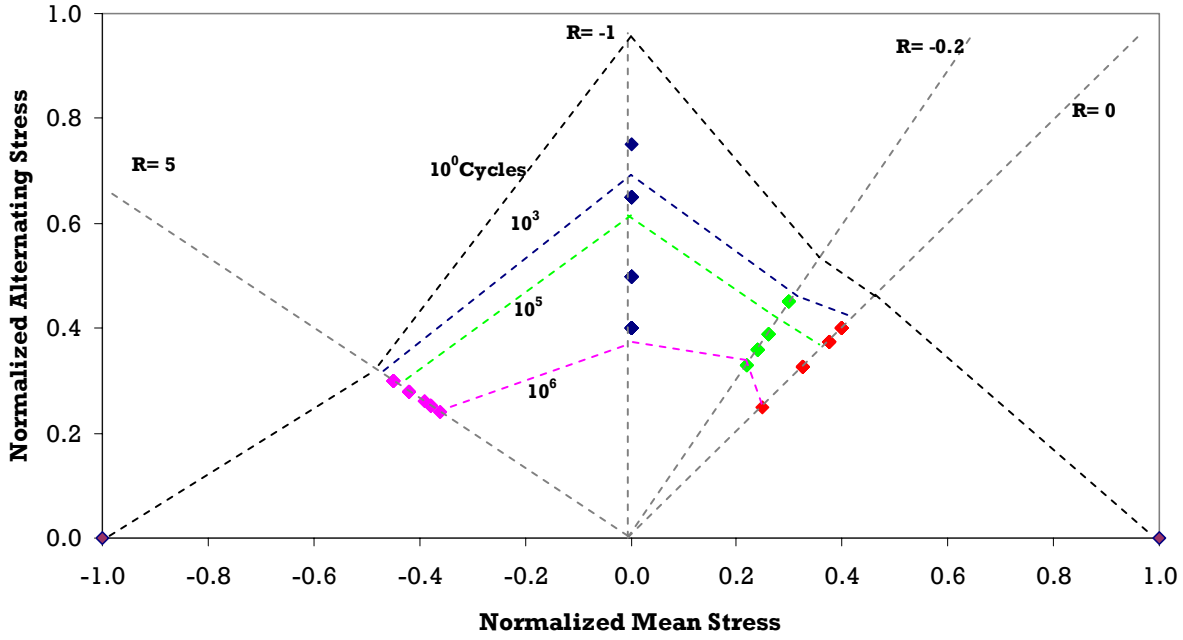

Figure A.15. Goodman diagram based on AS4/E7K8 PW OH test data.

A.2. Progressive Damage Failure and Compliance Change

The damage progression of several selected fatigue specimens was monitored by TTU C-scanning. The damage growth was then compared with the compliance change of those specimens during fatigue testing. Compliance was measured by the following: (a) stopping the fatigue test and periodically conducting a quasi-static test (Static), (b) collecting load-displacement data during fatigue at several fatigue interval (Dynamic), (c) using extensometer data (Ext.), and (d) using a laser extensometer (Laser). These data are shown in Figures A.16 though A.22 for several OHC and flexure specimens.

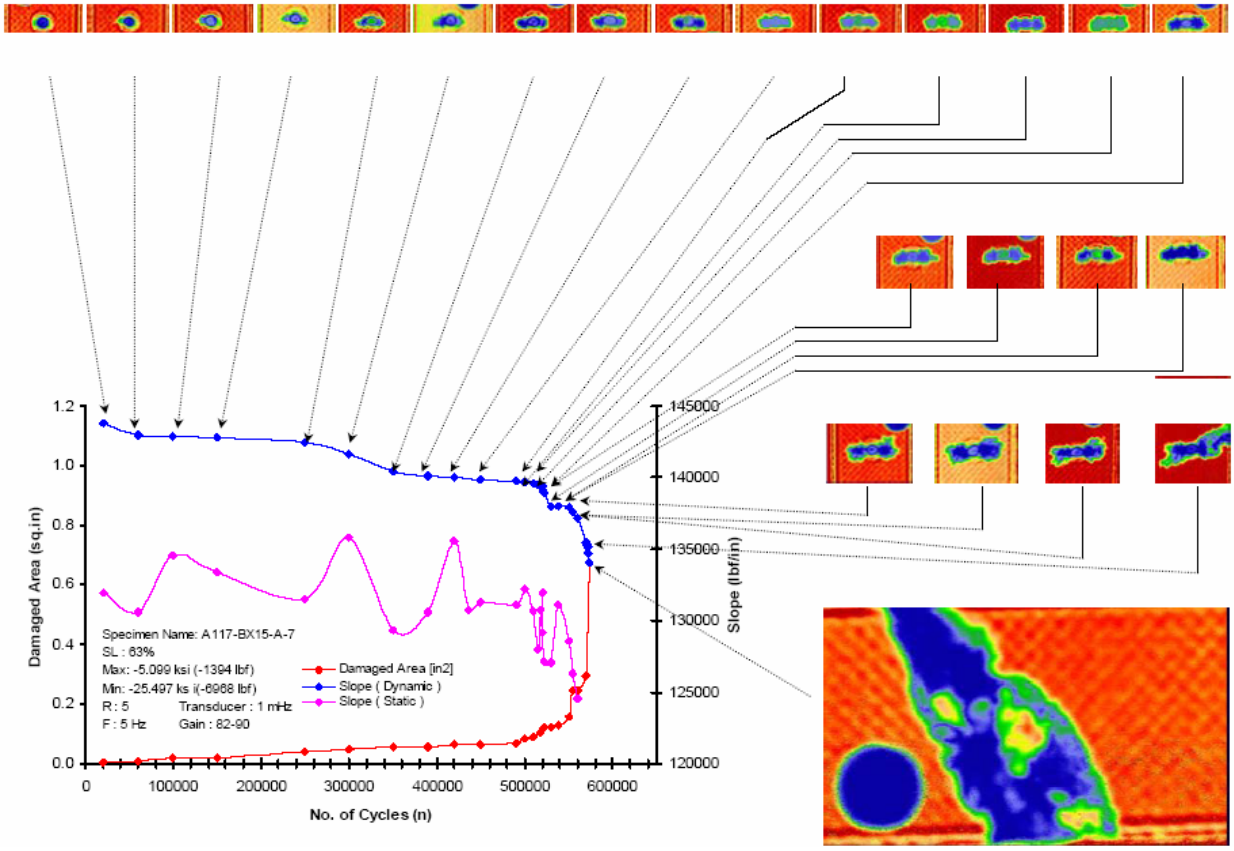

Figure A.16. AS4/E7K8 PW – 10/80/10, OHC, R=5, Stress Level=63% of static.

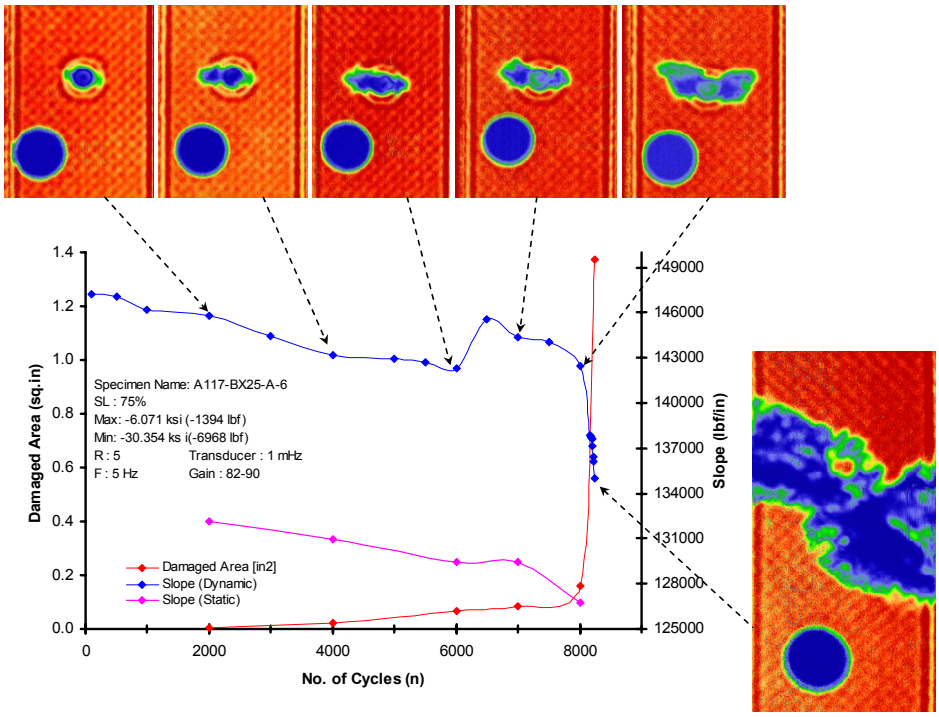

Figure A.17. AS4/E7K8 PW – 10/80/10, OHC, R=5, Stress Level=75% of static.

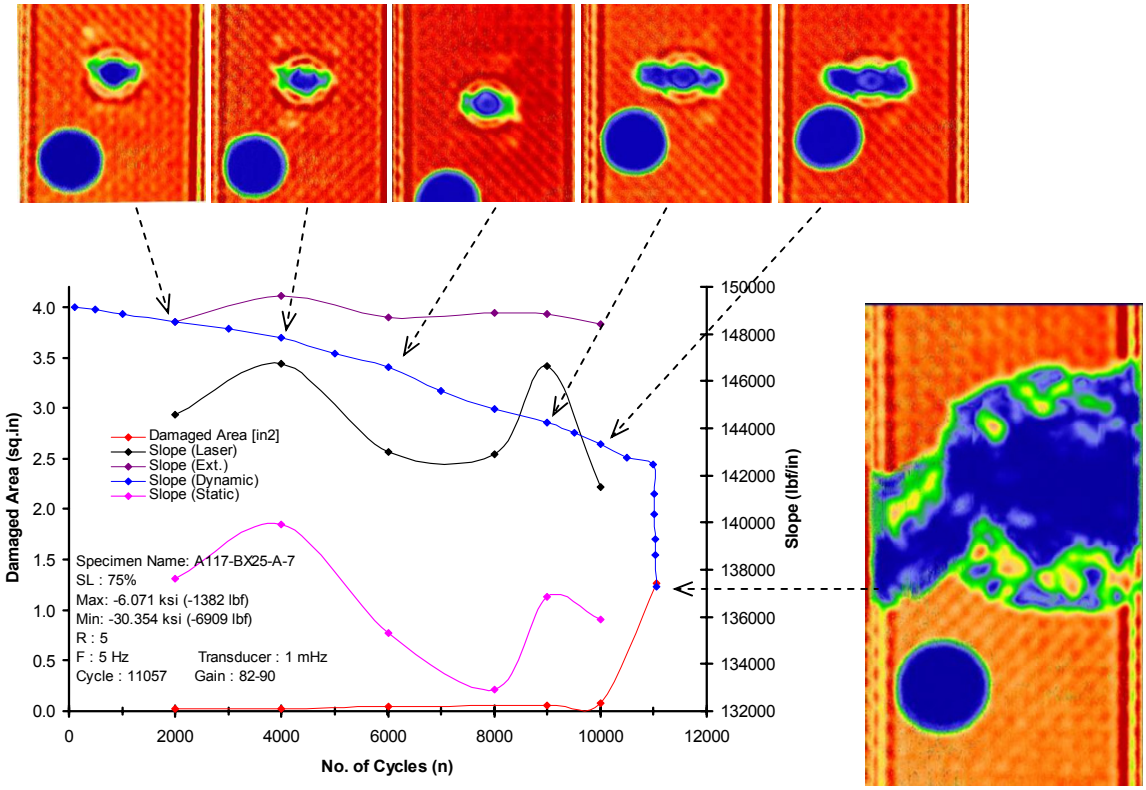

Figure A.18. AS4/E7K8 PW – 10/80/10, OHC, R=5, Stress Level=75% of static.

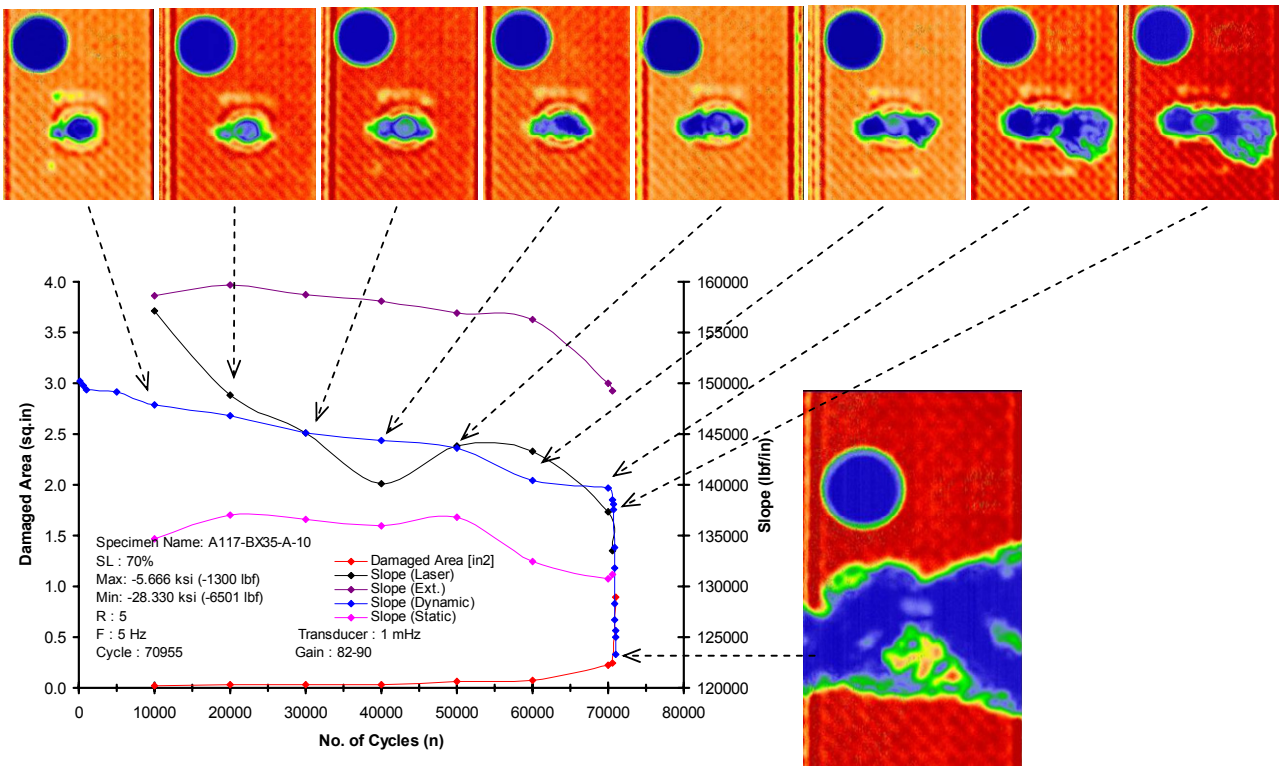

Figure A.19. AS4/E7K8 PW – 10/80/10, OHC, R=5, Stress Level=70% of static.

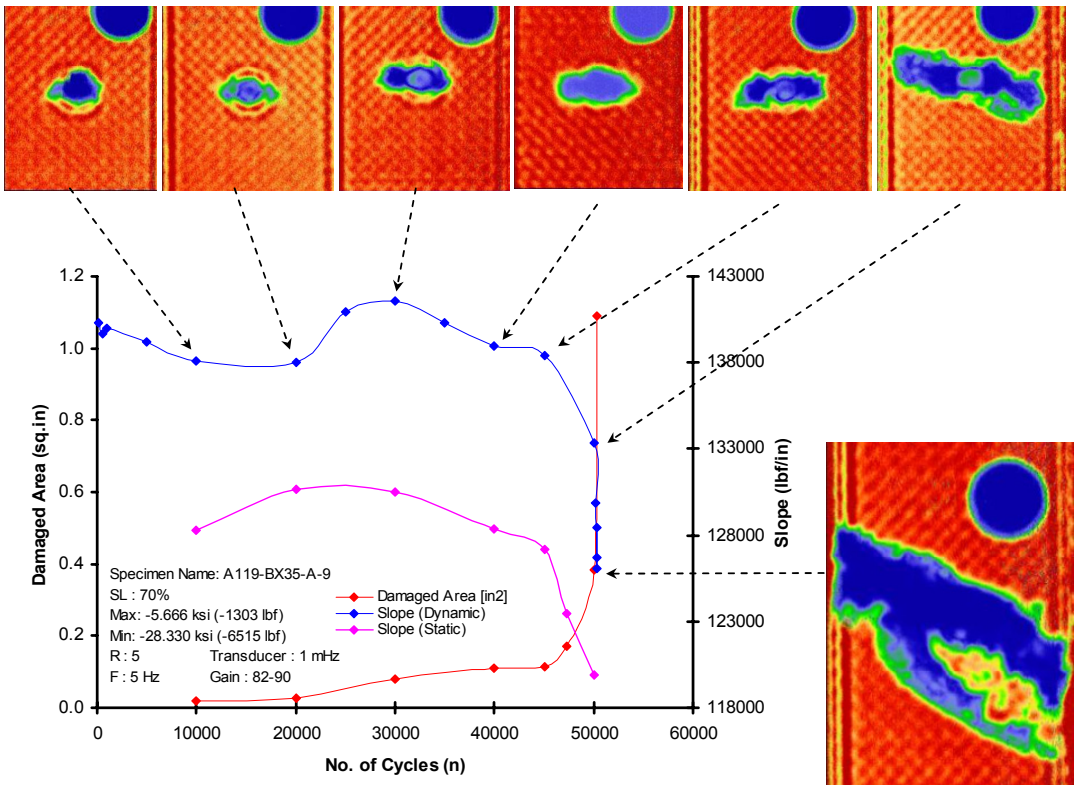

Figure A.20. AS4/E7K8 PW – 10/80/10, OHC, R=5, Stress Level=70% of static.

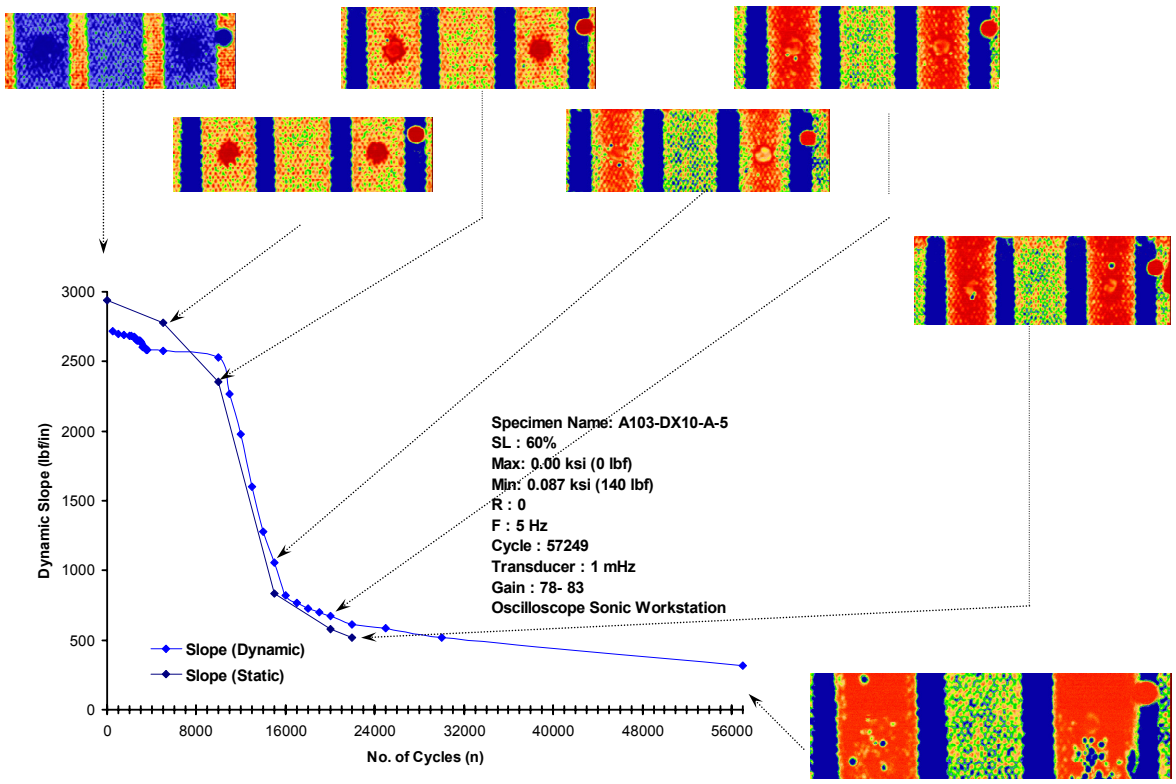

Figure A.21. AS4/E7K8 PW and HRH10 – sandwich, Flexure, R=0, Stress Level=60% of static.

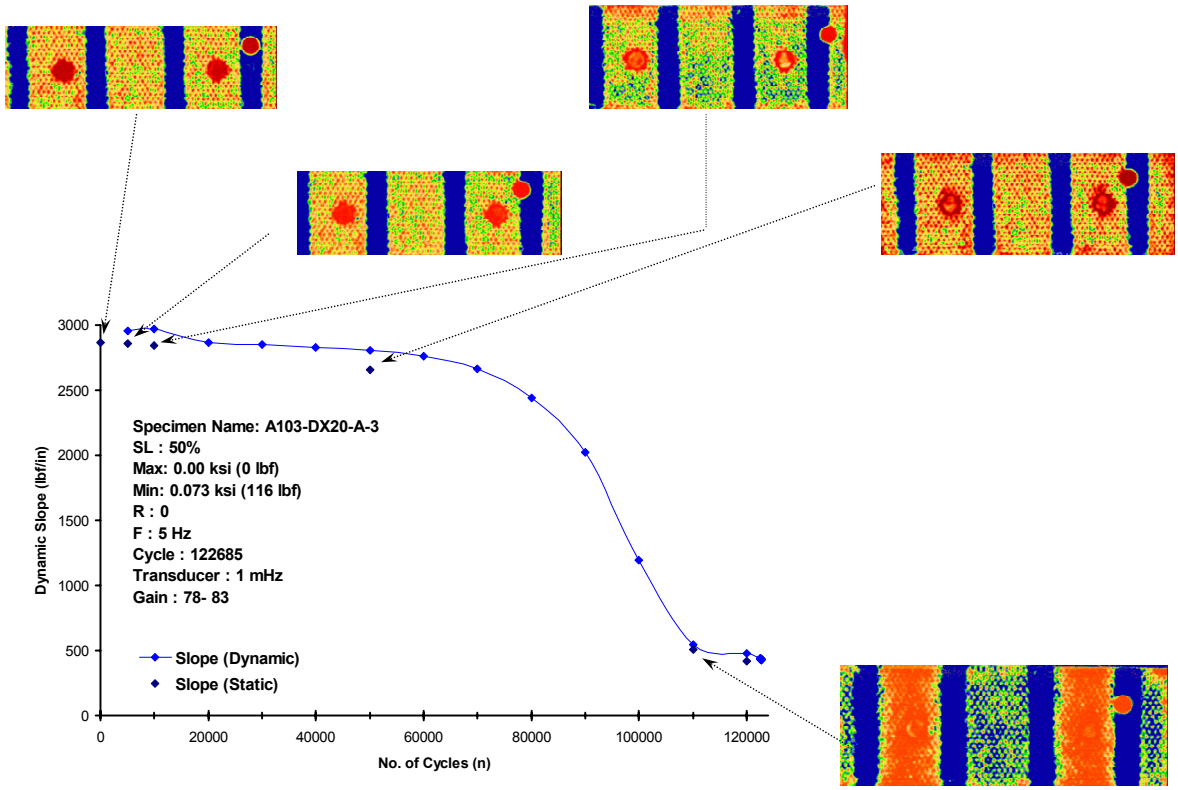

Figure A.22. AS4/E7K8 PW and HRH10 – sandwich, Flexure, R=0, Stress Level=50% of static.

Figures A.21 and A.22 show that the sandwich specimens carried the fatigue loads after significant damage propagation because the sandwich facesheets carried most of the loads as in-plane tensile loads after the core shear capabilities were diminished. Therefore, after observing the compliance change, a ten percent decrease in compliance was considered as the fatigue failure and the corresponding cycles were recorded as the number of fatigue cycles that the sandwich survived.

The compliance changes and the corresponding C-scan damage area for the three stress levels, i.e., 75, 70, and 63 percent of OHC static strength, of several selected fatigue specimens with a stress ratio of 5 are superimposed for comparison in Figure A.23.

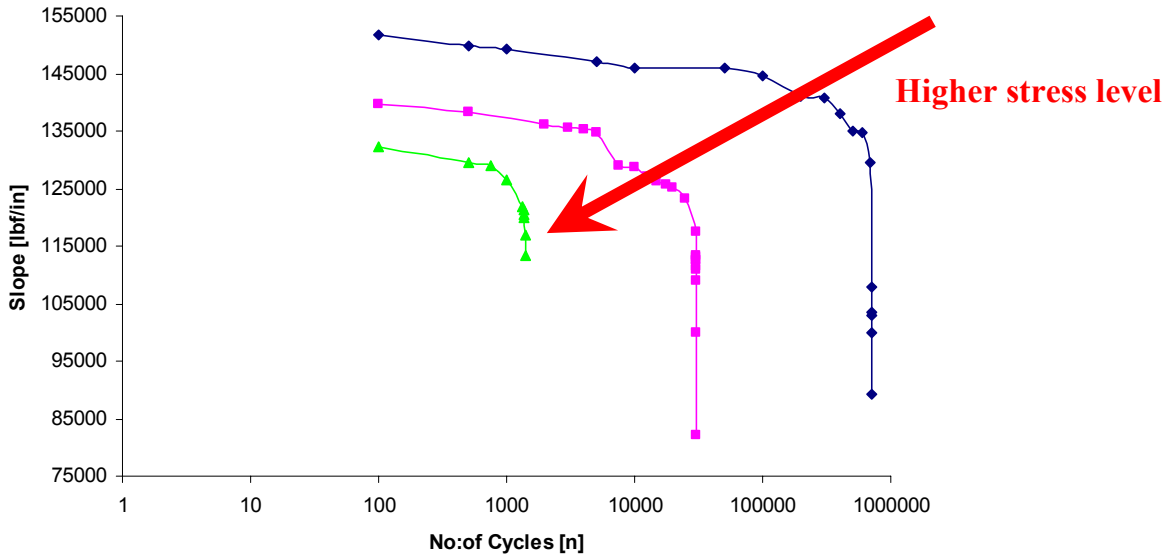

(a) Compliance change.

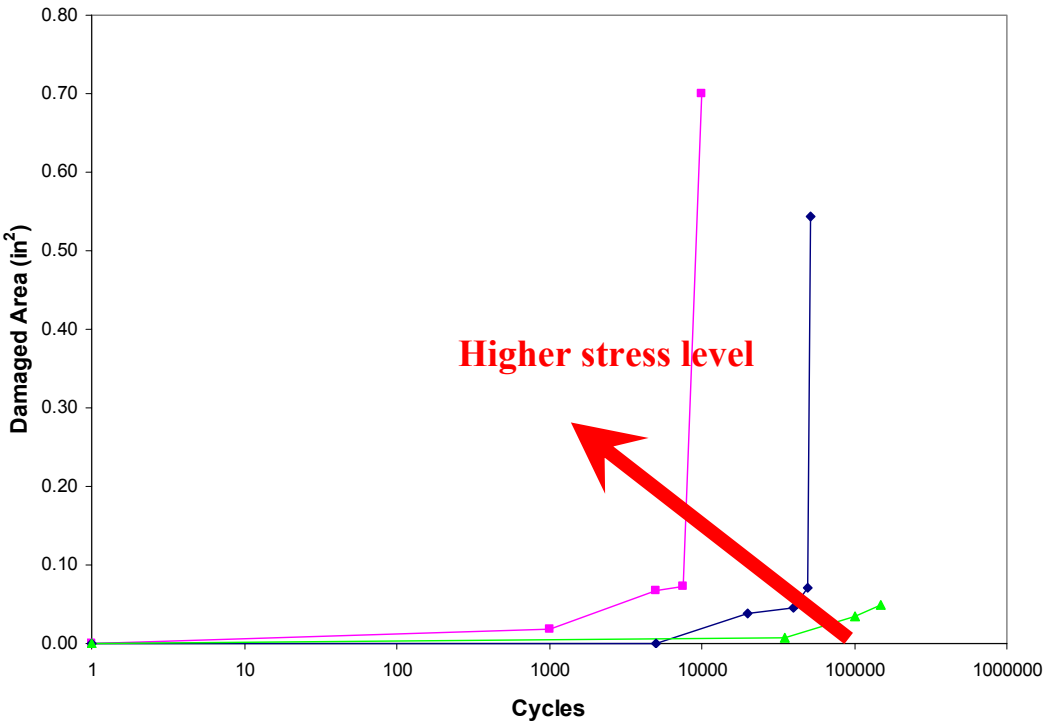

(b) Damage growth

Figure A.23. General trends of compliance change and damage growth for AS4-PW OH fatigue specimens.

A.3 S-N Data for T700/#2510 Pain-Weave Fabric

This section contains the S-N data for T700-PW test data included in the FAA-LEF database. Tables A.7 and A.8 include the individual data points, while Figures A.24 through A.27 show the S-N curves that were used for generating LEFs for T700-PW. In these tables, n is the number of cycles survived and n=1 indicate static failure. Also, σ_A and σ_R correspond to the fatigue stress level (or static failure stress level) and the residual strength after surviving the corresponding number of cycles, respectively.

TABLE A.7

S-N DATA FOR T700-PW OPEN-HOLE TESTS (FAA-LEF)

OHC/T (R = -1)			OHC (R = 5)			OHT (R = 0)			OHT (R = -0.2)		
σ_A	n	σ_R	σ_A	n	σ_R	σ_A	n	σ_R	σ_A	n	σ_R
33650	1		33650	1		41414	1		41414	1	
34576	1		34576	1		43186	1		43186	1	
35063	1		35063	1		41602	1		41602	1	
36487	1		36487	1		40934	1		40934	1	
35204	1		35204	1		42189	1		42189	1	
34936	1		34936	1		40789	1		40789	1	
24490	2532		31487	2185		35433	2338		33349	8451	
24490	2701		31487	1889		35433	780		33349	7003	
24490	3810		31487	1426		35433	500		33349	8196	
24490	3644		31487	4263		35433	331		33349	7766	
24490	5948		31487	2152		35433	1521		33349	11553	
24490	6102		31487	2466		34599	1879		33349	17718	
20992	47865		29738	27956		34599	3919		31264	36959	
20992	32017		29738	15207		34599	6211		31264	28014	
20992	34468		27989	89462		34599	12937		31264	43575	
20992	54001		27989	27907		34599	17960		31264	69444	
20992	32295		27989	38103		33349	21575		31264	71510	
20992	38393		27989	101532		33349	8256		31264	34351	
19242	231143		27989	16926		33349	17272		29180	157157	
19242	251069		27989	72487		33349	13863		29180	270388	
19242	245405		26239	455423		33349	18214		29180	524950	
19242	112840		26239	853210		33349	22073		29180	359994	
19242	116223		26239	427342		31264	169971		29180	381294	
19242	146589		26239	351708		31264	128793		29180	527262	
17493	1056026	29027	26239	218416		31264	188066		29180	1000183	29513
17493	1046017	29668	26239	614718		31264	65969				
17493	1000019	27191	26239	1000014	34559	31264	159350				
			24490	1032657	35164	31264	82926				
						30014	240064				
						29180	1089903				
						29180	1000000	35566			

TABLE A.8

S-N DATA FOR T700-PW DNC AND SANDWICH TESTS (FAA-LEF)

DNC (R = -1)			DNC (R = -0.2)			Flexure (R = 0)		
σ_A	n	σ_R	σ_A	n	σ_R	σ_A	n	σ_R
2878	1		2878	1		131	1	
3244	1		3244	1		137	1	
2786	1		2786	1		139	1	
3245	1		3245	1		138	1	
3009	1		3009	1		138	1	
2878	1		2878	1		141	1	
1503	5331		1804	6616		82	11500	
1503	7402		1804	5045		82	5100	
1503	7835		1804	7781		82	5500	
1503	1512		1804	4842		82	21000	
1503	1661		1804	1757		82	22500	
1503	11515		1804	6017		82	6750	
1353	10811		1503	26712		82	24673	
1203	51912		1503	40696		82	34800	
1203	54388		1503	55920		82	24006	
1203	44383		1503	38398		69	44036	
1203	53626		1503	209297		69	60000	
1203	174360		1503	40675		69	114000	
1203	51686		1503	76358		69	78025	
1203	43064		1353	403412		69	140000	
1052	293357		1353	361713		69	123500	
1052	243965		1353	226962		62	310133	
1052	94645		1353	115567		62	110000	
1052	207966		1353	150687		62	370000	
1052	46212		1353	347703		62	340000	
1052	291053		1203	473922		62	375000	
1052	74427		1203	981488		62	492500	
1052	32596		1203	1000023		62	364181	
1052	132350							
1052	144424							
902	1000029	2190						

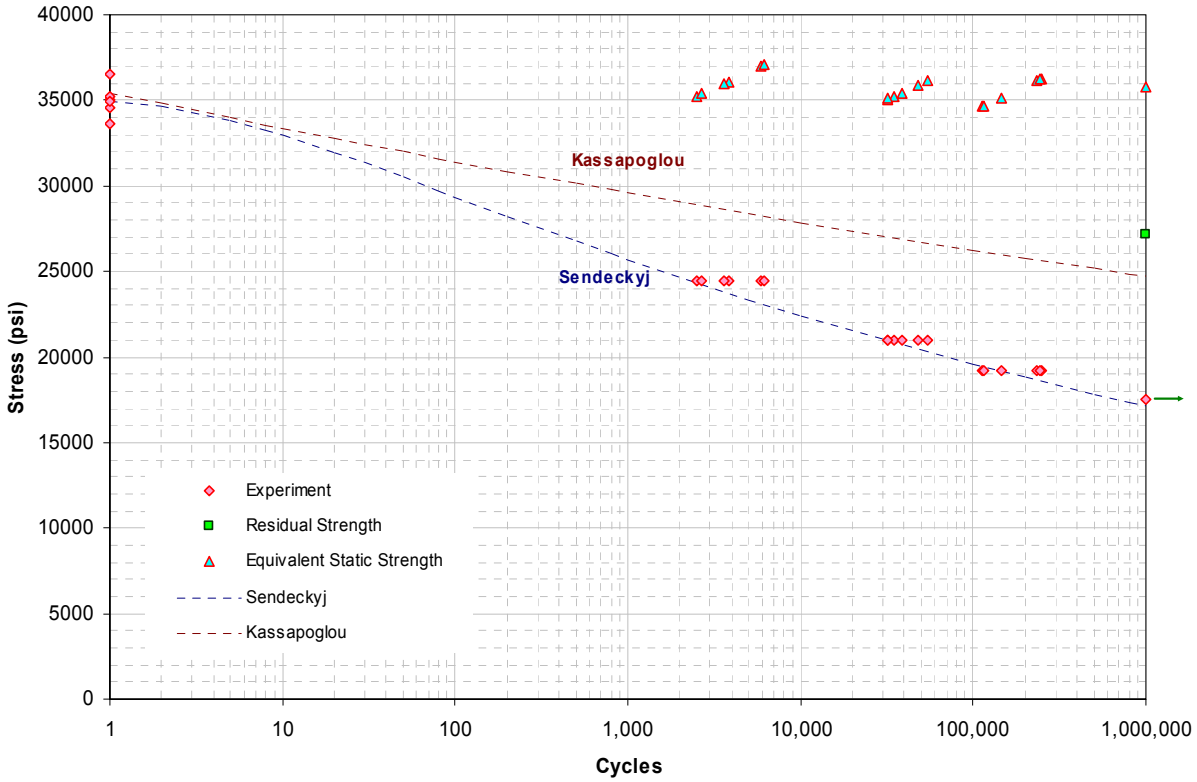

Figure A.24. T700-PW – 10/80/10, OH, R=-1.

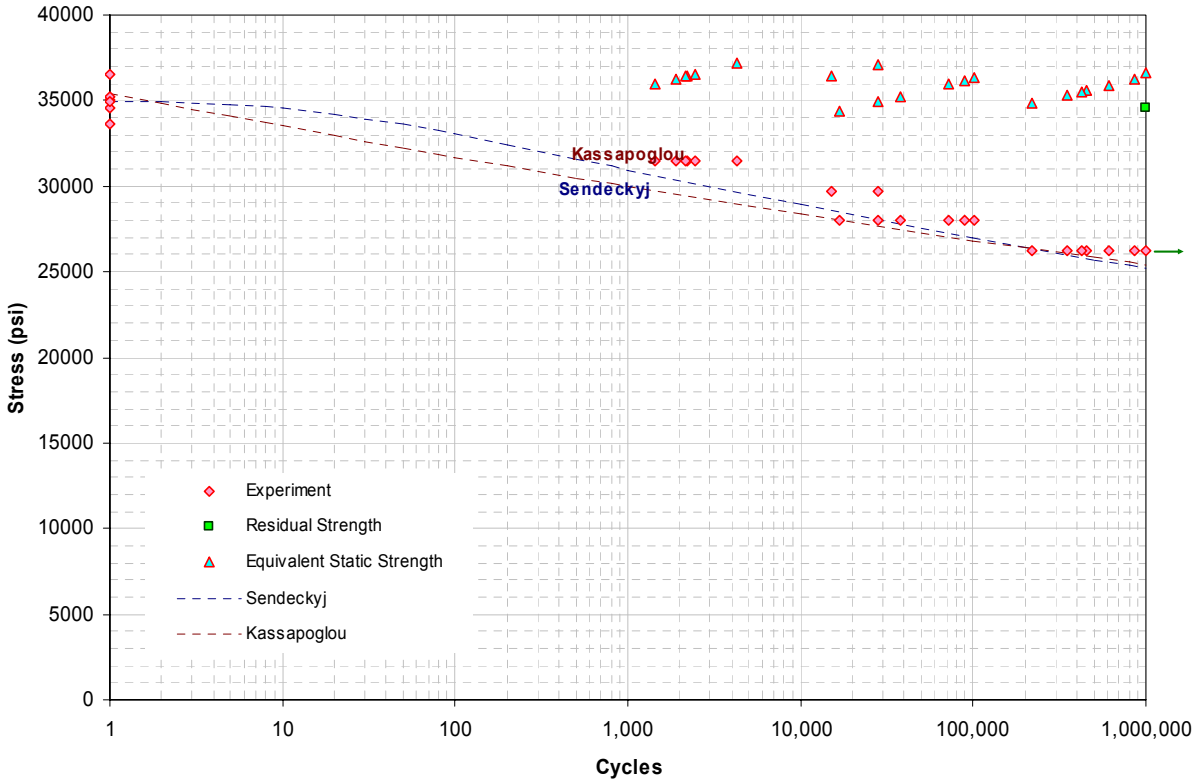

Figure A.25. T700-PW – 10/80/10, OH, R=5.

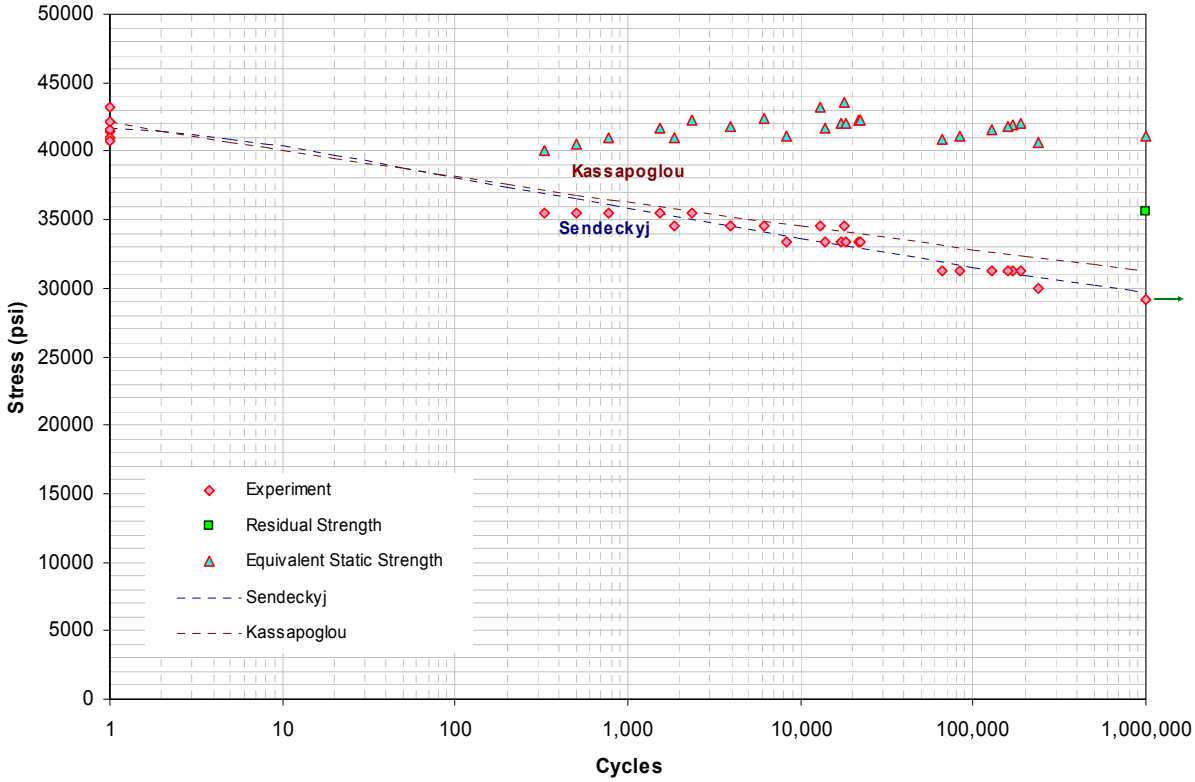

Figure A.26. T700-PW – 10/80/10, OH, R=0.

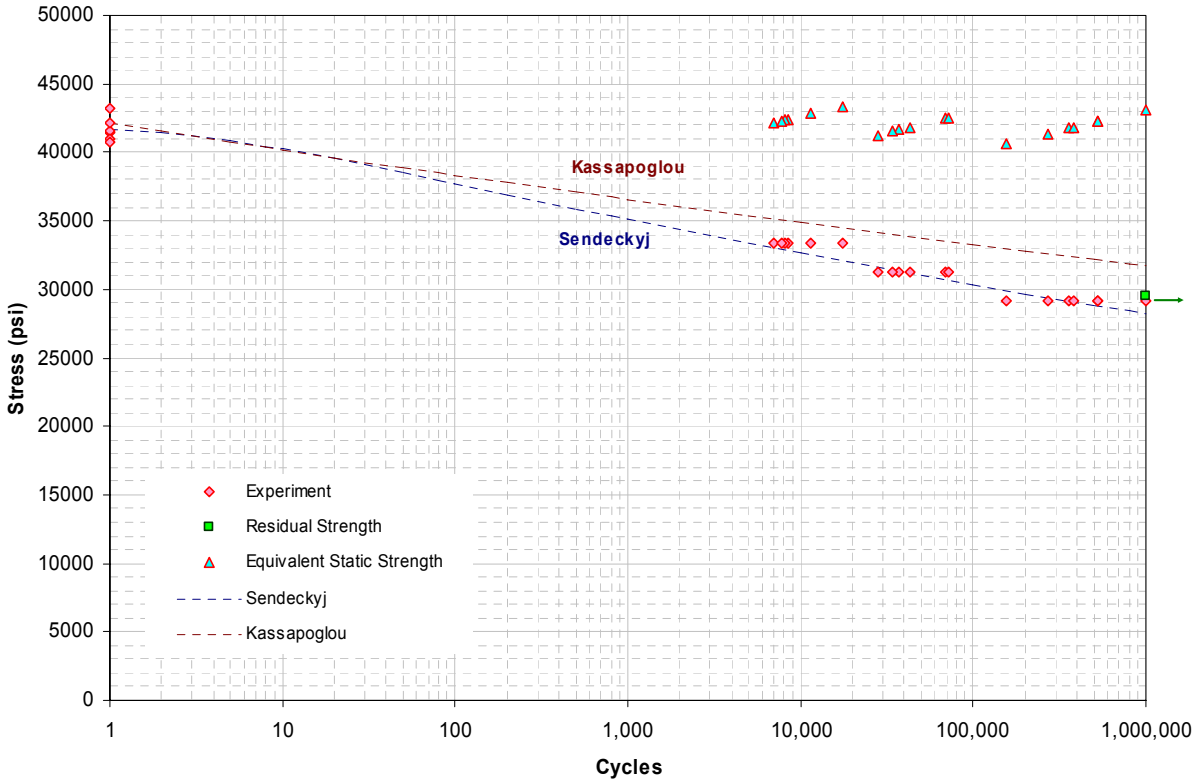

Figure A.27. T700-PW – 10/80/10, OH, R=-0.2.

A.4. S-N Data for 7781/#2510 8-Harness Satin-Weave Fabric

This section contains the S-N data for 7781-8HS test data included in the FAA-LEF database. Tables A.9 and A.10 include the individual data points, while Figures A.28 through A.31 show the S-N curves that were used for generating LEFs for 7781-8HS. In these tables, n is the number of cycles survived and n=1 indicate static failure. Also, σ_A and σ_R correspond to the fatigue stress level (or static failure stress level) and the residual strength after surviving the corresponding number of cycles, respectively.

TABLE A.9

S-N DATA FOR 7781-8HS OPEN-HOLE TESTS (FAA-LEF)

OHC/T (R = -1)			OHC (R = 5)			OHT (R = 0)			OHT (R = -0.2)		
σ_A	n	σ_R	σ_A	n	σ_R	σ_A	n	σ_R	σ_A	n	σ_R
33130	1		33130	1		27267	1		27267	1	
33141	1		33141	1		27150	1		27150	1	
33506	1		33506	1		26895	1		26895	1	
33514	1		33514	1		26613	1		26613	1	
33407	1		33407	1		26294	1		26294	1	
32666	1		32666	1		26632	1		26632	1	
23256	260		26582	2813		16085	4879		16085	4159	
16621	756		26582	2254		16085	4689		16085	3290	
13297	7502		26582	1587		16085	5153		16085	4340	
13292	4575		26582	1716		16085	4695		16085	4006	
13292	5335		26582	1673		16085	4478		16085	3901	
10723	32634		26582	1949		16085	5230		16085	5410	
10723	32224		24921	9408		13404	31239		13404	19991	
10723	33829		24921	29368		13404	29110		13404	26597	
10723	40038		24921	16482		13404	24024		13404	25380	
10723	30692		24921	27249		13404	23870		13404	24603	
10723	38903		24921	8833		13404	25278		13404	24317	
10723	40451		24921	13012		13404	29622		13404	22742	
10013	74386		24921	23041		10723	377715		10723	87248	
9973	81665		24921	7358		10723	352927		10723	193468	
9973	70390		24921	8213		10723	272790		10723	227929	
9973	362895		23259	216131		10723	353214		10723	193446	
9959	111843		23259	274091		10723	325874		10723	177910	
9383	123527		23259	595433		10723	288778		10723	193217	
9383	145031		23259	189941							
9383	134683		23259	347856							
9383	165288		23259	362656							
9383	179403		22595	1106426	29906						
9383	193388		21598	1000000	31661						
8043	593003		19936	1000100	30532						
8043	1000032										
8043	883245										
8043	942271										
8043	769637										
8043	778751										
8043	1144259	25937									

TABLE A.10

S-N DATA FOR 7781-8HS DNC AND SANDWICH TESTS (FAA-LEF)

DNC (R = -1)			DNC (R = -0.2)			Flexure (R = 0)		
σ_A	n	σ_R	σ_A	n	σ_R	σ_A	n	σ_R
3630	1		3630	1		140.342	1	
3625	1		3625	1		141.508	1	
3429	1		3429	1		141.772	1	
3195	1		3195	1		143.715	1	
3614	1		3614	1		139.256	1	
3468	1		3468	1		139.038	1	
1747	3121		2446	1692		83	28924	
1747	5270		2096	9267		83	42000	
1747	2028		2096	12301		83	39000	
1747	6133		2096	18245		83	50000	
1747	2759		2096	5612		83	36500	
1747	3916		2096	15366		83	64000	
1572	4004		2096	11326		70	265000	
1572	10732		1747	65045		70	216004	
1572	6779		1747	45870		70	205000	
1397	28078		1747	99557		70	230000	
1397	18684		1747	85112		70	167500	
1397	5724		1747	105136		70	262000	
1397	2138		1747	83695		70	70000	
1397	6291		1572	320302		63	410000	
1397	23500		1572	37069		63	270000	
1223	451048		1572	455873		63	190000	
1223	47332		1572	237356		60	325000	
1223	31537		1572	281584		60	490000	
1048	146896		1572	107805		60	625000	
1048	206313		1572	168387		60	1000042	
1048	379484		1397	1000088	2745	60	1000042	
1048	157833					60	790000	
1048	197364					60	1000042	
1048	57311					60	1000042	
						60	1000042	
						60	1000042	
						56	940000	

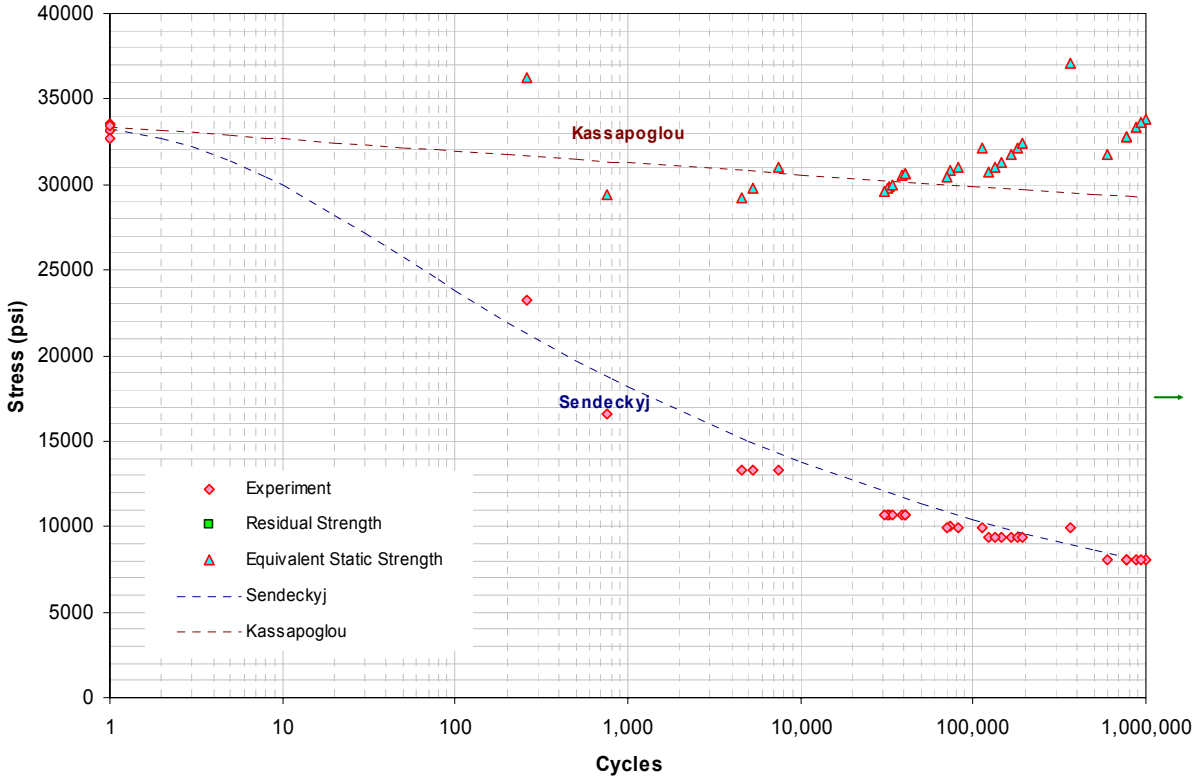

Figure A.28. 7781-8HS – 10/80/10, OH, R=-1.

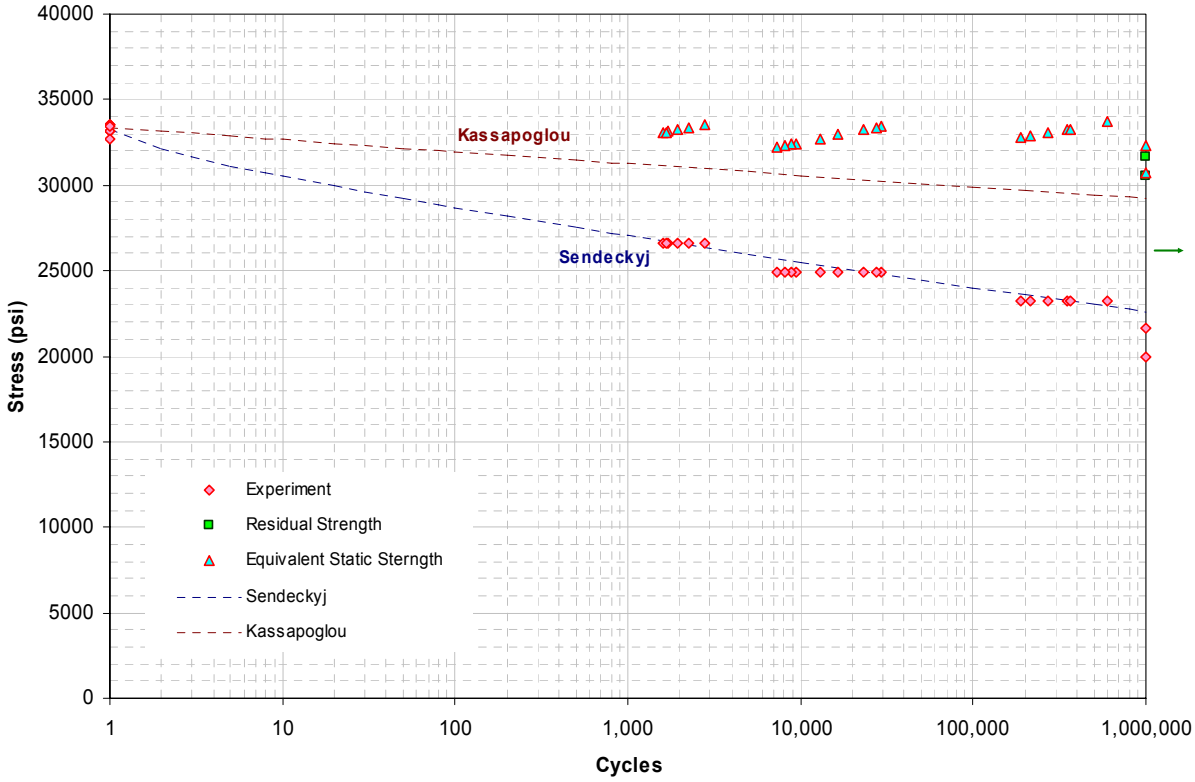

Figure A.29. 7781-8HS – 10/80/10, OH, R=5.

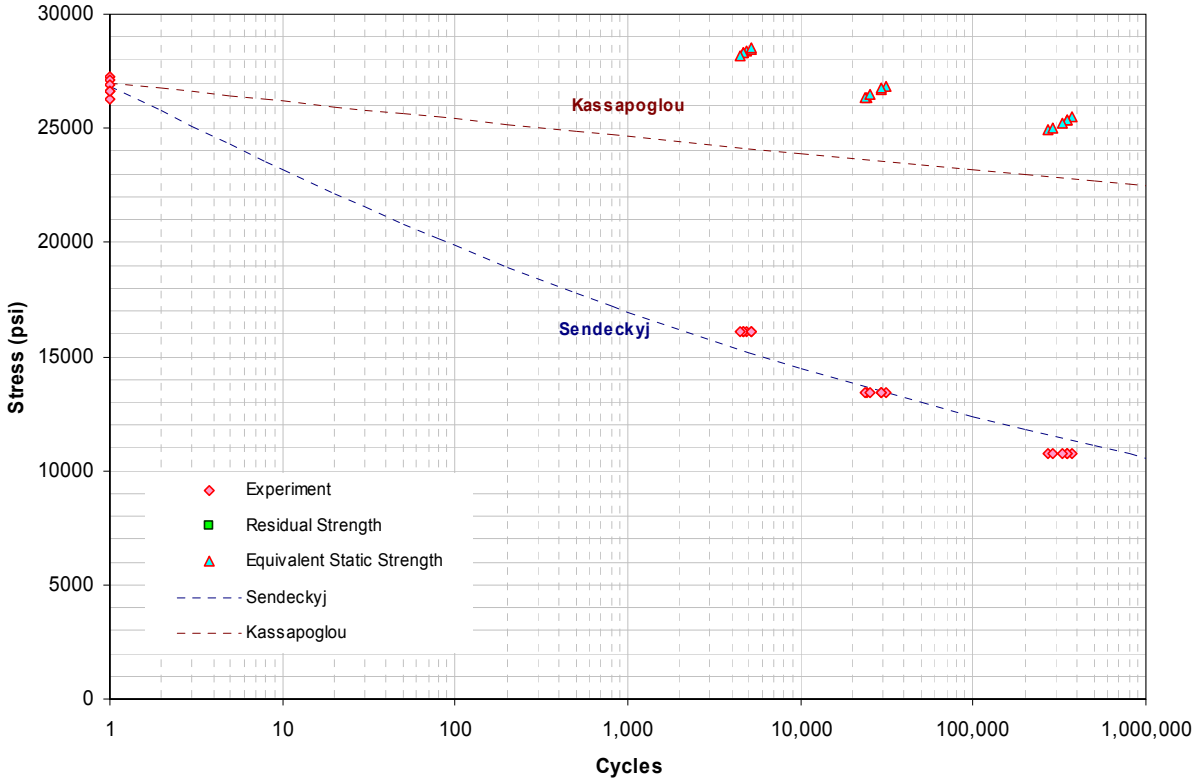

Figure A.30. 7781-8HS – 10/80/10, OH, R=0.

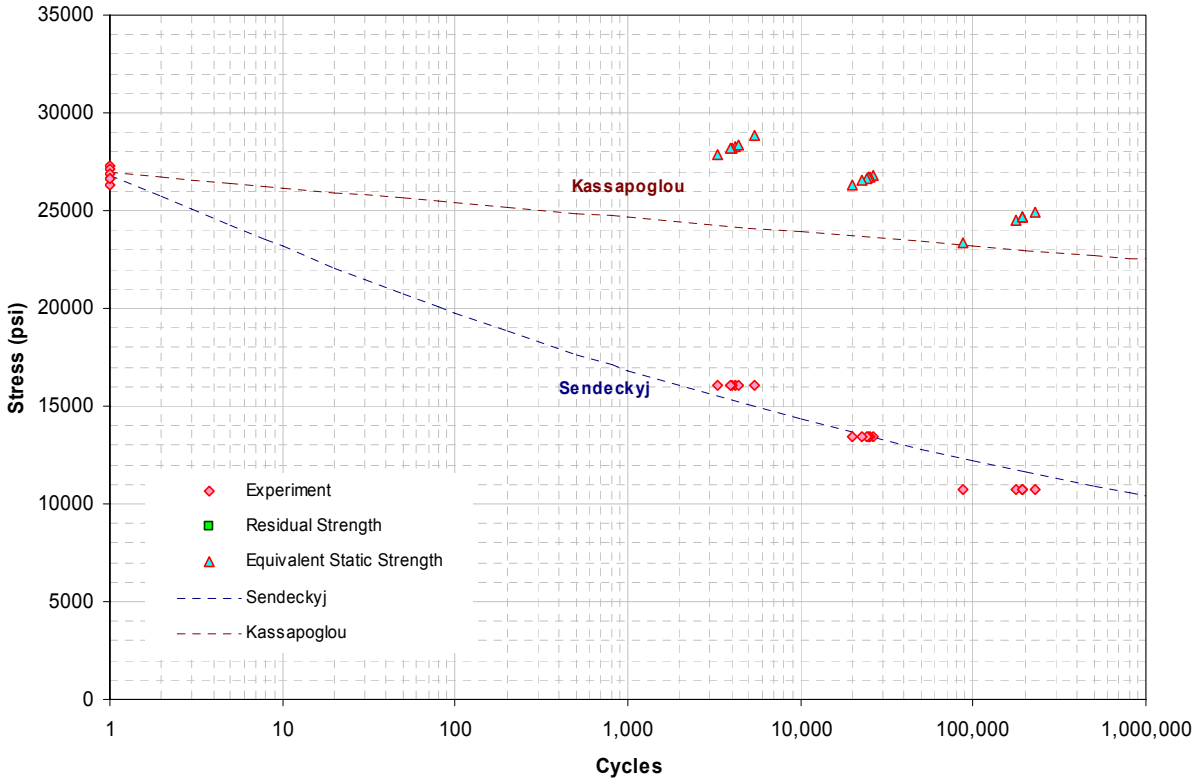

Figure A.31. 7781-8HS – 10/80/10, OH, R=-0.2.

A.5. Static Scatter Analysis of T700/#2510 Unidirectional Tape

This section contains the shape parameters of 853 T700-UT specimens from 47 data sets obtained from FAA-LVM database. Tables A.1, A.2, and A.3 contain shape parameters corresponding to static strength distributions of individual test methods and environmental conditions of hard (50/40/10), quasi-isotropic (25/50/25), and soft (10/80/10) laminates, respectively. The scatter analysis in section 4.1.4 was conducted by analyzing the shape parameters in these three tables.

TABLE A.11

WEIBULL PARAMETERS FOR STATIC-STRENGTH DISTRIBUTIONS OF 50/40/10 T700-UT (FAA-LVM)

Test Description	Test Environment	Shape Parameter, α	Number of Specimens
Single Shear Bearing-Tension	RTA	52.085	19
Double Shear Bearing-Tension	RTA	40.405	20
Bearing-Bypass 50%-Compression	RTA	38.043	15
Bearing-Bypass 50%-Tension [t/D=0.320]	RTA	41.398	18
Bearing-Bypass 50%-Tension [t/D=0.384]	RTA	44.098	18
Bearing-Bypass 50%-Tension [t/D=0.640]	RTA	42.257	17
Bearing-Bypass 50%-Tension [t/D=0.480]	RTA	59.840	15
No Hole-Tension	RTA	20.702	19
No Hole-Compression	RTA	33.121	19
Open Hole-Compression	RTA	22.705	21
Filled Hole-Tension	CTD	36.224	18
Filled Hole-Tension	RTA	17.585	18
Filled Hole-Tension	ETW	20.516	19
V-Notched Rail Shear	RTA	22.705	18
Open Hole-Tension [w/D=3]	RTA	22.553	18
Open Hole-Tension [w/D=4]	RTA	20.420	18
Open Hole-Tension [w/D=8]	RTA	32.794	19

TABLE A.12

WEIBULL PARAMETERS FOR STATIC-STRENGTH DISTRIBUTIONS OF 25/50/25 T700-UT (FAA-LVM)

Test Description	Test Environment	Shape Parameter, α	Number of Specimens
Double-Shear Bearing Tension	CTD	31.499	22
Double-Shear Bearing Tension	RTA	10.310	19
Double-Shear Bearing Tension	ETW	41.221	18
Single-Shear Bearing Tension	CTD	37.563	18
Single-Shear Bearing Tension	RTA	14.452	18
Single-Shear Bearing Tension	ETW	18.924	18
Bearing-Bypass 50% Tension	RTA	74.669	15
Bearing-Bypass 50% Compression	RTA	57.956	15
Open Hole-Tension [w/D=6]	CTD	37.058	18
Open Hole-Tension [w/D=6]	RTA	25.000	18
Open Hole-Tension [w/D=6]	ETW	27.714	21
No Hole-Tension	CTD	45.075	18
No Hole-Tension	RTA	39.641	18
No Hole-Tension	ETW	32.490	18
No Hole-Compression	CTD	23.026	18
No Hole-Compression	RTA	22.034	18
No Hole-Compression	ETW	34.869	18
Open Hole-Compression	CTD	37.455	21
Open Hole-Compression	RTA	27.930	18
Open Hole-Compression	ETW	22.122	22
V-Notched Rail Shear	RTA	9.054	18

A.6. Static Scatter Analysis of AS4C/MTM45 Unidirectional Tape

This section contains the shape parameters of 1151 AS4C-UT specimens from 86 data sets obtained from FAA-LVM database. Tables A.4, A.5, and A.6 contain shape parameters corresponding to static strength distributions of individual test methods and environmental conditions of hard (50/40/10), quasi-isotropic (25/50/25), and soft (10/80/10) laminates, respectively. In addition, shape parameters corresponding to AS4C-UT lamina data are included in Table A.7. The scatter analysis in section 4.1.5 was conducted by analyzing the shape parameters in these three tables.

TABLE A.13

WEIBULL PARAMETERS FOR STATIC-STRENGTH DISTRIBUTIONS OF 10/80/10 T700-UT (FAA-LVM)

Test Description	Test Environment	Shape Parameter, α	Number of Specimens
Bearing-Bypass 50% Tension	RTA	64.772	15
Bearing-Bypass 50% Compression	RTA	49.444	15
Open-Hole Tension [w/D=6]	RTA	67.241	18
No-Hole Tension	RTA	20.186	18
No-Hole Compression	RTA	26.157	18
Open-Hole Compression	RTA	41.378	18
V-Notched Rail Shear	CTD	7.262	18
V-Notched Rail Shear	RTA	19.659	19
V-Notched Rail Shear	ETW	10.595	18

TABLE A.14

WEIBULL PARAMETERS FOR STATIC-STRENGTH DISTRIBUTIONS OF 50/40/10 AS4C-UT (FAA-LVM)

Test Description	Test Environment	Shape Parameter, α	Number of Specimens
Unnotched Tension	CTD	36.6884	7
Unnotched Tension	RTD	39.6101	6
Unnotched Tension	ETW2	105.7766	6
Open-Hole Tension	CTD	8.2884	18
Open-Hole Tension	RTD	46.3690	6
Open-Hole Tension	ETW2	60.1876	6
Filled-Hole Tension	CTD	18.7167	6
Filled-Hole Tension	RTD	18.1374	6
Unnotched Compression	RTD	46.4812	6
Unnotched Compression	ETW	39.6044	7
Open-Hole Compression	RTD	51.4916	6
Open-Hole Compression	ETW2	28.7315	19
Filled-Hole Compression	RTD	7.6270	7
Filled-Hole Compression	ETW2	13.1700	21
Double-Shear Bearing	RTD	52.4169	6
Double-Shear Bearing	ETW2	30.4239	20

TABLE A.15

WEIBULL PARAMETERS FOR STATIC-STRENGTH DISTRIBUTIONS OF 25/50/25 AS4C-UT (FAA-LVM)

Test Description	Test Environment	Shape Parameter, α	Number of Specimens
Unnotched Tension	CTD	36.9107	18
Unnotched Tension	RTD	36.7091	18
Unnotched Tension	ETW2	73.1509	6
Open-Hole Tension	CTD	27.1127	15
Open-Hole Tension	RTD	35.9034	16
Open-Hole Tension	ETW	45.0771	5
Open-Hole Tension	ETW2	29.5619	18
Filled-Hole Tension	CTD	30.4239	18
Filled-Hole Tension	RTD	32.5909	6
Unnotched Compression	RTD	35.8363	19
Unnotched Compression	ETW	45.5883	7
Unnotched Compression	ETW2	25.0000	18
Open-Hole Compression	RTD	24.9999	14
Open-Hole Compression	ETW	23.6168	6
Open-Hole Compression	ETW2	28.0623	17
Filled-Hole Compression	RTD	24.9999	6
Filled-Hole Compression	ETW2	21.4617	7
Double-Shear Bearing	RTD	21.0857	18
Double-Shear Bearing	ETW2	22.9000	18
Compression After Impact	RTD	16.0114	6

TABLE A.16

WEIBULL PARAMETERS FOR STATIC-STRENGTH DISTRIBUTIONS OF 10/80/10 AS4C-UT (FAA-LVM)

Test Description	Test Environment	Shape Parameter, α	Number of Specimens
Unnotched Tension	CTD	35.1583	6
Unnotched Tension	RTD	31.4154	6
Unnotched Tension	ETW2	47.2541	6
Open-Hole Tension	CTD	48.8726	17
Open-Hole Tension	RTD	47.2759	5
Open-Hole Tension	ETW2	38.5491	6
Filled-Hole Tension	CTD	60.3965	6
Filled-Hole Tension	RTD	40.4534	6
Filled-Hole Tension	ETW2	38.2105	7
Unnotched Compression	RTD	33.1313	6
Unnotched Compression	ETW2	47.7841	6
Open-Hole Compression	RTD	33.2611	5
Open-Hole Compression	ETW2	27.2031	18
Filled-Hole Compression	RTD	38.5239	5
Filled-Hole Compression	ETW2	27.6622	21
Double-Shear Bearing	RTD	31.2818	6
Double-Shear Bearing	ETW2	18.3542	12
Short-Beam Shear	RTD	22.0431	18
Short-Beam Shear	ETW	23.9989	6
Short-Beam Shear	ETW2	27.0304	18

TABLE A.17

WEIBULL PARAMETERS FOR STATIC-STRENGTH DISTRIBUTIONS OF AS4C-UT LAMINA DATA (FAA-LVM)

Layup	Test Description	Test Environment	Shape Parameter, α	Number of Specimens
100/0/0	Longitudinal Tension	CTD	13.8596	20
	Longitudinal Tension	RTD	15.0419	18
	Longitudinal Tension	ETW	16.9554	12
	Longitudinal Tension	ETW2	18.9761	12
0/0/100	Transverse Tension	CTD	13.2656	20
	Transverse Tension	RTD	13.7326	20
	Transverse Tension	ETW	12.5037	23
	Transverse Tension	ETW2	16.5834	21
0/0/100	Transverse Compression	CTD	22.5142	19
	Transverse Compression	RTD	32.6974	18
	Transverse Compression	ETW	31.1187	18
	Transverse Compression	ETW2	23.3048	19
0/100/0	In-Plane Shear	CTD	30.8707	18
	In-Plane Shear	RTD	43.3159	18
	In-Plane Shear	ETW	37.3768	17
	In-Plane Shear	ETW2	31.4522	19
100/0/0	Short-Beam Shear	CTD	30.0698	20
	Short-Beam Shear	RTD	32.5469	20
	Short-Beam Shear	ETD	26.2652	20
	Short-Beam Shear	ETW	36.3365	21
	Short-Beam Shear	ETW2	19.1586	18
50/0/50	Unnotched Tension	CTD	18.9930	18
	Unnotched Tension	RTD	19.3424	18
	Unnotched Tension	ETW	16.0501	18
	Unnotched Tension	ETW2	17.8260	17
50/0/50	Unnotched Compression	CTD	14.1693	22
	Unnotched Compression	RTD	28.1360	18
	Unnotched Compression	ETD	20.7004	18
	Unnotched Compression	ETW	20.0349	18
	Unnotched Compression	ETW2	12.5308	18

A.7. Static Scatter Analysis of AS4C/MTM45 5-Harness Satin-Weave Fabric

This section contains the shape parameters of 1083 AS4C-5HS specimens from 78 data sets obtained from FAA-LVM database. Tables A.8, A.9, and A.10 contain shape parameters corresponding to static strength distributions of individual test methods and environmental conditions of hard (40/20/40), quasi-isotropic (25/50/25), and soft (10/80/10) laminates, respectively. In addition, shape parameters corresponding to AS4C-5HS lamina data are included in Table A.11. The scatter analysis in section 4.1.6 was conducted by analyzing the shape parameters in these three tables.

TABLE A.18

WEIBULL PARAMETERS FOR STATIC-STRENGTH DISTRIBUTIONS OF 40/20/40 AS4C-5HS (FAA-LVM)

Test Description	Test Environment	Shape Parameter, α	Number of Specimens
Unnotched Tension	CTD	50.3322	6
Unnotched Compression	RTD	13.4587	6
Unnotched Compression	ETW2	23.7333	6
Open-Hole Tension	CTD	25.5530	21
Open-Hole Tension	RTD	33.2549	7
Open-Hole Tension	ETW2	28.5810	6
Filled-Hole Tension	CTD	20.9094	6
Filled-Hole Tension	RTD	29.0854	6
Open-Hole Compression	RTD	32.2012	6
Open-Hole Compression	ETW2	27.0483	18
Filled-Hole Compression	RTD	14.1911	6
Filled-Hole Compression	ETW2	19.3906	20
Double-Shear Bearing	RTD	34.7686	6
Double-Shear Bearing	ETW2	15.5135	24

TABLE A.19

WEIBULL PARAMETERS FOR STATIC-STRENGTH DISTRIBUTIONS OF 25/50/25 AS4C-5HS (FAA-LVM)

Test Description	Test Environment	Shape Parameter, α	Number of Specimens
Unnotched Tension	CTD	62.6999	23
Unnotched Tension	RTD	34.3319	18
Unnotched Tension	ETW2	44.9484	6
Unnotched Compression	RTD	20.4637	18
Unnotched Compression	ETW	19.1119	6
Unnotched Compression	ETW2	19.6297	18
Open-Hole Tension	RTD	40.4981	18
Open-Hole Tension	CTD	24.3826	18
Open-Hole Tension	ETW	86.9983	6
Open-Hole Tension	ETW2	28.7676	18
Filled-Hole Tension	RTD	41.9103	6
Filled-Hole Tension	CTD	34.6634	18
Open-Hole Compression	RTD	29.5250	18
Open-Hole Compression	ETW	15.5124	6
Open-Hole Compression	ETW2	24.5294	18
Filled-Hole Compression	RTD	27.7953	6
Filled-Hole Compression	ETW2	31.8401	18
Double-Shear Bearing	RTD	13.9867	18
Double-Shear Bearing	ETW2	13.6569	23
Short-Beam Shear	RTD	35.7819	18
Short-Beam Shear	ETW	61.9031	6
Short-Beam Shear	ETW2	57.5735	18

TABLE A.20

WEIBULL PARAMETERS FOR STATIC-STRENGTH DISTRIBUTIONS OF 10/80/10 AS4C-5HS (FAA-LVM)

Test Description	Test Environment	Shape Parameter, α	Number of Specimens
Unnotched Tension	CTD	36.4157	6
Unnotched Tension	RTD	74.8199	6
Unnotched Tension	ETW2	26.8754	6
Unnotched Compression	RTD	23.2597	6
Unnotched Compression	ETW2	32.6546	6
Open-Hole Tension	CTD	41.9517	18
Open-Hole Tension	RTD	53.7592	9
Open-Hole Tension	ETW2	40.8813	6
Filled-Hole Tension	RTD	53.8676	6
Filled-Hole Tension	CTD	64.3808	6
Filled-Hole Tension	ETW2	43.5941	6
Open-Hole Compression	RTD	32.1458	6
Open-Hole Compression	ETW2	40.5532	18
Filled-Hole Compression	RTD	64.9168	6
Filled-Hole Compression	ETW2	41.6289	18
Double-Shear Bearing	RTD	21.9478	6
Double-Shear Bearing	ETW2	14.6494	24

A.8. Static Scatter Analysis of T700/E765 Unidirectional Tape

This section contains the shape parameters of 834 E765-UT specimens from 47 data sets obtained from FAA-LVM database. Tables A.12, A.13, and A.14 contain shape parameters corresponding to static strength distributions of individual test methods and environmental conditions of hard (50/40/10), quasi-isotropic (25/50/25), and soft (10/80/10) laminates, respectively. The scatter analysis in section 4.1.7 was conducted by analyzing the shape parameters in these three tables.

TABLE A.21

WEIBULL PARAMETERS FOR STATIC-STRENGTH DISTRIBUTIONS OF 50/0/50 AS4C-5HS (FAA-LVM)

Test Description	Test Environment	Shape Parameter, α	Number of Specimens
Warp Tension	CTD	41.7447	19
Warp Tension	RTA	31.7590	22
Warp Tension	ETW	34.1953	20
Warp Tension	ETW2	25.6064	22
Filled Tension	CTD	27.5161	18
Filled Tension	RTA	31.6162	18
Filled Tension	ETW	36.2862	21
Filled Tension	ETW2	25.4495	19
Warp Compression	CTD	11.9994	18
Warp Compression	RTA	16.1442	19
Warp Compression	ETW	12.2082	18
Warp Compression	ETW2	9.7697	18
Filled Compression	CTD	17.3767	18
Filled Compression	RTA	18.1475	18
Filled Compression	ETD	13.3973	18
Filled Compression	ETW	15.3266	18
Filled Compression	ETW2	18.4131	18
In-plane Shear	CTD	14.1296	16
In-plane Shear	RTA	14.7233	16
In-plane Shear	ETW	61.6350	16
In-plane Shear	ETW2	13.9587	16
Short-Beam Shear	CTD	24.7163	19
Short-Beam Shear	RTA	36.7471	17
Short-Beam Shear	ETW	26.2523	18
Short-Beam Shear	ETW2	28.0774	18

TABLE A.22

WEIBULL PARAMETERS FOR STATIC-STRENGTH DISTRIBUTIONS OF 50/40/10 E765-UT (FAA-LVM)

Test Description	Test Environment	Shape Parameter, α	Number of Specimens
Single Shear Bearing-Tension	RTA	30.814	18
Double Shear Bearing-Tension	RTA	17.957	21
Bearing-Bypass 50%-Compression	RTA	28.550	13
Bearing-Bypass 50%-Tension [t/D=0.320]	RTA	30.861	17
Bearing-Bypass 50%-Tension [t/D=0.384]	RTA	46.294	18
Bearing-Bypass 50%-Tension [t/D=0.640]	RTA	24.909	18
Bearing-Bypass 50%-Tension [t/D=0.480]	RTA	26.362	15
No Hole-Tension	RTA	7.347	20
No Hole-Compression	RTA	8.897	18
Open Hole-Compression	RTA	21.189	20
Filled Hole-Tension	CTD	31.088	18
Filled Hole-Tension	RTA	33.685	18
Filled Hole-Tension	ETW	18.421	18
V-Notched Rail Shear	RTA	19.226	18
Open Hole-Tension [w/D=3]	RTA	35.484	18
Open Hole-Tension [w/D=4]	RTA	77.305	16
Open Hole-Tension [w/D=8]	RTA	27.486	18

TABLE A.23

WEIBULL PARAMETERS FOR STATIC-STRENGTH DISTRIBUTIONS OF 25/50/25 E765-UT (FAA-LVM)

Test Description	Test Environment	Shape Parameter, α	Number of Specimens
Double-Shear Bearing Tension	CTD	13.077	19
Double-Shear Bearing Tension	RTA	28.116	18
Double-Shear Bearing Tension	ETW	8.356	21
Single-Shear Bearing Tension	CTD	17.509	18
Single-Shear Bearing Tension	RTA	26.754	18
Single-Shear Bearing Tension	ETW	31.724	20
Bearing-Bypass 50% Tension	RTA	40.112	16
Bearing-Bypass 50% Compression	RTA	30.226	15
Open Hole-Tension [w/D=6]	CTD	37.529	18
Open Hole-Tension [w/D=6]	RTA	50.949	18
Open Hole-Tension [w/D=6]	ETW	48.482	18
No Hole-Tension	CTD	14.611	19
No Hole-Tension	RTA	25.580	14
No Hole-Tension	ETW	24.874	18
No Hole-Compression	CTD	18.276	18
No Hole-Compression	RTA	28.061	17
No Hole-Compression	ETW	10.442	18
Open Hole-Compression	CTD	18.715	19
Open Hole-Compression	RTA	50.933	18
Open Hole-Compression	ETW	13.645	20
V-Notched Rail Shear	RTA	10.840	18

A.9. Static Scatter Analysis of T300/E765 3K Plain-Weave Fabric

This section contains the shape parameters of 722 E765-PW specimens from 48 data sets obtained from FAA-LVM database. Tables A.15, A.16, and A.17 contain shape parameters corresponding to static strength distributions of individual test methods and environmental conditions of hard (40/20/40), quasi-isotropic (25/50/25), and soft (10/80/10) laminates, respectively. The scatter analysis in section 4.1.8 was conducted by analyzing the shape parameters in these three tables.

TABLE A.24

WEIBULL PARAMETERS FOR STATIC-STRENGTH DISTRIBUTIONS OF 10/80/10 E765-UT (FAA-LVM)

Test Description	Test Environment	Shape Parameter, α	Number of Specimens
Bearing-Bypass 50% Tension	RTA	38.362	15
Bearing-Bypass 50% Compression	RTA	39.852	14
Open-Hole Tension [w/D=6]	RTA	32.358	18
No-Hole Tension	RTA	40.424	15
No-Hole Compression	RTA	27.476	18
Open-Hole Compression	RTA	28.881	20
V-Notched Rail Shear	CTD	6.335	18
V-Notched Rail Shear	RTA	16.180	18
V-Notched Rail Shear	ETW	11.573	18

TABLE A.25

WEIBULL PARAMETERS FOR STATIC-STRENGTH DISTRIBUTIONS OF 40/20/40 E765-PW (FAA-LVM)

Test Description	Test Environment	Shape Parameter, α	Number of Specimens
Single Shear Bearing-Tension	RTA	14.391	15
Double Shear Bearing-Tension	RTA	39.826	13
Bearing-Bypass 50%-Compression	RTA	34.680	9
Bearing-Bypass 50%-Tension [t/D=0.320]	RTA	49.915	12
Bearing-Bypass 50%-Tension [t/D=0.384]	RTA	43.274	12
Bearing-Bypass 50%-Tension [t/D=0.640]	RTA	2.986	6
Bearing-Bypass 50%-Tension [t/D=0.480]	RTA	27.165	12
No Hole-Tension	RTA	27.277	13
No Hole-Compression	RTA	23.693	13
Open Hole-Compression	RTA	31.510	12
Filled Hole-Tension	CTD	20.391	12
Filled Hole-Tension	RTA	45.561	12
Filled Hole-Tension	ETW	35.757	12
V-Notched Rail Shear	RTA	65.531	12
Open Hole-Tension [w/D=3]	RTA	34.781	12
Open Hole-Tension [w/D=4]	RTA	51.052	13
Open Hole-Tension [w/D=6]	RTA	29.581	12
Open Hole-Tension [w/D=8]	RTA	32.084	12

TABLE A.26

WEIBULL PARAMETERS FOR STATIC-STRENGTH DISTRIBUTIONS OF
25/50/25 E765-PW (FAA-LVM)

Test Description	Test Environment	Shape Parameter, α	Number of Specimens
Double-Shear Bearing Tension	CTD	19.297	20
Double-Shear Bearing Tension	RTA	38.719	20
Double-Shear Bearing Tension	ETW	28.345	19
Single-Shear Bearing Tension	CTD	12.403	18
Single-Shear Bearing Tension	RTA	22.420	18
Single-Shear Bearing Tension	ETW	19.406	18
Bearing-Bypass 50% Tension	RTA	40.069	10
Bearing-Bypass 50% Compression	RTA	34.458	8
Open Hole-Tension [w/D=6]	CTD	19.337	18
Open Hole-Tension [w/D=6]	RTA	18.427	18
Open Hole-Tension [w/D=6]	ETW	23.693	18
No Hole-Tension	CTD	43.886	18
No Hole-Tension	RTA	43.824	18
No Hole-Tension	ETW	42.304	21
No Hole-Compression	CTD	26.180	18
No Hole-Compression	RTA	33.422	15
No Hole-Compression	ETW	20.017	18
Open Hole-Compression	CTD	19.446	19
Open Hole-Compression	RTA	25.503	18
Open Hole-Compression	ETW	12.103	19
V-Notched Rail Shear	RTA	20.670	18

TABLE A.27

WEIBULL PARAMETERS FOR STATIC-STRENGTH DISTRIBUTIONS OF
10/80/10 E765-PW (FAA-LVM)

Test Description	Test Environment	Shape Parameter, α	Number of Specimens
Bearing-Bypass 50% Tension	RTA	8.873	10
Bearing-Bypass 50% Compression	RTA	25.206	13
Open-Hole Tension [w/D=6]	RTA	28.001	18
No-Hole Tension	RTA	44.073	18
No-Hole Compression	RTA	41.200	18
Open-Hole Compression	RTA	39.190	18
V-Notched Rail Shear	CTD	12.622	12
V-Notched Rail Shear	RTA	7.238	19
V-Notched Rail Shear	ETW	14.961	15

A.10. A- and B-Basis Load-Enhancement Factors

Tables A.28 and A.29 include A- and B-basis load-enhancement factors, respectively, using the equation (9) in section 3.3.

TABLE A.28

A-BASIS LOAD ENHANCEMENT FACTORS

	n	1							2							3						
N	α_L / α_R	1.00	1.25	1.50	1.75	2.00	2.25	2.50	1.00	1.25	1.50	1.75	2.00	2.25	2.50	1.00	1.25	1.50	1.75	2.00	2.25	2.50
1	17.5	1.385	1.378	1.373	1.369	1.366	1.363	1.361	1.366	1.360	1.355	1.351	1.348	1.345	1.343	1.357	1.350	1.345	1.341	1.338	1.336	1.334
	20.0	1.330	1.324	1.319	1.316	1.314	1.312	1.310	1.314	1.308	1.304	1.301	1.298	1.296	1.295	1.306	1.300	1.296	1.293	1.290	1.288	1.287
	22.5	1.288	1.283	1.279	1.277	1.274	1.273	1.271	1.275	1.270	1.266	1.263	1.261	1.259	1.258	1.268	1.263	1.259	1.257	1.254	1.253	1.251
	25.0	1.256	1.251	1.248	1.246	1.244	1.242	1.241	1.244	1.240	1.237	1.234	1.232	1.231	1.229	1.238	1.234	1.231	1.228	1.226	1.225	1.223
	27.5	1.230	1.226	1.223	1.221	1.219	1.218	1.217	1.220	1.216	1.213	1.211	1.209	1.208	1.207	1.214	1.210	1.208	1.205	1.204	1.202	1.201
	30.0	1.209	1.206	1.203	1.201	1.199	1.198	1.197	1.200	1.196	1.194	1.192	1.190	1.189	1.188	1.195	1.191	1.189	1.187	1.185	1.184	1.183
	32.5	1.192	1.188	1.186	1.184	1.183	1.182	1.181	1.183	1.180	1.178	1.176	1.174	1.173	1.172	1.179	1.175	1.173	1.171	1.170	1.169	1.168
	35.0	1.177	1.174	1.172	1.170	1.169	1.168	1.167	1.169	1.166	1.164	1.162	1.161	1.160	1.159	1.165	1.162	1.160	1.158	1.157	1.156	1.155
1.5	17.5	1.353	1.338	1.326	1.314	1.304	1.294	1.285	1.335	1.321	1.308	1.297	1.287	1.277	1.268	1.326	1.312	1.299	1.288	1.278	1.268	1.259
	20.0	1.303	1.291	1.280	1.270	1.261	1.253	1.245	1.288	1.276	1.265	1.256	1.247	1.239	1.231	1.280	1.268	1.257	1.248	1.239	1.231	1.223
	22.5	1.265	1.255	1.245	1.237	1.229	1.222	1.215	1.252	1.242	1.232	1.224	1.217	1.209	1.203	1.245	1.235	1.226	1.218	1.210	1.203	1.196
	25.0	1.236	1.226	1.218	1.211	1.204	1.198	1.192	1.224	1.215	1.207	1.200	1.193	1.187	1.181	1.218	1.209	1.201	1.194	1.187	1.181	1.175
	27.5	1.212	1.204	1.197	1.190	1.184	1.178	1.173	1.202	1.194	1.186	1.180	1.174	1.168	1.163	1.197	1.188	1.181	1.175	1.169	1.163	1.158
	30.0	1.193	1.185	1.179	1.173	1.167	1.162	1.157	1.184	1.176	1.170	1.164	1.158	1.153	1.148	1.179	1.171	1.165	1.159	1.154	1.149	1.144
	32.5	1.177	1.170	1.164	1.159	1.154	1.149	1.144	1.168	1.162	1.156	1.150	1.145	1.141	1.136	1.164	1.157	1.151	1.146	1.141	1.136	1.132
	35.0	1.163	1.157	1.151	1.147	1.142	1.138	1.133	1.155	1.149	1.144	1.139	1.134	1.130	1.126	1.151	1.145	1.140	1.135	1.130	1.126	1.122
2	17.5	1.331	1.311	1.294	1.277	1.262	1.247	1.233	1.313	1.294	1.276	1.260	1.245	1.231	1.217	1.304	1.285	1.267	1.251	1.236	1.222	1.208
	20.0	1.284	1.268	1.253	1.239	1.226	1.213	1.201	1.269	1.253	1.238	1.224	1.211	1.199	1.187	1.262	1.245	1.230	1.217	1.204	1.192	1.180
	22.5	1.249	1.235	1.222	1.210	1.198	1.187	1.177	1.236	1.222	1.209	1.197	1.186	1.175	1.165	1.229	1.215	1.202	1.191	1.179	1.169	1.158
	25.0	1.222	1.209	1.197	1.187	1.177	1.167	1.158	1.210	1.198	1.186	1.176	1.166	1.156	1.147	1.204	1.192	1.180	1.170	1.160	1.151	1.142
	27.5	1.200	1.188	1.178	1.168	1.159	1.151	1.143	1.189	1.178	1.168	1.159	1.150	1.141	1.133	1.184	1.173	1.163	1.153	1.145	1.136	1.128
	30.0	1.182	1.171	1.162	1.153	1.145	1.137	1.130	1.172	1.162	1.153	1.144	1.136	1.129	1.121	1.168	1.157	1.148	1.140	1.132	1.124	1.117
	32.5	1.166	1.157	1.149	1.141	1.133	1.126	1.119	1.158	1.149	1.140	1.133	1.125	1.118	1.111	1.154	1.144	1.136	1.128	1.121	1.114	1.107
	35.0	1.154	1.145	1.137	1.130	1.123	1.117	1.110	1.146	1.137	1.130	1.123	1.116	1.109	1.103	1.142	1.134	1.126	1.119	1.112	1.105	1.099
3	17.5	1.301	1.274	1.249	1.226	1.205	1.184	1.164	1.283	1.257	1.233	1.210	1.189	1.168	1.148	1.274	1.248	1.224	1.202	1.180	1.160	1.140
	20.0	1.259	1.236	1.215	1.196	1.177	1.159	1.142	1.244	1.222	1.201	1.182	1.163	1.146	1.129	1.236	1.214	1.194	1.174	1.156	1.139	1.122
	22.5	1.227	1.207	1.189	1.172	1.156	1.140	1.125	1.214	1.195	1.177	1.160	1.144	1.128	1.113	1.208	1.188	1.170	1.154	1.138	1.122	1.107
	25.0	1.202	1.185	1.169	1.154	1.139	1.125	1.112	1.191	1.174	1.158	1.143	1.129	1.115	1.102	1.185	1.168	1.152	1.137	1.123	1.109	1.096
	27.5	1.182	1.167	1.152	1.139	1.126	1.113	1.101	1.172	1.157	1.142	1.129	1.116	1.104	1.092	1.167	1.151	1.137	1.124	1.111	1.099	1.087
	30.0	1.166	1.152	1.139	1.126	1.115	1.103	1.092	1.157	1.143	1.130	1.118	1.106	1.095	1.084	1.152	1.138	1.125	1.113	1.102	1.090	1.080
	32.5	1.152	1.139	1.127	1.116	1.105	1.095	1.085	1.144	1.131	1.119	1.108	1.098	1.087	1.077	1.139	1.127	1.115	1.104	1.093	1.083	1.073
	35.0	1.140	1.129	1.118	1.107	1.098	1.088	1.079	1.133	1.121	1.110	1.100	1.090	1.081	1.072	1.129	1.117	1.106	1.096	1.086	1.077	1.068
4	17.5	1.279	1.248	1.219	1.192	1.166	1.141	1.117	1.262	1.231	1.203	1.176	1.150	1.126	1.102	1.254	1.223	1.194	1.168	1.142	1.118	1.094
	20.0	1.241	1.214	1.189	1.166	1.144	1.122	1.101	1.226	1.200	1.175	1.152	1.130	1.109	1.089	1.219	1.192	1.168	1.145	1.123	1.102	1.082
	22.5	1.211	1.188	1.166	1.146	1.127	1.108	1.090	1.199	1.176	1.154	1.134	1.115	1.096	1.078	1.192	1.169	1.148	1.128	1.109	1.090	1.073
	25.0	1.188	1.168	1.149	1.131	1.113	1.097	1.080	1.177	1.157	1.138	1.120	1.103	1.086	1.070	1.171	1.151	1.132	1.115	1.098	1.081	1.065
	27.5	1.170	1.151	1.134	1.118	1.102	1.087	1.073	1.160	1.142	1.125	1.109	1.093	1.078	1.064	1.155	1.137	1.120	1.104	1.088	1.073	1.059
	30.0	1.155	1.138	1.122	1.108	1.094	1.080	1.067	1.146	1.129	1.114	1.099	1.085	1.071	1.058	1.141	1.124	1.109	1.095	1.081	1.067	1.054
	32.5	1.142	1.127	1.112	1.099	1.086	1.074	1.061	1.134	1.119	1.105	1.091	1.078	1.066	1.054	1.129	1.114	1.100	1.087	1.074	1.062	1.050
	35.0	1.131	1.117	1.104	1.092	1.080	1.068	1.057	1.124	1.110	1.097	1.084	1.072	1.061	1.050	1.120	1.106	1.093	1.081	1.069	1.057	1.046
5	17.5	1.263	1.228	1.196	1.165	1.136	1.109	1.082	1.246	1.212	1.180	1.150	1.121	1.094	1.067	1.238	1.203	1.172	1.142	1.113	1.086	1.060
	20.0	1.227	1.197	1.169	1.143	1.118	1.094	1.071	1.213	1.183	1.156	1.130	1.105	1.082	1.059	1.205	1.176	1.149	1.123	1.099	1.075	1.052
	22.5	1.199	1.173	1.149	1.126	1.105	1.083	1.063	1.187	1.161	1.137	1.115	1.093	1.072	1.052	1.180	1.155	1.131	1.109	1.087	1.066	1.046
	25.0	1.178	1.155	1.133	1.113	1.094	1.075	1.057	1.167	1.144	1.123	1.103	1.083	1.065	1.047	1.161	1.138	1.117	1.097	1.078	1.060	1.042
	27.5	1.160	1.140	1.121	1.102	1.085	1.068	1.051	1.150	1.130	1.111	1.093	1.076	1.059	1.042	1.145	1.125	1.106	1.088	1.071	1.054	1.038
	30.0	1.146	1.127	1.110	1.093	1.077	1.062	1.047	1.137	1.119	1.101	1.085	1.069	1.054	1.039	1.132	1.114	1.097	1.080	1.065	1.049	1.035
	32.5	1.134	1.117	1.101	1.086	1.071	1.057	1.043	1.126	1.109	1.093	1.078	1.064	1.049	1.036	1.122	1.105	1.089	1.074	1.060	1.046	1.032
	35.0	1.124	1.108	1.094	1.080	1.066	1.053	1.040	1.116	1.101	1.086	1.072	1.059	1.046	1.033	1.113	1.097	1.082	1.069	1.055	1.042	1.030

TABLE A.29

B-BASIS LOAD ENHANCEMENT FACTORS

	n	1							2							3						
N	α_L / α_R	1.00	1.25	1.50	1.75	2.00	2.25	2.50	1.00	1.25	1.50	1.75	2.00	2.25	2.50	1.00	1.25	1.50	1.75	2.00	2.25	2.50
1	17.5	1.211	1.205	1.200	1.197	1.194	1.192	1.190	1.195	1.189	1.184	1.181	1.178	1.176	1.175	1.186	1.180	1.176	1.173	1.170	1.168	1.166
	20.0	1.182	1.177	1.173	1.170	1.168	1.166	1.165	1.168	1.163	1.160	1.157	1.154	1.153	1.151	1.161	1.156	1.152	1.150	1.147	1.146	1.144
	22.5	1.160	1.156	1.153	1.150	1.148	1.146	1.145	1.148	1.144	1.141	1.138	1.136	1.135	1.133	1.142	1.138	1.134	1.132	1.130	1.128	1.127
	25.0	1.143	1.139	1.136	1.134	1.132	1.131	1.130	1.133	1.129	1.126	1.124	1.122	1.120	1.119	1.127	1.123	1.120	1.118	1.116	1.115	1.114
	27.5	1.129	1.126	1.123	1.121	1.120	1.118	1.117	1.120	1.116	1.114	1.112	1.110	1.109	1.108	1.115	1.111	1.109	1.107	1.105	1.104	1.103
	30.0	1.118	1.115	1.112	1.111	1.109	1.108	1.107	1.109	1.106	1.104	1.102	1.100	1.099	1.098	1.105	1.102	1.099	1.097	1.096	1.095	1.094
	32.5	1.108	1.105	1.103	1.102	1.100	1.099	1.098	1.101	1.098	1.095	1.094	1.092	1.091	1.090	1.096	1.093	1.091	1.090	1.088	1.087	1.086
	35.0	1.100	1.098	1.096	1.094	1.093	1.092	1.091	1.093	1.090	1.088	1.087	1.086	1.085	1.084	1.089	1.086	1.084	1.083	1.082	1.081	1.080
1.5	17.5	1.183	1.170	1.159	1.149	1.140	1.132	1.123	1.167	1.155	1.144	1.134	1.125	1.117	1.108	1.159	1.147	1.136	1.126	1.117	1.109	1.101
	20.0	1.158	**1.148**	1.138	1.129	1.122	1.114	1.107	1.145	1.134	1.125	1.116	1.109	1.101	1.094	1.138	1.127	1.118	1.110	1.102	1.095	1.088
	22.5	1.140	1.130	1.122	1.114	1.107	1.101	1.095	1.128	1.118	1.110	1.103	1.096	1.090	1.083	1.122	1.112	1.104	1.097	1.090	1.084	1.077
	25.0	1.125	1.116	1.109	1.102	1.096	1.090	1.085	1.114	1.106	1.099	1.092	1.086	1.080	1.075	1.109	1.101	1.093	1.087	1.081	1.075	1.069
	27.5	1.113	1.105	1.099	1.093	1.087	1.082	1.077	1.104	1.096	1.089	1.083	1.078	1.073	1.068	1.099	1.091	1.084	1.079	1.073	1.068	1.063
	30.0	1.103	1.096	1.090	1.085	1.080	1.075	1.070	1.094	1.088	1.082	1.076	1.071	1.066	1.062	1.090	1.083	1.077	1.072	1.067	1.062	1.058
	32.5	1.095	1.088	1.083	1.078	1.073	1.069	1.065	1.087	1.081	1.075	1.070	1.065	1.061	1.057	1.083	1.077	1.071	1.066	1.061	1.057	1.053
	35.0	1.088	1.082	1.077	1.072	1.068	1.064	1.060	1.080	1.075	1.070	1.065	1.061	1.057	1.053	1.077	1.071	1.066	1.061	1.057	1.053	1.049
2	17.5	1.164	1.146	1.131	1.117	1.103	1.090	1.078	1.148	1.131	1.116	1.102	1.089	1.076	1.064	1.140	1.123	1.108	1.094	1.081	1.068	1.056
	20.0	1.142	1.127	1.114	1.101	1.090	1.079	1.068	1.129	1.114	1.101	1.089	1.077	1.066	1.056	1.122	1.107	1.094	1.082	1.071	1.060	1.049
	22.5	1.125	1.112	1.100	1.090	1.079	1.070	1.060	1.114	1.101	1.089	1.078	1.068	1.059	1.049	1.108	1.095	1.083	1.073	1.062	1.053	1.044
	25.0	1.112	1.100	1.090	1.080	1.071	1.062	1.054	1.102	1.090	1.080	1.070	1.061	1.053	1.044	1.096	1.085	1.075	1.065	1.056	1.047	1.039
	27.5	1.101	1.091	1.081	1.073	1.065	1.057	1.049	1.092	1.082	1.072	1.064	1.056	1.048	1.040	1.087	1.077	1.068	1.059	1.051	1.043	1.036
	30.0	1.093	1.083	1.074	1.067	1.059	1.052	1.045	1.084	1.075	1.066	1.058	1.051	1.044	1.037	1.080	1.070	1.062	1.054	1.047	1.039	1.033
	32.5	1.085	1.076	1.069	1.061	1.054	1.048	1.041	1.077	1.069	1.061	1.054	1.047	1.040	1.034	1.073	1.065	1.057	1.050	1.043	1.036	1.030
	35.0	1.079	1.071	1.063	1.057	1.050	1.044	1.038	1.072	1.064	1.056	1.050	1.043	1.037	1.031	1.068	1.060	1.053	1.046	1.040	1.034	1.028
3	17.5	1.137	1.114	1.092	1.072	1.053	1.035	1.017	1.122	1.099	1.078	1.058	1.039	1.021	1.004	1.114	1.091	1.070	1.051	1.032	1.014	
	20.0	1.119	1.099	1.080	1.063	1.046	1.031	1.015	1.106	1.086	1.068	1.051	1.034	1.019	1.003	1.099	1.079	1.061	1.044	1.028	1.012	
	22.5	1.105	1.087	1.071	1.056	1.041	1.027	1.014	1.094	1.076	1.060	1.045	1.030	1.017	1.003	1.088	1.070	1.054	1.039	1.025	1.011	
	25.0	1.094	1.078	1.064	1.050	1.037	1.024	1.012	1.084	1.068	1.054	1.040	1.027	1.015	1.003	1.079	1.063	1.049	1.035	1.022	1.010	
	27.5	1.085	1.071	1.058	1.045	1.034	1.022	1.011	1.076	1.062	1.049	1.037	1.025	1.014	1.002	1.071	1.057	1.044	1.032	1.020	1.009	
	30.0	1.078	1.065	1.053	1.042	1.031	1.020	1.010	1.069	1.057	1.045	1.034	1.023	1.012	1.002	1.065	1.052	1.040	1.029	1.019	1.008	
	32.5	1.072	1.060	1.049	1.038	1.028	1.019	1.009	1.064	1.052	1.041	1.031	1.021	1.011	1.002	1.060	1.048	1.037	1.027	1.017	1.008	
	35.0	1.066	1.055	1.045	1.036	1.026	1.017	1.009	1.059	1.048	1.038	1.029	1.019	1.011	1.002	1.056	1.045	1.035	1.025	1.016	1.007	
4	17.5	1.119	1.091	1.066	1.042	1.019			1.104	1.077	1.052	1.028	1.006			1.096	1.069	1.044	1.021			
	20.0	1.103	1.079	1.057	1.037	1.017			1.090	1.067	1.045	1.025	1.005			1.084	1.060	1.039	1.018			
	22.5	1.091	1.070	1.051	1.032	1.015			1.080	1.059	1.040	1.022	1.004			1.074	1.053	1.034	1.016			
	25.0	1.082	1.063	1.046	1.029	1.013			1.072	1.053	1.036	1.020	1.004			1.066	1.048	1.031	1.015			
	27.5	1.074	1.057	1.041	1.026	1.012			1.065	1.048	1.033	1.018	1.004			1.060	1.043	1.028	1.013			
	30.0	1.068	1.052	1.038	1.024	1.011			1.059	1.044	1.030	1.016	1.003			1.055	1.040	1.026	1.012			
	32.5	1.062	1.048	1.035	1.022	1.010			1.055	1.041	1.027	1.015	1.003			1.051	1.037	1.024	1.011			
	35.0	1.058	1.045	1.032	1.021	1.010			1.051	1.038	1.025	1.014	1.003			1.047	1.034	1.022	1.010			
5	17.5	1.104	1.074	1.046	1.019				1.090	1.060	1.032	1.005				1.082	1.052	1.025				
	20.0	1.091	1.064	1.040	1.017				1.078	1.052	1.028	1.005				1.072	1.046	1.021				
	22.5	1.080	1.057	1.035	1.015				1.069	1.046	1.025	1.004				1.063	1.040	1.019				
	25.0	1.072	1.051	1.032	1.013				1.062	1.041	1.022	1.004				1.057	1.036	1.017				
	27.5	1.065	1.046	1.029	1.012				1.056	1.038	1.020	1.003				1.052	1.033	1.016				
	30.0	1.060	1.042	1.026	1.011				1.051	1.034	1.018	1.003				1.047	1.030	1.014				
	32.5	1.055	1.039	1.024	1.010				1.047	1.032	1.017	1.003				1.043	1.028	1.013				
	35.0	1.051	1.036	1.023	1.009				1.044	1.029	1.016	1.003				1.040	1.026	1.012				

APPENDIX B

DAMAGE-TOLERANCE ELEMENT TEST RESULTS

This appendix contains the results and statistical analysis results for damage-tolerance element tests. In addition, for several selected DTE test specimens, full-field strain and displacement data using ARAMIS photogrammetry system are included. Such data are instrumental in evaluating the extent of damage after fatigue loading.

B.1. S-N data for AS4-PW Damage Tolerance Element Tests

Table A.28 includes the S-N data for damage-tolerance element tests. Figures B.1 through B.3 show the S-N diagrams as well as the Sendeckyj fitting data and Kassapoglou predictions.

TABLE A.30

S-N DATA FOR AS4-PW 25/50/25 OHT AND CAI TESTS (FAA-LEF)

CAI (R = 5) - BVID		CAI (R = 5) - VID		CAI (R = 5) - LID	
σ_A	n	σ_A	n	σ_A	n
37188	1	29149	1	25147	1
34745	1	31335	1	25601	1
35658	1	29443	1	24627	1
36526	1	29282	1	25370	1
36364	1	29950	1	25228	1
35669	1	28866	1	26695	1
28820	12243	22374	37690	19083	42897
28820	14342	22374	24001	19083	38476
28820	9651	22374	55768	19083	18155
28820	8152	22374	28958	19083	13719
28820	15155	22374	11897	19083	32463
28820	26005	22374	16335	19083	17564
27019	92926	20882	127451	16539	201380
27019	31634	20882	94625	16539	214807
27019	104891	20882	128689	16539	374375
27019	152023	20882	59749	16539	278234
27019	47635	20882	143030	16539	165086
27019	31642	20882	180742	16539	193821
25217	678421	19391	626039	15267	2233805
25217	596825	19391	397153	15267	1352887
25217	323026	19391	270784	15267	1618147
25217	252255	19391	638545	15267	1236307
25217	575983	19391	222775	15267	928401
25217	252433	19391	595875	15267	1228113

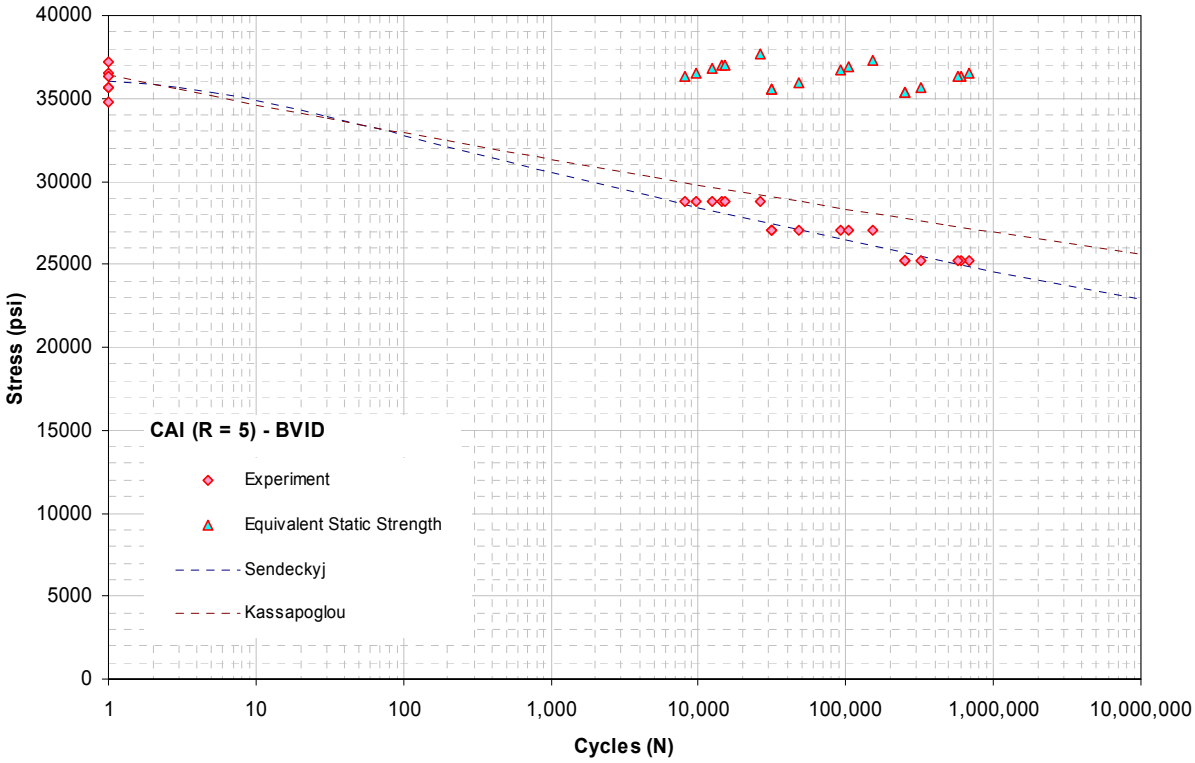

Figure B.1. AS4/E7K8 PW – 25/50/25, CAI - BVID, R=5.

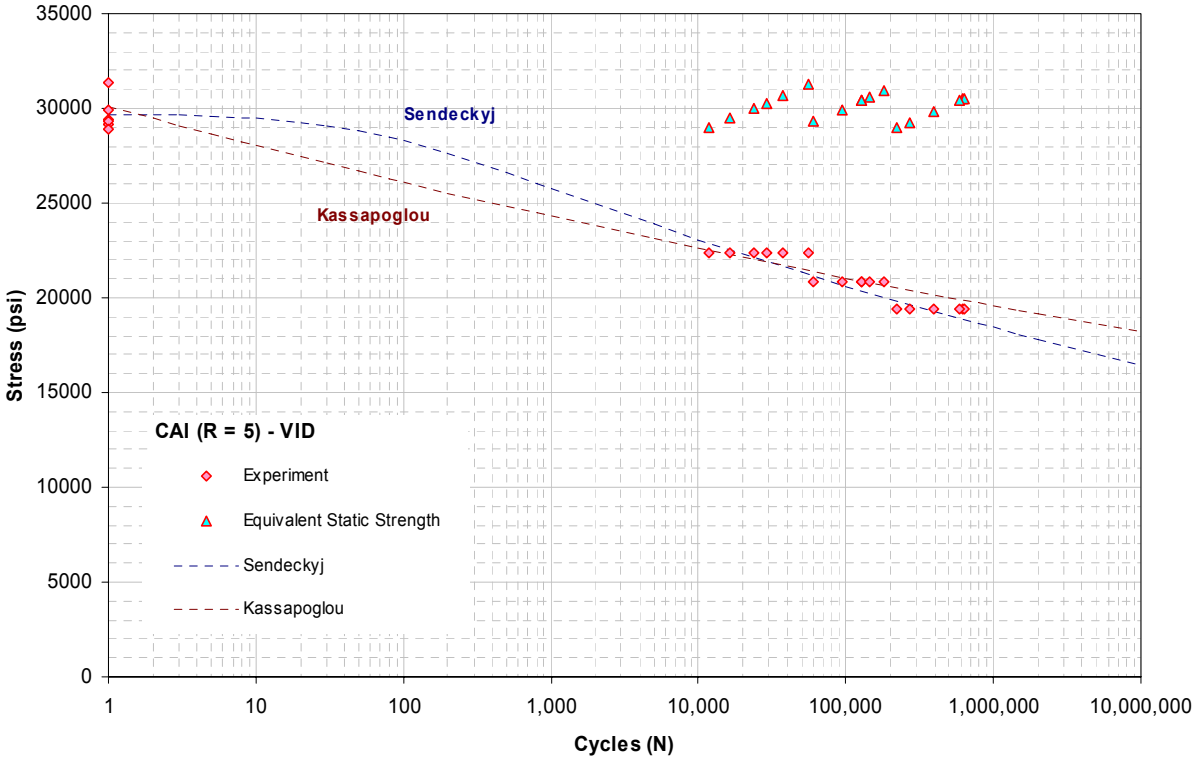

Figure B.2. AS4/E7K8 PW – 25/50/25, CAI - VID, R=5.

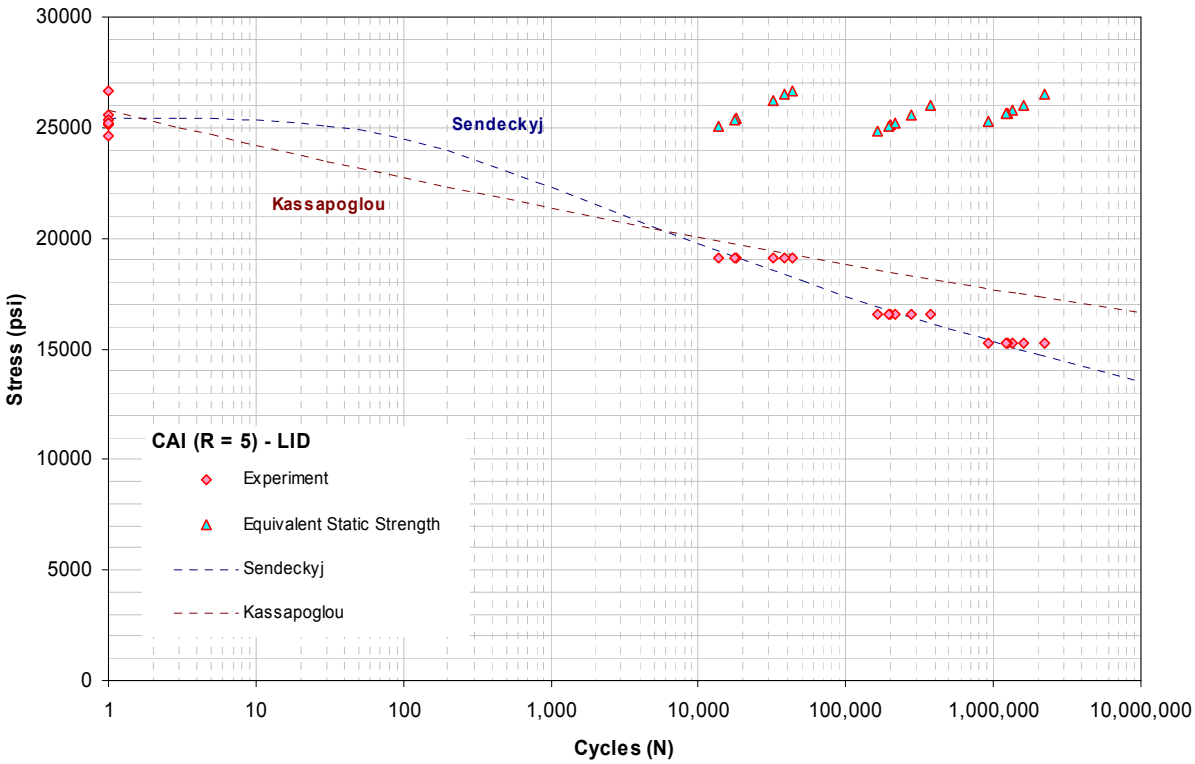

Figure B.3. AS4/E7K8 PW – 25/50/25, CAI - LID, R=5.

B.1. Full-field strain and Displacement data for Damage Tolerance Element Tests

Figure B.4 through B.10 show the full-field strain and displacement data for several DTE test specimens.

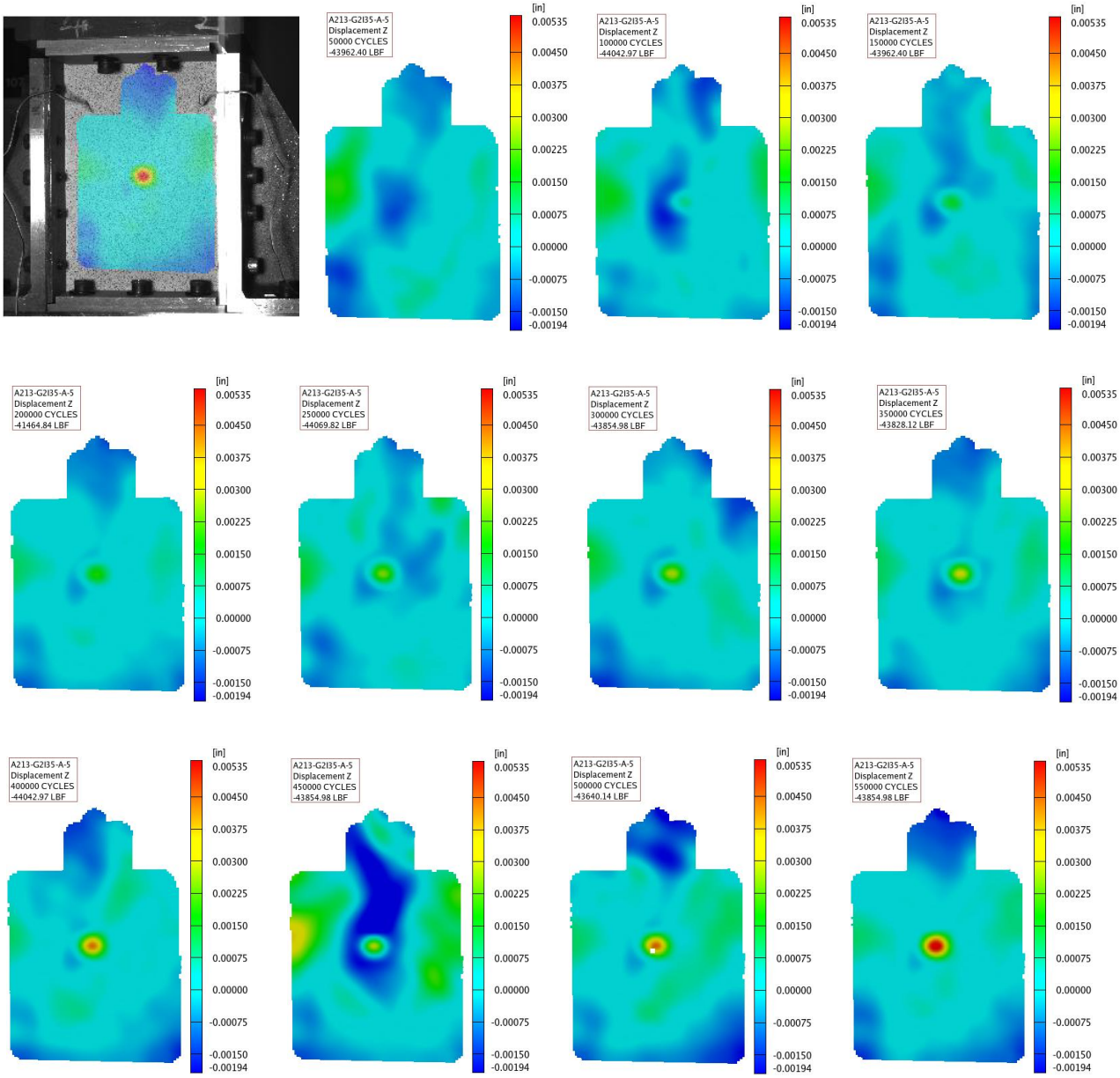

Figure B.4. Out-of-plane deformation for fatigue testing of DTE – BVID (750 in/lb/in), 70% of static strength, R=5.

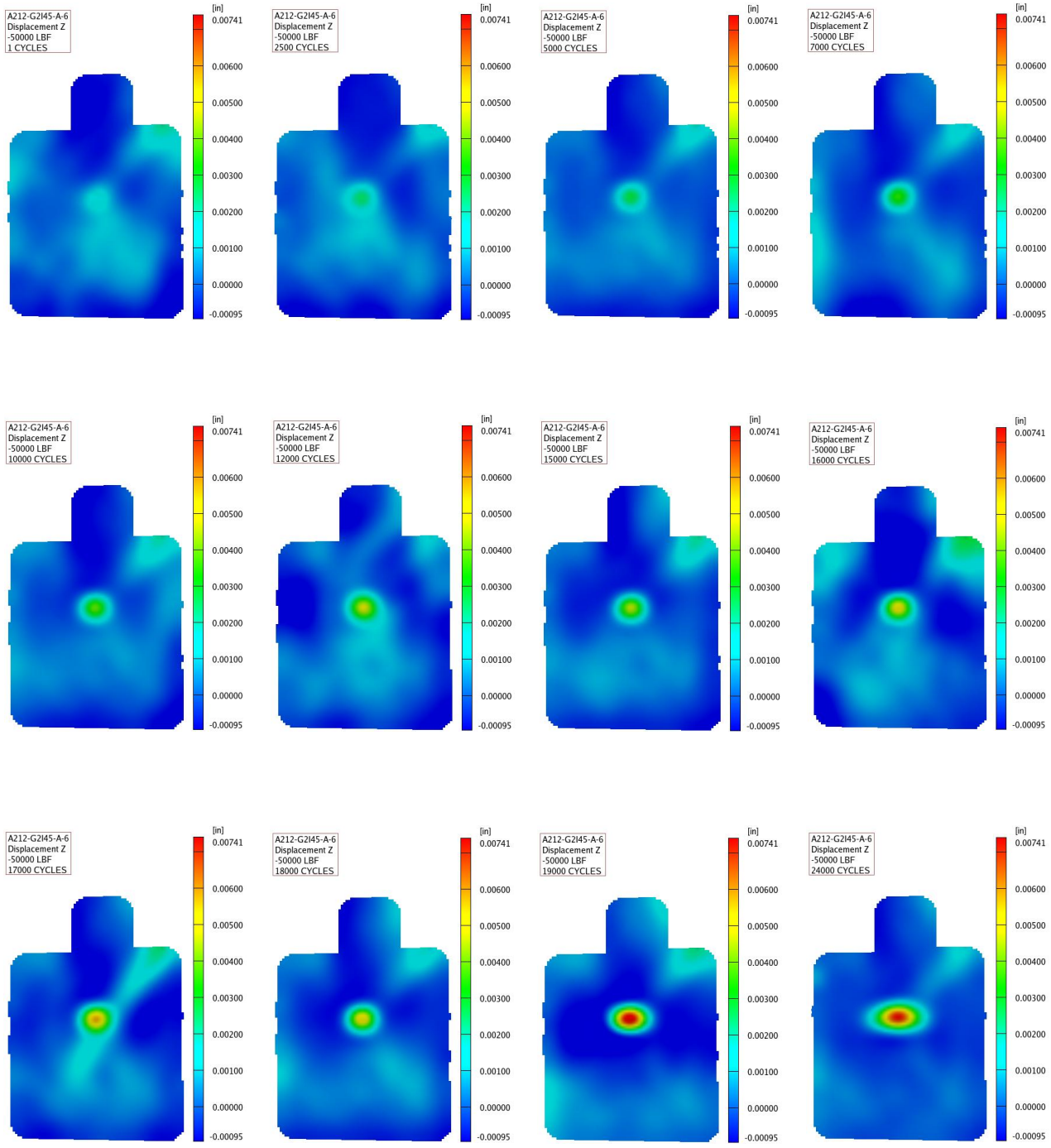

Figure B.5. Out-of-plane deformation for fatigue testing of DTE – BVID (750 in/lb/in), 80% of static strength, R=5.

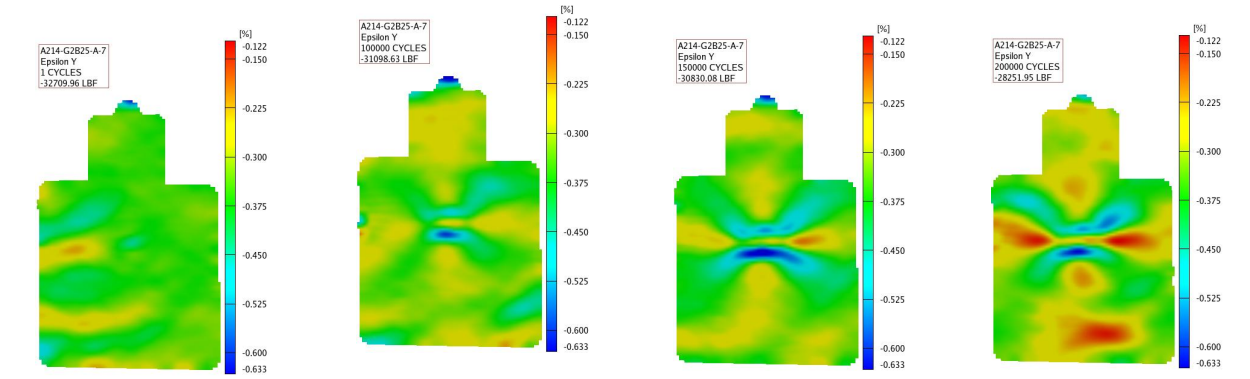

(a) Axial strain

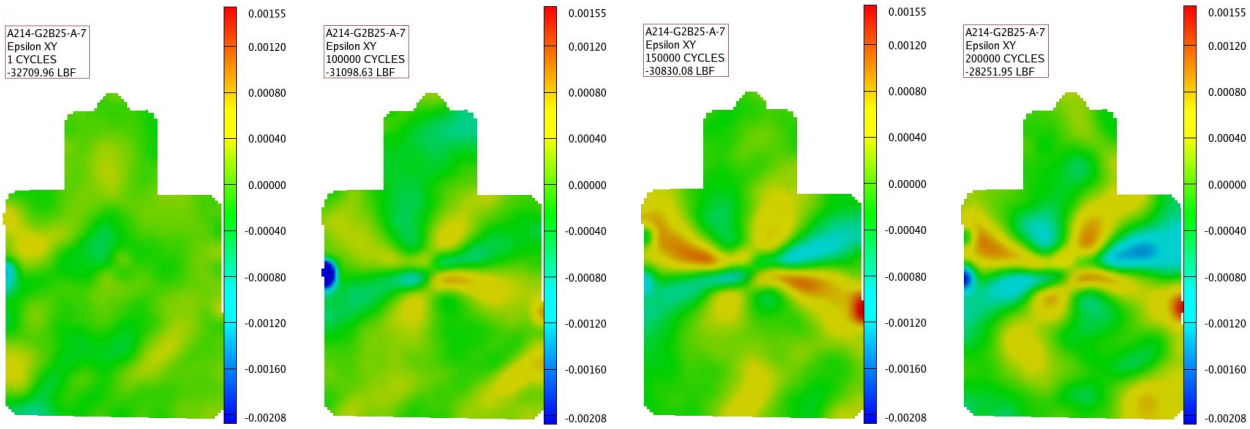

(b) Shear strain

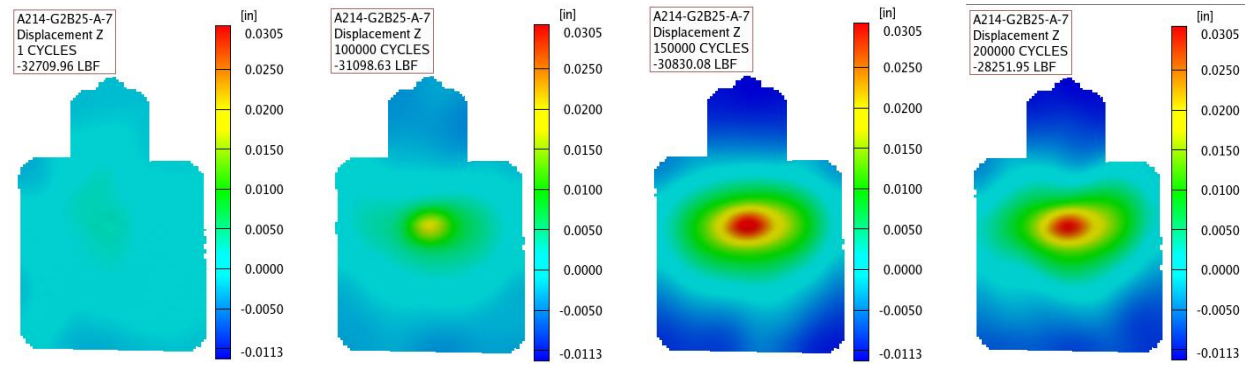

(C) Out-of-plane deformation

Figure B.6. Strain and displacement for fatigue testing of DTE – VID (1500 in/lb/in), 65% of static strength, R=5.

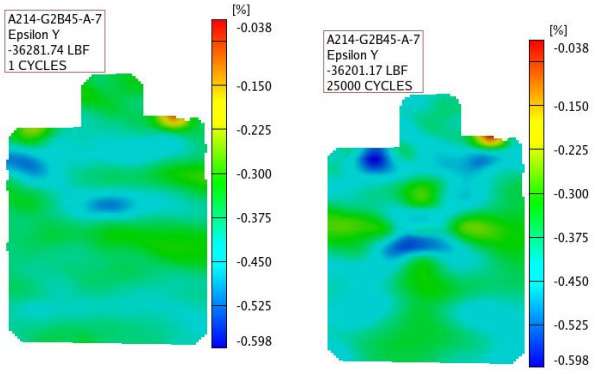

(a) Axial strain

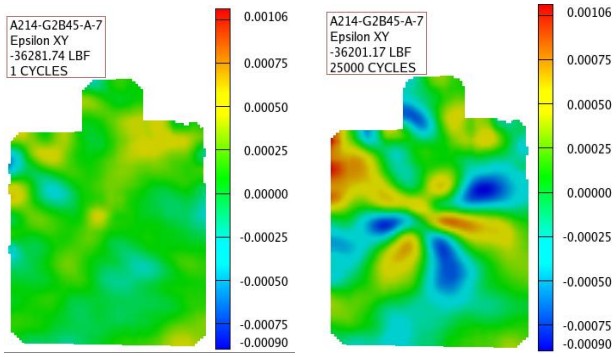

(b) Shear strain

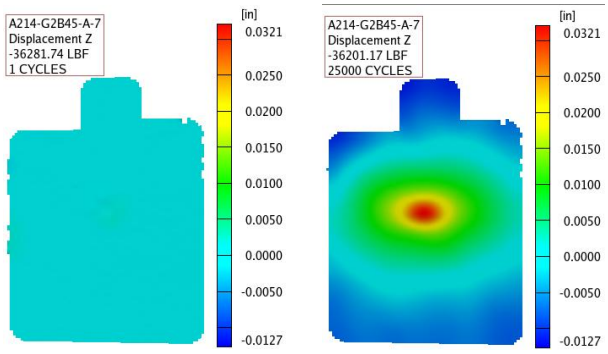

(C) Out-of-plane deformation

Figure B.7. Strain and displacement for fatigue testing of DTE – VID (1500 in/lb/in), 70% of static strength, R=5.

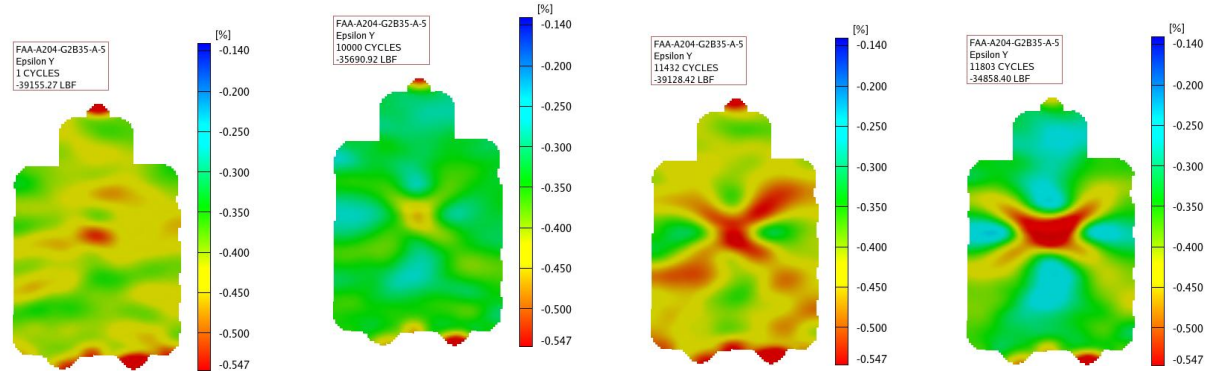

(a) Axial strain

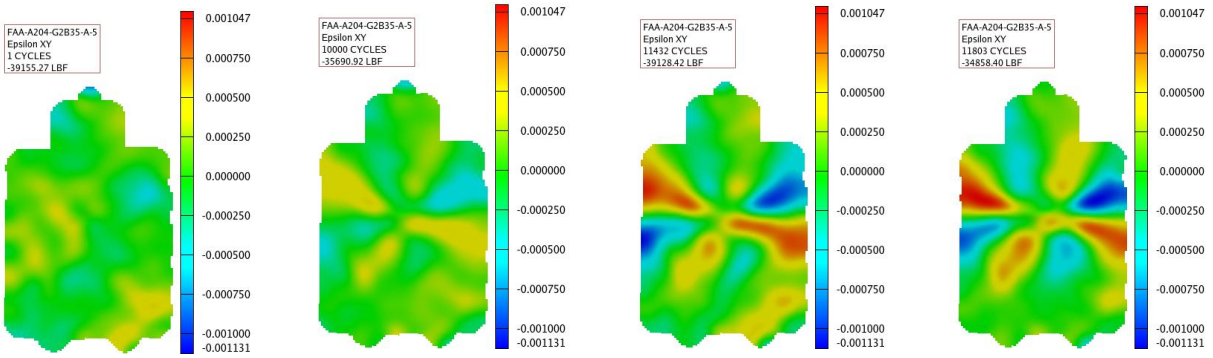

(b) Shear strain

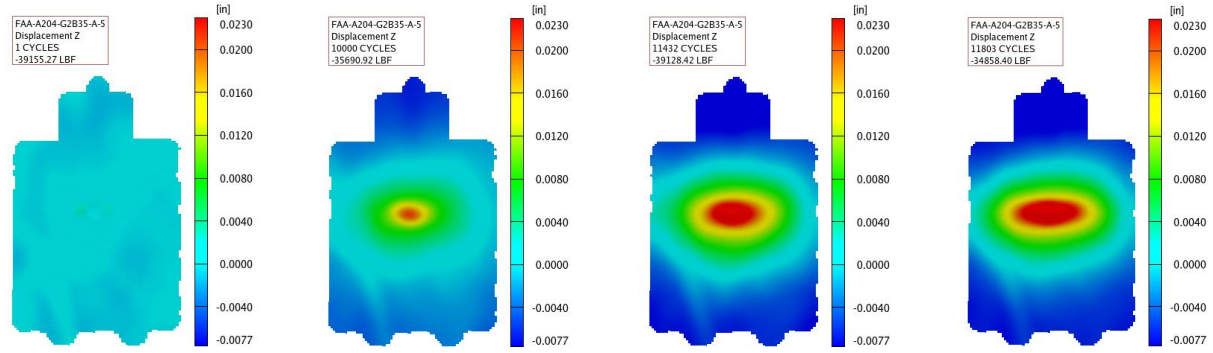

(C) Out-of-plane deformation

Figure B.8. Strain and displacement for fatigue testing of DTE – VID (1500 in/lb/in), 75% of static strength, R=5.

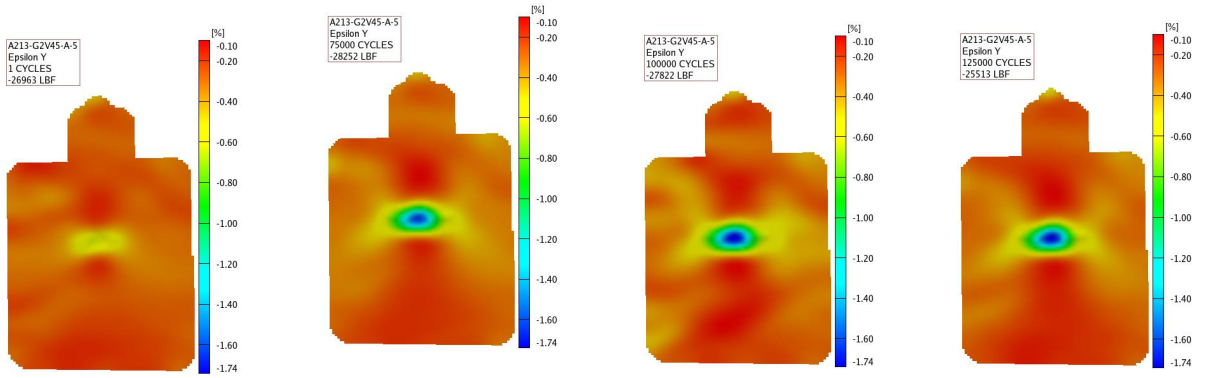

(a) Axial strain

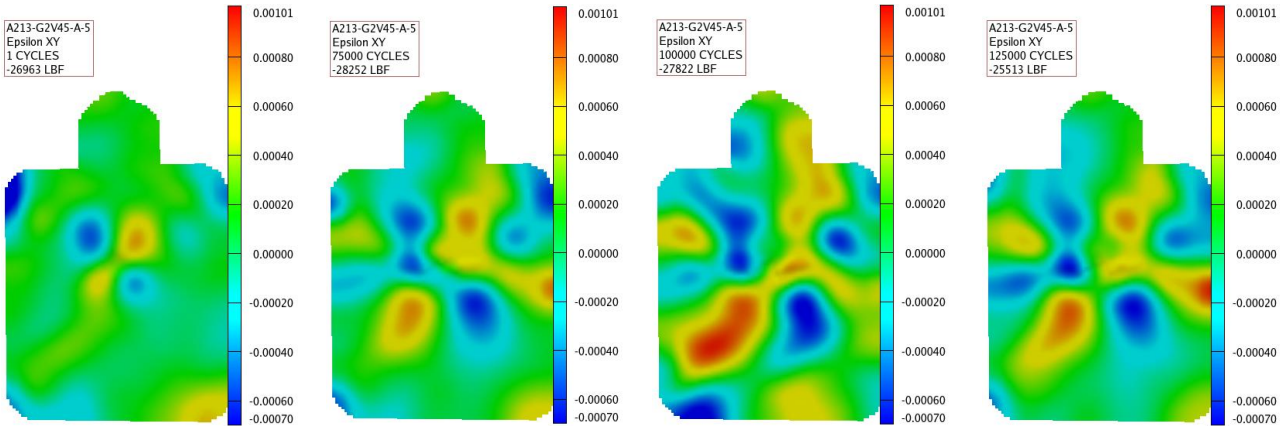

(b) Shear strain

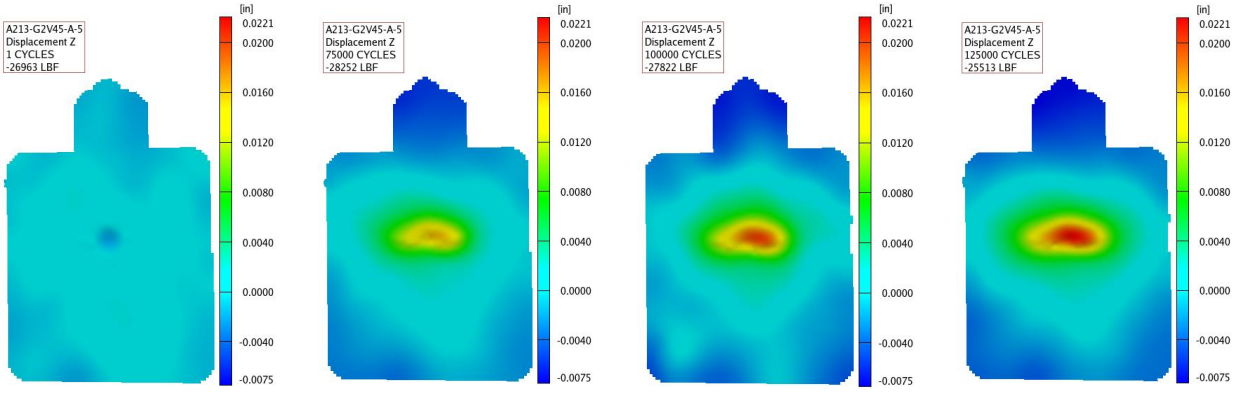

(C) Out-of-plane deformation

Figure B.9. Strain and displacement for fatigue testing of DTE - LID (3000 in/lb/in), 65% of static strength, R=5.

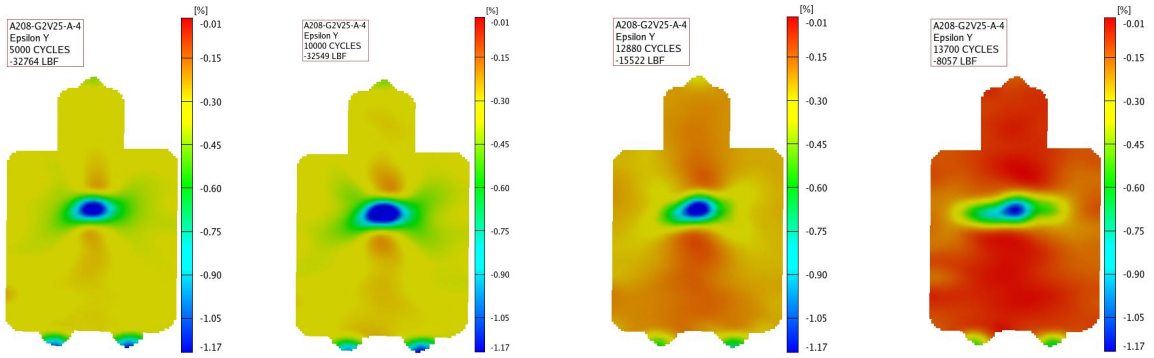

(a) Axial strain

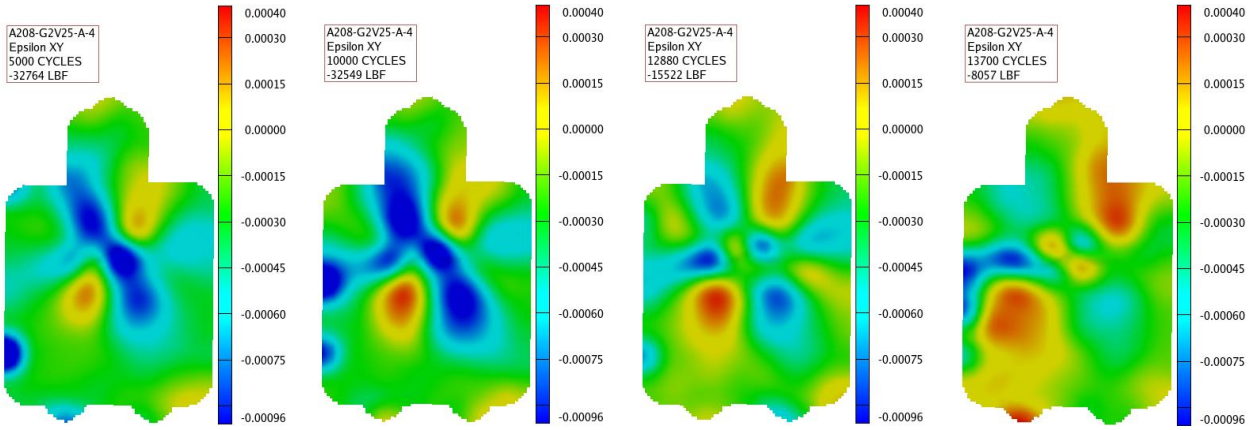

(b) Shear strain

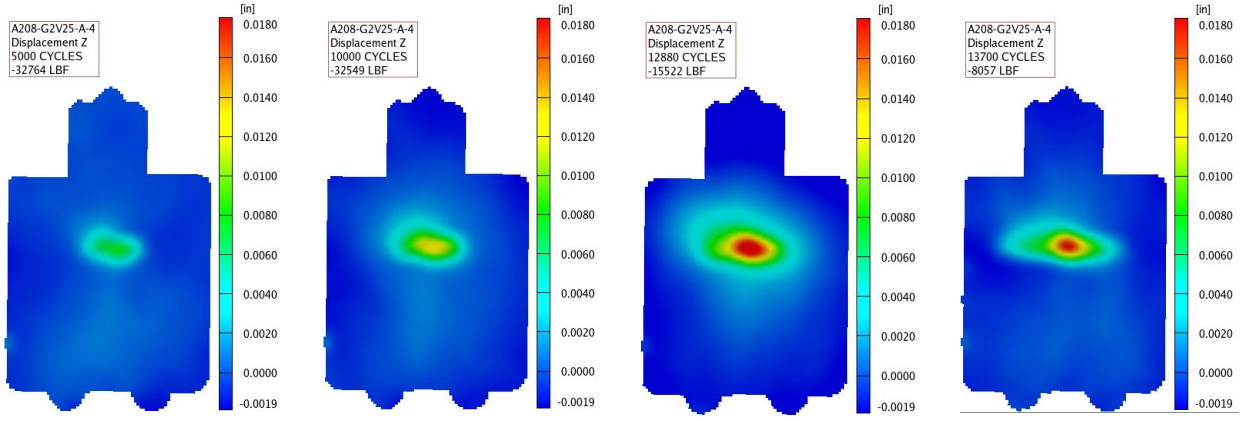

(C) Out-of-plane deformation

Figure B.10. Strain and displacement for fatigue testing of DTE - LID (3000 in/lb/in), 75% of static strength, R=5.

APPENDIX C

SPECTRUM LOADS FOR FULL-SCALE DADT TESTING

One RAC-defined lifetime of the test article is equivalent to 20,000 flight hours, which corresponds to a spectrum of 160,033 cycles, and which include 1-g and 3-g maneuvers as well as positive and negative gust conditions.

The origin of the axis system for forward-wing loads is at FWS 19.76 and lies on the central axis of the steel tube at the fixed end, as shown in Figure C.1. This figure shows the positive load, moment, and torque directions ($+P_Z$, $+M_x$, and $+T_y$, respectively) for the right-hand wing using the right-hand rule. For the left wing, the positive torque axis is oriented outboard so that the positive load axis is upward using the left-hand rule.

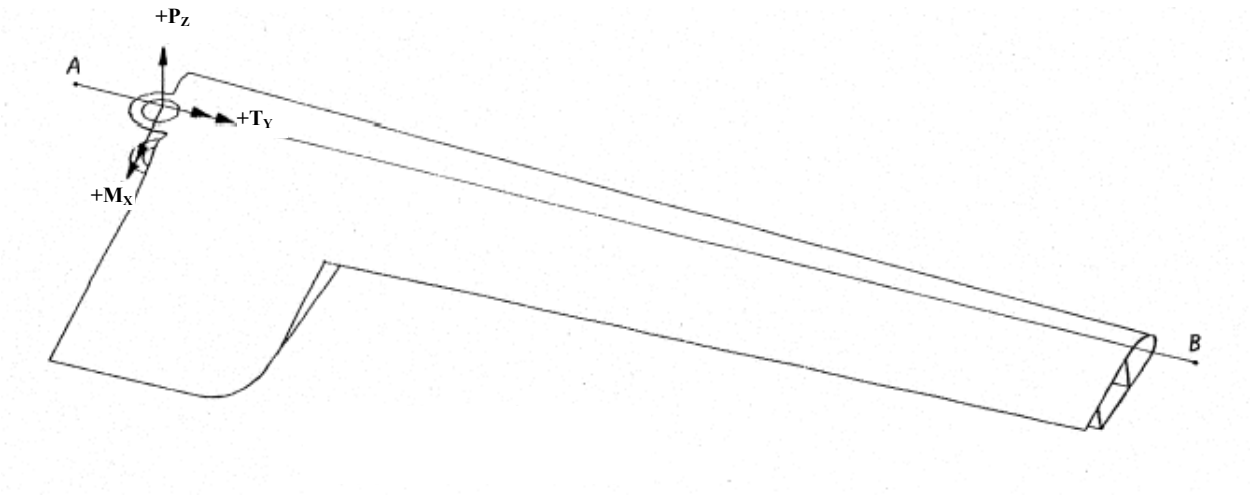

Figure C.1. Reference axis system for forward-wing loads.

Loads were applied to structures using load-formers (Figure C.2) and load-patch (Figure C.3) whiffletree settings for static and fatigue full-scale test articles, respectively. All static tests were performed only in the upbending configuration, and the majority of fatigue loads were in the upbending configuration, whereby the test articles were mounted upside down for ease of

inspection and safety. For fatigue tests, both top and bottom whiffletrees and four actuators were used so that both positive and negative SMT loads could be applied.

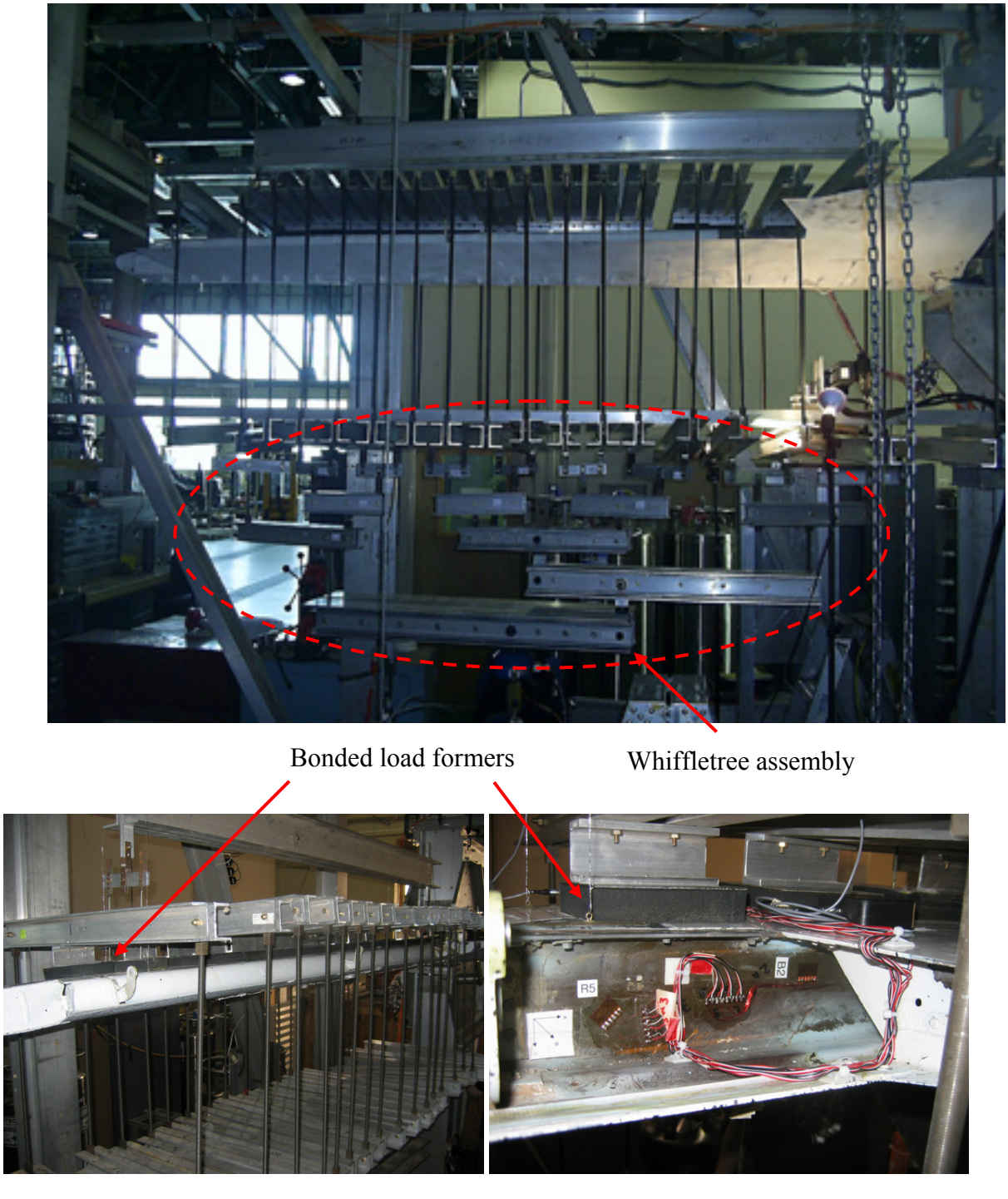

Figure C.2. Forward wing static test whiffletree setup with bonded load formers.

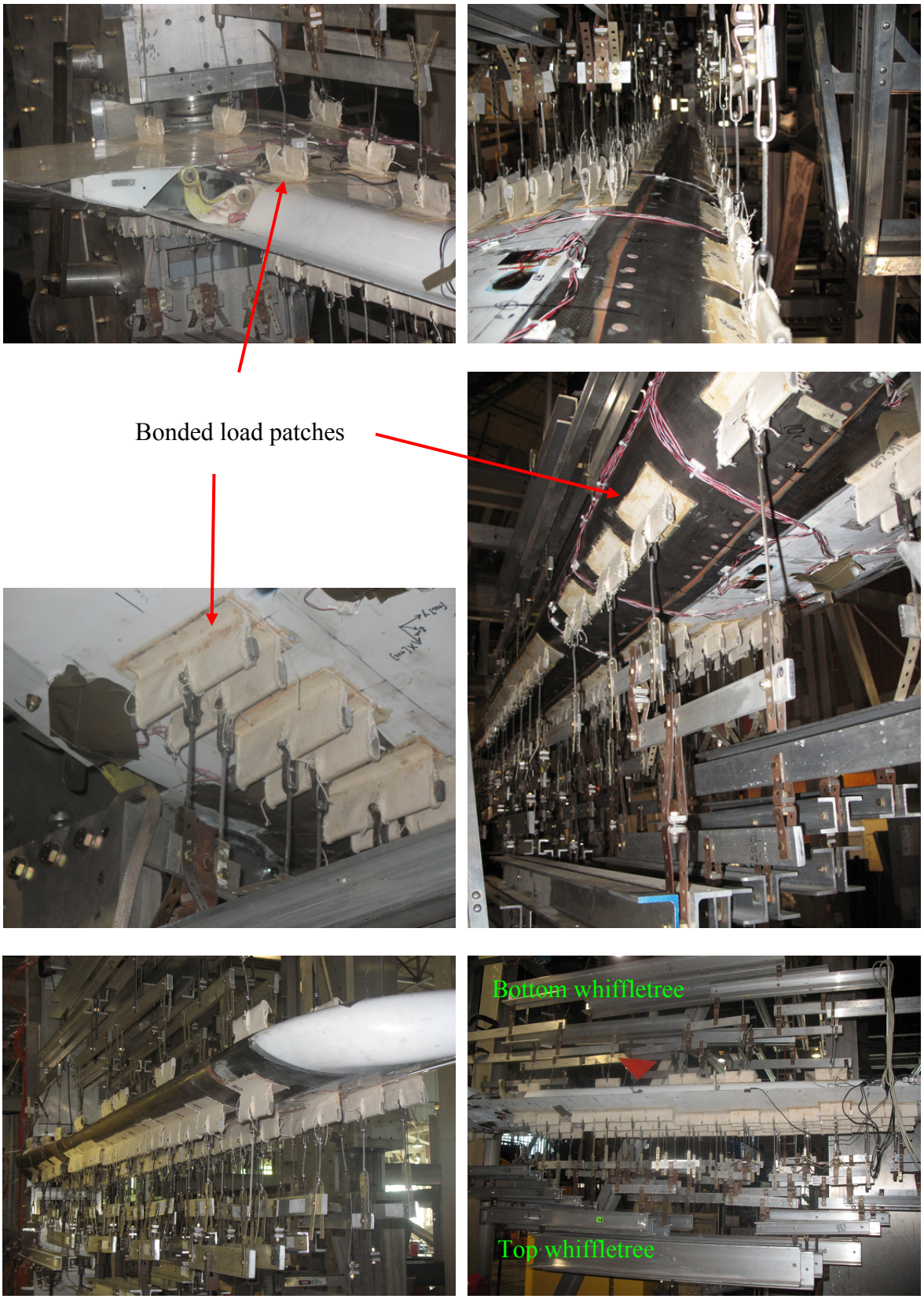

Figure C.3. Forward wing fatigue test whiffletree setup with bonded load patches.

Figures C.4 and C.5 show the maneuver and gust exceedences used for generating the Starship forward-wing load spectrum. Figures C.6 through C.9 show the Δg loads of the spectrum. Table C.1 contains the SMT loads with no load-enhancements.

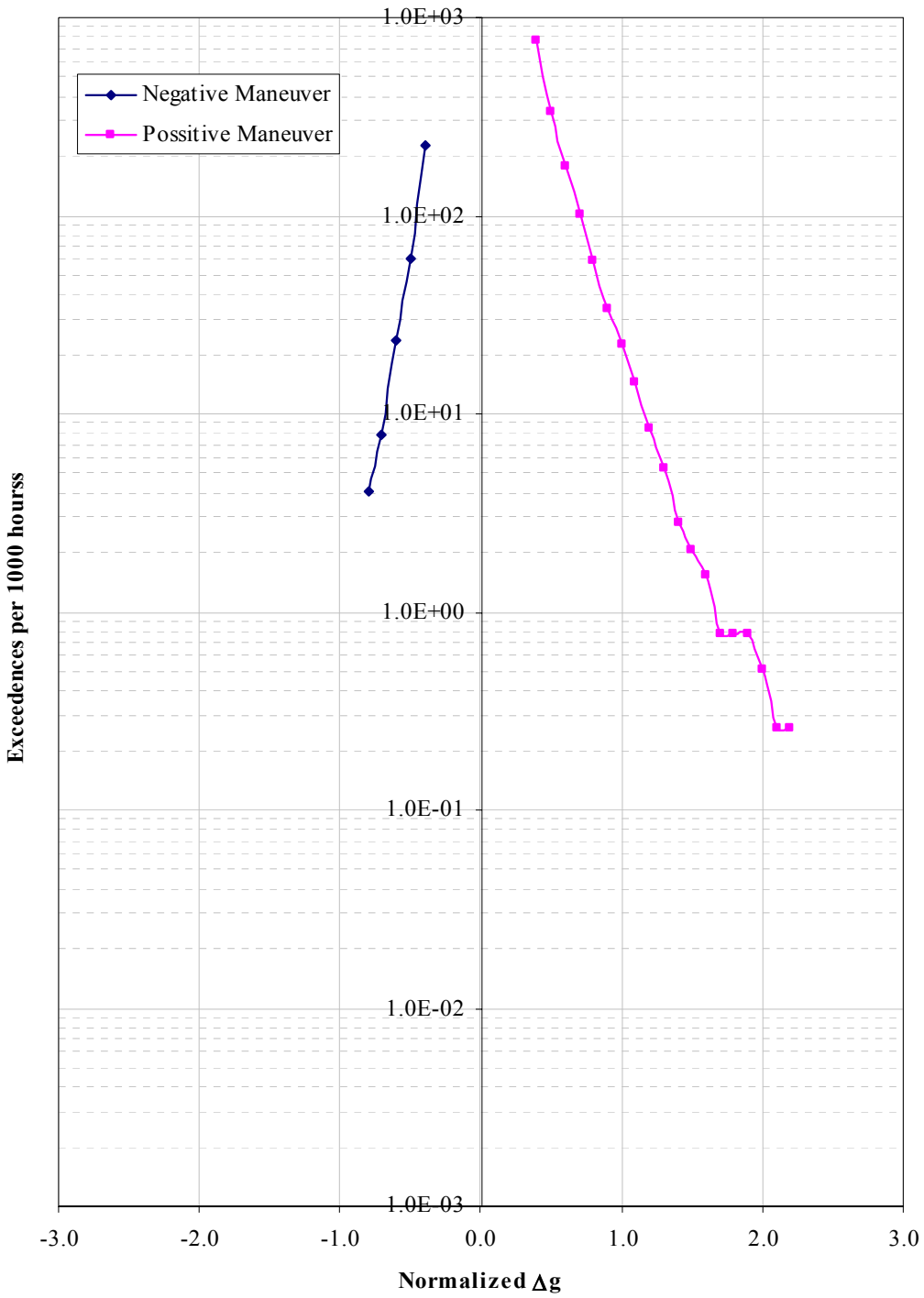

Figure C.4. Maneuver Δg's and exceedences.

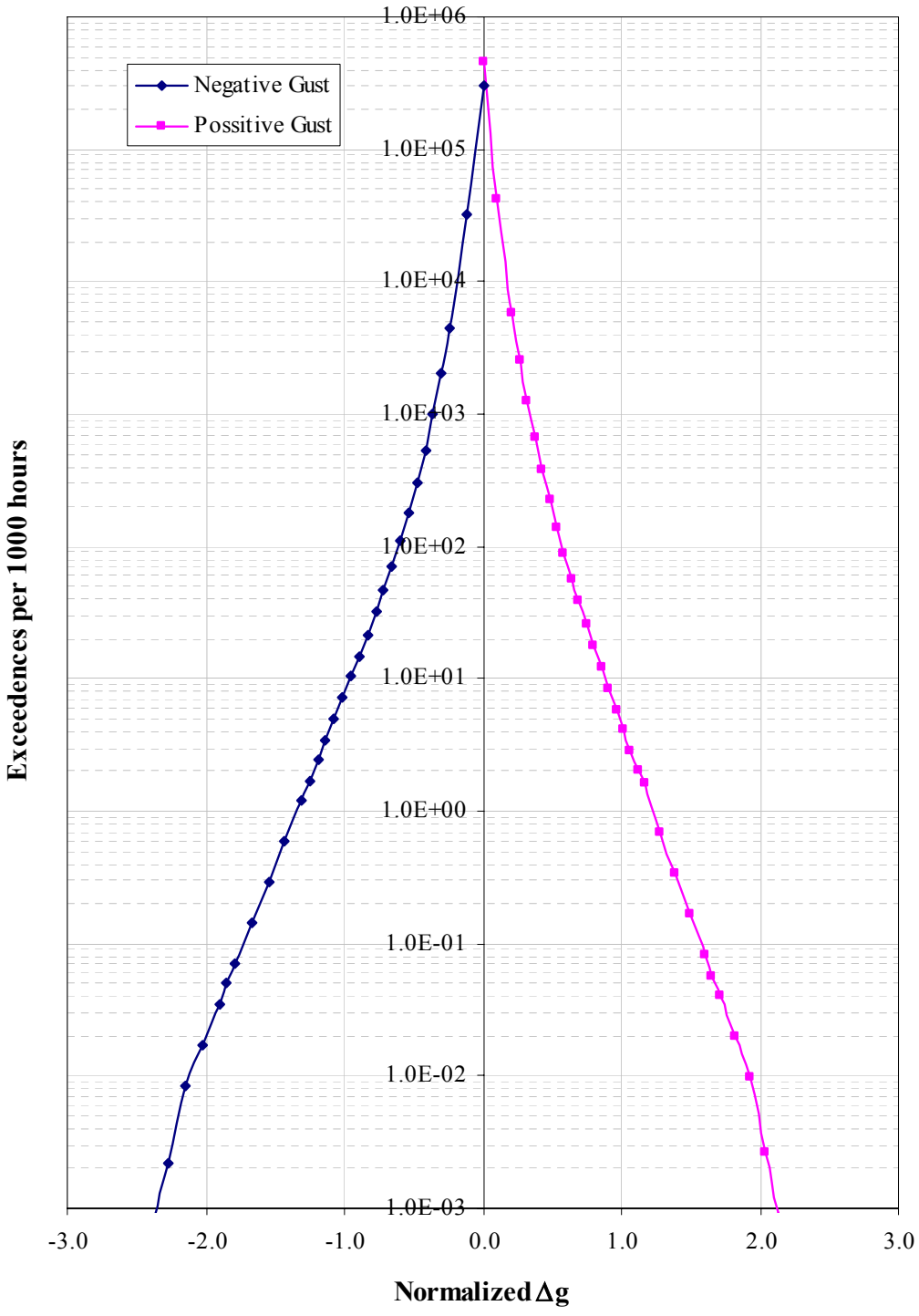

Figure C.5. Gust Δg's and exceedences.

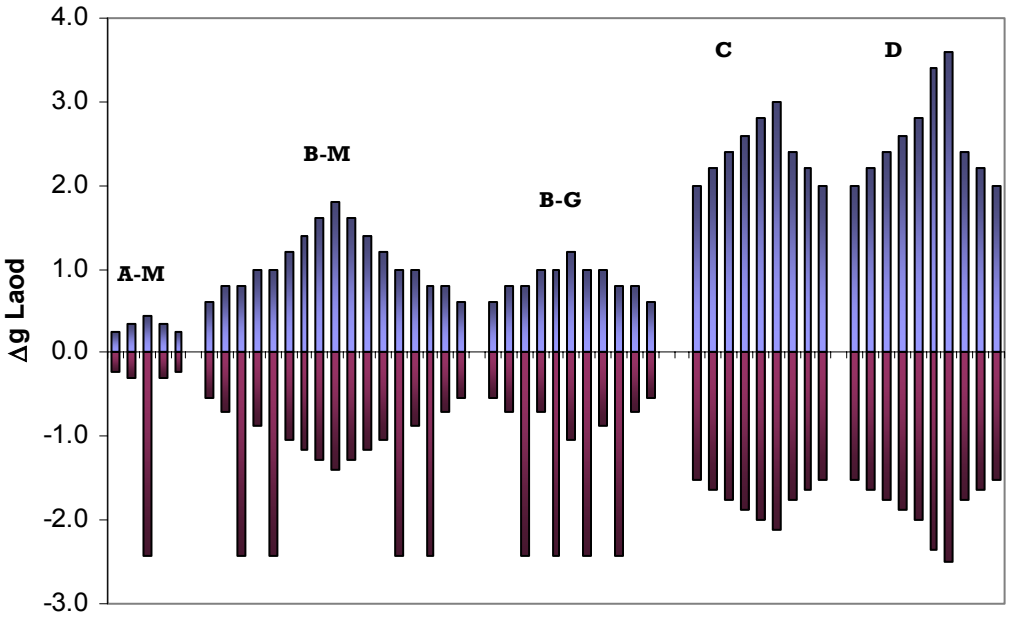

Figure C.6. Comparison of loading blocks.

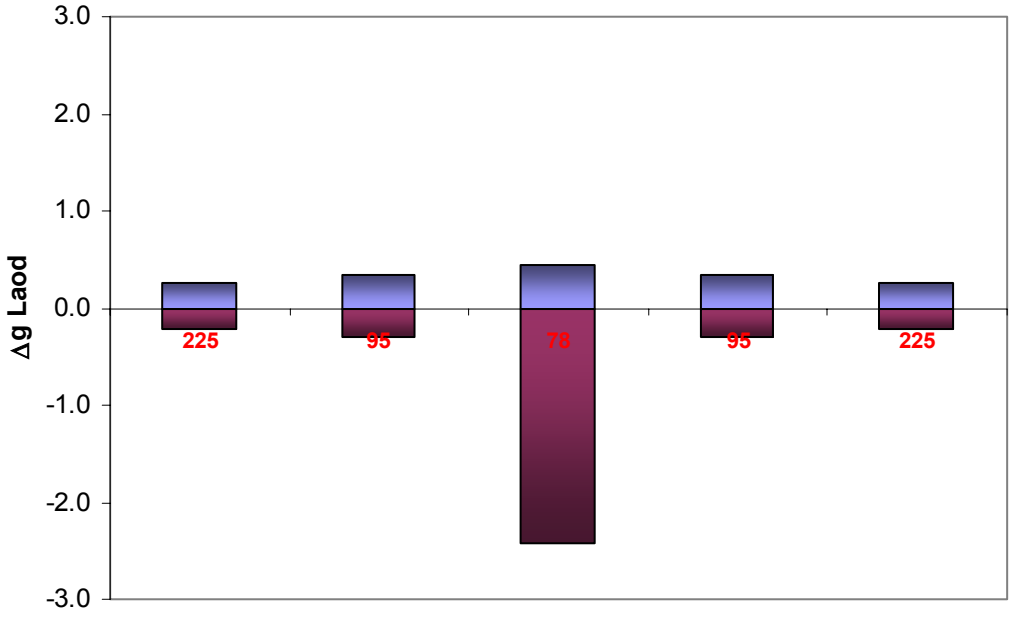

Figure C.7. Loading block A-Maneuver, occurrences/100 hours.

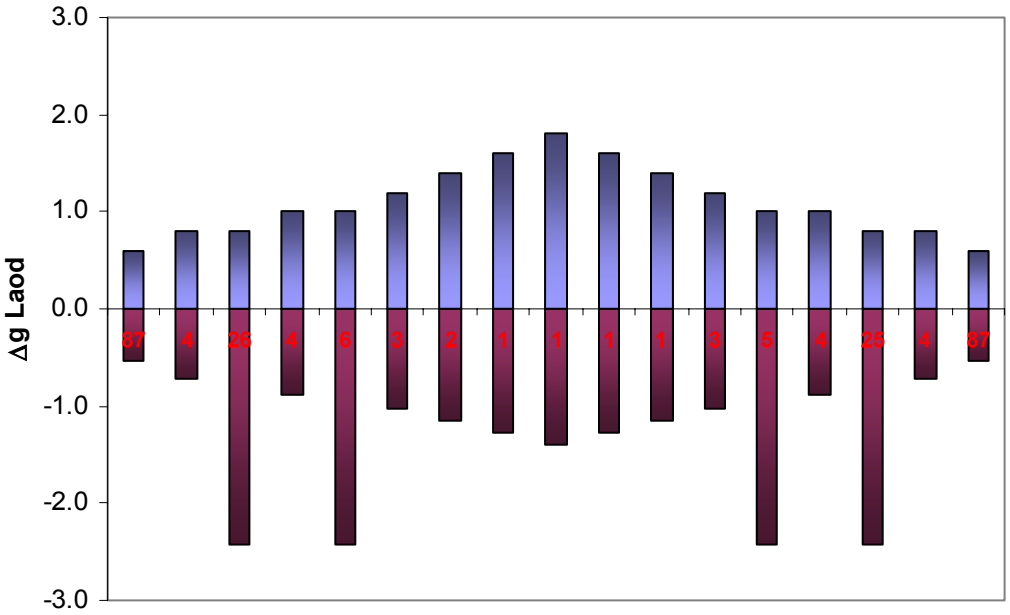

Figure C.8. Loading block B-Maneuver, occurrences/500 hours.

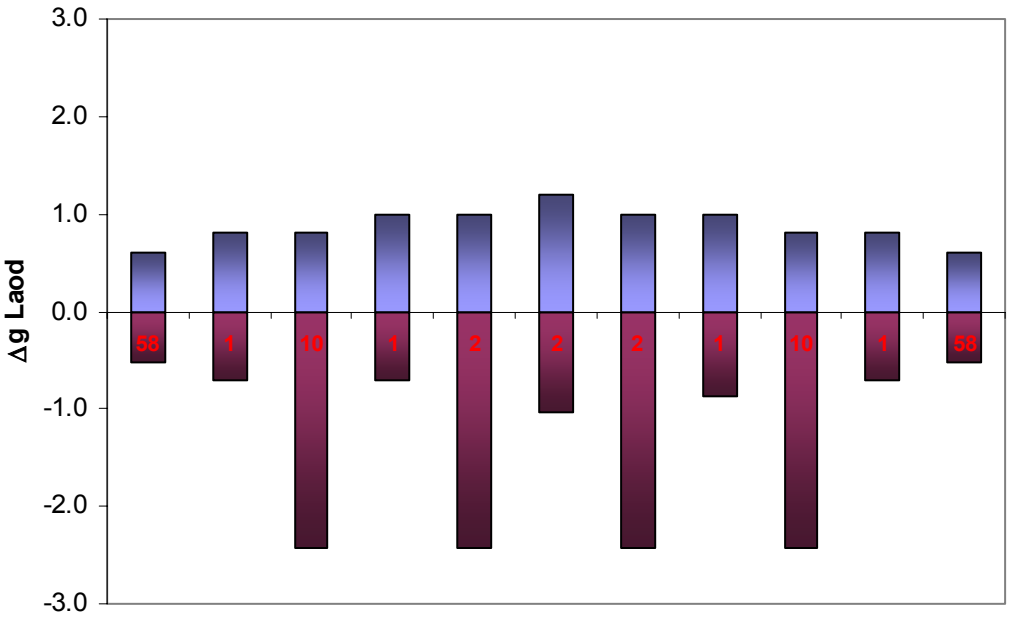

Figure C.9. Loading block B-Gust, occurrences/500 hours.

TABLE C.1

MANEUVER AND GUST LOADS FOR FORWARD WING (CF=1.0 AND LEF=1.0).

	Shear Loads (lbf)		Moments (in-lbf)		Torque (in-lbf)	
Block	**Max Load**	**Min Load**	**Max Load**	**Min Load**	**Max Load**	**Min Load**
Block A-M Maneuver	2,458	1,990	151,007	124,309	-5,578	-4,358
	2,627	1,860	160,648	116,893	-6,019	-4,019
	2,783	-649	169,548	-26,240	-6,425	2,522
	2,627	1,860	160,648	116,893	-6,019	-4,019
	2,458	1,990	151,007	124,309	-5,578	-4,358
Block B-M Maneuver	3,004	1,574	182,155	100,577	-7,001	-3,274
	3,264	1,366	196,988	88,711	-7,679	-2,731
	3,264	-649	196,988	-26,240	-7,679	2,522
	3,550	1,158	213,303	76,845	-8,425	-2,189
	3,550	-649	213,303	-26,240	-8,425	2,522
	3,810	950	228,136	64,979	-9,103	-1,647
	4,057	794	242,226	56,080	-9,746	-1,240
	4,304	638	256,317	47,180	-10,390	-833
	4,551	508	270,408	39,764	-11,034	-495
	4,304	638	256,317	47,180	-10,390	-833
	4,057	794	242,226	56,080	-9,746	-1,240
	3,810	950	228,136	64,979	-9,103	-1,647
	3,550	-649	213,303	-26,240	-8,425	2,522
	3,550	1,158	213,303	76,845	-8,425	-2,189
	3,264	-649	196,988	-26,240	-7,679	2,522
	3,264	1,366	196,988	88,711	-7,679	-2,731
	3,004	1,574	182,155	100,577	-7,001	-3,274
Block B-G Gust	3,004	1,574	182,155	100,577	-4,650	-5,233
	3,264	1,366	196,988	88,711	-4,544	-5,318
	3,264	-649	196,988	-26,240	-4,544	-6,139
	3,550	1,158	213,303	76,845	-4,427	-5,403
	3,550	-649	213,303	-26,240	-4,427	-6,139
	3,810	950	228,136	64,979	-4,321	-5,487
	3,550	-649	213,303	-26,240	-4,427	-6,139
	3,550	1,158	213,303	76,845	-4,427	-5,403
	3,264	-649	196,988	-26,240	-4,544	-6,139
	3,264	1,366	196,988	88,711	-4,544	-5,318
	3,004	1,574	182,155	100,577	-4,650	-5,233

TABLE C.1 (continued)

	Shear Loads (lbf)		Moments (in-lbf)		Torque (in-lbf)	
Block	**Max Load**	**Min Load**	**Max Load**	**Min Load**	**Max Load**	**Min Load**
Block C +Δg with Maneuver Torque -Δg with Gust Torque	4,798	352	284,499	30,865	-11,678	-5,731
	5,032	196	297,848	21,965	-12,288	-5,795
	5,266	53	311,197	13,807	-12,898	-5,853
	5,500	-90	324,546	5,650	-13,508	-5,911
	5,721	-207	337,154	-1,025	-14,084	-5,959
	5,942	-350	349,761	-9,183	-14,661	-6,017
	5,266	53	311,197	13,807	-12,898	-5,853
	5,032	196	297,848	21,965	-12,288	-5,795
	4,798	352	284,499	30,865	-11,678	-5,731
Block D +Δg with Maneuver Torque -Δg with Gust Torque	4,798	261	284,499	25,673	-11,678	-5,768
	5,032	92	297,848	16,032	-12,288	-5,837
	5,266	-51	311,197	7,875	-12,898	-5,896
	5,500	-220	324,546	-1,767	-13,508	-5,964
	5,721	-363	337,154	-9,924	-14,084	-6,023
	6,163	-844	362,369	-37,364	-15,237	-6,219
	5,266	-1,013	311,197	-47,005	-12,898	-6,288
	5,032	92	297,848	16,032	-12,288	-5,837
	4,798	261	284,499	25,673	-11,678	-5,768

Figures C.10 through C.15 shows the spectrum loads in Table C.1 with and without LEF=1.072, after applying the CF= 1.4.

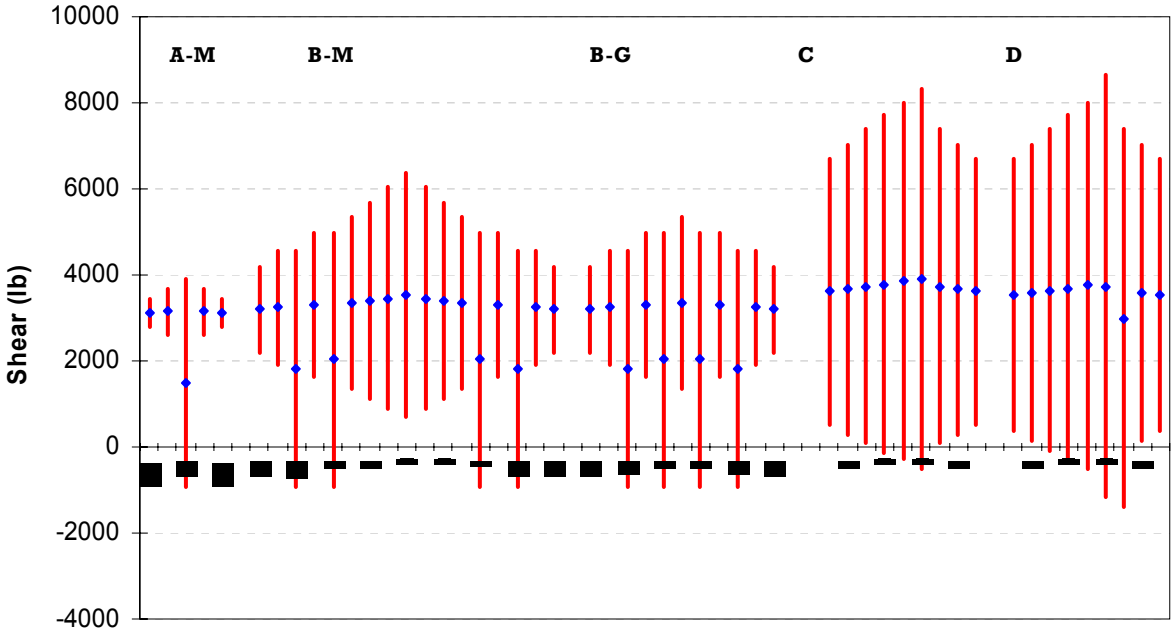

Figure C.10. Maneuver and gust shear spectrums, CF=1.4 and LEF=1.000.

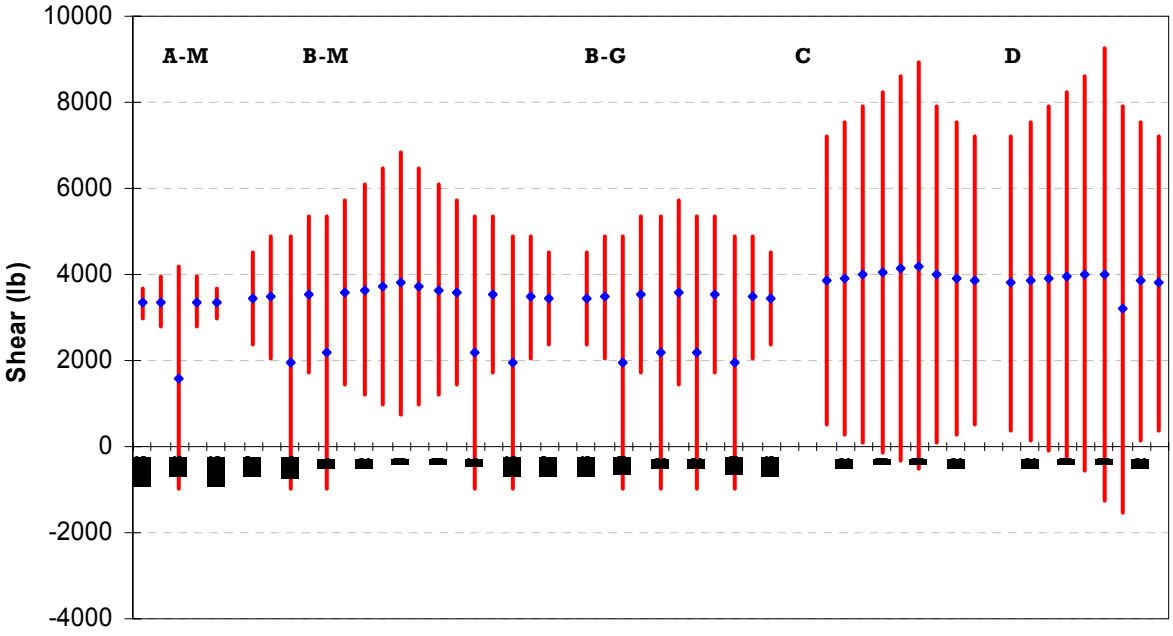

Figure C.11. Maneuver and gust shear spectrums, CF=1.4 and LEF=1.072.

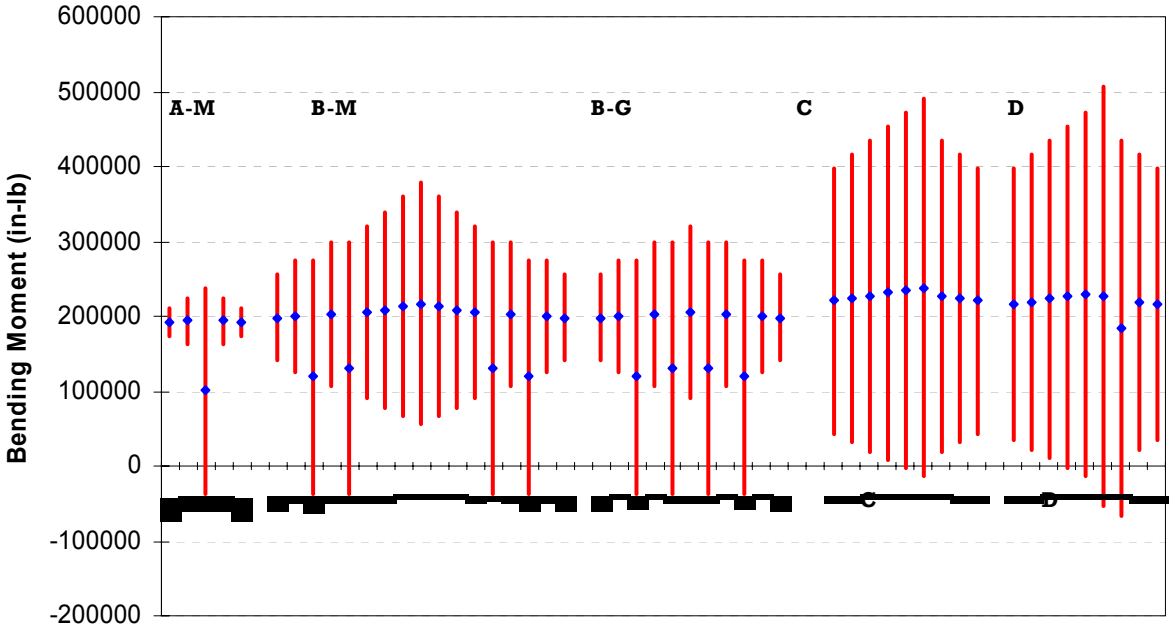

Figure C.12. Maneuver and gust bending moment spectrums, CF=1.4 and LEF=1.000.

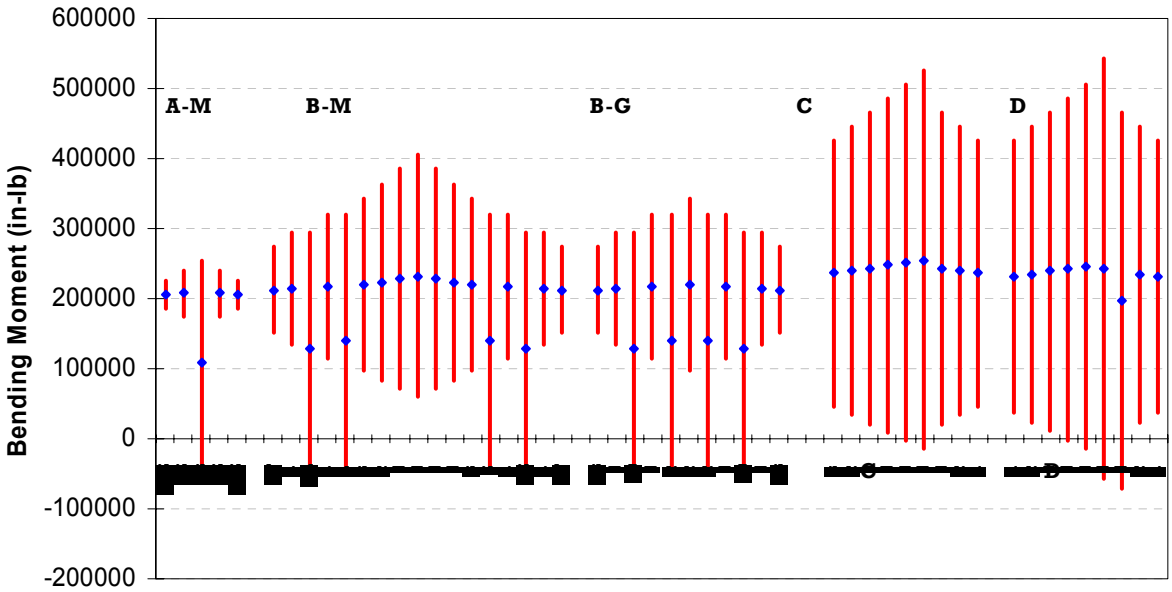

Figure C.13. Maneuver and gust bending moment spectrums, CF=1.4 and LEF=1.072.

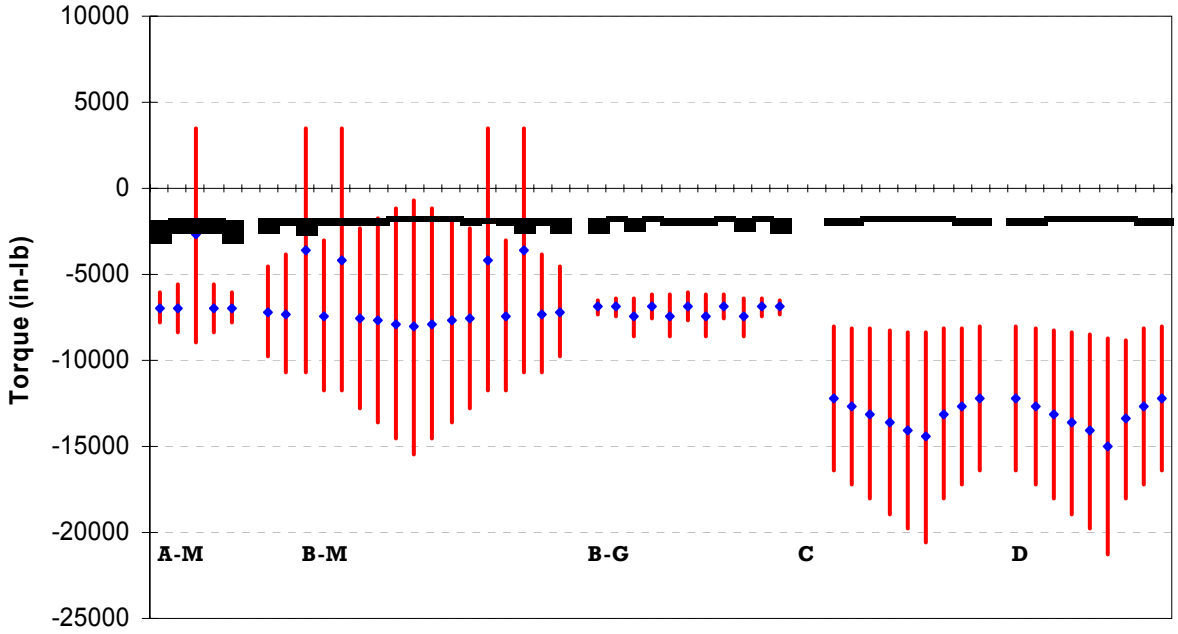

Figure C.14. Maneuver and gust torque spectrums, CF=1.4 and LEF=1.000.

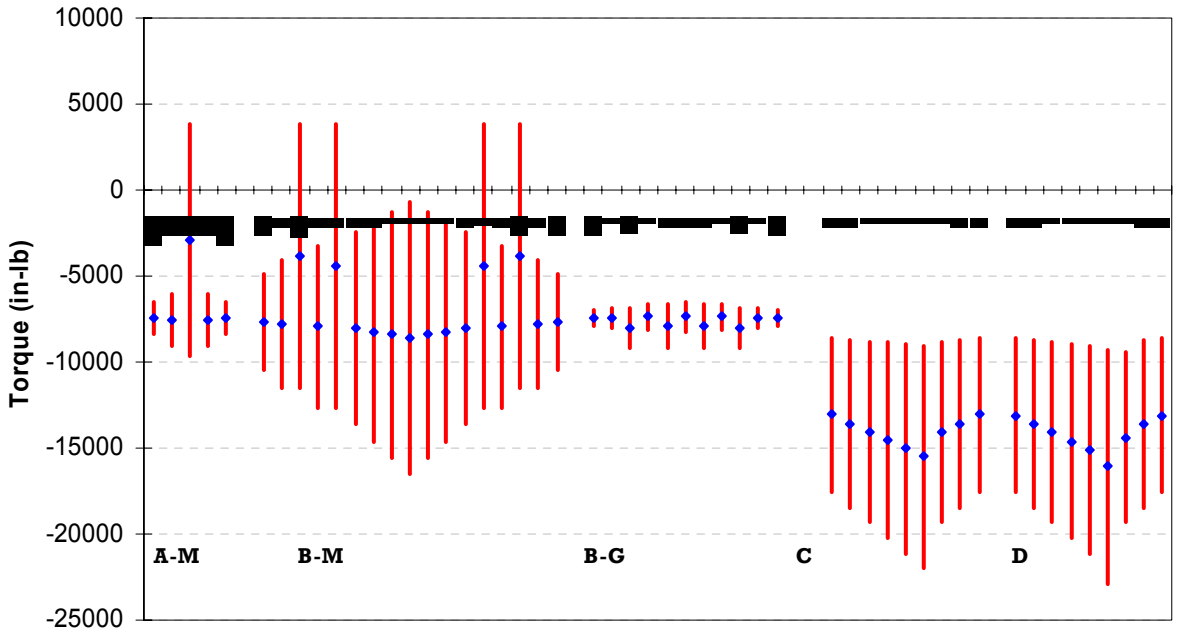

Figure C.15. Maneuver and gust torque spectrums, CF=1.4 and LEF=1.072.

APPENDIX D

FULL-SCALE TEST RESULTS

The following are locations of displacement transducers for all full-scale forward wing tests (Figure D.1):

D1 and D2 - FWS 51.05

D3 - FWS 76

D4 - FWS 100

D5 and D6 - FWS 130.90

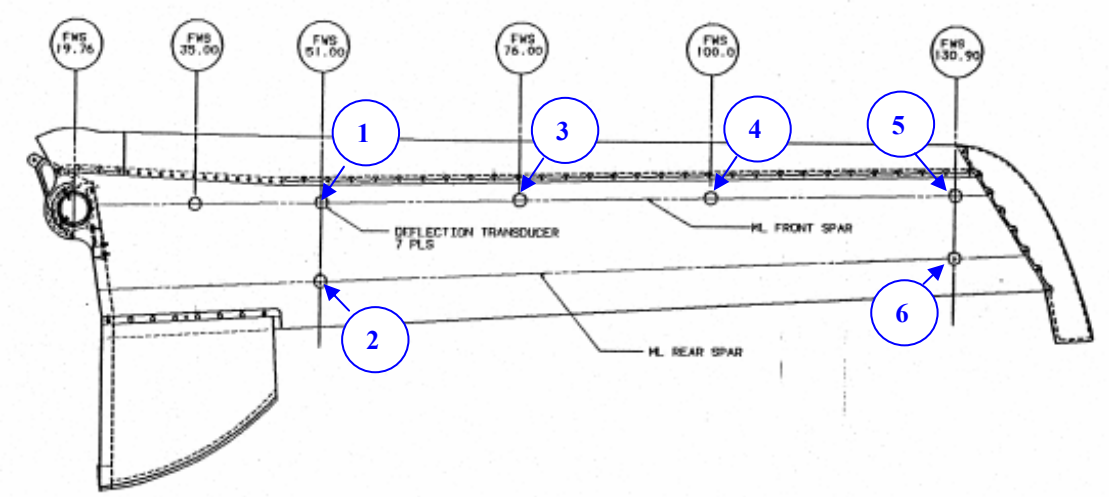

Figure D.1. Displacement transducer locations.

D.1 ST001 - Starship Forward-Wing Full-Scale Static Test

The first full-scale static-test article, ST001, was tested with a total of eleven axial gages and seven rosettes were used for strain measurements. A and R prefix indicate that the gages were either axial or rosette (three axial gages in 0°, 45°, and 90° directions that are named as A, B, and C, respectively), respectively.

A1 Lower skin FWS 24.8" on front spar

A2 Upper skin FWS 24.8" on front spar

A3 Upper skin FWS 27.0" on front spar

A4 Upper skin FWS 34.0" on rear spar

A5 Upper skin FWS 42.5" on rear spar

A6 Upper skin FWS 66.5" on front spar

A7 Upper skin FWS 66.5" on rear spar

A8 Upper skin FWS 90.5" on front spar

A9 Upper skin FWS 90.5" on rear spar

A10 Upper skin FWS 114.5" on front spar

A11 Upper skin FWS 114.5" on rear spar

R1 Root Rib at upper forward corner

R2 Lower skin FWS 24.8" and 2.5" outboard of front spar

R3 Upper skin FWS 24.8" on rear spar

R4 Lower skin FWS 38.0" on front spar

R5 Centered on rear web at FWS 50.44"

R6 Upper skin FWS 24.8" and 2.5" outboard of front spar

R7 Upper skin FWS 42.5" on front spar

The ST001 test article was quasi-statically loaded up to 200% BDLL and unloaded. Upon unloading a tap test and ultrasonic non-destructive inspections were performed around the rear and rear spar location and did not find any indications of delamination or disbonds. This article was later retested upon infliction of an impact damage at the aft spar.

In addition to strain gages, ARAMIS photogrammetry image-correlation system was used to obtain the full-field strain/displacement measurements during quasi-static loading of ST001. Since the fields of depth of the cameras were substantially low because of the whiffletree attachments, a rail system was designed to obtain full-field measurements along the length of the article at several different stations so that they can be later combined to form a single full-field image of the upper skin. ARAMIS measurements were first obtained for each section at multiple load steps till the limit load as shown in Figure D.2 (A). Then, the cameras were mounted away from the whiffletree as shown in Figure D.2 (B) to prevent possible damages to the sensors.

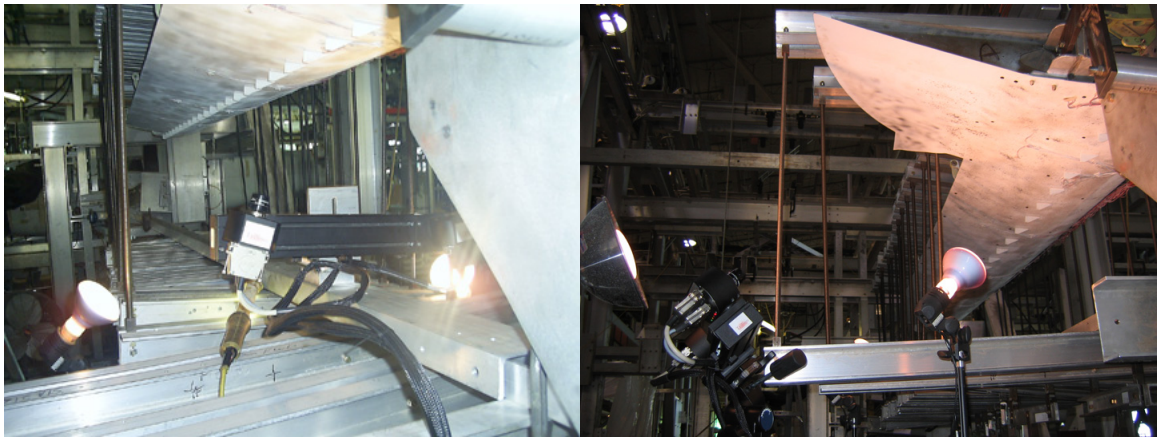

(A) (B)

Figure D.2. ARAMIS System setup (a) up to, and (b) after the limit load.

Vertical displacement readings (D1-D2 and D5-D6 in Figure D.3) indicated that there were minimal twisting at both the root and the tip of the test article. Overall displacements up to

200% BDLL were linear. Figure D.4 shows the axial strain data and Figure D.5 shows the strain data obtained from rosettes.

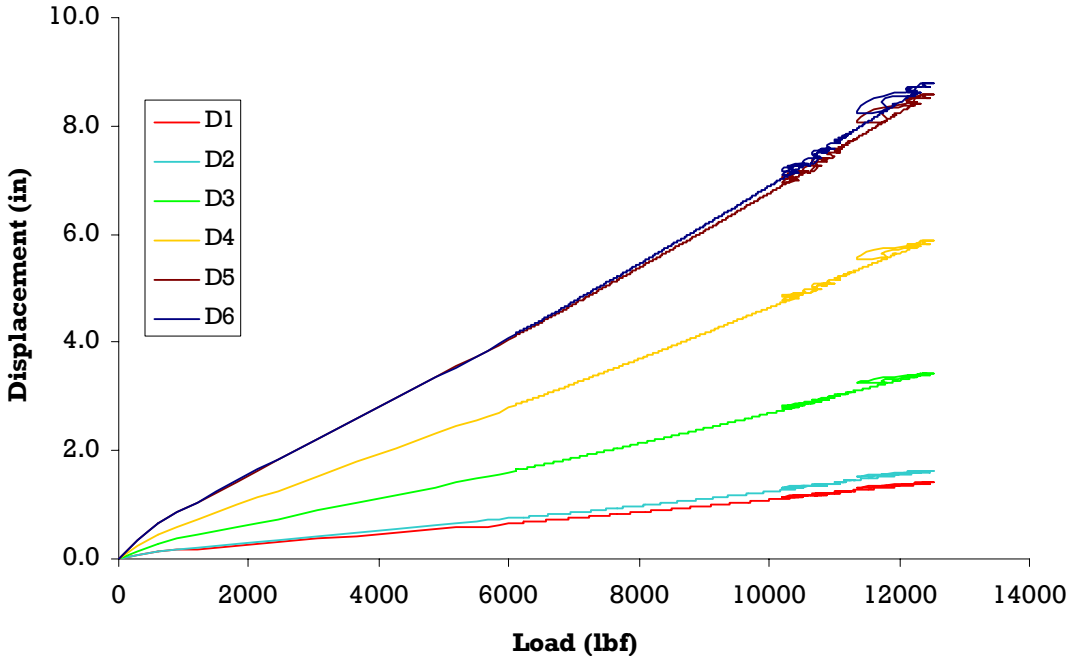

Figure D.3. Vertical displacements - ST001.

ARAMIS full-field strain data along the front and aft spars are compared with strain gage data in Figure D.6. Strain gage data on both front and rear spars were linear until the maximum applied load.

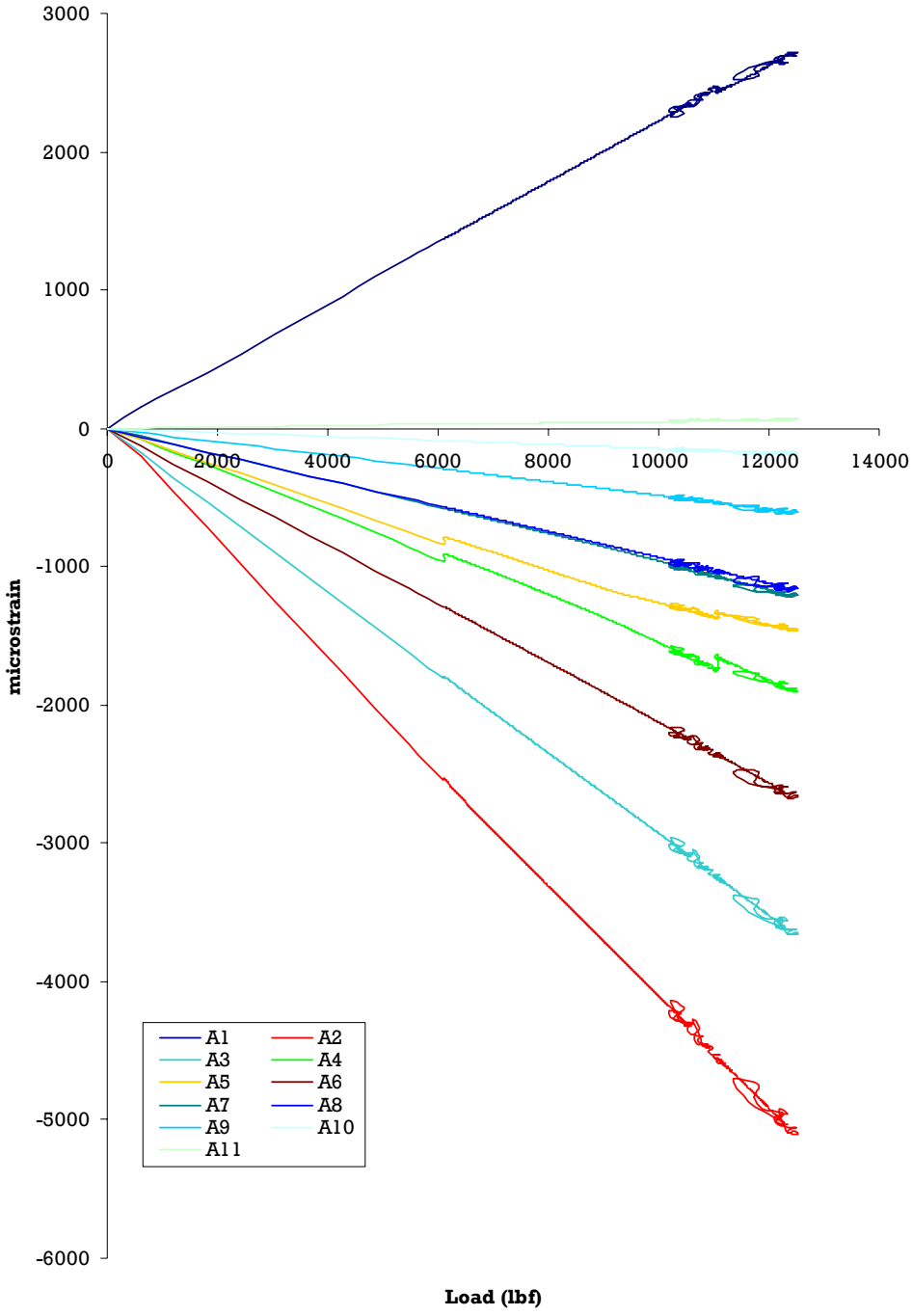

Figure D.4. Axial strain gage data for ST001.

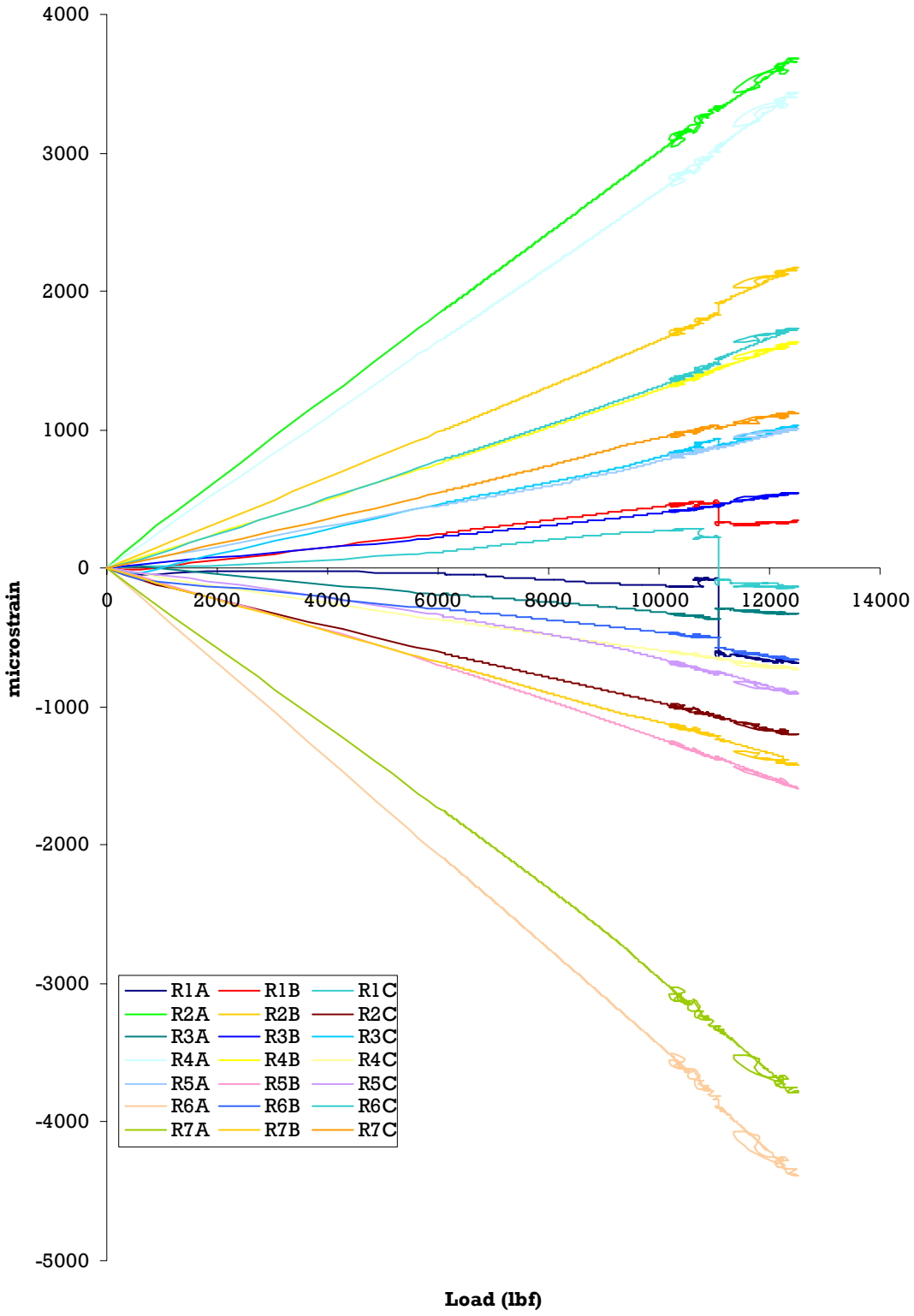

Figure D.5. Strain rosette data for ST001.

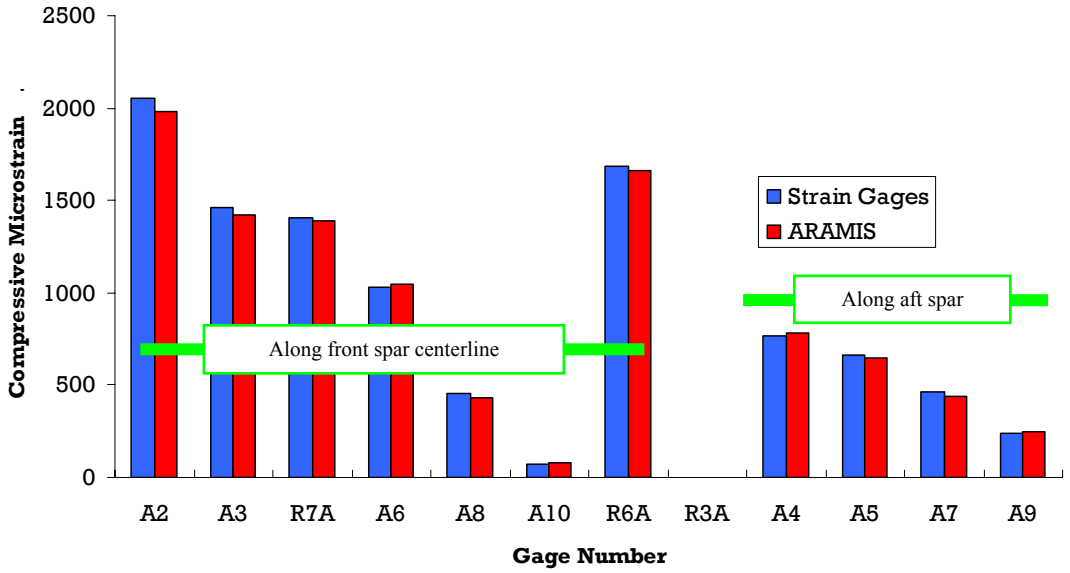

Figure D.6. Comparison of ARAMIS and strain gage data along front and aft spars of ST001.

D.2 ST002 - Starship Forward-Wing Full-Scale Static Test

The second full scale static test article, ST002, was tested with similar strain gage arrangement as ST001, except for the axial gages A9 through A11 and the rosette R3; these gages were replaced by the axial gages A12 through A14 and the rosette R8, respectively. The gage A12 was placed at FWS 46.6, where the leading edge assembly fastener pitch increases. The gage A14 was installed over the front spar at FWS 134.05, while the gage A13 was installed at FWS 137.45 over the closure rib on the tip fairing (Figure D.7).

Prior to installing the whiffletree, a point load was applied at FWS 100 in stepwise, while recording the strain gage data, so that the full-field strain survey can be carried out. This allowed the photogrammetry sensors to be placed at a distance further away from the upper skin to capture data from a larger field of view. The upper skin was divided into three overlapping segments for ARAMIS measurements so that the data can be "stitched" as a single image. The maximum point load applied was 1059.26 lbf, and the corresponding maximum strain was

recorded as -962.7 microstrain from the gages A2. Figure D.8 shows the full-field axial strain, and a comparison of the ARAMIS and strain gage data along the front and aft spars.

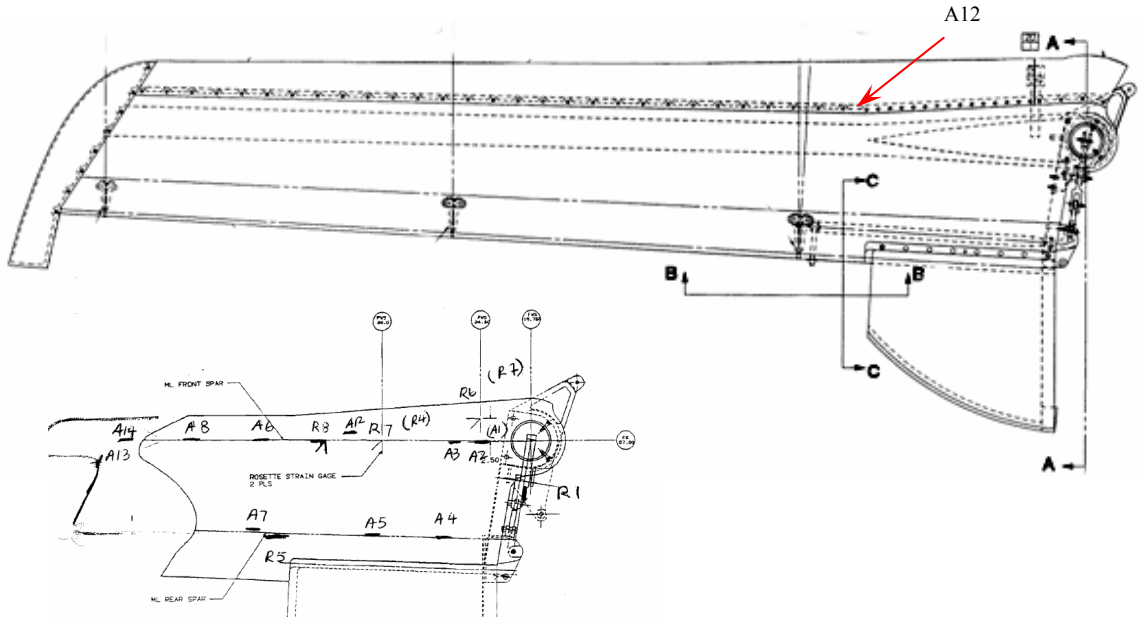

Figure D.7. Strain gage location for ST002 static test article.

During quasi-static loading of ST002 with the whiffletree test setup, the load was initially applied in 5% increments till BDLL and then continuously till fracture. The vertical displacement gages indicated minimal twisting of the article during loading (Figure D.9). The strain gages on the aft spar towards the root end (A4) indicated a sudden decrease in strain followed by an audible noise indicating an initial debond/delamination around 185% of BDLL (Figure D.10). The rosette R1 located at the root rib (Figure D.11) also indicated sudden changes in strain data around this load level.

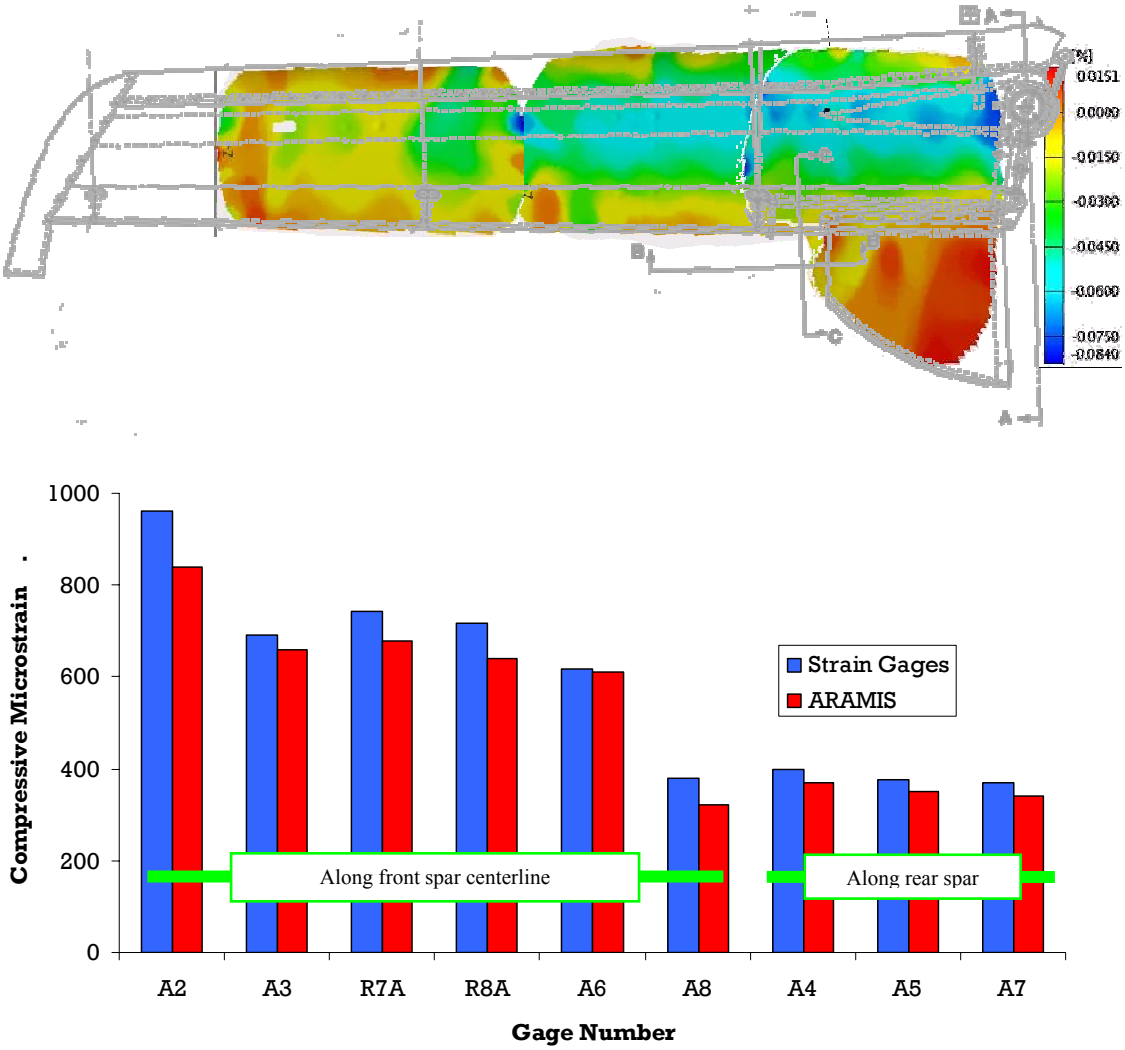

Figure D.8. Full-field strain survey and comparison with strain gage data for ST002.

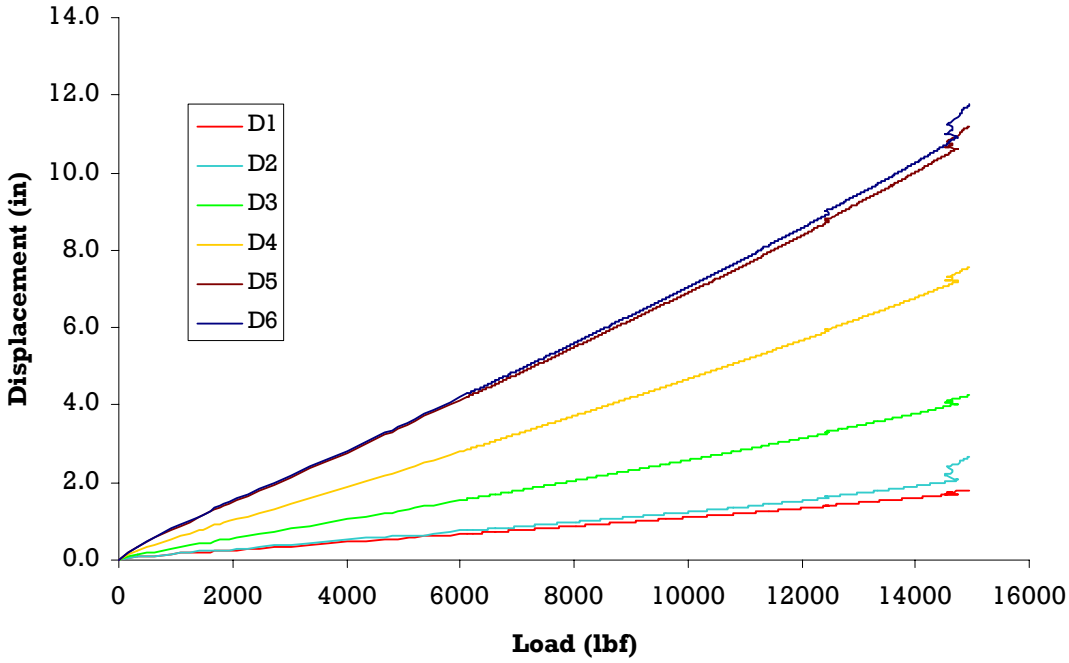

Figure D.9. Vertical displacements - ST002.

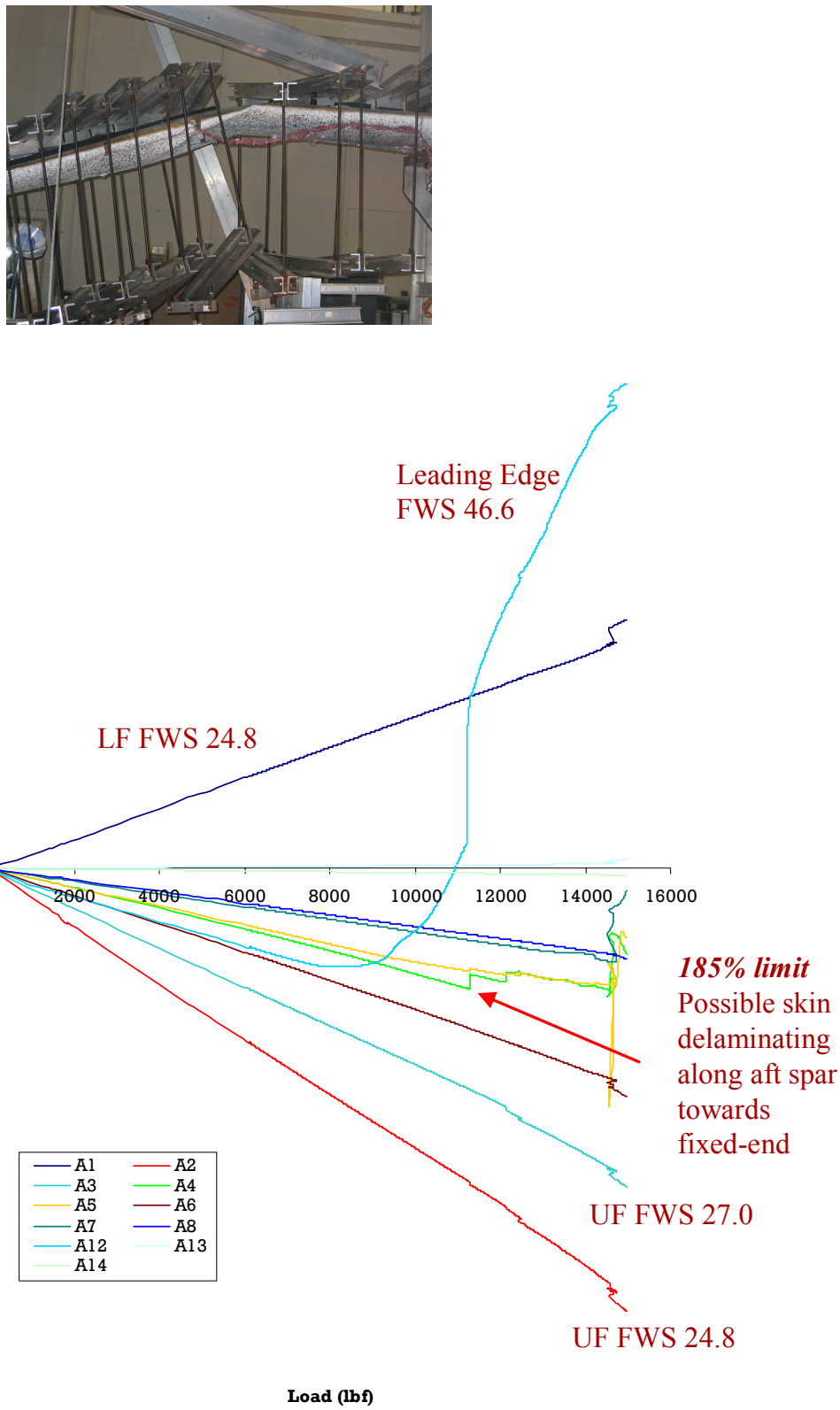

Figure D.10. Axial strain gage data for ST002.

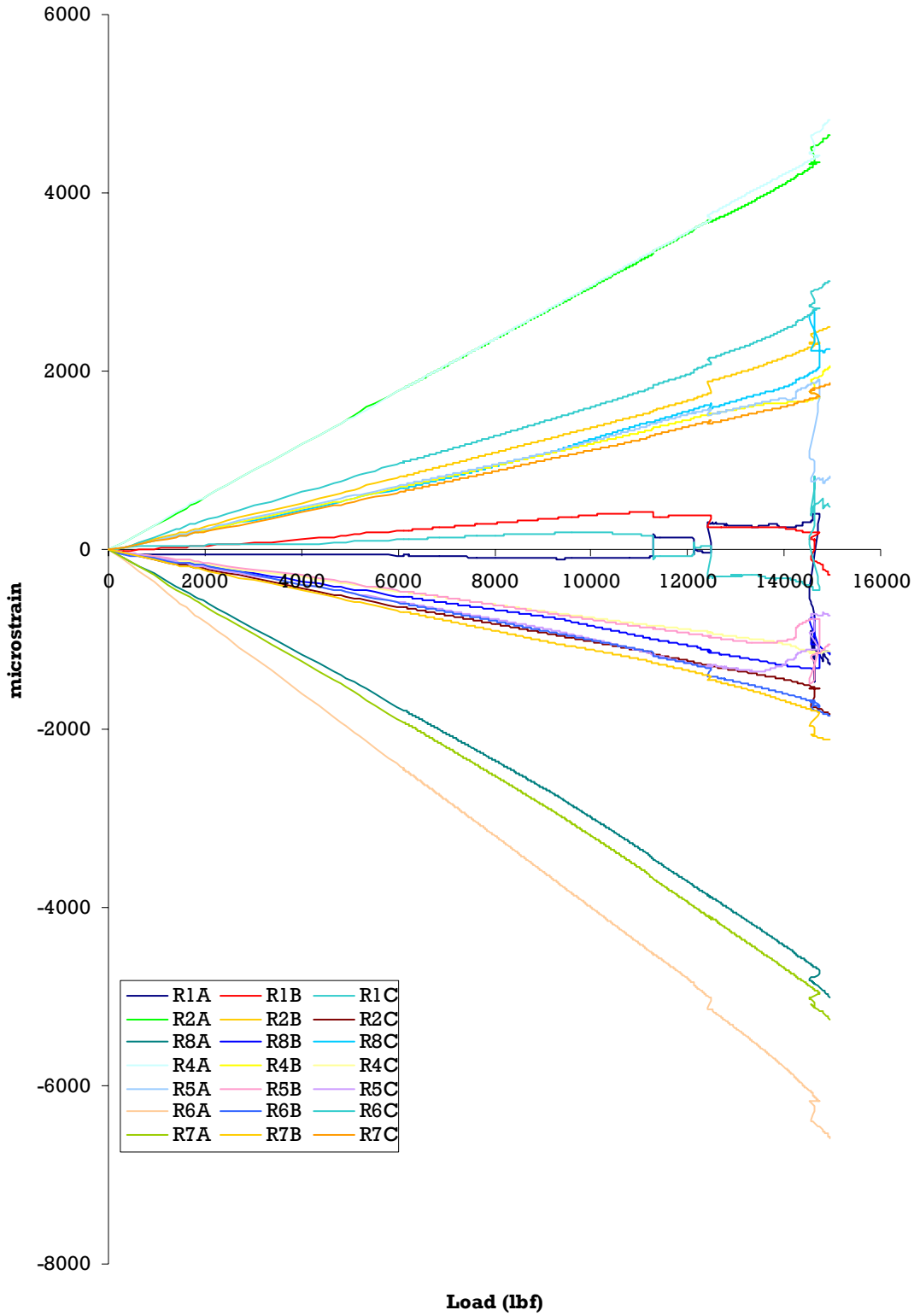

Figure D.11. Strain rosette data for ST002.

D.3 ST003 - Starship Forward-Wing Full-Scale Static Test

The third full-scale static test article, ST003, was tested with modified strain gage locations to detect damage initiation and propagation around the fracture locations noted during ST002 test. Strain gage locations are shown in Figure D.12. A total of eight axial gages and eight rosettes were mounted. The axial gages A2 and A6 were replaced by the rosettes R9 and R10. The rosette R7 was replaced with the axial gage A15. The rosette R6 was removed and the rosette R11 was added at FWS 59.5 on aft spar.

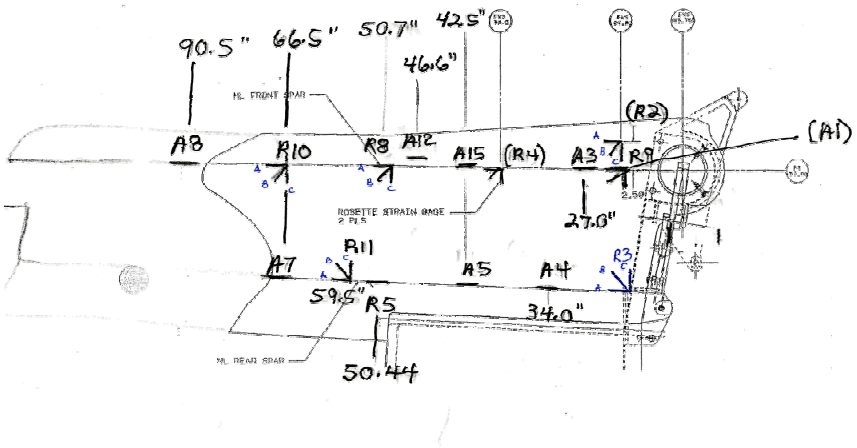

Figure D.12. Strain gage location for ST003 static test article.

Similar to ST002, a point load was applied at FWS 100 and the full-field strain survey was conducted. The maximum point load was 1000 lbf and the corresponding maximum strain was -677.8 microstrain recorded from the rosette gage R9A. Figure D.13 shows the stitched full-field axial strain, and a comparison of the ARAMIS and strain gage data.

Figure D.14 shows the vertical displacement reading of ST003 during quasi-static loading with the whiffletree test setup. Figure D.15 shows the axial strain data during static loading. The axial gage A12 indicated leading-edge buckling around 4000 lbf. The axial gage A4 and

the rosette R3 (Figure D.16) indicated delamination between top skin along aft spar that was initiated at the root end.

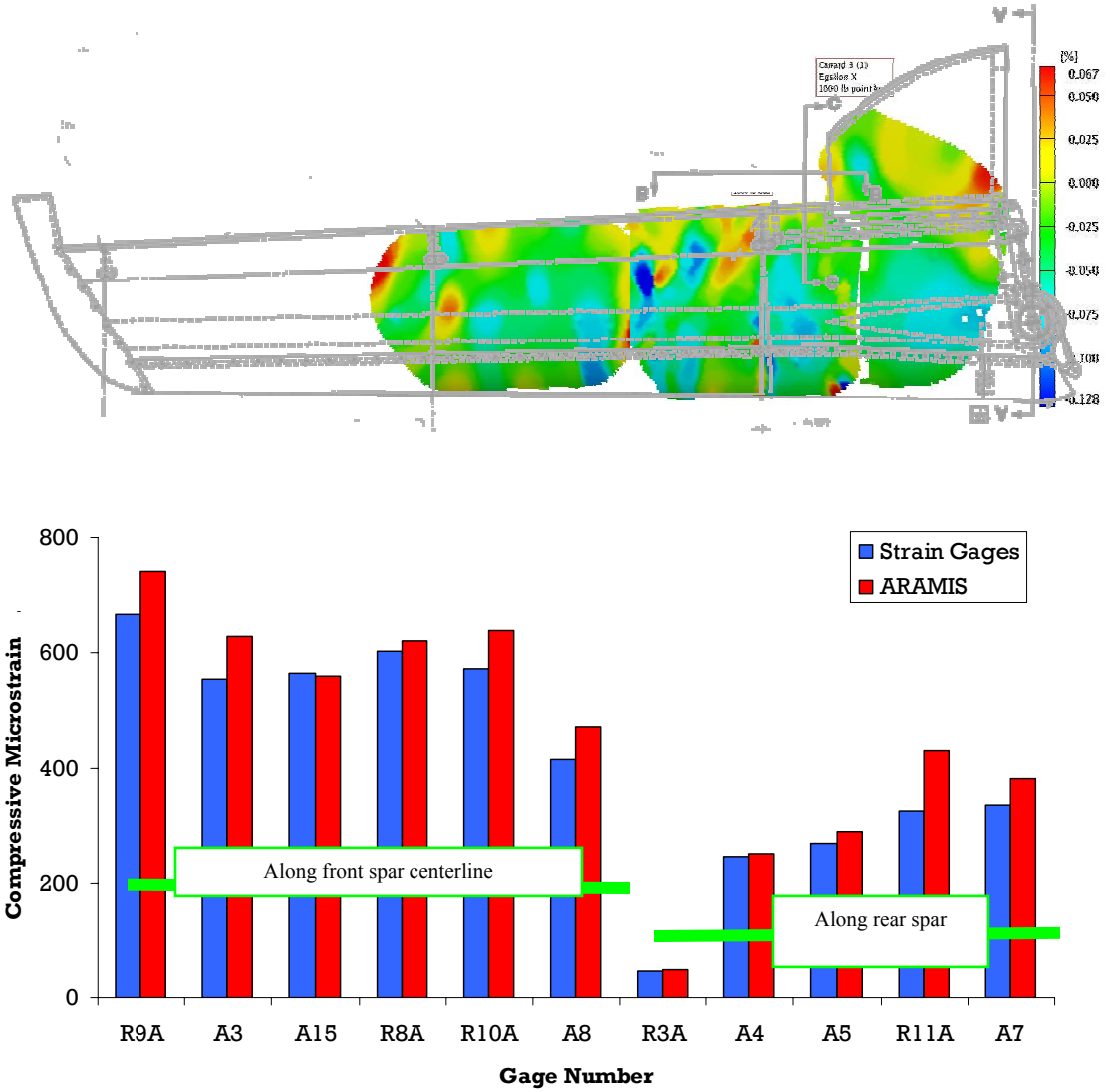

Figure D.13. Full-field strain survey and comparison with strain gage data for ST003.

The strain gage data along the front (F) and aft (A) spar on the upper (U) and lower (L) skins were compared for all three full-scale static test articles in Figure D.17 at 100 and 200 percent of BDLL. Overall strain distributions along both the front and aft spars for all three static articles were comparable.

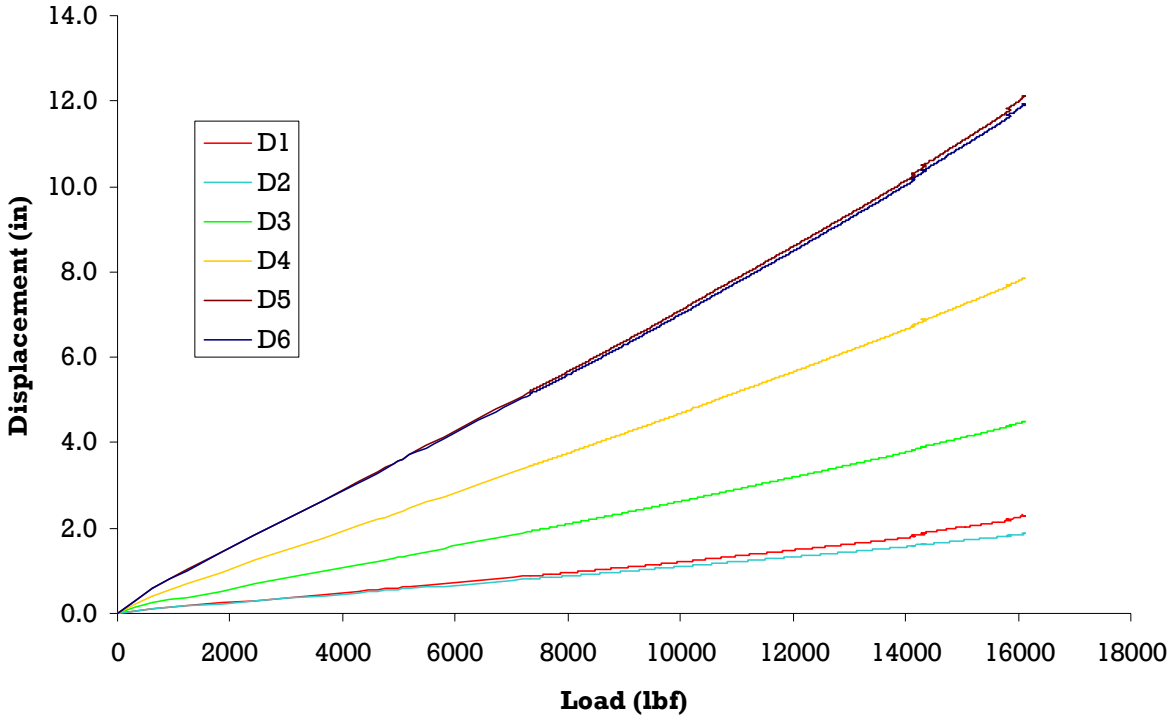

Figure D.14. Vertical displacements - ST003.

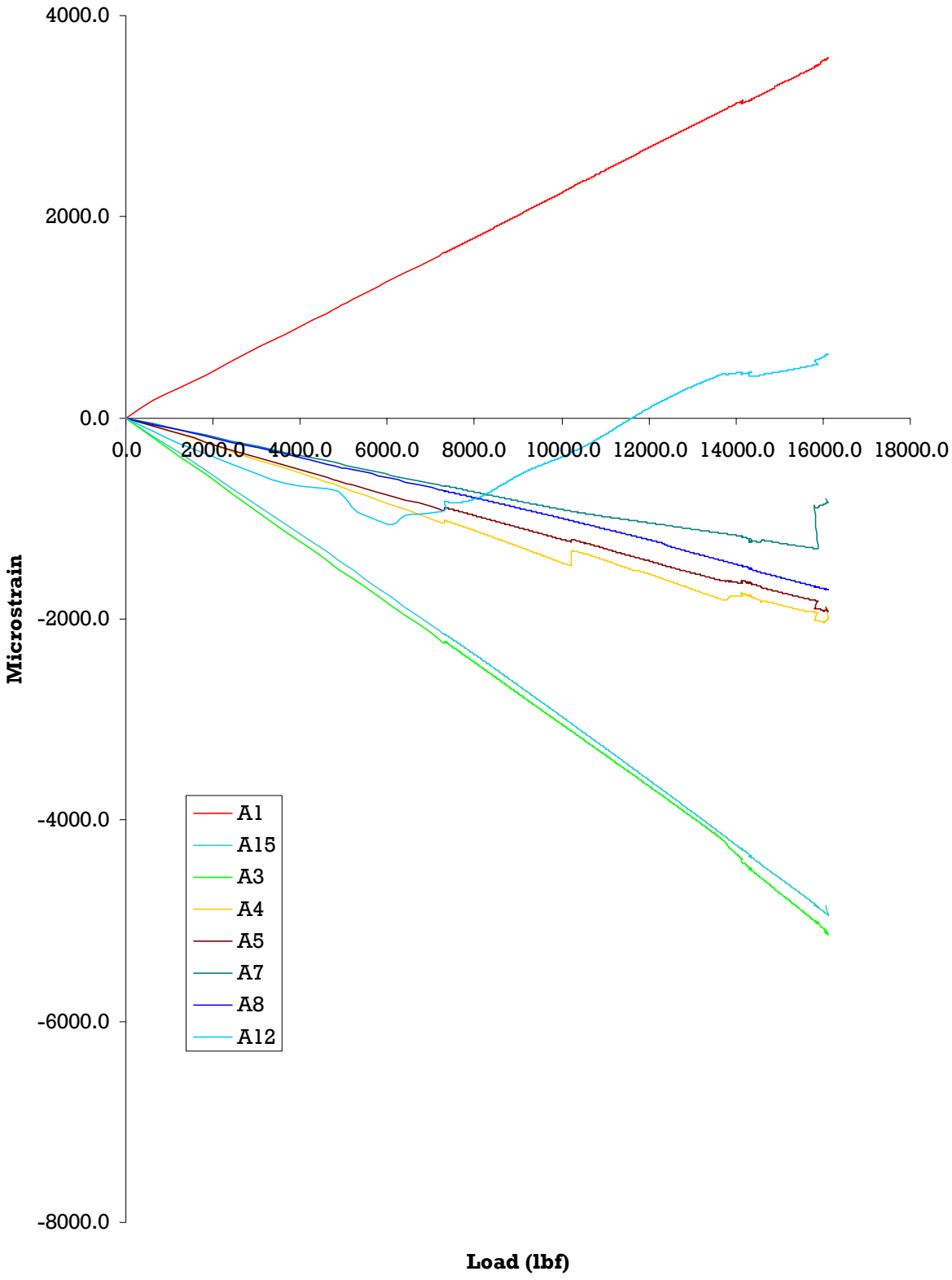

Figure D.15. Axial strain gage data for ST003.

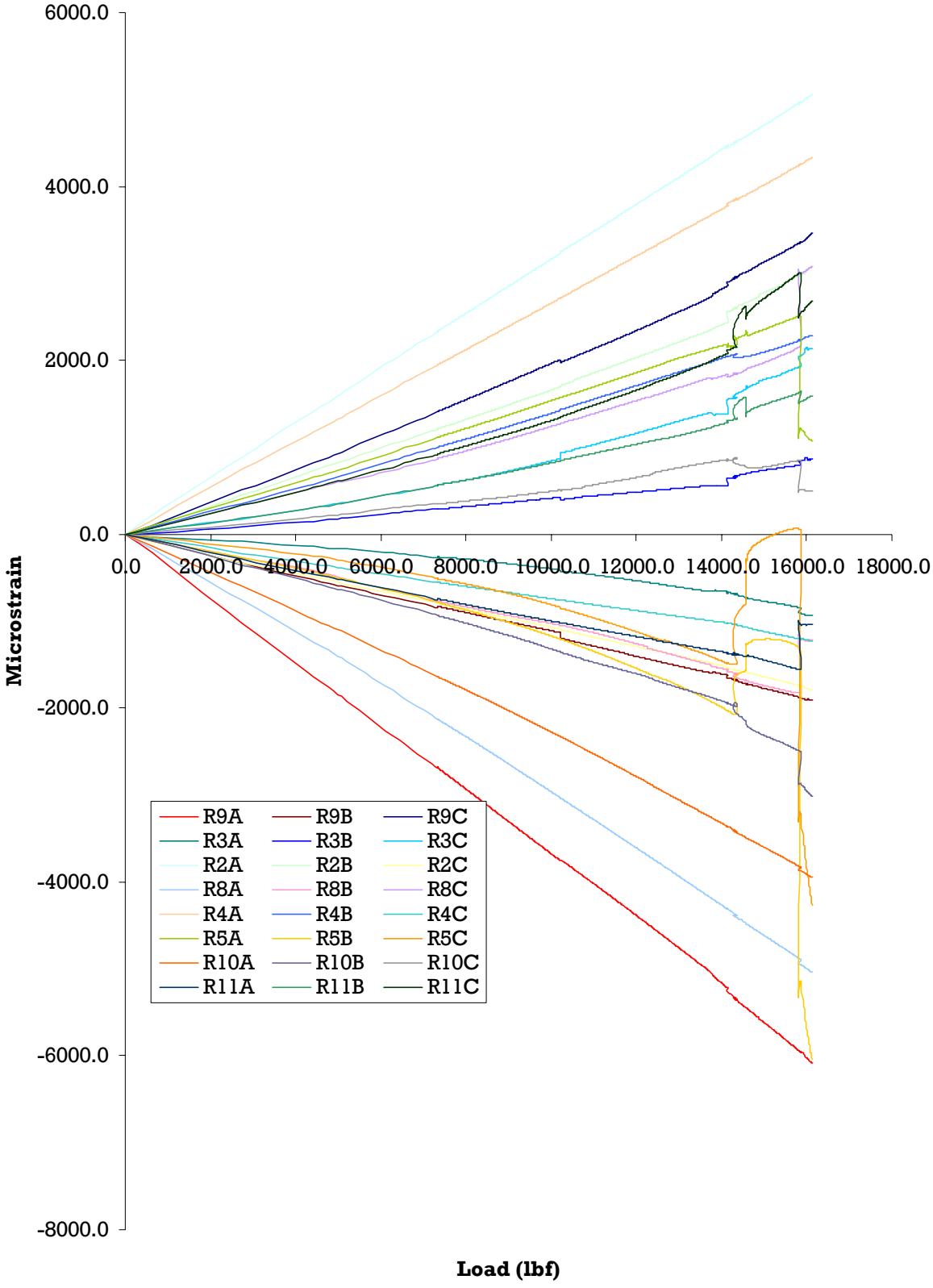

Figure D.16. Strain rosette data for ST003.

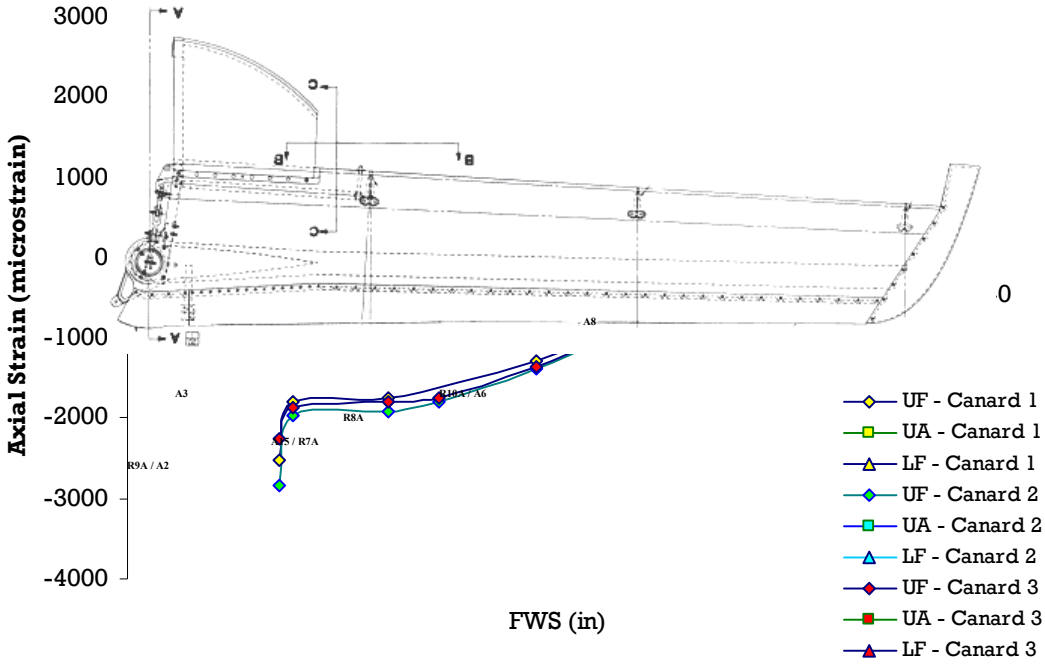

(A) 100% BDLL

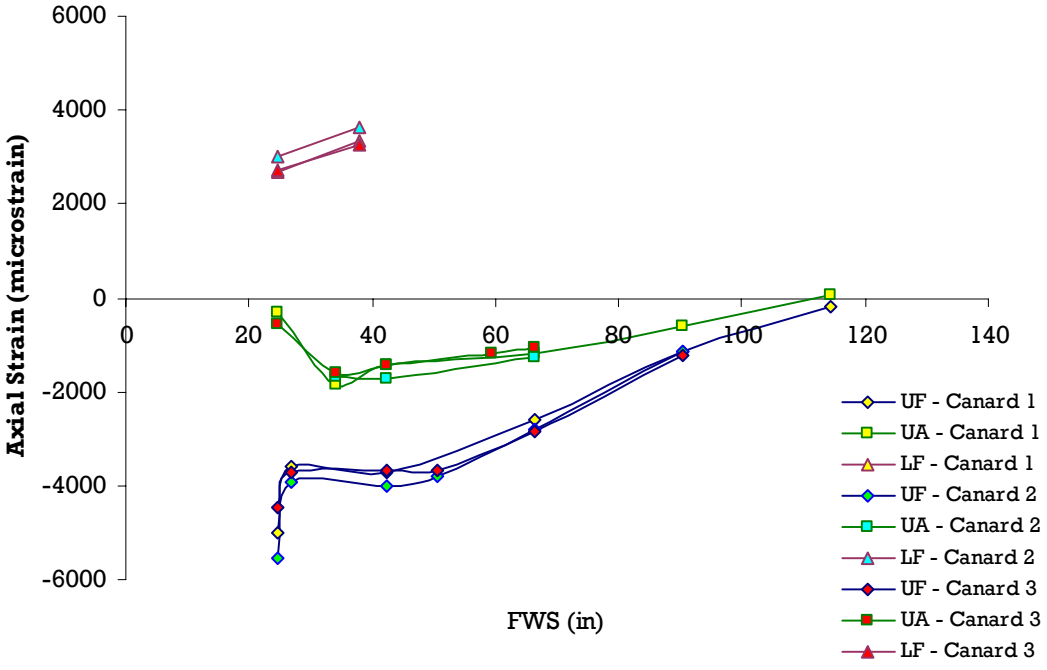

(B) 200% BDLL

Figure D.17. Strain comparison for all three test articles.

D.4 ST001(R) - Starship Forward-Wing Full-Scale Damage Tolerance Test

The third full-scale static test, ST001(R), was tested with an impact damage at FWS 45 on the top skin of the aft spar. A total of eleven axial gages, three bi-axial gages and nine rosettes were used for strain measurements (Figure 105) for article ST001(R). The following gage locations were used for the ST004 DaDT test article.

A1 Lower skin FWS 24.8 on Fwd spar

A2 Upper skin FWS 24.8 on Fwd spar

A3 Upper skin FWS 27.0 on Fwd spar

A4 Upper skin FWS 34.0 on Aft spar

A5 Upper skin FWS 42.5 on Aft spar

A6 Upper skin FWS 66.5 on Fwd spar

A7 Upper skin FWS 66.5 on Aft spar

A8 Upper skin FWS 90.5 on Fwd spar

A9 Upper skin FWS 90.5 on Aft spar

A10 Upper skin FWS 114.5 on Fwd spar

A11Upper skin FWS 114.5 on Aft spar

R1 Root Rib at upper forward corner

R2 Lower skin FWS 24.8 and 2.5 forward of Fwd spar

R3 Upper skin FWS 24.8 on Aft spar

R4 Lower skin FWS 38.0 on Fwd spar

R5 Centered on Aft Web at FWS 50.44

R6 Upper skin FWS 24.8 and 2.5 forward of Fwd spar

R7 Upper skin FWS 42.5 on Fwd spar

R12 Upper skin at FWS 45 and 2.05 forward of aft spar

R13 Upper skin at FWS 47 on aft spar

B1 Upper skin at FWS 45 and 2.3 aft of aft spar

B2 Rear spar Web at 43.44

B3 Rear spar Web at 38.84

In addition to A5, which was mounted closer to the damage location, R12, R13, and B1 rosettes were mounted to monitor damage propagation. Further, three gyro-enhanced orientation sensors (MicroStrain model 3DM-GX1) and one high-sensitivity accelerometer (Crossbow Technology CXL-LF series) were mounted as shown in Figure 105. They were mounted on this test article to support a validation of a health-monitoring technique (for discovering and recovering the unused service life) developed by Boeing Phantom Works, St Louis, Missouri.

Figure D.18 shows the vertical displacement results for the ST001(R) static-test article. Displacement gages D1 and D2 indicated that there was a rotation of the test article in $-T_Y$ direction (reference axis system may be found in Figure C.1) at the root end possibly due to damage propagation. The axial strain gages (Figure D.19), biaxial gages (Figure D.20) and rosettes (Figure D.21) around the damage location indicated significant nonlinearity due to damage propagation.

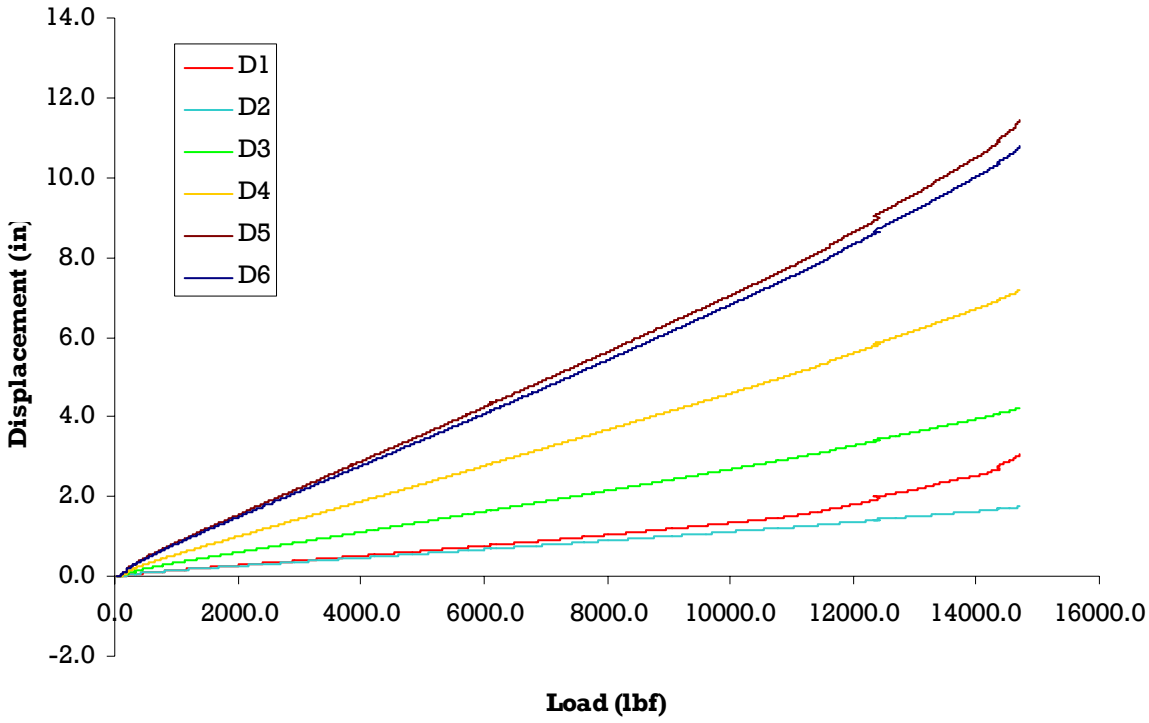

Figure D.18. Vertical displacements - ST001(R).

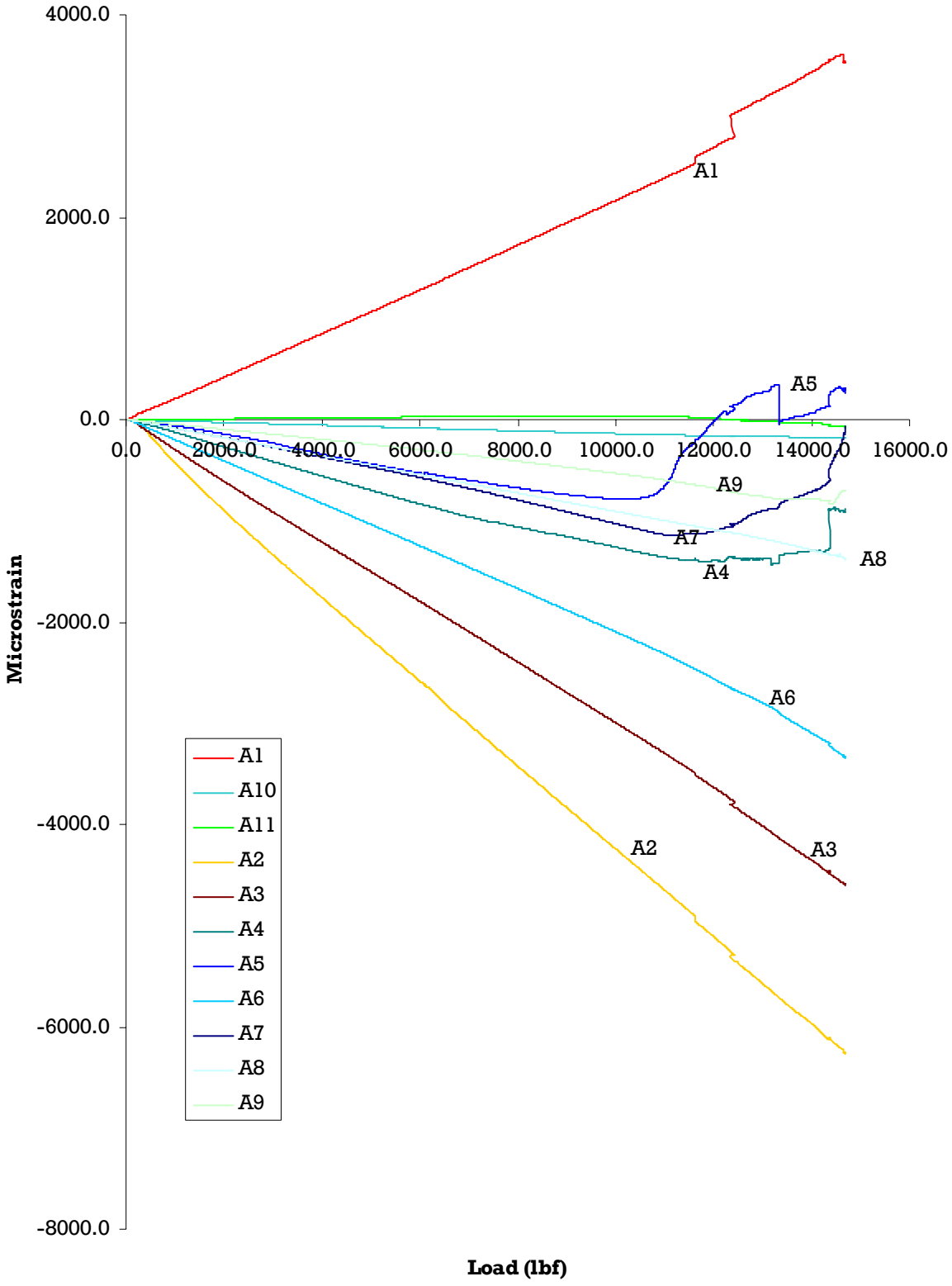

Figure D.19. Strains from axial gages – ST001(R).

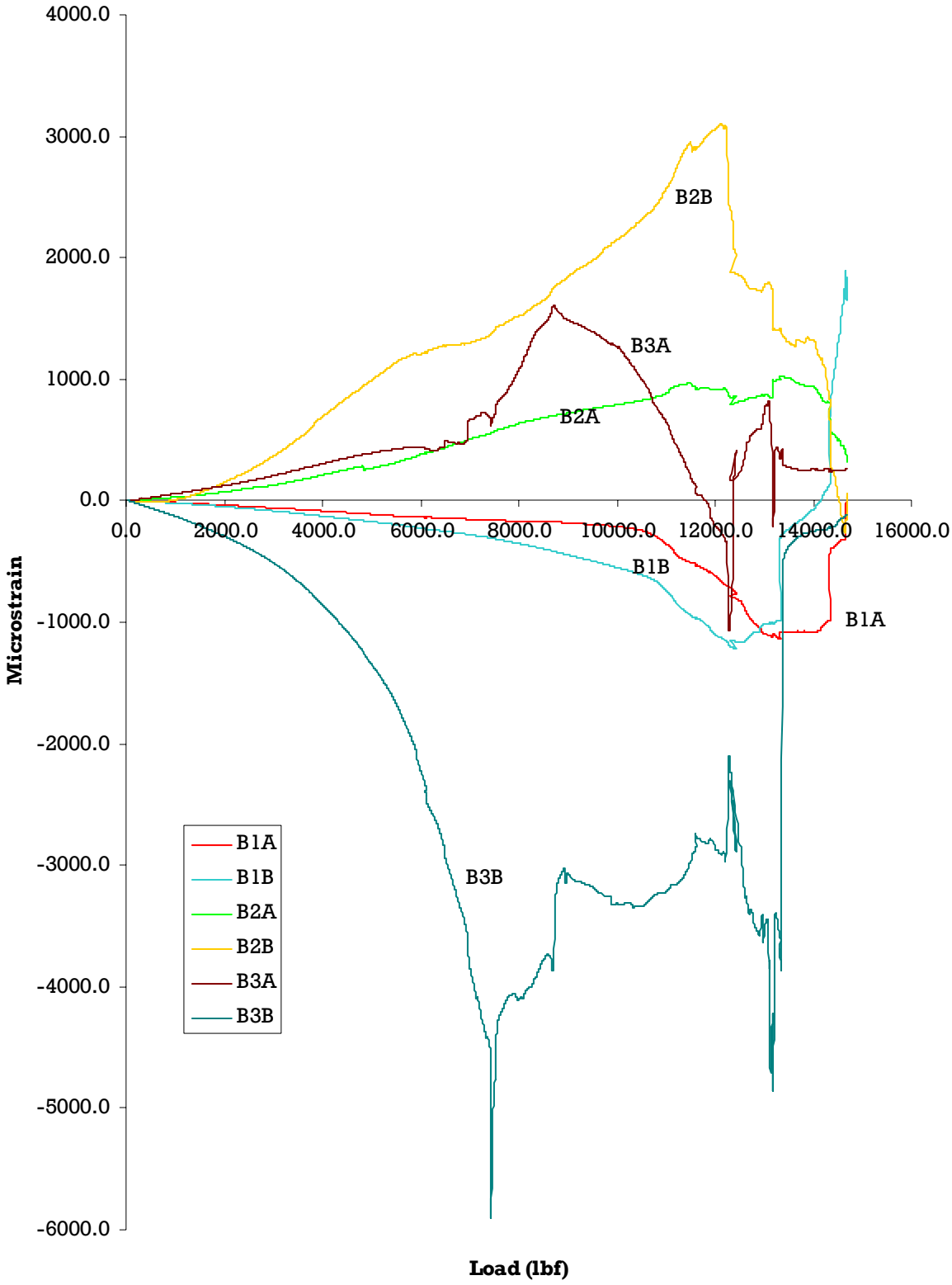

Figure D.20. Strains from biaxial gages – ST001(R).

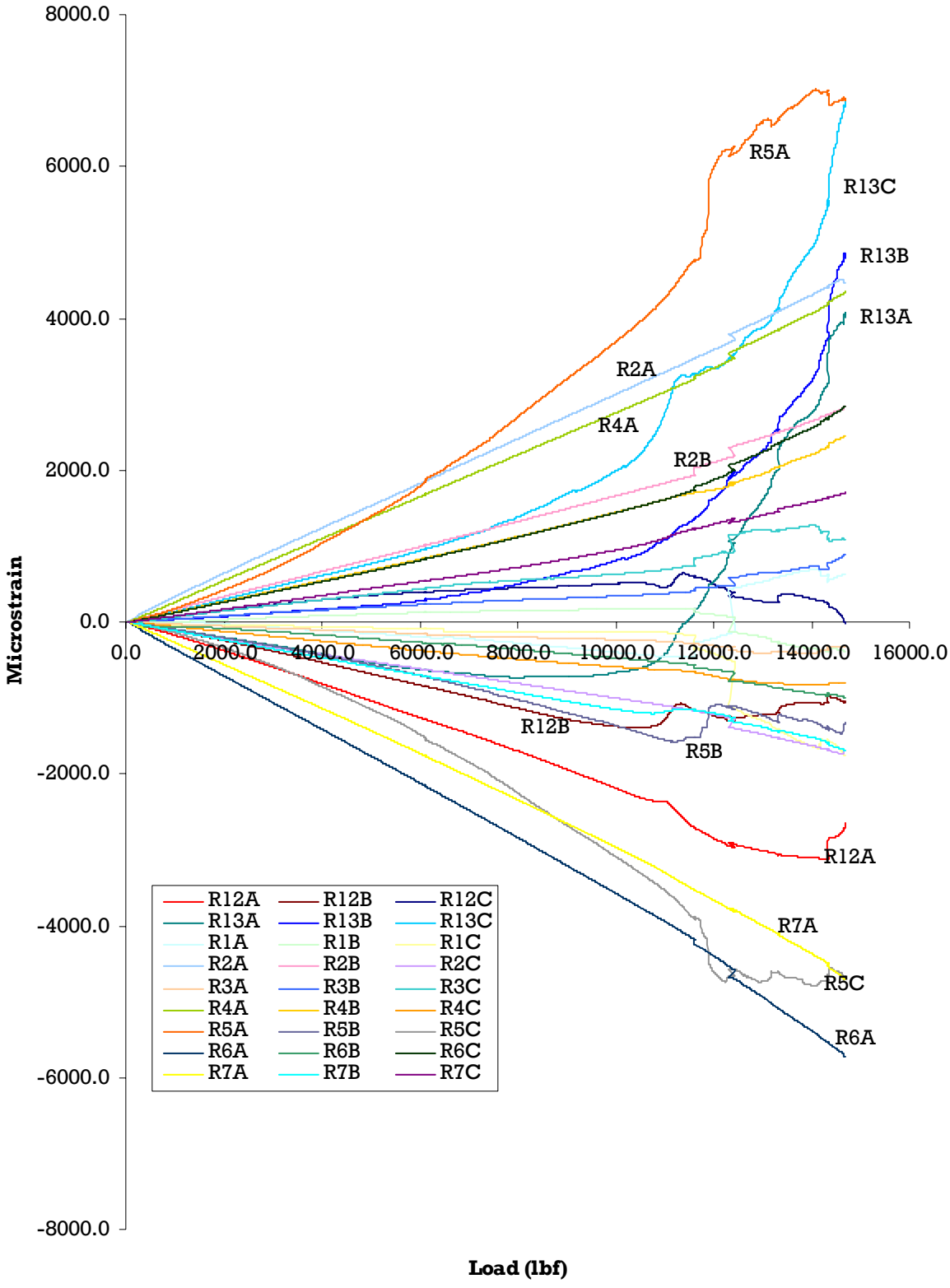

Figure D.21. Strains from rosettes – ST001(R).

D.5 Residual Strength Test Data of ST004 after 2-DLT Cyclic Test

The following gage locations were used for the ST004 DaDT test article. They are graphically illustrated in Figure 112.

A1 Lower skin FWS 24.8 on Fwd spar

A2 Upper skin FWS 24.8 on Fwd spar

A3 Upper skin FWS 27.0 on Fwd spar

A16 Upper skin FWS 37.0 on Aft spar

A17 Upper skin FWS 39.0 on Aft spar

A18 Upper skin FWS 51.75 on Aft spar

A19 Upper skin FWS 64.7 on Fwd spar

A20 Upper skin FWS 64.7 on Aft spar

R2 Lower skin FWS 24.8 and 2.5" forward of Fwd spar

R3 Upper skin FWS 24.8 on Aft spar

R4 Lower skin FWS 38.0 on Fwd spar

R5 Centered on Aft web at FWS 50.44

R6 Upper skin FWS 24.8 and 2.5" forward of Fwd spar

R7 Upper skin FWS 42.5 on Fwd spar

R14 Upper skin FWS 44.0 and 4.5" forward of Aft spar

R15 Upper skin FWS 49.7 and 5.0" on Aft spar

B4 Upper skin FWS 44.0 and 4.45" aft of Aft spar

Figure D.2 shows the displacement results for post-DaDT residual strength of ST004. Displacement gages D1 and D2 indicated that there was a rotation of the test article in $-T_Y$ direction (reference axis system may be found in Figure C.1), which was observed in videos.

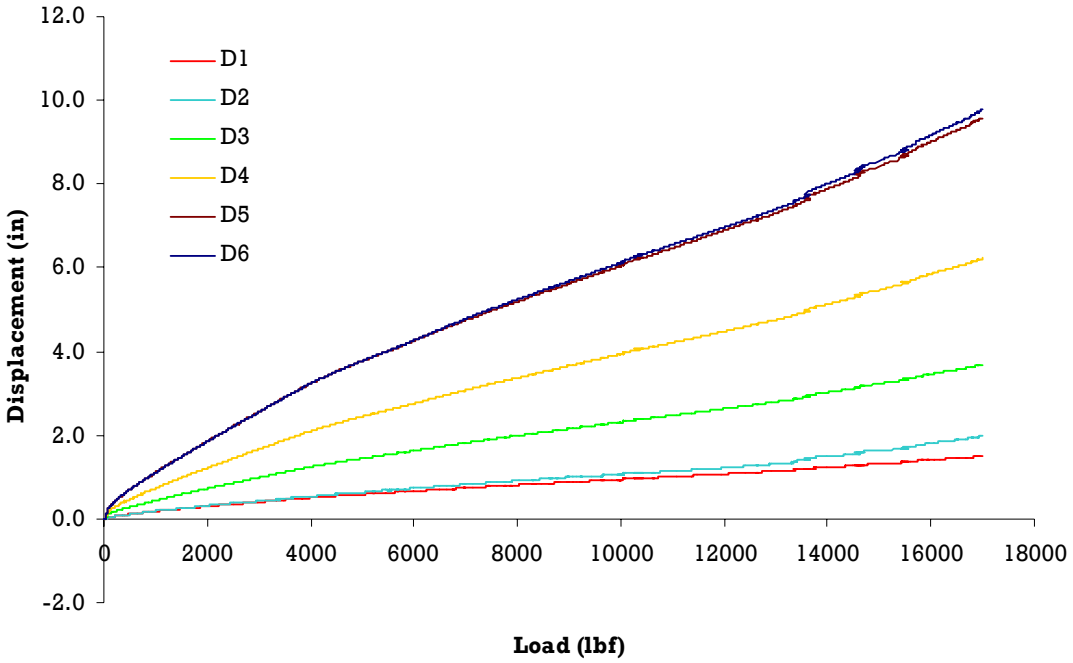

Figure D.22. Vertical displacements – ST004.

Figure D.3 shows the strain gage reading around the impact damage on aft spar (top skin) of the ST004 test article during post-DaDT residual strength test.

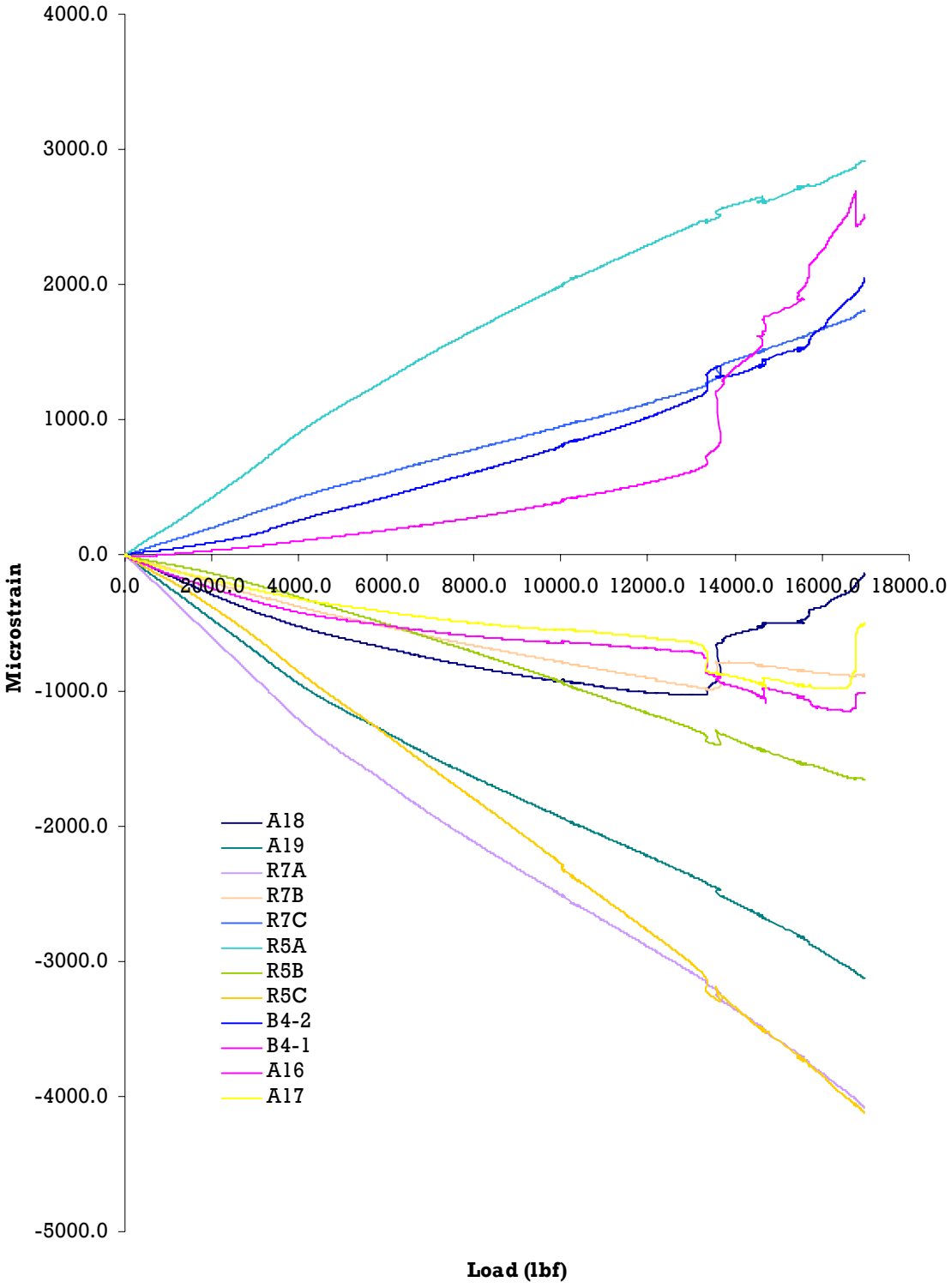

Figure D.23. Strains around CAT2 damage – ST004.

D.6 Static Strength Test Data for ST005

The following gage locations were used for the ST005 DaDT test article. They are graphically illustrated in Figure 109.

A1 Lower skin FWS 24.8 on Fwd spar

A2 Upper skin FWS 24.8 on Fwd spar

A3 Upper skin FWS 27.0 on Fwd spar

A7 Upper skin FWS 66.5 on Aft spar

A8 Upper skin FWS 90.5 on Fwd spar

A21 Upper skin FWS 38.25 on Fwd spar

A22 Upper skin FWS 38.25 on Aft spar

A23 Lower skin FWS 38.0 on Fwd spar

R1 Root sib at upper forward corner

R2 Lower Skin FWS 24.8 and 2.5" forward of Fwd spar

R3 Upper skin FWS 24.8 on Aft spar

R7 Upper skin FWS 42.5 on Fwd spar

R16 Upper skin FWS 63.0 on Fwd spar (2" Inboard of damage location FWS 65.0")

R17 Upper skin FWS 65.0 on Fwd spar (2" Aft of damage location FWS 65.0")

R18 Upper skin FWS 67.0 on Fwd spar (2" Outboard of damage location FWS 65.0")

B5 Upper skin FWS 50.7 centered between Fwd and Aft spar

B6 Upper skin FWS 65.0 (2" Fwd of damage location FWS 65.0")

B7 Lower skin FWS 65.0 (2" Fwd of damage location FWS 65.0")

B8 Upper skin FWS 65.0 centered between Fwd and Aft spar

Fgiure D.4 shows the displacement results for the ST005 static-test article. Displacement gages D1 and D2 indicated that there was a rotation of the test article in $-T_Y$ direction (reference axis system may be found in Figure C.1).

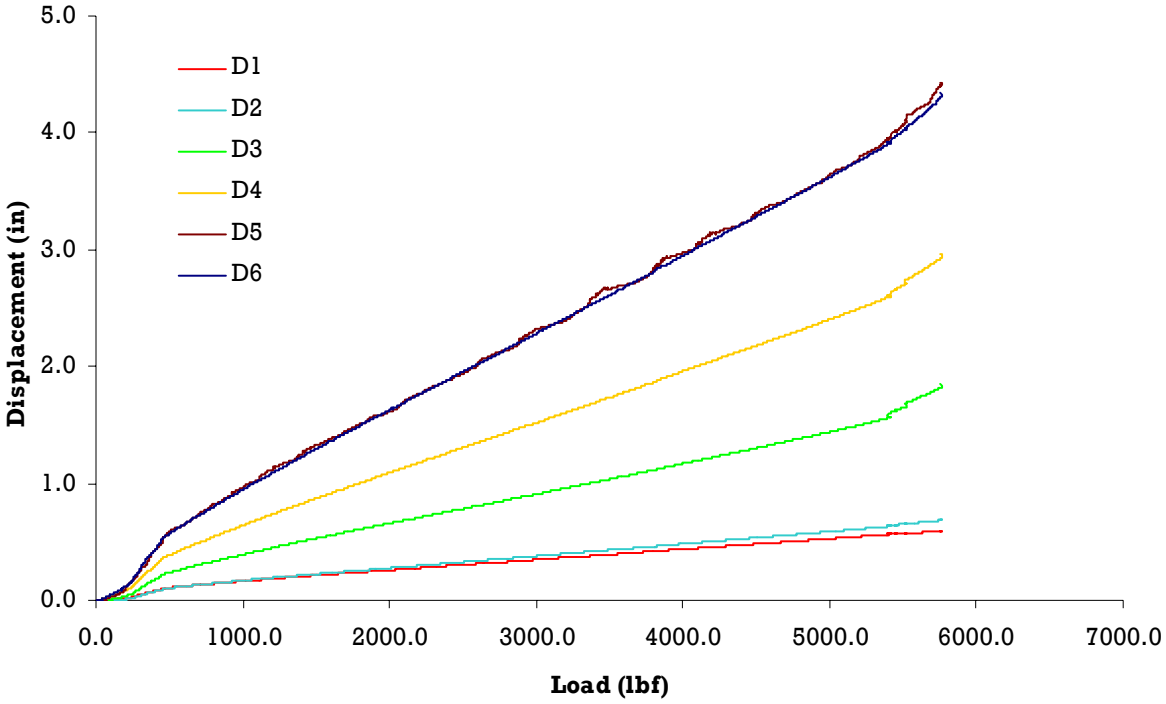

Figure D.24. Vertical displacements – ST005.

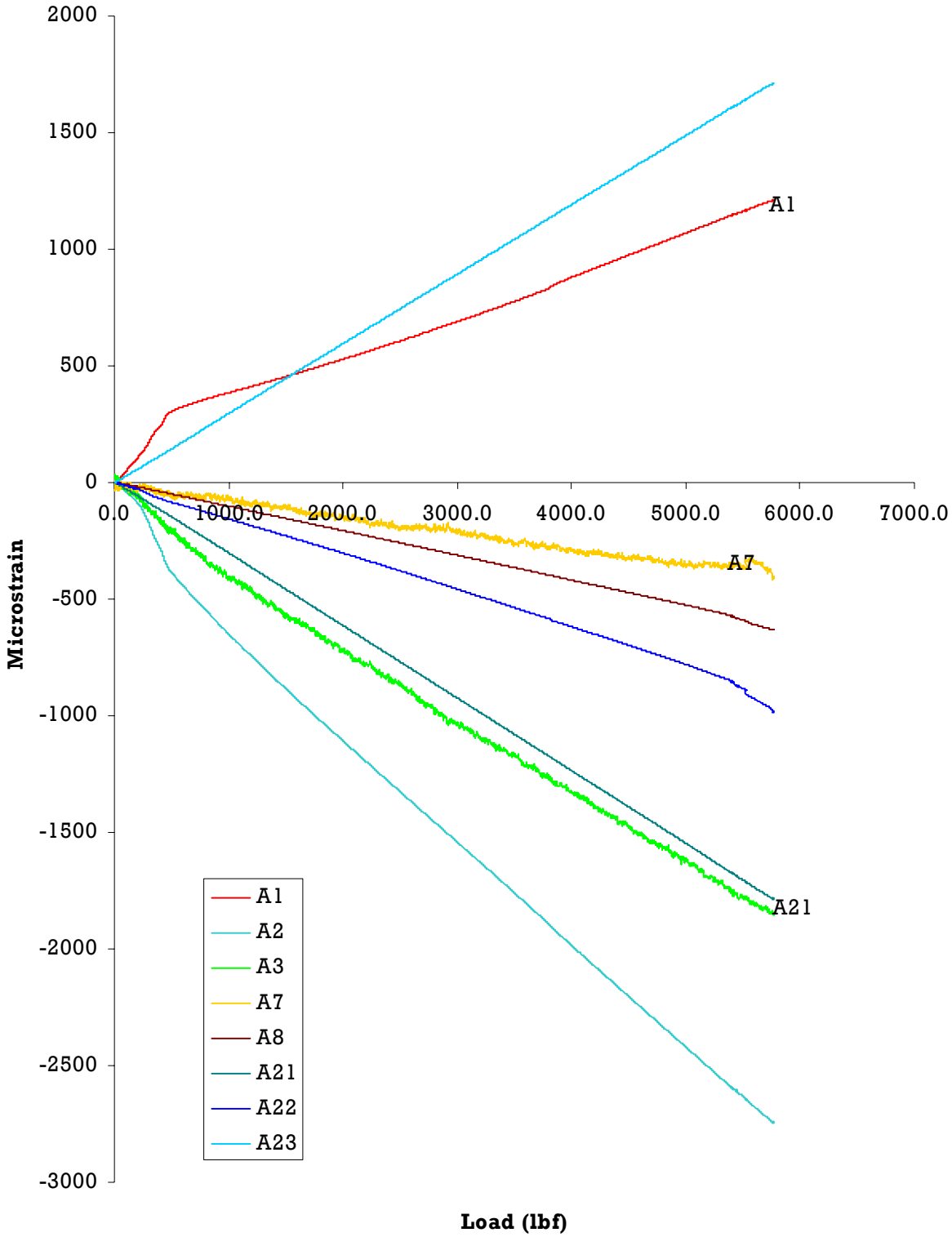

Figure D.25. Strains from axial gages – ST005.

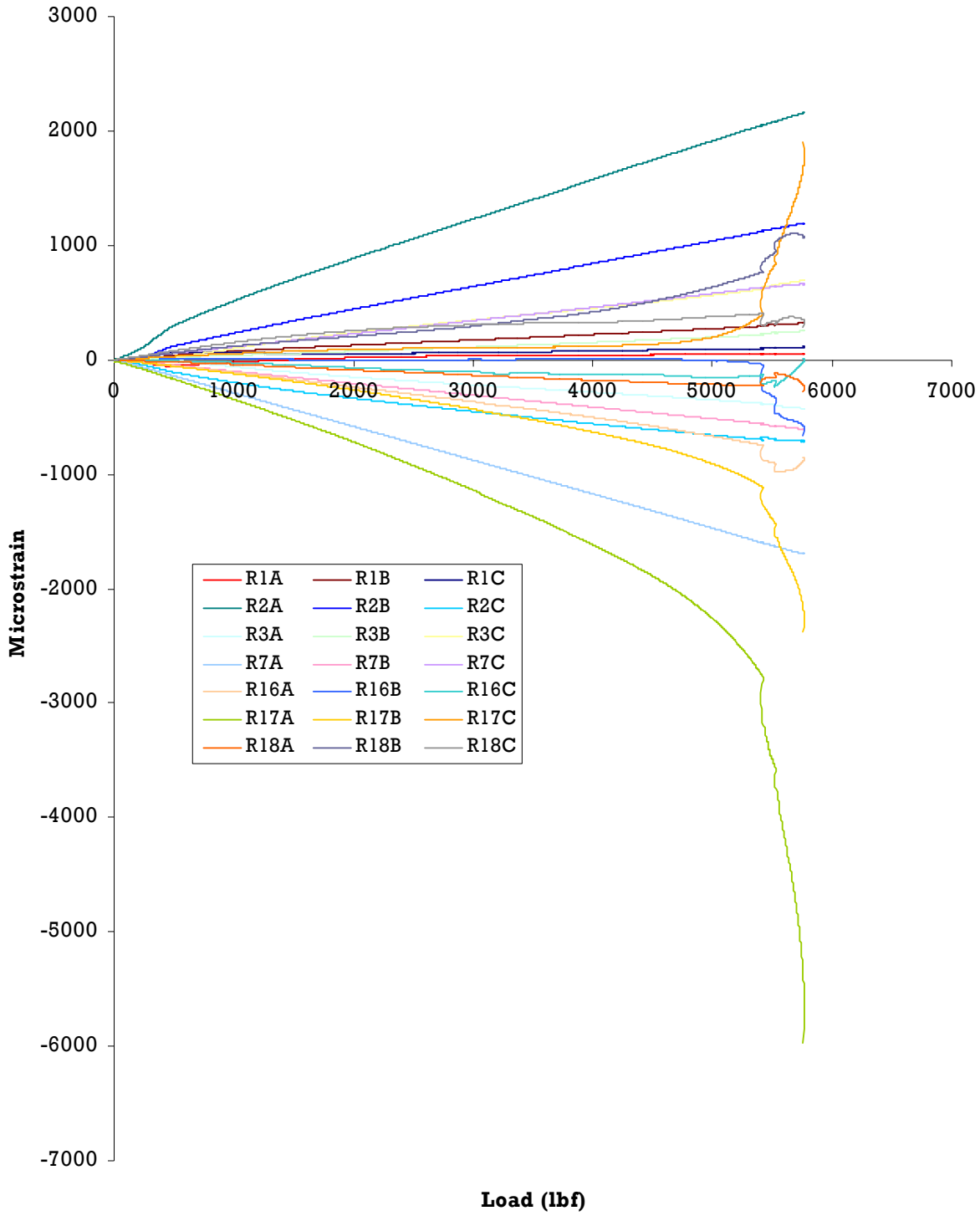

Figure D.26. Strains from rosettes – ST005.

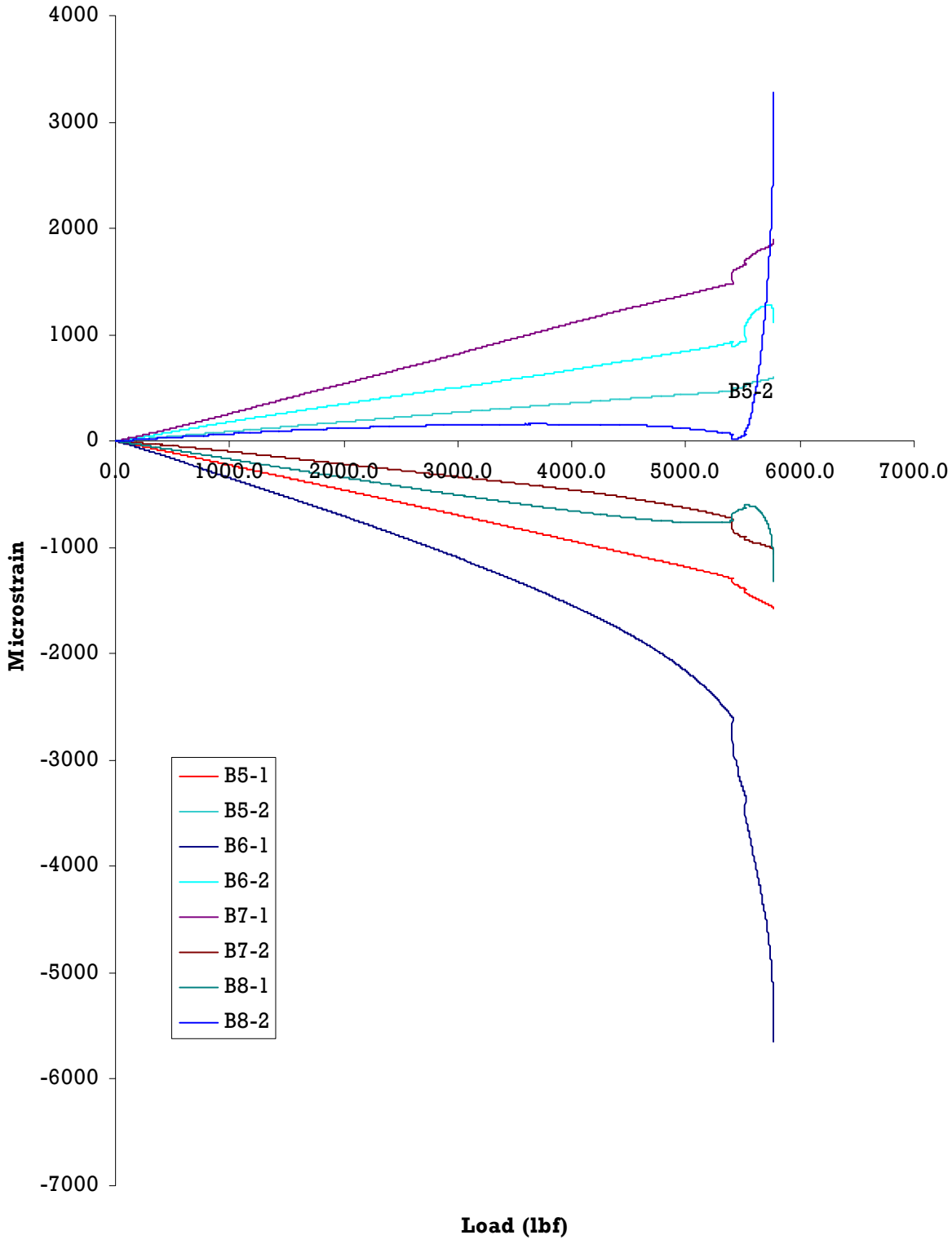

Figure D.27. Strains from biaxial gages – ST005.

D.7 Residual Strength Test Data of ST006 after 1/2-DLT Cyclic Test

The following gage locations were used for the ST006 DaDT test article. They are graphically illustrated in Figure 118.

A1 Lower skin FWS 24.8" on Fwd spar - Fatigue # 006 RH

A2 Upper skin FWS 24.8" on Fwd spar - Fatigue # 006 RH

A3 Upper skin FWS 27.0" on Fwd spar - Fatigue # 006 RH

A7 Upper skin FWS 66.5" on Aft spar - Fatigue # 006 RH

A8 Upper skin FWS 90.5" on Fwd spar - Fatigue # 006 RH

A15 Upper skin FWS 42.5" on Fwd spar - Fatigue # 006 RH

A21 Upper skin FWS 38.25" on Fwd spar - Fatigue # 006 RH

A22 Upper skin FWS 38.25" on Aft spar - Fatigue # 006 RH

A23 Lower skin FWS 38.0" on Fwd spar - Fatigue # 006 RH

A24 Upper skin FWS 53.25" on Fwd spar - Fatigue # 006 RH

A25 Lower skin FWS 53.25" on Fwd spar - Fatigue # 006 RH

A26 Upper skin FWS 76.25" on Fwd spar - Fatigue # 006 RH

A27 Lower skin FWS 76.25" on Fwd spar - Fatigue # 006 RH

R1 Root rib at upper fwd corner - Fatigue # 006 RH

R2 Lower skin FWS 24.8" and 2.5" forward of Fwd spar- Fatigue # 006 RH

R3 Upper skin FWS 24.8" on Aft spar - Fatigue # 006 RH

R16 Upper skin FWS 61.2." on Fwd spar - Fatigue # 006 RH

R17 Upper skin FWS 64.4" on Fwd spar - Fatigue # 006 RH

R18 Upper skin FWS 68.15" on Fwd spar - Fatigue # 006 RH

B5 Upper skin FWS 50.7" centered between Fwd and Aft spar - Fatigue # 006 RH

B6 Upper skin FWS 64.4" - Fatigue # 006 RH(1.67" Fwd of damage FWS 64.4")

B7 Lower skin FWS 64.4" - Fatigue # 006 RH (1.67" Fwd of damage FWS 64.4")

B8 Upper skin FWS 64.4" centered between Fwd and Aft spar - Fatigue # 006 RH

Figure D.8 shows the vertical displacement results for post-DaDT residual strength of the ST006 test article. Displacement gages D1 and D2 indicated that there was a rotation of the test article in $-T_Y$ direction (reference axis system may be found in Figure C.1).

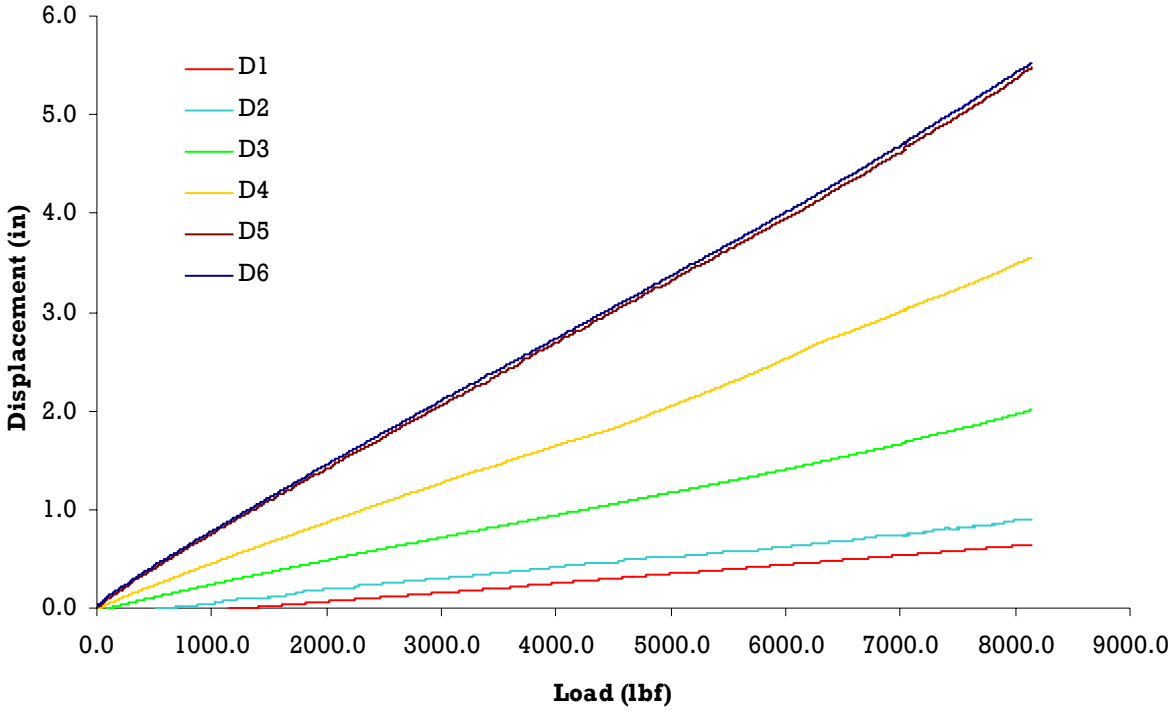

Figure D.28. Vertical displacements – ST006.

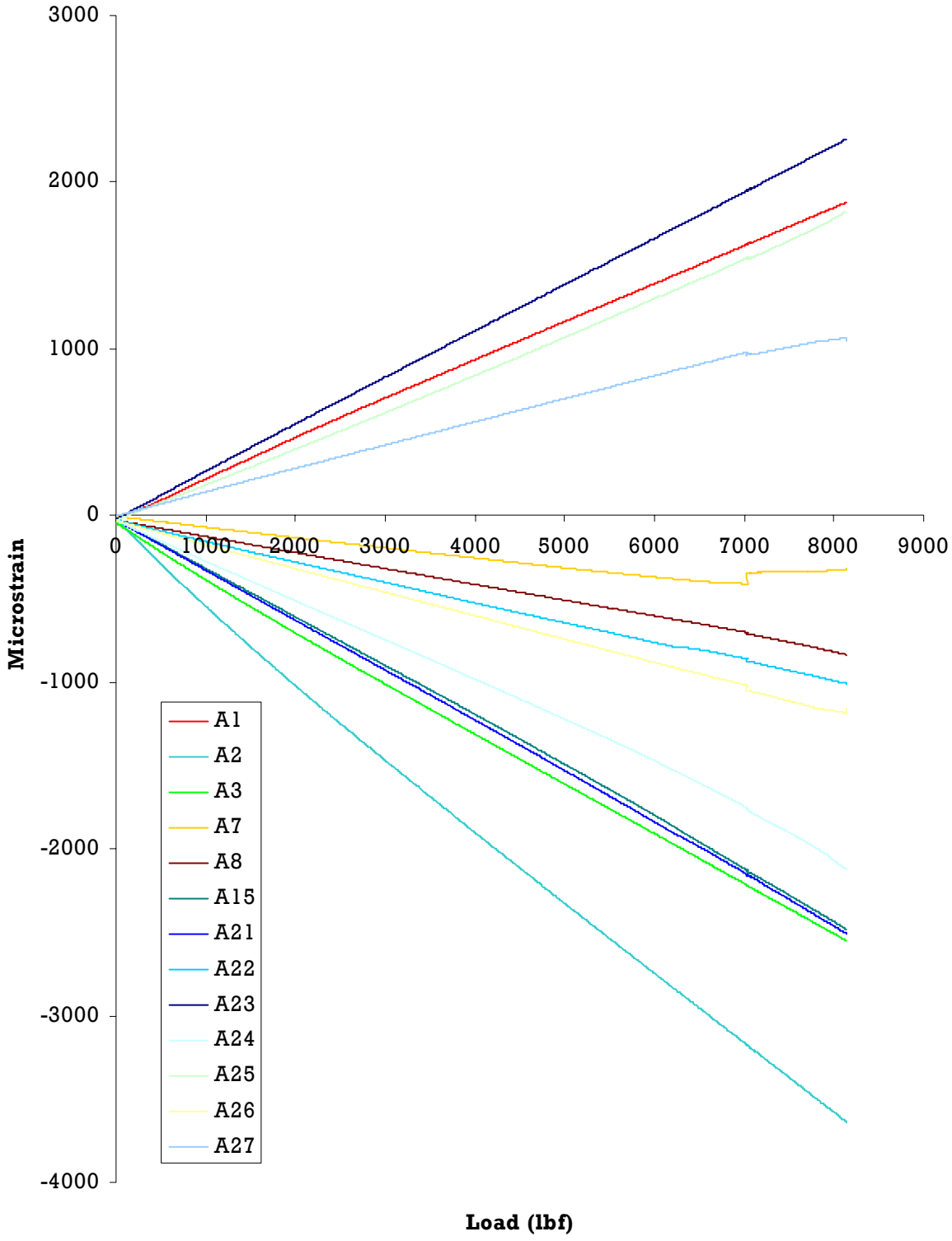

Figure D.29. Strains from axial gages – ST006.

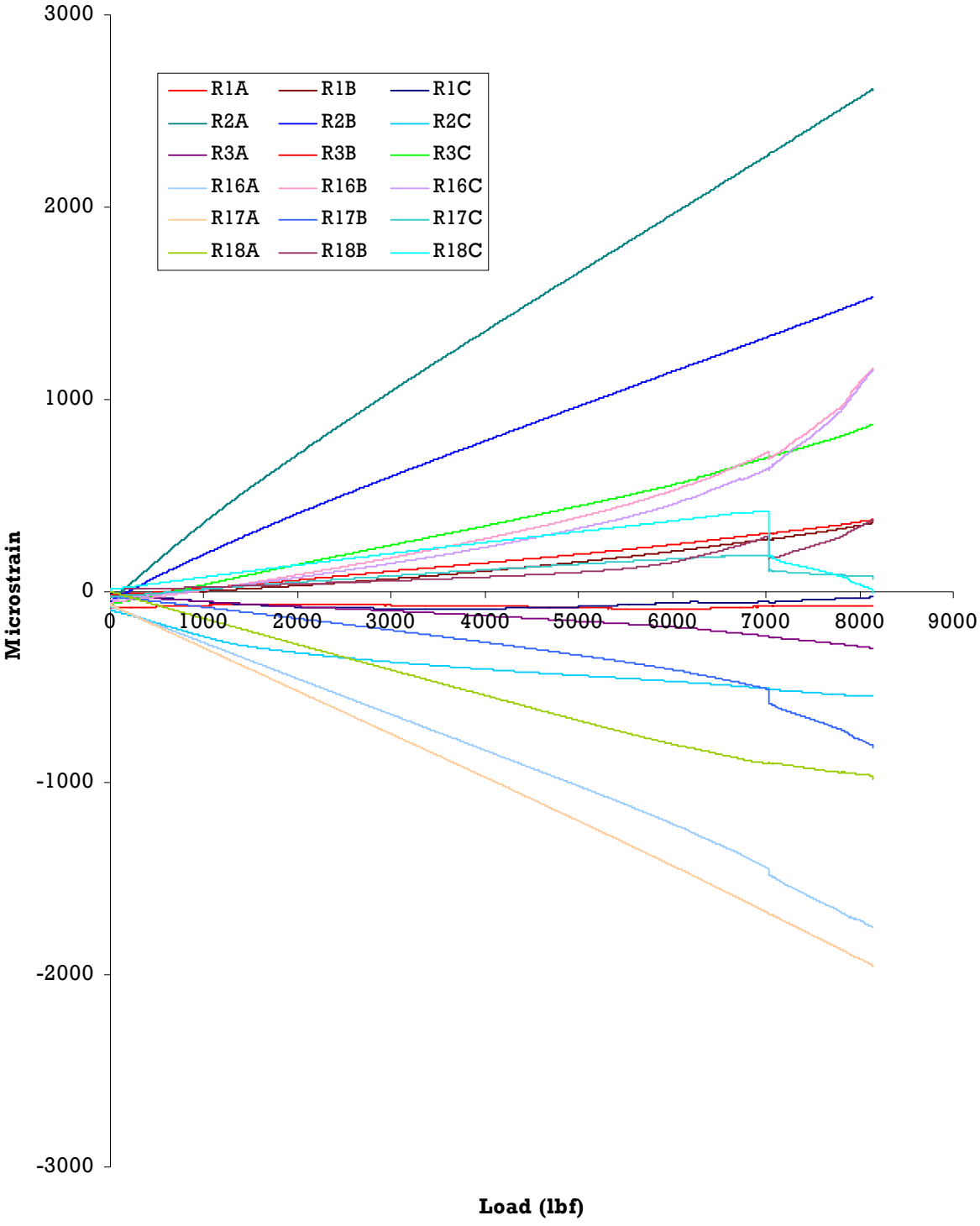

Figure D.30. Strains from rosettes – ST006.

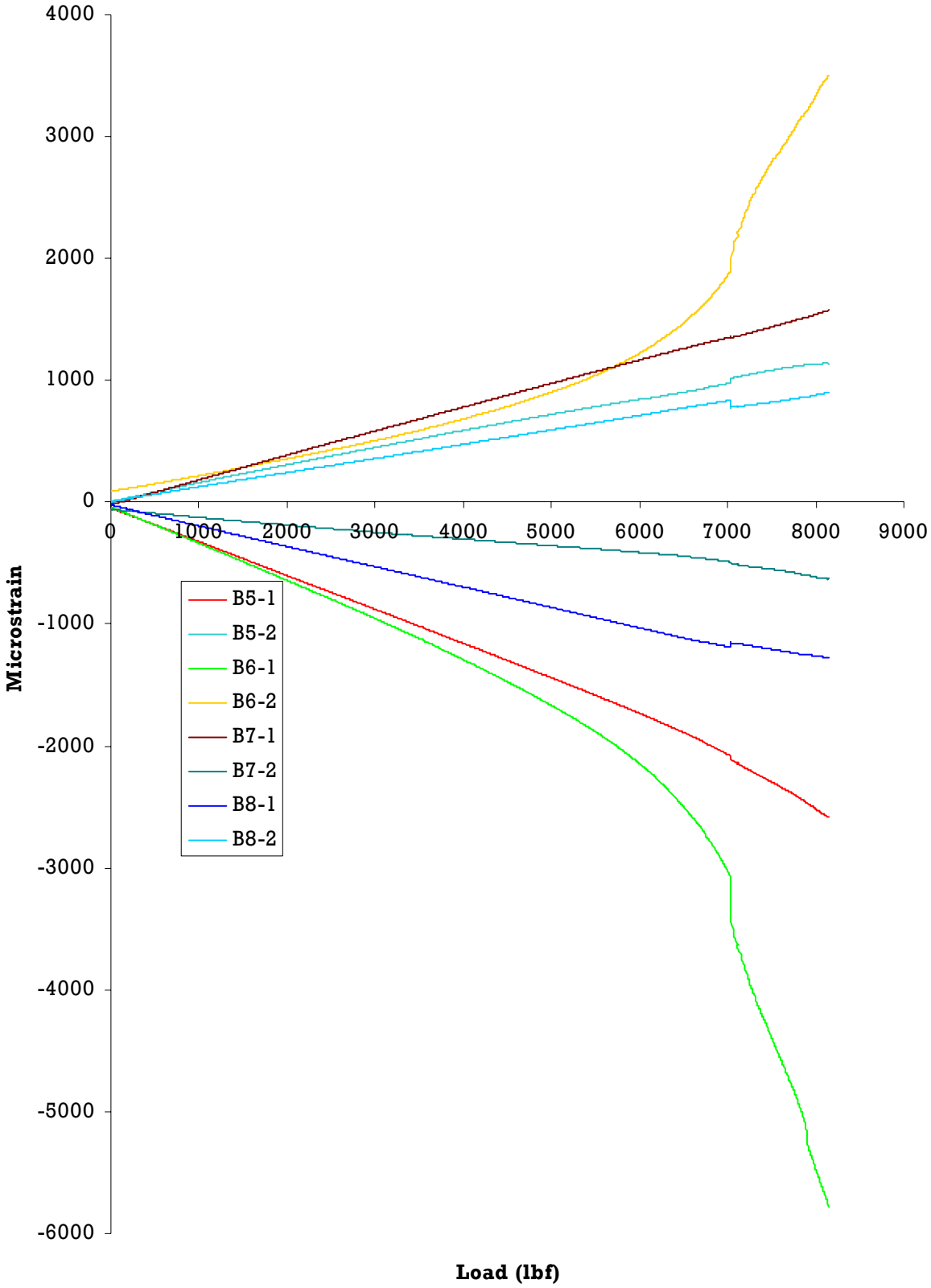

Figure D.31. Strains from biaxial gages – ST006.

This page left blank intentionally.